Volcanic Archives of Past Glacial Environments: Tindfjallajökull Volcano, Iceland

Thesis

VOLCANIC ARCHIVES OF PAST GLACIAL ENVIRONMENTS:

TINDFJALLAJÖKULL VOLCANO, ICELAND

Jonathan David Moles

MGeol (University of Leicester) 2014

A thesis submitted for the degree of

Doctor of Philosophy

School of Environment, Earth and Ecosystem Sciences

The Open University, United Kingdom

September 2018

ABSTRACT

Volcanoes preserve evidence of past glacial environments in the characteristics of their erupted products and in the sediments and landforms that occupy their flanks. By investigating volcanic stratigraphies and by dating palaeoenvironmental evidence, the glacial history of volcanic regions can be reconstructed. This thesis presents a geological and palaeoenvironmental survey of Tindfjallajökull volcano (Eastern Volcanic Zone, Iceland), followed by a focussed study of the glacial environments associated with the Ring Fracture Rhyolites eruption of neighbouring Torfajökull volcano.

Geological mapping, supplemented by whole-rock geochemistry and $^{40}Ar/^{39}Ar$ geochronology, gives insights into the evolution of Tindfjallajökull during the late Pleistocene. Prior to 358 ± 15 ka, a basalt-dominated stratocone of lavas and fragmental rocks was constructed, which was then capped with rhyolitic and basaltic lavas. Following this stage, there was a period of erosion and further rhyolitic volcanism occurred in the area of the present-day summit (126 ± 18 ka). Minor basaltic to trachyandesitic and basaltic andesitic flank eruptions continued through to the end of the last glacial period. Eruptions have commonly interacted with ice and the resulting glaciovolcanic deposits provide a record of fluctuating glacial environments on the volcano.

The Torfajökull Ring Fracture Rhyolites eruption (~55 ka) breached an ice sheet >400 m thick, dispersing tephra 'II-RHY-1' up to 2300 km from Iceland and depositing the Thórsmörk Ignimbrite in an area of little or no ice ~30 km from source. Due to the presence of the II-RHY-1 tephra horizon in regional palaeoclimate records (e.g. the Greenland ice cores), the eruption can be precisely dated to the end of Greenland Interstadial 15.2. The widely dispersed products of the eruption are used to reconstruct coeval glacial environments in southern Iceland and across the wider North Atlantic region.

ACKNOWLEDGEMENTS

First and foremost, I am extremely grateful to my supervisors – Dave McGarvie, John Stevenson and Sarah Sherlock – for providing the opportunity for me to undertake this project and for their support over the past 4 years. A huge thank you goes to Dave for being a dedicated yet hands-off lead supervisor, a reliable source of mild amusement, and my greatest advocate regardless of other work commitments and retirement. Thank you to John for frequently working late at night to provide me with all manner of useful advice and comments. Thank you to Sarah for being ready to efficiently solve any query that I ventured downstairs with.

I am grateful for the funding provided by the Natural Environment Research Council (NERC) via the Central England NERC Training Alliance (CENTA). Additional funding has been provided by the Volcanic and Magmatic Studies Group (VMSG), the International Union for Quaternary Research (INQUA) and the School of Environment, Earth and Ecosystem Sciences (EEES).

During my fieldwork in Iceland, I was ably assisted by Björn Oddson, Mike Widdowson, Matthew Saker-Clark, Jack McGarvie and Eleni Wood, as well as Dave McGarvie and John Stevenson. Matt and Eleni deserve particular recognition for their tolerance of the Icelandic conditions and for daring to follow me across the fastest rivers and steepest slopes. Thank you to Paul and Judi Stevens for always giving us a warm welcome (and a glass of rhubarb wine) when we stumbled into their wonderful hostel at Fljótsdalur. Thank you to Matthew Roberts and Sara Barsotti for hosting me on a two-week placement at Veðurstofa Íslands.

Laboratory assistance and advice has kindly been provided by Sam Hammond, Alison Halton, Frances Jenner, James Malley, Andy Tindle, Michelle Higgins and Kay Green at The Open University, and Nick Marsh and Tom Knott at the University of Leicester. Peter Abbott provided access to marine sediment cores at Swansea University and gave valuable assistance and advice on the extraction, preparation and analysis of tephra.

Thank you to the community at EEES, particularly my friends Matt, Costanza, Kerry, Peter, Katrina, Simone, Eleni, Laura and Stacy. Thank you to Clare Warren for having an open door just down the corridor.

Thank you to my parents for inspiring me to explore our world and for supporting me through all my endeavours.

Finally, thank you to Katie. For joining me in Milton Keynes and for making our home a happy one. For suggesting that I title this thesis "Volcanoes, ice and blah blah blah."

Approaching the summit of Tindfjallajökull, July 2016

CONTENTS

LIST OF FIGURES

LIST OF TABLES

LIST OF MATERIAL NOT BOUND INTO THESIS

PUBLICATIONS AND CONFERENCE PRESENTATIONS RESULTING FROM THIS THESIS

Published material that has been incorporated into this thesis is my own work and was completed with guidance from my supervisors and other co-authors. The contributions made by co-authors to the published and submitted paper are detailed below.

Articles

Moles, J.D., McGarvie, D., Stevenson, J.A., and Sherlock, S.C., 2018. Geology of Tindfjallajökull volcano, Iceland: Journal of Maps, v. 14, p. 22–31, doi:10.1080/17445647.2018.1425163.

Co-author contributions:

Dave McGarvie and *John Stevenson* assisted with field mapping and provided guidance on the interpretation of the field evidence, the style of the map, and the writing of the manuscript.

Sarah Sherlock provided guidance on the conversion of this paper into a thesis chapter.

Moles, J.D., 2019. Volcanic ash: a research tool that goes far beyond volcanoes: Proceedings of the Open University Geological Society, v.5 (in prep).

Moles, J.D., McGarvie, D., Stevenson, J., Sherlock, S., Abbott, P., Jenner, F., Halton, A. Widespread tephra dispersal and ignimbrite emplacement from a subglacial volcano: the rhyolitic eruption of Torfajökull, Iceland, ~55 ka: Geology (in prep for resubmission pending moderate revision).

Co-author contributions:

Dave McGarvie and *John Stevenson* assisted with sample collection and data interpretation, and provided guidance on the manuscript.

Sarah Sherlock assisted with the interpretation of $^{40}Ar/^{39}Ar$ data, and provided guidance on the manuscript.

Peter Abbott provided access to marine tephra samples, and provided guidance on sample preparation, sample analysis, and the manuscript.

Frances Jenner assisted with LA-ICP-MS analysis and data interpretation, and provided guidance on the manuscript.

Alison Halton assisted with $^{40}Ar/^{39}Ar$ analysis and data interpretation, and provided guidance on the manuscript.

Conference presentations

Moles, J., McGarvie, D., Widdowson, M., Stevenson, J., Sherlock, S., 2015. Volcano-ice interactions at Tindfjallajökull volcano, Iceland. Volcanic and Magmatic Studies Group conference (poster).

Moles, J., McGarvie, D., Sherlock, S., Stevenson, J., Widdowson, M., 2015. Glaciovolcanism at Tindfjallajökull, Iceland. Lancaster volcano-ice and Iceland Volcanism conference (talk).

Moles, J., McGarvie, D., Sherlock, S., Stevenson, J., Widdowson, M., 2016. Pleistocene glacial environments at Tindfjallajökull volcano, Iceland: the volcanic and sedimentary record. Volcanic and Magmatic Studies Group conference (poster).

Moles, J., McGarvie, D., Sherlock, S., Stevenson, J., 2016. A glaciolacustrine archive of volcanism and sedimentation at Tindfjallajökull, Iceland: the proximal counterpart of North Atlantic Ash Zone II? Lancaster volcano-ice and Iceland Volcanism conference (talk).

Moles, J., McGarvie, D., Sherlock, S., Abbott, P., Stevenson, J., 2017. In search of the source of North Atlantic Ash Zone II and the Thórsmörk Ignimbrite. Volcanic and Magmatic Studies Group conference (talk).

Moles, J., McGarvie, D., Sherlock, S., Stevenson, J., Abbott, P., Tindle, A., 2017. Far-flung tephra transport and ignimbrite emplacement from a rhyolitic glaciovolcanic eruption. Lancaster volcano-ice and Iceland Volcanism conference (talk).

Moles, J., McGarvie, D., Stevenson, J., Sherlock, S., 2017. Geological map of Tindfjallajökull volcano, Iceland. Lancaster volcano-ice and Iceland Volcanism conference (poster).

Moles, J., McGarvie, D., Sherlock, S., Stevenson, J., Abbott, P., Tindle, A., Jenner, F., 2017. Long-range tephra dispersal and ignimbrite emplacement from a large rhyolitic glaciovolcanic eruption. IAVCEI General Assembly (poster).

Moles, J., McGarvie, D., Stevenson, J., Sherlock, S., Abbott, P., Jenner, F., Halton, A., 2018. Widespread dispersal of rhyolitic tephra from a subglacial volcano: linking the terrestrial palaeoenvironment with climate records. INQUA–INTAV International Field Conference and Workshop (talk).

Chapter 1

Introduction

1.1 Overall rationale

On Earth, ice-clad volcanoes are distributed from the equator to the poles, with ~20% of volcanoes currently hosting areas of ice or permanent snow (Curtis and Kyle, 2017). Volcanic eruptions at these volcanoes are known for their hazards, particularly the lahars (volcanic mud flows; Major and Newhall, 1989) or jökulhlaups (glacial outburst floods; Gudmundsson et al., 2004) that can be generated through rapid melting of the ice. A considerably larger proportion of volcanoes may have hosted ice during the repeated glacial periods of the Pleistocene.

Volcano-ice interactions are recorded in the volcanic and sedimentary rocks of glaciated volcanoes. Thus, as a volcano grows over time, it builds an archive of the local glacial history (Lescinsky and Fink, 2000). Through the use of geochronology techniques, such as the radiometric dating of lavas, this archive of past glacial environments can be compared to other palaeoenvironmental records (e.g. McGarvie et al., 2006). For instance, with high precision geochronology, the glacial history of an Icelandic volcano could be linked to the high resolution climate records sourced from North Atlantic marine sediments and Greenland ice cores.

As archives of past glacial environments, volcanoes provide a chronology of terrestrial ice advance and retreat. By building these chronologies and linking them to regional climate records, the response of glacial environments to climatic change can be assessed. This approach requires a thorough reconstruction of volcanic histories, an understanding of the interactions between volcanoes and ice, and a precise method of linking disparate sources of palaeoenvironmental information.

1.2 GEOLOGICAL SETTING

1.2.1 Geology of Iceland

Iceland provides a rare terrestrial window into one of the fundamental processes on our planet: the formation of oceanic crust. The island is bisected by the Mid-Atlantic Ridge, which is expressed as zones of active rifting and volcanism linked by transform fault zones (Palmason and Saemundsson, 1974). However, Iceland is a highly unusual area of oceanic crust, formed through the interaction of this divergent plate boundary with a hotspot or mantle plume (Óskarsson et al., 1985; Schilling, 1973). This interaction generates an atypically thick and buoyant area of crust; a region of high volcanic productivity centred over the hotspot. The active rift zones, which gradually migrate north-westwards over time, periodically relocate south-eastwards in order to remain near the hotspot (Helgason, 1984). These rift jumps lead to a complex rifting pattern involving the repeated propagation of new rifts into areas of older crust.

Currently, the actively rifting sections of Iceland are the Western Volcanic Zone, the northern part of the Eastern Volcanic Zone (sometimes referred to as the Eastern Rift Zone) and the Northern Volcanic Zone (Figure 1.1). These are areas of active volcanism and crustal accretion (Sæmundsson, 1974). Outside of these zones, volcanism also occurs in non-rifting volcanic zones: the southern part of the Eastern Volcanic Zone (sometimes referred to as the Southern Flank Zone), the Öræfajökull Volcanic Zone and the Snæfellsnes Volcanic Zone. Rifting on the northern part of the Eastern Volcanic Zone is thought to have initiated ~3 Ma, with the southward propagation of the rift into older crust (Meyer et al., 1985). This process will probably continue until the full length of the Eastern Volcanic Zone is actively rifting, completing a rift jump from the Western Volcanic Zone (Einarsson, 1991).

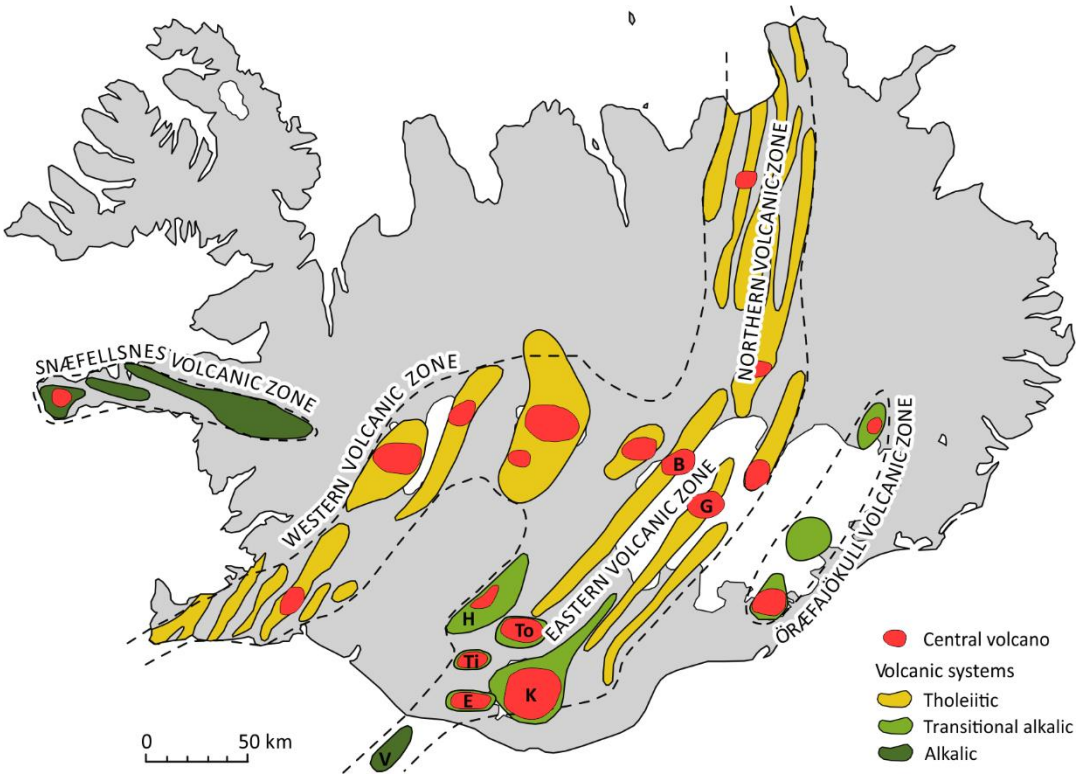

Figure 1.1. Map of Iceland showing the active volcanic zones and their volcanic systems, modified from Voelker and Haflidason (2015). The volcanic systems are coloured according to magma series (Jakobsson et al., 2008). Tholeiitic magmas are produced in actively-rifting zones. Transitional alkalic and alkalic magmas are generated in non-rifting flank zones. Volcanic systems in the Eastern Volcanic Zone are labelled. These are Bárðarbunga (B), Grímsvötn (G), Hekla (H), Torfajökull (To), Tindfjallajökull (Ti), Katla (K) Eyjafjallajökull (E) and Vestmannaeyjar (V).

Volcanism in Iceland occurs within discrete volcanic systems, which typically consist of a fissure swarm with or without a central volcano (Figure 1.1; Jakobsson, 1979). Fissure swarms make up most of the active rift zones and are typically 10–100 km long. Focusing of volcanism in one part of the system leads to the construction of a central volcano (Einarsson, 1991). Central volcanoes are often characterised by high geothermal activity and the production of evolved magma. Each volcanic system typically has unique geochemical and petrographic characteristics (Jakobsson, 1979; Sæmundsson, 1974).

1.2.2 Tindfjallajökull and Torfajökull volcanoes

Tindfjallajökull (63°47'N 19°35'W; alternatively known as Tindfjöll) is the main focus of this thesis but Torfajökull (63°57'N 19°08'W) also features in Chapters 5 and 6. Tindfjallajökull

and Torfajökull are neighbouring volcanic systems within the non-rifting part of the Eastern Volcanic Zone (Figure 1.2). The general characteristics of the central volcanoes in this area – which also include Katla, Hekla and Eyjafjallajökull – are summarised in Table 1.1.

The names 'Tindfjallajökull' and 'Torfajökull' strictly refer to ice caps, but are also used to refer to the volcanoes that host those ice caps (in this thesis, the names refer to the volcanoes). Both volcanoes host a high proportion of evolved rocks, a possible caldera structure, and a hydrothermal system (Jakobsson, 1979). However, the volcanoes have distinct morphologies. Tindfjallajökull (~300 km^2) is a stratovolcano that rises to 1464 m above mean sea level, with a ~13 km^2 ice cap currently hosted on the upper flanks. Torfajökull, Iceland's largest active silicic centre (~450 km^2), consists of a dissected rhyolite plateau partly overlain by Holocene rhyolite lava and tephra (Gunnarsson et al., 1998; Macdonald et al., 1990; McGarvie, 1984; McGarvie et al., 2006; Sæmundsson and Friðleifsson, 2001; Walker, 1966).

Figure 1.2. Oblique view (facing east) of the southern part of the Eastern Volcanic Zone with central volcanoes labelled. Image courtesy of NASA and acquired by the Operational Land Imager, Landsat 8 on 20th September 2014. The ice cap covering Katla (Mýrdalsjökull) is ~26 km in diameter.

Table 1.1. General characteristics of the central volcanoes of the southern part of the Eastern Volcanic Zone. Information compiled from the Catalogue of Icelandic Volcanoes (Gudmundsson, 2015; Gudmundsson and Höskuldsson, 2016; Larsen and Gudmundsson, 2016; Larsen and Thordarson, 2016; Sæmundsson and Larsen, 2016).

	Dimensions; summit elevation	Type	Ice cap dimensions	Average eruption interval	Magma type
Tindfjallajökull	20 × 15 km; 1464 m	Central volcano with caldera	5 × 3 km	No known eruptions in past 8000 years	Basaltic, intermediate and silicic
Torfajökull	30 × 18 km; 1280 m	Rhyolite volcano with resurgent caldera	3 × 2 km	~600 years between the last two eruptions	Silicic
Eyjafjallajökull	25 × 15 km; 1651 m.	Steep shield-like central volcano	12 × 7 km	300–400 years (in past 1500 years)	Intermediate to silicic, basalts on lower flanks
Katla	34 × 30 km; 1490 m	Subglacial volcano with caldera	26 × 24 km	55 years (in past 1100 years)	Basalt dominant, silicic infrequent
Hekla	20 × 10 km; 1490 m	Elongated stratovolcano	None	53 years (in past 1000 years)	Basaltic, intermediate and silicic

1.2.3 Glacial history of Iceland

Physical evidence, derived from sedimentary and volcanic successions in Iceland, suggests that localised ice cover first developed on the island ~4 Ma (Geirsdóttir, 2011). Like in other areas of the Northern Hemisphere, extensive glaciation began ~2.5 Ma. Glacial/interglacial cyclicity was established around this time, and it is thought that ice periodically covered the whole of

Iceland during glacial maxima (Geirsdóttir, 2011). During the Last Glacial Maximum (LGM; ~23 ka), the Icelandic Ice Sheet reached the shelf edge surrounding Iceland in all sectors (Norðdahl and Pétursson, 2005; Patton et al., 2017). Reconstruction of past ice extents and thicknesses is limited by a lack of dated physical evidence. The fragmentary nature of the geological record means that ice sheet modelling has only been attempted for the past 35 ka (Hubbard et al., 2006; Patton, 2013; Patton et al., 2017).

The setting of Iceland on the Mid-Atlantic Ridge has a considerable influence on its glacial history. The high geothermal heat flux results in a fast, dynamic ice sheet that has a low aspect ratio (Patton et al., 2017). Additionally, the high rate of precipitation enables the ice sheet to respond rapidly to changes in temperature. Modelling by Hubbard et al. (2006) indicates that a 3 °C cooling (relative to modern climate) would result in ice sheet advance across most of the present-day landmass. Such an ice sheet would attain an equilibrium state in ~1200 years. In response to a cooling of 5 °C, ice would advance beyond the present-day coastline in almost all sectors (Hubbard et al., 2006).

Iceland is located near to the polar front, where there is a strong N–S temperature gradient in both the ocean and the atmosphere (Geirsdóttir, 2011). In the present configuration of ocean circulation, the North Atlantic Current draws warm tropical water to the south coast of Iceland. Small changes in ocean and atmospheric circulation can shift the polar front, leading to significant climate changes in Iceland (Geirsdóttir, 2011). It is likely that the extent and thickness of ice in Iceland was highly responsive to the abrupt shifts in climate that occurred throughout the Pleistocene. Rapid fluctuations in climate punctuated the last glacial period, producing a series of century- to millennia-scale warm (interstadial) and cold (stadial) events in the regional climate record (Dansgaard et al., 1993).

1.3 RECONSTRUCTING PAST ENVIRONMENTS

In order to understand how the environment in Iceland has changed in the past (with a focus on glacial environments), it is necessary to:

a) Reconstruct past environments using physical evidence. This evidence typically consists of sediments, landforms and/or glaciovolcanic sequences.
b) Apply a dating technique to provide temporal context or to compare to other palaeoenvironmental records. This can be achieved through absolute or relative dating techniques.

1.3.1 Sediments and landforms

Sedimentary successions are widely used to reconstruct past environments. Marine-deposited sediments found offshore and in the coastal areas of Iceland provide a valuable record of the maximum ice extent and its retreat during the last glacial period (Norðdahl and Pétursson, 2005). The age of these sediments can be determined through radiocarbon dating of the shells of marine organisms. However, the terrestrial record prior to the LGM is very fragmentary. Typically, pre-LGM sediments are only preserved in Iceland where they have been protected by overlying lavas (Eiríksson and Geirsdóttir, 1991; Geirsdóttir, 2011). Detailed investigation of these sedimentary and volcanic sequences can provide information on how local environments have evolved through time (e.g. Geirsdóttir and Eiríksson, 1994). Correlations between isolated sequences can be made using magnetostratigraphy and radiometric ($^{40}K/^{40}Ar$ or $^{40}Ar/^{39}Ar$) dating (Eiríksson and Geirsdóttir, 1991).

Glacial landforms, such as moraines, striations and trimlines, also provide evidence of ice cover in Iceland (Patton, 2013). These landforms have a particularly low preservation potential, and rarely pre-date the LGM. The most commonly employed technique for dating glacial landforms – cosmogenic exposure dating – is useful for establishing chronologies of deglaciation (e.g. Principato et al., 2006). Chronologies of Holocene glacier fluctuations in

Iceland have also been deduced using dated tephra layers that are stratigraphically associated with ice-marginal moraines (Kirkbride and Dugmore, 2008, 2006).

1.3.2 Glaciovolcanism

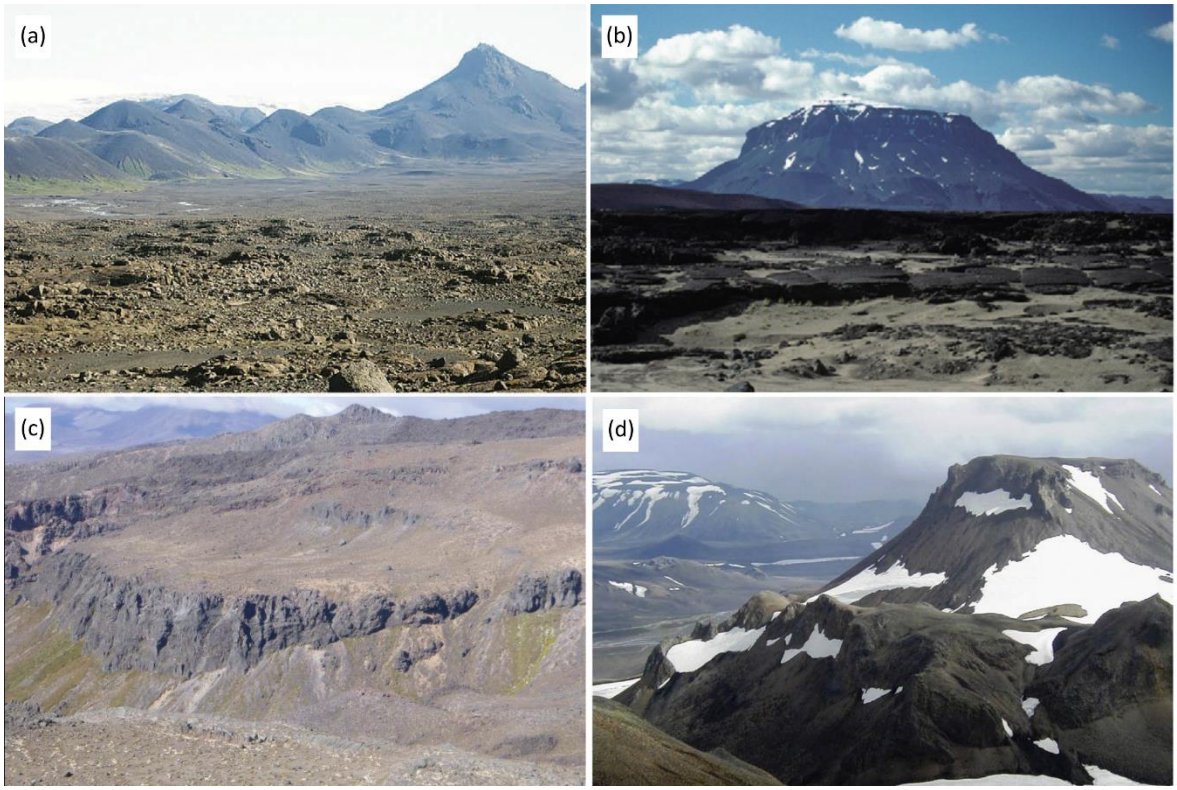

Figure 1.3. Examples of selected glaciovolcanic landforms documented in the literature. (a) Brekknafjöll–Jarlhettur ridge, Iceland (Bennett et al., 2009): an ice-confined ridge composed of basaltic hyaloclastite and pillow lava. (b) Herðubreið, Iceland (Licciardi et al., 2007): a basaltic 'tuya' (defined by Mathews (1947) as a flat-topped, steep-sided volcanic edifice that was confined by ice during its emplacement). (c) A dacite lava at Ruapehu, New Zealand (Conway et al., 2015): the lava was dammed by ice that infilled the valley at the time of the eruption. (d) A rhyolitic tuya at SE Rauðfossafjöll, Iceland (McGarvie, 2009), demonstrating the similar morphology of rhyolitic tuyas to basaltic tuyas.

'Glaciovolcanism' refers to any interaction between volcanism and ice, snow or meltwater (Edwards et al., 2015b; Kelman et al., 2002). This interaction will typically have an influence on the morphology of the resultant volcanic edifice and the lithofacies produced by the eruption (Figures 1.3 and 1.4). Ice and meltwater act to confine the erupted products close to the vent or along restricted pathways, producing edifices that are steep-sided and atypically thick (e.g. Lescinsky and Sisson, 1998; Stevenson et al., 2006). Interaction between magma and

(melt)water can trigger phreatomagmatic explosions, which enhances the fragmentation of the magma to form hyalotuffs (Honnorez and Kirst, 1975; Smellie et al., 2018). Additionally, enhanced cooling of lava through interaction with water can produce pillow lavas, hyaloclastites and jointing patterns (e.g. columnar joints, pseudopillow fractures; Lescinsky and Fink, 2000).

Figure 1.4. The glaciovolcanic landscape NE of Tindfjallajökull. Mafic and silicic fissure eruptions have been confined by ice, producing steep-sided parallel ridges (e.g. Sultarfell, the grey ridge in the centre of the photo). Sediments infill the valleys between the ridges. In the distance (under cloud) the ~2 km^3 rhyolitic tuya of Laufafell (Torfajökull volcano) is visible.

Glaciovolcanic eruption sequences preserve a record of the presence of ice at the time of the eruption (Edwards et al., 2015b; Mathews, 1947). However, many of the characteristics of these deposits (e.g. evidence of water interaction) are not diagnostic of an interaction with ice, and multiple lines of evidence and the context of the deposit must be taken into account when determining whether an eruption was glaciovolcanic. As well as indicating the presence of ice, glaciovolcanic sequences have been used to provide estimates of ice thickness (e.g. McGarvie et al., 2006; Smellie and Skilling, 1994) and to determine the basal thermal regime of the ice (e.g. Smellie et al., 2011a). Therefore, it is possible to gain insights into the glacial history of volcanic areas through the mapping of glaciovolcanic sequences.

Glaciovolcanic eruptions, and the associated ice reconstructions, are typically dated using $^{40}Ar/^{39}Ar$ geochronology (e.g. Clay et al., 2015; Conway et al., 2015; Flude et al., 2010; McGarvie et al., 2006; Mee et al., 2009; Smellie et al., 2008). In cases where the edifices have not been eroded and/or covered with thick snow/ice since the eruption, cosmogenic exposure dating can alternatively be used (Licciardi et al., 2007). Once dated, the eruptions can then be compared to climate archives such as ice core $\delta^{18}O$ records. However, this approach is limited by the uncertainties associated with all absolute dating techniques (Clay et al., 2015; Smellie et al., 2008). The chronology of both the glaciovolcanic eruptions and the climate record must be of sufficient accuracy and precision to allow a meaningful comparison between them. This problem is most acute in regions that have experienced frequent and rapid environmental change, such as Iceland. Clay et al. (2015) suggested that an eruption age uncertainty of ± 2–5 ka is required. If an eruption occurred during a period of rapid environmental change, it could be argued that this uncertainty would still be too large, considering that the response time of the Icelandic Ice Sheet has been modelled as ~1.2 ka (3 °C cooling; Hubbard et al., 2006).

1.4 THESIS AIMS AND STRUCTURE

The primary aims of this thesis are to investigate the geological development of glaciated volcanoes in Iceland, with an initial focus on the little known Tindfjallajökull volcano, and to study the record of past glacial environments that is preserved on and around these volcanoes. The key research questions of the thesis are:

- What are the geological characteristics of the Tindfjallajökull volcanic system (i.e. the stratigraphy, physical volcanology and magmatic geochemistry) and how has the volcano developed through time?
- What is the role of ice in the shaping of Tindfjallajökull and is a record of past glacial environments preserved on the volcano?

- Can eruptive environments on Tindfjallajökull (and other glaciated volcanoes) be precisely linked to climate records, e.g. using radiometric dating techniques?
- To what extent can glaciated volcanoes and their eruptive products be used to reconstruct local and regional palaeoenvironments?

These questions are addressed using multiple research techniques including geological mapping, geochemistry and geochronology.

Chapter 2 documents the geological mapping of Tindfjallajökull and the physical volcanology of the volcano. A 1:50,000 geological map is presented in Appendix 8. Field mapping was carried out with a focus on indicators of past environments. The geological mapping of Tindfjallajökull gives insights into the evolution of the volcano and the influence of ice in its development. The contents of this chapter and the geological map have been published in the *Journal of Maps* (Moles et al., 2018).

Chapter 3 provides an overview of the whole-rock geochemistry of Tindfjallajökull. The different magma compositions that occur at Tindfjallajökull are defined and the relationships between the magmas are explored.

Chapter 4 uses $^{40}Ar/^{39}Ar$ geochronology to date selected volcanic units at Tindfjallajökull. The successfully dated eruptions provide a chronostratigraphic framework for the evolution of the volcano. The climate at the time of each dated eruption is determined, by comparing the eruption dates with ice core climate chronologies.

Chapter 5 investigates how rhyolitic tephra is dispersed from subglacial volcanoes, focussing on a glaciovolcanic eruption of Torfajökull volcano during the last glacial period (~55 ka). The explosive behaviour of the eruption is assessed by correlating its products across multiple depositional settings (using geochemistry and geochronology). Tephra from the eruption is present in palaeoclimate archives (e.g. ice cores), allowing the climate at the time of the eruption to be precisely determined. The contents of this chapter have been reviewed by *Geology* and will be resubmitted pending moderate revision.

Chapter 6 is a synthesis of the palaeoenvironmental information associated with the ~55 ka eruption of Torfajökull volcano. Information is sourced from published literature and through investigation of depositional successions in Iceland. Palaeoenvironmental reconstructions are linked to the regional climate record using the tephra produced by the eruption.

Chapter 7 integrates the key outcomes of the thesis. These findings are summarised with reference to the research questions, and suggestions are made for further work.

Chapter 2

Geological mapping of Tindfjallajökull volcano

This chapter documents the geological mapping of Tindfjallajökull and accompanies the map presented in Appendix 8. The stratigraphic units that make up the volcano are described with a focus on evidence of past environments. This chapter and the associated geological map are adapted from a paper published in the *Journal of Maps* (Moles et al., 2018).

2.1 Introduction

Tindfjallajökull volcano (Figure 2.1) has been the subject of little geological investigation. A study of gabbro nodules by Larsen (1979) includes the most detailed geological map previously published. Jakobsson (1979) speculated that Tindfjallajökull is the oldest active volcano in the Eastern Volcanic Zone, and that it probably last erupted in late-glacial or postglacial time.

Tindfjallajökull is best known as a proposed source of the Thórsmörk Ignimbrite (Jørgensen, 1980). This 1.5–2 km^3 (dense-rock equivalent) peralkaline ignimbrite outcrops to the SE of the volcano (Thórarinsson, 1969) and has been correlated with the rhyolitic component of the widespread North Atlantic Ash Zone II (Lacasse et al., 1996; Sigurdsson, 1982; Tomlinson et al., 2010).

A 1:50,000 geological map of Tindfjallajökull (Appendix 8) is presented here with the aim of documenting the volcano's eruptive products and to provide context for further research. The geological mapping of Tindfjallajökull gives insights into its volcanological development and the role of ice in the shaping of the volcano. As is common for Icelandic volcanoes, the influence of past ice is evident in the geomorphology of the volcano, in the presence of glacially worked sediments and in the characteristics of the erupted products.

Figure 2.1. Oblique aerial photograph of Tindfjallajökull from the SE, August 1999. Source: Oddur Sigurðsson. To the right of the glacier-covered shoulder are the orange/brown twin peaks of Ýmir and Ýma, the highest points of the central silicic edifice. The mafic-dominated ridge of Tindfjöll is to the left. The valleys in front contain sediments deposited during the last glacial period.

2.2 METHODS

Geological mapping was undertaken at Tindfjallajökull during the summers of 2014 (10 days), 2015 (21 days) and 2016 (19 days). In the field, lithofacies were mapped onto topographic maps (USA Defence Mapping Agency, 1989) and aerial images (Google Earth Pro, 2010). Lithofacies were categorised in the field into approximately mafic (<52 wt% SiO_2; Le Bas et al., 1986), intermediate (52–63 wt% SiO_2) and silicic (>63 wt% SiO_2) compositional groups. Geological boundaries were then digitised using Google Earth Pro and imported into ESRI ArcGIS for construction of the map and cross sections. A UTM (Zone 27N) projection and the Hjörsey 1955 datum were used on the map, for easy comparison with most Icelandic topographic maps.

Geographical data of topography (contours and spot heights), place names, hydrology, buildings and tracks were sourced from the IS 50V digital map database (Landmælingar

Íslands, 2016). A hillshade was generated from the elevation data in order to enhance the topography of the map. These data were supplemented by field mapping of geomorphological features (mass-wasting scarps and subsidence pits) and superficial deposits (mass-wasting deposits and moraines).

To transform the mapped lithofacies data into the classes displayed on the final map, a division was first made according to volcanic system. Although most of the mapped area consists of the products of Tindfjallajökull volcano, the products of neighbouring and older systems are also present. Sediments, which potentially include material from multiple volcanic systems, form a separate category.

Within the categories defined above, divisions were then made based on relative age. Due to a lack of widespread marker horizons, major stratigraphic discontinuities or radiometric dates, it is only possible to divide Tindfjallajökull into broad stratigraphic groups: Early, Middle and Late Tindfjallajökull (the latter group is subdivided into A and B). The presence of the Thórsmörk Ignimbrite aids the identification of sediments and volcanic units deposited during the last glacial period (i.e. the Weichselian). The ignimbrite has an unpublished $^{40}Ar/^{39}Ar$ age of 54.5 ± 2 ka (see Sigurdsson et al., 1998) and a new $^{40}Ar/^{39}Ar$ age of 51.3 ± 4.2 ka is presented in Chapter 5.

Within the broad stratigraphic groups defined above, volcanic rocks were further subdivided according to composition and lithofacies. The compositional terms used in the field (i.e. mafic, intermediate and silicic) were used to define the mapped classes (more specific terms are assigned to analysed samples in Chapter 3). Subdividing by both composition and lithofacies groups together eruptive units that formed through similar processes and that may have formed in similar environments (Loughlin, 2002). Classification in this way is useful for the study of past glacial environments. However, the constituents of each subdivision are not strictly related in time and will represent a range of ages that are likely to overlap with other subdivisions of the same stratigraphic group (Figure 2.2). Distinct assemblages of related

lithofacies are grouped into lithofacies associations (e.g. hyaloclastite-dominated units, which can also include pillow lavas and lobate or sheet-like intrusions). Note that the term hyaloclastite is used here to encompass fragmental rocks generated through both quench fragmentation (hyaloclastite; Rittman, 1958) and explosive phreatomagmatic fragmentation (hyalotuff; Honnorez and Kirst, 1975) of magma.

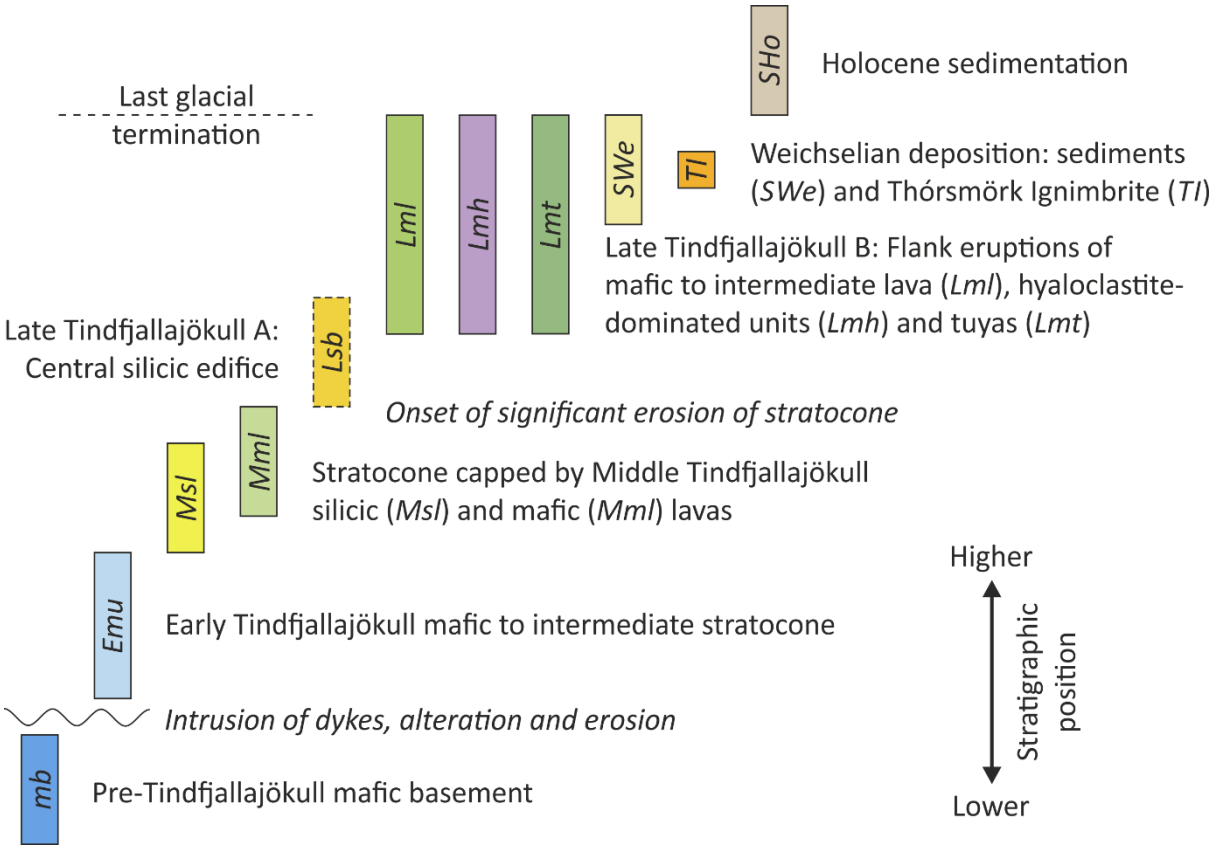

Figure 2.2. Stratigraphy of the mapped classes on Tindfjallajökull (not drawn to scale). It is not known if there is stratigraphic overlap between Late Tindfjallajökull A and Late Tindfjallajökull B. The eruptive products of Katla volcanic system and the fissure swarm NE of Tindfjallajökull are not included.

Vent locations relating to individual eruptive units were identified at numerous locations and are marked on the map. These vents are all extant scoria cones that are associated with the mafic to intermediate lavas and tuyas of Late Tindfjallajökull B. The vents of the older rocks of Early and Middle Tindfjallajökull have been removed by erosion and their locations could

not be determined. Additional ornamentations on the map highlight tuya lava caps, areas of lava delta, and highly-jointed lava.

Where the position of a geological boundary has an uncertainty of more than ±50 m (due to the presence of overlying superficial deposits and/or soils), it is classed as an approximate geological boundary.

2.3 GEOLOGY AND PAST ENVIRONMENTS OF TINDFJALLAJÖKULL VOLCANO

In this section, the products of Tindfjallajökull volcanic system are described, from oldest stratigraphic group to youngest, with a focus on indicators of past environments. Mapped units that are associated with other volcanic systems are then described, followed by the sediments and superficial deposits. UTM grid references are abbreviated to four digits representing 1×1 km squares, e.g. Sindri: *71 76*.

2.3.1 Early Tindfjallajökull

Mafic to intermediate, undifferentiated (Emu)

Most of the volume of Tindfjallajökull consists of a mafic-dominated succession of interbedded hyaloclastite and lava sheets, overlying the Pre-Tindfjallajökull basement. The basal contact has not been directly observed. Dykes and alteration in the basement have not been seen to pass into the overlying succession, suggesting that the contact is unconformable. In general, the Early Tindfjallajökull sheets dip gently outward from a central point roughly coincident with the present-day main ice cap. This parallel stratification is occasionally disrupted by minor palaeo-valleys and -gulleys. As a whole, the structure forms a dissected stratocone with an observed vertical extent of 1200 m (present-day maximum elevation: 1299 m above mean sea level, *69 76*).

2.3.2 Middle Tindfjallajökull

Silicic lava (Msl)

Three main areas of silicic lava are present on Tindfjallajökull, all of which immediately overlie the Early Tindfjallajökull stratocone. Erosion of the lavas has revealed lava lobe thicknesses of 20–60 m. Individual lava lobes have folded glassy margins with some areas of columnar jointing, and microcrystalline interiors which often develop platy structures. Ogives are preserved, or have been exhumed, on the surface of the upper lava lobe at Jökulskarð (~20 m wavelength; *73 76*). The vents of these lavas have not been preserved. A fragmental deposit (0–30 m thick) underlies the lava at Hestur (*72 68*) and is thought to have been emplaced during an initial phase of the same eruption.

These silicic lavas are not diagnostic of a particular eruptive environment, though the presence of ogives suggests that the upper lava lobe at Jökulskarð was emplaced in a subaerial setting.

Mafic lava (Mml)

Much of the west flank of Tindfjallajökull consists of a plateau surfaced with mafic lavas, capping the Early Tindfjallajökull stratocone. Isolated outcrops of capping lava are located on Vestriöxl (*75 75*) and on the NE side of Austurdalur (*66 77*). Individual lavas and vents are not distinct and have not been mapped in these areas. The unconfined nature of the lavas and the lack of evidence of enhanced cooling indicate that the eruptive environment was ice-free.

Since the formation of the Early Tindfjallajökull stratocone and the Middle Tindfjallajökull capping lavas, glacial erosion has cut the major valleys that emanate from the present-day ice cap.

2.3.3 Late Tindfjallajökull A: Central silicic edifice

Silicic breccia with coherent lava lobes (Lsb).

The summit of Tindfjallajökull (*70 74*) marks the top of a voluminous steep-sided pile of silicic breccia (Figure 2.3(a)), covering an area of perhaps 10 km^2 (when overlying volcanic rock and ice is removed). The breccia comprises poorly consolidated angular clasts 1–50 mm across. Coherent lobes of columnar-jointed silicic lava (~100 m wide) are present within the pile, and lava clasts are present within the surrounding breccia. The breccia has been subjected to pervasive hydrothermal alteration, and a hot spring in Hitagil (>60°C, Ármannsson, 2016; *72 71*) indicates that hydrothermal circulation is still active.

The base of the central silicic edifice was not observed. The lowest outcrop is at ~600 m elevation, over 800 m beneath the highest outcrop. Significant erosion and/or down-faulting of Early and Middle Tindfjallajökull material, which forms ridges up to 1300 m altitude surrounding the central edifice, must have occurred before the breccias were emplaced. It is possible that a caldera formed at Tindfjallajökull (as marked by Jóhannesson and Sæmundsson (1989), but no direct evidence for subsidence (e.g. displacement on a fault) has been observed. Syn- or post-eruption subsidence into the top of a magma chamber is necessary for a volcanic structure to be termed a caldera, as defined by (Cole et al., 2005).

Extensive fragmentation of silicic lava and the confinement of a steep-sided pile of erupted material can indicate the presence of ice during an eruption (McGarvie et al., 2007; Stevenson et al., 2011; Tuffen et al., 2001). Angular clasts and jointed lava lobes at all levels of the central silicic edifice suggest that cooling may have been enhanced by a thick body of ice, though further work is needed to reduce ambiguity.

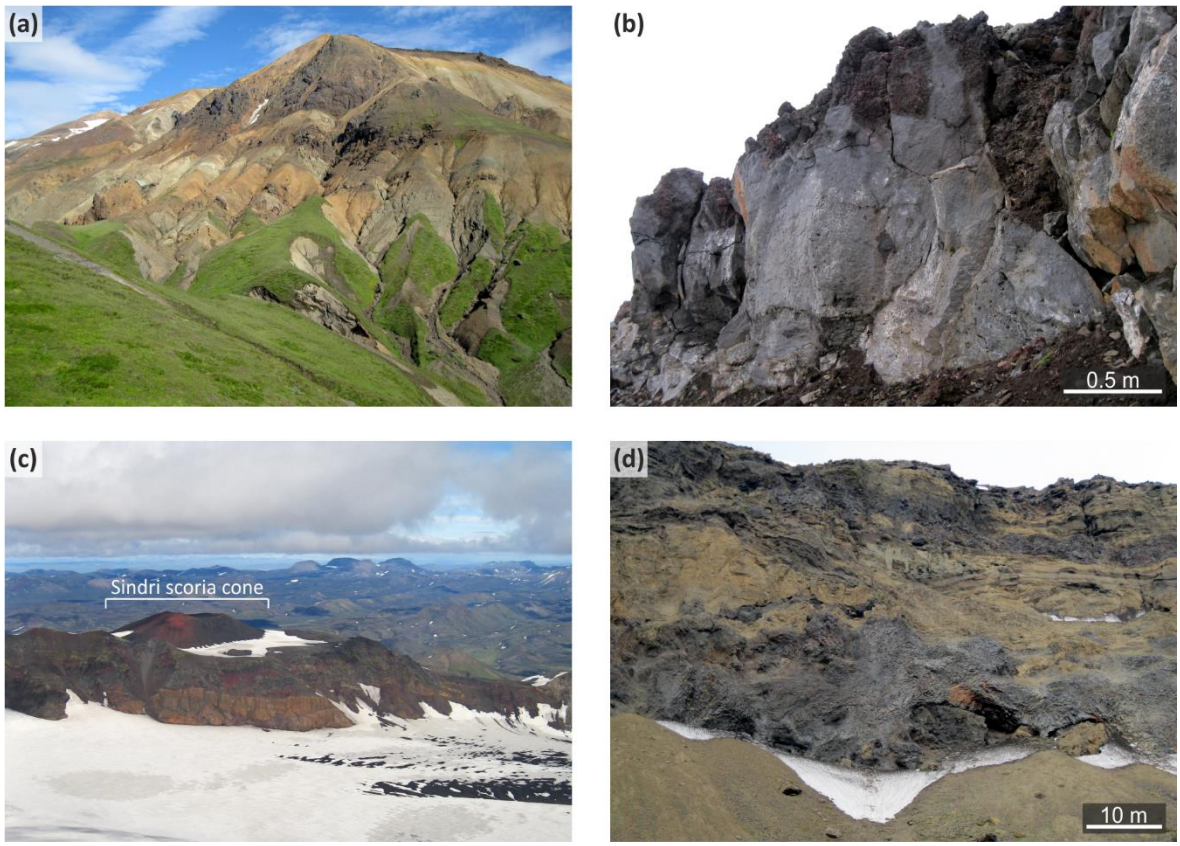

Figure 2.3. Photographs of selected geological features of Late Tindfjallajökull. (a) The view north from Botn of the pile of altered silicic breccia and lava lobes (dark) that make up the central silicic edifice of the volcano (Late Tindfjallajökull A). (b) A ~3 m thick mafic a'a lava in Tindfjallajökulsdalur (Late Tindfjallajökull B; *67 72*). This lava flowed into the valley from the Búri scoria cone. (c) Sindri scoria cone (*70 76*) viewed from Ýmir. The 500 m wide scoria cone sits on top of the Early Tindfjallajökull succession. (d) The interior of a tuff cone has been exposed through mass-wasting at Hitagilsbrún (*72 71*). Mafic sills (grey) intrude bedded hyaloclastite (brown).

2.3.4 Late Tindfjallajökull B: Flank volcanism

This category consists of a variety of well-preserved eruptive units that are sourced from dispersed vents and fissures on the flanks of Tindfjallajökull. The preservation of features such as scoria cones and the stratigraphic association of some of the units with the Thórsmörk Ignimbrite suggests that the majority of the units were emplaced during the Weichselian glacial period. There is likely to be chronological overlap between the members of this category (Figure 2.2), as they are subdivided by lithofacies rather than stratigraphic position.

Mafic to intermediate lava (Lml).

Twelve mafic to intermediate lavas that have experienced little erosion have been mapped on Tindfjallajökull's upper flanks. The lavas are typically a'a with autobrecciated bases and tops (where preserved; Figure 2.3(b)). The remnants of scoria cones are visible at the vents of nine of the lavas; the vents of the remaining three lavas are obscured by younger lava or ice. The scoria cone at Sindri (Figure 2.3(c); 70 76) is particularly well preserved, suggesting that it has not been subjected to glaciation and probably post-dates the last glacial maximum. Unconfined lavas with no evidence of enhanced cooling are indicative of an ice-free eruptive environment.

Highly jointed lava: In some instances, lavas that have flowed down steep slopes transition from a normal widely spaced jointing pattern to closely spaced pseudopillow fractures, cube-jointing and/or columnar jointing. This occurs on the south side of Sindri (*71 76*), on the southern rim of Austurdalur (*65 74*) and on the east side of Tindur (Figure 2.4; *70 70*). The closely-spaced jointing patterns indicate that the lavas were cooled rapidly due to the presence of water (Forbes et al., 2012). Topographic depressions suitable for the ponding of water are not present in these localities, so it is likely that water was instead derived through the melting of ice or snow. The elevation of the transition from subaerial lava to highly jointed lava (marked with white lines on the map) provides constraints on the upper limits of ice or snow within glaciated valleys at the time of each eruption (Table 2.1).

Table 2.1. Highly-jointed lavas and associated palaeoenvironmental interpretations.

Locality	Palaeoenvironment at the time of the eruption
South side of Sindri (*71 76*) 1180 m elevation	The depression to the south of Sindri, currently occupied by Tindfjallajökull ice cap, was filled with ice or snow. It is likely that ice (not snow) was the dominant source of meltwater, given the thickness required. The upper limit of the ice was ~160 m higher than the present-day ice cap.

Locality	Palaeoenvironment at the time of the eruption
Southern rim of Austurdalur (*65 74*) 940 m elevation	Ice or snow was present on the north-facing side of Austurdalur or ice infilled the whole valley (the valley is currently ~300 m deep in this area).
East side of Tindur (*70 70*) 1000 m elevation	Ice was present on the east side of Tindur (as a >40 m thick inclined sheet) or infilled the Vestri-Botná valley (as a >300 m thick valley glacier).

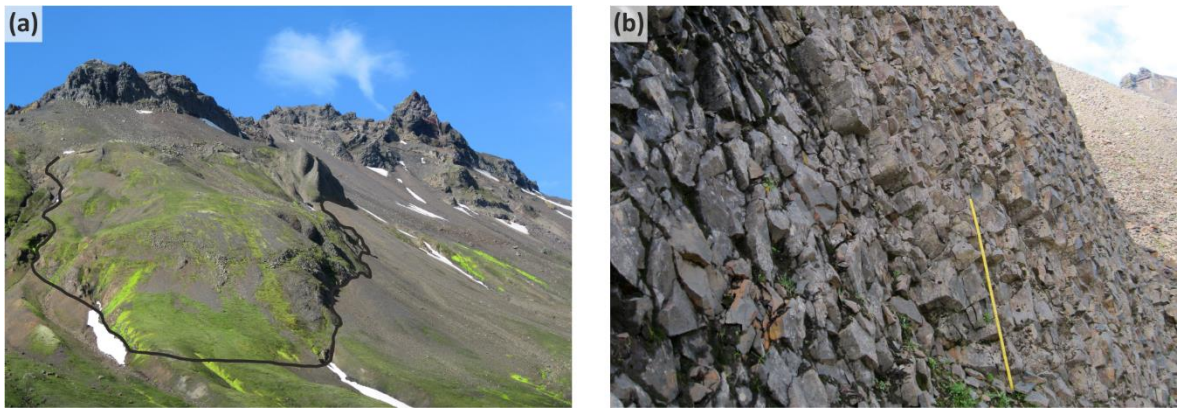

Figure 2.4. Photographs of the highly-jointed lava on the east side of Tindur (*70 70*). This lava has an intermediate composition (a) View west from Botn. The lava, outlined in black and ~250 m wide, becomes highly jointed where it has descended into the valley from a vent on the ridge. (b) Columnar jointing (~10 cm spacing) in the same lava. The columns are orientated perpendicular to the outer margin of the lava lobe, suggesting that the lava chilled against a body of ice or ice-confined meltwater that occupied the valley. Metre ruler for scale.

Mafic hyaloclastite-dominated units (Lmh).

Hyaloclastite-dominated units on Tindfjallajökull exist as hyaloclastite ridges, tuff cones, breccia mounds and hyaloclastite sheets. Each type can include a variable proportion of pillow lava and/or intrusive dykes, sills or lobes (Figure 2.3(d)), but capping lavas are not present.

Hyaloclastite ridges on Tindfjallajökull have a range of fissure orientations, with approximate groupings at 040–067° (perpendicular to the regional spreading direction), 104–111° and ~155°. Tuff cones and breccia mounds are sourced from point vents with no linear

orientation. Hyaloclastite sheets (2–10 m thick) typically constitute the more distal deposits of tuff cones and are common within a succession of Weichselian sediments on the SE side of Tindfjallajökull (around *73 70*; this succession is investigated further in Chapter 6).

Both hyaloclastite and pillow lava lithofacies indicate the presence of water during an eruption. This is commonly an indicator for the presence of ice in this topographical setting (Jones, 1969; Mathews, 1947). The prevalence of water interaction throughout all lithofacies in these units suggests that water or ice was present at the vent for the duration of each eruption.

Mafic to intermediate tuyas (Lmt).

Tuyas are defined here as hyaloclastite-dominated units that are capped with shallow-dipping lavas. Eight tuyas have been mapped on Tindfjallajökull, predominantly on the western upper flank. The footprint area of the tuyas ranges from 0.1 km^2 to the 8 km^2 Þórólfsfell tuya (*66 66*). Scoria cones are preserved at the vents of some of the tuyas. The five largest tuyas have extensive lava deltas preserved on their flanks, composed of steeply dipping highly jointed lava lobes and lava breccia.

Tuyas are common in Iceland and are interpreted to form when subglacial eruptions breach the upper ice surface (Jones, 1966; Mathews, 1947). When this occurs, the eruption transitions from phreatomagmatic conditions, producing pillow lavas and hyaloclastites, to 'dry' conditions during which a lava cap is emplaced. Meltwater is typically ponded around the growing tuya during the eruption. Where lava flows from the shallow-dipping top into the ice-dammed lake, a lava delta is formed, and the change in lithofacies at this water level is called a passage zone (Jones, 1969).

Passage zones are significant for palaeoenvironmental reconstruction because they can be used to estimate the thickness of ice that surrounded the tuya at the time of emplacement (Russell et al., 2014; Skilling, 2009). However, the relationship between the water level defined by the passage zone and the associated ice thickness is difficult to resolve, because the water

level can be controlled by release of water through subglacial pathways or through the upper layer of the ice (or a variable combination of these processes; Smellie, 2006). The water level must always be some way below the ice surface, because a) the upper layer of ice is permeable and thus cannot impound water, and b) the ice will float if water rises to 90% of the ice thickness, which would result in subglacial water release (Smellie et al., 2008). In cases where water outflow through the upper ice layer is dominant, the passage zone marks the height of the impermeable-permeable transition, which may be ~100 m below the ice surface (Smellie and Skilling, 1994). This drainage mechanism may produce relatively stable water levels – recorded by horizontal passage zones – in comparison to subglacial water drainage which is likely to be an unstable drainage mechanism (Smellie, 2006).

The palaeoenvironmental information derived from the tuya passage zones at Tindfjallajökull is presented in Table 2.2. Without precisely determined ages of the tuyas, it is not possible to link this information to regional climate records. However, the good preservation of the tuyas suggest that they were emplaced during the Weichselian glacial period.

Table 2.2. Passage zones preserved at tuyas on Tindfjallajökull.

Locality and passage zone elevation	Palaeoenvironmental information
Bláfell (*66 71*) 880 m elevation	Horizontal passage zone indicates stable meltwater drainage. Subglacial drainage may have been restricted by high ground to the N/E and thicker ice (thus high basal pressures) to the S/W. Thickness of impermeable ice at southern edge of tuya: 180 m.
Vörðufell (*63 72*) 800 m elevation	Horizontal passage zone indicates stable meltwater drainage. Thickness of impermeable ice: 100 m.
Rauðaborg (*65 73*) 940 m elevation	Horizontal passage zone indicates stable meltwater drainage. Thickness of impermeable ice: 40 m.
Þrífjöll (*62 74*)	Two passage zones indicate a change in water level or the occurrence of two separate eruption events.

Locality and passage zone elevation	Palaeoenvironmental information
760 m and 800 m elevation	Thickness of impermeable ice: 60 m (S section), 100 m (N section).
Þórólfsfell (*66 66*) 500–540 m elevation	The passage zone elevation is poorly constrained. Ice >400 m thick filled the Markarfljót valley.

Bláfell, an a'a lava-dominated tuya: The exterior lithofacies and structure of Bláfell tuya (*66 71*) are particularly well preserved, and are described in more detail here. It is assumed that hyaloclastites (not exposed) were deposited during the initial subglacial stage of the eruption. A scoria cone is present at the summit of the tuya (Figure 2.5(a)), with scoriaceous bombs up to 50 cm across. The upper surface of the tuya is composed of shallow-dipping lavas with clastogenic textures. Multiple lavas overlie one another, with each lava a few hundred metres across and 1–5 m thick. Rubbly autobreccia at the top and base of each lava indicates that the lavas are a'a, and jointing is widely spaced (~1 m). There are three subsidence pits on the surface of the tuya, which may have been formed through the draining of subsurface magma or meltwater.

On reaching a subaqueous environment at the margins of the tuya, lavas have formed prograding lava deltas (Figure 2.5(b)). The transition to subaqueous lava emplacement is marked by the budding of steeply-dipping (~30°) lobes that have quenched rinds, an aphanitic texture, and pervasive cube-jointing and pseudopillow fractures (Figure 2.5(c–e)), indicating rapid cooling and infiltration of water (Forbes et al., 2012). The lobes can be tube-like or sheet-like, and have cross-sectional profiles 5–20 m across. Coherent lava has flowed ~200 m to the foot of the tuya, via the primary lobes and/or secondary break-out lobes and pillows. Hyaloclastite breccias are interbedded with the lobes, and are composed of a palagonitised matrix, angular clasts of lava (0.5–10 cm) and isolated pillows (up to 40 cm). Around 30–70% of the delta is made up of these hyaloclastite breccia foresets (Figure 2.5(f)), some of which

exhibit slope-parallel bedding (~30°). This lithofacies is derived from the disintegration of quenched lava on the delta front.

The a'a lava delta at Bláfell tuya has similar characteristics to the few published descriptions of a'a lavas that have flowed from a subaerial to a subaqueous environment (Moore et al., 1973; Smellie et al., 2013, 2011a; Stevenson et al., 2012). In contrast to pahoehoe lavas, which usually break up at the waterline, a'a lavas typically flow subaqueously as coherent lobes with a smaller degree of brecciation (though the lobes still have pervasive in-situ fracturing). The lobes are insulated by the quenched outer layer, allowing the molten core to continue downslope and to break out to form secondary lobes and pillows (Smellie et al., 2013). Like in pahoehoe lavas, passage zones in a'a lavas can be identified by a characteristic change in lithofacies and structure, and are valuable as palaeoenvironmental indicators.

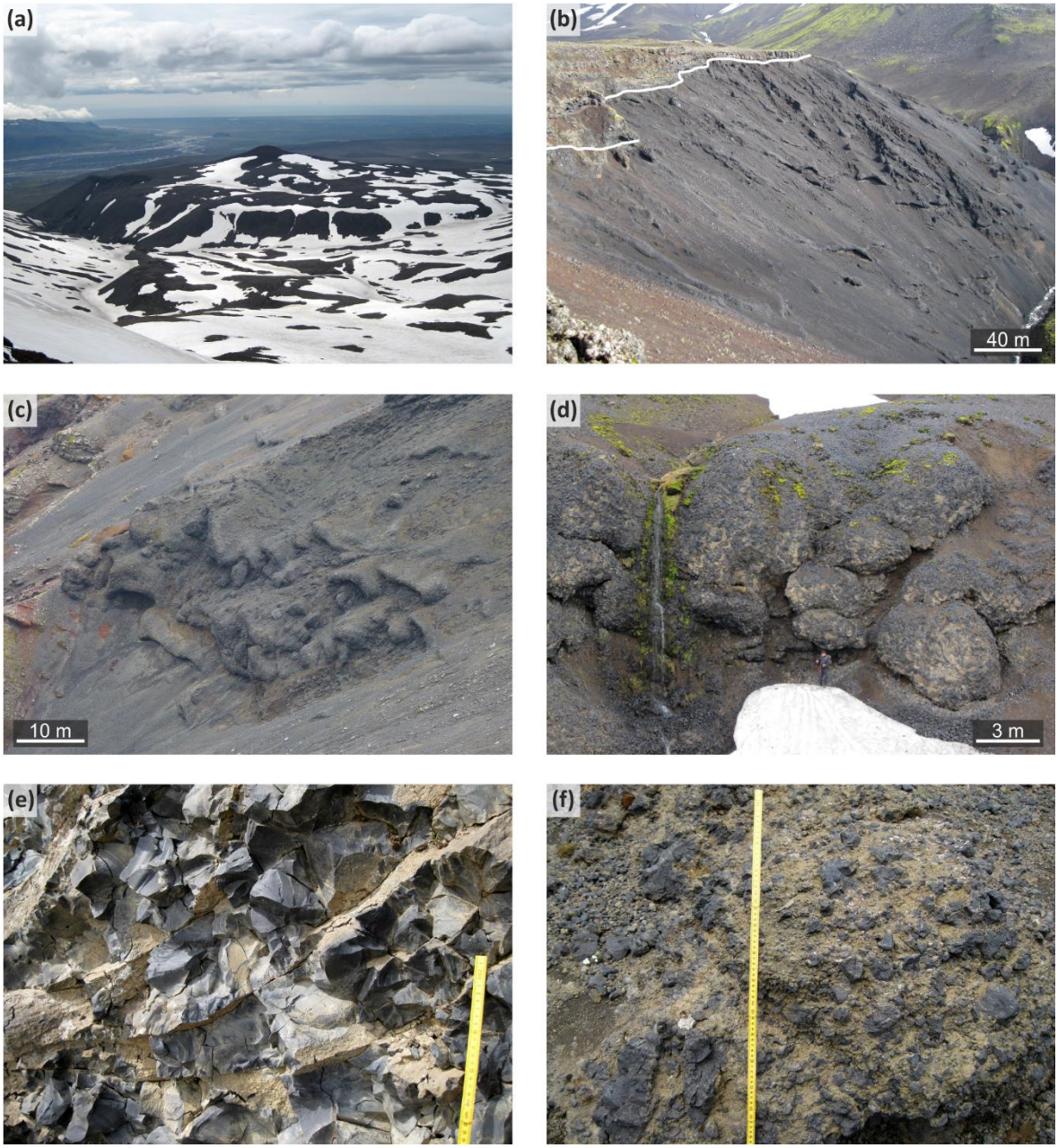

Figure 2.5. Photographs of Bláfell tuya (*66 71*). (a) View of Bláfell from the NE. The summit scoria cone is visible as the rounded knoll in the centre of the photo. The lava cap is surrounded by steep slopes composed of lava deltas. (b) The lava cap (top left) and lava delta exposed on the SE side of Bláfell. The white line indicates the passage zone between shallow-dipping a'a lavas and steeply-dipping lava lobes and breccia. (c, d) Jointed lava lobes and pillows near the base of the lava delta. (e) Pseudopillow fractures in a jointed lava lobe. The master fractures are sub-horizontal and intersect each other at low angles. (f) Hyaloclastite breccia near the base of the lava delta.

2.3.5 Other volcanic systems

Pre-Tindfjallajökull (volcanic system unknown)

Mafic basement (mb). The oldest rocks on the map are found on the SE side of Tindfjallajökull (Figure 2.6(a); *73 70*). These mafic hyaloclastites and lavas have been extensively altered, intruded by dykes, and their pore spaces have been infilled through secondary mineralisation. The extent of alteration and intrusion suggests that these rocks pre-date the unaltered rocks of Tindfjallajökull and most likely constitute part of an older volcanic system that has been largely buried by recent volcanic activity.

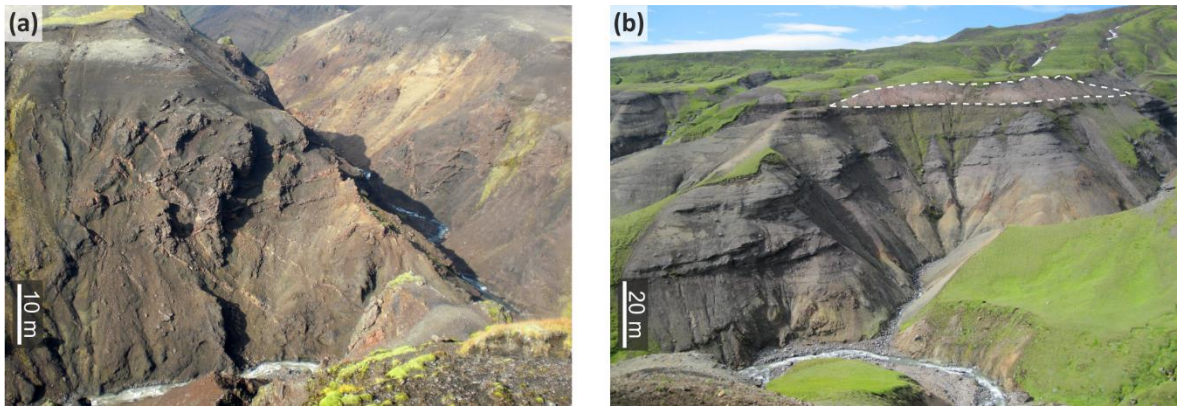

Figure 2.6. (a) Pre-Tindfjallajökull mafic basement exposed in a gorge (*73 70*). The lavas and hyaloclastites have been altered and intruded by numerous dykes. (b) The Weichselian depositional succession at Botn (*71 70*) composed of bedded diamict and the Thórsmörk Ignimbrite (outlined with white dashes).

Torfajökull volcanic system (speculative)

Mafic hyaloclastite-dominated units in fissure swarm between Tindfjallajökull and Torfajökull (mh). The fissure swarm stretching NE from Tindfjallajökull has been the subject of little study, but is tentatively considered to be part of the Torfajökull volcanic system (Sæmundsson and Larsen, 2016). Mafic eruptions in this area have produced SW–NE oriented parallel hyaloclastite ridges. Pillow lavas are found in the cores of the ridges, where exposed through fluvial erosion. The confinement of material along eruptive fissures and the prevalence of magma-

water interaction indicates that these ridges were emplaced subglacially. The ridges show relatively little sign of glacial erosion, suggesting that they were emplaced during the Weichselian glacial period.

Silicic breccia with coherent lava lobes in fissure swarm (sb). Sultarfell is a pale-coloured steep-sided hill (~0.03 km^3; *74 79*) situated in the fissure swarm NE of Tindfjallajökull. It is composed of jointed silicic lava lobes (a few metres across) bounded by an unconsolidated breccia of cogenetic silicic lava blocks. Lobes of fractured lava can be seen in close association with lava fragments that have spalled off the lobes during cooling, which may have been enhanced by the presence of water and/or ice. Like the neighbouring mafic hyaloclastite ridges, the level of preservation of Sultarfell suggests it was emplaced during the Weichselian glacial period.

Thórsmörk Ignimbrite (TI). Most of the preserved volume of the Thórsmörk Ignimbrite outcrops to the south of the Markarfljót, beyond the scope of this map (Jørgensen, 1980). The internal structure of the ignimbrite is complex and both welded and unwelded domains are present. Within the area of the map, the ignimbrite is intercalated within a succession of diamict (Figures 2.6(b) and 2.8; detailed further in Chapter 6) and typically forms a layer up to 10 m thick, though it is sometimes entirely absent from the stratigraphy. Within 5 km of Tindfjallajökull's summit, lithic clasts make up <5% of the ignimbrite and are <3 mm in diameter. In comparison, exposures south of the Markarfljót have a thickness of ~30 m with ~10% lithic clasts, which are up to 20 cm in diameter (Jørgensen, 1980).

Jørgensen (1980) proposed that Tindfjallajökull is the source of the Thórsmörk Ignimbrite, based on the broad patterns of welding, crystallisation and outcrop distribution of the deposit. However, geological mapping on Tindfjallajökull has not found evidence to support this. In particular, the relatively low abundance and small size of lithic clasts entrained within the ignimbrite close to Tindfjallajökull and the continuity of diamict deposition before and after ignimbrite emplacement suggests that Tindfjallajökull is not the source of this major eruption. Torfajökull volcano is a possible alternative source, as Grönvold et al. (1995) noted a

geochemical similarity between rhyolites at Torfajökull and North Atlantic Ash Zone II (the distal correlative of the Thórsmörk Ignimbrite). The source of the ignimbrite is assessed further in Chapter 5, and its depositional environment is investigated in Chapter 6.

Katla volcanic system

Mafic lava (Kml). A series of Holocene pahoehoe lavas have infilled the Markarfljót valley SE of Tindfjallajökull (*74 66*, SE extremity of map). The source of the lavas is located to the east of the map margin in the Katla volcanic system (Larsen, 2000). The interiors of the lavas have developed an entablature jointing pattern during cooling, and the lavas have subsequently been scoured by jökulhlaups (Smith and Dugmore, 2006). The unconfined nature of the lavas indicates a subaerial eruptive environment, with the entablature interiors indicating enhanced cooling of the lava following the introduction of river water (Lyle, 2000). This indicates that the valley was occupied by an active river at the time of lava emplacement.

2.3.6 Sediments

Last glacial period (Weichselian; SWe)

A depositional succession (maximum observed thickness of 160 m) extends from the Vestri-Botná valley (*71 71*) to the low-lying Fauskheiði ridge (*71 65*). The dominant lithofacies is diamict (Figure 2.7(a)), with occasional water-lain gravels. Clast sizes in the diamict range from silt to boulders 60 cm across. The clasts are typically faceted and striated, indicating a glacial influence in their transport. Crucially, the 51.3 ± 4.2 ka Thórsmörk Ignimbrite is present within the succession, dating it to the last glacial period (Chapter 5). A detailed study of this succession is presented in Chapter 6. Other pre-Holocene outcrops of glacially worked material are found on the southern flank of Tindfjallajökull (*68 68*) and in the Eystri-Botná valley (*74 73*).

Holocene and last glacial termination (SHo)

Sediments deposited during and after the retreat of the Weichselian Icelandic Ice Sheet infill valleys to the NE and S of Tindfjallajökull. The youngest sediments are conglomerates that are associated with the presently active fluvial systems, such as the braided river plain of the Markarfljót (in the extreme south of the map). Between the hyaloclastite ridges to the NE of Tindfjallajökull, rhythmites are common (Figure 2.7(b)). These deposits have 3–10 mm thick laminae of alternating fine sands and silts which are characteristic of lacustrine depositional environments, and suggest that lakes (now drained) once occupied the valleys between the parallel ridges.

Figure 2.7. Photographs of sediments deposited (a) during and (b) after the last glacial period. (a) Diamict exposed in Hitagil (*73 71*). Inset: striated cobble within the diamict. (b) Rhythmite with alternating laminae of fine sand and silt (*76 74*).

2.3.7 Superficial deposits

With the exception of tephra, the present-day ice cap entrains only a small volume of rock debris. This is reflected in the lack of significant deposits of moraine around the margins of the ice. Only one area of hummocky moraine has been mapped, near to the eastern and lowest altitude termination of the present ice cap (*73 74*).

Features produced through the collapse of ice-eroded and ice-confined eruptive units are present on Tindfjallajökull. Mass-wasting has taken place as coherent slumps (e.g. at Bláfell tuya *65 71*) or more chaotic rockslides and falls (e.g. at Hitagilsbrún *73 72*).

2.4 GEOLOGICAL DEVELOPMENT OF TINDFJALLAJÖKULL VOLCANO

2.4.1 Evolution of Tindfjallajökull

Geological mapping of Tindfjallajökull has given insight into the evolution of the volcano over time. Mafic basement rocks were emplaced during a volcanic episode prior to the construction of Tindfjallajökull. Volcanism in this area has been ongoing for perhaps 1–2 million years, building on top of crust that formed several million years ago (Óskarsson et al., 1985; Sæmundsson, 1974).

The construction of the Early Tindfjallajökull stratocone, a thick succession with consistent radial dip, was a highly productive phase of Tindfjallajökull's initial development. It is likely that the volcano was glaciated during much of this stage and that some erosion took place, but glacial erosion was surpassed by volcanism as the main driver of landscape evolution. Following the construction of the stratocone, all or most of its surface was capped by the subaerially-emplaced Middle Tindfjallajökull lavas of mafic and silicic compositions (Figure 2.8). Glacial erosion has subsequently resulted in extensive modification of the Early–Middle Tindfjallajökull edifice, particularly through the deepening of the valleys that radiate from the centre of the volcano.

At the onset of the Late Tindfjallajökull stage, the eruption of silicic breccia with coherent lava lobes formed the central silicic edifice. It is unclear if the eruption of this material was accompanied by caldera subsidence. Mafic to intermediate flank volcanism has continued through to the end of the last glacial period during various ice-thickness conditions. These eruptions, on the upper west flank in particular, produced a variety of landforms including hyaloclastite ridges, tuyas and lavas.

On the SE side of Tindfjallajökull, a depositional succession records a detailed history of glacially-influenced sedimentation and local mafic volcanism during the last glacial period. The Thórsmörk Ignimbrite provides a valuable chronostratigraphic marker within this succession (Figure 2.8; Chapter 6). During and after the retreat of the Weichselian glaciation, sedimentation has occurred in lacustrine and fluvial settings around the foot of Tindfjallajökull.

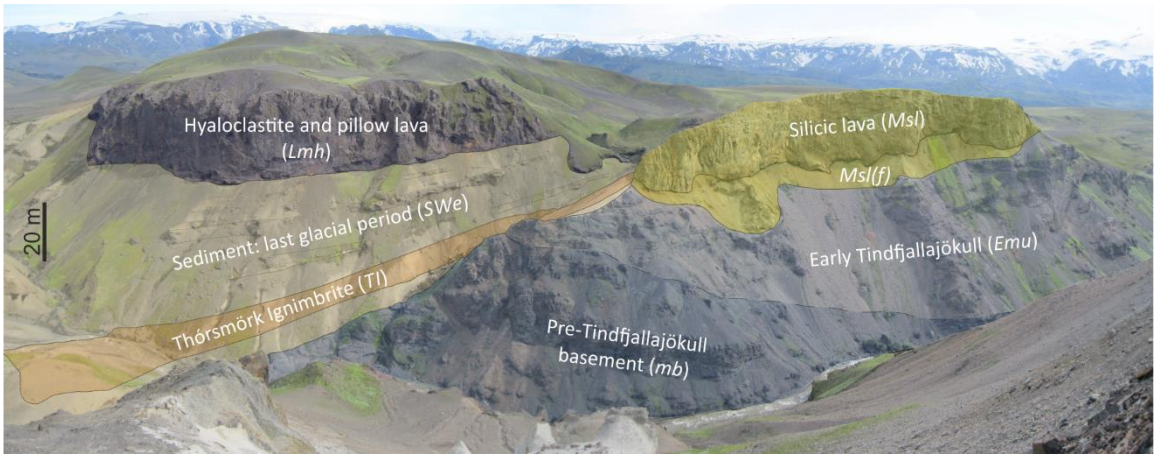

Figure 2.8. Annotated panorama of the SE side of the Gilsá gorge (*73 68*) viewed from Hestur. Sedimentary and volcanic deposits dating to the last glacial period (left) onlap onto an older succession of volcanic rocks (right).

2.4.2 Comparison to neighbouring volcanoes

Several broad characteristics of Tindfjallajökull volcano are comparable to Eyjafjallajökull volcano. The summit of Eyjafjallajökull is only 18 km south of the summit of Tindfjallajökull, and the two volcanoes are of similar size.

The oldest mapped rocks on Eyjafjallajökull are the Laugará Group, exposed on the southern flank of the volcano (Jónsson, 1988). Like the Pre-Tindfjallajökull basement, the Laugará Group is composed of altered basaltic hyaloclastite, pillow breccia and fragmented lava, with numerous intrusive sheets (Loughlin, 1995). The oldest rocks at Eyjafjallajökull were emplaced prior to the Brunhes-Matuyama geomagnetic reversal (~780 ka), and a K/Ar date of 780 ± 30 ka has been obtained from a lava with reversed polarity (Kristjansson et al., 1988).

Like Tindfjallajökull, much of Eyjafjallajökull consists of a thick succession of mafic to intermediate hyaloclastites and lavas (Loughlin, 2002). Furthermore, this succession is capped by lavas that surface much of the upper flanks of both volcanoes (Jónsson, 1988; Loughlin, 1995).

Glacial valleys are thought to have formed in the mid-late period of Eyjafjallajökull's development (Loughlin, 1995). Dissection of Tindfjallajökull's edifice is more advanced than at Eyjafjallajökull. The existence of accommodation space for sedimentary successions within a few kilometres of Tindfjallajökull's summit attests to the greater degree of focussed dissection that has occurred. It is not clear if caldera subsidence is an additional factor that may have contributed to the accommodation of sediment at Tindfjallajökull.

Finally, the mapping of Tindfjallajökull has indicated that it has more extensive deposits of silicic rock in comparison to Eyjafjallajökull (Loughlin, 1995). The presence of a suspected caldera and a high ratio of evolved rock to basalt led Jakobsson (1979) to speculate that Tindfjallajökull is the most mature active volcano in the Eastern Volcanic Zone. However, possible caldera structures and significant volumes of silicic material are also features of the larger nearby volcanoes of Katla and Torfajökull (Jóhannesson and Sæmundsson, 1989).

2.5 CONCLUSIONS

A 1:50,000 scale geological map of Tindfjallajökull provides the first comprehensive survey of this ice-capped stratovolcano. The map enables a reconstruction of the evolution of

Tindfjallajökull through time and a comparison to other nearby volcanoes. Much of the volcano is similar to neighbouring Eyjafjallajökull, though Tindfjallajökull has a higher proportion of silicic volcanic rocks and a higher degree of erosion.

Field mapping of volcanic lithofacies and lithofacies associations allows the mapped classes to broadly reflect the environment at the time of each eruption. As is typical in Iceland, ice has had a significant influence on the development of Tindfjallajökull, though the extent of ice has varied widely through time. Lavas, tuyas and hyaloclastite-dominated units have interacted with ice of variable thicknesses. A depositional succession on the SE side of Tindfjallajökull records glacially-influenced sedimentation and eruptions dating to the last glacial period. Information on past glacial environments on Tindfjallajökull, if combined with chronological data, could fit into larger-scale models of late Pleistocene to Holocene palaeoenvironments in Iceland.

Chapter 3

Geochemistry of Tindfjallajökull volcano

This chapter documents the geochemical characteristics of the Tindfjallajökull volcanic system, determined using whole-rock analytical methods. Compositional terms used in the field (i.e. mafic, intermediate, silicic (Chapter 2)) are replaced by more specific terms to define the geochemistry of the analysed samples (e.g. basalt, trachybasalt etc.; Le Bas et al., 1986). The compositional groups that are present at Tindfjallajökull are described and interpreted to investigate the processes that may be active in the magmatic system.

3.1 Introduction

The geochemistry of Tindfjallajökull volcano has been the subject of little previous work. Previously published studies consist of two papers on xenoliths/nodules that are hosted within mafic hyaloclastites on Tindfjallajökull (Gurenko et al., 2015; Larsen, 1979), and two basalt lava analyses have been published (Jakobsson, 1979; Larsen, 1979). Two additional papers provide geochemical data on the Thórsmörk Ignimbrite (Jørgensen, 1980; Tomlinson et al., 2010), and use physical evidence to suggest that the ignimbrite is sourced from Tindfjallajökull (Jørgensen, 1980). However, the evidence presented elsewhere in this thesis (Chapters 2 and 5) indicates that Tindfjallajökull is not the source of the Thórsmörk Ignimbrite. The geochemistry of the ignimbrite is therefore not relevant to the geochemistry of Tindfjallajökull and is not discussed in this chapter.

The two published studies on xenoliths/nodules from Tindfjallajökull were undertaken to study magmatic processes in the Icelandic crust, not to characterise the geochemistry of Tindfjallajökull. Larsen (1979) analysed gabbro nodules collected from Rauðaborg and Litla-Bláfell (referred to as Hanakambur in his paper) on the upper west flank of Tindfjallajökull. These nodules were interpreted as follows: Type I nodules are derived from a highly

crystallised portion of a pre-eruptive magma reservoir; Type II nodules are true xenoliths that have undergone 2–10% partial melting. Gurenko et al. (2015) analysed granitic and quartz-monzonitic xenoliths from the north foot of Tindfjallajökull. These xenoliths have also undergone partial melting, producing rhyolitic interstitial melts.

The magmatic geochemistry of the wider Eastern Volcanic Zone, within which Tindfjallajökull is situated, is comparatively well known. Basalt compositions transition from tholeiitic basalts in the northern actively-rifting section (e.g. Grímsvötn and Bárðarbunga volcanoes) to alkali basalts in Vestmannaeyjar, off the south coast of Iceland (Jakobsson, 1972). All of the onshore volcanoes of the southern non-rifting section of the Eastern Volcanic Zone (sometimes referred to as the Southern Flank Zone) are characterised by transitional alkali rocks (Figure 1.1). The transitional alkalic affinity of Tindfjallajökull was indicated by Jakobsson (1979) and Larsen (1979).

The work presented in this chapter provides a whole-rock geochemical dataset of Tindfjallajökull. The dataset is used to define the different magma compositions that occur at Tindfjallajökull, as part of the comprehensive geological survey of the volcano developed in Chapters 2–4. Relationships between the various magma types are assessed and the influence of fractional crystallisation, magma mixing and crustal melting is explored, though detailed petrogenetic modelling is beyond the scope of this study.

3.2 METHODS

Rock samples were collected at Tindfjallajökull during field seasons in 2014, 2015 and 2016. Samples were collected from in situ exposures, except for sample JM-218 which is a rhyolite obsidian clast extracted from diamict. Igneous rock samples were typically sourced from extrusive eruptive units, and include subaerial lavas, subaqueous lavas, scoria and hyaloclastites. Intrusive lobes or sheets, interpreted to have been emplaced within cogenetic hyaloclastites or breccias during the same eruptive event, were occasionally sampled in order

to obtain less altered material. Two samples were collected from intrusions that are not cogenetic with their host rock: sample JM-145 is from a lobate rhyolite intrusion in mafic basement and sample JM-101 is from a basalt dyke intruding sediments. Gabbro nodules (JM-26 and JM-27) were extracted from their host hyaloclastite at Rauðaborg, the same locality as Larsen (1979). The mineral phases present in the samples were identified using hand specimens and optical microscopy of thin sections.

A suite of 93 samples from a wide range of locations and stratigraphic positions (Figure 3.1) was selected for whole-rock X-ray Fluorescence (XRF) spectrometry.

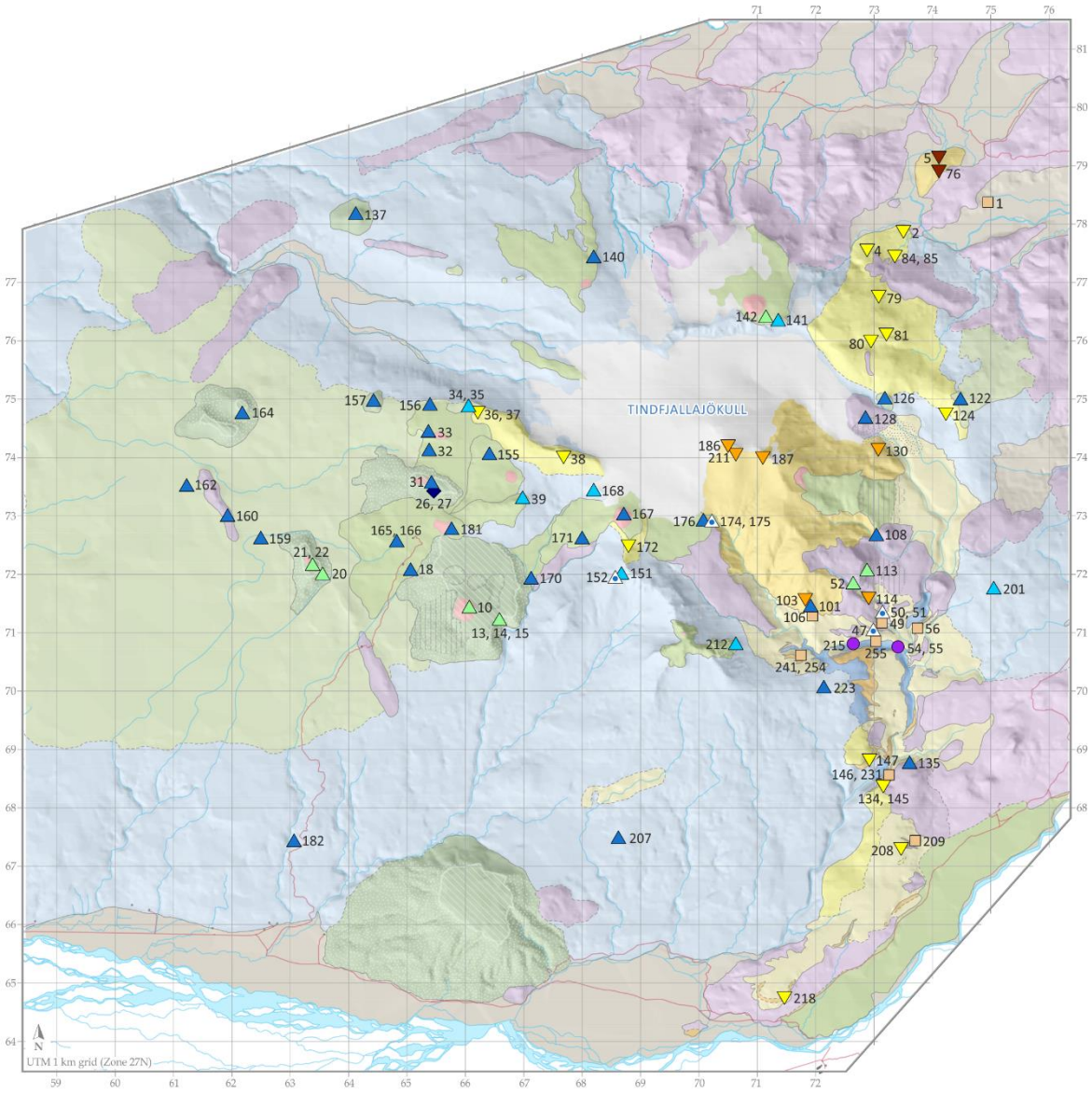

Figure 3.1. Location map of samples used for geochemical analysis. Samples were selected from a range of locations and stratigraphic positions. For key to geological units, see main geological map

(Appendix 8). For key to sample markers, see Figure 3.2. 'JM-' prefixes of sample numbers are omitted on the map.

Samples were prepared for XRF analysis using the standard technique employed at the University of Leicester. First, any altered rinds on the samples were removed using a manual rock splitter. Fine rock powders were then obtained using a jaw crusher followed by an agate planetary mill. For major element analysis, loss on ignition (LOI) was determined by igniting dry powders at 950 °C. Fused glass beads were then produced using the ignited powder mixed with flux (80% lithium metaborate: 20% lithium tetraborate) at a sample to flux ratio of 1:5. Trace elements were determined on pressed powder pellets (binding agent: 7% PVA solution). Major and trace elements were analysed using a PANalytical Axios Advanced XRF spectrometer at the Department of Geology, University of Leicester. The data were acquired over three separate analytical sessions. The full geochemical dataset is provided in Appendices 2.1 (major element oxides) and 2.2 (trace elements).

Precision and accuracy were monitored using a suite of reference materials, and 6 internal reference samples were also run during each of the three analytical sessions (reference material data is provided in Appendices 2.3 and 2.4). There is good agreement between these two measures of precision when reference materials of similar composition are compared (e.g. the precision on multiple analyses of reference material BCR-1 is similar to that of internal reference basalt JM-31). Relative standard deviations (RSDs) are typically 1–2% for major element oxides, except where abundance is low (e.g. MgO in rhyolites). Trace elements that are routinely below detection limits and/or have high RSDs are not used for geochemical plots or interpretations. The plotted element with the highest RSD, due to low abundances, is thorium (BCR-1 RSD = 6.1%). This is equal to a 2σ uncertainty of $\pm$ 0.7 ppm for this element.

3.3 CLASSIFICATION OF ANALYSED SAMPLES

3.3.1 Compositional groups

The analysed samples can be classified into 9 groups based on their geological context and their geochemical compositions (Figure 3.2). The geological context of the samples, such as their lithology and stratigraphic position, is derived from the geological mapping presented in Chapter 2. The compositions of the samples (when unaltered: see section 3.3.2) are determined using a total-alkali vs. silica (TAS) plot (Figure 3.3).

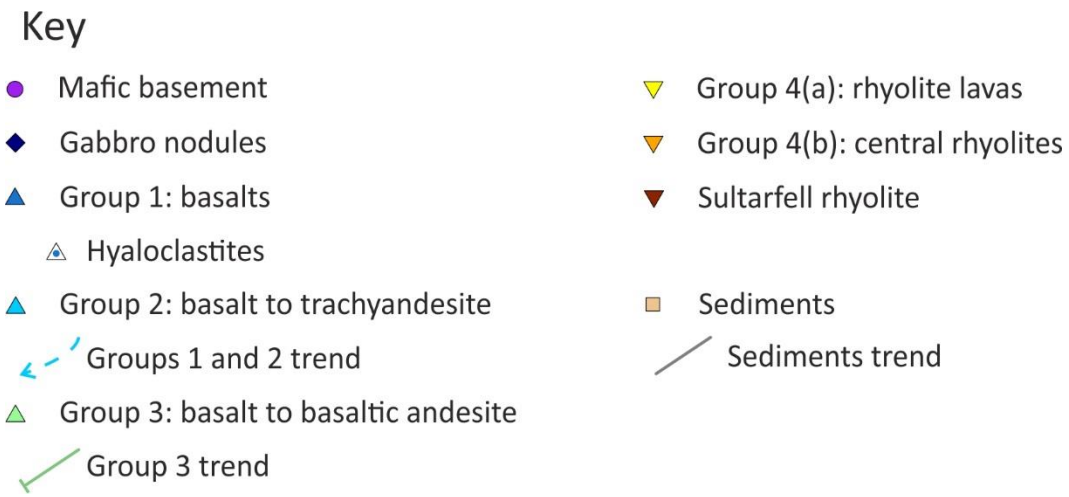

Figure 3.2. Key to geochemistry plots. The analysed samples have been allocated into the 9 groups based on their geological context and geochemical composition. The hyaloclastites in Group 1 may not be representative of the original magmatic geochemistry and are therefore marked with a different symbol. Geochemical trends are seen in the data, and these are annotated on the plots.

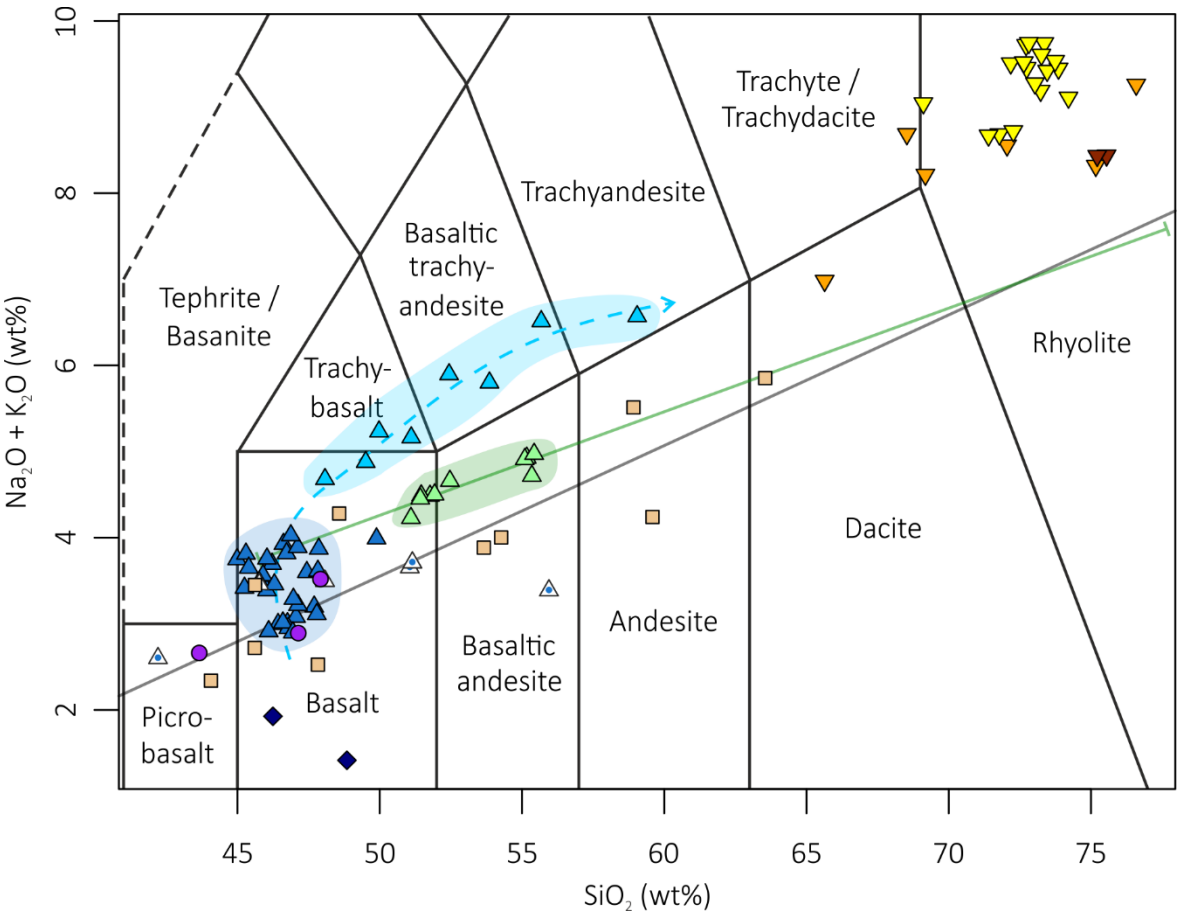

Figure 3.3. Total alkali vs silica (TAS) classification plot. Compositional fields from Le Bas et al. (1986). The compositions of unaltered samples are defined using this plot. Note that the TAS plot is not a reliable way of classifying altered samples (e.g. hyaloclastites, Group 4(b) rhyolites) – the classification of these samples is discussed in section 3.3.2. Shading is intended to highlight, not strictly define, compositional domains.

The 9 groups of analysed samples are defined as follows:

● *Mafic basement.* Samples belonging to the mafic basement stratigraphic group (defined in Chapter 2) may belong to a pre-Tindfjallajökull volcanic system and therefore form a distinct class of rocks.

▼ *Sultarfell rhyolite.* The Sultarfell rhyolite is a separate group due to its unusual location in the fissure swarm to the NE of Tindfjallajökull and its distinctive geochemistry relative to the other rhyolites in the dataset.

All the remaining igneous samples are considered part of the Tindfjallajökull central volcano and are defined in Table 3.1.

Table 3.1. Geochemical subdivision of igneous rocks at Tindfjallajökull.

▲ *Group 1*	A cluster of compositionally similar samples that define the typical Tindfjallajökull basalt geochemistry.
▲ *Group 2*	Samples along a trend from basalt to trachyandesite.
△ *Group 3*	Samples along a trend from basalt to basaltic andesite.
▽▼ *Group 4*	Rhyolites. This group is further subdivided on stratigraphic grounds into 4(a) – samples belonging to the Middle Tindfjallajökull stratigraphic group – and 4(b) – samples belonging to the Late Tindfjallajökull A stratigraphic group. These subgroups are not compositionally distinctive.
◆ *Gabbro nodules*	Gabbro nodules from Rauðaborg (a tuya with a Group 1 composition).

□ *Sediments.* Finally, sediments form a separate class due to their distinct mode of formation and mixed provenance.

The classification of the products of the Tindfjallajökull volcanic system (except the gabbro nodules) into Groups 1 to 4 is based on geochemistry and thus does not directly relate to the stratigraphy of the volcano. More than one compositional group can therefore be represented within each of the broad stratigraphic groups defined in Chapter 2 (Table 3.2).

Table 3.2. List of the compositional groups known to be present in each of the volcanic stratigraphic groups defined in Chapter 2.

Stratigraphic group	Compositional groups present
Tindfjallajökull volcanic system	
Early Tindfjallajökull	▲ Group 1: basalts ▲ Group 2: basalt to trachyandesite
Middle Tindfjallajökull	▲ Group 1: basalts ▽ Group 4(a): rhyolite lavas
Late Tindfjallajökull A: Central silicic edifice	▽ Group 4(b): central rhyolites
Late Tindfjallajökull B: Flank volcanism	▲ Group 1: basalts ◆ Gabbro nodules ▲ Group 2: basalt to trachyandesite ▲ Group 3: basalt to basaltic andesite
Other volcanic systems	
Pre-Tindfjallajökull mafic basement	● Mafic basement
Mafic hyaloclastite-dominated units in fissure swarm between Tindfjallajökull and Torfajökull	*No samples analysed*
Silicic breccia with coherent lava lobes in fissure swarm	▼ Sultarfell rhyolite
Thórsmörk Ignimbrite	*The geochemistry of the Thórsmörk Ignimbrite is investigated in Chapter 5*
Katla volcanic system: mafic lava	*No samples analysed*

3.3.2 Altered samples

For samples that may have undergone geochemical alteration after their emplacement, through hydrothermal alteration or secondary mineralisation processes (e.g. Furnes, 1978), classification by mobile elements such as the alkali metals is unreliable (Winchester and Floyd, 1977). Altered rocks typically exhibit a high degree of compositional variability in the mobile elements (Furnes, 1978; Macdonald et al., 1987) and have high loss on ignition (LOI) values. Although fresh samples were sought in the field, mapping of Tindfjallajökull (Chapter 2) identified that evidence of hydrothermal alteration (orange-stained surfaces; secondary mineralisation in veins and pore spaces) is pervasive in the Pre-Tindfjallajökull mafic basement and the Late Tindfjallajökull (A) central silicic edifice. Samples from these units have LOI values of up to 5.11 wt% (JM-215) and 3.99 wt% (JM-103) respectively. Additionally, mafic hyaloclastites are expected to undergo geochemical alteration through post-emplacement palagonitisation (Furnes, 1978); analysed hyaloclastite samples have LOI values up to 9.77 wt% (JM-152). For comparison, igneous rocks from the remainder of the dataset have a mean LOI value of 0.00 wt % (standard deviation: 0.70; some samples gained mass through oxidation).

The potentially altered sample groups identified above display compositional variability on the TAS plot (Figure 3.3). For instance, hyaloclastites occupy the picrobasalt, basalt and basaltic andesite fields. Two members of the Group 4(b) 'rhyolites' actually have a dacitic and a trachytic/trachydacitic composition according to the TAS plot. As well as variability in SiO_2, Na_2O and K_2O in these groups, other elements such as Sr (Figure 3.6) and Rb (Figure 3.7) have a relatively large range in concentrations. To test whether this variability represents original magmatic compositional variation or an alteration overprint, these samples are plotted on an immobile element classification plot (Figure 3.4; Winchester and Floyd, 1977). When only immobile elements are considered (i.e. elements that remain inert during alteration processes) it can be seen that the hyaloclastites and the Pre-Tindfjallajökull basement are highly comparable to the typical Group 1 basalt composition (Figure 3.4). Use of immobile

elements therefore supports the inclusion of the analysed hyaloclastites within the Group 1 basalts. The mafic basement is kept as a separate group due to its distinct geological context. Similarly, samples from the central silicic edifice (Group 4(b)) exhibit less geochemical variability when immobile elements are plotted, supporting the inclusion of all of these samples in one compositional group with a rhyolitic magmatic composition.

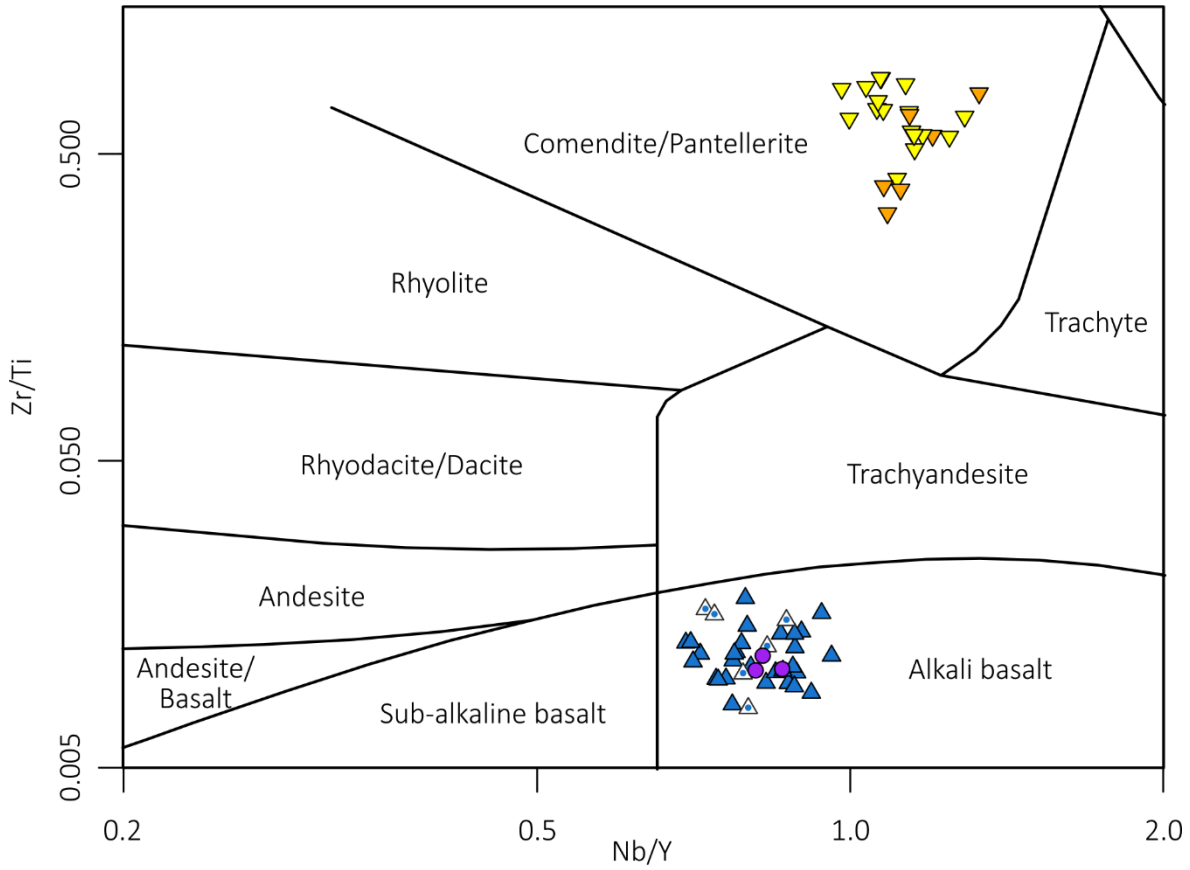

Figure 3.4. Immobile element classification plot showing the Group 4 rhyolites, Group 1 basalts (including hyaloclastites) and mafic basement. Compositional fields from Winchester and Floyd (1977). This figure demonstrates the coherency of the defined compositional groups when immobile elements are plotted, and the geochemical similarity between the mafic basement and the Group 1 basalts.

Note that, for consistency, the classification scheme defined by the TAS plot is used throughout this chapter. The immobile element classification plot is used to demonstrate the affinity of altered samples with the defined compositional groups, not as an additional classification scheme.

3.4 DESCRIPTION OF COMPOSITIONAL GROUPS

The geochemical characteristics of the defined groups are described in this section, before interpretations are presented in section 3.5.

3.4.1 Group 1: basalts

Group 1 is made up of 35 samples that are sourced from a wide range of locations on the Tindfjallajökull edifice (Figure 3.1) and were emplaced during the Early, Middle and Late stages of Tindfjallajökull's stratigraphy (Table 3.2). The members of this group form a cluster of compositionally similar samples on the TAS plot (Figure 3.3; excluding the hyaloclastites) and the immobile element classification plot (Figure 3.4; including the hyaloclastites). These plots show that the Group 1 samples make up the dominant basaltic component of the Tindfjallajökull magmatic system. The typical mineralogy of this group is plagioclase + olivine + clinopyroxene + Fe-Ti oxides (Table 3.3).

Within the Group 1 samples, there is a high degree of variability in the MgO content (typically 4–8 wt%). By plotting against MgO, compositional trends in the other elements can be assessed (Figure 3.5). As MgO decreases, the abundance of TiO_2, Fe_2O_3 and V is seen to increase and then decrease, with an inflection at ~6 wt% MgO. However, there is significant variability in the concentration of these elements within the 5–7 wt% MgO interval (e.g. there is a range of 3.0 – 4.3 wt% TiO_2 at ~6 wt% MgO). One sample (JM-176; circled in Figure 3.5) is rich in olivine phenocrysts and has a correspondingly high MgO content of 10.9 wt%.

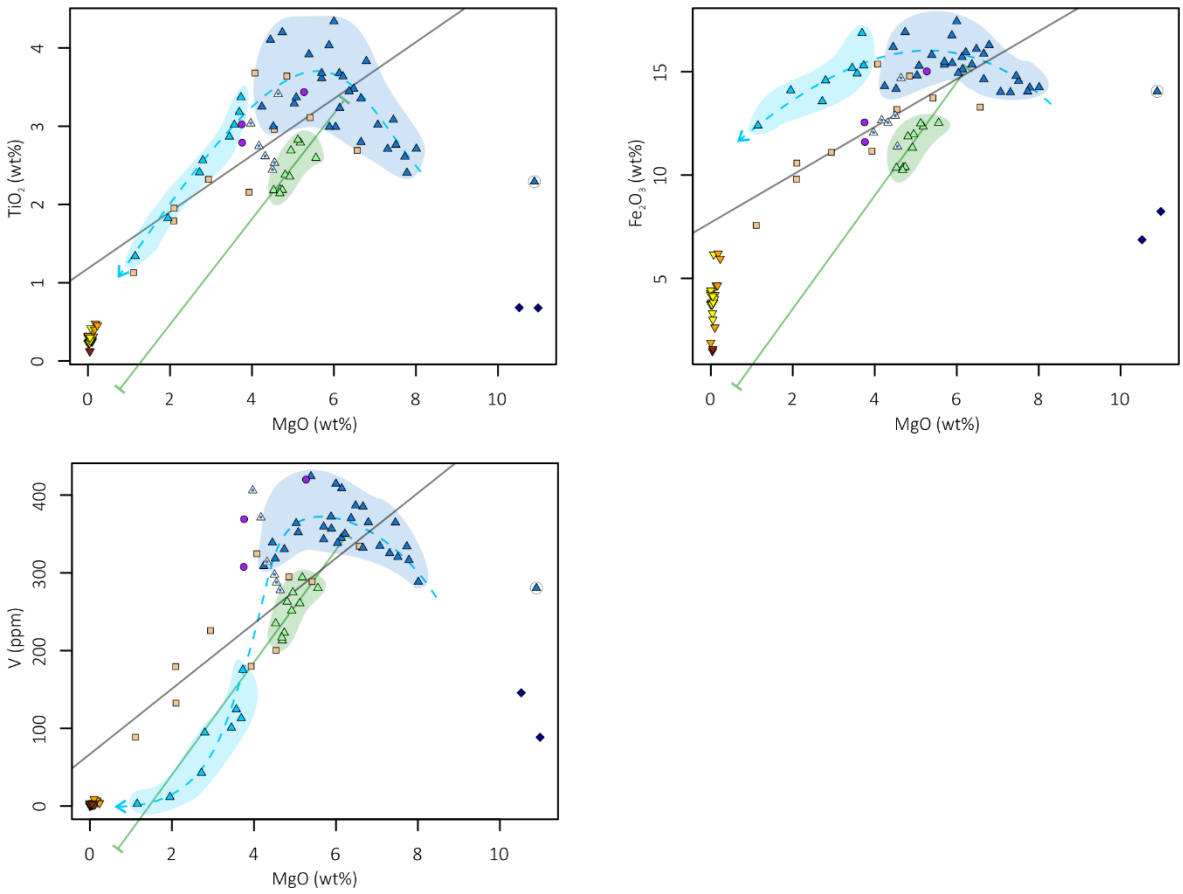

Figure 3.5. Plots to highlight compositional variation within the mafic rocks. MgO has high variability in these samples and is therefore useful for identifying compositional trends. In the Group 1 basalts, inflections occur in the evolution of TiO_2, Fe_2O_3 and V at ~6 wt% MgO, though compositional variability is high in this interval. MgO is not useful for identifying compositional trends in the rhyolites due to its low concentration and correspondingly poor analytical precision (MgO RSD for basalt JM-31: 2.1%; MgO RSD for rhyolite JM-2: 43.5% (Appendix 2.4)). The elements plotted here are susceptible to alteration during palagonitisation (Furnes, 1978), so are unreliable in determining the original magmatic composition of the hyaloclastites.

3.4.2 Mafic basement

The small number of analysed samples and the physical and chemical evidence of alteration (section 3.3.2) restricts a full assessment of the geochemistry of the mafic basement. However, elements that are relatively immobile during hydrothermal alteration can be used to determine the relationship between the mafic basement and the younger Tindfjallajökull rocks. The immobile element concentrations of the mafic basement samples (e.g. Figure 3.4) consistently plot within the envelope defined by the Group 1 basalts.

Table 3.3 (this page and next). Mineralogy of selected samples determined by thin section microscopy.

	Phenocrysts (% of thin section)						Groundmass		Comments
	Plagio-clase	Clino-pyroxene	Olivine	Fe-Ti oxides	Amphi-bole	Alkali feldspar	% of thin section	Feldspar lath length (μm)	
Group 1									
JM-31	8	1	2	1			88	100	Sieve texture in ~⅔ of plagioclase phenocrysts
JM-126	5	1	3	1			90	200	
JM-137	6	1	3				90	100	
JM-164	5	1	2				92	100	Sieve texture in ~⅓ of plagioclase phenocrysts
JM-166	8	1	2				89	80	
JM-171	9	1	3	1			86	100	
JM-176	1		8				91	200	
Mafic basement									
JM-54	30	1					69	200	
JM-55	28	1					56 (+ 15% amygdales)	100	Brown-stained amygdales composed of calcite
Gabbro nodules									
JM-26	55	15	20	5			5	(not visible: glassy)	500 μm crystal size
JM-27	45	30	20				5	(not visible: glassy)	500 μm crystal size
Group 2									
JM-35	2		1	1			96	100	
JM-39	1			1			98	(not visible: glassy)	Vesicular
JM-141	2		1	1			96	50	Flow banded / clastogenic texture

	Phenocrysts (% of thin section)						Groundmass		Comments
	Plagio-clase	Clino-pyroxene	Olivine	Fe-Ti oxides	Amphi-bole	Alkali feldspar	% of thin section	Feldspar lath length (μm)	
Group 3									
JM-13	1		1				98	100	
JM-15	1		1				98	100	
JM-20	1		1				98	(not visible: glassy)	
JM-22	1						99	100	Vesicular
JM-113	10	1	2	1			86	50	Sieve texture in ~⅒ of plagioclase phenocrysts
Group 4(a)									
JM-04				1	1	2	96	(not visible)	
JM-36					1	5	94	(not visible)	
JM-38				1	1	7	91	(not visible)	
JM-79				1	1	3	95	(not visible)	
JM-81				2	1	3	94	(not visible)	
JM-134				1		4	95	(not visible: glassy)	
Group 4(b)									
JM-103				2	3	6	89	(not visible: glassy)	
JM-130				1		5	94	(not visible: glassy)	
JM-186						6	94	(not visible: glassy)	Flow banded
JM-187				1	2	7	90	(not visible: glassy)	Flow banded
JM-211						5	95	(not visible: glassy)	Flow banded
Sultarfell rhyolite									
JM-05				1	1	5	93	(not visible: glassy)	Vesicular
JM-139					1	5	94	(not visible: glassy)	Vesicular

3.4.3 Gabbro nodules

The eruptive unit that hosts the gabbro nodules – Rauðaborg – has a Group 1 basalt composition and is part of the Late Tindfjallajökull (B) stratigraphic group. The gabbro nodules are identified as the Type I nodules of Larsen (1979), due to their euhedral phenocrysts and their mineralogy (plagioclase + clinopyroxene + olivine, with interstitial glass; Table 3.3). Therefore, the nodules represent a phenocryst-rich counterpart of the Rauðaborg basalt (sample JM-31) and are derived from a highly crystallised part of the same pre-eruptive magma body (Larsen, 1979). The analyses indicate that the nodules are enriched in MgO, Al_2O_3 and CaO relative to the Group 1 basalts.

3.4.4 Group 2: basalt to trachyandesite

Group 2 is a set of 8 samples with a more evolved composition than the Group 1 basalts. The samples follow an evolution path from a basaltic composition (~48 wt% SiO_2) through the trachybasalt and basaltic trachyandesite compositional fields on the TAS plot (Figure 3.3), with one sample having a trachyandesitic composition. This most-evolved sample (JM-212) contains 59.1 wt% SiO_2 and is a lava from the Late Tindfjallajökull (B) stratigraphic group. Overall, the samples that make up Group 2 have no clear geographic or stratigraphic pattern. For instance, both the Early and Late stages of Tindfjallajökull's stratigraphy are represented by samples in this group (Table 3.2).

Due to the range of SiO_2 concentrations in the Group 2 samples (48–59 wt%), compositional trends in the other elements can be identified when plotted against SiO_2 (Figure 3.6). The large range in SiO_2 concentrations in the Group 2 samples relative to the Group 1 basalts is demonstrated in these plots. Along the evolution trend (increasing SiO_2, decreasing MgO) the concentrations of TiO_2, Fe_2O_3, V and CaO decrease (Figures 3.5 and 3.6), while the incompatible elements increase (Figure 3.7). In contrast to the Group 1 basalts, the concentrations of Sr and P_2O_5 decrease with increasing evolution of the Group 2 samples. This switch in behaviour of these elements thus occurs at ~4 wt% MgO.

To highlight the evolutionary trends in the Group 1 and 2 samples, curved lines ('Groups 1 and 2 trend') have been added to the plots and pass continuously through these groups.

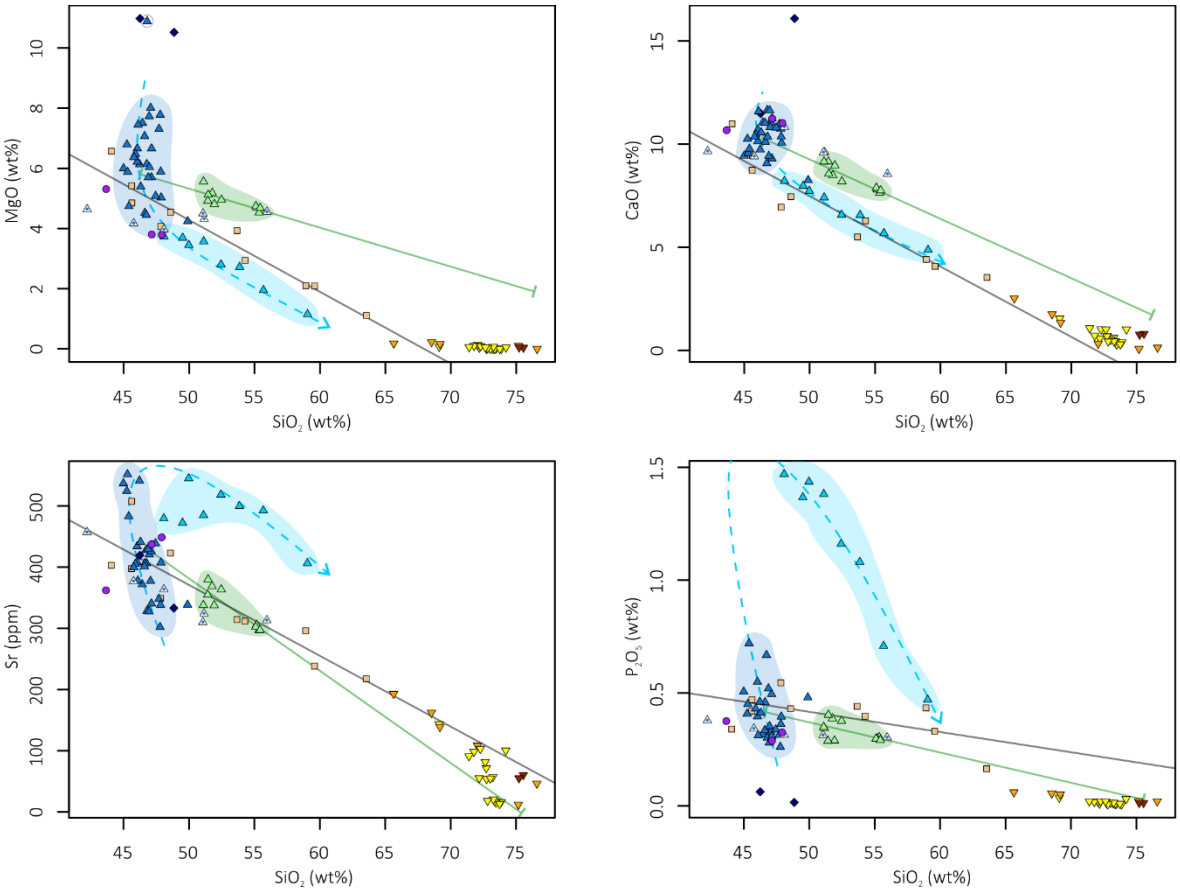

Figure 3.6. Plots to highlight compositional variation within the mafic to intermediate rocks. SiO_2 varies little within the Group 1 basalts but has a larger range in the Group 2 samples. SiO_2 is therefore useful for identifying compositional trends in the Group 2 rocks. The blue dashed line highlights the evolutionary trend of the Group 1 and 2 samples. The concentration of Sr and P_2O_5 increases with evolution of the Group 1 samples then decreases with evolution of the Group 2 samples.

3.4.5 Group 3: basalt to basaltic andesite

Ten samples from 4 eruptive units make up Group 3 – another group with a more silica-rich composition than the Group 1 basalts. This group is distinct from Group 2 in its different (i.e. less alkalic) compositional trend, which passes from basalt to basaltic andesite on the TAS plot (Figure 3.3). There is no apparent geographical control on Group 3, but all of the eruptions are part of the Late Tindfjallajökull (B) stratigraphic group. The most silica-rich samples are from Bláfell tuya (samples JM-10, -13, -14, -15; ~55 wt% SiO_2).

As well as having a less alkalic geochemistry than the Group 2 samples, the Group 3 rocks do not have a curved compositional trend. This is demonstrated in Figure 3.6 (particularly the plots of Sr and P_2O_5), where the Group 3 samples do not show the same transitions in behaviour as the Group 1 and 2 samples. Instead, Group 3 has a linear orientation between basaltic and basaltic andesitic compositions on these plots. The difference between Group 2 and Group 3 is supported by plots of elements that typically increase in concentration during magmatic evolution (i.e. incompatible elements; Figure 3.7). Rather than showing a proportional increase with magmatic evolution, the incompatible elements in Group 3 either increase in concentration (e.g. Th, Ba, K_2O, Rb) or remain at a similar concentration to the Group 1 basalts (e.g. Nb, Zr, La).

In order to test whether Group 3 is a product of the mixing of two different magma compositions, linear regressions ('Group 3 trend') have been fitted to this group and added to the plots. Each regression line has been extrapolated back to its intersection with the Group 1 basalts, which may represent a basaltic endmember composition. The amount of extrapolation in the 'evolved' direction is proportional in each plot, with the Bláfell tuya samples situated 30% of the distance along each line. The silicic end of the regression line therefore models the composition of a rhyolite that, if mixed with Group 1 basalt at a ratio of 30% rhyolite to 70% basalt, would produce the composition of Bláfell tuya. The regression line on the plot of Zr vs Nb has been omitted due to a lack of spread in the data (Figure 3.7).

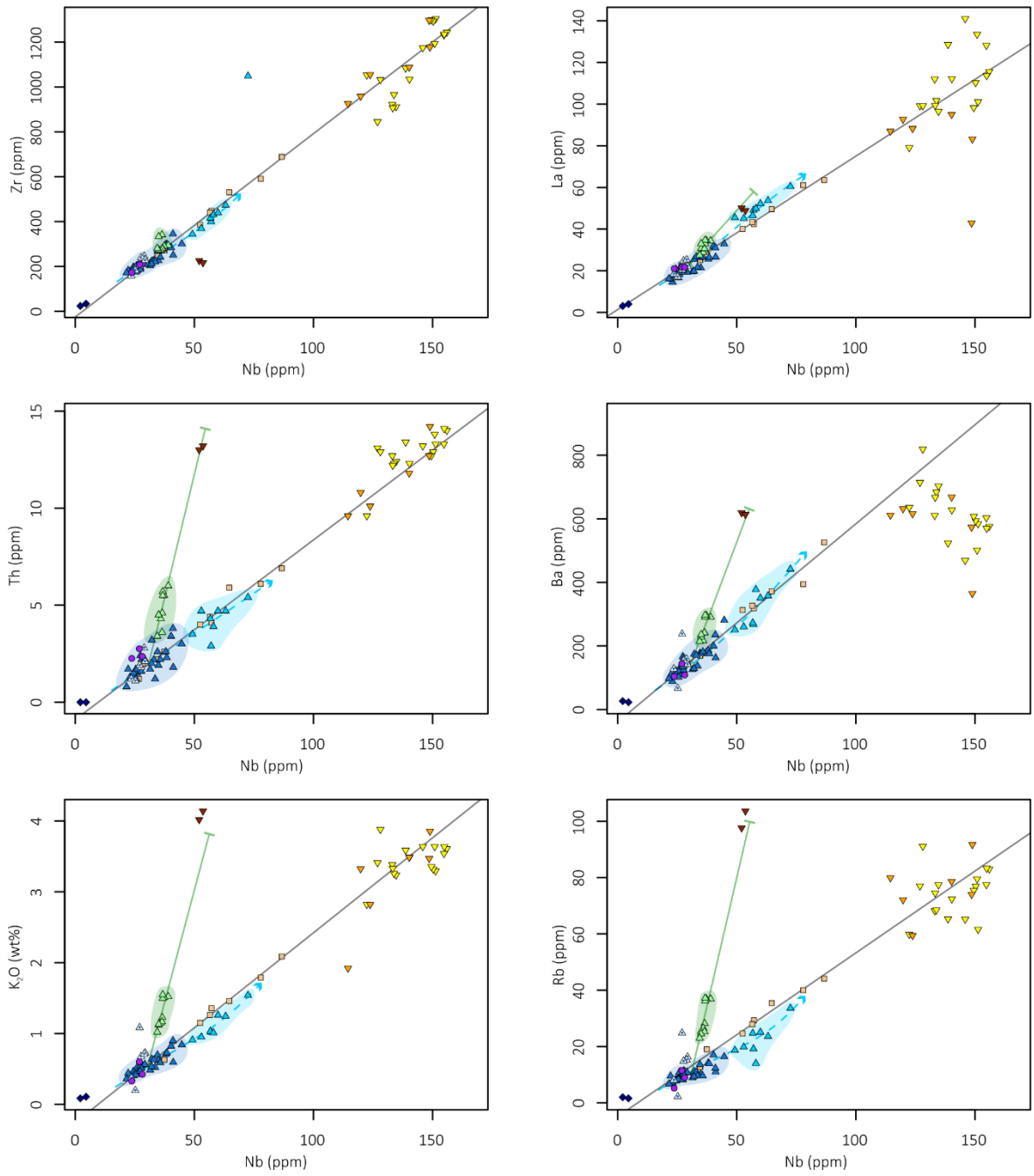

Figure 3.7. Plots of elements that are typically incompatible during magmatic evolution at Tindfjallajökull. Elements are plotted against Nb, which is highly incompatible in the dataset (i.e. there is a large relative increase in its concentration from basalts to rhyolites) and does not show evidence of alteration (e.g. hyaloclastites have little variation in Nb). The ratios of the incompatible elements remain approximately constant in the Group 1, Group 2 and Group 4 samples. The Group 3 samples deviate from this trend. The Sultarfell rhyolite has a distinct incompatible element composition and is dissimilar to the other rhyolites in the dataset.

3.4.6 Group 4: rhyolites

Group 4 includes all of the analysed rhyolite samples that were collected from the Tindfjallajökull edifice (i.e. excludes the Sultarfell rhyolite which is situated NE of Tindfjallajökull). The group can be divided into two subgroups on stratigraphic grounds. Group 4(a) rhyolite lavas are from the Middle Tindfjallajökull stratigraphic group and the Group 4(b) central rhyolites are from the Late Tindfjallajökull (A) stratigraphic group. Despite the different stratigraphic positions of the rhyolite subgroups, they have similar geochemical characteristics (e.g. Figure 3.4). The typical phenocryst assemblage is alkali feldspar + amphibole + Fe-Ti oxides (Table 3.3).

Although alteration has affected some elements in the Group 4(b) rhyolites (section 3.3.2), the unaltered samples and the immobile elements in altered samples define the rhyolitic component of the Tindfjallajökull magmatic system. The alkali versus alumina saturation of the samples can be calculated using the peralkalinity index: molar $(Na_2O + K_2O)/Al_2O_3$, with peralkaline rocks having a value greater than 1 (Figure 3.8). The Group 4(a) rhyolite lavas at Saxi (JM-36, -37, -38, -172) and Jökulskarð (JM-2, -4, -79, -80, -81, -84, -85, -124) are mildly peralkaline (comenditic) with mean peralkalinity indices of 1.07 and 1.11 respectively. The Group 4(a) rhyolite lava at Hestur (JM-134, -145, -147, -208) is metaluminous, having a mean peralkalinity index of 0.96. Alteration may have affected the peralkalinity indices of the Group 4(b) central rhyolite samples, which range from 0.82 (sample JM-103) to 1.05 (sample JM-211).

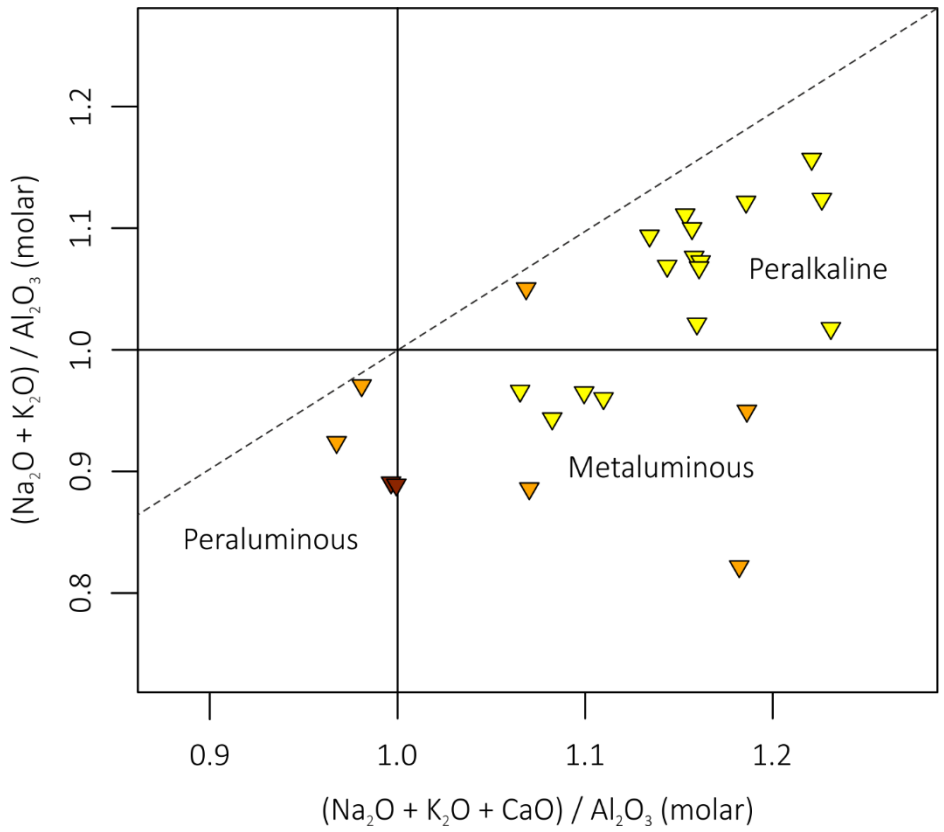

Figure 3.8. Saturation of alkalis with respect to alumina in the rhyolitic samples. Most of the Group 4(a) samples have a peralkaline composition. The variability of the Group 4(b) samples is attributed to post-emplacement alteration. The Sultarfell rhyolite sits on the boundary between peraluminous and metaluminous compositions.

The Group 4 samples are highly depleted (relative to the mafic and intermediate samples) in MgO, TiO_2, Fe_2O_3, V (Figure 3.5), CaO, Sr and P_2O_5 (Figure 3.6), and enriched in Nb, Zr, La, Th, K_2O and Rb (Figure 3.7). Barium concentrations are relatively high in these samples but decrease with increasing Nb content (Figure 3.7).

3.4.7 Sultarfell rhyolite

Sultarfell is a high-silica rhyolite (~75 wt% SiO_2) located in the fissure swarm to the NE of Tindfjallajökull. This rhyolite has a peralkalinity index of 0.89 and an equal ratio of molar (Na_2O + K_2O + CaO) to Al_2O_3, placing it at the boundary between metaluminous and peraluminous compositions (Figure 3.8). The mineral assemblage is alkali feldspar + amphibole + Fe-Ti oxides (Table 3.3). Similar to the Group 4 rhyolites, Sultarfell has relatively low concentrations of the compatible elements MgO, TiO_2, Fe_2O_3, V (Figure 3.5), CaO, Sr

and P_2O_5 (Figure 3.6). Although some incompatible elements have high concentrations (Th, Ba, K_2O and Rb) and are comparable to the Group 4 rhyolites, other elements that are enriched in the Group 4 rhyolites have low concentrations in the Sultarfell rhyolite (Nb, Zr, La; Figure 3.7). There are therefore some key differences in incompatible element ratios between the Sultarfell rhyolite and the Group 4 rhyolites. The pattern of high concentration and low concentration trace elements in the Sultarfell rhyolite matches the pattern of enriched and constant elements observed in the Group 3 trend. This relationship is demonstrated by the consistent plotting of the Sultarfell rhyolite near to the modelled rhyolitic endmember of the Group 3 trend (Figure 3.7).

3.4.8 Sediments

The analysed sediments are of Weichselian age (dated through their association with the Thórsmörk Ignimbrite; Chapter 2), except for JM-1 which is of post-glacial age. It is assumed that the geochemistry of the sediments provides information on the erosion and transport of material from the volcanic source areas on Tindfjallajökull. Four sediment samples have compositions close to the Group 1 basalts (samples JM-1, -209, -231, -254). The remaining samples show a varying degree of incorporation of more evolved material. Sediments in close proximity to the central rhyolites (samples JM-106, -255, -49 and -56) and a sample close to the rhyolite lava at Hestur (sample JM-146) have incorporated the largest proportion of silicic rock.

Linear regressions ('Sediments trend') have been fitted to the sediment compositional data and added to the plots. These regressions provide approximate mixing lines between the dominant volcanic components of Tindfjallajökull. Some loss of mobile elements such as Na_2O may have occurred in the sedimentary process.

3.5 INTERPRETATION OF MAGMATIC PROCESSES AND RELATIONSHIPS

Drawing on the descriptions of the compositional groups provided above, the potential relationships between the magmas at Tindfjallajökull and the processes that may have contributed to their evolution are discussed in this section.

3.5.1 Groups 1 and 2 trend

The geochemical trend through Groups 1 and 2 includes inflections that are attributed to the onset of crystallisation of mineral phases during evolution of the magmas. It is therefore interpreted that the compositional variation in these groups is primarily driven by fractional crystallisation. Gabbro nodules, representing crystal-rich portions of the Group 1 basalts, reveal the bulk composition when the principal mineral phases are accumulated (i.e. the opposite of fractional crystallisation). The 50% decrease in MgO within the Group 1 basalts is attributed to fractionation driven by olivine and clinopyroxene. At ~6 wt% MgO, the removal of Fe_2O_3, TiO_2 and V is initiated by the onset of Fe-Ti oxide crystallisation (as is the case at Eyjafjallajökull (Loughlin, 1995)). The large range in TiO_2, Fe_2O_3 and V concentrations around this transition may indicate that the onset of Fe-Ti oxide crystallisation occurs at subtly different stages of evolution in different batches of magma and under different conditions of crystallisation. For instance, the crystallisation of Fe-Ti oxides is influenced by the oxygen fugacity of the magma (Lapin et al., 1985).

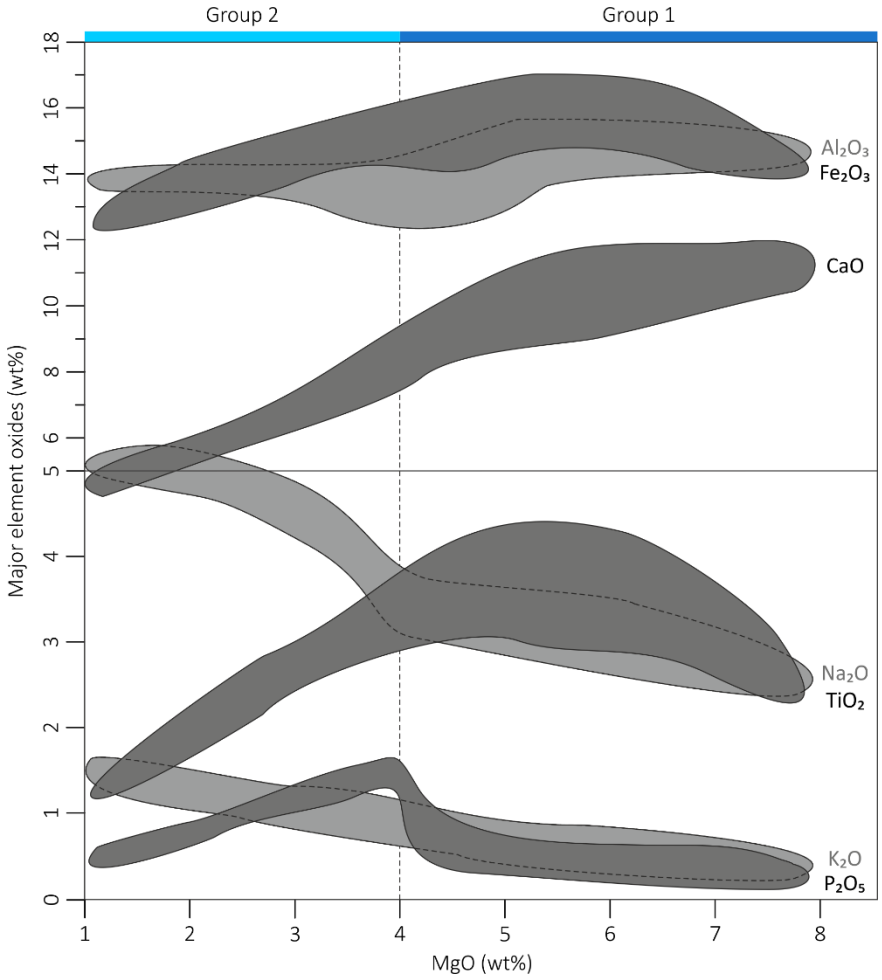

Figure 3.9. Behaviour of major element oxides (vs. MgO) in the Group 1 and 2 samples (hyaloclastites excluded). These elements have continuous evolution trends through Groups 1 and 2, which go from right to left (i.e. decreasing MgO) on the plot. Inflections in the trends are consistent with the evolution of the magmas through fractional crystallisation.

It is interpreted that continued fractional crystallisation of the Group 1 basalts produces magma with a Group 2 composition (Figure 3.9). Significant enrichment of SiO_2 in the magmas starts to occur at the transition from Group 1 to Group 2. Within Group 2, P_2O_5 decreases rapidly following the onset of apatite crystallisation at ~4 wt% MgO, and continued fractionation of plagioclase reduces the concentration of CaO and Sr. Incompatible elements (e.g. K_2O) steadily increase in concentration as the compatible elements are removed from the melt. In summary, fractional crystallisation of basaltic magmas at Tindfjallajökull results in the eruption of a continuous range of magma compositions from basalt to trachyandesite.

3.5.2 Petrogenesis of the Group 4 rhyolites

There is a striking lack of geochemical evidence for hybridisation (i.e. straight mixing lines) between the basalts and the Group 4 rhyolites, despite these being the dominant magma types at Tindfjallajökull. In the Group 4 rhyolites, concentrations of compatible elements MgO, TiO_2 and V are consistently very low, indicating an absence of basaltic contamination. This is in contrast to neighbouring volcanoes, where mixing between the dominant magma types is common (e.g. Torfajökull (Blake, 1984; McGarvie, 1984) and Katla (Lacasse et al., 2007)). Without the masking effect of hybridisation, there is a prominent 'Daly gap' between the Group 1 & 2 rocks and the Group 4 rhyolites. Only one of the Group 2 samples in the dataset has evolved to a trachyandesitic composition (Figure 3.3).

The bimodal geochemical distribution of volcanic rocks is characteristic of Icelandic magmatism (Sigurdsson, 1977; Walker, 1966), in contrast to 'typical' oceanic crust where volcanic rocks are almost entirely basaltic. The origin of the rhyolitic rocks in Iceland has been the subject of much debate, with authors typically advocating either extensive fractional crystallisation of basaltic magmas (Table 3.4(a) and references therein) or the partial melting of crustal rocks to produce rhyolitic compositions. Proposed mechanisms for the production of Icelandic rhyolites by crustal melting require a pre-existing source rock of either metamorphosed/ hydrothermally altered mafic composition (Table 3.4(b) and references therein) or silicic composition (Table 3.4(c) and references therein).

Table 3.4. Three proposed mechanisms for the petrogenesis of rhyolitic magma in Iceland.

	Source	Process of rhyolite petrogenesis	Example references
a)	Mafic magma that has accumulated in the crust.	Fractional crystallisation. Extensive (≥90%) crystallisation of mafic magma is needed to produce a rhyolitic melt.	Macdonald et al., 1990 (Torfajökull); Portnyagin et al., 2012 (Hekla); Prestvik et al., 2001 (Öræfajökull)

b)	Hydrothermally altered and/or metamorphosed mafic crust, heated by intruding mafic magma.	Partial melting of the mafic crust, forming an evolved (dacitic or rhyolitic) melt. Partial melts may subsequently evolve through fractional crystallisation and/or assimilation of other magmas.	Elders et al., 2011 (Krafla); Sigmarsson et al., 1991 (Hekla, Krafla, Askja); Zierenberg et al., 2013 (Krafla)
c)	Silicic rock in the crust (e.g. silicic segregations in the upper parts of intrusions or the evolved products of older volcanic systems), heated by intruding mafic magma.	Partial melting of the silicic bodies in the crust, forming a rhyolitic melt. Further interaction and evolution of the partial melts may occur.	Gunnarsson et al., 1998 (Torfajökull); Gurenko et al., 2015 (Tindfjallajökull); Sigurdsson, 1977 (Vestmannaeyjar, Askja and others)

The scarcity of intermediate rocks in Iceland suggests that the continuous evolution of magma from basaltic to rhyolitic compositions does not occur. Intermediate compositions would be expected to be common if rhyolite petrogenesis occurred through the traditional model of fractional crystallisation in near-liquidus conditions (Yoder, 1973). Instead, rhyolites may be produced through the extraction of evolved interstitial melts from a near-solidus crystal mush – conditions that can occur either during the cooling of a magma body or through the partial melting of pre-existing rock (Jónasson, 2007). Whether the rhyolites at a particular Icelandic volcano are generated through the cooling of a basaltic magma or the heating of a pre-existing crustal source may be a function of the local geothermal gradient (Martin and Sigmarsson, 2007). For instance, rhyolite petrogenesis at rift-zone volcanoes (i.e. areas of high geothermal gradient) may be dominated by the partial melting of mafic crust (e.g. Krafla volcano; Elders et al., 2011), whilst fractional crystallisation may be dominant at off-rift volcanoes (e.g. Öræfajökull volcano; Prestvik et al., 2001). As Tindfjallajökull is situated on a propagating rift, in transition from an off-rift zone to a rift zone, it is unclear whether the local geothermal gradient is high enough for the partial melting of altered mafic crust to occur.

From the perspective of the data presented here, it is possible that the Group 4 rhyolites are derived from the Group 1 basalts through continued evolution along the Group 2 fractionation trend. This interpretation is supported by the relative abundances of incompatible elements across the various groups (Figure 3.7). The ratios of the highly incompatible elements are consistent throughout Groups 1, 2 and 4, suggesting that these magmas have a common source. To produce the observed gap from intermediate to silicic compositions, the fractionation process that produced the Group 4 rhyolites may have involved the extraction of evolved melt from a highly crystallised body of Group 1 basalt, potentially followed by further fractional crystallisation within the magmatic system beneath Tindfjallajökull. However, the observation that the mafic basement has a similar composition to the Group 1 basalts means that the pre-existing basement rocks cannot be ruled out as the source of the Group 4 rhyolites. Partial melting of the mafic basement at depth may also be a viable process for producing a rhyolitic melt with the geochemical characteristics of the Group 4 rhyolites. The observed depletion of Ba in the Group 4 rhyolites suggests that alkali feldspar was present in the source rock or as a fractionating phase.

In order to investigate the contribution of pre-existing crust to the origin and evolution of Icelandic rhyolites, previous studies have employed Th, O and/or H isotopes to determine the influence of 'old' (low (^{230}Th/^{232}Th)), hydrothermally altered (low $\delta^{18}O$, low δD) crust (e.g. Elders et al., 2011; Nicholson et al., 1991; Sigmarsson et al., 1991). A similar approach could be used to examine the role of pre-existing crust in the formation of the Group 4 rhyolites, but this is beyond the scope of this thesis.

3.5.3 Group 3 trend

Unlike the Group 2 samples, the compositional trend of the Group 3 samples does not have inflections that would indicate the influence of fractional crystallisation in the evolution of these magmas. For example, Group 3 samples lack the pattern of P_2O_5 enrichment and depletion associated with the onset of apatite crystallisation in the Group 2 samples (Figure

3.6). Additionally, the unusual behaviour of incompatible elements in the Group 3 samples (e.g. Rb increases whilst Nb remains approximately constant; Figure 3.7) is not consistent with fractional crystallisation of olivine, pyroxene, Fe-Ti oxide, plagioclase and apatite mineral phases.

Instead, the linear trend of the Group 3 samples suggests that they are the product of mixing of two different magma compositions. Consistent intersection of the Group 3 trend with the Group 1 basalts indicates that the mafic end-member was of the typical Tindfjallajökull basalt composition (~6 wt% MgO). It is interpreted that magma with a Group 1 composition has mixed with a more silicic magma to produce the Group 3 composition.

The extrapolation of the Group 3 trend to more evolved compositions allows the composition of the possible silicic end-member to be assessed. On plots of incompatible elements (Figure 3.7), the orientation of the Group 3 trend rules out the Group 4 rhyolites as the silicic end-member. Specifically, the Group 3 trend does not show an enrichment in Nb, Zr and La, as would be expected if Group 1 basalts were mixed with the Group 4 rhyolites. Instead, the Group 3 trend passes close to the Sultarfell rhyolite composition on all plots, and the Sultarfell rhyolite has a similar composition to the modelled rhyolitic end-member of the Group 3 trend (which considers the mixing of a Group 1 basaltic magma (70%) and a rhyolitic magma (30%) to produce the Bláfell tuya composition; section 3.4.5). It is interpreted that magmas of Group 3 composition are produced through the mixing of Group 1 basaltic magma with a rhyolitic magma of similar composition to the Sultarfell rhyolite.

3.5.4 Petrogenesis of the 'Sultarfell-type' rhyolites

Given the apparent geochemical similarity between the Sultarfell rhyolite and the silicic end-member of the Group 3 trend, these magmas (termed the 'Sultarfell-type' magmas) may have been generated through a similar process. Such a process must:

a) Produce rhyolitic magma with a different incompatible element composition to all the other magmas known at Tindfjallajökull, including the Group 4 rhyolites.

b) Allow for the eruption of rhyolitic magma away from Tindfjallajökull (i.e. at Sultarfell) and mixed magmas at scattered locations on the Tindfjallajökull edifice (Figure 3.10).

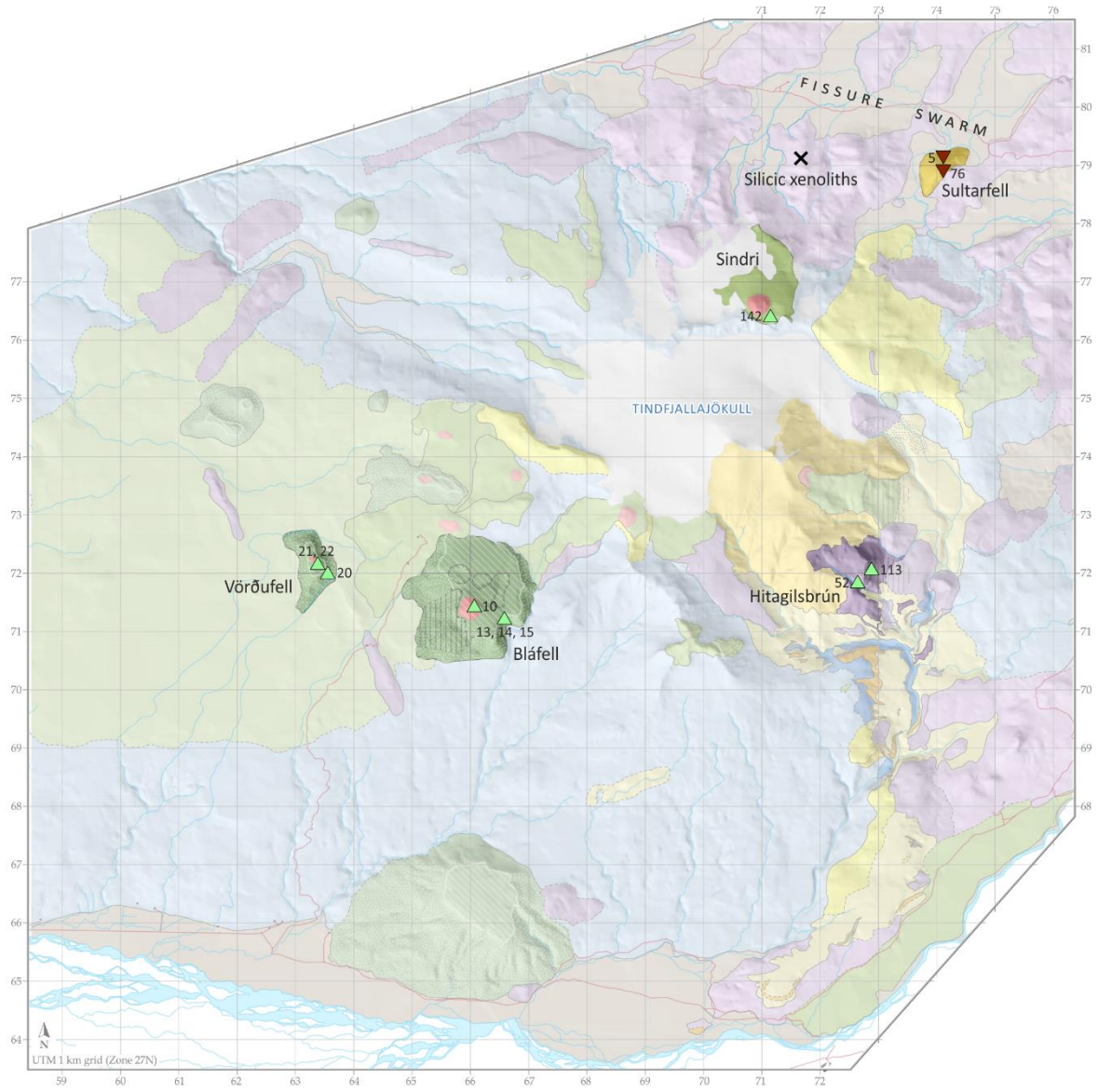

Figure 3.10. Location map of the Sultarfell rhyolite, the silicic xenoliths investigated by Gurenko et al. (2015), and eruptive units known to have a Group 3 composition. The xenolith locality and Sultarfell are both located in the fissure swarm to the NE of Tindfjallajökull. Eruptions with a Group 3 composition have occurred at scattered locations on the Tindfjallajökull edifice.

The significant differences in composition between the Sultarfell-type rhyolites and the Group 4 rhyolites suggest that more than one process of rhyolite petrogenesis occurs at Tindfjallajökull. Unlike the Group 4 rhyolites, the Sultarfell-type rhyolites do not have comparable incompatible element ratios to the Group 1 basalts or the mafic basement,

indicating that there is not a genetic relationship between the Sultarfell-type rhyolite and the local basaltic magmas or the known pre-existing mafic rocks. Both the atypical composition of the Sultarfell-type magmas and the location of Sultarfell in a fissure swarm suggest that the production of these magmas may be decoupled from the central volcano magmatic system.

A potentially viable mechanism for producing rhyolitic magma both on and away from a central volcano is the partial melting of pre-existing silicic rocks in the crust (Table 3.4(c)). This process could generate rhyolitic magma without requiring the high degree of fractional crystallisation or the partial melting of mafic crust that occurs at central volcanoes. The existence of silicic rocks in the crust in this area is demonstrated by the presence of granitic and quartz monzonitic xenoliths at Hungurfit (Gurenko et al., 2015), only 2.4 km west of Sultarfell (Figure 3.10). Silicic xenoliths have been identified at numerous localities in Iceland, including Hekla, Surtsey and Katla (Jakobsson, 1966; Lacasse et al., 2007; Sigurdsson, 1968). The xenoliths are most abundant where rift-jumping has initiated recent volcanism on areas of older crust (Sigurdsson, 1977). Sigurdsson (1977) suggested that the xenoliths are derived from silicic bodies within the crust, such as plagiogranites. The remelting and mobilisation of this silicic material could be a significant source of rhyolitic magma in Iceland and an important consequence of rift propagation into pre-existing crust (Gunnarsson et al., 1998; Sigurdsson, 1977).

The silicic xenoliths at Hungurfit contain interstitial glass (Gurenko et al., 2015) that has a metaluminous to peraluminous composition (molar $(Na_2O + K_2O + CaO)/Al_2O_3 = 0.93$ to 1.19). Gurenko et al. (2015) interpreted that the glass formed through partial melting of the silicic rock, and dated this partial melting episode (using U-Pb zircon geochronology) to ~0.15–0.25 Ma. The interstitial glass has a diverse range of compositions, making it difficult to assess if the glass represents the source melt of rhyolites at Tindfjallajökull or Sultarfell (Figure 3.11). However, Gurenko et al. (2015) noted that the xenoliths are rich in zircons and contain allanite or chevkinite as an accessory mineral. These minerals may have controlled the partitioning of Zr, Nb, Y and the rare earth elements during crystallisation of the original

magma and/or during the later partial melting (Gurenko et al., 2015). The pattern of trace element concentrations seen in the Sultarfell-type magmas, such as the low concentrations of Zr, Nb and La presented in Figure 3.7, could be explained by the presence of zircon, allanite and/or chevkinite in the source rock during partial melting.

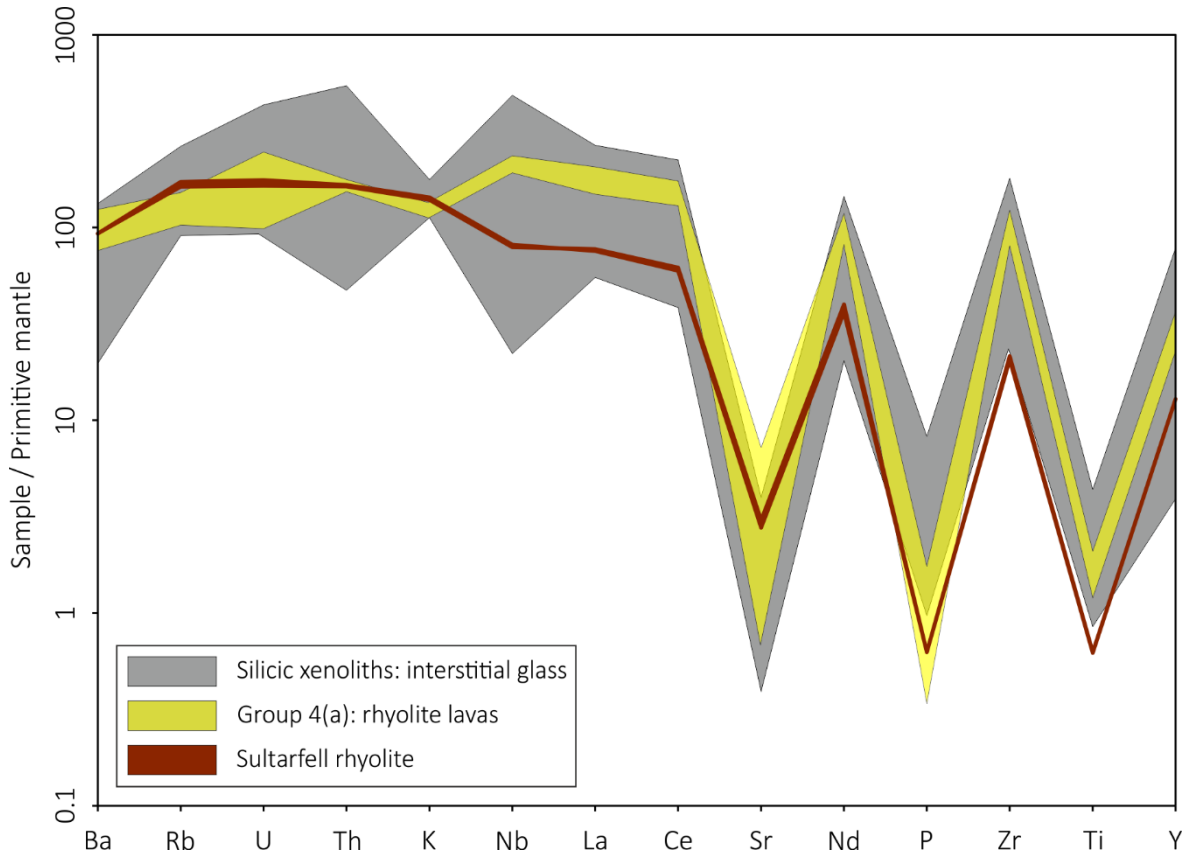

Figure 3.11. Multi-element diagram comparing the trace element composition of the Group 4(a) and Sultarfell rhyolites with the interstitial glass of silicic xenoliths analysed by Gurenko et al. (2015; analysis by EPMA and LA-ICP-MS). The xenoliths were collected from a hyaloclastite ridge 2.4 km to the west of Sultarfell by Gurenko et al. (2015), who interpreted the interstitial glass to be a product of partial melting. The geochemical diversity of partial melts in the xenoliths means that it is difficult to ascertain if these melts have contributed to the rhyolites erupted on Tindfjallajökull and at Sultarfell. Data normalised to primitive mantle using values from Sun and McDonough (1989).

It is interpreted that the Sultarfell-type magmas are derived from partial melting of pre-existing silicic rock in the crust, and that this source rock is represented by the silicic xenoliths found at Hungurfit by Gurenko et al. (2015). The relationship between the Sultarfell-type rhyolites and the xenoliths is evidenced by their spatial proximity, their metaluminous to peraluminous

composition, the presence of zircon, allanite and/or chevkinite in the xenoliths and correspondingly low Zr, Nb, Y and rare earth element concentrations in the Sultarfell-type rhyolites, and the evidence for recent partial melting in the xenoliths. The production of the Sultarfell-type magmas through this process explains their atypical composition relative to the other magmas at Tindfjallajökull. Continued evolution of the rhyolitic magmas may have occurred after their formation, such as through fractional crystallisation of the mineral assemblage observed in the Sultarfell rhyolite (alkali feldspar + Fe-Ti oxides + amphibole).

The origin of the silicic rocks below Tindfjallajökull, brought to the surface as xenoliths at Hungurfit, is unknown (Gurenko et al., 2015). The crust in this area is thought to have formed at the Western Rift Zone ~8 million years ago (Óskarsson et al., 1985; Sæmundsson, 1974). Silicic rocks may have been emplaced at this time (e.g. as silicic differentiates in the crust such as plagiogranites; Sigurdsson, 1977) or during more recent volcanism associated with the Eastern Volcanic Zone (as intrusive or extrusive bodies at a central volcano).

The partial melting of the silicic rocks, dated to ~0.15–0.25 Ma at Hungurfit (Gurenko et al., 2015), may have been triggered by basaltic magmatism at and around Tindfjallajökull. Gurenko et al. (2015) noted that the partial melting of the xenoliths at Hungurfit may be temporally associated with magmatic activity on the fissure swarm in this area. Sultarfell is similarly located in the fissure swarm to the NE of Tindfjallajökull (Figure 3.10), and it is proposed that basaltic magmatism in the fissure swarm resulted in partial melting of silicic rocks and the consequent eruption of the Sultarfell rhyolite. Sultarfell is thus a possible example of rhyolitic volcanism that is not directly associated with a central volcano, but is instead a product of the heating of the crust by fissure swarm magmatism. As the fissure swarm is not thought to be part of the Tindfjallajökull volcanic system (Chapter 2; Sæmundsson and Larsen, 2016), there is not considered to be any association between Sultarfell and Tindfjallajökull.

Although basaltic magma may have provided the crucial heat source to produce the Sultarfell-type rhyolite, there is no evidence to indicate that mixing of basaltic and rhyolitic magmas occurred at Sultarfell itself. Conversely, the Group 3 magmas are made up of basaltic magma mixed with a subordinate component of Sultarfell-type magma. Of the analysed samples, those from Bláfell tuya contain the highest proportion of Sultarfell-type magma: ~30%. This is equivalent to a volume of ~0.08 km^3 of Sultarfell-type magma in the tuya (total volume of Bláfell tuya: ~0.26 km^3). The Sultarfell-type magmas in the Group 3 samples may have been produced during the same partial melting episode as at Hungurfit (associated with fissure swarm magmatism) or may instead be associated with basaltic magmatism at Tindfjallajökull. The four known eruptive units with a Group 3 composition are all thought to date from the last glacial period (based on preservation; Chapter 2), which may indicate that Sultarfell-type magmas have only interacted with basaltic magmas during the most recent stage of Tindfjallajökull's evolution.

The partial melting of pre-existing silicic rock may explain other occurrences of rhyolite in Iceland that are seemingly unrelated to central volcanoes. The Prestahnúkur volcanic system in the Western Volcanic Zone lacks a topographically distinct central volcano (Sæmundsson, 2016), but does host a rhyolitic edifice with a volume of ~0.6 km^3 (McGarvie et al., 2007). The whole-rock composition of the Prestahnúkur rhyolite (reported by McGarvie et al., 2007) is highly comparable to the composition of Sultarfell, and displays the same trace element characteristics (Figure 3.12). Another example of an isolated rhyolitic edifice with a similar composition to Sultarfell is Mælifell, located in the Northern Volcanic Zone (McGarvie, unpublished). Both Prestahnúkur and Mælifell are situated where recent (Late Pleistocene) volcanism has occurred on older crust. It is proposed that these rhyolites, like Sultarfell, are derived from the partial melting of pre-existing silicic rock following the onset of recent magmatism. Further work is needed to confirm this hypothesis, such as the comparison of isotopic ratios in xenoliths with those of the erupted rhyolites.

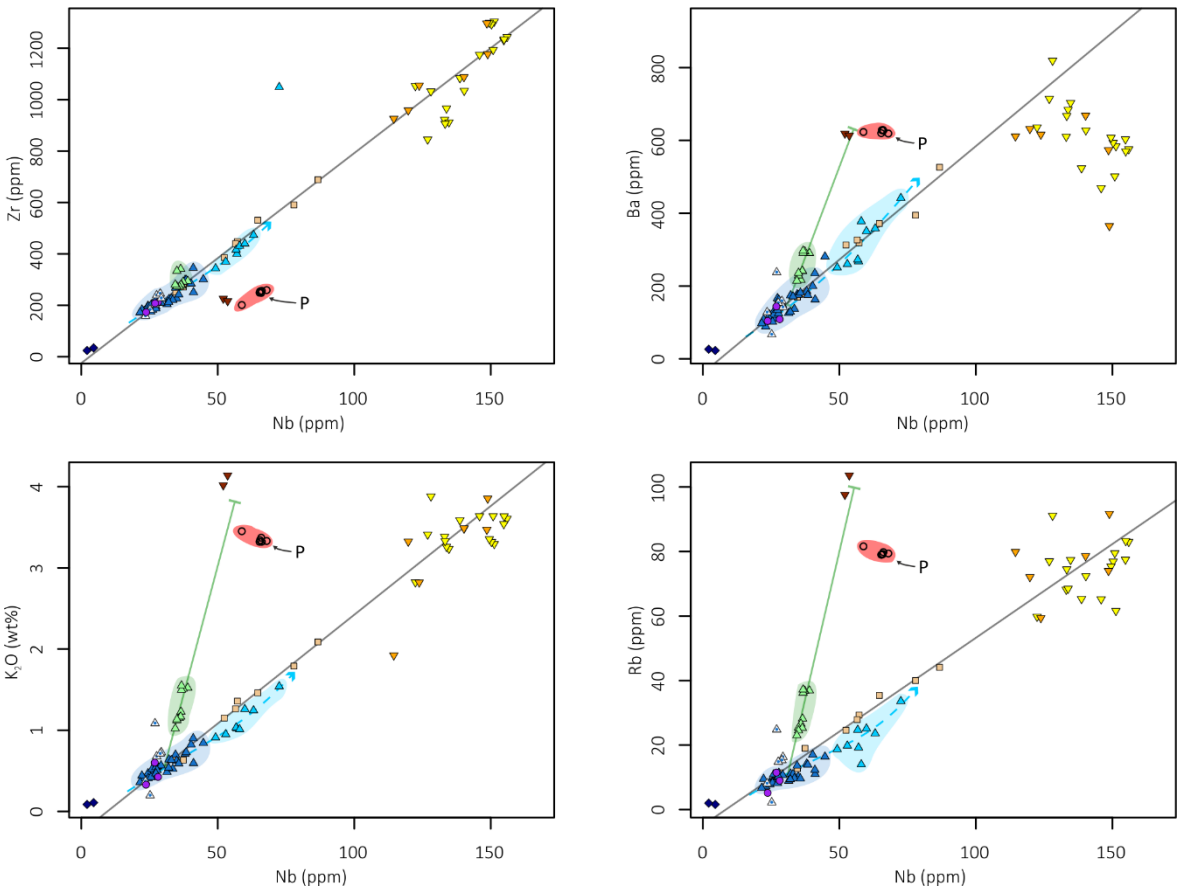

Figure 3.12. The incompatible element geochemistry of the Prestahnúkur rhyolite (highlighted in red and labelled 'P') compared to Tindfjallajökull and the Sultarfell rhyolite. Prestahnúkur data from McGarvie et al. (2007); analysed by whole-rock XRF. The Prestahnúkur rhyolite has a similar composition to the Sultarfell rhyolite, sharing its incompatible element characteristics, which may indicate that the petrogenesis of these magmas was controlled by similar processes.

3.6 CONCLUSIONS

A thorough whole-rock geochemical study of Tindfjallajökull volcano has revealed the dominant magma types and the relationships between them (Figure 3.13). Tindfjallajökull has a broadly bimodal composition with most of the analysed samples defining the basaltic and rhyolitic components of the magmatic system.

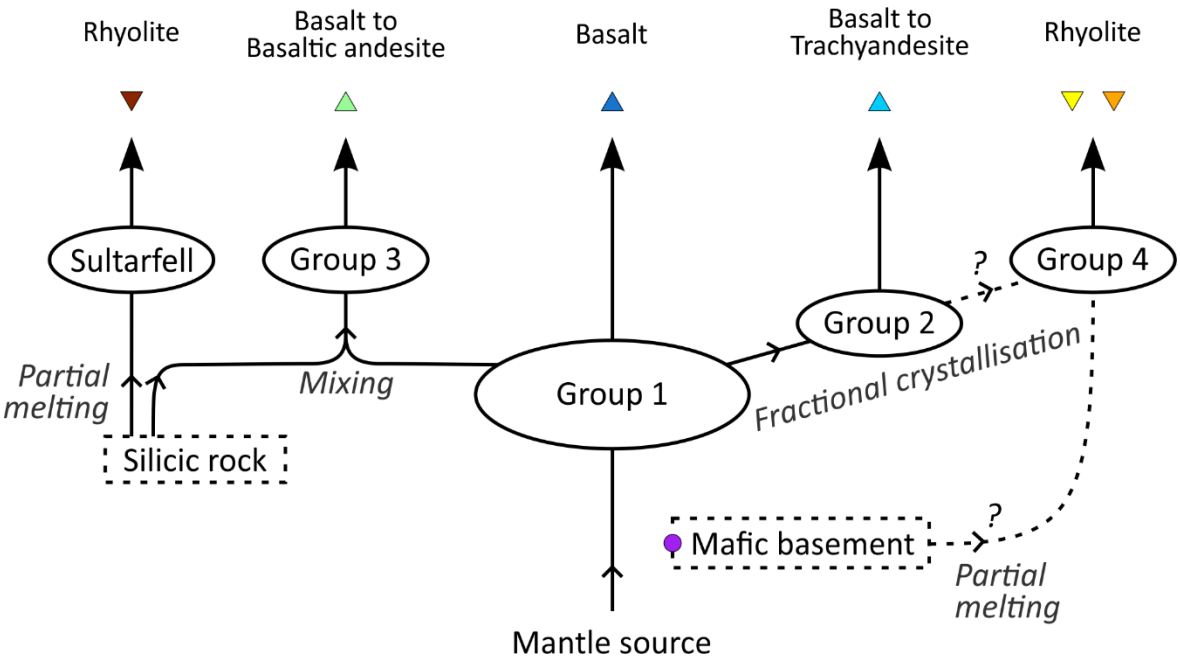

Figure 3.13. Relationships of the various magma groups at Tindfjallajökull. The figure is intended to be a schematic representation of the identified magmas and the processes involved in their evolution – the structure of the plumbing system under Tindfjallajökull is not known. It is interpreted that magmatic evolution has been driven by partial melting, fractional crystallisation, and magma mixing processes.

Geochemical variation within the basalts is predominantly driven by fractional crystallisation of olivine, clinopyroxene, plagioclase and Fe-Ti oxides. Continued fractional crystallisation of basaltic magma has produced a suite of magmas with a basaltic to trachyandesitic evolution path, with apatite as an additional fractionating phase.

The presence of two distinct rhyolite compositions in the Tindfjallajökull area sheds some light on the origins of Icelandic rhyolites. On the Tindfjallajökull edifice itself, rhyolites are interpreted to be derived from the near-solidus differentiation of a mafic source. It is unclear if this source was cooling magma associated with Tindfjallajökull or pre-existing mafic rock that has undergone partial melting during recent magmatism.

The Sultarfell rhyolite, located in the fissure swarm to the NE of Tindfjallajökull, is interpreted to be a product of the partial melting of silicic rock in the crust. Partial melting of the pre-existing silicic rock may have occurred as a consequence of local basaltic magmatism. Rhyolitic

magma produced through the same process has mixed with basaltic magma to erupt as hybrid magmas on the Tindfjallajökull edifice.

Chapter 4

Geochronology of Tindfjallajökull volcano

This chapter employs $^{40}Ar/^{39}Ar$ geochronology to date selected volcanic units at Tindfjallajökull, in order to produce a chronostratigraphic framework for the evolution of the volcano and to link eruptions to the regional climate record. The results of $^{40}Ar/^{39}Ar$ dating are described and discussed, and the limitations of this approach for integrating palaeoenvironmental information are identified.

4.1 Introduction

The absolute dating of volcanic rocks, through radiometric dating methods, can be used to understand the temporal evolution of volcanoes (e.g. Conway et al., 2016; Flude et al., 2008) and to link volcano-derived palaeoenvironmental information with the regional climate record (e.g. McGarvie et al., 2006). Quaternary volcanic eruptions are commonly dated using $^{40}Ar/^{39}Ar$ geochronology, which is based on the decay of ^{40}K to ^{40}Ar (Kelley, 2002). In this technique, the ^{40}K content is determined indirectly through neutron irradiation of the sample – converting a portion of the ^{39}K (which occurs at a constant ratio to ^{40}K) to ^{39}Ar – and the subsequent measurement of ^{39}Ar (Merrihue and Turner, 1966). Therefore, unlike the related $^{40}K/^{40}Ar$ method, it is only necessary to acquire Ar isotopic data and this can be achieved simultaneously on one aliquot of sample (Merrihue and Turner, 1966). $^{40}Ar/^{39}Ar$ geochronology can be applied to the dating of both potassium-bearing phenocrysts and groundmass material, though problems are often encountered in samples that are hydrated, have a non-atmospheric initial Ar ratio, and/or have a low concentration of radiogenic ^{40}Ar (Flude et al., 2017).

The use of $^{40}Ar/^{39}Ar$ geochronology for dating glaciovolcanic sequences is well established (e.g. Clay et al., 2015; Conway et al., 2015; Flude et al., 2010, 2008, McGarvie et al., 2007,

2006; Mee et al., 2009; Smellie et al., 2008, 2018, 2011a, 2011b). An ability to precisely date these eruptions is necessary to put the associated palaeoenvironmental information in a climatic context and to inform models of ice sheet evolution. However, it has proved challenging to determine $^{40}Ar/^{39}Ar$ ages with sufficient precision and accuracy to allow a meaningful comparison to rapidly fluctuating climate (Clay et al., 2015; Flude et al., 2010; Smellie et al., 2008). Previous studies have successfully used $^{40}Ar/^{39}Ar$ techniques to date eruptions to glacial/interglacial periods (e.g. McGarvie et al., 2006) but uncertainties currently preclude the linking of eruptions to century- to millennia-scale climatic episodes (e.g. stadials/interstadials). In this chapter the $^{40}Ar/^{39}Ar$ method is applied to samples from Tindfjallajökull to assess whether the technique is suitable for precisely dating eruptions relative to the regional climate record.

4.2 METHODS

Samples were selected for $^{40}Ar/^{39}Ar$ dating from volcanic units representing the Early, Middle and Late stages of Tindfjallajökull's stratigraphy (Table 4.1; Figure 4.1). Mafic, intermediate and silicic compositions are represented in the selected samples, allowing the dating technique to be tested on the full range of compositions present on Tindfjallajökull. Additionally, the units selected for dating have a variety of eruptive environments. In particular, the selected Late Tindfjallajökull B units include lavas emplaced in ice-free conditions (JM-34 & JM-165), and hyaloclastite-dominated units and tuyas that show evidence of interaction with ice (JM-160, JM-12, JM-14, JM-20 & JM-164; Chapter 2). All selected samples consist of unaltered lava. Analyses were undertaken in two batches: 5 samples in 2015 and 10 samples in 2016 (of which 2 samples were repeat analyses from 2015).

Table 4.1. Stratigraphic context of the samples selected for $^{40}Ar/^{39}Ar$ geochronology. Samples marked with an asterisk were analysed in both 2015 and 2016.

Stratigraphic unit	Sample number (Locality name)
Early Tindfjallajökull: mafic to intermediate, undifferentiated	JM-151 (Tindfjöll) JM-168 (Búraskarð)
Middle Tindfjallajökull: silicic lavas	JM-36 & JM-37 (Saxi) JM-124 (Vestriöxl)
Late Tindfjallajökull A: Central silicic edifice	JM-186 (Ýmir)
Late Tindfjallajökull B: mafic to intermediate lavas	JM-34 (Suðurhlíð); JM-165 (Miðdalur)
Late Tindfjallajökull B: mafic hyaloclastite-dominated units	JM-160 (Litla-Bláfell)
Late Tindfjallajökull B: mafic to intermediate tuyas	JM-12* & JM-14 (Bláfell); JM-20* (Vörðufell); JM-164 (Þrífjöll)

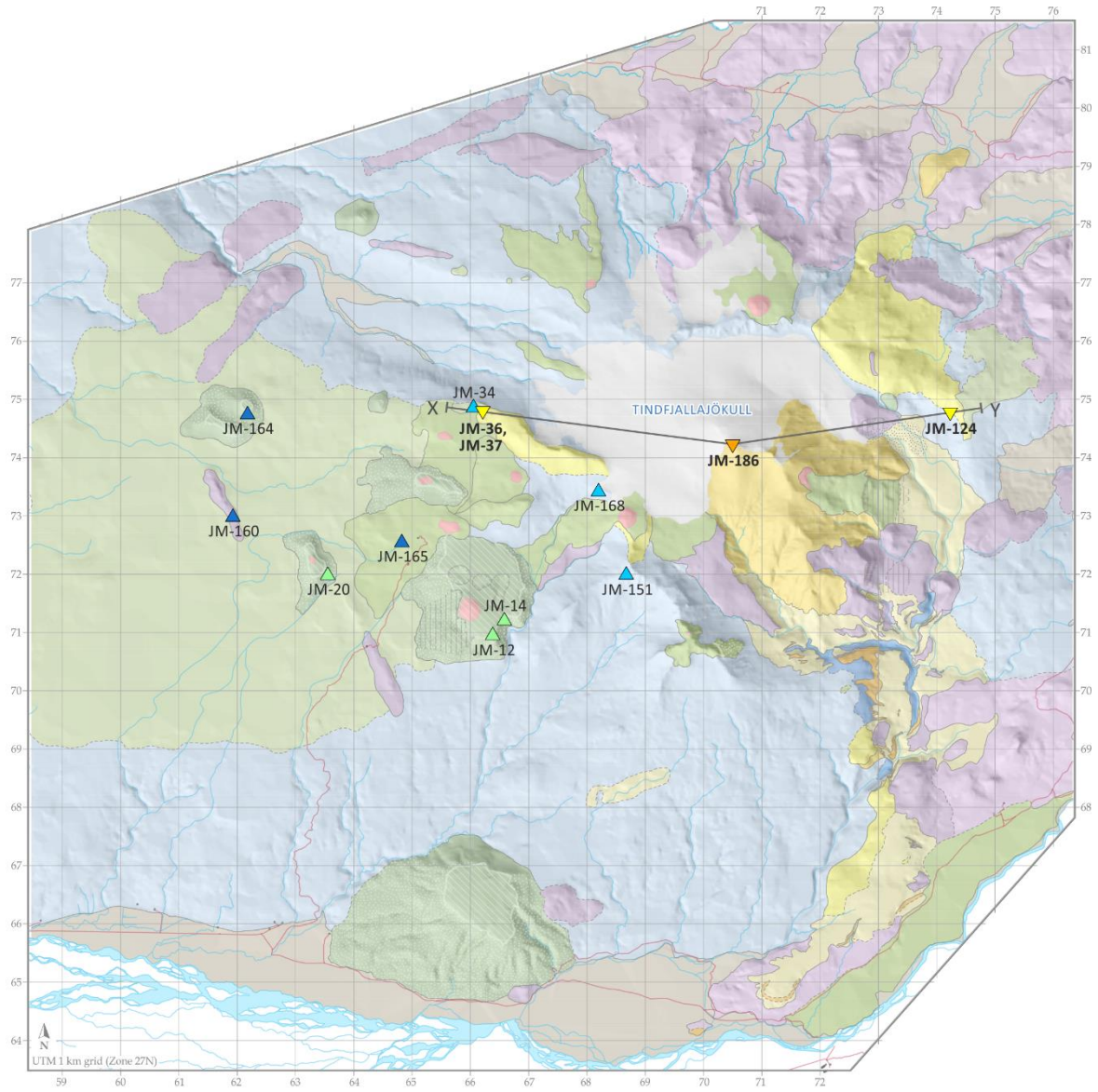

Figure 4.1. Location map of samples selected for $^{40}Ar/^{39}Ar$ geochronology. Marker colours relate to geochemical composition: see Chapter 3. Silicic samples are labelled in bold. The line X–Y marks the position of the cross section in Figure 4.6.

Samples were prepared for $^{40}Ar/^{39}Ar$ analysis using the standard technique employed at The Open University. First, samples were crushed using a jaw crusher and sieved to isolate the 250–500 μm size fraction. For each sample, this size fraction was picked under a binocular microscope to isolate the groundmass component for dating, discarding any altered material or visible phenocrysts. The picked material was ultrasonically cleaned in acetone followed by deionised water. After drying, two ~50 mg splits of each sample were loaded into aluminium foil packets. The samples and GA-1550 biotite standards were irradiated (with cadmium

shielding) at McMaster Nuclear Reactor, Canada for ~4 hours. Foil packets containing GA-1550 were sited between every 10 sample packets to monitor the neutron fluence in the reactor.

Step-heating experiments were carried out using an SPI infrared continuous wave fibre laser (1050–1250 nm) coupled to a Nu Instruments Noblesse noble gas mass spectrometer at The Open University. Samples and standards were loaded into aluminium sample holders in an ultra-high vacuum extraction line. The filled holders were placed under a heat lamp (250 W) for 8 hours prior to analysis, to remove atmospheric gases adhering to the sample surface. Standards were analysed through single-grain total-fusion. Samples were step-heated by rastering the laser across the grains at incrementally higher laser powers until fused (10–15 steps; ~5 minutes heating per step). The advantage of step-heating over total-fusion techniques is that the Ar released by the sample at progressively higher temperatures can be monitored, which may reveal heterogeneities and disturbances in the Ar system (Kelley, 2002). The extraction line was fitted with a ball bearing-filled u-tube cooled with liquid nitrogen, and two getters (room temperature and ~400 °C) to remove unwanted gas species. Automatic inlet into the mass spectrometer was timed to occur ~2 minutes after the end of sample heating (total gettering time: 7 minutes). Argon isotopes ^{36}Ar, ^{37}Ar, ^{38}Ar, ^{39}Ar and ^{40}Ar were measured by the mass spectrometer. Blank measurements were made at the beginning of each day and between every sample step.

The following corrections were applied to the argon isotopic data using *ArMaDiLo* software (Schwanethal, 2008):

- Blank levels: the average blank level of each day was subtracted from the corresponding sample and standard data.
- Mass discrimination: a correction specific to the mass spectrometer, which accounts for bias associated with the mass spectrometer (Table 4.2(a)).

- Radioactive decay: a correction for the decay of ^{37}Ar and ^{39}Ar between the time of irradiation and the time of analysis (Table 4.2(b and c)).
- Neutron-induced interference reactions: corrections for unwanted ^{36}Ar, ^{39}Ar and ^{40}Ar produced through irradiation of Ca and K. These reactions are minimised through the use of cadmium shielding in the reactor. Correction factors are based on the analysis of Ca and K salts (Table 4.2(d–f)).
- Atmospheric argon: the component of the ^{40}Ar that is attributed to an atmospheric source was subtracted from the data to determine the radiogenic ^{40}Ar content ($^{40}Ar^*$). The atmospheric ^{40}Ar content is assumed to be 298.56 × the measured ^{36}Ar content (using the atmospheric $^{40}Ar/^{36}Ar$ ratio determined by Lee et al. (2006); Table 4.2(g)).

Table 4.2. Values used for corrections, decay constants and age of standard in $^{40}Ar/^{39}Ar$ dating.

a)	Mass discrimination ($^{40}Ar/^{36}Ar$)	295
b)	^{37}Ar decay constant	1.975×10^{-2} day^{-1}
c)	^{39}Ar decay constant	7.055×10^{-6} day^{-1}
d)	$(^{36}Ar/^{37}Ar)_{Ca}$	0.000265 ± 0.000001325
e)	$(^{39}Ar/^{37}Ar)_{Ca}$	0.00065 ± 0.00000325
f)	$(^{40}Ar/^{39}Ar)_{K}$	0.0085 ± 0.0000425
g)	Atmospheric $^{40}Ar/^{36}Ar$	298.56 (Lee et al., 2006)
h)	GA-1550 age	99.738 ± 0.104 Ma (Renne et al., 2011)
i)	$^{40}K_{tot}$ decay constant (λ)	$(5.5305 \pm 0.0150) \times 10^{-10}$ yr^{-1} (Renne et al., 2011)

ArMaDiLo was used to calculate J-values, representing the neutron dose received during irradiation, for the GA-1550 biotite standards (age used: Table 4.2(h)). J-values were then linearly interpolated for all the samples according to their position in the irradiated sample tube. Argon isotopic ratios, apparent ages and propagated uncertainties were calculated for

each incremental heating step using *ArMaDiLo* ($^{40}K_{tot}$ decay constant: Table 4.2(i)). The $^{40}Ar/^{39}Ar$ age equation is:

$$t = \frac{1}{\lambda}\ln\left(1 + J\frac{^{40}Ar^*}{^{39}Ar}\right)$$

where t is the time since closure, λ is the total decay constant of ^{40}K, J is the J-value and $^{40}Ar^*$ is the radiogenic ^{40}Ar content (Kelley, 2002).

4.3 RESULTS

The results of the step-heating experiments are assessed with the use of age spectra (apparent age vs. cumulative release of ^{39}Ar) and inverse isochrons ($^{36}Ar/^{40}Ar$ vs. $^{39}Ar/^{40}Ar$). An age spectrum displays the apparent age calculated from each incremental heating step, allowing variations in the Ar released at increasing temperatures to be assessed. If the apparent age of a series of contiguous steps is consistent (i.e. the heating steps form a plateau), a plateau age can be calculated as the error-weighted mean of those steps (McDougall and Harrison, 1999). Age plateaux presented here adhere to the recommendations of Fleck et al. (1977) – i.e. they include >50% of the ^{39}Ar over >3 contiguous steps with similar apparent ages at the 95% confidence level – and were calculated using *Isoplot 4.15* (Ludwig, 2012).

Inverse isochrons represent a mixing line between the radiogenic argon component of a sample ($^{39}Ar/^{40}Ar^*$) and the initial argon component ($^{36}Ar/^{40}Ar$; argon trapped in the sample that has not been generated through radioactive decay, e.g. atmospheric argon). By fitting a regression line to the isotopic data, an isochron is produced that defines: a) the radiogenic argon ratio at the intercept with the x-axis, and b) the initial argon ratio at the intercept with the y-axis (Figure 4.2; Kelley, 2002). Inverse isochrons can therefore be used to determine the age of the sample and to assess whether the initial argon component has an atmospheric composition. Inverse isochron ages and initial argon ratios were calculated using *Isoplot 4.15* (Ludwig, 2012).

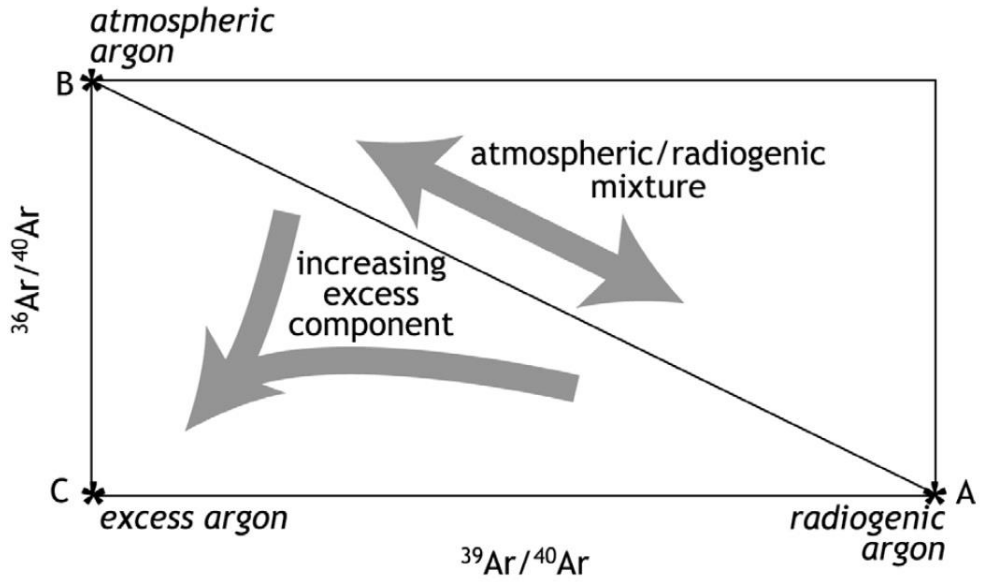

Figure 4.2. Schematic inverse isochron diagram from Kelley (2002). The isochron (diagonal line) represents a mixing line between atmospheric and radiogenic argon compositions. Some samples have an excess of ^{40}Ar that has not formed through radioactive decay ('excess argon'). The presence of excess argon in the sample will decrease the $^{36}Ar/^{40}Ar$ value where the isochron intercepts the y-axis. This is identified as a non-atmospheric initial $^{36}Ar/^{40}Ar$ ratio.

The ages that were successfully determined for the Tindfjallajökull samples are presented in Table 4.3, and a full dataset is provided in Appendix 3. Ages could only be reliably determined on the silicic samples. These samples contain >3 wt.% K_2O, while the mafic and intermediate samples have 0.4–1.5 wt.% K_2O (Chapter 3). The low initial potassium content of the mafic and intermediate samples and their assumed young age results in low yields of radiogenic ^{40}Ar. The mafic and intermediate samples are therefore not suitable for $^{40}Ar/^{39}Ar$ dating without considerably enhanced analytical precision.

Table 4.3 (next page). $^{40}Ar/^{39}Ar$ plateau ages and inverse isochron ages for the successfully dated samples. Mean square weighted deviation (MSWD) values provide a measure of goodness of fit (acceptable range (n=10): 0.5 – 2; Wendt and Carl, 1991) and indicate whether analytical uncertainties are overestimated (low MSWD) or underestimated (high MSWD).

Unit *Sample, material*	Plateau age (ka) ± 2σ	MSWD	Inverse isochron age (ka) ± 2σ	MSWD	Initial $^{40}Ar/^{36}Ar$ ± 2σ
Saxi *JM-36, silicic non-glassy groundmass*	358 ± 15	0.8	364 ± 39 (steps 1–5 only)	1.16	289 ± 38
Saxi *JM-37, silicic glass*	350 ± 27	0.95	310 ± 61	2.1	311 ± 11
Vestriöxl *JM-124, silicic non-glassy groundmass*	209.5 ± 2.8	0.63	253 ± 13	2.8	274 ± 34
Ýmir *JM-186, silicic non-glassy groundmass*	126 ± 18	1.12	125 ± 97	1.3	298 ± 76

4.3.1 Saxi

Two samples (JM-36 & JM-37) from the Middle Tindfjallajökull silicic lava at Saxi were dated and their age spectra and inverse isochron diagrams are presented in Figure 4.3. Both samples yielded anomalously old apparent ages in the higher temperature heating steps (Figure 4.3: light grey steps in age spectra), suggesting that excess ^{40}Ar is contained within a component of the sample (e.g. phenocrysts that were too fine-grained to be removed during sample preparation) and is released at higher temperatures. Plateau ages of 358 ± 15 ka (JM-36) and 350 ± 27 ka (JM-37) were successfully determined using the results of the lower temperature heating steps.

Excess argon in the higher temperature steps is also observed on the inverse isochron diagram of JM-36 (Figure 4.3), which resembles the pattern shown in Figure 4.2. In order to determine a reasonable inverse isochron age for this sample, the high temperature heating steps were excluded (giving an inverse isochron age of 364 ± 39 ka). An isochron could be constructed

for sample JM-37 without excluding steps (inverse isochron age: 310 ± 61 ka). However, the MSDW for this isochron (2.1) is high (according to the recommendations of Wendt and Carl (1991)), suggesting that uncertainties are underestimated. The plotted isochrons of both samples indicate an approximately atmospheric initial $^{40}Ar/^{36}Ar$ ratio (i.e. close to the atmospheric ratio of 298.56 (Lee et al., 2006)), though the slightly high initial $^{40}Ar/^{36}Ar$ ratio in sample JM-37 (311 ± 11) may be an additional indicator that excess ^{40}Ar is present in part of the sample.

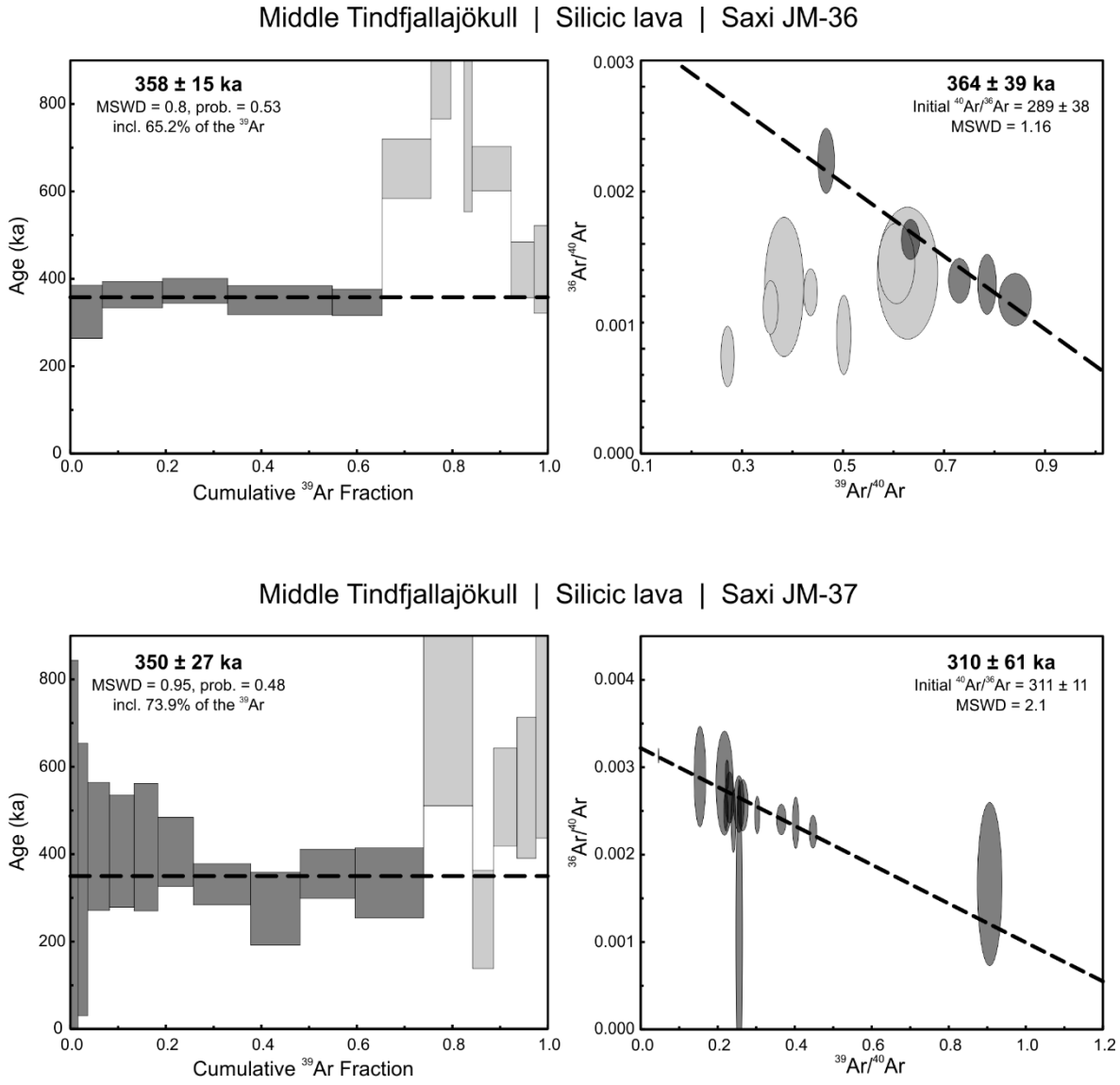

Figure 4.3. $^{40}Ar/^{39}Ar$ age spectra (left) and inverse isochron diagrams (right) for samples JM-36 and JM-37. Light grey steps were not included in plateau/isochron calculations. Plateaux and isochrons are displayed as a black dashed line. The $^{40}Ar/^{39}Ar$ results derived from each plot are shown. Ages are consistent (within uncertainty) across both samples and both methods of calculation.

The ages determined for the Saxi silicic lava overlap for both samples and for both methods of age calculation. The plateau ages, which provide the lowest uncertainties and have acceptable MSWD values, are the preferred ages for these samples.

4.3.2 Vestriöxl

Sample JM-124, from the Middle Tindfjallajökull lava at Vestriöxl, yielded a uniform plateau with an age of 209.5 ± 2.8 ka (Figure 4.4). The inverse isochron gives an older age of 253 ± 13 ka, though its MSWD (2.8) is unacceptably high. It is possible that the isochron is negatively affected by the poor spread of data, with most steps having a low atmospheric argon content. The plateau age is therefore the preferred age for this sample.

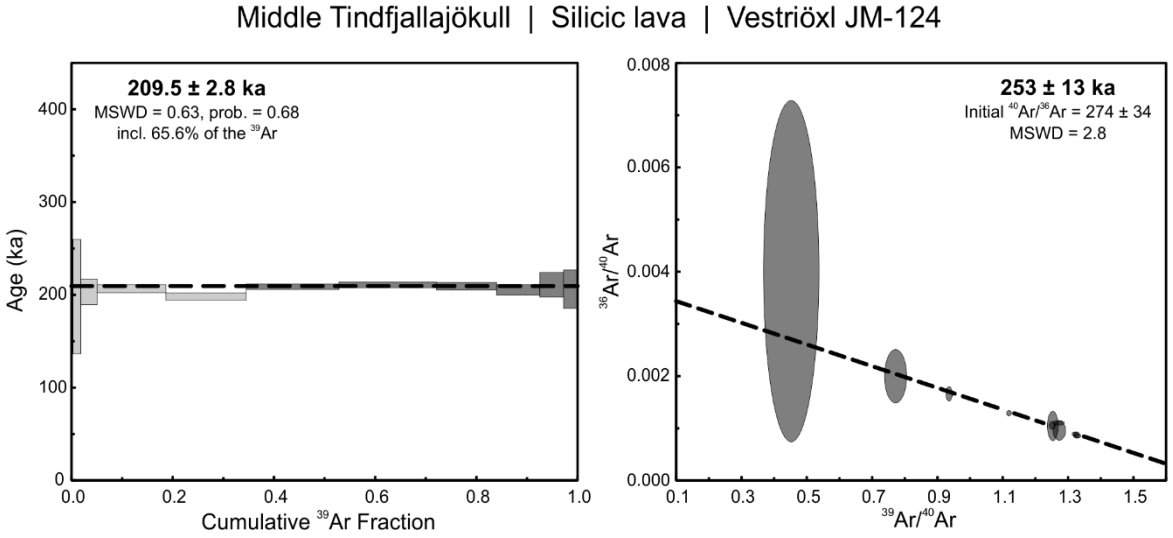

Figure 4.4. $^{40}Ar/^{39}Ar$ age spectrum and inverse isochron diagram for sample JM-124. The age spectrum is uniform and provides a precise plateau age. The inverse isochron age is affected by a poor spread of data and has a high MSWD.

4.3.3 Ýmir

Sample JM-186, from the Late Tindfjallajökull A central silicic edifice at Ýmir, gave a uniform plateau with an age of 126 ± 18 ka (Figure 4.5). A similar age was calculated using an inverse isochron (125 ± 97 ka) and the initial $^{40}Ar/^{36}Ar$ ratio has an atmospheric composition, though the uncertainties are high. High uncertainties may be a result of the low yield of Ar

(particularly ^{36}Ar) measured on this sample (full data: Appendix 3). The plateau age is the preferred age for this sample.

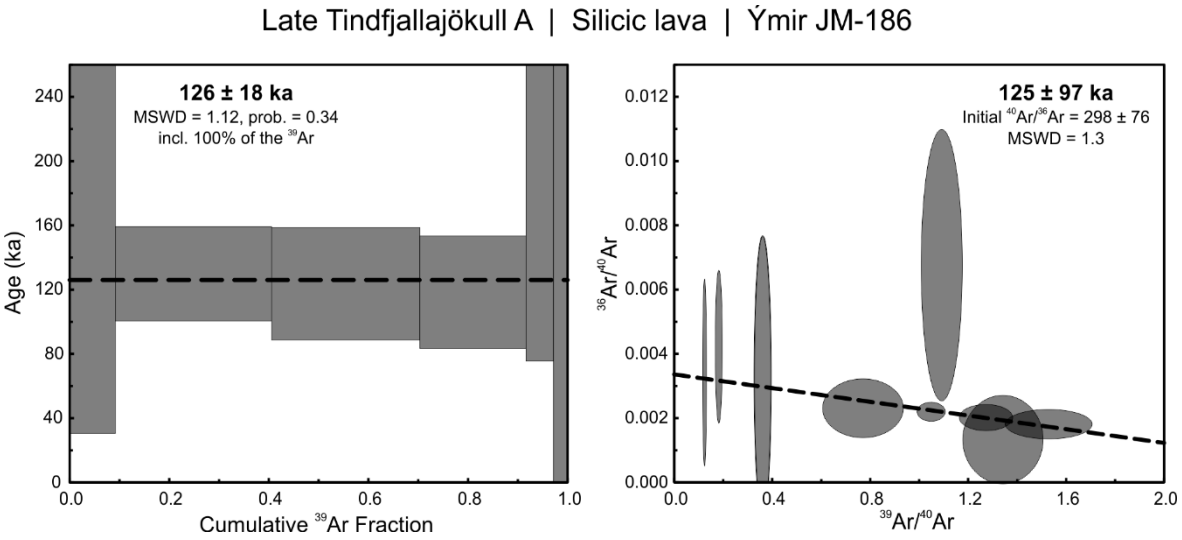

Figure 4.5. $^{40}Ar/^{39}Ar$ age spectrum and inverse isochron diagram for sample JM-186. Both methods of calculating the age give similar results, though uncertainties are high on the inverse isochron.

4.4 DISCUSSION

4.4.1 Temporal evolution of Tindfjallajökull volcano

The new $^{40}Ar/^{39}Ar$ ages are the first geochronological data to be sourced from Tindfjallajökull and they provide a preliminary chronostratigraphic framework for the evolution of the volcano. The age of the Middle Tindfjallajökull silicic lava at Saxi (JM-36 and JM-37) suggests that most of the volume of the volcano – consisting of the Early Tindfjallajökull stratocone – was constructed prior to 358 ± 15 ka (Figure 4.6). The lifespan of Tindfjallajökull therefore extends back hundreds of thousands of years (minimum), consistent with other Icelandic volcanoes that have been the subject of $^{40}Ar/^{39}Ar$ investigation (Torfajökull: >384 or >255 ka (Clay et al., 2015; McGarvie et al., 2006); Ljósufjöll: >653 ka (Flude et al., 2008); Kerlingarfjöll: >345 ka (Flude et al., 2010)).

Samples from the Middle Tindfjallajökull silicic lavas yielded different ages at Saxi (358 ± 15 ka (JM-36) and 350 ± 27 ka (JM-37)) compared to Vestriöxl (209.5 ± 2.8 ka (JM-124); Figure

4.6), suggesting that the lavas that make up this stratigraphic group were emplaced during separate events over a protracted time period. These samples have indistinguishable whole-rock geochemical compositions (Chapter 3) despite this apparent ~150 ka age gap. Further geochronological analyses of the Middle Tindfjallajökull silicic lavas are needed to fully constrain their temporal relationships.

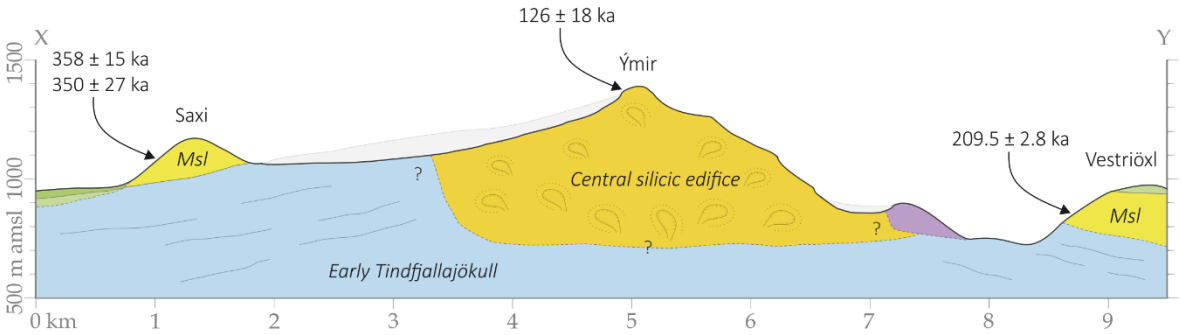

Figure 4.6. Cross section of upper Tindfjallajökull intersecting the successfully dated stratigraphic units (see Figure 4.1 for line of cross section). *Msl* = Middle Tindfjallajökull silicic lava. 2× vertical exaggeration. The Early Tindfjallajökull stratocone predates the Middle Tindfjallajökull silicic lavas (Saxi: 358 ± 15 ka (JM-36)). The Middle Tindfjallajökull silicic lava at Vestriöxl is ~150 ka younger than the lava at Saxi. Lava at the present-day summit of the central silicic edifice (Ýmir: 126 ± 18 ka (JM-186)) post-dates the Middle Tindfjallajökull silicic lavas.

As established through the geological mapping of Tindfjallajökull (Chapter 2), the central silicic edifice (Late Tindfjallajökull A) formed during a later stage of silicic volcanism. The 126 ± 18 ka age of the lava at the present-day summit of the edifice (Ýmir; JM-186) is consistent with this stratigraphy (Figure 4.6). It is not known if the central silicic edifice was constructed during one eruptive event at this date or during multiple eruptive events over a period of time.

In Chapter 2, it was identified that caldera subsidence or a period of significant erosion occurred between emplacement of the Middle Tindfjallajökull lavas and the Late Tindfjallajökull A central silicic edifice. This dissection of the volcano must have occurred within the time interval bracketed by the eruption ages of Vestriöxl (209.5 ± 2.8 ka (JM-124)) and Ýmir (126 ± 18 ka (JM-186)).

4.4.2 Linking dated eruptions to regional climate conditions

The dated Tindfjallajökull eruptions are compared to a record of past climate in Figure 4.7. The eruptions pre-date the ~120 kyr climate record derived from the Greenland ice cores, so δD climate proxy data from the EPICA Dome C (EDC) ice core in Antarctica are used instead (data from Jouzel et al. (2007)). In order to gain a closer approximation of climate in the North Atlantic region, Barker et al. (2011) have modelled a synthetic Greenland climate record using the EDC data (Figure 4.7). The regional climate state can therefore be deduced for each dated eruption.

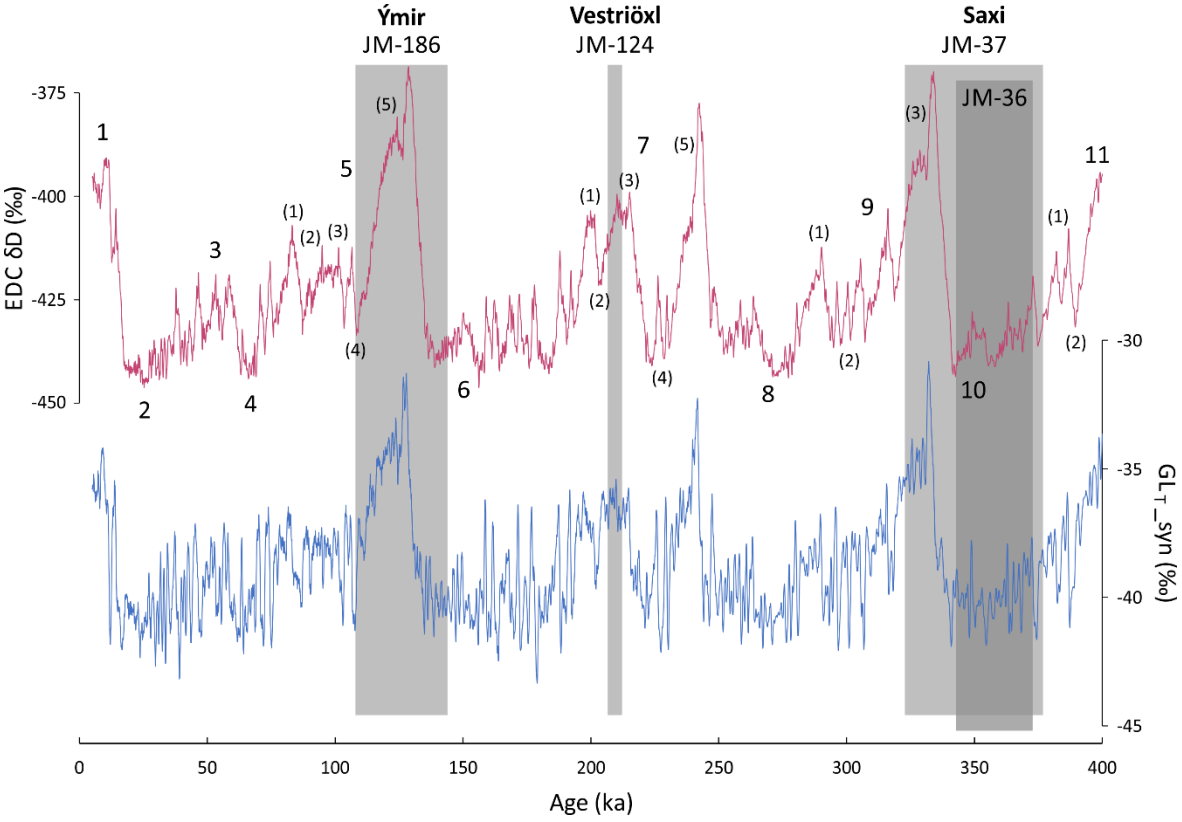

Figure 4.7. Comparison of Tindfjallajökull $^{40}Ar/^{39}Ar$ plateau ages (± 2σ; grey boxes) with the climate record. EDC δD data (upper plot) from Jouzel et al. (2007). Synthetic Greenland climate data (GL_T_syn; lower plot) from Barker et al. (2011). The climate data is fitted to the EDC3 timescale which has a 2σ uncertainty of ~6 kyr (Parrenin et al., 2007). Marine isotope stages (according to Jouzel et al. (2007)) are labelled, with substages in brackets. Cold (glacial) periods have even Marine Isotope Stage (MIS) numbers; warm (interglacial) periods have odd MIS numbers. The lava at Saxi was emplaced during MIS 10, the Vestriöxl lava was emplaced during MIS 7.3, and Ýmir was emplaced during MIS 5.5 or 6.

The $^{40}Ar/^{39}Ar$ age of Saxi sample JM-37 (350 ± 27 ka) has a relatively large uncertainty and consequently overlaps with more than one Marine Isotope Stage: MIS 9.3 and MIS 10 (Figure 4.7). However, the lower uncertainty achieved on sample JM-36 (358 ± 15 ka) means that the Saxi lava can be dated to MIS 10, a glacial period. The lava at Vestriöxl (JM-124: 209.5 ± 2.8 ka) was emplaced during a period of warmer climate: MIS 7.3. Physical features diagnostic of a particular eruptive environment have not been observed in either of these lavas (Chapter 2), so the palaeoenvironment at Tindfjallajökull during these climatic stages cannot currently be reconstructed.

Due to the uncertainty in the eruption date, the Ýmir sample (JM-186: 126 ± 18 ka) cannot be assigned to a specific climate period. The eruption could have occurred during the final part of MIS 6 – a glacial period – or during MIS 5.5 – an interglacial period. The steep-sided morphology and the fragmental lithologies of the central silicic edifice may indicate that the eruption interacted with a thick body of ice (Chapter 2). This environment would be most consistent with the cold conditions at the end of MIS 6, though the available evidence does not allow a robust linking of environment to climatic stage.

The dissection of the volcano between the emplacement of the Middle Tindfjallajökull lavas and the Late Tindfjallajökull A central silicic edifice can be dated to MIS 6 or the latter part of MIS 7 (i.e. MIS 7.1 or 7.2). It is possible that this dissection was associated with glacial erosion during the cold MIS 6, though further geochronological data are needed to constrain the timing of this episode.

4.4.3 Limitations of using absolute dating to link eruptions to the climate record

The attempt at linking Tindfjallajökull eruptions to the climate record using $^{40}Ar/^{39}Ar$ geochronology demonstrates the limitations of using absolute dating techniques for this purpose. Firstly, dating of the mafic and intermediate samples was not successful, highlighting

the critical influence of geochemical composition on the suitability of young samples for $^{40}Ar/^{39}Ar$ dating.

Secondly, uncertainties in the eruption dates limit the precision that can be achieved when comparing these dates to climate. If an eruption is dated with relatively low uncertainty to a time of stable climate (e.g. the dating of sample JM-124 to MIS 7.3), it is possible to make a meaningful estimate of the climate at the time of the eruption. However, if an eruption date overlaps with a large range of climatic conditions, as demonstrated by sample JM-186 (Figure 4.7), it is not possible to determine the climatic state at the time of the eruption. This problem is exacerbated by the highly unstable climate of the Pleistocene, with abrupt shifts in climate occurring over decadal timescales (Kindler et al., 2014).

Thirdly, this approach involves the comparison of two independent absolute dating techniques: the radiometric eruption dates and the ice core chronology (constructed using annual layer counting (e.g. Svensson et al., 2008) or a combination of modelling and independent age markers (e.g. Parrenin et al., 2007)). There are uncertainties associated with the climate chronology as well as the radiometric eruption dates; for instance the EDC timescale used in Figure 4.7 has a 2σ uncertainty of ~6 kyr (Parrenin et al., 2007). Uncertainties will always limit the degree of precision that can be achieved when attempting to compare the results of two different absolute dating techniques. Therefore, without a considerable decrease in uncertainties, absolute dating alone is not well suited for precisely dating volcanic eruptions (and associated palaeoenvironmental information) relative to the rapidly fluctuating climate of the Pleistocene.

4.5 CONCLUSIONS

Absolute dating of Tindfjallajökull eruptions, using $^{40}Ar/^{39}Ar$ geochronology, provides a preliminary chronostratigraphic framework for the evolution of the volcano. Plateau ages of the dated silicic eruptions range from 358 ± 15 ka (Saxi) to 126 ± 18 ka (Ýmir). Dating of

mafic and intermediate samples was unsuccessful, due to their low content of radiogenic argon.

By comparing the $^{40}Ar/^{39}Ar$ ages to the regional climate record, eruptions can be dated to climatic stages. The Middle Tindfjallajökull silicic lavas at Saxi and Vestriöxl were emplaced during the cold MIS 10 and the warm MIS 7.3 respectively. The present-day summit of the central silicic edifice (Ýmir; Late Tindfjallajökull A) was emplaced during the latter part of the MIS 6 glacial period or during the MIS 5.5 interglacial.

Although silicic eruptions can be dated to Marine Isotope Stages using $^{40}Ar/^{39}Ar$ geochronology, uncertainties in the eruption ages and in climate chronologies limit the precision with which eruptive environments can be linked to climate. This absolute dating technique is not well suited for precisely dating volcanic eruptions relative to rapidly fluctuating climate.

Chapter 5

The rhyolitic eruption of Torfajökull ~55 ka: widespread tephra dispersal and ignimbrite emplacement from a subglacial volcano

This chapter addresses the issue raised in Chapter 4: the need for an alternative approach to absolute dating if glaciovolcanic sequences are to be precisely linked to records of past climate. Here, a different approach is tested that involves the correlation of rhyolitic eruption products across multiple depositional settings. If rhyolitic glaciovolcanic eruptions can result in widespread tephra dispersal (as is suspected but unconfirmed), it is possible that known rhyolitic tephra horizons in distal settings can be correlated to glaciovolcanic sequences at their source volcano. Distal tephras are commonly found in palaeoclimate archives (e.g. ice cores) and can therefore be used to precisely date volcanic eruptions relative to the climate stratigraphy. Correlating a glaciovolcanic sequence with a distal tephra horizon would provide a direct tie-line between glaciovolcanism-derived palaeoenvironmental information and the regional climate record.

This chapter has been adapted from a paper (including supplementary materials) submitted to and reviewed by *Geology*. Moderate revision of the paper is required before resubmission to the journal.

5.1 Introduction

The stratigraphic correlation of volcanic products, particularly tephra, is a powerful means of studying the past eruptive behaviour of volcanoes and linking together disparate palaeoenvironmental records (Lowe, 2011). The more depositional settings in which an

eruption is identified, the more information can be pooled together to understand the eruption and the prevailing environmental conditions. However, it can be challenging to find correlations of volcanic products between different realms (e.g. Abbott et al., 2016), especially in terrestrial settings that are subjected to periodic glaciation (Larsen and Eiríksson, 2008). In this chapter, correlation methods are used to a) assess the tephra dispersal mechanisms of rhyolitic glaciovolcanic eruptions, and b) precisely integrate glaciovolcanism-derived palaeoenvironmental data with the regional climate record.

Current knowledge of the behaviour of rhyolitic glaciovolcanic eruptions is drawn from proximal deposits, which show that the explosivity of these eruptions is driven by magmatic volatiles regardless of ice cover (Owen et al., 2013a; Stevenson et al., 2011). However, without any established correlations between glaciovolcanic rhyolites and distal tephras, it is not known if these eruptions have produced widespread tephra deposits (McGarvie, 2009; Tuffen et al., 2007, 2002). Identification of tephra from a rhyolitic glaciovolcanic eruption in distal settings would provide information on tephra dispersal processes and, importantly, establish a direct link between the eruption and the regional paleoclimate archive.

The distal tephra in this study is II-RHY-1, the rhyolitic component of North Atlantic Ash Zone II, which has been correlated with the Thórsmörk Ignimbrite in south Iceland (Lacasse et al., 1996; Sigurdsson, 1982; Tomlinson et al., 2010). The eruption has been dated to the last glacial period at 55,380 ± 2367 (2σ) yr b2k (Greenland Ice Core Chronology 2005 (GICC05); Svensson et al., 2008). II-RHY-1 is an important part of the tephrostratigraphy of the North Atlantic region due to its widespread distribution and occurrence during an abrupt climate transition: the cooling at the end of Greenland Interstadial (GI) 15.2 (Austin et al., 2004; Austin and Abbott, 2010; Bramlette and Bradley, 1941; Zielinski et al., 1997). Atmospheric transport of the tephra resulted in distal fallout onto the Greenland ice sheet and sea ice (Ram and Gayley, 1991; Ruddiman and Glover, 1972), leading to sea-ice rafting of the tephra up to 2300 km to the south and southwest of Iceland (Ruddiman and Glover, 1972; Wastegård et al., 2006). The volume of airfall tephra, ice-rafted tephra and redeposited tephra in the marine

stratigraphy is substantial, but not well quantified (Brendryen et al., 2011; Lackschewitz and Wallrabe-Adams, 1997; Ruddiman and Glover, 1972; Voelker and Haflidason, 2015).

The source of the eruption that produced the Thórsmörk Ignimbrite and II-RHY-1 has not yet been identified (Chapter 2). It has been suggested that Tindfjallajökull volcano is the source of the ignimbrite (Jørgensen, 1980). However, Grönvold et al. (1995) noted a geochemical similarity between II-RHY-1 and rhyolites at Torfajökull volcano, particularly the Ring Fracture Rhyolites. These suggested source volcanoes, as well as other local volcanoes Eyjafjallajökull and Katla, are considered in this chapter.

5.2 SAMPLES AND METHODS

Potential correlations between samples from distal, medial and proximal settings were investigated using both geochemistry and geochronology.

5.2.1 II-RHY-1 sample information and preparation

II-RHY-1 tephra shards were extracted from four North Atlantic marine sediment cores (Figure 5.1; Table 5.1). The occurrence and stratigraphic position of II-RHY-1 in the sediment cores were determined by Abbott et al. (2018). Samples of freeze-dried sediment core known to contain II-RHY-1 were immersed in dilute (10%) hydrochloric acid overnight. Fine sediment was then removed by passing through a 25 μm nylon mesh. Density separation was carried out by centrifuging the >25 μm fraction in sodium polytungstate (SPT) prepared to 2.3 g/cm^3, to remove low density biogenic material. The target density fraction of 2.3–2.5 g/cm^3 was then floated and extracted using SPT prepared to 2.5 g/cm^3 to separate the rhyolitic shards from denser minerogenic material. SPT was removed from the extracted tephra by centrifuging three times in distilled water. In preparation for geochemical analysis, tephra shards were evaporated onto a frosted glass slide, before being covered in epoxy resin. Shards were exposed using 14 μm silicon carbide paper and polished using a 3 μm diamond suspension.

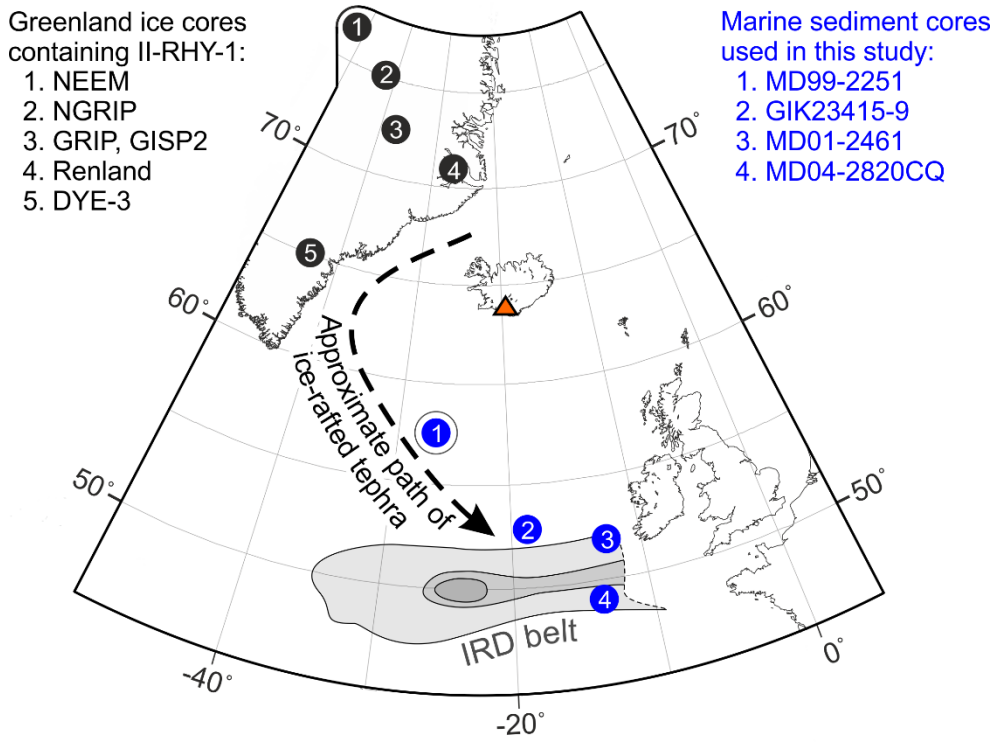

Figure 5.1. Location map of II-RHY-1 samples used in this study, and dispersal of II-RHY-1 in the North Atlantic. The location of the ice-rafted debris (IRD) belt is specific to the time period (early isotope stage 3) and is sourced from Ruddiman (1977). Path of ice-rafted tephra from Ruddiman and McIntyre (1984).

Table 5.1. II-RHY-1 sample locations and analyses undertaken. *Age not determined.

Core	Depth	Latitude (° N)	Longitude (° W)	EPMA	LA-ICP-MS	$^{40}Ar/^{39}Ar$
MD99-2251	2014-2015 cm	57.4478	27.9078	✓	✓	✓*
GIK23415-9	429-430 cm	53.1783	19.1450	✓	✓	
MD01-2461	947-948 cm	51.7483	12.9150	✓	✓	
MD04-2820CQ	610-611 cm	49.0697	13.4128	✓	✓	

The tephra shards are up to 300 μm across and their morphologies include cuspate shards, platy shards and pumiceous shards (Figure 5.2).

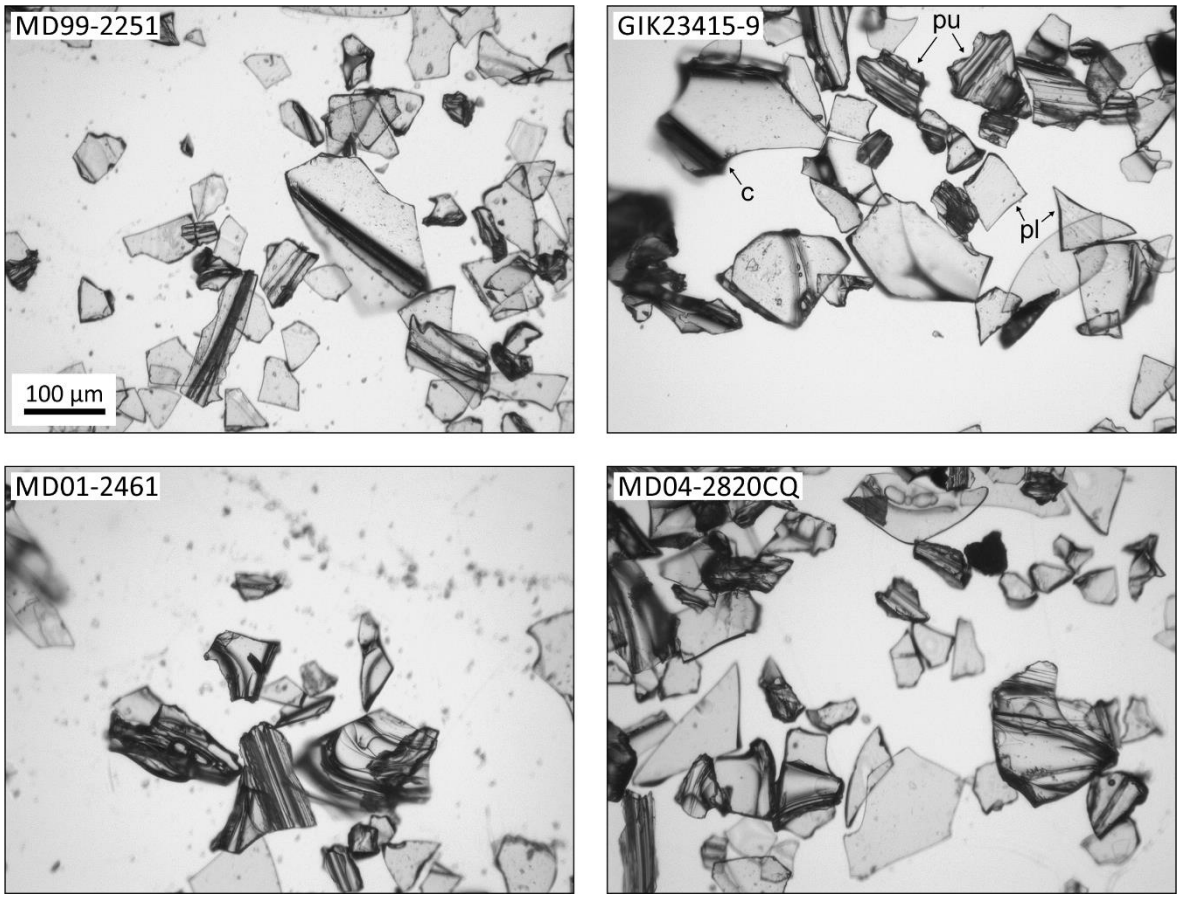

Figure 5.2. Photomicrographs (greyscale) of II-RHY-1 ash shards from each of the four marine sediment cores. A range of shard morphologies is present including platy (pl), cuspate (c) and pumiceous (pu) shards (labelled in the GIK23415-9 image), which are formed at vesicle walls, at vesicle junctions, and in microvesicular magmas respectively (McPhie et al., 1993). All photos are the same scale and show the extracted sediment core material after removal of the <25 µm size fraction, the <2.3 g/cm^3 density fraction and the >2.5 g/cm^3 density fraction.

5.2.2 Thórsmörk Ignimbrite sample information and preparation

Ash samples were collected from the non-welded domains of the Thórsmörk Ignimbrite during field mapping of Tindfjallajökull volcano (Figure 5.3; Table 5.2). The samples were cleaned in acetone, followed by deionised water, in a sonic bath. Shards were then mounted in epoxy resin blocks, exposed using 14 µm silicon carbide paper and polished using a 3 µm diamond suspension. The shards are up to 600 µm across and have cuspate morphologies (Figure 5.4).

Glassy fiamme samples – flattened pumices from a welded domain of the ignimbrite – were collected from the main area of ignimbrite outcrop (Figure 5.3; Table 5.2). Crystals of anorthoclase, pyroxene, Fe-Ti oxides and fayalite are also present in the ignimbrite, as well as pumice, xenoliths and basaltic juvenile clasts.

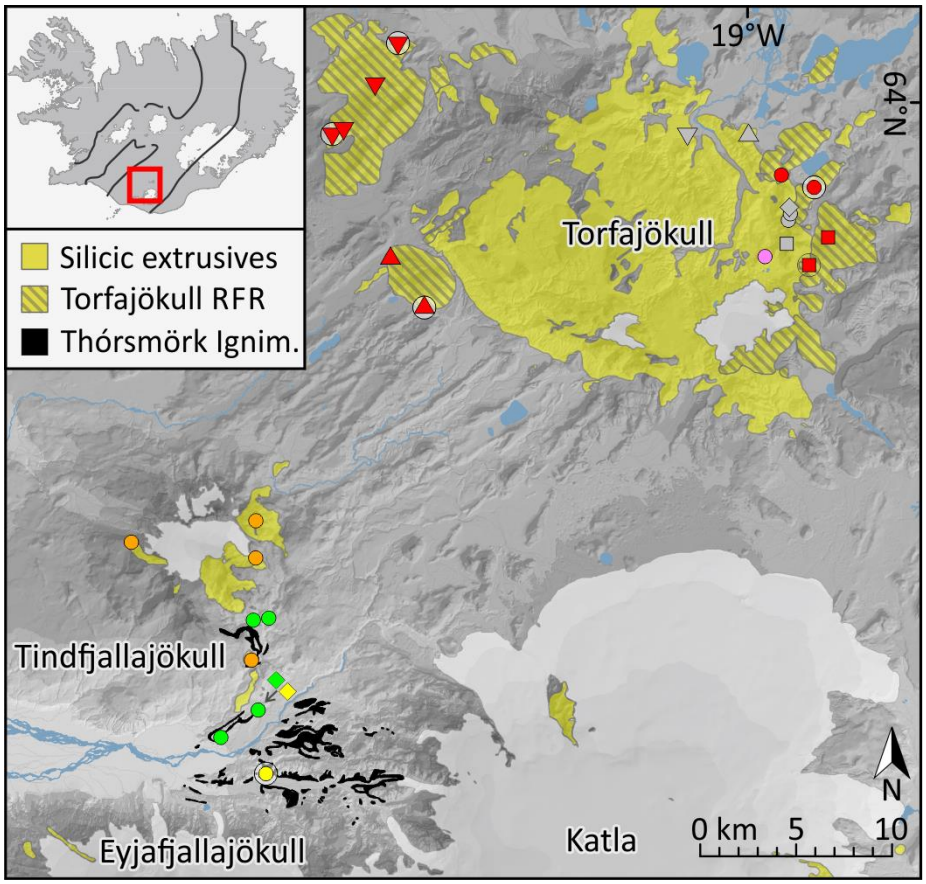

Figure 5.3. Location map of the Thórsmörk Ignimbrite and neighbouring volcanoes in southern Iceland. Geological mapping from Jørgensen (1980), Jóhannesson and Sæmundsson (1989), Sæmundsson and Friðleifsson (2001) and Moles et al. (2018). RFR: Ring Fracture Rhyolites. Markers indicate sample locations (Key: Figure 5.5).

Table 5.2. Thórsmörk Ignimbrite sample locations and analyses undertaken.

Sample type	Sample name	Latitude (° N)	Longitude (° W)	EPMA	LA-ICP-MS	$^{40}Ar/^{39}Ar$
Ash	JM-184	63.7571	19.5215	✓	✓	
Ash	JM-205	63.7015	19.5548	✓	✓	

Sample type	Sample name	Latitude (° N)	Longitude (° W)	EPMA	LA-ICP-MS	$^{40}Ar/^{39}Ar$
Ash	JM-219	63.7147	19.5156	✓	✓	
Ash	JM-228	63.7583	19.5054	✓	✓	
Fiamme	JM-252	63.6846	19.5076	✓	✓	✓
Fiamme	JM-253	63.6846	19.5076	✓	✓	

Tomlinson et al. (2010) samples were collected from the same location as JM-219 (E. Tomlinson, pers. comm. 2017).

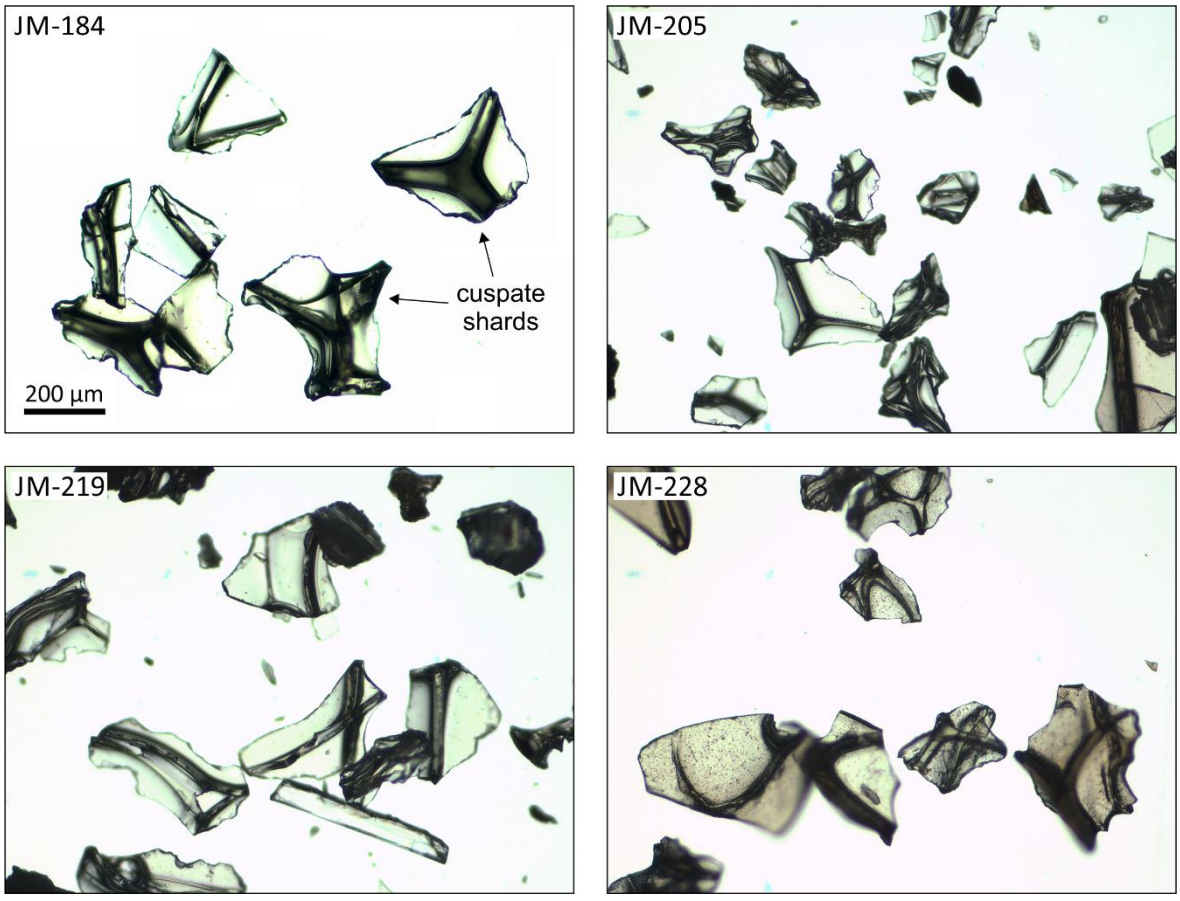

Figure 5.4. Photomicrographs (colour) of ash shards from each of the four Thórsmörk Ignimbrite ash samples. These ash shards are larger than the II-RHY-1 shards and are dominated by cuspate morphologies, often having y-shaped structures formed at the junctions between vesicles (McPhie et al., 1993). All photos are the same scale and show the ash samples after they were cleaned (submersion in acetone followed by deionised water in sonic bath).

5.2.3 Tindfjallajökull lavas sample information

Four rhyolite lava samples were selected from Tindfjallajökull (Table 5.3; Appendix 1). Samples JM-37, JM-80 and JM-147 are glassy rhyolite lavas from the Middle Tindfjallajökull stratigraphic group (Chapter 2). Sample JM-130 is also a glassy rhyolite and is from an intrusive lava lobe within the Late Tindfjallajökull A central silicic edifice (Chapter 2). Phenocrysts and microphenocrysts are typically alkali feldspar > amphibole > Fe-Ti oxides.

Table 5.3. Tindfjallajökull sample locations and analyses undertaken. *$^{40}Ar/^{39}Ar$ dating of JM-37 is presented in Chapter 4.

Unit	Sample name	Latitude (° N)	Longitude (° W)	EPMA	LA-ICP-MS	$^{40}Ar/^{39}Ar$
Saxi	JM-37	63.7926	19.6517	✓		✓*
Jökulskarð	JM-80	63.8028	19.5200	✓		
Hestur	JM-147	63.7382	19.5197	✓		
Ymir (East)	JM-130	63.7856	19.5161	✓		

5.2.4 Torfajökull lavas sample information

Proximal lavas were sampled at Torfajökull (17 samples; Table 5.4). These eruptions produced a significant proportion of fragmental material (e.g. hyaloclastite, ash), though samples were sourced from lava lobes and/or capping lavas to avoid alteration effects. All samples are glassy rhyolite except non-glassy rhyolite samples JM-250 and JM-247. Phenocrysts and microphenocrysts are typically anorthoclase > clinopyroxene (or amphibole) > Fe-Ti oxides ± fayalite. The selected lavas include eruptions known to have occurred during the last glacial period (i.e. Ring Fracture Rhyolites, Bláhnúkur and Unnamed Ridge B (McGarvie, 1984; McGarvie et al., 2006; Clay et al., 2015)). Previously published $^{40}Ar/^{39}Ar$ ages are compiled in Table 5.5.

Table 5.4. Torfajökull sample locations and analyses undertaken. *Age not determined for TJ97-16.

	Unit	Sample name	Latitude (° N)	Longitude (° W)	EPMA	LA-ICP-MS	$^{40}Ar/^{39}Ar$
Ring Fracture Rhyolites	Kirkjufell	TJ99-2	63.9607	18.9275	✓	✓	
	Kirkjufell	TJ99-4	63.9655	18.9615	✓	✓	✓
	Illihnúkur	TJ97-16	63.9241	18.9345	✓	✓	✓*
	Illihnúkur	TJ97-18	63.9374	18.9141	✓	✓	
	Laufafell	JM-40	63.9278	19.3790	✓	✓	
	Laufafell	JM-250	63.9030	19.3479			✓
	Rauðfossafjöll	TJ97-29	63.9862	19.4297	✓	✓	
	Rauðfossafjöll	TJ98-18	64.0071	19.3965	✓	✓	
	Rauðfossafjöll	TJ98-43	64.0263	19.3723	✓	✓	✓
	Rauðfossafjöll	JM-247	63.9830	19.4467			✓
Other Rhyolites	Unnamed ridge A	TJ98-05	63.9276	18.9812	✓	✓	
	Unnamed ridge B	TJ97-09	63.9478	18.9542	✓		
	Unnamed ridge B	TJ97-12	63.9446	18.9563	✓	✓	
	Bláhnúkur	TJ98-40	63.9839	19.0636	✓		
	Hábarmur	TJ97-14	63.9341	18.9581	✓	✓	
	North Hábarmur	TJ98-34	63.9509	18.9553	✓	✓	
	Gvendarhyrna	TJ97-22	63.9861	18.9986	✓		

Table 5.5. Previously published $^{40}Ar/^{39}Ar$ ages of Torfajökull samples used in this study, and unpublished Thórsmörk Ignimbrite $^{40}Ar/^{39}Ar$ age. Published ages are recalculated to the updated decay constant and standard age values used in this study. RFR: Ring Fracture Rhyolites. *Note that Clay et al. (2015) demonstrated that feldspars give erroneously old ages at Torfajökull, so ages determined on feldspars should be treated with caution. **Clay et al. (2015) dated a different sample from Hábarmur (TJ97-15, rhyolite glass), which yielded an age of 255 ± 20 ka (recalculated to 258 ± 20 ka).

Unit *Sample, material*	Age (ka) ± 2σ	Recalculated age (ka) ± 2σ	Reference
RFR – Rauðfossafjöll *TJ97-29, feldspar**	67 ± 18	68 ± 18	McGarvie et al., 2006
RFR – Illihnúkur *TJ97-18, feldspar**	72 ± 14	73 ± 14	McGarvie et al., 2006
Unnamed Ridge B *TJ97-09, rhyolite glass*	83 ± 12	84 ± 12	McGarvie et al., 2006
Bláhnúkur *TJ98-40, rhyolite glass*	108 ± 22	110 ± 22	Clay et al., 2015
Gvendarhyrna *TJ97-22, feldspar**	278 ± 36	281 ± 36	McGarvie et al., 2006
Hábarmur** *TJ97-14, rhyolite glass*	384 ± 40	388 ± 40	McGarvie et al., 2006
Thórsmörk Ignimbrite *Feldspar*	54.5 ± 2	Standard and decay constant used not known	Abstract: Sigurdsson et al., 1998

5.2.5 EPMA procedures

The major element geochemistry of tephras and glassy lavas was determined using electron probe microanalysis (EPMA). Analyses were carried out using a Cameca SX100 WDS electron probe microanalyser at The Open University. For unconsolidated tephras, analyses were made on individual shards. For fiamme and lava samples, multiple matrix glass analyses were made

per thin section. Normal operating conditions were an accelerating voltage of 20 keV, beam current of 20 nA, and spot size of 10 μm. In samples susceptible to volatilisation, Na_2O was analysed first with a reduced beam current (10 nA) and a larger spot size (20 μm). Rhyolite glass standard VG-568 was analysed concurrently with all samples.

Glass shard data often have major elements totals <100% due to hydration, and the data are normalised to 100% totals prior to comparison with other samples. Compositional data of lava and fiamme samples were also normalised to maintain consistency, despite hydration not being apparent in these samples. As totals are typically 99–101.5%, this has little effect on the data. However, normalisation may be detrimental where alteration has caused preferential mobilisation of particular element oxides (e.g. Na_2O). Tindfjallajökull samples JM-130 and JM-147 have variable mobile element concentrations (Figure 5.6(E–H)), suggesting that alteration has occurred. The mobile element data from these samples are therefore treated with caution. In normalising the data from these samples, all element abundances have been increased by 3.0% and 1.9% respectively, despite alteration not having a proportional effect on all elements. This effect does not influence the interpretations made in this chapter.

5.2.6 LA-ICP-MS procedures

The trace element geochemistry of tephras and lavas was determined using laser ablation inductively coupled plasma mass spectrometry (LA-ICP-MS). Analyses were carried out using an Agilent 8800 Triple Quadrupole ICP-MS coupled to a Teledyne CETAC Analyte G2 Excimer Laser Ablation System at The Open University. The ICP-MS was tuned at the beginning of each session for optimum sensitivity and minimum oxide production. As per EPMA, unconsolidated tephra analyses were made on individual glass shards, whereas lava and fiamme matrices were analysed multiple (~16) times. NIST SRM 612 was analysed at the beginning and end of each batch of 8–16 sample spots, and was used for external calibration (preferred values from Jenner and O'Neill (2012)). SiO_2 values from EPMA, normalised to an anhydrous basis, were used for internal calibration (shard-specific SiO_2 values for each ash

shard; average SiO_2 value for each thin section). BCR-2G was used as a secondary standard. Data reduction was performed using Iolite v3.5 on Wavemetrics Igor Pro v6.37. A secondary correction was made using BCR-2G and preferred values from Jenner and O'Neill (2012) to correct for differences between analytical sessions. Further LA-ICP-MS settings are listed in Table 5.6.

Table 5.6. LA-ICP-MS operating conditions

Teledyne CETAC Analyte G2 193 nm Excimer Laser Ablation System	
Fluence	3.91 J/cm^2
Repetition rate	5, 7, 10 Hz
Spot sizes	25, 40, 50, 85, 110, 130 μm
Cell gas flow	0.9 Lmin^{-1} He
Nitrogen	Later sessions included 5 mLmin^{-1} N to increase sensitivity (Hu et al., 2008)
Ablation duration	30 s

5.2.7 $^{40}Ar/^{39}Ar$ procedures

A glassy fiamme from the Thórsmörk Ignimbrite, glass shards from II-RHY-1 and 5 lava samples from the Torfajökull Ring Fracture Rhyolites were selected for groundmass $^{40}Ar/^{39}Ar$ dating. Despite mobilisation of K during welding of the fiamme (section 5.3.1), this material is suitable for $^{40}Ar/^{39}Ar$ dating as alteration was essentially instantaneous with deposition (Quane et al., 2009). The sample preparation and analytical procedures were the same as those described in Chapter 4 (Section 4.2), except that the mass spectrometer used was a MAP-215-50 noble gas mass spectrometer (mass discrimination: 283).

Blank measurements descended during the day of analysis of sample JM-247, so a moving average was used for blank correction of this sample. In comparison to a full-day average blank correction, this method has an insignificant effect on calculated ages but improves the MSWD.

5.3 RESULTS AND INTERPRETATION

5.3.1 Geochemistry results

The geochemistry data are plotted in Figures 5.6 and 5.7 (Full dataset: Appendices 4 and 5). In the left column of both figures, lava samples are plotted as the mean composition of multiple analyses of each sample ± the standard deviation. Individual shard data are plotted for tephras, in order to identify any compositional variation or multiple populations. In the right column, all data points from this study are plotted to show the full spread of data. The major element composition of Katla is defined using data from Lacasse et al. (2007), and Eyjafjallajökull (1821–23 eruption) data is from Larsen et al. (1999).

Figure 5.5. Key to geochemistry plots. Thórsmörk Ignimbrite data from Tomlinson et al. (2010) are included on the trace element plots.

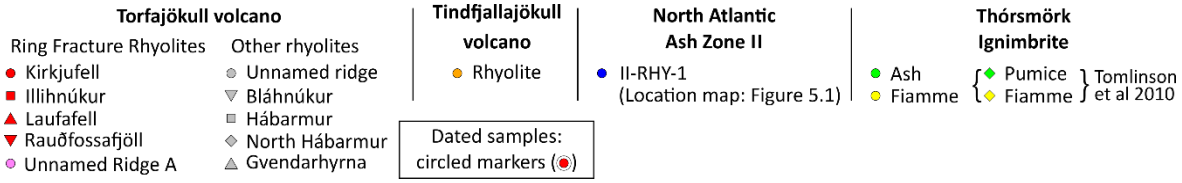

Figure 5.6. Plots of major elements. All plots demonstrate a compositional overlap between II-RHY-1 (blue markers), the Thórsmörk Ignimbrite (green and yellow markers) and the Torfajökull Ring Fracture Rhyolites (red markers). Unnamed Ridge A (pink marker) also has a similar composition to the Ring Fracture Rhyolites. Other analysed samples from Torfajökull (grey markers), Tindfjallajökull (orange markers), Eyjafjallajökull and Katla do not have a comparable composition to II-RHY-1 or the Thórsmörk Ignimbrite.

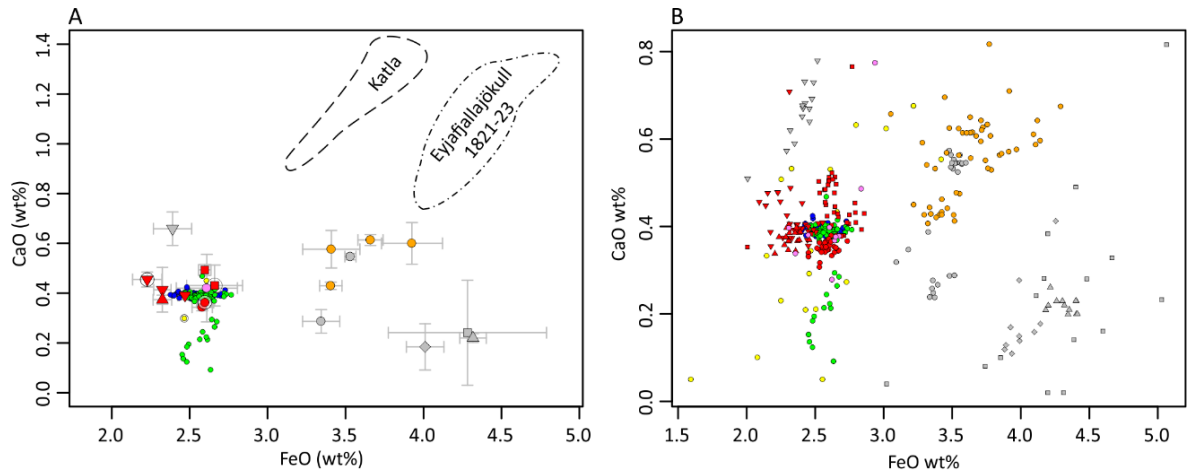

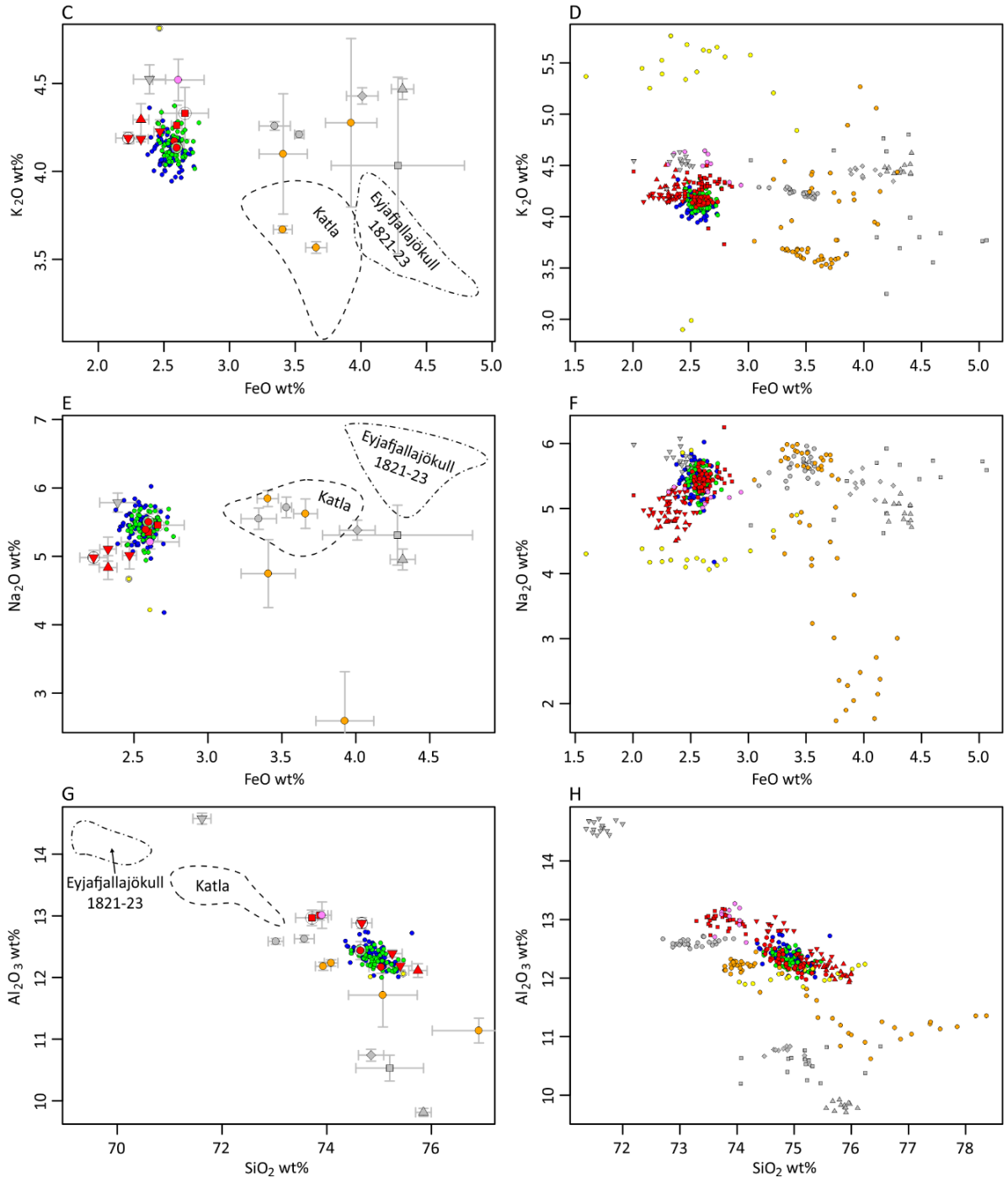

Figure 5.7 (next two pages). Plots of trace elements. There is more compositional variability seen in the trace elements compared to the major elements, particularly for the Thórsmörk Ignimbrite ash samples which range from 808 to 1215 ppm Zr. In the Ring Fracture Rhyolites, distinct geochemical subgroups are apparent in some elements, particularly Ba (plots G and H). Three of the Ring Fracture Rhyolite samples (from Illihnúkur and Rauðfossafjöll) and the Unnamed Ridge A sample have elevated Sr concentrations relative to the other Ring Fracture Rhyolite samples (plots C and D). Nevertheless, all plots show a compositional overlap between II-RHY-1, the Thórsmörk Ignimbrite and the Torfajökull Ring Fracture Rhyolites. The other analysed Torfajökull lavas are compositionally distinct from II-RHY-1 and the Thórsmörk Ignimbrite, for instance they have higher Zr concentrations.

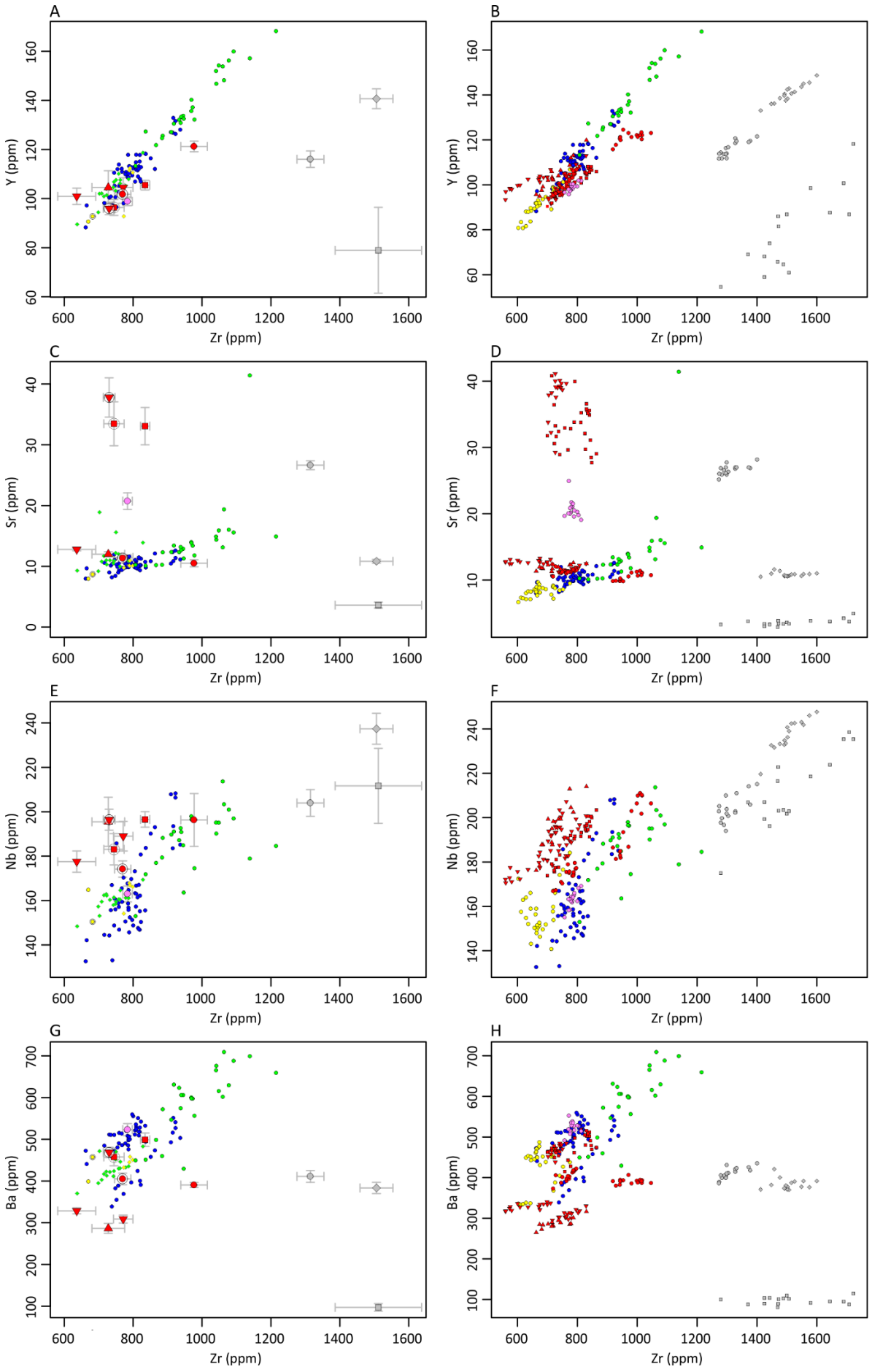
A
Y (ppm)
Zr (ppm)
B
Y (ppm)
Zr (ppm)
C
Sr (ppm)
Zr (ppm)
D
Sr (ppm)
Zr (ppm)
E
Nb (ppm)
Zr (ppm)
F
Nb (ppm)
Zr (ppm)
G
Ba (ppm)
Zr (ppm)
H
Ba (ppm)
Zr (ppm)

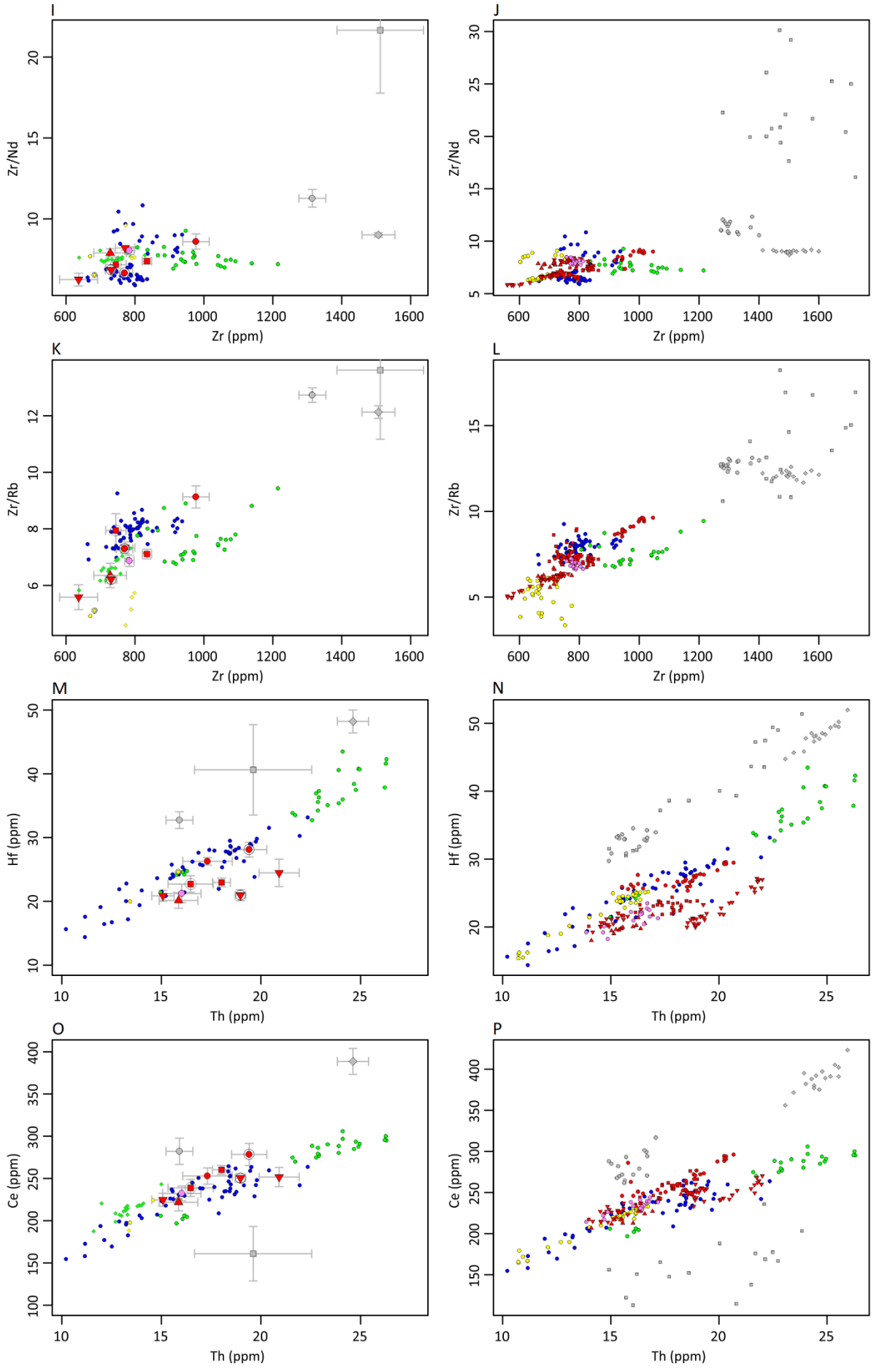
I
Zr/Nd
Zr (ppm)
J
Zr/Nd
Zr (ppm)
K
Zr/Rb
Zr (ppm)
L
Zr/Rb
Zr (ppm)
M
Hf (ppm)
Th (ppm)
N
Hf (ppm)
Th (ppm)
O
Ce (ppm)
Th (ppm)
P
Ce (ppm)
Th (ppm)

The major element data for II-RHY-1 and the Thórsmörk Ignimbrite overlap on all bivariate plots (Figure 5.6), confirming that these tephra deposits have highly comparable major element compositions (as first identified by Sigurdsson (1982)). Lower CaO abundances seen in Thórsmörk Ignimbrite ash sample JM-228 (Figure 5.6(A–B)) may be due to heterogeneities and/or alteration in these glass shards (shards appear discoloured and heterogeneous in Figure 5.4). The trace element compositions of II-RHY-1 and the Thórsmörk Ignimbrite also overlap for all analysed elements (Figure 5.7), though there is more compositional variation than in the major elements. In particular, there is a trend to more evolved compositions (e.g. higher Zr and Th) in the Thórsmörk Ignimbrite ash that is not apparent in the fiamme or in pumice data from Tomlinson et al. (2010). As noted by Tomlinson et al. (2010), fiamme are enriched in elements susceptible to mobility during welding (K_2O, Rb & Li; e.g. the higher concentration of K_2O in fiamme relative to Thórsmörk Ignimbrite ash in Figure 5.6(D)).

Comparison of the major element geochemistry of II-RHY-1 and the Thórsmörk Ignimbrite with data from Tindfjallajökull, Katla and Eyjafjallajökull indicates that there is no geochemical correlation with known compositions from these volcanoes (Figure 5.6). For example, these volcanoes produce rhyolites with >3 wt% FeO, whereas II-RHY-1 and the Thórsmörk Ignimbrite have ~2.5 wt% FeO (Figure 5.6 (A–F)).

The composition of the Torfajökull Ring Fracture Rhyolites overlaps with II-RHY-1 and the Thórsmörk Ignimbrite on all major and trace element plots (Figures 5.6 and 5.7), indicating a strong geochemical similarity between these groups. Unnamed ridge A has a previously unidentified geochemical affinity with the Ring Fracture Rhyolites (Figures 5.6 and 5.7) and it is suggested that this unit is an additional constituent of the Ring Fracture Rhyolites, though its age has not been determined. The Ring Fracture Rhyolite samples (including Unnamed Ridge A) are the only analysed samples from Torfajökull that show a compositional overlap with II-RHY-1 and the Thórsmörk Ignimbrite. Other Torfajökull units can be distinguished from the Ring Fracture Rhyolites based on, for example, their higher Zr concentration (as identified by McGarvie et al. (1990), post-glacial rhyolites excepted).

There are some geochemical differences between samples of the Ring Fracture Rhyolites. In particular, samples from Illihnúkur, Rauðfossafjöll (TJ98-43 only) and Unnamed Ridge A are enriched in Al_2O_3, MnO, MgO and TiO_2, and have elevated Sr at a given Zr (Figures 5.6(G) and 5.7(C)). These offsets may indicate that mixing has occurred between the typical Ring Fracture Rhyolite magma and a less evolved magma. The mafic and intermediate magmas of the Torfajökull volcanic system are characteristically high in TiO_2 and Sr (Gunnarsson et al., 1998; Macdonald et al., 1990; McGarvie et al., 1990), and mixing with a subordinate amount of these magmas would be consistent with the observed geochemical offsets.

Additionally, there are other subtle variations in trace elements within the Ring Fracture Rhyolites (e.g. Nb, Ba, Nd, Rb, Hf), which are most apparent in the plot of Ba vs Zr (Figure 5.7(H)). In this plot, distinct geochemical subgroups within the Ring Fracture Rhyolites can be identified, each with a different Ba concentration. Notably, most of these geochemical subgroups are also represented in the II-RHY-1 and/or Thórsmörk Ignimbrite data, with the exception of the subgroup with the lowest Ba concentration (Rauðfossafjöll sample TJ97-29 and Laufafell sample JM-40). Representation of the same geochemical subgroups in both the Ring Fracture Rhyolites and the tephras is an additional indicator of the geochemical similarity of these deposits.

5.3.2 Mahalanobis distances

In order to assess the geochemical similarity/dissimilarity between the analysed tephras, and between the tephra and lavas, Mahalanobis distances (D^2_m) were calculated. The Mahalanobis distance is a statistical measure of the separation between two groups of multivariate data (Cronin et al., 1997). Both the mean and the variance of each variable are taken into account. The unitless D^2_m value can be calculated between various deposits, allowing their similarity/dissimilarity to be compared (Lowe et al., 2017).

Prior to the calculation of D^2_m, values, the data were normalised and log-ratio-transformed (SiO_2 divisor; this transformation is the natural log of the ratios of all variables to silica

content). D^2_m values were then calculated using the *D.sq* function of the *asbio* package in the R programming language (Usage: *D.sq (g1, g2)*, where g1 and g2 are the two matrices being compared; Aho, 2016; R Core Team, 2014). In the major elements, MnO and MgO were not included in the calculation because they have low concentrations which would have had a large effect on the D^2_m results (Pearce et al., 2008). Na_2O was also not included due to the volatility of sodium during EPMA. For trace elements, elements with a typical concentration > 50 ppm were used (Zn, Rb, Y, Zr, Nb, Ba, La, Ce and Nd). Fiamme from the Thórsmörk Ignimbrite were not included, due to the mobility of some elements (e.g. K_2O and Rb) during welding.

The low D^2_m values between II-RHY-1 and the Thórsmörk Ignimbrite (Table 5.7) support the geochemical correlation of these deposits.

Table 5.7. D^2_m between II-RHY-1 tephra and Thórsmörk Ignimbrite tephra.

Major elements D^2_m	Trace elements D^2_m
1.3	16.0

Data from II-RHY-1 and the Thórsmörk Ignimbrite were then combined into one group, and D^2_m values were calculated between individual lava samples and this tephra group (Table 5.8). D^2_m values were also calculated between the combined tephra group and a combined Ring Fracture Rhyolites group. Unnamed ridge A was not included in this group as it has not previously been recognised as a constituent of the Ring Fracture Rhyolites and its age has not been determined.

Statistical distances between the combined tephra dataset and the Tindfjallajökull rhyolites are relatively high (D^2_m (major elements) > 90; Table 5.8), supporting the previous observation that there is no geochemical correlation between the tephras and the analysed Tindfjallajökull samples.

Table 5.8. D^2_m between lavas and the combined tephra group.

	Unit	Sample name	Major elements D^2_m	Rank	Trace elements D^2_m	Rank
Torfajökull: Ring Fracture Rhyolites	Kirkjufell	TJ99-2	2.6	2	95.5	5
	Kirkjufell	TJ99-4	2.3	1	109.7	6
	Illihnúkur	TJ97-16	43.3*	7	46.5	2
	Illihnúkur	TJ97-18	40.3*	6	54.4	3
	Laufafell	JM-40	19.2	5	207.9	9
	Rauðfossafjöll	TJ97-29	5.4	3	156.5	7
	Rauðfossafjöll	TJ98-18	14.4	4	178.6	8
	Rauðfossafjöll	TJ98-43	57.1*	8	89.1	4
	All above combined		**3.4**		**64.8**	
	Unnamed ridge A	TJ98-05	59.8*	9	30.9	1
Torfajökull: Other rhyolites	Unnamed ridge B	TJ97-09	101.7	11		
	Unnamed ridge B	TJ97-12	160.5	13	401.4	10
	Bláhnúkur	TJ98-40	355.5	17		
	Hábarmur	TJ97-14	310.3	16	1955.7	12
	North Hábarmur	TJ98-34	415.4	18	651.2	11
	Gvendarhyrna	TJ97-22	767.7	19		
Tindfjallajökull: Rhyolites	Saxi	JM-37	214.9	14		
	Jökulskarð	JM-80	136.1	12		
	Ymir (E)	JM-130	279.6	15		
	Hestur	JM-147	93.3	10		

*The different composition of these samples relative to the rest of the Ring Fracture Rhyolites may have been caused by mixing with a compositionally distinct magma.

D^2_m values between the tephra (combined) and the Ring Fracture Rhyolites (RFR) are low in comparison to other Torfajökull rhyolites (D^2_m (RFR combined) = 3.4 (majors) and 64.8 (traces > 50 ppm); (D^2_m (other Torfajökull) > 100 (majors) and > 400 (traces > 50 ppm); Table 5.8). This indicates a close geochemical similarity between the tephra and the Ring Fracture Rhyolites, as identified in the geochemical plots (Figures 5.6 and 5.7).

5.3.3 $^{40}Ar/^{39}Ar$ results

The results of $^{40}Ar/^{39}Ar$ step-heating experiments are assessed with the use of age spectra (cumulative release of ^{39}Ar vs. apparent age) and inverse isochrons ($^{39}Ar/^{40}Ar$ vs. $^{36}Ar/^{40}Ar$). Calculated ages are presented in Figure 5.8 and Table 5.9 (Full dataset: Appendix 6). Age plateaux adhere to the recommendations of Fleck et al. (1977), i.e. they include >50% of the ^{39}Ar over >3 contiguous steps with similar apparent ages at the 95% confidence level.

Figure 5.8. $^{40}Ar/^{39}Ar$ age spectra (left) and inverse isochron diagrams (right) for successfully dated samples. Light grey steps were not included in plateau calculations. Plateaux and isochrons are displayed as a black dashed line. The $^{40}Ar/^{39}Ar$ results derived from each plot are shown.

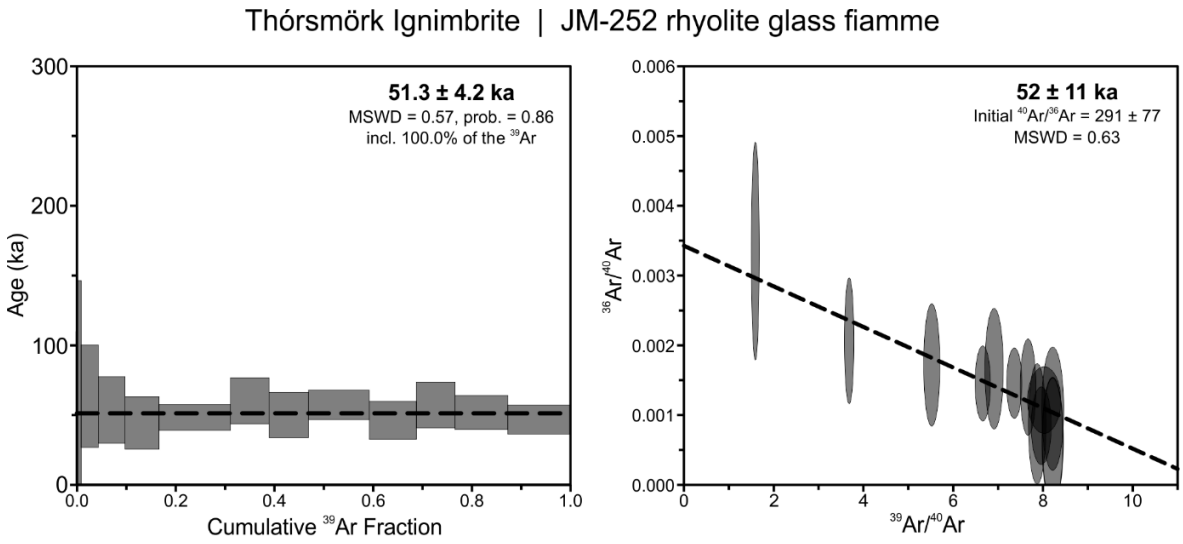

Ring Fracture Rhyolites | Kirkjufell area | TJ99-4 rhyolite glass

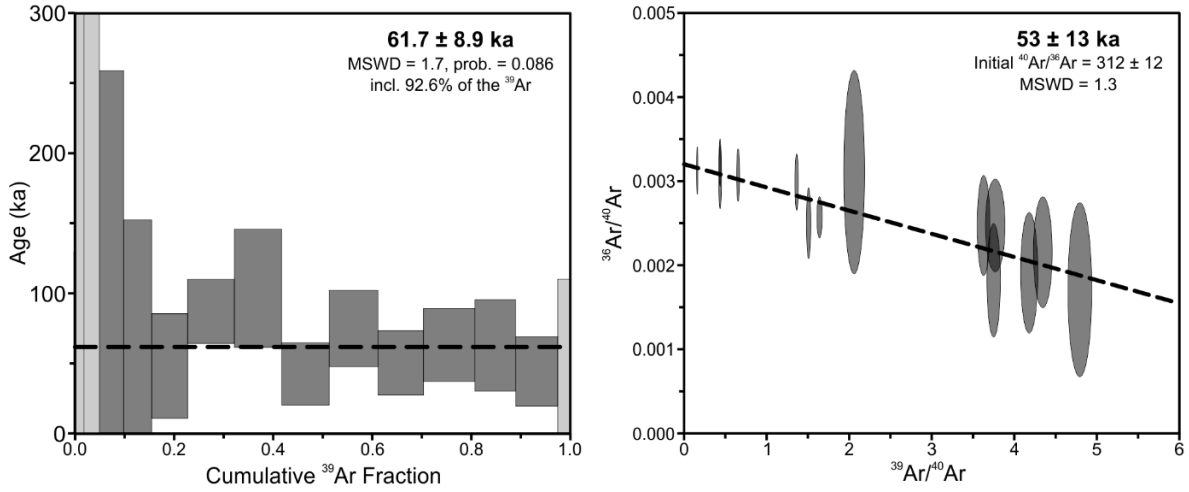

Ring Fracture Rhyolites | Rauðfossafjöll (N) | TJ98-43 rhyolite glass

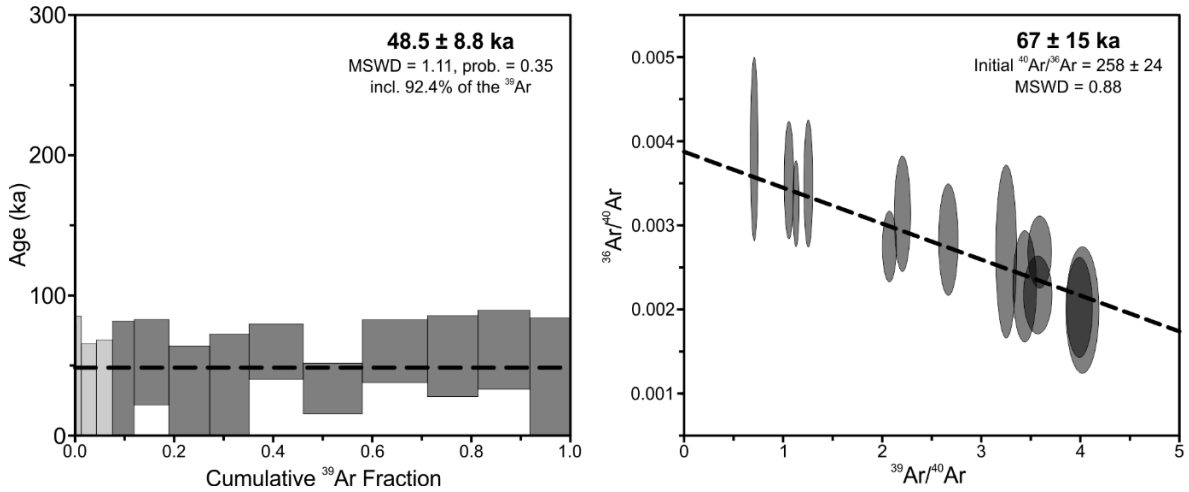

Ring Fracture Rhyolites | Rauðfossafjöll (SW) | JM-247 rhyolite non-glassy groundmass

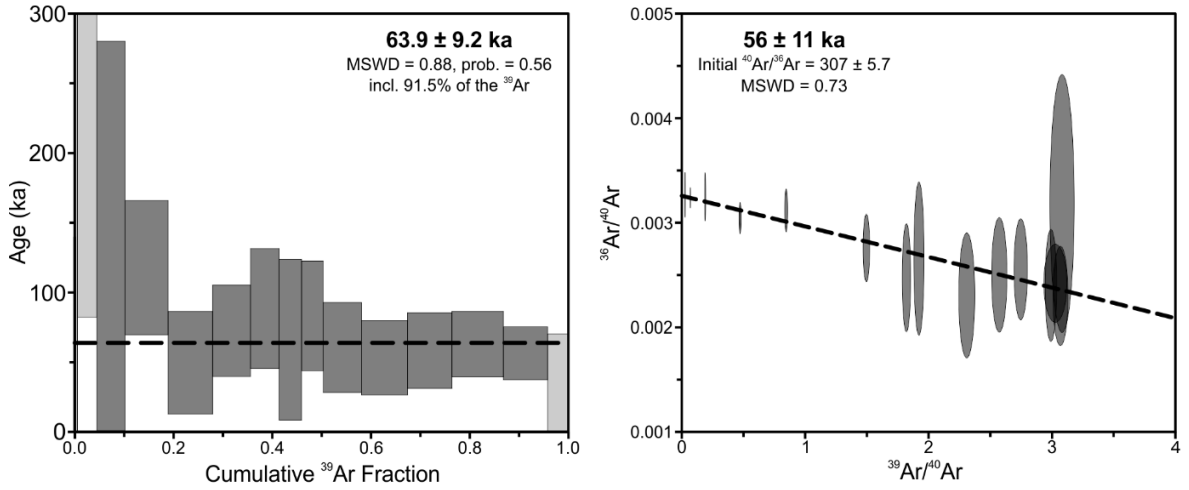

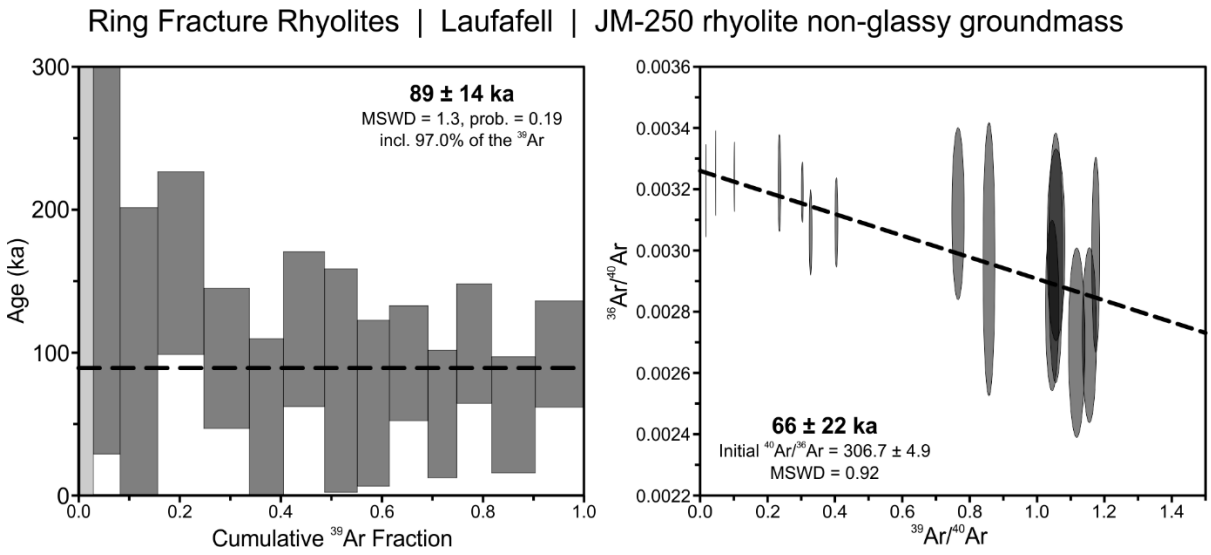

Table 5.9. $^{40}Ar/^{39}Ar$ plateau ages and inverse isochron ages. RFR: Torfajökull Ring Fracture Rhyolites. **Recommended age in bold** (choice of recommended age discussed below). All MSWD values are within the acceptable range according to Wendt and Carl (1991).

Unit *Sample, material*	Plateau age (ka) ± 2σ	MSWD	Inverse isochron age (ka) ± 2σ	MSWD	Initial $^{40}Ar/^{36}Ar$
Thórsmörk Ignimbrite *JM-252, rhyolite glass fiamme*	**51.3 ± 4.2**	0.57	52 ± 11	0.63	291 ± 77
II-RHY-1 *MD99-2251: 2014-2015 cm, rhyolite glass shards*	Age not determined		Age not determined		
RFR – Kirkjufell *TJ99-4, rhyolite glass*	61.7 ± 8.9	1.7	**53 ± 13**	1.3	312 ± 12
RFR - Rauðfossafjöll (N) *TJ98-43, rhyolite glass*	48.5 ± 8.8	1.11	**67 ± 15**	0.88	258 ± 24
RFR - Rauðfossafjöll (SW) *JM-247, rhyolite non-glassy groundmass*	63.9 ± 9.2	0.88	**56 ± 11**	0.73	307 ± 5.7

Unit *Sample, material*	Plateau age (ka) ± 2σ	MSWD	Inverse isochron age (ka) ± 2σ	MSWD	Initial $^{40}Ar/^{36}Ar$
RFR – Laufafell *JM-250, rhyolite non-glassy groundmass*	89 ± 14	1.3	**66 ± 22**	0.92	306.7 ± 4.9
RFR – Illihnúkur *TJ97-16, rhyolite glass*	Age not determined		Age not determined		

For the Thórsmörk Ignimbrite fiamme sample, similar results are obtained for the plateau age (51.3 ± 4.2 ka) and the inverse isochron age (52 ± 11 ka). The plateau is uniform with a consistent age determined for each heating step (Figure 5.8). The inverse isochron indicates a near-atmospheric initial $^{40}Ar/^{36}Ar$ ratio (291 ± 77), but the uncertainty on the isochron age is negatively affected by the limited spread of data along the isochron (Figure 5.8). The plateau age is therefore the recommended age for this sample. The age of the Thórsmörk Ignimbrite (51.3 ± 4.2 ka) overlaps with the GICC05 age of II-RHY-1 (55,380 ± 2367 yr b2k; Figure 5.9). Thus, both the geochemical and geochronological data confirm and strengthen the previously recognized correlation between these medial and distal tephra deposits.

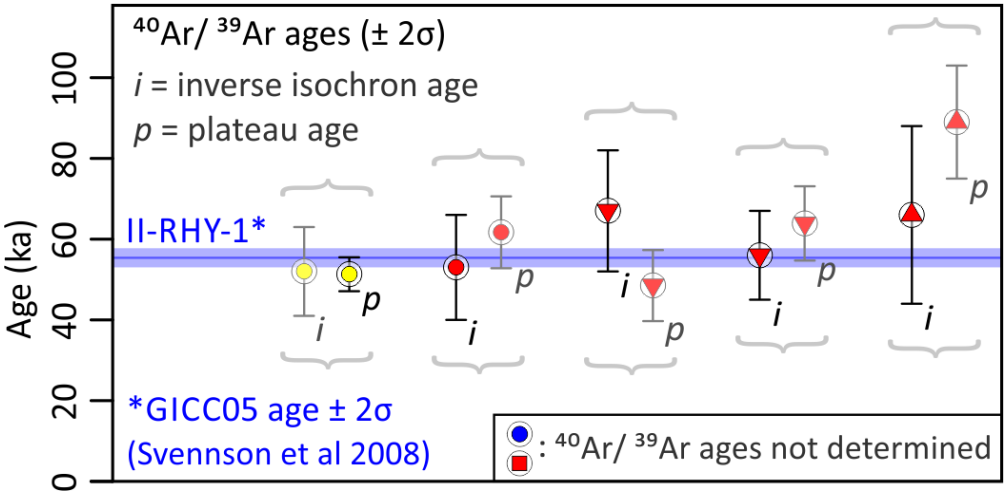

Figure 5.9. $^{40}Ar/^{39}Ar$ ages and comparison with the Greenland Ice Core Chronology 2005 (GICC05) age of II-RHY-1. Inverse isochron and plateau ages are shown for each sample, with the recommended ages in black.

In the Ring Fracture Rhyolite samples, there is typically an offset between the plateau ages and the isochron ages (Table 5.9; Figure 5.9), suggesting a more complex Ar system. In comparison to the fiamme, these samples contain a higher non-radiogenic ^{40}Ar content that may be partly derived from a non-atmospheric argon reservoir. Older apparent ages on age spectra are typically explained by an excess of ^{40}Ar, commonly encountered in volcanic rocks that have not completely degassed (Flude et al., 2017). Three of the Ring Fracture Rhyolite samples have above-atmosphere initial argon ratios (>298.56; Lee et al., 2006) that could explain the high plateau ages. Sample TJ98-43 has a below-atmosphere initial argon ratio (258 ± 24; excess ^{36}Ar), and a correspondingly low plateau age. Excess ^{36}Ar was encountered in similar samples by Clay et al. (2015). Inverse isochrons give a calculated age that is independent of the initial argon ratio, so are the preferred way of determining the ages of these samples. Therefore the inverse isochron ages are the recommended ages for the Ring Fracture Rhyolite samples.

Two of the analysed samples – Torfajökull lava TJ97-16 and glass shards from II-RHY-1 – have very high non-radiogenic ^{40}Ar contents, yielding ~21 and ~12 times more ^{40}Ar than ^{39}Ar respectively. Ages could not be determined on these samples, which may be explained by the large proportion of non-radiogenic ^{40}Ar to radiogenic ^{40}Ar. The non-radiogenic ^{40}Ar may be present due to incomplete degassing of the magma or, in the case of the II-RHY-1 glass shards, was likely incorporated into the shards during post-depositional hydration (Flude et al., 2017).

Inverse isochron ages of the Ring Fracture Rhyolites overlap with the GICC05 age of II-RHY-1 and the $^{40}Ar/^{39}Ar$ age of the Thórsmörk Ignimbrite (Figures 5.8 and 5.9; Table 5.9). None of the other Torfajökull rhyolites dated in previous studies (Clay et al., 2015; McGarvie et al., 2006; Table 5.5) have comparable ages to the tephras.

The combined geochemical and geochronological evidence strongly suggests that II-RHY-1, the Thórsmörk Ignimbrite and the Torfajökull Ring Fracture Rhyolites are the products of the same eruptive event.

5.4 DISCUSSION

5.4.1 The source of II-RHY-1 and the Thórsmörk Ignimbrite

Contrary to the conclusion of Jørgensen (1980), the evidence presented here suggests that Tindfjallajökull is not the source of the Thórsmörk Ignimbrite. This is supported by the observation that ignimbrite deposits on the flanks of Tindfjallajökull lack proximal facies, in fact lithic clasts reduce in size and abundance towards the volcano (Chapter 2). Additionally, there was no significant change in local sediment deposition regimes at Tindfjallajökull, as would be expected following a major eruption (Chapter 2; further investigation of this depositional succession is undertaken in Chapter 6).

Instead, the geochemical and geochronological data show that Torfajökull, specifically the Ring Fracture Rhyolites eruption, is the source of II-RHY-1 and the Thórsmörk Ignimbrite. This is the largest known rhyolitic eruption in Iceland. Approximately 18 km^3 (DRE: dense-rock equivalent) of tephra and lava is preserved at Torfajökull (McGarvie, 2009). A ring of tuyas was emplaced during the eruption, confined by an ice sheet >400 m thick (McGarvie et al., 2006; Tuffen et al., 2002). Magmatic volatiles drove explosive fragmentation before the effusive emplacement of intrusions and lava caps (Owen et al., 2013a, 2013b; Tuffen et al., 2008).

5.4.2 Tephra dispersal during rhyolitic glaciovolcanic eruptions

The new correlation provides the first documented link between rhyolite tuya-forming eruptions and distal tephra deposits. This confirms that widespread and voluminous tephra dispersal can be an important feature, and hazard, of rhyolitic glaciovolcanism (as hypothesized by Tuffen et al., (2002) and Stevenson et al. (2011)).

Furthermore, the correlation of rhyolite tuyas with an ignimbrite demonstrates that pyroclastic density currents can occur during such eruptions (Figure 5.10) and can travel tens of kilometres across an ice sheet. Pyroclastic density currents have previously been known to have descended the ice-clad flanks of steep-sided stratovolcanoes (e.g. Nevado del Ruiz, Colombia: Pierson et al., 1990; Redoubt, Alaska: Trabant et al., 1994), but their propagation across an ice sheet (>400 m thick at the vent in this instance) has not previously been documented. Welded ignimbrite deposits are present >30 km from Torfajökull (Jørgensen, 1980), indicating that the pyroclastic density current was still hot after travelling over ice or tephra-covered ice. It is likely that a significant volume of tephra was deposited on the ice surface proximal to the eruption, and is now lost from the terrestrial record (Stevenson et al., 2011; Tuffen et al., 2002). The preserved ignimbrite volume is estimated to be 1.5–2 km^3 DRE (Thórarinsson, 1969).

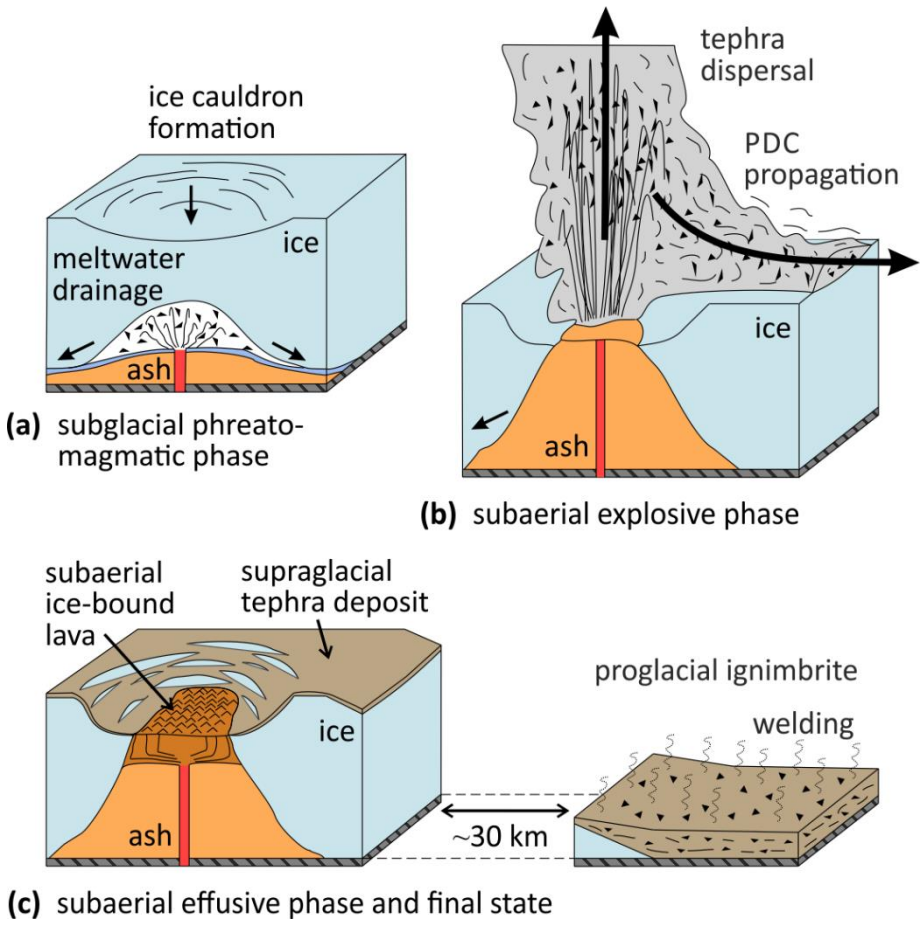

Figure 5.10. Model of rhyolite tuya formation modified from Tuffen et al. (2002) to show tephra dispersal and ignimbrite emplacement. PDC: pyroclastic density current. Despite the eruption

commencing in a subglacial environment (a), with a phreatomagmatic initial eruption phase (Tuffen et al., 2002), breaching of the ice leads to a subaerial explosive eruption (b) which is little influenced by ice. The eruptive products that remain at the vent are confined by ice to form a steep-sided tuya (c), but ice does not prevent the widespread dispersal of tephra and the emplacement of welded ignimbrite.

5.4.3 Linking glaciovolcanism-derived palaeoenvironmental information with other records

II-RHY-1 is a precise, widely dispersed, chronostratigraphic tie-line that marks the Torfajökull Ring Fracture Rhyolites eruption directly within an array of proxy records, such as ice core $\delta^{18}O$ profiles (Austin et al., 2004; Grönvold et al., 1995; Zielinski et al., 1997). These records document the rapid cooling transition (end GI-15.2) during which the eruption occurred (Austin et al., 2004) and the associated environmental conditions (e.g. sea ice extent, ice rafting patterns (Ruddiman and Glover, 1972)). Reconstructions of ice conditions in south Iceland at the time of the eruption (e.g. ice >400 m thick at Torfajökull) can now be precisely linked to this vast archive of palaeoenvironmental information. The palaeoenvironmental information that can be integrated using the products of this eruption is detailed in Chapter 6.

5.5 CONCLUSIONS

The Ring Fracture Rhyolites of Torfajökull volcano, south Iceland, are identified as the source of the Thórsmörk Ignimbrite and the distal tephra II-RHY-1. This correlation demonstrates that explosive rhyolitic eruptions at subglacial volcanoes can result in widespread tephra dispersal. Additionally, it shows that pyroclastic density currents propagated across an ice sheet to emplace a variably welded ignimbrite ~30 km from source. Rhyolitic glaciovolcanic eruptions produce tephra layers in a variety of depositional settings, making them valuable tools for stratigraphic correlation, while preserving a record of ice cover at the vent. For the first time, glaciovolcanism-derived palaeoenvironmental information can be precisely linked to the regional paleoclimate archive.

Chapter 6

Disparate palaeoenvironmental records linked by the Ring Fracture Rhyolites – Thórsmörk Ignimbrite – II-RHY-1 tephra isochron

The ~55 ka eruption of Torfajökull volcano (studied in Chapter 5) is represented in multiple depositional settings and therefore provides a valuable link between disparate palaeoenvironmental records. In this chapter, the products of the eruption are used to reconstruct past environments and to integrate palaeoenvironmental information from across the North Atlantic region. Data are sourced from published literature and through the investigation of depositional successions in south Iceland.

6.1 Introduction

In Chapter 5, it was established that the Ring Fracture Rhyolites, the Thórsmörk Ignimbrite and the rhyolitic component of North Atlantic Ash Zone II (II-RHY-1) are sourced from one major eruption of Torfajökull volcano. Such a complete correlation of volcanic products from proximal to distal settings is unique in the pre-Holocene record of Icelandic eruptions (Abbott and Davies, 2012). The widely dispersed products of the eruption provide a chronostratigraphic tie-line that links palaeoenvironmental records in terrestrial, marine and ice core settings. It is particularly rare to be able to incorporate terrestrial palaeoenvironmental information with marine and ice core data, given the degree to which glaciation has inhibited the storage and preservation of a terrestrial volcanic and depositional record (Larsen and Eiríksson, 2008).

Widespread tephra horizons are unmatched in their value as tools for precise stratigraphic correlation across multiple settings, especially for the Quaternary period (Lowe, 2011). Though absolute dating techniques (e.g. radiocarbon dating, $^{40}Ar/^{39}Ar$ dating) are useful over long timescales or for certain applications, these methods are limited by the uncertainties associated with all geochronometric results (as discussed in Chapter 4). As well as analytical uncertainties, radiocarbon dating, which is often used to integrate sedimentary successions deposited after ~50 ka (Bird et al., 1999), has uncertainties associated with the variable proportion of ^{14}C in the atmosphere and the need for reservoir age corrections (Austin et al., 2004). For precise integration of stratigraphic information, it is therefore necessary to use event horizons (e.g. geomagnetic excursions, tephra horizons) that directly link records without the need for absolute dating. Event horizons should represent an essentially instantaneous event (relative to the timescales of study) and are most valuable when found across multiple depositional settings (Gale, 2009).

Geomagnetic excursions are an example of a relative dating tool that links palaeoenvironmental information on a worldwide scale (Laj and Channell, 2007). Numerous short-lived reversals of the Earth's magnetic field occurred during the Pleistocene, and these events are represented in volcanic, sedimentary and ice core records (Laj and Channell, 2007; Svensson et al., 2008). A number of glaciovolcanic edifices on the Reykjanes peninsula, south Iceland, were emplaced during one such excursion: the Laschamp event (Kristjansson and Gudmundsson, 1980; Levi et al., 1990). In the Greenland ice core stratigraphy, the same event is expressed as a cosmogenic nuclide excursion around Greenland Interstadial 10 (Yiou et al., 1997; GICC05 age: 41,250 ± 1628 (2σ) yr b2k (Svensson et al., 2006)). Using the Laschamp event as a time marker, the ice conditions recorded by the eruptions in Iceland can be linked to palaeoenvironmental information from sedimentary successions and ice cores worldwide. However, this link has not yet been recognised in the literature; for example Norðdahl and Pétursson (2005) quote eruption $^{40}K/^{40}Ar$ ages (mean age: 42.9 ± 7.8 ka (2σ); Levi et al., 1990) without mentioning the more precise relative dating to GI-10. This relative dating technique is

limited by the infrequency of geomagnetic excursions and the need to independently date records to deduce which excursion they are associated with. Additionally, the non-instantaneous nature of the events limits the dating precision that can be achieved. For instance, the eruptions on Reykjanes could have occurred at any time during the Laschamp excursion, which lasted a few hundred years (Nowaczyk et al., 2012).

Tephra horizons are found in a wide variety of depositional settings, carry a geochemical fingerprint for correlation, and are typically (though not always, see section 6.2.2) erupted and deposited over short time-scales (i.e. hours to months; Lowe, 2011). It is these qualities, combined with the high frequency of events (in comparison to geomagnetic reversals), that make tephra a valuable tool for stratigraphic correlation (Lowe, 2011). There are challenges in using tephra however, such as the incomplete nature of the volcanic record and the difficulties in finding tephra correlatives between different settings (e.g. Abbott et al., 2016).

This chapter is a synthesis of the palaeoenvironmental information derived from the broad range of depositional settings where the Ring Fracture Rhyolites eruption is represented. Published studies of II-RHY-1 and the Ring Fracture Rhyolites are reviewed, before original research on the palaeoenvironments associated with the Thórsmörk Ignimbrite is presented. Finally, palaeoenvironmental information derived from the terrestrial deposits is linked with the regional climate record using II-RHY-1.

6.2 II-RHY-1 IN MARINE AND ICE CORE SETTINGS

North Atlantic Ash Zone II, including rhyolitic tephra of the II-RHY-1 component, was first discovered by Bramlette and Bradley (1941) in marine sediment cores taken along a transect of the North Atlantic at ~50° N. The II-RHY-1 tephra has a notably widespread distribution, and is now known to occur in marine sediments across millions of square kilometres of the ocean floor (Figure 6.1). Additionally, II-RHY-1 was the first ancient tephra horizon to be reported in an ice core (the DYE-3 core from southern Greenland; Ram and Gayley (1991)),

and it remains one of only a few tephra horizons that have been correlated between Greenland ice cores (Abbott and Davies, 2012; Grönvold et al., 1995). The correlation of II-RHY-1 between the Greenland ice sheet and North Atlantic marine sediments has been achieved through major element geochemistry in tandem with a well-constrained event stratigraphy and dating control (Austin et al., 2004; Grönvold et al., 1995; Ram et al., 1996; Ram and Gayley, 1991; Zielinski et al., 1997). Since its discovery, II-RHY-1 has been established as a valuable chronostratigraphic marker for correlating stratigraphic successions and for linking disparate palaeoenvironment records (Austin et al., 2004; Austin and Abbott, 2010; Ruddiman and McIntyre, 1977).

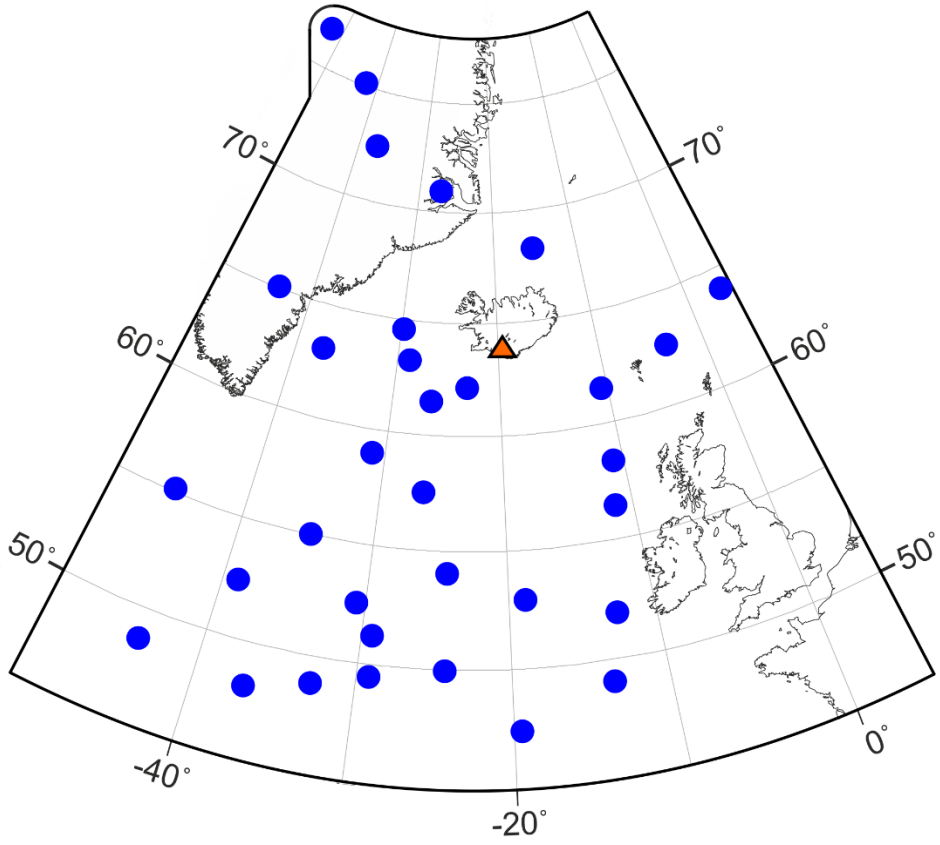

Figure 6.1. Map of reported occurrences of II-RHY-1 (blue circles) in North Atlantic marine sediment cores and Greenland ice cores. The tephra has also been reported to the west of Greenland in Baffin Bay (Aksu and Piper, 1979). Core locations from Austin et al., 2004; Bramlette and Bradley, 1941; Brendryen et al., 2011, 2010; Davies et al., 2012; Grönvold et al., 1995; Haflidason et al., 2000; Heinrich, 1988; Hodell et al., 2010; Kvamme et al., 1989; Lacasse et al., 1996; Lacasse and Garbe-Schönberg, 2001; Lackschewitz and Wallrabe-Adams, 1997; Ram et al., 1996; Ram and Gayley, 1991; Ruddiman and Glover, 1972; Ruddiman and McIntyre, 1984; Smythe et al., 1985; Wastegård et al., 2006; Zielinski et al., 1997.

6.2.1 Climate at the time of II-RHY-1 deposition

The climate at the time of II-RHY-1 deposition is well constrained due to the presence of the tephra in the Greenland ice cores. This places the tephra directly within the high resolution proxy records derived from the ice cores, such as the $\delta^{18}O$ and δD temperature proxies. Figure 6.2 displays the $\delta^{18}O$ record of the last glacial period from the NGRIP ice core (Rasmussen et al., 2014; Seierstad et al., 2014). Full glacial conditions during ~70.5 – 59.5 kyr b2k (indicated by low $\delta^{18}O$) transitioned to a generally milder but variable climate (~59.5 to ~35.0 kyr b2k) during which II-RHY-1 was deposited.

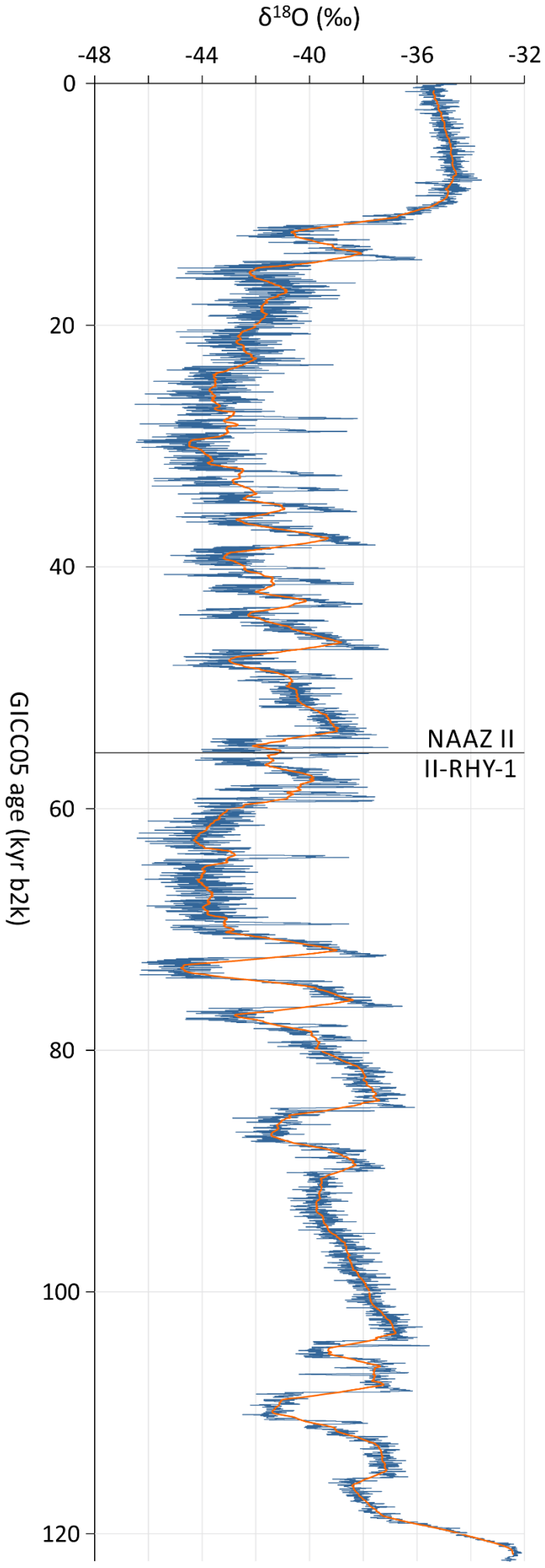

Figure 6.2. Oxygen isotope record from the North Greenland Ice Core Project (NGRIP), stretching back to the last (Eemian) interglacial period. Colder conditions are indicated by lower $\delta^{18}O$ values. The timescale used is the Greenland Ice Core Chronology 2005 (GICC05), which is measured in years before 2000 CE (b2k). A 1200 yr moving average of the oxygen isotope data has been added to the plot (orange line). Isotope and age data from Rasmussen et al., 2014 and Seierstad et al., 2014.

The Greenland climate record of the last glacial period is punctuated by abrupt shifts in climate known as Dansgaard-Oeschger events (Dansgaard et al., 1993). Equivalent fluctuations in climate have been found in records throughout the northern hemisphere (e.g. speleothems in northern China; Duan et al. (2016)). The II-RHY-1 layer occurs mid-way through a transition from interstadial (warm) conditions to stadial (cold) conditions (Austin et al., 2004; Zielinski et al., 1997). Within the climatostratigraphy of Rasmussen et al. (2014), the interglacial preceding II-RHY-1 is known as Greenland Interstadial 15.2 (GI-15.2) and the subsequent stadial is known as Greenland Stadial 15.2 (GS-15.2; Figure 6.3). Modelling of the past surface temperature at the NGRIP (North Greenland Ice Core Project) site using $\delta^{15}N$ suggests that the temperature decreased by ~8.5 °C across this stadial-interstadial transition, which was complete within decades (Kindler et al., 2014).

Marine sediments containing II-RHY-1 also host climate proxies, such as foraminiferal assemblages, that can be used to understand the climate in the marine realm at the time of the eruption. For instance, Ruddiman and McIntyre (1977) used II-RHY-1 to bring together *Neogloboquadrina pachyderma* (sinistral) relative abundance data from a wide area of the North Atlantic. The relative abundance of this foraminifer is a proxy for sea-surface temperatures, and was used by the authors to locate the transition (known as the polar front) between polar and sub-polar water masses. They found that the polar front was located at a latitude of 45–55° N at the time of II-RHY-1 deposition, similar to the average polar front position during the whole of the last glacial period. Austin et al. (2004) used II-RHY-1 to precisely link an ice core $\delta^{18}O$ profile with the record of *N. pachyderma* (sinistral) relative abundance in marine sediment core MD95-2006 (Figure 6.3). By directly linking these palaeoclimate proxies, it was demonstrated that the cooling event at the end of GI-15.2 was synchronous on a decadal scale across the North Atlantic.

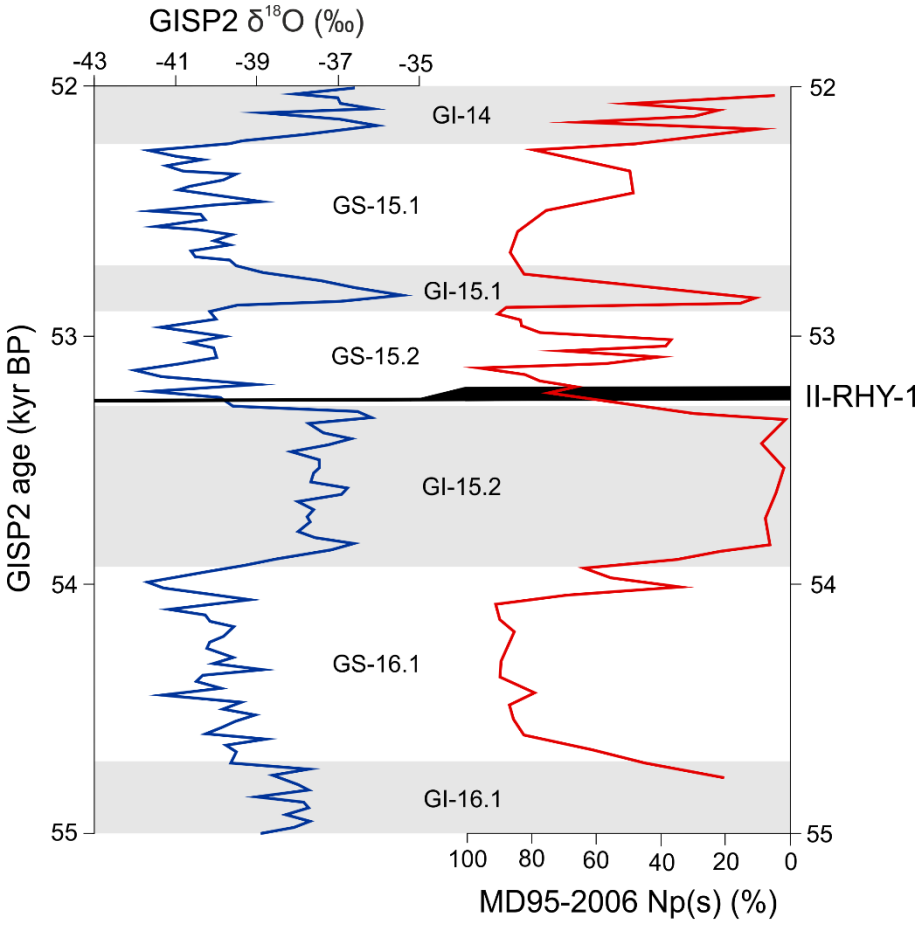

Figure 6.3. Precise synchronisation of ice core (left) and marine sediment (right) palaeoclimate records using II-RHY-1 (figure modified from Austin et al., 2004). In this plot, the ice core oxygen isotope record is from Greenland Ice Core Project 2 (GISP2) and is dated using the GISP2 time-scale (Meese et al., 1997). The marine proxy for sea-surface temperatures is the *Neogloboquadrina pachyderma* (sinistral) relative abundance, from sediment core MD95-2006 (Austin et al., 2004). By linking these records using II-RHY-1, Austin et al. (2004) demonstrated that the cooling in climate at the end of GI-15.2 was synchronous across the North Atlantic region. The II-RHY-1 isochron allows precise synchronisation of records regardless of the uncertainties in absolute age (e.g. offset between GISP2 age and GICC05 age). Climatostratigraphy from Rasmussen et al., 2014.

The widespread distribution of II-RHY-1 and its occurrence during a rapid climatic transition makes it ideal for testing the phase relationships of abrupt climate events between different settings (Davies et al., 2012). In fact, Blockley et al. (2014) identified II-RHY-1 as "the tephra that offers the greatest potential for constraining the rapid climatic events of the last glacial period."

6.2.2 Transport and deposition of II-RHY-1 and the associated environmental conditions

The presence of II-RHY-1 tephra in numerous North Atlantic sediment cores (Figure 6.1) allows a vast archive of information on marine depositional environments to be linked together. Ruddiman and Glover (1972) recognised that the southward dispersal of the tephra was largely driven by ice-rafting rather than solely atmospheric processes. Airfall tephra was initially deposited on sea ice near to Iceland, possibly to the north of the island (Lacasse et al., 1996). The tephra-bearing sea ice was subsequently rafted far to the south, releasing the tephra as it melted. The distribution of the tephra in marine sediments is therefore a function of the trajectory of the rafting sea ice and the regions of ice melting (Smythe et al., 1985). II-RHY-1 thus provides a measure of the extent of sea ice formation and southward rafting at the time of the eruption (i.e. extensive sea ice near to Iceland; rafting as far as 47° N), and the tephra can be used as a tracer of the past trajectory of ocean surface currents (Ruddiman and Glover, 1972; Smythe et al., 1985).

In a deep marine basin ~200 km to the south of Iceland, Lacasse et al. (1996) reported that II-RHY-1 was deposited by turbidity currents that transported tephra from the southern shelf of Iceland. It is possible that the turbidity currents were triggered by jökulhlaups or pyroclastic density currents entering the ocean during the eruption (Lacasse et al., 1996), or through the rapid build-up of volcanic material on the shelf.

Throughout the dispersal area of II-RHY-1, shards with an identical geochemical composition are commonly found higher up in the stratigraphic sequence. Although these shards have been used to propose that further eruptions with the same composition occurred (Jennings et al., 2014), the stratigraphic repetition of II-RHY-1 material is typically attributed to resedimentation within, or delayed transport to, the marine realm (Brendryen et al., 2011; Voelker and Haflidason, 2015). Tephra shards can be redistributed in marine settings through biological (e.g. bioturbation) and physical (e.g. erosion and transport by bottom currents)

processes (Abbott et al., 2013). Transport to marine settings will be delayed if tephra is first deposited on ice sheets or land surfaces before being transported to the ocean. In particular, tephra entrained in ice sheets can subsequently be dispersed across the seafloor through iceberg rafting (over longer timescales than dispersal via sea ice; Brendryen et al. (2011)).

The known existence of time delays in the transport and deposition of II-RHY-1 tephra means that caution is required when using II-RHY-1 as a chronostratigraphic marker in marine settings. However, high resolution shard concentration profiles through marine sediments in a number of cores have demonstrated that the integrity of the II-RHY-1 isochron is robust (Abbott et al., 2018a). The isochron within a layer of sea-ice rafted or airfall tephra can typically be defined at 1 cm resolution (Abbott et al., 2018a), and it is thought that sea-ice rafting will impart a delay of less than a decade (Austin et al., 2004; Brendryen et al., 2010). Tephra horizons that may not be isochronous include those where shard concentration profiles are diffuse and/or have multiple peaks (Abbott et al., 2018b), those where there are multiple geochemical and grain size populations (Austin et al., 2004), and those that are deposited in close association with debris rafted by icebergs (Brendryen et al., 2011).

The II-RHY-1 tephra has been reported as an airfall deposit (i.e. it was deposited directly as fallout through the atmosphere and, in marine settings, the water column) on the Greenland ice sheet (Ram and Gayley, 1991) and in marine sediments SW of Iceland (Lackschewitz and Wallrabe-Adams, 1997). Grain size characteristics of the tephra in the Greenland ice sheet have been used to study the conditions of atmospheric circulation at the time of the eruption. Ram and Gayley (1991) noted that II-RHY-1 shards are as large as 300 μm in the DYE-3 ice core. The atmospheric transport of these particles for >1000 km requires powerful injection of tephra high into the stratosphere and/or stronger atmospheric circulation than seen today (Lacasse, 2001; Ram and Gayley, 1991). Simulations by Lacasse (2001) suggest that the grain size of some Pliocene and Pleistocene tephra deposits, particularly II-RHY-1, cannot be explained by present-day atmospheric circulation patterns. However, further work is required

to understand the atmospheric transport of II-RHY-1 in light of recent advances in knowledge of long-range tephra dispersal (e.g. Bourne et al., 2016; Stevenson et al., 2015).

6.3 ERUPTIVE ENVIRONMENT OF THE RING FRACTURE RHYOLITES, TORFAJÖKULL VOLCANO

The Ring Fracture Rhyolites are a discontinuous ring of rhyolitic edifices situated around the outer margin of Torfajökull volcano (McGarvie, 1984; Tuffen et al., 2002; Chapter 5). The edifices are typically composed of steep-sided tephra piles capped with lava. It was first noted by McGarvie (1984) that the eruption of the rhyolites had interacted with ice. A detailed study of part of the Ring Fracture Rhyolites at SE Rauðfossafjöll led Tuffen et al. (2002) to identify the edifices as rhyolitic tuyas which had erupted through a substantial ice sheet. Torfajökull hosts a high concentration of rhyolitic tuyas including the largest known in Iceland, Laufafell (~2 km^3), which is a part of the Ring Fracture Rhyolites (McGarvie, 2009; Chapter 5).

Rhyolitic tuyas are similar to basaltic tuyas in their steep-sided 'table mountain' morphology, which is a result of the confinement of the edifices by ice during their emplacement (Stevenson et al., 2011). Additionally, both basaltic and rhyolitic tuyas typically consist of a pile of fragmental material that is overlain by sub-horizontal lava caps (Tuffen et al., 2002). However, in contrast to basaltic tuya-forming eruptions, the influence of meltwater in rhyolitic tuya-forming eruptions is relatively minor and no evidence has been found for the ponding of significant volumes of water around the vent (Stevenson et al., 2011; Tuffen et al., 2002). Passage zones, which record the level of water that ponded around basaltic tuyas (Chapter 2), are therefore absent in rhyolitic tuyas (McGarvie, 2009; Stevenson et al., 2011). Without the presence of passage zones as palaeoenvironmental indicators, other features must be used to estimate the thickness of ice that was present at the time of rhyolitic tuya emplacement (Stevenson et al., 2011).

Where preservation is good, the lava caps that make up the upper parts of rhyolitic tuyas typically have columnar joints that are oriented perpendicular to the lava margins. This has been reported in the Ring Fracture Rhyolites at SE Rauðfossafjöll (Tuffen et al., 2002) and at Kerlingarfjöll volcano (Stevenson et al., 2011). The sub-horizontal columnar joints indicate that the capping lavas chilled against a steep wall of ice (Tuffen et al., 2002). Combined with the thick and steep-sided morphology of the tuyas, this evidence suggests that the edifices were confined by a thick body of ice during their emplacement. The height of the tuyas represents the minimum thickness of ice that was present at the time of the eruption (McGarvie et al., 2006). Equally, the summit elevation of the tuyas corresponds to the minimum estimate of ice sheet surface elevation. This is a more appropriate measure across areas of uneven topography, where ice thickness will vary even if ice surface elevation is constant. However, using the present-day summit elevation of the tuyas does not take into account of any vertical lithospheric deformations that occurred during and since the eruption.

Vertical deformation of the lithosphere is likely to have occurred as a result of ice loading and unloading since the eruption. For instance, isostatic adjustment of the lithosphere raised the elevation of Iceland following the deglaciation at the end of the last glacial period (Sigmundsson, 1991). Where post-glacial rebound has occurred, physical features used to reconstruct past ice sheets will overestimate the surface elevation of the ice. In order to estimate the effect of isostatic adjustment on the elevation of the tuyas at Torfajökull, McGarvie et al. (2006) used a simple Airy isostatic model:

$$\text{Glacial isostatic adjustment} = (\varrho_{ice} \times \text{ice thickness})/\varrho_{mantle}$$

The density of ice (ϱ_{ice}) is 920 kgm^{-3} and the density of the Icelandic mantle (ϱ_{mantle}) is approximately 3100 kgm^{-3} (Sigmundsson, 1991). The model assumes that the reconstructed ice sheet was in isostatic equilibrium with the lithosphere; an assumption that may be reasonable given Iceland's rapid (<1000 yr) response to ice unloading at the end of the last glacial period (Sigmundsson, 1991). However, the model also does not take into account of variations in ice

thickness across the area, which are likely to have been significant considering the local relief (present-day elevation range: ~700 m). According to the model, the removal of a 400 m thick ice sheet would cause the lithosphere to rebound by ~120 m.

In addition to vertical movements due to ice loading and unloading, it is possible that the substantial evacuation of magma during the eruption resulted in subsidence (e.g. Hildreth and Mahood, 1986), though no evidence for this has been reported. Syn- or post-eruptive subsidence would lead to an underestimation of the elevation of the reconstructed ice sheet. Given the uncertainties in correcting for vertical lithospheric deformations, the estimate of ice sheet surface elevation below is taken directly from the present-day topography without correction.

The tuyas of the Ring Fracture Rhyolites have consistent summit elevations of ~1200 m above mean sea level (Figure 6.4). Two tuyas near Kirkjufellsvatn in the NE of the complex are an exception, reaching ~950 m elevation. As the summit elevations represent minimum estimates of ice sheet surface elevation, the differences in height between individual tuyas is unlikely to correspond to actual differences in ice sheet surface elevation at the time of the eruption. As a large proportion of the tuyas have elevations ~1200 m, and none are considerably higher, it is interpreted that the ice sheet overlying Torfajökull at the time of the eruption had a minimum surface elevation of 1200 m. The present-day high point of the volcano, which pre-dates the Ring Fracture Rhyolites (Clay et al., 2015), is only marginally higher than the summits of the tuyas (1281 m; Figure 6.4). Therefore it is likely that the reconstructed ice sheet was thick enough to cover all of the Torfajökull area.

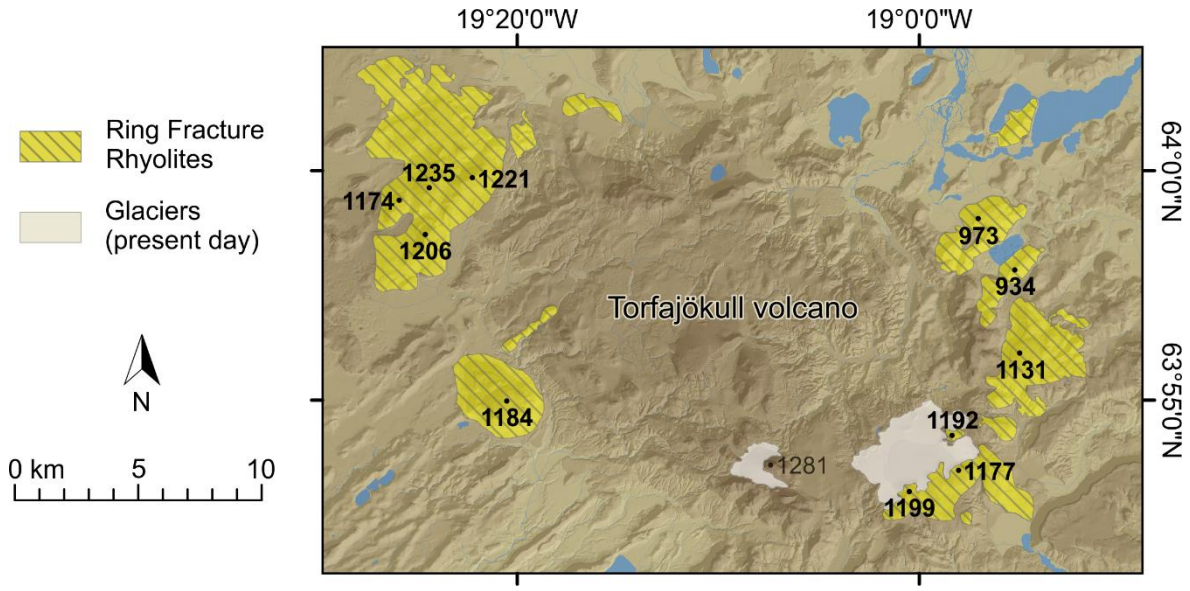

Figure 6.4. Map of the Ring Fracture Rhyolites, Torfajökull volcano. The summit elevations of tuyas are shown in metres above mean sea level. The highest point of the volcano, Háskerðingur (1281 m), is also marked.

There are some products of the Ring Fracture Rhyolites eruption preserved at Torfajökull that do not take the form of tuyas (e.g. Dalakvísl: Owen et al., 2013a, 2013b; Tuffen et al., 2008). The pyroclastic material and associated intrusions at Dalakvísl were emplaced in an entirely subglacial environment (Tuffen et al., 2008), which is consistent with the evidence from the tuyas of an ice surface >1200 m elevation (Owen et al., 2013b).

6.4 THE PALAEOENVIRONMENTAL RECORD ASSOCIATED WITH THE THÓRSMÖRK IGNIMBRITE

In this section, stratigraphic successions that include the Thórsmörk Ignimbrite horizon are investigated, in order to assess the palaeoenvironmental record hosted by the ignimbrite and the associated deposits. Since the physical volcanology of the ignimbrite was first mapped and described by Jørgensen (1980), little work has been published on the physical characteristics of the ignimbrite or the bracketing deposits. A set of composite stratigraphic logs were produced

by Roberts (2001), which show that the ignimbrite is commonly overlain by basaltic units that were emplaced in a subglacial environment.

Six sites were chosen for detailed study, stretching from the deeply incised SE flank of Tindfjallajökull to the wide valley of the Markarfljót (Table 6.1; Figure 6.5). As well as geographical spread, sites were chosen where both the ignimbrite and bracketing deposits are exposed. The lithologies and structures at each site are documented in Tables 6.2–6.7 and Figures 6.6–6.11.

Table 6.1. Locations of the sites chosen for palaeoenvironmental investigation.

Site number	Site name	Site location
1	Botn	63.754° N 19.547° W
2	Vestri-Botná	63.756° N 19.522° W
3	Eystri-Botná	63.758° N 19.506° W
4	Gilsá	63.736° N 19.516° W
5	Tröllagjá	63.715° N 19.516° W
6	Kápa	63.702° N 19.480° W

On the flanks of Tindfjallajökull (Sites 1–5) the ignimbrite is bracketed by sediments, of which diamict is the dominant lithofacies (Chapter 2; Appendix 8). Basaltic volcanic units are also found within the depositional succession, all of which belong to the Late Tindfjallajökull (B) stratigraphic group (Chapter 2). Similar lithofacies are present in the area of Site 6 south of the Markarfljót (Roberts, 2001), though detailed geological mapping of this area has not been carried out. Unlike the Ring Fracture Rhyolites palaeoenvironmental record discussed above, which is representative of a moment in time (the time of the eruption), the succession containing the ignimbrite was deposited over a period of time. As the ignimbrite is the only widespread event horizon and dated horizon in the succession, the time taken to deposit the whole succession at each site is unknown.

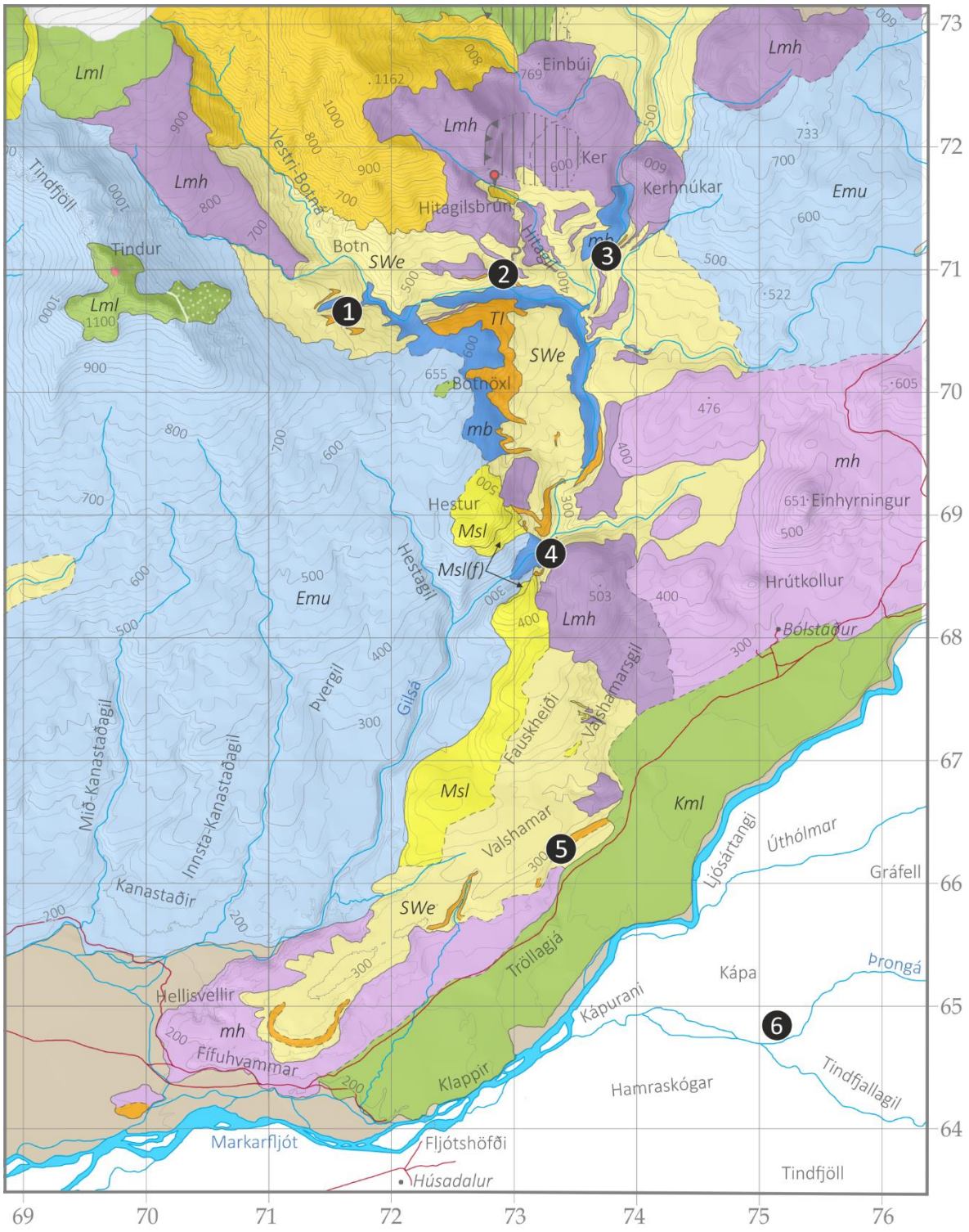

Figure 6.5. Part of the geological map of Tindfjallajökull (Chapter 2) showing the location of the palaeoenvironment study sites in this chapter. Topography and geology are not mapped south of the Markarfljót. The Thórsmörk Ignimbrite (orange; *Tl*) outcrops at all study sites. For key to other geological units and symbols, see main map (Appendix 8). Grid: 1 km² squares, UTM Zone 27N.

6.4.1 Description of lithofacies at each study site

Site 1 (Botn) is situated in a steep-sided valley flanked by the mafic Tindfjöll ridge on the west side and the central silicic edifice to the north (Figure 6.5). The depositional succession at this site overlies the basement, and the Thórsmörk Ignimbrite is present near the top of the succession (Figure 6.6; Table 6.2).

Figure 6.6. Overview and annotated photographs of Site 1. Inset photographs: (a) Diamict package containing basalt boulders. (b) Well-sorted gravel, sand and silt layers in the upper part of a diamict package. (c) Striated boulder (striation direction indicated by arrows). (d) Range of clast sizes and compositions in a diamict exposure.

Table 6.2. Lithofacies descriptions, Site 1.

Unit (thickness)	Description
i) Diamict packages (20–60 m)	Unconformably overlies basement (palaeosurface slopes to SE). Discrete packages of sediment ~1–5 m thick, inclined at 5–10° to SE. The dominant lithology is diamict with a continuous range of clast sizes from silt to boulders (up to 1 m; Figure 6.6 (a, d)). Clasts are typically sub-rounded, though some have faceted and striated surfaces (Figure 6.6 (c)). Basaltic (>70%) and rhyolitic (<30%) clast types are present. The basal part of each package is usually prominent, and contains the highest abundance of large clasts. In the upper parts of some of the packages, diamict is overlain by beds (1–20 cm thick) of gravel, laminated sand and/or laminated silt (Figure 6.6 (b)). Individual beds/laminae are well sorted and sometimes graded. Beds are discontinuous over distances >1 m. In well exposed sections, the beds of finer sediment are observed to be truncated by the overlying diamict package.
ii) Thórsmörk Ignimbrite (0–10 m)	Conformably overlies (i). Unconsolidated buff ash overlain by brecciated incipiently-welded pink ignimbrite. Poorly exposed.
iii) Diamict packages (0–10 m)	The ignimbrite is cross-cut by diamict packages with the same characteristics as (i). Ignimbrite clasts are also present (<10%).

Site 2 (Vestri-Botná) is located 1.3 km down-valley (E) of Site 1, and is similarly situated to the south of the central silicic edifice (Figure 6.5). The depositional succession at this site overlies the basement and, in addition to the Thórsmörk Ignimbrite, units emplaced during local basaltic volcanism are present (Figure 6.7; Table 6.3).

Figure 6.7 (next page). Overview and annotated photographs of Site 2. Inset photographs: (a) Diamict exposed close to the basal unconformity of the succession. (b) Laminated ash in stream bed (underwater) at the base of the Thórsmörk Ignimbrite. (c) Laminated sands with imbricated outsize diamict clasts. Palaeoflow direction is to the right (SE). (d) Rhyolite lithic clast in basaltic lapilli tuff.


Site 2: Vestri-Botná
10 m
SE

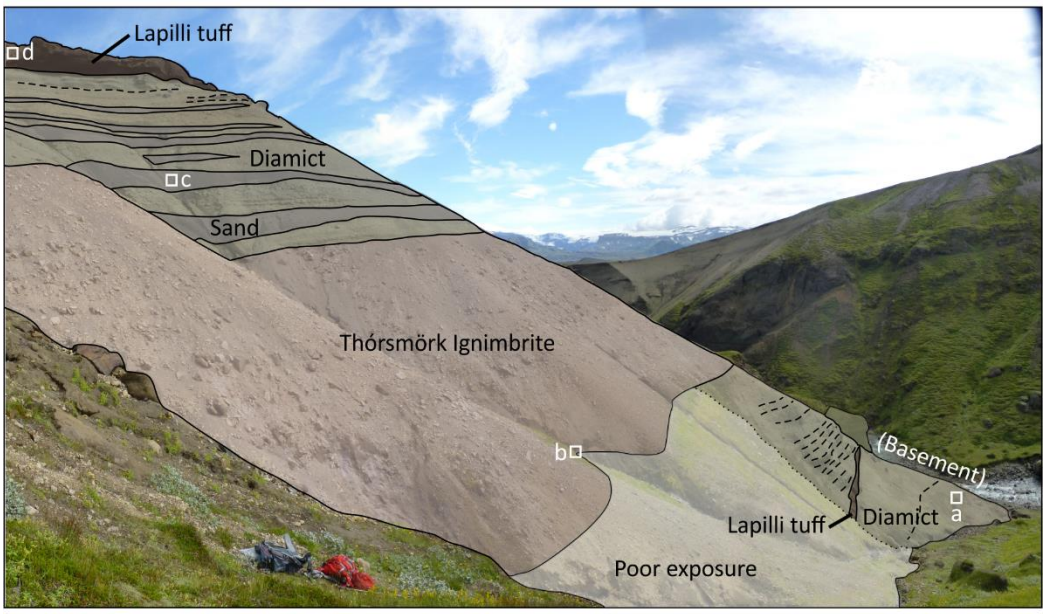
Lapilli tuff
d
Diamict
c
Sand
Thórsmörk Ignimbrite
b
(Basement)
a
Lapilli tuff
Diamict
Poor exposure

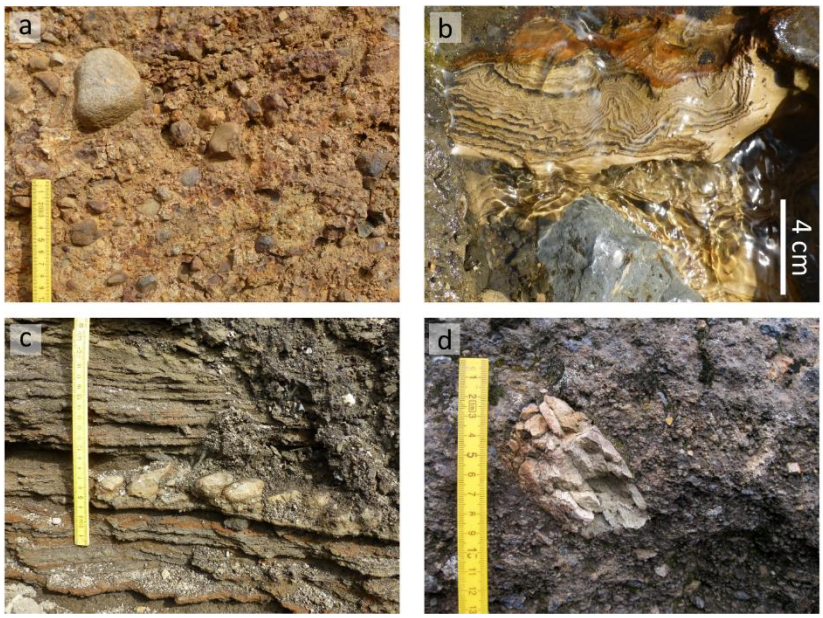
a
b
4 cm
c
d

Table 6.3. Lithofacies descriptions, Site 2.

Unit (thickness)	Description
i) Diamict (0–10 m)	Unconformably overlies basement (irregular palaeotopography). Clast sizes have a continuous range from silt to cobbles, and the clasts are typically sub-rounded to rounded (Figure 6.7 (a)). A range of clast types is present, but most clasts in the basal part are altered lithologies derived from the underlying basement. This unit lacks distinctive sedimentary structures.
ii) Lapilli tuff (basaltic; 1.2 m)	Basaltic scoria lapilli and palagonitised ash. A 4 cm thick bed of sand (including basaltic clasts) is present 35 cm above the base of the unit.
iii) Diamict (~15 m)	Similar to (i), clasts are silt to cobble sized, sub-rounded, and have a range of compositions (basalt and rhyolite). The lower ~2 m also contains rounded basaltic lapilli derived from the underlying unit. Metre-scale parallel bedding is present, with subtle variations in clast sizes between beds.
iv) Thórsmörk Ignimbrite (~20 m)	A layer of fine ash (8 cm thick) with convolute laminations is exposed at the base of the ignimbrite (Figure 6.7 (b)). This is overlain by an unconsolidated deposit (~4 m thick) primarily composed of well sorted sub-angular pumice lapilli. Within this deposit, there are angular blocks of pink and grey welded ignimbrite (2–15 cm) and irregularly-shaped domains of ash. The upper 10–15 m of the ignimbrite are poorly exposed, but appear to be an unconsolidated breccia composed of angular blocks of pale pink welded ignimbrite.
v) Interbedded diamict and sand (~25 m)	Above a sharp basal contact with the underlying ignimbrite, this unit consists of alternating beds of diamict and sand. The diamict is similar to unit (iii), but additionally contains clasts of ignimbrite and crystals derived from the ignimbrite. However, <10% of the cobble-sized clasts are ignimbrite, with other rhyolite and basaltic clast types dominant. The sand beds (1–1.5 m thick) are composed of well sorted fine to medium sand. Laminations (0.5–8 mm thick) are present throughout and are either parallel or low-angle cross-stratified. Rounded outsize pebbles of diamict are imbricated, and indicate palaeoflow to the SE (Figure 6.3 (c)).
vi) Lapilli tuff (basaltic; ~4 m)	Palagonitised basaltic lapilli tuff with cross-stratification and graded bedding. The juvenile clasts are coarse ash to fine lapilli. Rhyolite lithics clasts are found throughout (Figure 6.7 (d)). Vent located at Hitagilsbrún ~1 km to the NNW.

Site 3 (Eystri-Botná) is located 800 m east of Site 2, immediately south of a steep basement palaeoslope (Figure 6.5). The Thórsmörk Ignimbrite and local basaltic units are present in the succession (Figure 6.8; Table 6.4).

Further deposits of diamict and basaltic lapilli tuff (correlating with unit (vi) of Site 2) are present above the studied succession – these were not studied in detail due to poor exposure.

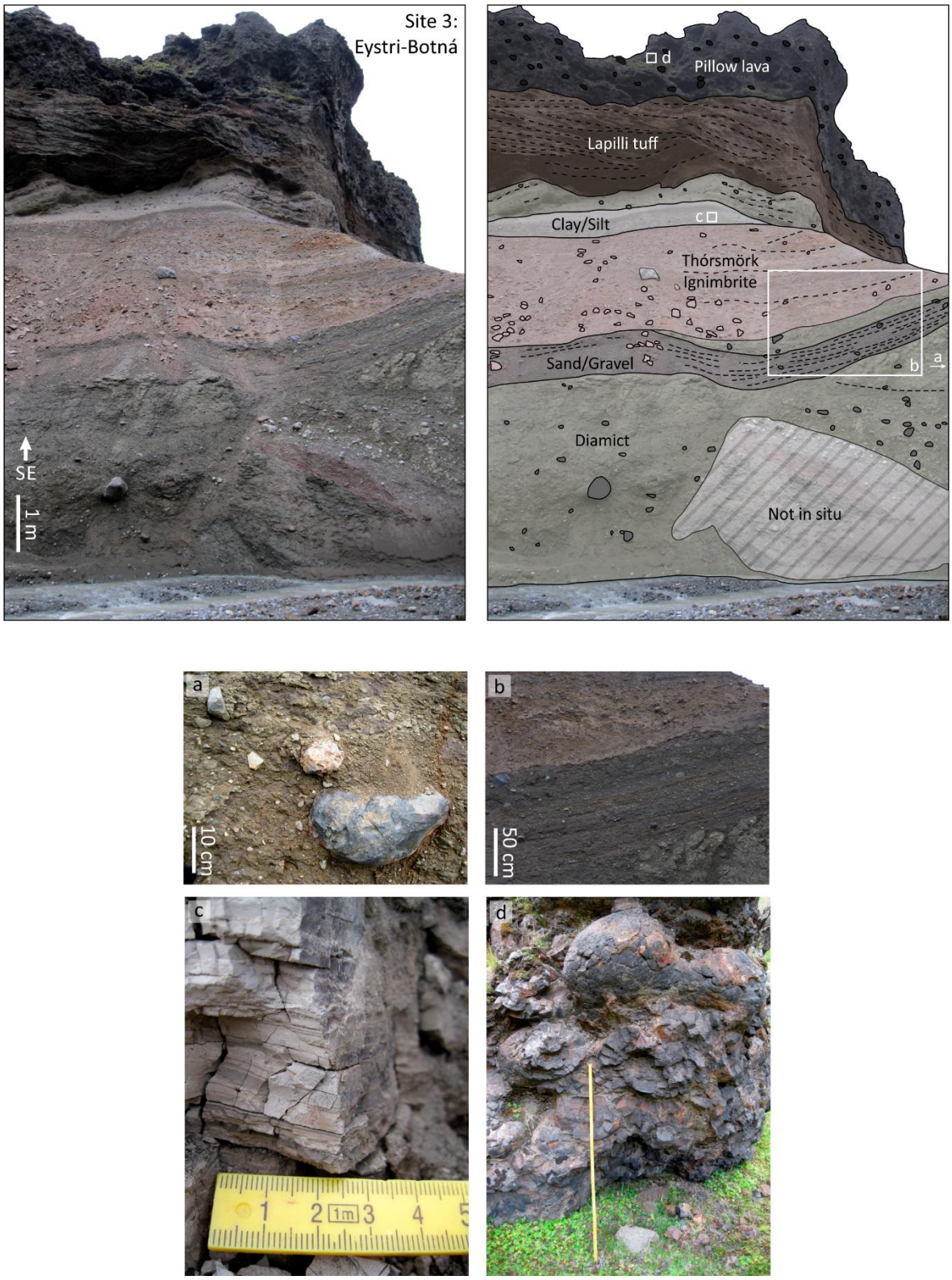

Figure 6.8. Overview and annotated photographs of Site 3. Inset photographs: (a) Diamict exposed near the base of the observed succession. (b) Bedded sand and gravel unit between layers of diamict, with the Thórsmörk Ignimbrite at the top of the photo. (c) Fine-grained laminated unit with alternating pale and dark laminae. (d) Pillow lava exposed in a fallen block.

Table 6.4. Lithofacies descriptions, Site 3.

Unit (thickness)	Description
i) Diamict (5 m minimum)	The basal contact is not seen at this site, but basement is observed to underlie this diamict unit ~400 m to the south. Additionally, basement with a steep palaeotopography is exposed on the opposite riverbank ~25 m north of this site. Clasts range from silt to boulders (up to 80 cm) and basalt to rhyolite compositions (Figure 6.8 (a)). Clasts are typically sub-rounded but some retain facets and striations. Beds with laterally variable thickness (typically 1 m) are present, with some beds truncating the bed underlying them at up to 5°.
ii) Sand/gravel (~1 m)	This unit consists of parallel bedded medium sand to gravel, with outsize cobbles (Figure 6.8 (b)). The components of individual beds are moderately well sorted, and both basaltic and rhyolitic clasts are present.
iii) Diamict (0–0.5 m)	A lens of diamict, with the same characteristics as unit (i), truncates unit (ii) at a low angle.
iv) Thórsmörk Ignimbrite (~10 m)	The basal part of the ignimbrite (bottom 5–10 cm) is a layer of fine ash, pale pink in colour and containing matrix vesicles. Also present in this layer are crystals, lithic clasts, accretionary lapilli, cored lapilli and angular clasts of welded ignimbrite up to 15 cm. A 5 cm layer of deep pink ash overlies this, with less abundant matrix vesicles and domains of grey ash. This is then overlain by a buff-coloured medium ash with black domains (5–10 cm across). The black domains are rich in lapilli that are cored with lithic clasts ~8 mm across. The remaining thickness of the ignimbrite is poorly exposed, but jointed blocks of grey and pink welded ignimbrite are present. An ignimbrite exposure ~120 m NE of this site has a highly convolute structure. The ignimbrite is laterally discontinuous in this area.
v) Clay/silt (~3 m)	Well sorted clays and silts with laminae 1–5 mm thick, poorly exposed. The laminae have pale-dark alternate layering (Figure 6.8 (c)). This unit has a minimum lateral extent of 200 m.
vi) Diamict (~3 m)	Similar to unit (i), but clasts of welded ignimbrite are also present.
vii) Lapilli tuff (basaltic; ~5 m)	Parallel bedded unit of palagonitised basaltic lapilli tuff. Individual beds are 5–20 cm thick. Vent possibly located at Kerhnúkar, 800 m to the NNE.
viii) Pillow lava (~10 m)	Basalt pillows ~60 cm across with radial jointing and vesicular interiors (Figure 6.8 (d)). The vent is located at Kerhnúkar, 800 m to the NNE.

Site 4 (Gilsá) is located ~2 km south of Sites 1–3. At this site, the succession is deposited on a sloping palaeosurface made up of mafic basement, Early Tindfjallajökull mafic rocks and Middle Tindfjallajökull silicic lava (Figure 6.5; Chapter 2). The units drape the slope – they are not horizontal – with only a gradual thinning towards higher elevations. The Thórsmörk Ignimbrite is near the base of the succession and three distinct basaltic units are present (Figure 6.9; Table 6.5).

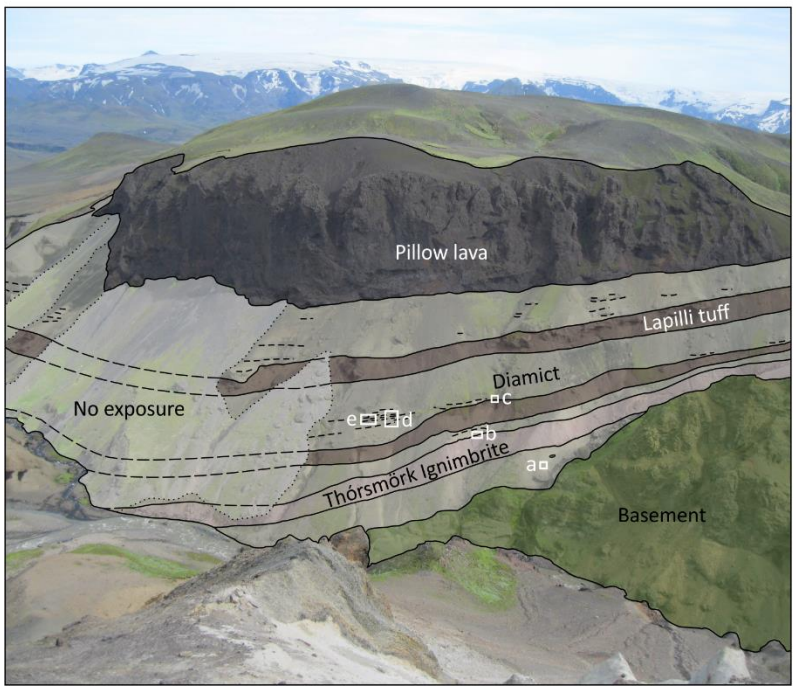

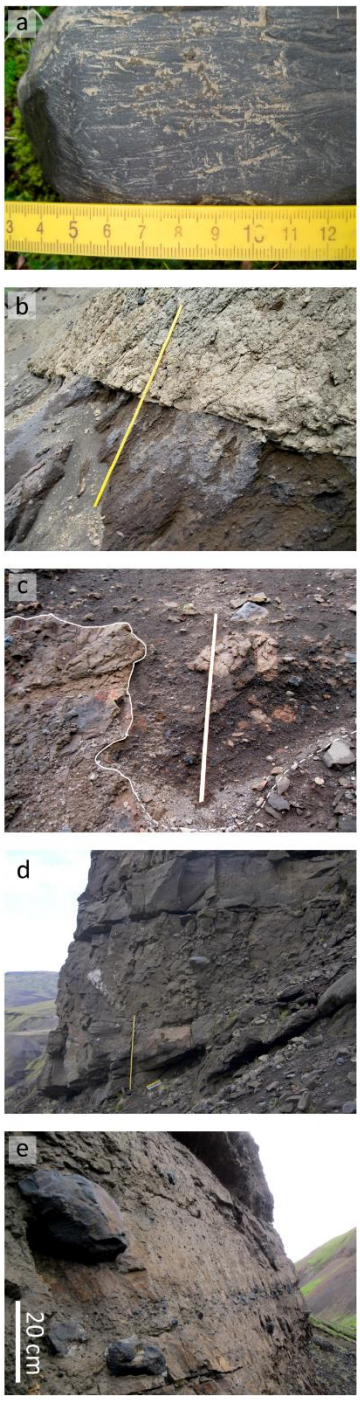

Figure 6.9 (previous page). Overview and annotated photographs of Site 4. Inset photographs: (a) Striated cobble extracted from the lowermost diamict. (b) Sharp contact at the top of the Thórsmörk Ignimbrite (dark grey lithology). (c) Basaltic lapilli tuff containing diamict clasts, with metre-deep scour into underlying diamict (contact highlighted with white line). (d) Diamict packages with lateral variations in thickness over several metres. (e) Diamict with boulders and a horizon rich in cobbles (lower part of photo).

Table 6.5. Lithofacies descriptions, Site 4.

Unit (thickness)	Description
i) Diamict (2–8 m, thins up palaeoslope)	Unconformably overlies basement (palaeosurface slopes to NE). Grain size from silt to cobbles. Occasional boulders up to 1.5 m are locally derived rhyolite lava. However, most clasts are basaltic (~75%). Clasts are typically sub-rounded, though some retain facets and striations (Figure 6.9 (a)). No distinct structures observed.
ii) Thórsmörk Ignimbrite (~10 m)	Conformably overlies (i). The lower parts are poorly exposed, but include layers of unconsolidated ash (pink, grey and brown) and angular pumice. This appears to be overlain by grey and pink domains of brecciated welded ignimbrite. The upper part of the ignimbrite has lateral variations in the degree of welding, transitioning continuously from welded (pink-grey) to unconsolidated (buff) ignimbrite over ~5 m. The welded parts are jointed and contain rare fiamme, and the unconsolidated parts contain ~2% pumice. Additionally, there is an irregularly-shaped contact between the buff ignimbrite and a dark grey lithology (also unconsolidated).
iii) Diamict (~4 m)	Basal contact is sharp and truncates structures in the underlying ignimbrite (Figure 6.9 (b)). This unit is similar to (i), but also contains clasts of welded ignimbrite. There are two distinct beds in this unit – the upper bed is more prominent and has a lower silt content.
iv) Lapilli tuff (basaltic; ~6 m)	Basaltic unit composed of sub-rounded to sub-angular vesicular lapilli (0.5–20 mm). Grain size fluctuates up through the unit, but no other structures are visible. There are metre deep scours into the underlying diamict (Figure 6.9 (c)). The lower part of the unit contains diamict clasts 2–150 cm across, with lobate or cuboidal shapes. Other lithic clasts are present, which are derived from break-up of the diamict. Diamict clasts are most abundant near the base and where the lapilli are most coarse.

v) Diamict (~20 m)	Sharp contact with underlying unit. This diamict unit is made up of multiple packages of sediment, similar to Site 1 (units (i) and (iii)). Each bed has lateral variations in thickness (Figure 6.9 (d)). Grain size is from silt to boulders but the proportions vary through the sequence. For instance, cobbles and boulders usually make up <5% of the sediment, but there is a 20 cm thick bed containing ~30% cobbles (Figure 6.9 (e)). The clasts are sub-rounded to rounded and are predominantly basaltic (~90%), with subordinate rhyolite lava and ignimbrite clasts. The upper part of this unit is poorly exposed.
vi) Lapilli tuff (basaltic; ~5 m)	Similar to unit (iv). The finer-grained parts of the deposit are cross-stratified.
vi) Diamict (~20 m)	Sharp contact with underlying unit. Similar to unit (v), though >95% of clasts are basaltic. Bottom ~30 cm contains scoria from the underlying unit. The upper part of the unit is poorly exposed.
vii) Pillow lava (~50 m)	A thick pile of pillow lavas caps the succession at this site. Columnar-jointed lavas intrude the interior of the pile.

Site 5 (Tröllagjá) is located 2.4 km south of Site 4 at the edge of the wide Markarfljót valley (Figure 6.5). The base of the depositional succession is not exposed in this area, but the Thórsmörk Ignimbrite and overlying sediments are well exposed (Figure 6.10; Table 6.6).

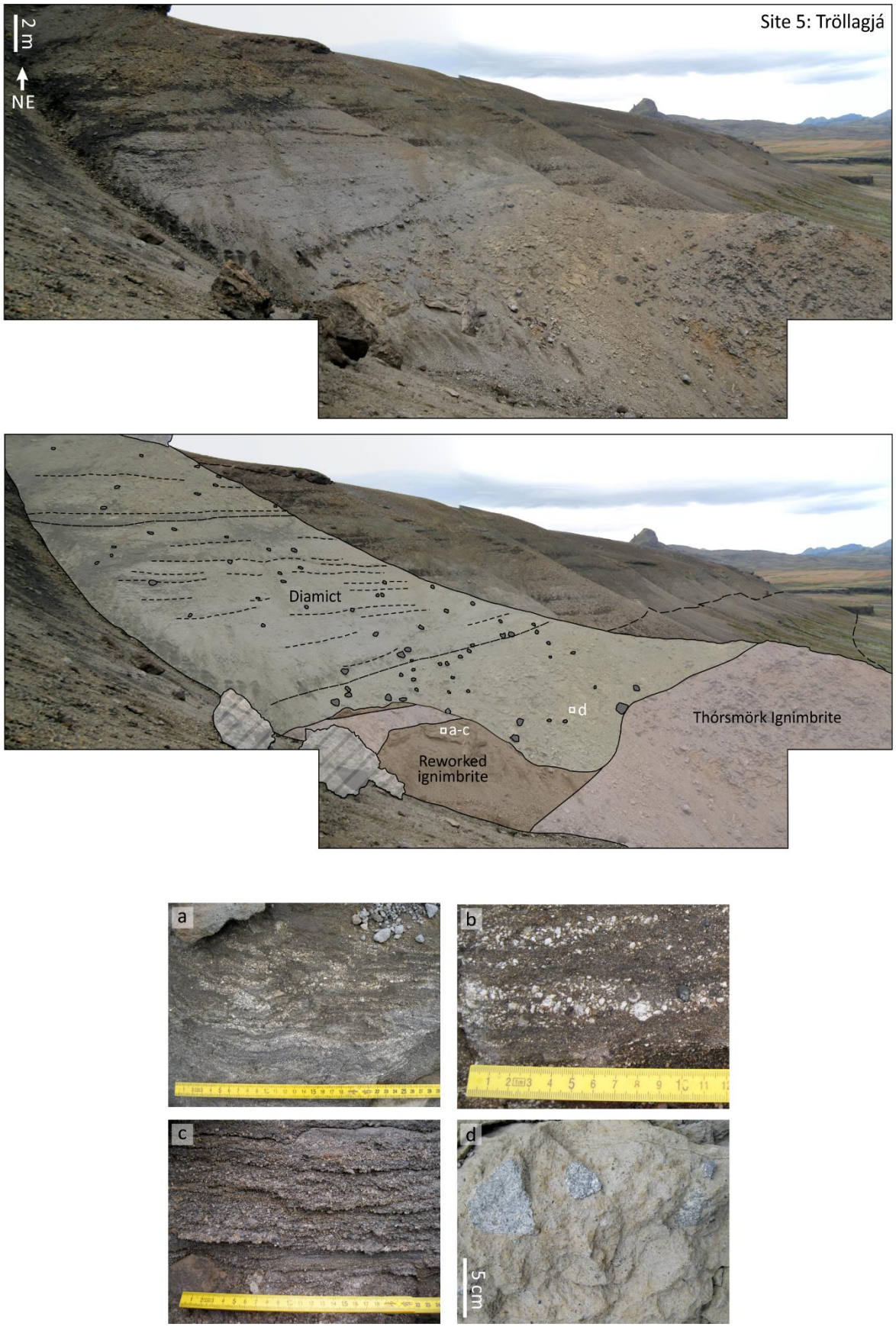

Figure 6.10. Overview and annotated photographs of Site 5. Inset photographs: (a–c) Well sorted lenses of reworked ignimbrite material. The pale clasts in (a) and (b) are composed of pumice. (d) Buff-coloured diamict with clasts of welded ignimbrite.

Table 6.6. Lithofacies descriptions, Site 5.

Unit (thickness)	Description
i) Diamict (3 m minimum)	Not shown in Figure 6.10. Base not seen. Clast size is predominantly silt but ranges from clay to cobbles. Pebbles and cobbles make up ~5% of the deposit and are rounded basaltic clasts. No visible structures.
ii) Thórsmörk Ignimbrite (~10 m)	Base not seen. At this site, the ignimbrite is dominated by a grey welded lithology with columnar joints (~15 cm joint spacing). Joint surfaces have an orange staining. The degree of welding decreases up through the ignimbrite, from strongly welded to incipiently welded. The upper ~30 cm of the ignimbrite is brecciated and has a red/orange stained cement.
iii) Reworked ignimbrite (0–3 m)	Sand to gravel sized clasts of welded ignimbrite, rounded pumice, feldspar crystals and lithic clasts. The deposit consists of lenses with different grain sizes and different proportions of the various reworked ignimbrite components (Figures 6.10 (a–c)). Lenses rich in pumice are clearly visible in Figures 6.10 (a–b). Individual lenses are typically ~1 cm thick, extend 5–15 cm laterally and are well sorted. Erosion of some lenses has occurred before deposition of the next lens. Some areas have been distorted through slumping.
iv) Thórsmörk Ignimbrite (0–1 m)	A layer of buff fine ash with occasional pumice clasts (up to 5 cm across) overlies unit (iii).
v) Reworked ignimbrite (0–0.2 m)	Sharply overlies unit (iv). Bedded gravels composed of sub-angular to sub-rounded clasts of welded ignimbrite, feldspar crystals and basaltic lithic clasts. Orange-stained cement.
vi) Diamict (15 m minimum)	Truncates units (iii) to (v). Clasts range from silt to cobbles, with occasional boulders. In the lower ~10 m, most coarse sand to cobble-sized clasts are sub-rounded welded ignimbrite (Figure 6.10(d)), with basaltic clasts and feldspar crystals also present. The fine component of the lower ~5 m is pale buff colour, containing a large proportion of reworked ash. Above this, the unit is light grey, with a high proportion of comminuted welded ignimbrite. In the upper ~5 m, the abundance of basaltic clasts outweighs ignimbrite clasts. At approximately the level of this transition, there is a ~40 cm thick interval that contains ~20% scoriaceous basaltic lapilli (initially sub-angular, but rounded higher in the succession).

Site 6 (Kápa) is situated in a low-lying area to the south of the Markarfljót (Figure 6.4). The base of the Thórsmörk Ignimbrite is not seen at this site, but the overlying reworked ignimbrite material and sediments are well exposed (Figure 6.11; Table 6.7).

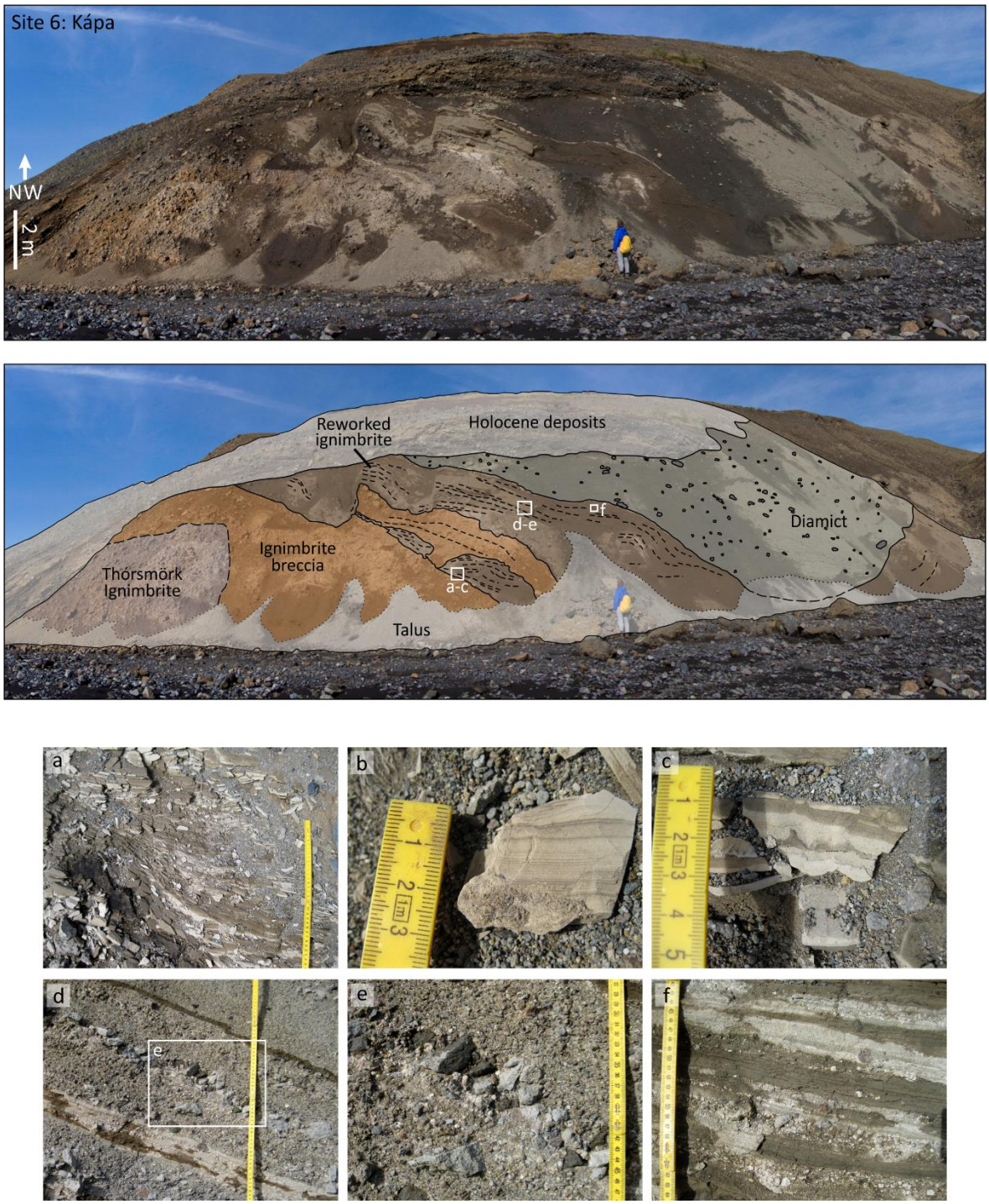

Figure 6.11. Overview and annotated photographs of Site 6. Inset photographs: (a) Laminated reworked tephra. (b) Close-up of pale and dark alternating laminae in reworked tephra. (c) Load and flame structures in laminated reworked tephra. (d) Reworked ignimbrite material with well sorted beds of silt (ash-dominated) to pebbles (welded ignimbrite-dominated). (e) Imbrication of pebbles in reworked ignimbrite. (f) Laminated reworked tephra containing rounded pumice clasts.

Table 6.7. Lithofacies descriptions, Site 6.

Unit (thickness)	Description
i) Thórsmörk Ignimbrite (4 m minimum)	Base not seen at this site. Jointed welded ignimbrite, poorly exposed.
ii) Ignimbrite breccia (1–4 m)	Diffuse and irregular contact with underlying ignimbrite. Angular blocks of ignimbrite (5–25 cm) supported by a matrix of reworked ash and pumice (silt to fine sand grain size). The matrix is well sorted and laminated (1–10 mm thick laminae).
iii) Reworked ignimbrite (0–0.8 m)	This unit is composed of reworked tephra, similar to the matrix of unit (ii). Silt to fine sand with laminae <1 mm – 10 mm thick (Figure 6.11 (a, b). Laminae commonly alternate between pale (~fine sand) and dark (~silt), with load and flame structures observed at lamination interfaces (Figure 6.11 (c)).
iv) Ignimbrite breccia (0–1.2 m)	Breccia composed of angular to sub-angular clasts of welded ignimbrite, from gravel (0.2 cm) to blocks up to 50 cm.
v) Reworked ignimbrite (~2 m)	Truncates units (iii) and (iv). Bedded unit consisting of reworked tephra and welded ignimbrite material (Figure 6.11 (d)). Grain size and componentry fluctuates from silt (ash) to coarse sand (ash, crystals and lithic clasts) to pebbles (sub-angular welded ignimbrite clasts). Silt/sand beds are laminated, as per unit (iii), and sand/gravel layers often additionally contain rounded pumices (Figure 6.11 (f)). Individual beds/laminae are well sorted by mass. Welded ignimbrite clasts are observed to be imbricated (palaeoflow to NE in Figure 6.11 (e)).
vi) Diamict (6 m minimum)	Slight truncation of underlying unit. Sub-rounded clasts from silt to cobble size. Approximately 90% of the gravel-cobble sized clasts are composed of ignimbrite, and feldspar crystals are found in the sand-sized component. Rhyolite and basalt lava clasts are also present. No distinct structures.

The units at Site 6 have been distorted following deposition. This deformation is picked out as tilted and folded bedding planes in units (ii) to (v). The other units lack structures that would indicate that deformation has taken place.

6.4.2 Palaeoenvironment interpretations

In this section, the depositional environment of each of the described lithofacies is interpreted. Marine environments are not considered, as all sites are at a higher elevation than the maximum marine limit in Iceland at the end of the last glacial period (~150 m elevation inferred from marine terraces; Ingólfsson and Norddahl, 2001).

Diamict

Diamict (including 'Diamict packages') is found at all 6 study sites, and is the dominant sedimentary lithofacies in the studied successions. The wide range of clast sizes and clast types is typical of glacially worked debris, and the presence of facetted and striated clasts confirms that glacial transport contributed to the formation of the diamict. Abrasion of clasts, producing facets and striations, occurs during transport of debris in the basal part of the ice (Eyles et al., 1985). Clasts that do not have abraded surfaces may have undergone little erosion due to their transport within and on top of the ice (e.g. through mass-wasting onto the glacier from adjacent slopes (Evans, 2005)).

Many different processes can contribute to the final sedimentation of glacially worked debris, and it is often difficult to define what processes controlled deposition following release of the material from the ice (Martini et al., 2011). The presence of diamict units that are laterally extensive (>100 m), thick (>10 m) and devoid of evidence of shearing suggests that deposition did not occur in a subglacial setting. Additionally, the widespread distribution of diamict, from the low-lying Markarfljót valley (200 m elevation) to the flanks of Tindfjallajökull (up to 700 m elevation), makes lacustrine deposition unlikely. It is proposed that, in most or all sites, diamict was deposited in a subaerial environment by debris flows.

Debris flows – highly concentrated mixtures of debris and water – are a common mechanism for the remobilisation of unconsolidated glacially worked debris (Blikra and Nemec, 1998). As observed in the studied successions, debris flow deposits retain the poorly sorted characteristics of the original debris, and sedimentary structures (e.g. grading, stratification) are

scarce or entirely absent (Eyles et al., 1985). Each debris flow produces one bed or 'package' of sediment that may take the form of a broad lobe (Blikra and Nemec, 1998). After deposition, water flowing over the debris flow deposit can produce thin layers and lenses of sorted sand and gravel, as observed at Site 1, which may be removed by subsequent erosion (Lawson, 1981).

The thick successions of diamict indicate that a significant volume of glacially worked debris was available at the time of deposition, possibly following a period of ice retreat. Draping of diamict units onto the valley sides at Tindfjallajökull (e.g. Site 4) indicates that the debris flows transported material down the local slopes, rather than inundating the low-lying areas from a more distant source. Some of the debris may be derived directly from the local slopes without glacial transport. For instance, the central silicic edifice of Tindfjallajökull is steep-sided, hydrothermally-altered, water-saturated and unconsolidated: unstable material that could easily be incorporated into debris flows. Additionally, other lithofacies that make up the local depositional successions are incorporated into subsequent diamict units. For instance, clasts derived from the Thórsmörk Ignimbrite are present in the overlying diamict units, and in some cases may have been redeposited over very short distances (perhaps less than 100 m; e.g. ignimbrite material in lower part of unit (vi), Site 5).

Debris flows commonly occur on ice-clad volcanoes such as Mount Rainier (Scott et al., 1995). The flows are often triggered by the water-saturation of unconsolidated debris, which increases the pore water pressure (Lawson, 1981). At Mount Rainier, saturation fluctuates with the seasons due to the melting of ice and snow during spring/summer and rainfall events in the autumn (Scott et al., 1995). Similarly, the debris flows on the flanks of Tindfjallajökull may have been triggered by seasonal processes such as the thawing of ice and snow during summer.

Sand/Gravel

The layers of sand at Site 2 and sand/gravel at Site 3 have undergone a greater degree of sorting compared to the diamict. The presence of parallel and cross-stratified laminations, and the lack of silt-sized clasts, suggests that these units were transported and deposited by flowing water. This is supported by the rounding and imbrication of outsize clasts at Site 2, which indicate a flow direction down the Vestri-Botná valley. These clasts are composed of diamict derived from a previously-deposited diamict unit. The overall range of clast types observed in the sand/gravel are similar to those observed in the diamicts, suggesting that the sand and gravel is derived from reworking of previously-deposited diamict units and/or mobilisation of the same source material.

It is interpreted that streams of flowing water resulted in erosion of diamict, transport of this material down valleys, and subsequent deposition of sorted sands and gravels in valley bottoms. At Site 2, the lateral extent of sand layers (>100 m) and the close association with debris flow deposits suggests that the valley was not filled with ice at the time. It is not clear if ice was present at Site 3, as it is possible that the sand/gravel was deposited in a subglacial cavity. There may be a degree of seasonality associated with the deposition of the sand/gravel. In the context of the climate of the last glacial period, the formation of surface streams may only have occurred during the summer, and may have been associated with rainfall and/or the melting of ice and snow. Water may alternatively have been derived from hot springs associated with the hydrothermal system that is still active locally (Chapter 2).

Clay/Silt

The laminated clay/silt at Site 3 is interpreted to have been deposited through the settling out of suspended sediment in a body of still water. This type of deposit is typical of lacustrine environments where the lake bed is not affected by bottom current activity (e.g. Bennett et al., 2000a). The alternating dark/pale laminae may have a seasonal control, or may represent individual depositional events.

The minimum lateral extent of this unit (200 m) provides a minimum size of the body of water in which it was deposited. The water may have infilled a topographic hollow on the surface of the Thórsmörk Ignimbrite (the underlying unit). It is possible that the lake was dammed by ice, but there is no evidence of ice calving into the lake (e.g. dropstones or iceberg scours).

Thórsmörk Ignimbrite

The complex lithologies and structure of the Thórsmörk Ignimbrite are poorly understood, making it difficult to identify which characteristics of the ignimbrite provide palaeoenvironmental information. However, some of the unusual features of the ignimbrite may be a result of the environmental conditions at the time of the eruption.

Jørgensen (1980) noted that the welded parts of the ignimbrite are pink in colour close to Tindfjallajökull, and attributed this to hydrothermal alteration occurring around the central volcano. However, alteration is not evident in the deposits above and below the ignimbrite in this area (Sites 1–4). Instead, the pink colour of the ignimbrite on the flanks of Tindfjallajökull (at elevations above 350 m) may be due to thermal oxidation, driven by the interaction of water vapour with the deposit immediately following emplacement (Walker and Croasdale, 1971). Cowlyn (2016) suggested that the patchy red colour of an ignimbrite on Ruapehu volcano, New Zealand, was a result of thermal oxidation, and that the water vapour was sourced from melting snow or ice. Although oxidation of pyroclastic deposits is not diagnostic of ice or snow interaction (Cowlyn, 2016), the localised oxidation of the Thórsmörk Ignimbrite at higher elevations could be an indicator that ice or snow was present in these areas at the time of ignimbrite deposition.

Emplacement of the ignimbrite on ice or snow may partly explain the complex lithologies and structure of the deposit. Interaction between the ignimbrite and meltwater could have triggered secondary hydrovolcanic explosions and/or debris flows of ignimbrite material entrained in meltwater. Additionally, the melting of ice or snow under the ignimbrite could

have resulted in subsided stratigraphy and brecciation. At Site 3, the basal pink ash deposits containing matrix vesicles, cored lapilli and clasts of welded ignimbrite may have been produced through hydrovolcanic explosions. At Site 2 and Site 4 (and an exposure NE of Site 3), the complex and non-horizontal contacts between different domains of the ignimbrite may be due to slumping and/or subsidence caused by melting ice or snow. However, other explanations for these latter structures are possible, such as the emplacement of the ignimbrite on unconsolidated sediments and sloping surfaces, and the potential for later deformation by glacial and permafrost processes. The relative impact of these processes cannot be understood without a more detailed examination of the structure of the ignimbrite.

Although some parts of the ignimbrite may have been emplaced on ice or snow, the preservation of the ignimbrite as a whole suggests that there was not a substantial body of ice in this area at the time of the eruption. Deposition of ignimbrite on a thick body of ice would likely result in the removal and break-up of the deposit as the ice moved and melted. It is possible that some ignimbrite deposits would be preserved after stagnation and melting of the ice, but these would be significantly modified from the original ignimbrite. Despite widespread brecciation in the Thórsmörk Ignimbrite, many original structures remain intact that would probably not have been preserved if thick ice was present. These include the stratified ash deposits at Sites 2–4 (including matrix vesicles at Site 3) and the intact columnar jointing at Site 5. Furthermore, no glacially worked debris has been found associated with the ignimbrite that could convincingly be derived through melt-out from stagnating ice.

Reworked ignimbrite (including Ignimbrite breccia)

Reworking of pyroclastic material on the surface of the Thórsmörk Ignimbrite has produced a range of volcaniclastic lithologies at Sites 5 and 6. Laminated and well sorted lenses of tephra and welded ignimbrite clasts (some of which are imbricated) indicate that much of this material was transported and deposited by flowing water. Frequent depositional events formed the pale and dark alternating laminae with load and flame structures in the silty layers at Site 6

(Bennett et al., 2000b). Erosion occurred between deposition of some of the layers/units, to create the observed truncations in stratigraphy. The presence of reworked ignimbrite between primary ignimbrite layers at Site 5 suggests that some reworking occurred during the course of the Thórsmörk Ignimbrite eruption.

In the sites studied here, the reworked material was probably sourced locally from the surface of the ignimbrite. In the ignimbrite breccias, the angularity of the welded ignimbrite clasts indicates that transport only occurred over short distances. The angular blocks of welded ignimbrite within a laminated silt matrix (Site 6, unit ii) may have simply fallen into this deposit from the adjacent outcrop of jointed ignimbrite. Towards the margins of the ignimbrite, volcaniclastic material may also have been sourced from adjacent topographic highs and/or ice margins.

At both Sites 5 and 6, the reworked ignimbrite units have been deformed after deposition (at Site 6, the overlying diamict may also have been deformed). This deformation may have occurred through subsidence of the underlying ignimbrite, slumping of the unconsolidated sediments on the irregular surface of the ignimbrite, or later glaciotectonism (Eyles et al., 1985).

Pillow lava

Pillow lavas are indicative of the eruption of magma into water (Jones, 1966). The basaltic pillow lava piles at Sites 3 and 4 both reach elevations of ~500 m. At these locations and elevations, there are no topographic barriers suitable for damming a lake. Therefore, it is interpreted that the pillow lavas erupted into a body of meltwater confined in a subglacial environment (as is commonly concluded at other glaciated volcanoes, e.g. Jones, 1969; Smellie and Skilling, 1994). There is no evidence, such as subaerial lavas, to indicate that the eruptions breached the surface of the water and/or ice.

The pillow lavas provide minimum constraints on the thickness of ice that was present during the eruption of each unit. In order to impound the water, there must have been a body of

impermeable ice with a surface elevation over 500 m. If the permeable snow, firn and crevassed ice in the upper part of the ice is also included, the minimum ice surface elevation at the time of the eruptions was ~600 m (see Chapter 2 for details on estimating ice surface elevations from impounded water levels).

Lapilli tuffs

Similar to the pillow lavas, the lapilli tuffs at Sites 2–4 are the products of local basaltic eruptions and contain evidence that water was present during the eruptions. The presence of a high proportion of ash in the deposits is attributed to quench fragmentation and explosive fragmentation during magma-water interaction (Honnorez and Kirst, 1975; Rittman, 1958). Additionally, the structures in some of the units, such as cross-stratification (Sites 2 (vi) and 4 (vi)) and the erosion and incorporation of material from underlying deposits (Site 4 (iv)), suggest that transport occurred as a flow of pyroclasts mixed with water.

Unlike the pillow lavas, not all of the lapilli tuffs are diagnostic of the presence of ice at the site of deposition. Water could potentially have been sourced from ice limited to the area around the vent (the location of which is often unknown), groundwater or, at low elevations, a lake (though there is no evidence of lacustrine sedimentation in deposits immediately underlying or overlying the lapilli tuffs). At Site 2, lapilli tuff unit (vi) is seen to be sourced from Hitagilsbrún, a steep-sided tuff cone constructed during the same eruption which has since partly collapsed (Chapter 2, Figure 2.3(d)). In this example, the formation of a steep-sided edifice (up to ~900 m elevation), with magma-water interaction throughout, indicates that thick ice was present at the time of the eruption, with an ice surface elevation >900 m.

6.4.3 Summary of palaeoenvironmental information

The depositional environments of the studied successions are summarised as follows.

Environment before emplacement of the Thórsmörk Ignimbrite

The ignimbrite is consistently underlain by diamict. Unconsolidated debris was transported down the local slopes as debris flows, and deposited in a subaerial environment. The contribution of glacial processes to the production of the debris indicates that ice was locally present or had recently retreated from the area. Flowing water remobilised some of the debris at Sites 1 and 3 (Figure 6.12(A)).

Environment at the time of ignimbrite emplacement

As the ignimbrite is typically conformable with the underlying sediments, it is assumed that the depositional environment reconstructed from the underlying sediments was largely unchanged by the time of ignimbrite emplacement. The ignimbrite indicates that the area of study was devoid of thick ice at the time of the eruption, consistent with the pre-eruptive environment described above. Some accumulations of ice or snow may have been present, particularly at elevations >350 m (Figure 6.12(A)).

Environment after ignimbrite emplacement

Pyroclastic material on the surface of the ignimbrite was remobilised by flowing water. At Site 5 there is evidence that this may have occurred before the end of the eruption. Erosion of the ignimbrite at Sites 1–5 (including the reworked ignimbrite at Site 5) has resulted in an unconformable contact with the overlying sediments. The length of time represented by this period of erosion in unknown. However, the good preservation of the ignimbrite, despite much of the deposit being unconsolidated, suggests that erosion was short-lived and was limited to the upper parts of the ignimbrite or to areas of focussed dissection.

Following this stage of ignimbrite reworking and erosion, deposition of diamict continued largely unchanged from the pre-eruptive conditions (Figure 6.12(B)). A body of standing water existed on the surface of the ignimbrite at Site 3 before diamict deposition returned. Flowing water, which may have been derived from hot springs, rainfall and/or the seasonal melting of

snow, periodically remobilised sedimentary material in the Vestri-Botná valley (Site 2). Lapilli tuffs at Site 4 record local basaltic eruptions, but their eruptive environment is not certain.

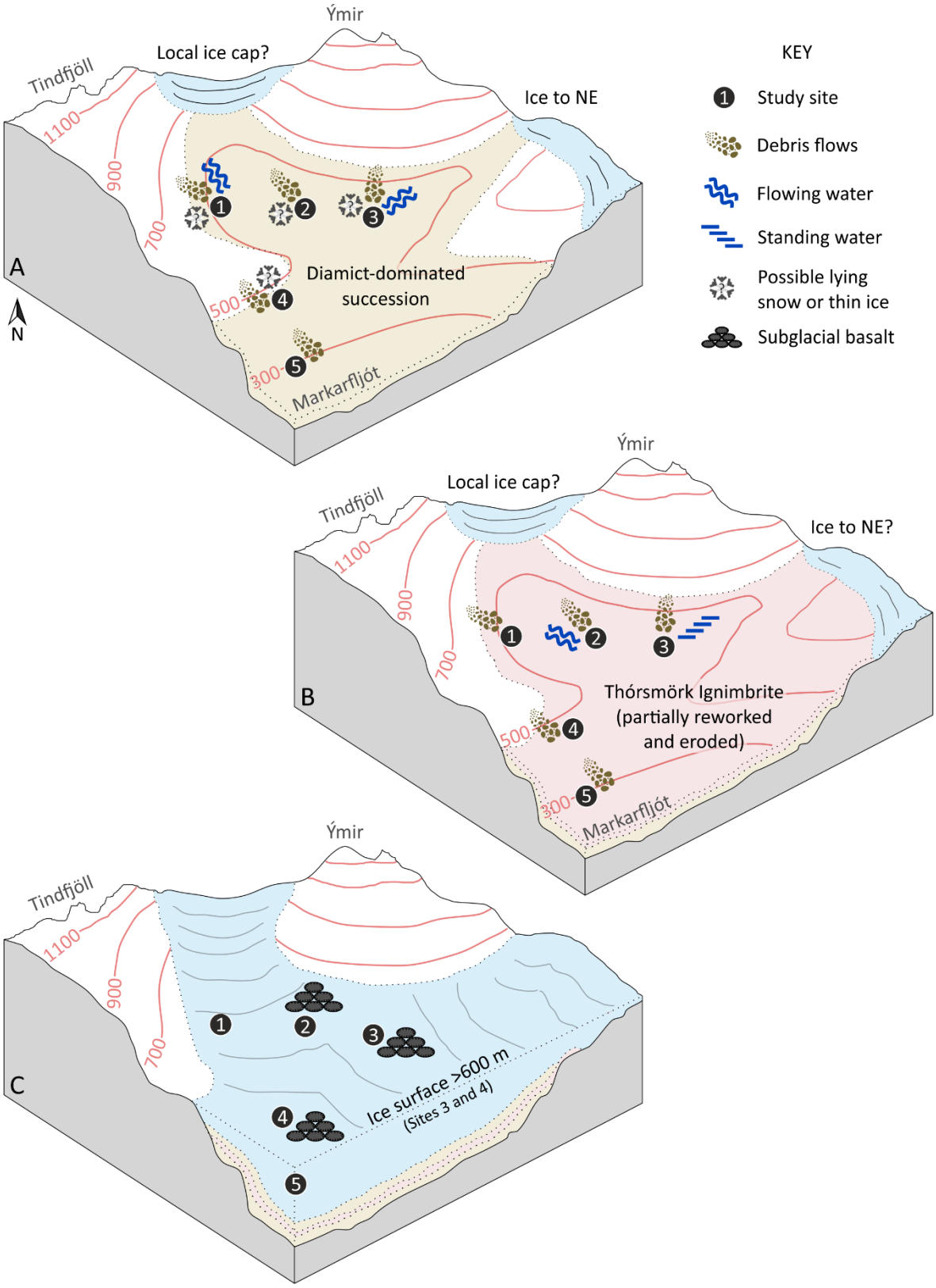

Figure 6.12. Depositional environments on the SE flank of Tindfjallajökull (Sites 1–5) around the time of the Thorsmörk Ignimbrite eruption. A) Environmental context of ignimbrite emplacement (end GI-15.2). Prior to the ignimbrite-forming eruption, a diamict-dominated succession was deposited through

subaerial debris flows, with some action by flowing water. Snow or thin ice may have been present at the time of the eruption, particularly at higher elevations. B) Environment after ignimbrite emplacement. Deposition through subaerial debris flows continued, as well as spatially limited areas of flowing and standing water. It is unknown if areas of snow or ice were also present during deposition of these units. C) Later on, the occurrence of subglacial basaltic eruptions indicates the presence of ice in the landscape. The surface elevation of the ice was >600 m during eruptions at Sites 3 and 4, and may have been >900 m during an eruption recorded at Site 2. The timing of these events is poorly constrained.

Continuing evolution of the environment

Basaltic eruptions, preserved at the top of the studied successions at Sites 2–4, record the presence of ice cover at the time of their emplacement (Figure 6.12(C)). The eruptions are distinct localised events with different vent locations. Without dated marker horizons in this part of the stratigraphy, the timing of these events is unknown. However, the eruptive units do not significantly truncate the underlying sediments, indicating that there was not a major period of erosion between deposition of the sediments and subglacial emplacement of the capping basaltic units.

6.5 INTEGRATION OF TERRESTRIAL PALAEOENVIRONMENTAL INFORMATION WITH THE CLIMATE RECORD

Using the chronostratigraphic marker formed by the products of the Ring Fracture Rhyolites eruption, the terrestrial palaeoenvironmental information derived from the Ring Fracture Rhyolites (section 6.3) and from successions containing the Thórsmörk Ignimbrite (section 6.4) can be linked together and integrated with the regional climate record (section 6.2).

6.5.1 Terrestrial palaeoenvironment at the end of Greenland Interstadial 15.2

Palaeoenvironmental evidence that has a direct temporal association with the Ring Fracture Rhyolites and the Thórsmörk Ignimbrite can be dated to the end of Greenland Interstadial

15.2 using the II-RHY-1 tephra isochron in the Greenland ice core climatostratigraphy (Section 6.2.1).

The reconstructed glacial conditions in south Iceland at end-GI-15.2 are summarised in Figure 6.13. Whilst the Torfajökull area was covered by ice with a surface elevation >1200 m, there was no or little ice in the Thórsmörk area ~30 km to the south-southwest. The area of ignimbrite outcrop represents the minimum extent of this ice-poor area, which may not have been entirely free from thin ice or snow, particularly above 350 m elevation. It is likely that there was also little or no ice cover further down the Markarfljót valley, though any ignimbrite deposits there have been buried by Holocene alluvium.

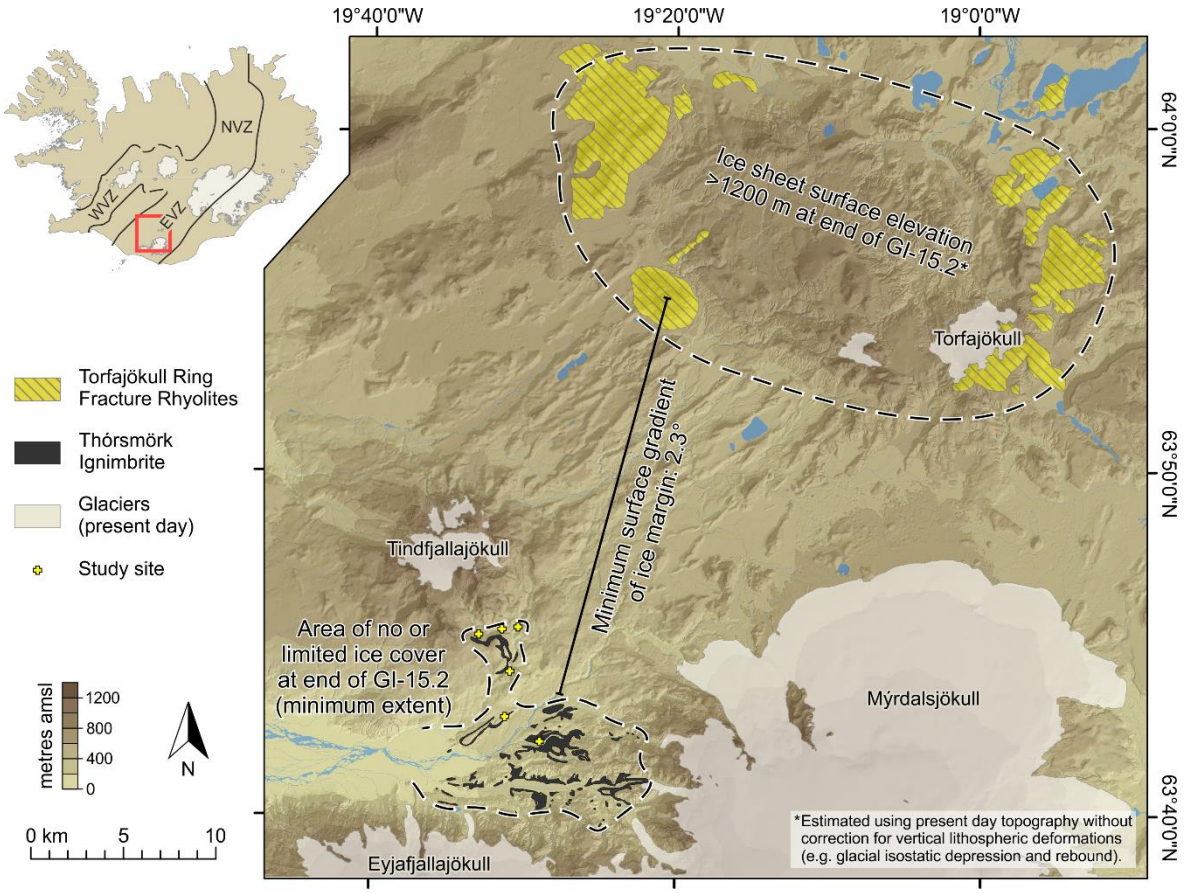

Figure 6.13. Map of the Torfajökull Ring Fracture Rhyolites and the Thórsmörk Ignimbrite, with palaeoenvironment study locations marked. The geometries of the outcrops of both units can be used to reconstruct the glacial environment at the time of the eruption. Geological mapping from Jørgensen (1980) and Sæmundsson and Friðleifsson (2001). Topography and hydrology data from Landmælingar Íslands (2016).

The average gradient from Thórsmörk to the top of Laufafell tuya is 2.3°. This figure represents a minimum estimate of the ice surface gradient at the time of the eruption (Figure 6.13). The estimate is a minimum because it assumes that the ice extended all the way to Thórsmörk and that the ice surface elevation at Laufafell was no higher than the top of the tuya. An ice surface gradient of 2.3° is similar to the present-day northern margin of Vatnajökull (average gradients of ~2.4° (west sector) and ~1.9° (east sector)) and shallower than the present-day northern margin of Mýrdalsjökull (~5.2°).

Given the high susceptibility of Iceland to large-scale glaciation (Bingham et al., 2003; Hubbard et al., 2006; Patton et al., 2017), it has been considered likely that a substantial ice mass was present on the island throughout much of the last glacial period (Patton, 2013). However, the physical record of ice conditions before the last glacial maximum (~23 ka) is sparse and poorly time-constrained (Norddahl and Pétursson, 2005; Patton, 2013). Due to this lack of precisely-dated physical evidence, numerical modelling of the Icelandic Ice Sheet has not been attempted for the period prior to 35 ka (Patton et al., 2017). The evidence for a thick body of ice at Torfajökull at the end of GI-15.2 (~55 ka) confirms that Iceland did host a large volume of ice at this time. It is possible that the ice at Torfajökull was part of an extensive ice sheet that covered much of Iceland's interior, linking up with present-day Vatnajökull to the NE of Torfajökull. The existence of an ice-poor area at Thórsmörk indicates that the ice sheet margin in this sector was grounded in a terrestrial environment. The ice thickness and extent data derived from the Ring Fracture Rhyolites and the Thórsmörk Ignimbrite can be used to constrain numerical models of the glacial evolution of Iceland.

Although numerical modelling of the Icelandic Ice Sheet has not been attempted for the studied time period (end GI-15.2; ~55 ka), the reconstructed glacial environment can be compared to existing models (post-35 ka) to assess whether a similar ice configuration may have occurred later in the Pleistocene. The reconstructed extent of ice in the Thórsmörk/Torfajökull area at the end of GI-15.2 is similar to that modelled at 14.04 ka by Patton et al. (2017). This time-slice of the model occurs during the retreat of the Icelandic Ice

Sheet in GI-1, and shows no ice in the Thórsmörk area whilst Torfajökull is completely ice-covered (Figure 6.14). The simultaneous existence of a substantial (~50,000 km^2) inland ice sheet and relatively small ice caps on outlying topographic highs (e.g. Tindfjallajökull, which is almost ice-free in Figure 6.14) may be characteristic of periods of ice retreat (A. Dugmore, pers. comm. 2018).

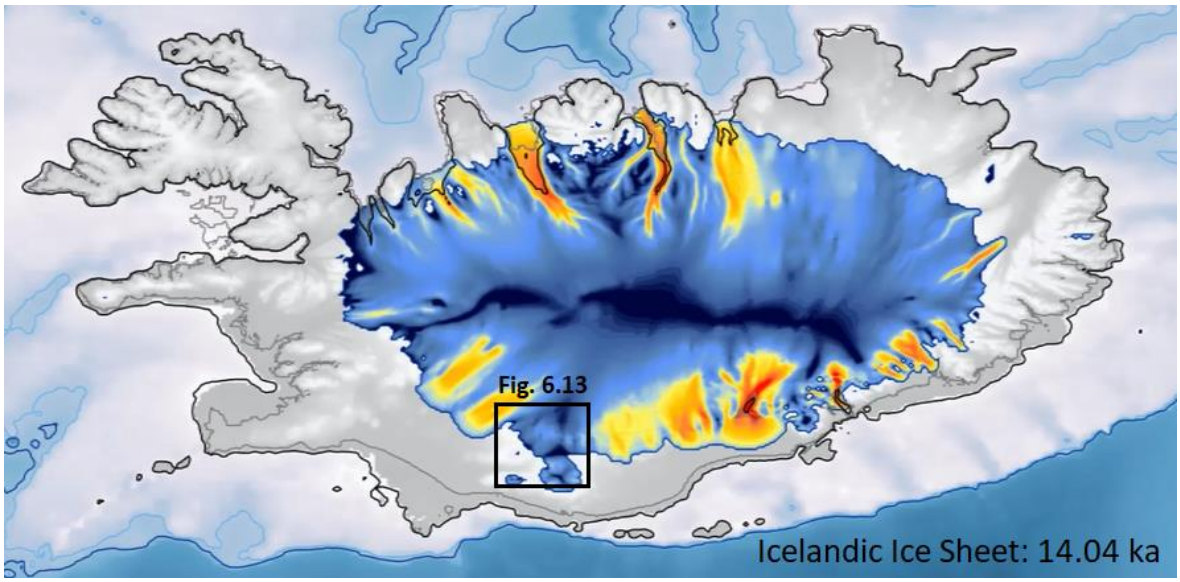

Figure 6.14. Model of the Icelandic Ice Sheet at 14.04 ka by Patton et al. (2017). Colours indicate the surface-ice velocity (warmer colours: faster ice flow). The reconstructed glacial environment in the Thórsmörk/Torfajökull area at the end of GI-15.2 (Figure 6.13; ~55 ka) may be similar to the modelled extent of ice at 14.04 ka.

The heat released by the Ring Fracture Rhyolites eruption will have resulted in the melting of ice in proximity to the vents, generating meltwater which efficiently drained from the area during the eruption (Tuffen et al., 2002). Efficient subglacial drainage of the meltwater away from the vents suggests that the ice sheet had a wet-based thermal regime (i.e. was not frozen to its bed), as is likely considering the high geothermal heat flow in this area (Patton et al., 2017). Additionally, the drainage of water away from Torfajökull may have been facilitated by a pressure gradient in the subglacial drainage network associated with the thinning of the ice sheet towards Thórsmörk (Björnsson, 2002; Stevenson et al., 2009). The presence of a viable drainage pathway and a regular pressure gradient to the ice margin would reduce the risk of

storage and subsequent release of water as a sudden jökulhlaup (Stevenson et al., 2011; Tuffen et al., 2002). The potential for jökulhlaups may also be reduced by the release of thermal energy to the atmosphere during the subaerial phase of the eruption (Stevenson et al., 2011).

6.5.2 Palaeoenvironmental evolution of the Thórsmörk area and climate context

The depositional successions that contain the Thórsmörk Ignimbrite provide a local palaeoenvironmental record before and after ignimbrite emplacement. However, with no other dated horizons within the studied successions, the palaeoenvironments cannot be linked to climatic stages with certainty. Nevertheless, comparison of the local palaeoenvironmental information (section 6.4.3) with the regional climate record (Figure 6.15) gives some insights into the wider palaeoenvironmental evolution of the area as the climate changed.

Evidence that glacial processes were locally active either during or prior to the deposition of the diamicts is not surprising, considering that the successions were deposited during the last glacial period when conditions were consistently colder than today. Ice may have existed on the upper flanks of Tindfjallajökull throughout the time represented by the studied successions. Additionally, it is likely that the whole area had been glaciated during the full glacial conditions from ~70.5 to ~59.5 kyr b2k (GS-19.2, 19.1 and 18; Figure 6.15). During this time, conditions were similar to the last glacial maximum when it is known that Iceland was completely covered in ice (Patton et al., 2017). A large volume of glacially-worked debris may have been released during retreat of the ice at the end of this cold period. The ice that contributed to the formation of the diamict was erosive (evidenced by the abrasion of clasts), indicative of basal sliding in a wet-based thermal regime (Nelson et al., 2009).

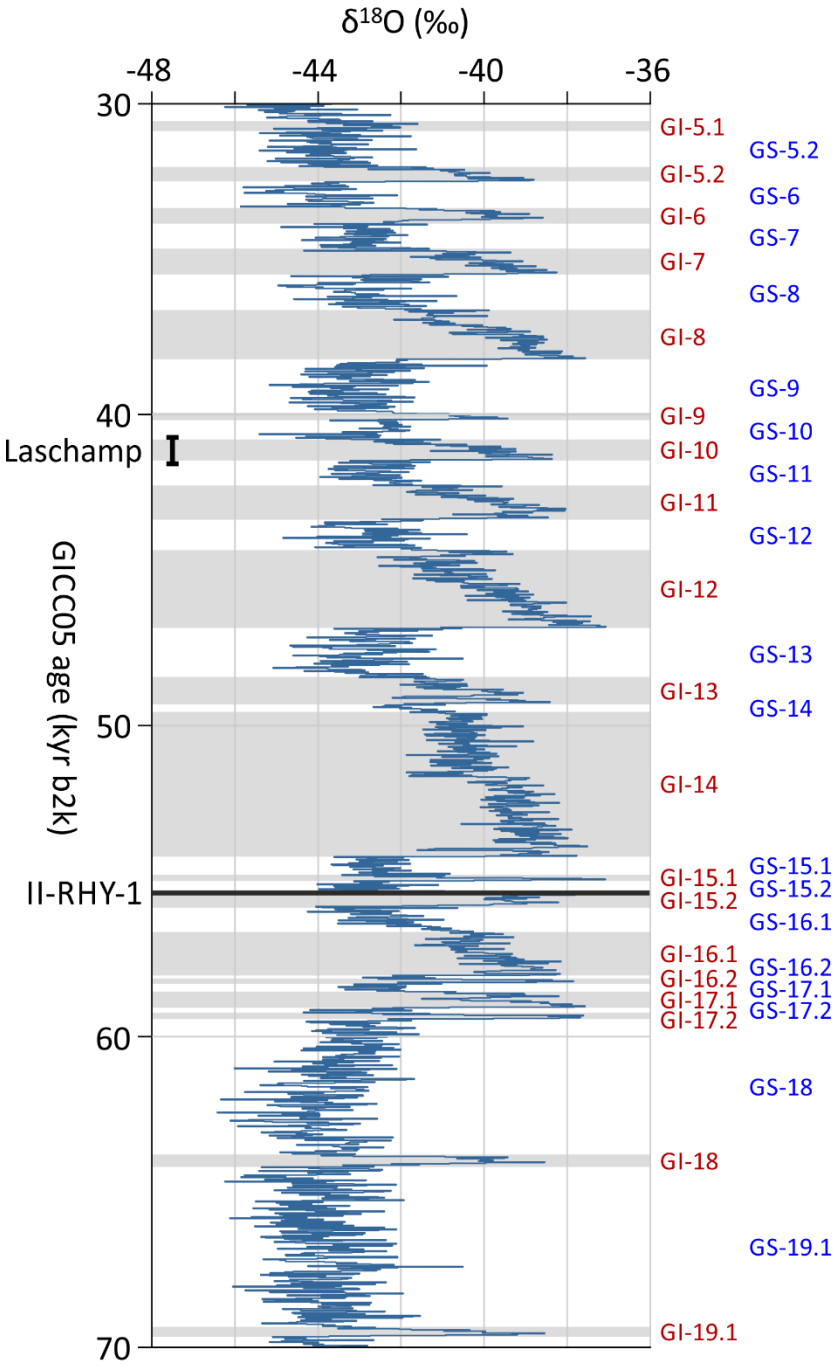

Figure 6.15. NGRIP oxygen isotope record 30–70 kyr b2k, with Greenland Interstadials (shaded grey) and Stadials labelled (data from Rasmussen et al., 2014 and Seierstad et al., 2014). Event horizons that are found in both the Greenland ice sheet and Iceland are marked. The timing of the Laschamp event is from Svensson et al. (2006) and II-RHY-1 is from Svensson et al. (2008).

The retreat of ice from the landscape, allowing subaerial deposition of sediment and ignimbrite, may have initiated at ~59.5 kyr b2k with a series of warm interstadials (GI-17.2, 17.1, 16.2, 16.1; Figure 6.15). Despite some colder stadials during this time (GS-17.2, 17.1,

16.2, 16.1), a subaerial environment persisted in the Thórsmörk area at the end of GI-15.2 (section 6.5.1). It is possible that some ice accumulated in the area during stadials GS-15.2 and 15.1, immediately after emplacement of the Thórsmörk Ignimbrite. However, warm conditions recommenced with GI-14, which lasted for ~4.5 kyr, closely followed by GI-13. Perhaps subaerial diamict deposition resumed during this warm stage, accompanied by reworking of sediments by flowing water (sand interbeds, Site 2) and formation of a lake (clay/silt, Site 3).

Ice later returned to the landscape, as recorded by the capping basaltic eruptions at Sites 2–4 (and at sites studied by Roberts (2001) south of the Markarfljót). Sufficient ice may have accumulated during the stadials from GS-13 onwards, but the timing of the return of ice is very uncertain. Climate conditions continued to fluctuate but generally deteriorated until the last glacial maximum (~23 ka), when the area was completely covered in ice (Bingham et al., 2003; Hubbard et al., 2006; Patton et al., 2017). The depositional successions remain remarkably well preserved despite the glaciation of the area during the last glacial maximum. This may be partly explained by the presence of palagonitised basalt units that protected the underlying sediments. Additionally, the successions close to Tindfjallajökull (Sites 1–4) are located away from the main focus of glacial erosion along the Markarfljót valley.

Overall, the Thórsmörk area was a dynamic environment during the last glacial period. Depositional successions >100 m thick accumulated, which include the Thórsmörk Ignimbrite and the products of local basaltic eruptions. During relatively mild times, the Thórsmörk area was largely ice-free and there were ephemeral lakes and streams. The interior of Iceland, including Torfajökull, remained ice-covered during GI-15.2 and was probably in a more persistent state of glaciation. It is likely that the Thórsmörk area was susceptible to ice advance from both local topographic highs (Katla, Eyjafjallajökull and Tindfjallajökull volcanoes) and from the interior of Iceland. The chronology of glaciation of Thórsmörk is not well constrained, but ice covered the whole region during the last glacial maximum and probably also during the cold period prior to deposition of the successions (~70.5 to ~59.5 kyr b2k).

6.6 CONCLUSIONS

The widespread products of the Ring Fracture Rhyolites eruption link together palaeoenvironmental information from across the North Atlantic region. Using the position of the II-RHY-1 tephra horizon in the Greenland ice cores, the eruption can be dated to the cooling transition at the end of Greenland Interstadial 15.2. The distribution of II-RHY-1 in marine settings indicates that the sea surface was frozen near to Iceland and that sea ice rafted as far south as 47° N. At the same time, Torfajökull volcano was covered by a wet-based ice sheet with a surface elevation >1200 m. Thirty kilometres to the south-southwest of Torfajökull, where the Thórsmörk Ignimbrite is preserved, little or no ice was present at the end of GI-15.2 and during other interstadials. The Thórsmörk area was a dynamic environment during the middle of the last glacial period, with considerable accumulation of volcanic and sedimentary deposits influenced by glacial, fluvial and lacustrine processes.

Chapter 7

Synthesis and conclusions

7.1 Introduction

The primary aims of this thesis were to investigate the geological development of glaciated volcanoes, with a primary focus on the little known Tindfjallajökull volcano, and to study the record of past glacial environments that is preserved on and around these volcanoes. These aims have been addressed using a wide range of approaches and analytical techniques (Figure 7.1). In this chapter, the findings of the thesis are discussed and summarised with reference to the original research questions that were presented in Chapter 1.

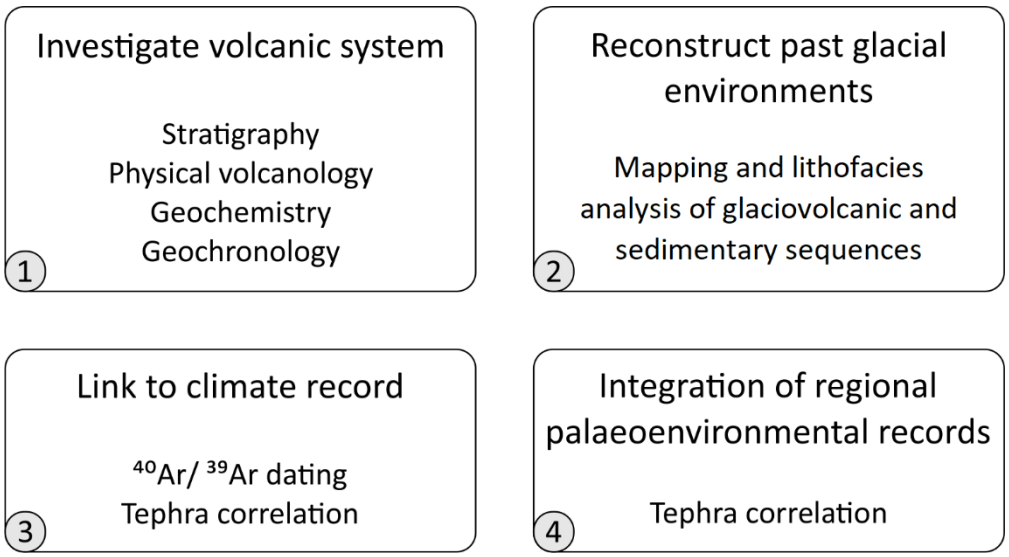

Figure 7.1. The methods and disciplines adopted in this thesis for reconstructing past environments using volcanoes.

7.2 SUMMARY OF FINDINGS

7.2.1 Volcanic and magmatic evolution of Tindfjallajökull volcano

Research question: What are the geological characteristics of the Tindfjallajökull volcanic system (i.e. the stratigraphy, physical volcanology and magmatic geochemistry) and how has the volcano developed through time?

Prior to this study, Tindfjallajökull volcano had been the subject of little geological investigation. A comprehensive overview of the volcano is now provided through a geological map and stratigraphy (Chapter 2; Appendix 8), a whole-rock geochemical dataset (Chapter 3; Appendix 2), and $^{40}Ar/^{39}Ar$ geochronology (Chapter 4; Appendix 3).

The early-formed part of the volcano is a broad stratocone predominantly composed of basalt (Figure 7.2: 'Early Tindfjallajökull'), similar to neighbouring Eyjafjallajökull. This stratocone overlies older basement rocks, has an observed vertical extent of 1200 m, and consists of interbedded fragmental rocks and lavas emplaced prior to ~358 ka (the maximum age is unknown). Rhyolite and basalt lavas then overlaid much of the upper surface of the stratocone (Figure 7.2: 'Middle Tindfjallajökull'); rhyolite lavas have been dated to 358 ± 15 ka (Saxi) and 209.5 ± 2.8 ka (Vestriöxl). Later (126 ± 18 ka), the eruption of rhyolitic breccia and lava lobes, which may have been accompanied by caldera subsidence, formed the present-day summit of the volcano (Figure 7.2: 'Late Tindfjallajökull A'). The rhyolites situated on the Tindfjallajökull edifice are interpreted to have been generated through the fractional crystallisation or partial melting of a mafic source. The dominance of fractional crystallisation or partial melting in the formation of the rhyolites may be a function of the local geothermal gradient (Martin and Sigmarsson, 2007), but it is currently uncertain which process was dominant at Tindfjallajökull.

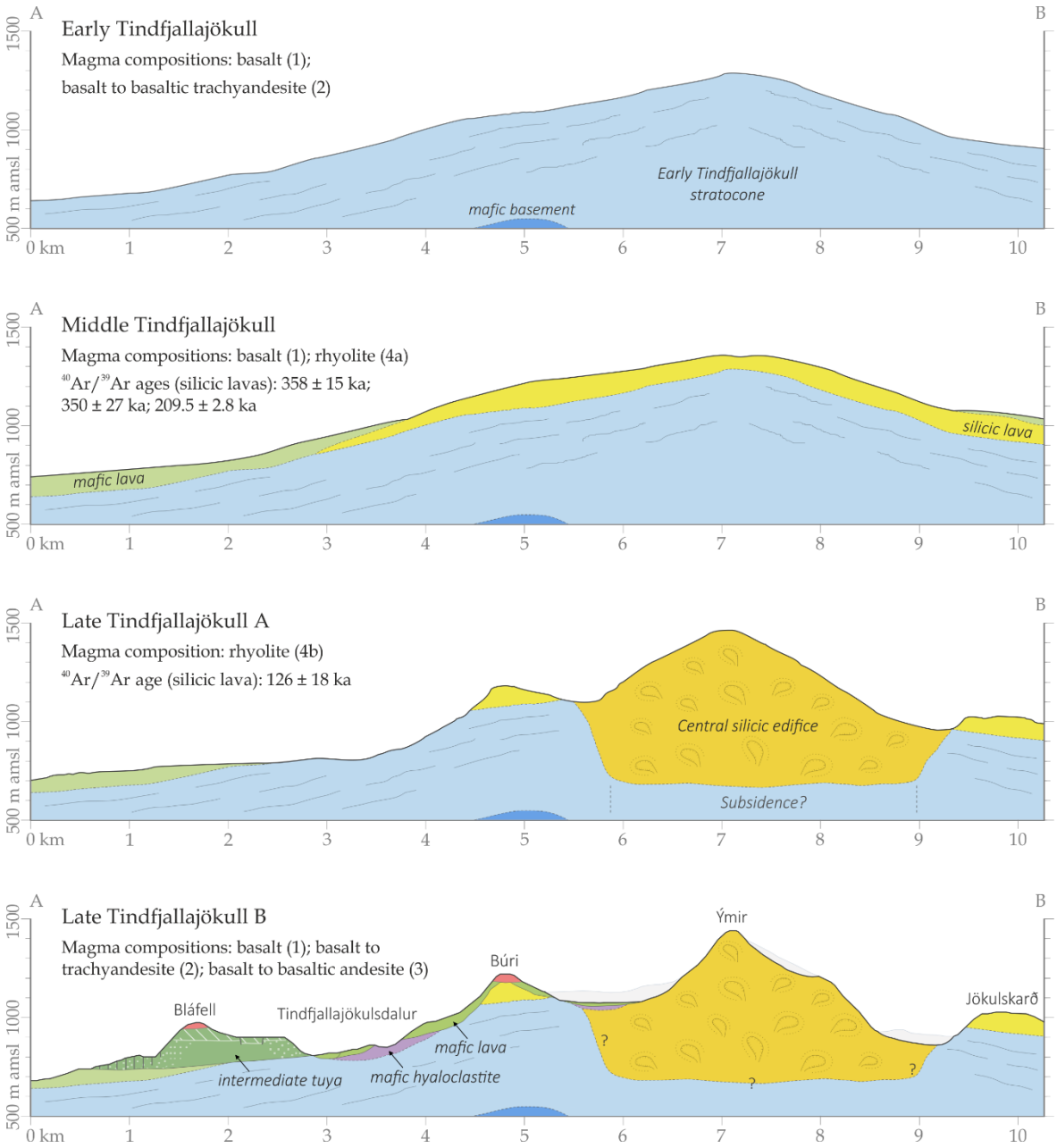

Figure 7.2. Speculative reconstruction of the temporal evolution of Tindfjallajökull, with $^{40}Ar/^{39}Ar$ ages and magma compositions annotated. For key to colours and position of cross section line (A–B), see main geological map (Appendix 8). Numbers in brackets refer to the compositional groups defined in Chapter 3. The Late Tindfjallajökull B panel consists of the present-day cross section and includes the present-day ice cap (ice is not included on the other panels). 2× vertical exaggeration. The broad temporal evolution of Tindfjallajökull can be subdivided into an initial stratocone-building stage ('Early Tindfjallajökull'), the surfacing of the stratocone with lavas ('Middle Tindfjallajökull'), the formation of the central silicic edifice ('Late Tindfjallajökull A') and the occurrence of a diverse set of minor eruptions on the volcano's flanks ('Late Tindfjallajökull B').

Volcanism at Tindfjallajökull during the last glacial period was characterised by minor flank eruptions (Figure 7.2: 'Late Tindfjallajökull B'). The magmas erupted during this time were typically basaltic, though some basaltic magmas had evolved to intermediate compositions (i.e. basaltic trachyandesite and trachyandesite) through fractional crystallisation. Additionally, some basaltic magmas mixed with silicic magmas in the crust. Rather than being similar in composition to the typical Tindfjallajökull rhyolites, these silicic magmas had a similar composition to the Sultarfell rhyolite, situated in the fissure swarm to the NE of Tindfjallajökull (a possible component of the Torfajökull volcanic system; Sæmundsson and Larsen, 2016). The Sultarfell rhyolite (and other magmas of a similar composition) may be a product of the partial melting of silicic rock in the crust. A possible source rock is represented by silicic xenoliths in the area, which are thought to have undergone partial melting in association with local basaltic magmatism (Gurenko et al., 2015).

Well-preserved scoria cones on Tindfjallajökull suggest that volcanism has occurred since the last glacial maximum (~23 ka), but no Holocene activity is known. This is in contrast to the other volcanic systems of the Eastern Volcanic Zone, all of which have erupted in the past 600 years (i.e. post-1477 AD, the most recent eruption of Torfajökull (Sæmundsson and Larsen, 2016)).

7.2.2 Reconstructing past glacial environments at Tindfjallajökull

Research question: What is the role of ice in the shaping of Tindfjallajökull and is a record of past glacial environments preserved on the volcano?

Ice has had a significant impact on the development of Tindfjallajökull volcano. Interactions between volcanism and ice have influenced eruption styles and the resultant eruption products (similar to, for example, neighbouring Eyjafjallajökull (Loughlin, 2002)). Deposits produced by glaciovolcanic eruptions are typically steep-sided and have a high proportion of fragmental material. Ice has also been influential in the erosion of Tindfjallajökull (e.g. the deepening of the valleys that radiate from the centre of the volcano) and the mobilisation and working of

sediment source material. Evidence for the presence of ice can be found throughout much of the stratigraphy, in the form of glaciovolcanic sequences and glacially-worked sediments.

Glaciovolcanic sequences provide the most complete record of past glacial environments, though it is typically only the well-preserved examples that provide unambiguous evidence for ice. Minor eruptions on Tindfjallajökull's flanks during the latter stage of the volcano's development (Late Tindfjallajökull B) are recorded as well-preserved eruptive units (described in Chapter 2). Due to the limited degree of subsequent (i.e. Holocene) volcanic activity at Tindfjallajökull, the products of these eruptions have not been obscured by more recent deposits. These eruptions thus provide a good record of past environments and can be used to deduce the variations in ice cover on the volcano. Some of the eruptions produced unconfined lavas (e.g. at Búri and Haki on the upper west flank of the volcano) that indicate an ice-free eruptive environment. In some instances lavas transition to a highly jointed facies that indicates the presence of snow or ice. For example, a highly jointed trachyandesitic lava on the east side of Tindur records the presence of ice in the Vestri-Botná valley at the time of the eruption. Other eruptions produced tuyas and hyaloclastite-dominated units that indicate that ice surrounded the vents during these eruptions. Passage zones in tuyas can be used to assess the stability of meltwater drainage and to estimate ice thicknesses (Smellie, 2006). For instance, Bláfell is an a'a lava-dominated tuya that records the presence of impermeable ice 180 m thick (passage zone elevation: 880 m). Meltwater drainage was stable during the eruption, suggesting a supraglacial (rather than subglacial) meltwater drainage pathway. Tuyas on Tindfjallajökull record impermeable ice thicknesses from 40 m (Rauðaborg; upper west flank; 940 m passage zone elevation) to >400 m (Þórólfsfell; Markarfljót valley; 500–540 m passage zone elevation).

A well-preserved Weichselian depositional succession on the SE flank of Tindfjallajökull provides a sedimentary and volcanic record of environmental change (presented in Chapter 6). Glacial erosion and transport influenced the production of debris, which was deposited by debris flows in a subaerial environment. Reworked debris was occasionally deposited in bodies

of flowing and standing water. Volcanic units in the succession include the Thórsmörk Ignimbrite, which was deposited when thick ice was absent from the area, though some accumulations of ice or snow may have been present at higher elevations. Basaltic glaciovolcanic units indicate the presence of ice later in the succession; for instance two pillow lava units record local ice surface elevations >600 m at the time of their emplacement.

7.2.3 Linking glaciovolcanism to the climate record

Research question: Can eruptive environments on Tindfjallajökull (and other glaciated volcanoes) be precisely linked to climate records, e.g. using radiometric dating techniques?

$^{40}Ar/^{39}Ar$ geochronology is an established method for linking glaciovolcanic eruptions to the record of past climate. In Chapter 4, the $^{40}Ar/^{39}Ar$ technique was used to date silicic lavas at Saxi and Vestriöxl to Marine Isotope Stages 10 (cold) and 7.3 (warm) respectively, and a silicic lava from Ýmir was dated to MIS 6 (cold) or 5.5 (warm). Dating of samples with mafic and intermediate compositions was unsuccessful, due to the low potassium content and young age of these rocks. The precision that can be achieved varies between samples; the lowest uncertainty obtained during this study was on the 209.5 ± 2.8 ka (2σ) age of the Vestriöxl lava. Uncertainties in the eruption ages and in the climate chronologies limit the precision with which eruptive environments can be linked to climate using absolute dating techniques. These uncertainties preclude the dating of eruptions to short-term (i.e. millennia-scale or shorter) climatic episodes such as stadials/interstadials.

By correlating rhyolitic tuyas at Torfajökull volcano (the Ring Fracture Rhyolites) with a widespread tephra horizon (II-RHY-1) in Chapter 5, it was established that tephra from rhyolitic glaciovolcanic eruptions can be found within climate archives such as ice cores. The presence of a tephra isochron within the climate stratigraphy provides a high-precision method of determining the eruption date relative to the record of past climate. This method does not require the comparison of different dating techniques that have been applied to different stratigraphic records, as was previously the case when only absolute dating

techniques were used. The emplacement of the rhyolitic tuyas at Torfajökull can now be precisely dated to the end of Greenland Interstadial 15.2 using the II-RHY-1 tephra horizon. This approach resolves the problem of high uncertainties when linking glaciovolcanism to the climate record, though it relies on the robust correlation of proximal glaciovolcanic sequences with distal tephra horizons.

7.2.4 Integrating disparate palaeoenvironmental records using a glaciovolcanic eruption

Research question: To what extent can glaciated volcanoes and their eruptive products be used to reconstruct local and regional palaeoenvironments?

Tephra dispersal is common during basaltic glaciovolcanic eruptions (e.g. Óladóttir et al., 2011; Larsen and Eiríksson, 2008) and, as demonstrated in Chapter 5, can also be an important feature of rhyolitic glaciovolcanism. The dispersal of tephra across multiple depositional settings produces a valuable marker horizon that can be used to integrate a wide range of palaeoenvironmental information (Lowe et al., 2017). By applying tephra correlation techniques to glaciovolcanic eruptions, the palaeoenvironmental information associated with their scattered eruption products can be combined.

The correlation of the Torfajökull Ring Fracture Rhyolites with the Thórsmörk Ignimbrite and II-RHY-1 (established in Chapter 5) provides a tie-line between terrestrial, marine and ice core palaeoenvironmental records (detailed in Chapter 6). According to ice core and marine palaeoclimate proxies, the regional climate was transitioning from interstadial conditions (GI-15.2) to stadial conditions (GS-15.2) at the time of the eruption (Austin et al., 2004). The terrestrial palaeoenvironment in Iceland can be reconstructed using the proximal and medial eruption products. The Ring Fracture Rhyolites provide evidence that Torfajökull volcano was covered by a wet-based ice sheet with a surface elevation >1200 m, whilst the outcrop of the Thórsmörk Ignimbrite defines an area (~30 km to the SSW of Torfajökull) that hosted little or

no ice. In the marine realm, the distribution of II-RHY-1 indicates the presence of sea ice near to Iceland, which rafted as far south as 47° N (Heinrich, 1988; Ruddiman and Glover, 1972).

The palaeoenvironmental information recorded by the terrestrial eruption products, combined with the dispersal of II-RHY-1 across a wide area of the North Atlantic, means that a vast archive of past environments can be linked together. The ability to precisely integrate these disparate datasets is crucial for understanding the environmental responses to climate change in the Quaternary.

7.3 VOLCANOES AS ARCHIVES OF PAST GLACIAL ENVIRONMENTS

Volcanoes host a unique archive of past glacial environments that can be used to reconstruct the glacial history of volcanic regions. As areas of overall crustal accretion, volcanoes accumulate evidence of past environments with each successive eruption. The resolution of this record therefore depends on the eruption frequency of the volcano and the extent to which each eruption sequence is preserved (Smellie et al., 2014). Subsequent eruptions may bury the products of previous eruptions, protecting them from erosion but also obscuring them from view. At Tindfjallajökull and Torfajökull, volcanic sequences from the last glacial period are particularly well preserved and have not been obscured by more recent volcanism, allowing past glacial environments from this time period to be reconstructed. In contrast, the Pleistocene volcanic record at nearby Katla and Hekla volcanoes is partly obscured by ice and recent lavas respectively (Jóhannesson and Sæmundsson, 1989).

Sedimentary successions are often present in volcanic zones and are another valuable source of palaeoenvironmental information. Whilst glaciovolcanic sequences can be used to infer ice thicknesses and basal thermal regimes, glacial sediments are more typical of wet-based ice and are shaped by processes at the margins and base of an ice sheet (Hambrey and Glasser, 2012). Terrestrial sedimentary deposits are vulnerable to erosion and well-preserved examples that pre-date the last glacial maximum are rare (Norðdahl and Pétursson, 2005). The Weichselian

sedimentary succession on the SE flank of Tindfjallajökull is an unusual record of pre-LGM depositional environments, which has been largely protected from erosion by overlying basaltic volcanic units.

The dating of palaeoenvironmental information and the integration of disparate palaeoenvironmental records presents a significant challenge to studies of past environments (Davies et al., 2012). Terrestrial glacial sediments often lack features that can be dated or linked to other successions (Smellie et al., 2014), such as carbon-bearing fossils or widespread marker horizons. Methods of absolute dating, such as $^{40}Ar/^{39}Ar$ dating of volcanic material, can be applied to many palaeoenvironmental records (e.g. glaciovolcanic sequences) but have uncertainties that inhibit the high-precision integration of disparate records. A solution is provided by the widely-dispersed products of volcanic eruptions, which extend the record of past volcanism far from volcanic zones. The products of one eruption can be used to precisely link palaeoenvironmental records from multiple depositional settings across a wide region.

Ice and volcanoes commonly co-exist on Earth (Curtis and Kyle, 2017), and consequently, many volcanic zones host archives of past glacial environments. The approach used in this thesis is therefore applicable to all volcanoes that are currently ice-clad or have been glaciated in the past. In particular, the use of tephra to link glaciovolcanism to climate records could be attempted for any glaciovolcanic eruption that produced widespread tephra deposits. Given that tephra dispersal can be a feature of both basaltic and rhyolitic glaciovolcanism, it is likely that glaciovolcanic eruptions are commonly represented in distal tephra stratigraphies. Further correlations between glaciovolcanic sequences and distal tephras are possible in all volcanic zones that are the subject of both glaciovolcanism and tephra research (e.g. Alaska (Jensen et al., 2014; Waythomas et al., 2014), Antarctica (Iverson et al., 2017; Smellie and Skilling, 1994), Kamchatka (Braitseva et al., 1997; Edwards et al., 2015a), New Zealand (Conway et al., 2015; Turner et al., 2011) and the Southern Andes (Alloway et al., 2017; Mee et al., 2009)).

However, this approach relies on the robust correlation of eruption products, which may not be possible when records are incomplete and/or tephra horizons are not uniquely identifiable. For example, multiple distal tephra horizons (including the ~12.1 ka Vedde Ash) have been identified as having a comparable geochemistry to the Sólheimar Ignimbrite of Katla volcano (Lane et al., 2012; Tomlinson et al., 2012), which may be the product of a glaciovolcanic eruption (Lacasse et al., 2007). Without good stratigraphic or dating control in the terrestrial setting, it is not currently possible to establish an unequivocal correlation between this ignimbrite and a distal tephra horizon (Lane et al., 2012; Tomlinson et al., 2012). As distal tephra stratigraphies continue to be systematically documented (e.g. Abbott et al., 2018a), it is often the proximal record of volcanic eruptions that is most incomplete and unexplored. The proximal-distal correlation of volcanic products is especially challenging when proximal material is poorly-preserved or buried under ice or rock. It therefore remains to be seen whether tephra correlation methods can be widely applied to other glaciovolcanic eruptions.

7.4 FURTHER WORK

The thorough investigation of Tindfjallajökull presented in this thesis provides context for further work on the volcano. Due to ice and sedimentary cover, it has not been possible to determine whether the central silicic edifice is situated within a caldera structure (Chapter 2). The potential existence of a caldera could be examined using geophysical survey techniques. Further study of the physical volcanology of the central silicic edifice would give insights into the eruption processes and eruptive environment. Was the edifice formed during one or multiple eruptions? What is the extent of any subsidence associated with the eruption(s)? How did the eruptive environment influence the eruption(s) and the structure of the resulting edifice?

The existence of two distinct types of rhyolite on and around Tindfjallajökull suggests that more than one process has driven rhyolite petrogenesis in this area (Chapter 3). The peralkaline and metaluminous rhyolites on Tindfjallajökull are interpreted to have been

derived from the near-solidus differentiation of a mafic source, whilst the high-silica Sultarfell rhyolite is thought to be a product of the partial melting of silicic rock in the crust. A detailed geochemical study of the rhyolites would provide further insights into the origin of Icelandic rhyolites and the relative contribution of the proposed sources and processes. In particular, isotopic analyses (e.g. (^{230}Th/^{232}Th), δ^{18}O, δD) of the rhyolites, as well as the potentially significant silicic xenoliths found in the area, would assist in identifying the role of pre-existing crust (e.g. Elders et al., 2011; Nicholson et al., 1991; Sigmarsson et al., 1991).

Although the source of the Thórsmörk Ignimbrite has now been identified and the eruptive environment at the vent is known (Chapter 5 and 6), a more detailed study of the physical volcanology of the ignimbrite is needed to understand its formation. Investigation of the complex structures and the wide variety of lithologies in the ignimbrite, through detailed logging and componentry analysis, may provide further clues to the processes that contributed to its emplacement. Did the presence of ice at the vent influence the initiation of pyroclastic density currents? Did pyroclastic density currents interact with ice as they travelled over the surface of the ice sheet? Exactly how did ice and/or snow affect the deposition of the ignimbrite?

Finally, information on past glacial environments derived from volcanoes can be used to constrain numerical ice sheet models. Well-dated physical evidence is crucial for refining models of the advance and retreat of the Icelandic Ice Sheet. The ice thickness and extent data derived from the Ring Fracture Rhyolites and the Thórsmörk Ignimbrite (~55 ka) could be used to constrain or validate models of the Icelandic Ice Sheet beyond the current 35 ka modelled timeframe (Patton, 2013; Patton et al., 2017). Further modelling would provide a longer-term insight into the evolution and dynamics of the Icelandic Ice Sheet. The past behaviour of the Iceland Ice Sheet may be of relevance to present-day ice masses, particularly those situated in volcanic zones such as the West Antarctic Ice Sheet (Patton et al., 2017; van Wyk de Vries et al., 2018).

References

Abbott, P. M., Austin, W. E. N., Davies, S. M., Pearce, N. J. G., & Hibbert, F. D. (2013). Cryptotephrochronology of the Eemian and the last interglacial-glacial transition in the North East Atlantic. *Journal of Quaternary Science*, *28*(5), 501–514. http://doi.org/10.1002/jqs.2641

Abbott, P. M., Bourne, A. J., Purcell, C. S., Davies, S. M., Scourse, J. D., & Pearce, N. J. G. (2016). Last glacial period cryptotephra deposits in an eastern North Atlantic marine sequence: Exploring linkages to the Greenland ice-cores. *Quaternary Geochronology*, *31*, 62–76. http://doi.org/10.1016/j.quageo.2015.11.001

Abbott, P. M., & Davies, S. M. (2012). Volcanism and the Greenland ice-cores: The tephra record. *Earth-Science Reviews*, *115*(3), 173–191. http://doi.org/10.1016/j.earscirev.2012.09.001

Abbott, P. M., Griggs, A. J., Bourne, A. J., Chapman, M. R., & Davies, S. M. (2018a). Tracing marine cryptotephras in the North Atlantic during the last glacial period: Improving the North Atlantic marine tephrostratigraphic framework. *Quaternary Science Reviews*, *189*, 169–186. http://doi.org/10.1016/j.quascirev.2018.03.023

Abbott, P. M., Griggs, A. J., Bourne, A. J., & Davies, S. M. (2018b). Tracing marine cryptotephras in the North Atlantic during the last glacial period: Protocols for identification, characterisation and evaluating depositional controls. *Marine Geology*, *401*, 81–97. http://doi.org/10.1016/j.margeo.2018.04.008

Aho, K. (2016). asbio: A Collection of Statistical Tools for Biologists. *R package version 1.3-1*. http://CRAN.R-project.org/package=asbio

Aksu, A. E., & Piper, D. J. W. (1979). Baffin Bay in the past 100,000 yr. *Geology*, *7*(5), 245–248. http://doi.org/10.1130/0091-7613(1979)7<245:BBITPY>2.0.CO;2

Alloway, B. V., Moreno, P. I., Pearce, N. J. G., De Pol-Holz, R., Henríquez, W. I., Pesce, O. H., … Outes, V. (2017). Stratigraphy, age and correlation of Lepué Tephra: A widespread c. 11 000 cal a BP marker horizon sourced from the Chaitén Sector of southern Chile. *Journal of Quaternary Science*, *32*, 795–829. http://doi.org/10.1002/jqs.2976

Ármannsson, H. (2016). The fluid geochemistry of Icelandic high temperature geothermal areas. *Applied Geochemistry*, *66*, 14–64. http://doi.org/10.1016/j.apgeochem.2015.10.008

Austin, W. E. N., & Abbott, P. M. (2010). Comment: Were last glacial climate events simultaneous between Greenland and France? A quantitative comparison using non-tuned chronologies. M. Blaauw, B. Wohlfarth, J. A. Christen, L. Ampel, D. Veres, K. Hughen, F. Preusser and A. Svensson (2009). *Journal of Quaternary Science*, *25*(6), 1045–1046. http://doi.org/10.1002/jqs.1366

Austin, W. E. N., Wilson, L. J., & Hunt, J. B. (2004). The age and chronostratigraphical significance of North Atlantic Ash Zone II. *Journal of Quaternary Science*, *19*(2), 137–146. http://doi.org/10.1002/jqs.821

Barker, S., Knorr, G., Edwards, R. L., Parrenin, F., Putnam, A. E., Skinner, L. C., … Ziegler, M. (2011). 800,000 Years of Abrupt Climate Variability. *Science*, *334*(6054), 347–351. http://doi.org/10.1126/science.1203580

Bennett, M. R., Huddart, D., & Gonzalez, S. (2009). Glaciovolcanic landsystems and large-scale glaciotectonic deformation along the Brekknafjöll–Jarlhettur, Iceland. *Quaternary Science Reviews*, *28*(7–8), 647–676. http://doi.org/10.1016/j.quascirev.2008.07.018

Bennett, M. R., Huddart, D., & McCormick, T. (2000a). An integrated approach to the study of glaciolacustrine landform and sediments: a case study from Hagavatn, Iceland. *Quaternary Science Reviews*, *19*, 633–665. http://doi.org/http://dx.doi.org/10.1016/S0277-3791(99)00013-X

Bennett, M. R., Huddart, D., & McCormick, T. (2000b). The glaciolacustrine landform-sediment assemblage at Heinabergsjokull, Iceland. *Geografiska Annaler: Series A, Physical Geography*, *82A*(1), 1–16. http://doi.org/10.1111/j.0435-3676.2000.00107.x

Bingham, R. G., Hulton, N. R. J., & Dugmore, A. J. (2003). Modelling the southern extent of the last Icelandic ice-sheet. *Journal of Quaternary Science*, *18*(2), 169–182. http://doi.org/10.1002/jqs.734

Bird, M. I., Ayliffe, L. K., Fifield, L. K., Turney, C. S. M., Cresswell, R. G., Barrows, T. T., & David, B. (1999). Radiocarbon dating of "old" charcoal using a wet oxidation, stepped-combustion procedure. In *Radiocarbon* (Vol. 41, pp. 127–140). Boston, MA: Springer US. http://doi.org/10.1007/978-1-4757-9694-0_3

Björnsson, H. (2002). Subglacial lakes and jökulhlaups in Iceland. *Global and Planetary Change*, *35*(3–4), 255–271. http://doi.org/10.1016/S0921-8181(02)00130-3

Blake, S. (1984). Magma mixing and hybridization processes at the alkalic, silicic, Torfajökull central volcano triggered by tholeiitic Veidivötn fissuring, south Iceland. *Journal of Volcanology and Geothermal Research*, *22*(1–2), 1–31. http://doi.org/10.1016/0377-0273(84)90033-7

Blikra, L. H., & Nemec, W. (1998). Postglacial colluvium in western Norway: depositional processes, facies and palaeoclimatic record. *Sedimentology*, *45*(5), 909–959. http://doi.org/10.1046/j.1365-3091.1998.00200.x

Blockley, S. P. E., Bourne, A. J., Brauer, A., Davies, S. M., Hardiman, M., Harding, P. R., … Zanchetta, G. (2014). Tephrochronology and the extended INTIMATE (Integration of Ice-core, Marine and Terrestrial records) event stratigraphy 8-128 ka b2k. *Quaternary Science Reviews*, *106*, 88–100. http://doi.org/10.1016/j.quascirev.2014.11.002

Bourne, A. J., Abbott, P. M., Albert, P. G., Cook, E., Pearce, N. J. G., Ponomareva, V., … Davies, S. M. (2016). Underestimated risks of recurrent long-range ash dispersal from

northern Pacific Arc volcanoes. *Scientific Reports*, *6*, 29837. http://doi.org/10.1038/srep29837

Braitseva, O. A., Ponomareva, V. V., Sulerzhitsky, L. D., Melekestsev, I. V., & Bailey, J. (1997). Holocene Key-Marker Tephra Layers in Kamchatka, Russia. *Quaternary Research*, *47*(2), 125–139. http://doi.org/10.1006/qres.1996.1876

Bramlette, M. N., & Bradley, W. H. (1941). Geology and Biology of North Atlantic Deep-Sea Cores: Lithology and geologic interpretations. *Geological Survey Professional Paper*, *196–A*.

Brendryen, J., Haflidason, H., & Sejrup, H. P. (2010). Norwegian Sea tephrostratigraphy of marine isotope stages 4 and 5: Prospects and problems for tephrochronology in the North Atlantic region. *Quaternary Science Reviews*, *29*, 847–864. http://doi.org/10.1016/j.quascirev.2009.12.004

Brendryen, J., Haflidason, H., & Sejrup, H. P. (2011). Non-synchronous deposition of North Atlantic Ash Zone II in Greenland ice cores, and North Atlantic and Norwegian Sea sediments: an example of complex glacial-stage tephra transport. *Journal of Quaternary Science*, *26*(7), 739–745. http://doi.org/10.1002/jqs.1499

Clay, P. L., Busemann, H., Sherlock, S. C., Barry, T. L., Kelley, S. P., & McGarvie, D. W. (2015). $^{40}Ar/^{39}Ar$ ages and residual volatile contents in degassed subaerial and subglacial glassy volcanic rocks from Iceland. *Chemical Geology*, *403*, 99–110. http://doi.org/10.1016/j.chemgeo.2015.02.041

Cole, J. W., Milner, D. M., & Spinks, K. D. (2005). Calderas and caldera structures: a review. *Earth-Science Reviews*, *69*, 1–26. http://doi.org/10.1016/j.earscirev.2004.06.004

Conway, C. E., Leonard, G. S., Townsend, D. B., Calvert, A. T., Wilson, C. J. N., Gamble, J. A., & Eaves, S. R. (2016). A high-resolution $^{40}Ar/^{39}Ar$ lava chronology and edifice construction history for Ruapehu volcano, New Zealand. *Journal of Volcanology and Geothermal Research*, *327*, 152–179. http://doi.org/10.1016/j.jvolgeores.2016.07.006

Conway, C. E., Townsend, D. B., Leonard, G. S., Wilson, C. J. N., Calvert, A. T., & Gamble, J. A. (2015). Lava-ice interaction on a large composite volcano: a case study from Ruapehu, New Zealand. *Bulletin of Volcanology*, *77*(3), 21. http://doi.org/10.1007/s00445-015-0906-2

Cowlyn, J. D. (2016). *Pyroclastic density currents at Ruapehu volcano; New Zealand*. PhD thesis, University of Canterbury.

Cronin, S. J., Neall, V. E., Palmer, A. S., & Stewart, R. B. (1997). Methods of identifying late Quaternary rhyolitic tephras on the ring plains of Ruapehu and Tongariro volcanoes, New Zealand. *New Zealand Journal of Geology and Geophysics*, *40*(2), 175–184. http://doi.org/10.1080/00288306.1997.9514751

Curtis, A., & Kyle, P. (2017). Methods for mapping and monitoring global glaciovolcanism. *Journal of Volcanology and Geothermal Research*, *333–334*, 134–144. http://doi.org/10.1016/j.jvolgeores.2017.01.017

Dansgaard, W., Johnsen, S. J., Clausen, H. B., Dahl-Jensen, D., Gundestrup, N. S., Hammer, C. U., … Bond, G. (1993). Evidence for general instability of past climate from a 250-kyr ice-core record. *Nature*, *364*(6434), 218–220. http://doi.org/10.1038/364218a0

Davies, S. M., Abbott, P. M., Pearce, N. J. G., Wastegård, S., & Blockley, S. P. E. (2012). Integrating the INTIMATE records using tephrochronology: Rising to the challenge. *Quaternary Science Reviews*, *36*, 11–27. http://doi.org/10.1016/j.quascirev.2011.04.005

Duan, W., Cheng, H., Tan, M., & Edwards, R. L. (2016). Onset and duration of transitions into Greenland Interstadials 15.2 and 14 in northern China constrained by an annually laminated stalagmite. *Scientific Reports*, *6*(1), 20844. http://doi.org/10.1038/srep20844

Edwards, B. R., Belousov, A., Belousova, M., & Melnikov, D. (2015a). Observations on lava, snowpack and their interactions during the 2012-13 Tolbachik eruption, Klyuchevskoy

Group, Kamchatka, Russia. *Journal of Volcanology and Geothermal Research*, *307*, 107–119. http://doi.org/10.1016/j.jvolgeores.2015.08.010

Edwards, B. R., Gudmundsson, M. T., & Russell, J. K. (2015b). Glaciovolcanism. In H. Sigurdsson, B. Houghton, H. Rymer, J. Stix, & S. McNutt (Eds.), *The Encyclopedia of Volcanoes* (pp. 377–393). Elsevier. http://doi.org/10.1016/B978-0-12-385938-9.00020-1

Einarsson, P. (1991). Earthquakes and present-day tectonism in Iceland. *Tectonophysics*, *189*, 261–279.

Eiríksson, J., & Geirsdóttir, Á. (1991). A record of Pliocene and Pleistocene glaciations and climatic changes in the North Atlantic based on variations in volcanic and sedimentary facies in Iceland. *Marine Geology*, *101*(1–4), 147–159. http://doi.org/10.1016/0025-3227(91)90068-F

Elders, W. a., Fridleifsson, G. Ó., Zierenberg, R. a., Pope, E. C., Mortensen, A. K., Gudmundsson, Á., … Schiffman, P. (2011). Origin of a rhyolite that intruded a geothermal well while drilling at the Krafla volcano, Iceland. *Geology*, *39*(3), 231–234. http://doi.org/10.1130/G31393.1

Evans, D. J. A. (2005). The glacier-marginal landsystems of Iceland. In *Developments in Quaternary Science* (Vol. 5, pp. 93–126). http://doi.org/10.1016/S1571-0866(05)80007-7

Eyles, C. H., Eyles, N., & Miall, A. D. (1985). Models of glaciomarine sedimentation and their application to the interpretation of ancient glacial sequences. *Palaeogeography, Palaeoclimatology, Palaeoecology*, *51*(1–4), 15–84. http://doi.org/10.1016/0031-0182(85)90080-X

Fleck, R. J., Sutter, J. F., & Elliot, D. H. (1977). Interpretation of discordant $^{40}Ar/^{39}Ar$ age-spectra of mesozoic tholeiites from antarctica. *Geochimica et Cosmochimica Acta*, *41*(1), 15–32. http://doi.org/10.1016/0016-7037(77)90184-3

Flude, S., Burgess, R., & McGarvie, D. W. (2008). Silicic volcanism at Ljósufjöll, Iceland: Insights into evolution and eruptive history from Ar–Ar dating. *Journal of Volcanology and Geothermal Research*, *169*(3–4), 154–175. http://doi.org/10.1016/j.jvolgeores.2007.08.019

Flude, S., McGarvie, D. W., Burgess, R., & Tindle, A. G. (2010). Rhyolites at Kerlingarfjöll, Iceland: the evolution and lifespan of silicic central volcanoes. *Bulletin of Volcanology*, *72*(5), 523–538. http://doi.org/10.1007/s00445-010-0344-0

Flude, S., Tuffen, H., & Sherlock, S. C. (2017). Spatially heterogeneous argon-isotope systematics and apparent $^{40}Ar/^{39}Ar$ ages in perlitised obsidian. *Chemical Geology*, (November 2016). http://doi.org/10.1016/j.chemgeo.2017.05.018

Forbes, A. E. S., Blake, S., McGarvie, D. W., & Tuffen, H. (2012). Pseudopillow fracture systems in lavas: Insights into cooling mechanisms and environments from lava flow fractures. *Journal of Volcanology and Geothermal Research*, *245–246*, 68–80. http://doi.org/10.1016/j.jvolgeores.2012.07.007

Furnes, H. (1978). Element mobility during palagonitization of a subglacial hyaloclastite in Iceland. *Chemical Geology*, *22*, 249–264. http://doi.org/10.1016/0009-2541(78)90034-7

Gale, S. J. (2009). Event chronostratigraphy: A high-resolution tool for dating the recent past. *Quaternary Geochronology*, *4*(5), 391–399. http://doi.org/10.1016/j.quageo.2008.12.003

Geirsdóttir, Á. (2011). Pliocene and Pleistocene Glaciations of Iceland. In *Developments in Quaternary Science* (Vol. 15, pp. 199–210). http://doi.org/10.1016/B978-0-444-53447-7.00016-7

Geirsdóttir, Á., & Eiríksson, J. (1994). Growth of an Intermittent Ice Sheet in Iceland during the Late Pliocene and Early Pleistocene. *Quaternary Research*, *42*, 115–130.

Google Earth Pro. (2010). Tindfjallajökull 63°47'N 19°35'W. DigitalGlobe 2012.

Grönvold, K., Óskarsson, N., Johnsen, S. J., Clausen, H. B., Hammer, C. U., Bond, G., & Bard, E. (1995). Ash layers from Iceland in the Greenland GRIP ice core correlated with

oceanic and land sediments. *Earth and Planetary Science Letters*, *135*(1–4), 149–155. http://doi.org/10.1016/0012-821X(95)00145-3

Gudmundsson, M. T. (2015). Tindfjallajökull. In E. Ilyinskaya, G. Larsen, & M. Gudmundsson (Eds.), *Catalogue of Icelandic Volcanoes*. IMO, UI, CPD-NCIP.

Gudmundsson, M. T., & Höskuldsson, Á. (2016). Eyjafjallajökull. In E. Ilyinskaya, G. Larsen, & M. Gudmundsson (Eds.), *Catalogue of Icelandic Volcanoes*. IMO, UI, CPD-NCIP.

Gudmundsson, M. T., Sigmundsson, F., Björnsson, H., & Högnadóttir, T. (2004). The 1996 eruption at Gjálp, Vatnajökull ice cap, Iceland: efficiency of heat transfer, ice deformation and subglacial water pressure. *Bulletin of Volcanology*, *66*(1), 46–65. http://doi.org/10.1007/s00445-003-0295-9

Gunnarsson, B., Marsh, B. D., & Taylor, H. P. (1998). Generation of Icelandic rhyolites: silicic lavas from the Torfajokull central volcano. *Journal of Volcanology and Geothermal Research*, *83*, 1–45. http://doi.org/10.1016/S0377-0273(98)00017-1

Gurenko, A. A., Bindeman, I. N., & Sigurdsson, I. A. (2015). To the origin of Icelandic rhyolites: insights from partially melted leucocratic xenoliths. *Contributions to Mineralogy and Petrology*, *169*(5), 49. http://doi.org/10.1007/s00410-015-1145-4

Haflidason, H., Eiriksson, J., & Kreveld, S. Van. (2000). The tephrochronology of Iceland and the North Atlantic region during the Middle and Late Quaternary: a review. *Journal of Quaternary Science*, *15*(1), 3–22. http://doi.org/10.1002/(SICI)1099-1417(200001)15:1<3::AID-JQS530>3.0.CO;2-W

Hambrey, M. J., & Glasser, N. F. (2012). Discriminating glacier thermal and dynamic regimes in the sedimentary record. *Sedimentary Geology*, *251–252*, 1–33. http://doi.org/10.1016/j.sedgeo.2012.01.008

Heinrich, H. (1988). Origin and consequences of cyclic ice rafting in the Northeast Atlantic Ocean during the past 130,000 years. *Quaternary Research*, *29*(2), 142–152. http://doi.org/10.1016/0033-5894(88)90057-9

Helgason, J. (1984). Frequent shifts of the volcanic zone in Iceland. *Geology*, *12*, 212–216. http://doi.org/10.1130/0091-7613(1984)12<212

Hildreth, W., & Mahood, G. (1986). Ring-fracture eruption of the Bishop Tuff. *Geological Society of America …*, *97*, 396–403. Retrieved from http://gsabulletin.gsapubs.org/content/97/4/396.short

Hodell, D. A., Evans, H. F., Channell, J. E. T., & Curtis, J. H. (2010). Phase relationships of North Atlantic ice-rafted debris and surface-deep climate proxies during the last glacial period. *Quaternary Science Reviews*, *29*(27–28), 3875–3886. http://doi.org/10.1016/j.quascirev.2010.09.006

Honnorez, J., & Kirst, P. (1975). Submarine basaltic volcanism: Morphometric parameters for discriminating hyaloclastites from hyalotuffs. *Bulletin Volcanologique*, *39*, 441. http://doi.org/10.1007/BF02597266

Hu, Z., Gao, S., Liu, Y., Hu, S., Chen, H., & Yuan, H. (2008). Signal enhancement in laser ablation ICP-MS by addition of nitrogen in the central channel gas. *Journal of Analytical Atomic Spectrometry*, *23*(8), 1093. http://doi.org/10.1039/b804760j

Hubbard, A., Sugden, D., Dugmore, A., Norddahl, H., & P??tursson, H. G. (2006). A modelling insight into the Icelandic Last Glacial Maximum ice sheet. *Quaternary Science Reviews*, *25*(17–18), 2283–2296. http://doi.org/10.1016/j.quascirev.2006.04.001

Ingólfsson, Ó., & Norddahl, H. (2001). High Relative Sea Level during the Bolling Interstadial in Western Iceland : A Reflection of Ice-Sheet Collapse and Extremely Rapid Glacial Unloading. *Arctic, Antarctic, and Alpine Research*, *33*(2), 231–243.

Iverson, N. A., Lieb-Lappen, R., Dunbar, N. W., Obbard, R., Kim, E., & Golden, E. (2017). The first physical evidence of subglacial volcanism under the West Antarctic Ice Sheet. *Scientific Reports*, *7*(1), 1–8. http://doi.org/10.1038/s41598-017-11515-3

Jakobsson, S. (1966). The Grimsnes lavas SW-Iceland. *Acta Naturalia Islandica*, *II*(6).

Jakobsson, S. P. (1972). Chemistry and distribution pattern of recent basaltic rocks in Iceland. *Lithos*, *5*(4), 365–386. http://doi.org/10.1016/0024-4937(72)90090-4

Jakobsson, S. P. (1979). Petrology of recent basalts of the Eastern Volcanic Zone, Iceland. *Acta Naturalia Islandica*, *26*. http://doi.org/10.1016/0198-0254(81)91274-7

Jakobsson, S. P., Jónasson, K., & Sigurðsson, I. A. (2008). The three igneous rock series of Iceland. *Jökull*.

Jenner, F. E., & O'Neill, H. S. C. (2012). Major and trace analysis of basaltic glasses by laser-ablation ICP-MS. *Geochemistry, Geophysics, Geosystems*, *13*(3), 1–17. http://doi.org/10.1029/2011GC003890

Jennings, A., Thordarson, T., Zalzal, K., Stoner, J., Hayward, C., Geirsdottir, A., & Miller, G. (2014). Holocene tephra from Iceland and Alaska in SE Greenland Shelf Sediments. *Geological Society, London, Special Publications*, *398*(1), 157–193. http://doi.org/10.1144/SP398.6

Jensen, B. J. L., Pyne-O'Donnell, S., Plunkett, G., Froese, D. G., Hughes, P. D. M., Sigl, M., … Pilcher, J. R. (2014). Transatlantic distribution of the Alaskan White River Ash. *Geology*, *42*(10), 875–878. http://doi.org/10.1130/G35945.1

Jóhannesson, H., & Sæmundsson, K. (1989). Geological Map of Iceland, 1:500,000, Bedrock Geology. *Icelandic Institute of Natural History, Reykjavik*.

Jónasson, K. (2007). Silicic volcanism in Iceland: Composition and distribution within the active volcanic zones. *Journal of Geodynamics*, *43*, 101–117. http://doi.org/10.1016/j.jog.2006.09.004

Jones, J. G. (1966). Intraglacial Volcanoes of South-west Iceland and their Significance in the Interpretation of the Form of the Marine Basaltic Volcanoes. *Nature*, *212*, 586–588. http://doi.org/10.1038/212586a0

Jones, J. G. (1969). Intraglacial volcanoes of the Laugarvatn region, south-west Iceland. *Quarterly Journal of the Geological Society of London*, *124*, 197–211. http://doi.org/10.1144/gsjgs.124.1.0197

Jónsson, J. (1988). Geological Map Eyjafjöll, 1:50,000. *Research Institute Neðri Ás Hveragerði*.

Jørgensen, K. A. (1980). The Thorsmörk ignimbrite: an unusual comenditic pyroclastic flow in southern Iceland. *Journal of Volcanology and Geothermal Research*, *8*(1), 7–22. http://doi.org/10.1016/0377-0273(80)90004-9

Jouzel, J., Masson-Delmotte, V., Cattani, O., Dreyfus, G., Falourd, S., Hoffmann, G., … Wolff, E. W. (2007). Orbital and Millennial Antarctic Climate Variability over the Past 800,000 Years. *Science*, *317*, 793–796. http://doi.org/104.239.165.217

Kelley, S. (2002). K-Ar and Ar-Ar Dating. *Reviews in Mineralogy and Geochemistry*, *47*(1), 785–818. http://doi.org/10.2138/rmg.2002.47.17

Kelman, M. C., Russell, J. K., & Hickson, C. J. (2002). Effusive intermediate glaciovolcanism in the Garibaldi Volcanic Belt, southwestern British Columbia, Canada. *Geological Society, London, Special Publications*, *202*(1), 195–211. http://doi.org/10.1144/GSL.SP.2002.202.01.10

Kindler, P., Guillevic, M., Baumgartner, M., Schwander, J., Landais, A., & Leuenberger, M. (2014). Temperature reconstruction from 10 to 120 kyr b2k from the NGRIP ice core. *Climate of the Past*, *10*(2), 887–902. http://doi.org/10.5194/cp-10-887-2014

Kirkbride, M. P., & Dugmore, A. J. (2006). Responses of mountain ice caps in central Iceland to Holocene climate change. *Quaternary Science Reviews*, *25*(13–14), 1692–1707. http://doi.org/10.1016/j.quascirev.2005.12.004

Kirkbride, M. P., & Dugmore, A. J. (2008). Two millennia of glacier advances from southern Iceland dated by tephrochronology. *Quaternary Research*, *70*(3), 398–411. http://doi.org/10.1016/j.yqres.2008.07.001

Kristjansson, L., & Gudmundsson, A. (1980). Geomagnetic excursion in late-glacial basalt outcrops in south-western Iceland. *Geophysical Research Letters*, *7*(5), 337–340.

Kristjansson, L., Johannesson, H., Eiriksson, J., & Gudmundsson, A. I. (1988). Brunhes-Matuyama paleomagnetism in three lava sections in Iceland. *Canadian Journal of Earth Sciences*, *25*(2), 215–225. http://doi.org/10.1139/e88-024

Kvamme, T., Mangerud, J., Furnes, H., & Ruddiman, W. F. (1989). Geochemistry of Pleistocene ash zones in cores from the North Atlantic. *Norsk Geologisk Tidsskrift*, *69*(4), 251–272.

Lacasse, C. (2001). Influence of climate variability on the atmospheric transport of Icelandic tephra in the subpolar North Atlantic. *Global and Planetary Change*, *29*(1–2), 31–55. http://doi.org/10.1016/S0921-8181(01)00099-6

Lacasse, C., & Garbe-Schönberg, C. D. (2001). Explosive silicic volcanism in Iceland and the Jan Mayen area during the last 6 Ma: Sources and timing of major eruprtions. *Journal of Volcanology and Geothermal Research*, *107*(1–3), 113–147. http://doi.org/10.1016/S0377-0273(00)00299-7

Lacasse, C., Sigurdsson, H., Carey, S. N., Jóhannesson, H., Thomas, L. E., & Rogers, N. W. (2007). Bimodal volcanism at the Katla subglacial caldera, Iceland: Insight into the geochemistry and petrogenesis of rhyolitic magmas. *Bulletin of Volcanology*, *69*, 373–399. http://doi.org/10.1007/s00445-006-0082-5

Lacasse, C., Sigurdsson, H., Carey, S., Paterne, M., & Guichard, F. (1996). North Atlantic deep-sea sedimentation of Late Quaternary tephra from the Iceland hotspot. *Marine Geology*, *129*(3–4), 207–235. http://doi.org/10.1016/0025-3227(96)83346-9

Lackschewitz, K. S., & Wallrabe-Adams, H. J. (1997). Composition and origin of volcanic ash zones in late quaternary sediments from the Reykjanes ridge: Evidence for ash fallout and ice-rafting. *Marine Geology*, *136*(3–4), 209–224. http://doi.org/10.1016/S0025-3227(96)00056-4

Laj, C., & Channell, J. E. T. (2007). Geomagnetic Excursions. In *Treatise on Geophysics* (Vol. 5, pp. 373–416). Elsevier. http://doi.org/10.1016/B978-044452748-6.00095-X

Landmælingar Íslands. (2016). IS 50V digital map database. Retrieved from http://www.lmi.is/en/stafraen-gogn/is-50v-nytt/; Licence: http://www.lmi.is/wp-content/uploads/2013/10/licenceNLSI.pdf

Lane, C. S., Blockley, S. P. E., Mangerud, J., Smith, V. C., Lohne, S., Tomlinson, E. L., … Lotter, A. F. (2012). Was the 12.1ka Icelandic Vedde Ash one of a kind? *Quaternary Science Reviews*, *33*(FEBRUARY), 87–99. http://doi.org/10.1016/j.quascirev.2011.11.011

Lapin, I. V, Lukanin, O. A., & Kadik, A. A. (1985). Effect of redox conditions on near-surface Icelandic basalt crystallisation and differentation. *Geokhimiya*, *6*, 747–760.

Larsen, G. (2000). Holocene eruptions within the Katla volcanic system, south Iceland: Characteristics and environmental impact. *Jökull*, *49*(49), 1–28.

Larsen, G., Dugmore, A., & Newton, A. (1999). Geochemistry of historical-age silicic tephras in Iceland. *The Holocene*, *9*(4), 463–471. http://doi.org/10.1191/095968399669624108

Larsen, G., & Eiríksson, J. (2008). Late Quaternary terrestrial tephrochronology of Iceland—frequency of explosive eruptions, type and volume of tephra deposits. *Journal of Quaternary Science*, *23*(2), 109–120. http://doi.org/10.1002/jqs.1129

Larsen, G., & Gudmundsson, M. T. (2016). Katla. In E. Ilyinskaya, G. Larsen, & M. Gudmundsson (Eds.), *Catalogue of Icelandic Volcanoes*. IMO, UI, CPD-NCIP.

Larsen, G., & Thordarson, T. (2016). Hekla. In E. Ilyinskaya, G. Larsen, & M. Gudmundsson (Eds.), *Catalogue of Icelandic Volcanoes*. IMO, UI, CPD-NCIP.

Larsen, J. G. (1979). Glass-bearing gabbro inclusions in hyaloclastites from Tindfjallajökull, Iceland. *Lithos*, *12*(4), 289–302. http://doi.org/10.1016/0024-4937(79)90021-5

Lawson, D. E. (1981). Distinguishing characteristics of Diamictons at the Margin of the Matanuska Glacier, Alaska. *Annals of Glaciology*, *2*(February), 78–84. http://doi.org/10.3189/172756481794352379

Le Bas, M. J., Le Maitre, R. W., Streckeisen, A., & Zanettin, B. (1986). A chemical classification of volcanic rocks based on the total alkali-silica diagram. *Journal of Petrology*, *27*(3), 745–750. http://doi.org/10.1093/petrology/27.3.745

Lee, J. Y., Marti, K., Severinghaus, J. P., Kawamura, K., Yoo, H. S., Lee, J. B., & Kim, J. S. (2006). A redetermination of the isotopic abundances of atmospheric Ar. *Geochimica et Cosmochimica Acta*, *70*(17), 4507–4512. http://doi.org/10.1016/j.gca.2006.06.1563

Lescinsky, D. T., & Fink, J. H. (2000). Lava and ice interaction at stratovolcanoes: Use of characteristic features to determine past glacial extents and future volcanic hazards. *Journal of Geophysical Research*, *105*(B10), 23711–23726.

Lescinsky, D. T., & Sisson, T. W. (1998). Ridge-forming, ice-bounded lava flows at Mount Rainier, Washington. *Geology*, *26*(4), 351–354.

Levi, S., Audunsson, H., Duncan, R. A., Kristjansson, L., Gillot, P. Y., & Jakobsson, S. P. (1990). Late Pleistocene geomagnetic excursion in Icelandic lavas: confirmation of the Laschamp excursion. *Earth and Planetary Science Letters*, *96*(3–4), 443–457. http://doi.org/10.1016/0012-821X(90)90019-T

Licciardi, J. M., Kurz, M. D., & Curtice, J. M. (2007). Glacial and volcanic history of Icelandic table mountains from cosmogenic3He exposure ages. *Quaternary Science Reviews*, *26*(11–12), 1529–1546. http://doi.org/10.1016/j.quascirev.2007.02.016

Loughlin, S. C. (1995). *The evolution of the Eyjafjöll volcanic system, southern Iceland*. PhD thesis, Durham University.

Loughlin, S. C. (2002). Facies analysis of proximal subglacial and proglacial volcaniclastic successions at the Eyjafjallajökull central volcano, southern Iceland. *Geological Society, London, Special Publications*, *202*, 149–178. http://doi.org/10.1144/GSL.SP.2002.202.01.08

Lowe, D. J. (2011). Tephrochronology and its application: A review. *Quaternary Geochronology*, *6*(2), 107–153. http://doi.org/10.1016/j.quageo.2010.08.003

Lowe, D. J., Pearce, N. J. G., Jorgensen, M. A., Kuehn, S. C., Tryon, C. A., & Hayward, C. L. (2017). Correlating tephras and cryptotephras using glass compositional analyses and numerical and statistical methods: Review and evaluation. *Quaternary Science Reviews*, *175*, 1–44. http://doi.org/10.1016/j.quascirev.2017.08.003

Ludwig, K. (2012). User's manual for Isoplot version 3.75-4.15: a geochronological toolkit for Microsoft Excel.

Lyle, P. (2000). The eruption environment of multi-tiered columnar basalt lava flows. *Journal of the Geological Society*, *157*, 715–722. http://doi.org/10.1144/jgs.157.4.715

Macdonald, R., Mcgarvie, D. W., Pinkerton, H., Smith, R. L., & Palacz, Z. A. (1990). Petrogenetic Evolution of the Torfajokull Volcanic Complex , Iceland I. Relationship Between the Magma Types. *Journal of Petrology*, *31*, 429–459.

Macdonald, R., Sparks, R. S. J., Sigurdsson, T., Mattey, D. P., McGarvie, D. W., & Smith, R. L. (1987). The 1875 eruption of Askja volcano, Iceland: combined fractional crystallization and selective contamination in the generation of rhyolitic magma. *Mineralogical Magazine*, *51*(360), 183–202. http://doi.org/10.1180/minmag.1987.051.360.01

Major, J. J., & Newhall, C. G. (1989). Snow and ice perturbation during historical volcanic eruptions and the formation of lahars and floods - A global review. *Bulletin of Volcanology*, *52*(1), 1–27. http://doi.org/10.1007/BF00641384

Martin, E., & Sigmarsson, O. (2007). Crustal thermal state and origin of silicic magma in Iceland: The case of Torfajökull, Ljósufjöll and Snæfellsjökull volcanoes. *Contributions to Mineralogy and Petrology*, *153*(5), 593–605. http://doi.org/10.1007/s00410-006-0165-5

Martini, I. P., French, H. M., & Pérez Alberti, A. (2011). Ice-Marginal and Periglacial Processes and Sediments, 1–13.

Mathews, W. H. (1947). "Tuyas," flat-topped volcanoes in northern British Columbia. *American Journal of Science*, *245*(9), 560–570. http://doi.org/10.2475/ajs.245.9.560

McDougall, I., & Harrison, T. M. (1999). *Geochronology and Thermochronology by the $^{40}Ar/^{39}Ar$ method*. New York: Oxford University Press.

McGarvie, D. (2009). Rhyolitic volcano–ice interactions in Iceland. *Journal of Volcanology and Geothermal Research*, *185*(4), 367–389. http://doi.org/10.1016/j.jvolgeores.2008.11.019

McGarvie, D. W. (1984). Torfajokull: a volcano dominated by magma mixing. *Geology*, *12*, 685–688. http://doi.org/10.1130/0091-7613(1984)12<685:TAVDBM>2.0.CO;2

McGarvie, D. W., Burgess, R., Tindle, A. G., Tuffen, H., & Stevenson, J. A. (2006). Pleistocene rhyolitic volcanism at Torfajökull, Iceland: eruption ages, glaciovolcanism, and geochemical evolution. *Jökull*, *56*, 57–75.

McGarvie, D. W., Macdonald, R., & Pinkerton, H. (1990). Petrogenetic Evolution of the Torfajokull Volcanic Complex, Iceland II. The Role of Magma Mixing. *Journal of Petrology*, *31*, 461–481.

McGarvie, D. W., Stevenson, J. A., Burgess, R., Tuffen, H., & Tindle, A. G. (2007). Volcano – ice interactions at Prestahnukur, Iceland: rhyolite eruption during the last interglacial – glacial transition. *Annals of Glaciology*, *45*, 38–47. http://doi.org/10.3189/172756407782282453

McPhie, J., Doyle, M., & Allen, R. (1993). *Volcanic textures: a guide to the interpretation of textures in volcanic rocks*. Centre for Ore Deposit and Exploration Studies, University of Tasmania.

Mee, K., Gilbert, J. S., McGarvie, D. W., Naranjo, J. A., & Pringle, M. S. (2009). Palaeoenvironment reconstruction, volcanic evolution and geochronology of the Cerro Blanco subcomplex, Nevados de Chillán volcanic complex, central Chile. *Bulletin of Volcanology*, *71*(8), 933–952. http://doi.org/10.1007/s00445-009-0277-7

Meese, D. A., Gow, A. J., Alley, R. B., Zielinski, G. A., Grootes, P. M., Ram, M., … Bolzan, J. F. (1997). The Greenland Ice Sheet Project 2 depth-age scale: Methods and results. *Journal of Geophysical Research: Oceans*, *102*(C12), 26411–26423. http://doi.org/10.1029/97JC00269

Merrihue, C., & Turner, G. (1966). Potassium-Argon Dating by Activation with Fast Neutrons. *Journal of Geophysical Research*, *71*(11), 2852–2857.

Meyer, P. S., Sigurdsson, H., & Schilling, J. (1985). Petrological and geochemical variations along Iceland's Neovolcanic Zones. *Journal of Geophysical Research*, *90*, 10043. http://doi.org/10.1029/JB090iB12p10043

Moles, J. D., McGarvie, D., Stevenson, J. A., & Sherlock, S. C. (2018). Geology of Tindfjallajökull volcano, Iceland. *Journal of Maps*, *14*(2), 22–31. http://doi.org/10.1080/17445647.2018.1425163

Moore, J. G., Phillips, R. L., Grigg, R. W., Peterson, D. W., & Swanson, D. A. (1973). Flow of lava into the sea, 1969-1971, Kilauea Volcano, Hawaii. *Bulletin of the Geological Society of America*, *84*(2), 537–546. http://doi.org/10.1130/0016-7606(1973)84<537:FOLITS>2.0.CO;2

Nelson, A. E., Smellie, J. L., Hambrey, M. J., Williams, M., Vautravers, M., Salzmann, U., … Regelous, M. (2009). Neogene glacigenic debris flows on James Ross Island, northern Antarctic Peninsula, and their implications for regional climate history. *Quaternary Science Reviews*, *28*(27–28), 3138–3160. http://doi.org/10.1016/j.quascirev.2009.08.016

Nicholson, H., Condomines, M., Fitton, J. G., Fallick, A. E., Grönvold, K., & Rogers, G. (1991). Geochemical and isotopic evidence for crustal assimilation beneath krafla, Iceland. *Journal of Petrology*, *32*(5), 1005–1020. http://doi.org/10.1093/petrology/32.5.1005

Norðdahl, H., & Pétursson, H. G. (2005). 3. Relative sea-level changes in Iceland: new aspects of the Weichselian deglaciation of Iceland. In *Developments in Quaternary Science* (Vol. 5, pp. 25–78). http://doi.org/10.1016/S1571-0866(05)80005-3

Nowaczyk, N. R., Arz, H. W., Frank, U., Kind, J., & Plessen, B. (2012). Dynamics of the Laschamp geomagnetic excursion from Black Sea sediments. *Earth and Planetary Science Letters*, *351–352*, 54–69. http://doi.org/10.1016/j.epsl.2012.06.050

Óladóttir, B. A., Sigmarsson, O., Larsen, G., & Devidal, J.-L. (2011). Provenance of basaltic tephra from Vatnajökull subglacial volcanoes, Iceland, as determined by major- and trace-element analyses. *The Holocene*, *21*(7), 1037–1048. http://doi.org/10.1177/0959683611400456

Óskarsson, N., Steinthórsson, S., & Sigvaldason, G. E. (1985). Iceland geochemical anomaly: Origin, volcanotectonics, chemical fractionation and isotope evolution of the crust. *Journal of Geophysical Research*, *90*(B12), 10011. http://doi.org/10.1029/JB090iB12p10011

Owen, J., Tuffen, H., & McGarvie, D. W. (2013a). Explosive subglacial rhyolitic eruptions in Iceland are fuelled by high magmatic H2O and closed-system degassing. *Geology*, *41*(2), 251–254. http://doi.org/10.1130/G33647.1

Owen, J., Tuffen, H., & McGarvie, D. W. (2013b). Pre-eruptive volatile content, degassing paths and depressurisation explaining the transition in style at the subglacial rhyolitic eruption of Dalakvísl, South Iceland. *Journal of Volcanology and Geothermal Research*, *258*, 143–162. http://doi.org/10.1016/j.jvolgeores.2013.03.021

Palmason, G., & Saemundsson, K. (1974). Iceland in Relation to the Mid-Atlantic Ridge. *Annual Review of Earth and Planetary Sciences*, *2*(1), 25–50. http://doi.org/10.1146/annurev.ea.02.050174.000325

Parrenin, F., Barnola, J. M., Beer, J., Blunier, T., Castellano, E., Chappellaz, J., … Wolff, E. (2007). The EDC3 chronology for the EPICA Dome C ice core. *Climate of the Past*, *3*(3), 485–497. http://doi.org/10.5194/cp-3-485-2007

Patton, H. (2013). *Modelling the dynamic evolution and sensitivities of two palaeo-ice masses: the Welsh Ice Cap and the Icelandic Ice Sheet*. PhD thesis, Aberystwyth University.

Patton, H., Hubbard, A., Bradwell, T., & Schomacker, A. (2017). The configuration, sensitivity and rapid retreat of the Late Weichselian Icelandic ice sheet. *Earth-Science Reviews*, *166*, 223–245. http://doi.org/10.1016/j.earscirev.2017.02.001

Pearce, N. J. G., Bendall, C. A., & Westgate, J. A. (2008). Comment on "Some numerical considerations in the geochemical analysis of distal microtephra" by A.M. Pollard, S.P.E. Blockley and C.S. Lane. *Applied Geochemistry*, *23*(5), 1353–1364. http://doi.org/10.1016/j.apgeochem.2008.01.002

Pierson, T. C., Janda, R. J., Thouret, J. C., & Borrero, C. A. (1990). Perturbation and melting of snow and ice by the 13 November 1985 eruption of Nevado del Ruiz, Colombia, and consequent mobilization, flow and deposition of lahars. *Journal of Volcanology and Geothermal Research*, *41*(1–4), 17–66. http://doi.org/10.1016/0377-0273(90)90082-Q

Portnyagin, M., Hoernle, K., Storm, S., Mironov, N., van den Bogaard, C., & Botcharnikov, R. (2012). H_2O-rich melt inclusions in fayalitic olivine from Hekla volcano: Implications for phase relationships in silicic systems and driving forces of explosive volcanism on Iceland. *Earth and Planetary Science Letters*, *357–358*, 337–346. http://doi.org/10.1016/j.epsl.2012.09.047

Prestvik, T., Goldberg, S., Karlsson, H., & Grönvold, K. (2001). Anomalous strontium and lead isotope signatures in the off-rift Öræfajökull central volcano in south-east iceland evidence for enriched endmember(s) of the iceland mantle plume? *Earth and Planetary Science Letters*, *190*(3–4), 211–220. http://doi.org/10.1016/S0012-821X(01)00390-9

Principato, S. M., Geirsdóttir, Á., Jóhannsdóttir, G. E., & Andrews, J. T. (2006). Late Quaternary glacial and deglacial history of eastern Vestfirdir, Iceland using cosmogenic isotope (36Cl) exposure ages and marine cores. *Journal of Quaternary Science*, *21*(3), 271–285. http://doi.org/10.1002/jqs.978

Quane, S. L., Russell, J. K., & Friedlander, E. A. (2009). Time scales of compaction in volcanic systems. *Geology*, *37*(5), 471–474. http://doi.org/10.1130/G25625A.1

R Core Team (2014). R: A language and environment for statistical computing. *R Foundation for Statistical Computing, Vienna, Austria.* http://www.R-project.org/

Ram, M., Donarummo, J., & Sheridan, M. (1996). Volcanic ash from Icelandic ~57,300 yr BP eruption found in GISP2 (Greenland) ice core. *Geophysical Research Letters*, *23*(22), 3167–3169.

Ram, M., & Gayley, R. I. (1991). Long-range transport of volcanic ash to the Greenland ice sheet. *Nature*, *349*(6308), 401–404. http://doi.org/10.1038/349401a0

Rasmussen, S. O., Bigler, M., Blockley, S. P., Blunier, T., Buchardt, S. L., Clausen, H. B., … Winstrup, M. (2014). A stratigraphic framework for abrupt climatic changes during the Last Glacial period based on three synchronized Greenland ice-core records: Refining and extending the INTIMATE event stratigraphy. *Quaternary Science Reviews*, *106*, 14–28. http://doi.org/10.1016/j.quascirev.2014.09.007

Renne, P. R., Balco, G., Ludwig, K. R., Mundil, R., & Min, K. (2011). Response to the comment by W.H. Schwarz et al. on " Joint determination of 40K decay constants and $^{40}Ar^*/^{40}K$ for the Fish Canyon sanidine standard, and improved accuracy for $^{40}Ar/^{39}Ar$

geochronology" by P.R. Renne et al. (2010). *Geochimica et Cosmochimica Acta*, *75*(17), 5097–5100. http://doi.org/10.1016/j.gca.2011.06.021

Rittman, A. (1958). Il meccanismo di formazione delle lave a pillows e dei cosidelti tufi palagonitici. *Atti Acc. Gioenia*, *4*, 310–317.

Roberts, S. J. (2001). *Quaternary tephrochronology in Iceland: dating principles and applications*. PhD thesis, University of Edinburgh.

Ruddiman, W. F. (1977). Late Quaternary deposition of ice-rafted sand in the subpolar North Atlantic (lat 40° to 65°N). *Bulletin of the Geological Society of America*, *88*(12), 1813–1827. http://doi.org/10.1130/0016-7606(1977)88<1813:LQDOIS>2.0.CO;2

Ruddiman, W. F., & Glover, L. K. (1972). Vertical Mixing of Ice-Rafted Volcanic Ash in North Atlantic Sediments. *Geological Society of America Bulletin*, *83*, 2817–2836.

Ruddiman, W. F., & McIntyre, A. (1977). Late Quaternary Surface Ocean Kinematics and Climatic Change in High Latitude North-Atlantic. *Journal of Geophysical Research-Oceans and Atmospheres*, *82*(27), 3877–3887.

Ruddiman, W. F., & McIntyre, A. (1984). Ice-age thermal response and climatic role of the surface Atlantic Ocean, 40°N to 63°N. *Geological Society of America Bulletin*, *95*(4), 381–396. http://doi.org/10.1130/0016-7606(1984)95<381:itracr>2.0.co;2

Russell, J. K., Edwards, B. R., Porritt, L., & Ryane, C. (2014). Tuyas: A descriptive genetic classification. *Quaternary Science Reviews*, *87*, 70–81. http://doi.org/10.1016/j.quascirev.2014.01.001

Sæmundsson, K. (1974). Evolution of the Axial Rifting Zone in Northern Iceland and the Tjörnes Fracture. *Geological Society of America Bulletin*, *85*, 495–504. http://doi.org/10.1130/0016-7606(1974)85<495

Sæmundsson, K. (2016). Prestahnúkur. In E. Ilyinskaya, G. Larsen, & M. Gudmundsson (Eds.), *Catalogue of Icelandic Volcanoes*. IMO, UI, CPD-NCIP.

Sæmundsson, K., & Friðleifsson, G. Ó. (2001). Geological Map of the Torfajökull Central Volcano, 1:40,000, 18.09.01-KS-GÓF.

Sæmundsson, K., & Larsen, G. (2016). Torfajökull. In E. Ilyinskaya, G. Larsen, & M. T. Gudmundsson (Eds.), *Catalogue of Icelandic Volcanoes*. IMO, UI, CPD-NCIP.

Schilling, J. G. (1973). Iceland mantle plume: Geochemical study of Reykjanes Ridge. *Nature*, *242*(5400), 565–571. http://doi.org/10.1038/242565a0

Schwanethal, J. (2008). ArMaDiLo (Argon Macro Direct Loader) Instruction Manual.

Scott, K. M., Vallance, J. W., & Pringle, P. T. (1995). Sedimentology, behavior, and hazards of debris flows at Mount Rainier, Washington. *U. S. Geological Survey Professional Paper*, *1547*, 1–66.

Seierstad, I. K., Abbott, P. M., Bigler, M., Blunier, T., Bourne, A. J., Brook, E., … Vinther, B. M. (2014). Consistently dated records from the Greenland GRIP, GISP2 and NGRIP ice cores for the past 104ka reveal regional millennial-scale ??18O gradients with possible Heinrich event imprint. *Quaternary Science Reviews*, *106*, 29–46. http://doi.org/10.1016/j.quascirev.2014.10.032

Sigmarsson, O., Hemond, C., Condomines, M., Fourcade, S., & Oskarsson, N. (1991). Origin of silicic magma in Iceland revealed by Th isotopes. *Geology*, *19*(6), 621–624. http://doi.org/10.1130/0091-7613(1991)019<0621:OOSMII>2.3.CO;2

Sigmundsson, F. (1991). Post-glacial rebound and asthenosphere viscosity in Iceland. *Geophysical Research Letters*, *18*(6), 1131–1134. http://doi.org/10.1029/91GL01342

Sigurdsson, H. (1968). Petrology of acid xenoliths from Surtsey. *Geological Magazine*, *105*(5), 440–453.

Sigurdsson, H. (1977). Generation of Icelandic rhyolites by melting of plagiogranites in the oceanic layer. *Nature*, *269*, 25–28.

Sigurdsson, H. (1982). Útbreidsla íslenskra gjóskulaga á botni Atlantshafs. In H. Thorarinsdóttir, O. H. Oskarsson, S. Steinthorsson, & T. Einersson (Eds.), *Eldur er í nordri* (pp. 119–127). Reykjavik: Sögufélag.

Sigurdsson, H., McIntosh, W. C., Dunbar, N., Lacasse, C., & Carey, S. N. (1998). Thorsmork Ignimbrite in Iceland; possible source of North Atlantic ash zone 2? In *AGU 1998 Spring Meeting. Eos (Transactions, American Geophysical Union) 79.* (p. 377).

Skilling, I. P. (2009). Subglacial to emergent basaltic volcanism at Hlöðufell, south-west Iceland: A history of ice-confinement. *Journal of Volcanology and Geothermal Research*, *185*(4), 276–289. http://doi.org/10.1016/j.jvolgeores.2009.05.023

Smellie, J. L. (2006). The relative importance of supraglacial versus subglacial meltwater escape in basaltic subglacial tuya eruptions: An important unresolved conundrum. *Earth-Science Reviews*, *74*(3–4), 241–268. http://doi.org/10.1016/j.earscirev.2005.09.004

Smellie, J. L., Johnson, J. S., McIntosh, W. C., Esser, R., Gudmundsson, M. T., Hambrey, M. J., & van Wyk de Vries, B. (2008). Six million years of glacial history recorded in volcanic lithofacies of the James Ross Island Volcanic Group, Antarctic Peninsula. *Palaeogeography, Palaeoclimatology, Palaeoecology*, *260*(1–2), 122–148. http://doi.org/10.1016/j.palaeo.2007.08.011

Smellie, J. L., Rocchi, S., & Armienti, P. (2011a). Late Miocene volcanic sequences in northern Victoria Land, Antarctica: Products of glaciovolcanic eruptions under different thermal regimes. *Bulletin of Volcanology*, *73*(1), 1–25. http://doi.org/10.1007/s00445-010-0399-y

Smellie, J. L., Rocchi, S., Gemelli, M., Di Vincenzo, G., & Armienti, P. (2011b). A thin predominantly cold-based Late Miocene East Antarctic ice sheet inferred from glaciovolcanic sequences in northern Victoria Land, Antarctica. *Palaeogeography, Palaeoclimatology, Palaeoecology*, *307*(1–4), 129–149. http://doi.org/10.1016/j.palaeo.2011.05.008

Smellie, J. L., Rocchi, S., Johnson, J. S., Di Vincenzo, G., & Schaefer, J. M. (2018). A tuff cone erupted under frozen-bed ice (northern Victoria Land, Antarctica): linking glaciovolcanic and cosmogenic nuclide data for ice sheet reconstructions. *Bulletin of Volcanology*, *80*(1). http://doi.org/10.1007/s00445-017-1185-x

Smellie, J. L., Rocchi, S., Wilch, T. I., Gemelli, M., Di Vincenzo, G., McIntosh, W., … Fargo, A. (2014). Glaciovolcanic evidence for a polythermal Neogene East Antarctic Ice Sheet. *Geology*, *42*(1), 39–41. http://doi.org/10.1130/G34787.1

Smellie, J. L., & Skilling, I. P. (1994). Products of subglacial volcanic eruptions under different ice thicknesses: two examples from Antarctica. *Sedimentary Geology*, *91*(1–4), 115–129. http://doi.org/10.1016/0037-0738(94)90125-2

Smellie, J. L., Wilch, T. I., & Rocchi, S. (2013). ʻAʻā lava-fed deltas: A new reference tool in paleoenvironmental studies. *Geology*, *41*(4), 403–406. http://doi.org/10.1130/G33631.1

Smith, K. T., & Dugmore, A. J. (2006). Jökulhlaups circa Landnám: Mid- to late first millennium AD floods in South Iceland and their implications for landscapes of settlement. *Geografiska Annaler*, *88 A*(2), 165–176. http://doi.org/10.1111/j.0435-3676.2006.00292.x

Smythe, F. ., Ruddiman, W. ., & Lumsden, D. . (1985). Ice-rafted evidence of long-term North Atlantic circulation. *Marine Geology*, *64*(1–2), 131–141. http://doi.org/10.1016/0025-3227(85)90164-1

Stevenson, J. A., Gilbert, J. S., McGarvie, D. W., & Smellie, J. L. (2011). Explosive rhyolite tuya formation: classic examples from Kerlingarfjöll, Iceland. *Quaternary Science Reviews*, *30*(1–2), 192–209. http://doi.org/10.1016/j.quascirev.2010.10.011

Stevenson, J. A., McGarvie, D. W., Smellie, J. L., & Gilbert, J. S. (2006). Subglacial and ice-contact volcanism at the Öræfajökull stratovolcano, Iceland. *Bulletin of Volcanology*, *68*(7–8), 737–752. http://doi.org/10.1007/s00445-005-0047-0

Stevenson, J. A., Millington, S. C., Beckett, F. M., Swindles, G. T., & Thordarson, T. (2015). Big grains go far: Understanding the discrepancy between tephrochronology and satellite infrared measurements of volcanic ash. *Atmospheric Measurement Techniques*, *8*(5), 2069–2091. http://doi.org/10.5194/amt-8-2069-2015

Stevenson, J. A., Mitchell, N. C., Mochrie, F., Cassidy, M., & Pinkerton, H. (2012). Lava penetrating water: the different behaviours of pāhoehoe and ʻaʻā at the Nesjahraun, Þingvellir, Iceland. *Bulletin of Volcanology*, *74*(1), 33–46. http://doi.org/10.1007/s00445-011-0480-1

Stevenson, J. A., Smellie, J. L., McGarvie, D. W., Gilbert, J. S., & Cameron, B. I. (2009). Subglacial intermediate volcanism at Kerlingarfjöll, Iceland: Magma–water interactions beneath thick ice. *Journal of Volcanology and Geothermal Research*, *185*(4), 337–351. http://doi.org/10.1016/j.jvolgeores.2008.12.016

Sun, S. -s., & McDonough, W. F. (1989). Chemical and isotopic systematics of oceanic basalts: implications for mantle composition and processes. *Geological Society, London, Special Publications*, *42*(1), 313–345. http://doi.org/10.1144/GSL.SP.1989.042.01.19

Svensson, A., Andersen, K. K., Bigler, M., Clausen, H. B., Dahl-Jensen, D., Davies, S. M., … Vinther, B. M. (2006). The Greenland Ice Core Chronology 2005, 15-42 ka. Part 2: comparison to other records. *Quaternary Science Reviews*, *25*(23–24), 3258–3267. http://doi.org/10.1016/j.quascirev.2006.08.003

Svensson, A., Andersen, K. K., Bigler, M., Clausen, H. B., Dahl-Jensen, D., Davies, S. M., … Vinther, B. M. (2008). A 60 000 year Greenland stratigraphic ice core chronology. *Climate of the Past*, *4*(1), 47–57. http://doi.org/10.5194/cp-4-47-2008

Thórarinsson, S. (1969). Ignimbrít í Þörsmórk. *Náttúrufræðingurinn*, *39*, 139–155.

Tomlinson, E. L., Thordarson, T., Lane, C. S., Smith, V. C., Manning, C. J., Müller, W., & Menzies, M. A. (2012). Petrogenesis of the Sólheimar ignimbrite (Katla, Iceland):

Implications for tephrostratigraphy. *Geochimica et Cosmochimica Acta*, *86*(JUNE 2012), 318–337. http://doi.org/10.1016/j.gca.2012.03.012

Tomlinson, E. L., Thordarson, T., Müller, W., Thirlwall, M., & Menzies, M. A. (2010). Microanalysis of tephra by LA-ICP-MS — Strategies, advantages and limitations assessed using the Thorsmörk ignimbrite (Southern Iceland). *Chemical Geology*, *279*(3–4), 73–89. http://doi.org/10.1016/j.chemgeo.2010.09.013

Trabant, D. C., Waitt, R. B., & Major, J. J. (1994). Disruption of Drift glacier and origin of floods during the 1989-1990 eruptions of Redoubt Volcano, Alaska. *Journal of Volcanology and Geothermal Research*, *62*(1–4), 369–385. http://doi.org/10.1016/0377-0273(94)90043-4

Tuffen, H., Gilbert, J., & McGarvie, D. (2001). Products of an effusive subglacial rhyolite eruption: Bláhnúkur, Torfajökull, Iceland. *Bulletin of Volcanology*, *63*(2–3), 179–190. http://doi.org/10.1007/s004450100134

Tuffen, H., McGarvie, D. W., & Gilbert, J. S. (2007). Will subglacial rhyolite eruptions be explosive or intrusive? Some insights from analytical models. *Annals of Glaciology*, *45*, 87–94. http://doi.org/10.3189/172756407782282534

Tuffen, H., McGarvie, D. W., Gilbert, J. S., & Pinkerton, H. (2002). Physical volcanology of a subglacial-to-emergent rhyolitic tuya at Rauðufossafjöll, Torfajökull, Iceland. *Geological Society, London, Special Publications*, *202*(1), 213–236. http://doi.org/10.1144/gsl.sp.2002.202.01.11

Tuffen, H., McGarvie, D. W., Pinkerton, H., Gilbert, J. S., & Brooker, R. A. (2008). An explosive–intrusive subglacial rhyolite eruption at Dalakvísl, Torfajökull, Iceland. *Bulletin of Volcanology*, *70*(7), 841–860. http://doi.org/10.1007/s00445-007-0174-x

Turner, M. B., Cronin, S. J., Bebbington, M. S., Smith, I. E. M., & Stewart, R. B. (2011). Integrating records of explosive and effusive activity from proximal and distal sequences:

Mt. Taranaki, New Zealand. *Quaternary International*, *246*(1–2), 364–373. http://doi.org/10.1016/j.quaint.2011.07.006

USA Defence Mapping Agency. (1989). Iceland DMA-C761 topographic maps, 1:50,000. Washington DC: Defence Mapping Agency.

van Wyk de Vries, M., Bingham, R. G., & Hein, A. S. (2018). A new volcanic province: an inventory of subglacial volcanoes in West Antarctica. *Geological Society, London, Special Publications*, *461*(1), 231–248. http://doi.org/10.1144/SP461.7

Voelker, A. H. L., & Haflidason, H. (2015). Refining the Icelandic tephrachronology of the last glacial period - The deep-sea core PS2644 record from the southern Greenland Sea. *Global and Planetary Change*, *131*, 35–62. http://doi.org/10.1016/j.gloplacha.2015.05.001

Walker, G. P. L. (1966). Acid volcanic rocks in Iceland. *Bulletin Volcanologique*, *29*(1), 375–402. http://doi.org/10.1007/BF02597164

Walker, G. P. L., & Croasdale, R. (1971). Characteristics of some basaltic pyroclastics. *Bulletin Volcanologique*, *35*(2), 303–317. http://doi.org/10.1007/BF02596957

Wastegård, S., Rasmussen, T. L., Kuijpers, A., Nielsen, T., & van Weering, T. C. E. (2006). Composition and origin of ash zones from Marine Isotope Stages 3 and 2 in the North Atlantic. *Quaternary Science Reviews*, *25*(17–18), 2409–2419. http://doi.org/10.1016/j.quascirev.2006.03.001

Waythomas, C. F., Haney, M. M., Fee, D., Schneider, D. J., & Wech, A. (2014). The 2013 eruption of Pavlof Volcano, Alaska: a spatter eruption at an ice- and snow-clad volcano. Bulletin of Volcanology, 76, 862. http://doi.org/10.1007/s00445-014-0862-2

Wendt, I., & Carl, C. (1991). The statistical distribution of the mean squared weighted deviation. *Chemical Geology: Isotope Geoscience Section*, *86*(4), 275–285. http://doi.org/10.1016/0168-9622(91)90010-T

Winchester, J., & Floyd, P. (1977). Geochemical discrimination of different magma series and their differentiation products using immobile elements. *Chemical Geology*, *20*, 325–343. Retrieved from http://www.sciencedirect.com/science/article/pii/0009254177900572

Yiou, F., Raisbeck, G. M., Baumgartner, S., Beer, J., Hammer, C., Johnsen, S., … Yiou, P. (1997). Beryllium 10 in the Greenland Ice Core Project ice core at Summit, Greenland. *Journal of Geophysical Research*, *102*(C12), 26,783-26,794.

Yoder, H. S. (1973). Contemporaneous basaltic and rhyolitic magmas. *American Mineralogist*, *58*, 153–171.

Zielinski, G. A., Mayewski, P. A., Meeker, L. D., Grönvold, K., Germani, M. S., Whitlow, S., … Taylor, K. (1997). Volcanic aerosol records and tephrochronology of the Summit, Greenland, ice cores. *Journal of Geophysical Research*, *102*(C12), 26625. http://doi.org/10.1029/96JC03547

Zierenberg, R. A., Schiffman, P., Barfod, G. H., Lesher, C. E., Marks, N. E., Lowenstern, J. B., … Elders, W. A. (2013). Composition and origin of rhyolite melt intersected by drilling in the Krafla geothermal field, Iceland. *Contributions to Mineralogy and Petrology*, *165*(2), 327–347. http://doi.org/10.1007/s00410-012-0811-z

Appendices

Appendix 1: Sample information

Information on samples collected as part of this thesis and analytical work undertaken.

A1.1 Samples collected in 2014

Sample	Lithology	Location	Strati-graphic code	°N	°E	XRF	EPMA	LA-ICP-MS	Ar/Ar
JM-1	Laminated silt	Hvitmaga	SHo	63.8224	-19.4778	✓			
JM-2	Platy rhyolite	SW of Sultarfell	Msl	63.8197	-19.5078	✓			
JM-3	Superficial diamict	SW of Sultarfell		63.8161	-19.5233				
JM-4	Platy rhyolite	SW of Sultarfell	Msl	63.8154	-19.5218	✓			
JM-5	Vesicular rhyolite	Sultarfell	sb	63.8308	-19.4943	✓			
JM-6	Basalt pillow in hyaloclastite	Faxi	mh	63.8309	-19.4631				
JM-7	Basalt lava	Faxi		63.8304	-19.4339				
JM-8	Pillow breccia	Lifrarfjöll	mh	63.8029	-19.4347				
JM-9	Scoria	Bláfell	Lmt	63.7657	-19.6664				
JM-10	Scoria	Bláfell	Lmt	63.7657	-19.6664	✓			
JM-11	Clastogenic lava	Bláfell	Lmt	63.7620	-19.6575				
JM-12	Jointed lava	Bláfell	Lmt	63.7569	-19.6536				✓
JM-13	Top lava	Bláfell	Lmt	63.7613	-19.6500	✓			
JM-14	2nd lava down	Bláfell	Lmt	63.7613	-19.6500	✓			✓
JM-15	3rd lava down	Bláfell	Lmt	63.7613	-19.6500	✓			
JM-16	Autobreccia below top lava	Bláfell	Lmt	63.7613	-19.6500				
JM-17	Jointed lava	Bláfell	Lmt	63.7679	-19.6787				
JM-18	Platy basalt	Miðdalur	Lml	63.7679	-19.6787	✓			
JM-19	Intrusive basalt	SE of Vörðufell		63.7680	-19.7077				
JM-20	Jointed lava	Vörðufell	Lmt	63.7680	-19.7105	✓			✓
JM-21	Clast from breccia	Vörðufell	Lmt	63.7681	-19.7138	✓			
JM-22	Scoria	Vörðufell	Lmt	63.7681	-19.7138	✓			
JM-23	Clastogenic lava	Vörðufell	Lmt	63.7699	-19.7153				
JM-24	Tuff	Vörðufell	Lmt	63.7714	-19.7156				
JM-25	Basalt lava	Smáfjöll		63.7584	-19.6997				
JM-26	Gabbro nodule	Rauðaborg	Lmt	63.7818	-19.6738	✓			
JM-27	Gabbro nodule	Rauðaborg	Lmt	63.7818	-19.6738	✓			
JM-28	Gabbro nodule	Rauðaborg	Lmt	63.7818	-19.6738				

Sample	Lithology	Location	Strati-graphic code	°N	°E	XRF	EPMA	LA-ICP-MS	Ar/Ar
JM-29	Gabbro nodule	Rauðaborg	Lmt	63.7818	-19.6738				
JM-30	Gabbro nodule	Rauðaborg	Lmt	63.7818	-19.6738				
JM-31	Clastogenic lava	Rauðaborg	Lmt	63.7818	-19.6738	✓			
JM-32	Basalt lava	N of Rauðaborg	Lml	63.7854	-19.6725	✓			
JM-33	Clastogenic lava	N of Rauðaborg	Lml	63.7891	-19.6741	✓			
JM-34	Basalt - upper lava	Suðurhlíð	Lml	63.7937	-19.6565	✓			✓
JM-35	Basalt - lower lava	Suðurhlíð	Lml	63.7937	-19.6565	✓			
JM-36	Rhyolite lava	Saxi	Msl	63.7931	-19.6544	✓			✓
JM-37	Rhyolite lava	Saxi	Msl	63.7926	-19.6517	✓	✓		✓
JM-38	Upper rhyolite lava	Saxi	Msl	63.7858	-19.6274	✓			
JM-39	Clastogenic lava	Haki	Lml	63.7791	-19.6410	✓			
JM-40	Glassy rhyolite	Laufafell	Torf RFR	63.9278	-19.3790		✓	✓	
JM-41	Non-glassy rhyolite	Laufafell	Torf RFR	63.9278	-19.3790				
JM-42	Rhyolite lava	Grænahlíð	Torf RFR?	64.0254	-19.2530				
JM-43	Sand	Eystri-Botná	SWe	63.7543	-19.5050				
JM-44	Vein fill within sand	Eystri-Botná	SWe	63.7543	-19.5050				
JM-45	Lapilli tuff	Eystri-Botná	Lmh	63.7543	-19.5050				
JM-46	Lapilli tuff	Hitagilsbrún	Lmh	63.7572	-19.5201				
JM-47	Lapilli tuff	Hitagilsbrún	Lmh	63.7572	-19.5201	✓			
JM-48	Sediment or tuff	Hitagil	SWe	63.7575	-19.5175				
JM-49	Diamict	Hitagil	SWe	63.7580	-19.5164	✓			
JM-50	Lapilli tuff	Hitagil	Lmh	63.7595	-19.5153	✓			
JM-51	Lapilli tuff	Hitagil	Lmh	63.7595	-19.5153	✓			
JM-52	Basalt column	Hitagilsbrún	Lmh	63.7595	-19.5153	✓			
JM-53	Dyke intruding basement	Vestri-Botná	mb	63.7549	-19.5103				
JM-54	Basement lava	Vestri-Botná	mb	63.7549	-19.5103	✓			
JM-55	Basement lava	Vestri-Botná	mb	63.7549	-19.5103	✓			
JM-56	Diamict	Eystri-Botná	SWe	63.7576	-19.5081	✓			
JM-57	Basalt lava	Grænafjall	Emu	63.7671	-19.4379				
JM-58	Lapilli tuff	N of Einhyrningur	Emu	63.7509	-19.4742				
JM-59	Basalt lava	N of Einhyrningur	Emu	63.7534	-19.4693				
JM-60	Basalt lava	N of Einhyrningur	Emu	63.7509	-19.4742				
JM-61	Basalt lava	N of Einhyrningur	Emu	63.7534	-19.4734				
JM-62	Clast from lapilli tuff	N of Einhyrningur	Emu	63.7509	-19.4742				
JM-63	Lapilli tuff	Einhyrningur	Lmh	63.7408	-19.4715				

Sample	Lithology	Location	Strati-graphic code	°N	°E	XRF	EPMA	LA-ICP-MS	Ar/Ar
JM-64	Clast from lapilli tuff	Einhyrningur	Lmh	63.7408	-19.4715				
JM-65	Clast from lapilli tuff	Einhyrningur	Lmh	63.7408	-19.4715				
JM-66	Lower lava	Tröllagjá	Kml	63.7183	-19.5003				
JM-67	2nd lava up	Tröllagjá	Kml	63.7183	-19.5003				
JM-68	3rd lava up	Tröllagjá	Kml	63.7183	-19.5003				
JM-69	4th lava up	Tröllagjá	Kml	63.7183	-19.5003				
JM-70	Basalt lobe	Mögugil, Þórólfsfell	Lmt	63.7076	-19.6990				
JM-71	Lapilli tuff	Hafrafell	mh	63.8452	-19.8209				
JM-72	Lapilli tuff	Kerlingarfjöll	mh	63.8555	-19.6269				
JM-73	Lapilli tuff	Hungurskarð	mh	63.8427	-19.5657				
JM-74	Pillow basalt	Reiðskarð	mh	63.8386	-19.4994				
JM-75	Basalt dyke	Reiðskarð	mh	63.8386	-19.4994				
JM-76	Rhyolite lobe	Sultarfell	sb	63.8285	-19.4946	✓			
JM-77	Rhyolite breccia	Sultarfell	sb	63.8295	-19.4920				
JM-78	Basalt lobe	S of Sultarfell	Lmh	63.8129	-19.5168				
JM-79	Rhyolite lava	S of Sultarfell	Msl	63.8103	-19.5141	✓			
JM-80	Glassy rhyolite	S of Sultarfell	Msl	63.8028	-19.5200	✓	✓		
JM-81	Platy rhyolite	S of Sultarfell	Msl	63.8029	-19.5147	✓			
JM-82	Basalt lobe	S of Sultarfell	Lmh	63.8110	-19.5100				
JM-83	Glassy rhyolite (lava base)	S of Sultarfell	Msl	63.8143	-19.5117				
JM-84	Rhyolite (lava base)	S of Sultarfell	Msl	63.8143	-19.5117	✓			
JM-85	Glassy rhyolite	S of Sultarfell	Msl	63.8143	-19.5117	✓			
JM-86	Possible mafic inclusions	Sultarfell	sb	63.8295	-19.4920				

A1.2 Samples collected in 2015

Sample	Lithology	Location	Strati-graphic code	°N	°E	XRF	EPMA	LA-ICP-MS	Ar/Ar
JM-101	Dyke intruding diamict	Vestri-Botná		63.7603	-19.5390	✓			
JM-102	Rhyolite lava	S cent. silicic edifice	Lsb	63.7609	-19.5401				
JM-103	Columnar rhyolite	S cent. silicic edifice	Lsb	63.7629	-19.5424	✓			
JM-104	Altered fragmented rhyolite	S cent. silicic edifice	Lsb	63.7638	-19.5435				

Sample	Lithology	Location	Strati-graphic code	°N	°E	XRF	EPMA	LA-ICP-MS	Ar/Ar
JM-105	Rhyolite lava	S cent. silicic edifice	Lsb	63.7645	-19.5414				
JM-106	Diamict	Vestri-Botná	SWe	63.7603	-19.5390	✓			
JM-107	Diamict	Vestri-Botná	SWe	63.7581	-19.5211				
JM-108	Columnar basalt	Einbúi	Lsb	63.7727	-19.5191	✓			
JM-109	Basalt breccia	Einbúi	Lsb	63.7727	-19.5191				
JM-110	Rhyolite breccia	SE cent. silicic edifice	Lsb	63.7739	-19.5220				
JM-111	Rhyolite breccia	SE cent. silicic edifice	Lsb	63.7739	-19.5220	✓			
JM-112	Altered fragmented rhyolite	SE cent. silicic edifice	Lsb	63.7739	-19.5220				
JM-113	Basalt sill	Hitagilsbrún	Lmh	63.7667	-19.5225	✓			
JM-114	Platy rhyolite	Hitagil	Lsb	63.7626	-19.5198	✓			
JM-115	Diamict	Hitagil	SWe	63.7576	-19.5125				
JM-116	Pebbles from diamict	Hitagil	SWe	63.7576	-19.5125				
JM-117	Basement breccia	Eystri-Botná	mb	63.7598	-19.5025	✓			
JM-118	Pillow basalt	Kerhnúkar	Lmh	63.7552	-19.5073				
JM-119	Rhyolite lava	Mosar	Msl	63.7873	-19.4648				
JM-120	Lapilli tuff	Mosar	Emu	63.7873	-19.4648				
JM-121	Basalt lava	Vestriöxl	Mml	63.7936	-19.4699				
JM-122	Basalt lava	Vestriöxl	Mml	63.7934	-19.4904	✓			
JM-123	Rhyolite lava	Vestriöxl	Msl	63.7936	-19.4941				
JM-124	Columnar rhyolite	Vestriöxl	Msl	63.7879	-19.4959	✓			✓
JM-125	Lapilli tuff	Jökulskarð	Lmt	63.7919	-19.5137				
JM-126	Intrusive basalt	Jökulskarð	Lmt	63.7934	-19.5146	✓			
JM-127	Lapilli tuff	Jökulskarð	Lmh	63.7906	-19.5215				
JM-128	Basalt sill	Jökulskarð	Lmh	63.7906	-19.5215	✓			
JM-129	Rhyolite breccia	E cent. silicic edifice	Lsb	63.7865	-19.5188				
JM-130	Columnar rhyolite	E cent. silicic edifice	Lsb	63.7865	-19.5188	✓	✓		
JM-131	Breccia	Vestriöxl	Emu	63.7830	-19.4898				

Sample	Lithology	Location	Strati-graphic code	°N	°E	XRF	EPMA	LA-ICP-MS	Ar/Ar
JM-132	Welded ignimbrite	Hestur	TI	63.7376	-19.5145				
JM-133	Dark ash	Hestur	TI	63.7364	-19.5155				
JM-134	Rhyolite lava	Hestur	Msl	63.7350	-19.5182	✓			
JM-135	Intrusive basalt	Hestur	Lmh	63.7381	-19.5099	✓			
JM-136	Lapilli tuff	Klofningar	Lmh	63.8175	-19.7388				
JM-137	Basalt lava	Valahnúkur	Lmt	63.8230	-19.6964	✓			
JM-138	Rhyolite breccia matrix	Sultarfell	sb	63.8308	-19.4943				
JM-139	Rhyolite lobe	Sultarfell	sb	63.8308	-19.4943				
JM-140	Basalt lava	Blesárjökull	Lml	63.8152	-19.6124	✓			
JM-141	Basalt lava	Ásgrindur	Emu	63.8062	-19.5514	✓			
JM-142	Basalt lava	Sindri	Lml	63.8052	-19.5542	✓			
JM-143	Basalt lava	Sindri	Lml	63.8126	-19.5467				
JM-144	Diamict	Hestur	SWe	63.7343	-19.5171				
JM-145	Intrusive rhyolite	Hestur	Msl	63.7351	-19.5169	✓			
JM-146	Diamict	Hestur	SWe	63.7351	-19.5169	✓			
JM-147	Columnar rhyolite lobe	Hestur	Msl	63.7383	-19.5183	✓	✓		
JM-148	Rhyolite lava base	Hestur	Msl	63.7383	-19.5183				
JM-149	Fragmented rhyolite matrix	Hestur	Msl	63.7383	-19.5183				
JM-150	Plutonic river boulder	Hestur		63.7419	-19.5124				
JM-151	Basalt lava	Tindfjöll	Emu	63.7672	-19.6071	✓			✓
JM-152	Lapilli tuff	Tindfjöll	Emu	63.7672	-19.6071	✓			
JM-153	Jointed lava	Tindfjalla-jökulsdalur	Lmh	63.7678	-19.6318				
JM-154	Clastogenic lava	Rauðaborg	Lmt	63.7810	-19.6699				
JM-155	Clastogenic lava	Hakaskarð	Lml	63.7858	-19.6511	✓			
JM-156	Jointed lava	Suðurhlíð	Lml	63.7946	-19.6709	✓			
JM-157	Basalt lava	Suðurhlíð	Lmt	63.7937	-19.6918	✓			
JM-158	Basalt lobe	Vörðufell	Lmt	63.7742	-19.7227				
JM-159	Basalt lava	W of Vörðufell	Mml	63.7734	-19.7306	✓			

Sample	Lithology	Location	Strati-graphic code	°N	°E	XRF	EPMA	LA-ICP-MS	Ar/Ar
JM-160	Basalt dyke	Litla-Bláfell	Lmh	63.7766	-19.7434	✓			✓
JM-161	Gabbro nodules	Litla-Bláfell	Lmh	63.7766	-19.7434				
JM-162	Basalt lava	W of Litla-Bláfell	Mml	63.7811	-19.7565	✓			
JM-163	Jointed lava	Þrífjöll	Lmt	63.7959	-19.7528				
JM-164	Basaltic intrusions	Þrífjöll	Lmt	63.7930	-19.7396	✓			✓
JM-165	Platy lava	Miðdalur	Lml	63.7733	-19.6848	✓			✓
JM-166	Jointed lava	Miðdalur	Lml	63.7733	-19.6848	✓			
JM-167	Agglutinate	Búri	Lml	63.7764	-19.6058	✓			
JM-168	Columnar lava	Búraskarð	Emu	63.7793	-19.6172	✓			✓
JM-169	Breccia	Bláfell	Lmt	63.7637	-19.6403				
JM-170	Jointed lava	Tindfjalla-jökulsdalur	Lml	63.7654	-19.6377	✓			
JM-171	Basalt lava	Búri	Lml	63.7718	-19.6200	✓			
JM-172	Platy rhyolite	Hornklofi	Msl	63.7726	-19.6053	✓			
JM-173	Pillow breccia	Vestri-Botná	Lmh	63.7685	-19.5898				
JM-174	Breccia	Vestri-Botná	Lmh	63.7769	-19.5750	✓			
JM-175	Breccia	Vestri-Botná	Lmh	63.7769	-19.5750	✓			
JM-176	Olivine basalt lava	Vestri-Botná	Lml	63.7760	-19.5780	✓			
JM-177	Altered rhyolite breccia	Ýmir	Lsb	63.7868	-19.5686				
JM-178	Columnar rhyolite	Ýmir	Lsb	63.7868	-19.5686				
JM-179	Glassy rhyolite	Ýmir	Lsb	63.7868	-19.5686				
JM-180	Rhyolite breccia	Ýmir	Lsb	63.7858	-19.5644				
JM-181	Agglutinate	Miðdalur	Lml	63.7745	-19.6658	✓			
JM-182	Hyaloclastite	Fljótsdalsheiði	Emu	63.7272	-19.7239	✓			
JM-183	Welded ignimbrite	Vestri-Botná	TI	63.7571	-19.5215				
JM-184	Ash	Vestri-Botná	TI	63.7571	-19.5215		✓	✓	
JM-185	Pumice	Vestri-Botná	TI	63.7571	-19.5215				
JM-186	Rhyolite lava	Ýmir	Lsb	63.7868	-19.5686	✓			✓

Sample	Lithology	Location	Strati-graphic code	°N	°E	XRF	EPMA	LA-ICP-MS	Ar/Ar
JM-187	Dark lava	Ýma	Lsb	63.7851	-19.5558	✓			

A1.3 Samples collected in 2016

Sample	Lithology	Location	Strati-graphic code	°N	°E	XRF	EPMA	LA-ICP-MS	Ar/Ar
JM-201	Basalt lava	Grænafjall	Emu	63.7657	-19.4729	✓			
JM-202	Basalt lava	Grænafjall	Emu	63.7548	-19.4444				
JM-203	Welded ignimbrite	Tröllagjá	TI	63.7151	-19.5149				
JM-204	Diamict	Tröllagjá	SWe	63.7151	-19.5149				
JM-205	Ash	Fífuhvammar	TI	63.7015	-19.5548		✓	✓	
JM-206	Welded ignimbrite	Fífuhvammar	TI	63.7127	-19.5300				
JM-207	Basalt lava	S of Tindur	Emu	63.7269	-19.6102	✓			
JM-208	Rhyolite lava	Valshamarsgil	Msl	63.7245	-19.5096	✓			
JM-209	Diamict	Valshamarsgil	SWe	63.7245	-19.5096	✓			
JM-210	Diamict	Hitagil	SWe	63.7641	-19.5234				
JM-211	Rhyolite breccia	Ýmir	Lsb	63.7858	-19.5644	✓			
JM-212	Jointed intermediate lava	Tindur	Lml	63.7565	-19.5641	✓			
JM-213	Ignimbrite	Botn	TI	63.7538	-19.5473				
JM-214	Ignimbrite	Botn	TI	63.7538	-19.5473				
JM-215	Basement lava	Botn	mb	63.7559	-19.5279	✓			
JM-216	Pumice	Vestri-Botná	TI	63.7565	-19.5219				
JM-217	Welded ignimbrite	Fífuhvammar	TI	63.6966	-19.5860				
JM-218	Obsidian clast in diamict	Fífuhvammar	Msl	63.7015	-19.5548	✓			
JM-219	Ash	Tröllagjá	TI	63.7144	-19.5150		✓	✓	
JM-220	Diamict	Tröllagjá	SWe	63.7144	-19.5150				
JM-221	Diamict	Tröllagjá	SWe	63.7144	-19.5150				
JM-222	Basement lava	Botnöxl	mb	63.7529	-19.5262				

Sample	Lithology	Location	Strati-graphic code	°N	°E	XRF	EPMA	LA-ICP-MS	Ar/Ar
JM-223	Basalt lava	Botnöxl	Emu	63.7510	-19.5338	✓			
JM-224	Porphyritic basalt lava	Botnöxl	Emu	63.7483	-19.5408				
JM-225	Basalt boulder	Eystri-Botná		63.7505	-19.4753				
JM-226	Deep pink ash	Eystri-Botná	TI	63.7584	-19.5063				
JM-227	Pale pink ash	Eystri-Botná	TI	63.7584	-19.5063				
JM-228	Buff ash	Eystri-Botná	TI	63.7584	-19.5063		✓	✓	
JM-229	Ash	Hestur	TI	63.7364	-19.5156				
JM-230	Incipiently welded ignimbrite	Hestur	TI	63.7364	-19.5156				
JM-231	Diamict	Hestur	SWe	63.7364	-19.5156	✓			
JM-232	Pumice in reworked ignimbrite	Þröngá	TI	63.7022	-19.4799				
JM-233	Altered lithics in ignimbrite	Þröngá	TI	63.7035	-19.4787				
JM-234	Fiamme	Þröngá	TI	63.7035	-19.4787				
JM-235	Dark pumice	Þröngá	TI	63.7105	-19.4565				
JM-236	Pumice	Steinholts-dalur	TI	63.6731	-19.5876				
JM-237	Fiamme	Steinholts-dalur	TI	63.6731	-19.5876				
JM-238	Basal ash	Vestri-Botná	TI	63.7565	-19.5219				
JM-239	Welded ignimbrite	Vestri-Botná	TI	63.7578	-19.5229				
JM-240	Columnar rhyolite	Botn	Lsb	63.7620	-19.5524				
JM-241	Diamict	Botn	SWe	63.7538	-19.5473	✓			
JM-242	Porphyritic basalt clasts in diamict	Botn	SWe	63.7538	-19.5473				
JM-243	Rhyolite lava	Kirkjufell	Torf RFR	63.9913	-18.9331				
JM-244	Rhyolite lava	Kirkjufell	Torf RFR	63.9913	-18.9331				
JM-245	Rhyolite lava	Rauðfossafjöll	Torf RFR	64.0266	-19.3956				
JM-246	Rhyolite lava	Rauðfossafjöll	Torf RFR	64.0266	-19.3956				
JM-247	Rhyolite lava	Rauðfossafjöll	Torf RFR	63.9830	-19.4467				✓
JM-248	Rhyolite lava	Laufafell	Torf RFR	63.9332	-19.3785				

Sample	Lithology	Location	Strati-graphic code	°N	°E	XRF	EPMA	LA-ICP-MS	Ar/Ar
JM-249	Rhyolite lava	Laufafell	Torf RFR	63.9332	-19.3785				
JM-250	Rhyolite lava	Laufafell	Torf RFR	63.9030	-19.3479				✓
JM-251	Rhyolite lava	Laufafell	Torf RFR	63.9030	-19.3479				
JM-252	Fiamme (1)	Langidalur	TI	63.6846	-19.5076		✓	✓	✓
JM-253	Fiamme (2)	Langidalur	TI	63.6846	-19.5076		✓	✓	
JM-254	Diamict	Botn	SWe	63.7538	-19.5473	✓			
JM-255	Diamict	Vestri-Botná	SWe	63.7565	-19.5219	✓			

A2.1 Major element oxides (wt%)

All volcanic samples are lava (intrusive or extrusive) except where indicated.

Sample	Session		SiO_2	TiO_2	Al_2O_3	Fe_2O_3	MnO	MgO	CaO	Na_2O	K_2O	P_2O_5	SO_3	LOI	Total
Mafic basement															
JM-54	1		47.92	3.008	17.43	12.49	0.153	3.75	10.96	2.90	0.586	0.320	<0.002	0.70	100.23
JM-55	1		47.14	2.774	17.89	11.54	0.218	3.76	11.17	2.55	0.314	0.283	<0.002	2.42	100.06
JM-117	2		53.91	2.323	13.95	13.29	0.200	2.77	6.19	3.33	1.255	0.543	0.179	2.44	100.20
JM-215	3		43.66	3.42	13.33	14.96	0.19	5.27	10.61	2.22	0.41	0.37	0.042	5.11	99.58
Group 1															
JM-18	1		46.30	3.918	14.05	15.81	0.212	5.39	10.56	2.99	0.468	0.412	<0.003	-0.80	99.30
JM-31	1		46.60	3.018	14.95	14.02	0.184	7.07	11.02	2.59	0.420	0.335	<0.002	-0.04	100.17
JM-32	1		45.78	3.445	14.73	15.35	0.206	6.37	10.35	2.94	0.536	0.431	<0.002	-0.70	99.44
JM-33	2		45.90	3.479	14.69	16.10	0.222	6.48	10.46	3.04	0.523	0.431	<0.003	-0.49	100.84
JM-47	1	Hyaloclastite	55.95	2.533	12.98	11.38	0.160	4.55	8.55	2.66	0.728	0.303	0.125	0.11	100.03
JM-50	1	Hyaloclastite	51.15	2.616	15.16	12.53	0.184	4.32	9.60	3.00	0.712	0.345	0.089	0.39	100.09
JM-51	1	Hyaloclastite	51.06	2.443	14.98	12.87	0.197	4.50	9.59	2.98	0.677	0.313	0.081	0.46	100.15
JM-101	2		46.62	2.997	14.20	14.17	0.211	4.52	10.10	3.10	0.823	0.459	0.102	3.30	100.50
JM-108	2		46.73	4.104	13.53	16.20	0.325	4.45	9.07	2.97	0.843	0.668	0.343	1.12	100.03
JM-122	2		46.22	3.678	15.45	15.71	0.205	6.13	9.73	3.06	0.638	0.461	<0.003	-0.86	100.42
JM-126	2		46.43	2.762	14.32	14.55	0.201	7.51	11.05	2.57	0.428	0.317	<0.003	-0.07	100.06
JM-128	2		47.06	2.712	14.36	14.25	0.198	8.01	11.03	2.63	0.453	0.327	<0.003	-0.61	100.42
JM-135	2		47.86	3.289	15.25	14.82	0.210	5.03	10.06	3.17	0.698	0.395	0.039	-0.34	100.45
JM-137	2		47.70	2.710	14.51	14.00	0.197	7.31	10.97	2.68	0.521	0.314	0.029	-0.16	100.76
JM-140	2		44.99	4.339	14.71	17.44	0.227	6.00	9.43	3.13	0.623	0.506	<0.003	-0.72	100.67

Sample	Session		SiO_2	TiO_2	Al_2O_3	Fe_2O_3	MnO	MgO	CaO	Na_2O	K_2O	P_2O_5	SO_3	LOI	Total
JM-152	2	Hyaloclastite	42.21	3.410	13.15	14.69	0.205	4.64	9.65	2.23	0.370	0.378	0.063	9.77	100.77
JM-155	2		46.97	2.991	15.42	14.94	0.209	6.04	10.81	2.73	0.555	0.353	<0.003	-0.13	100.88
JM-156	2		46.04	3.355	14.93	15.87	0.218	6.66	10.69	2.90	0.485	0.396	0.012	-0.92	100.62
JM-157	2		46.04	3.635	14.95	15.94	0.225	6.22	10.13	3.16	0.594	0.549	0.014	-0.79	100.67
JM-159	2		47.44	3.367	15.47	15.29	0.210	5.08	10.79	3.05	0.544	0.338	<0.003	-0.76	100.82
JM-160	2		46.10	3.082	14.78	14.80	0.196	7.45	11.58	2.51	0.400	0.312	0.070	-0.65	100.57
JM-162	2		45.30	4.034	15.21	16.76	0.219	5.88	9.55	3.18	0.632	0.450	<0.003	-0.39	100.82
JM-164	2		47.79	2.405	14.80	14.23	0.198	7.78	10.74	2.67	0.440	0.261	0.005	-0.47	100.85
JM-165	2		45.25	3.832	15.02	16.29	0.206	6.79	10.25	2.85	0.566	0.408	<0.003	-0.91	100.56
JM-166	2		47.13	2.797	15.23	14.64	0.207	6.66	11.23	2.81	0.407	0.308	0.009	-0.69	100.73
JM-167	2		47.12	3.612	14.73	15.34	0.217	5.70	9.30	3.18	0.709	0.495	<0.003	0.20	100.60
JM-170	2		46.95	2.610	14.91	14.04	0.197	7.73	11.63	2.54	0.359	0.280	<0.003	-0.56	100.70
JM-171	2		46.88	3.678	14.69	15.48	0.213	5.70	9.42	3.30	0.728	0.520	<0.003	-0.22	100.38
JM-174	2	Hyaloclastite	45.77	2.746	15.48	12.65	0.191	4.17	9.40	2.37	1.085	0.342	0.262	7.00	101.47
JM-175	2	Hyaloclastite	48.08	3.035	14.59	12.05	0.239	3.97	10.83	3.30	0.197	0.315	0.093	3.68	100.37
JM-176	2		46.79	2.292	13.21	14.05	0.191	10.89	10.35	2.48	0.468	0.302	<0.003	-0.44	100.57
JM-181	2		47.83	2.991	14.95	15.42	0.220	5.89	10.36	3.11	0.509	0.362	<0.003	-0.55	101.09
JM-182	2		46.76	3.233	14.17	15.12	0.208	6.14	11.64	2.55	0.457	0.327	0.008	0.10	100.71
JM-207	3		45.40	4.20	12.93	16.92	0.28	4.74	9.77	3.06	0.59	0.72	<0.002	-0.08	98.53
JM-223	3		49.89	3.25	13.91	14.30	0.23	4.24	8.25	3.09	0.90	0.48	0.014	0.59	99.15
Gabbro nodules															
JM-26	1		46.25	0.678	20.84	8.24	0.101	10.98	11.48	1.82	0.108	0.062	0.013	0.18	100.76
JM-27	1		48.85	0.682	15.74	6.87	0.102	10.52	16.08	1.33	0.086	0.015	<0.002	0.25	100.53

Sample	Session		SiO_2	TiO_2	Al_2O_3	Fe_2O_3	MnO	MgO	CaO	Na_2O	K_2O	P_2O_5	SO_3	LOI	Total
Group 2															
JM-34	1		49.98	2.866	13.43	15.18	0.311	3.45	7.73	4.21	1.021	1.436	0.117	-0.66	99.08
JM-35	1		51.11	3.017	13.14	14.91	0.294	3.57	7.41	4.13	1.032	1.381	<0.002	-0.25	99.74
JM-39	1		52.44	2.564	13.68	14.58	0.320	2.80	6.57	4.88	1.011	1.161	0.010	-0.29	99.73
JM-141	2		55.68	1.824	14.07	14.10	0.344	1.95	5.68	5.27	1.244	0.708	<0.003	-0.40	100.46
JM-151	2		49.51	3.181	12.85	16.87	0.345	3.69	7.97	3.97	0.910	1.367	0.084	-0.01	100.65
JM-168	3		48.08	3.37	12.73	15.30	0.28	3.73	8.21	3.73	0.95	1.47	0.144	0.76	98.77
JM-201	3		53.86	2.41	14.08	13.57	0.31	2.72	6.56	4.54	1.26	1.08	0.063	0.02	100.46
JM-212	3		59.05	1.34	13.88	12.40	0.35	1.15	4.87	5.03	1.54	0.47	0.065	0.58	100.72
Group 3															
JM-10	1	Scoria	55.35	2.182	14.75	10.35	0.155	4.53	7.64	3.19	1.523	0.304	0.007	0.19	100.17
JM-13	1		55.17	2.190	14.74	10.37	0.155	4.69	7.80	3.42	1.510	0.298	<0.003	-0.15	100.18
JM-14	1		55.10	2.184	14.72	10.38	0.153	4.74	7.88	3.41	1.497	0.297	<0.003	-0.14	100.22
JM-15	1		55.43	2.143	14.68	10.24	0.152	4.68	7.75	3.42	1.550	0.291	<0.003	-0.33	100.00
JM-20	1		52.47	2.690	14.68	11.97	0.175	4.95	8.19	3.43	1.228	0.376	0.007	-0.32	99.85
JM-21	1	Scoria	51.77	2.790	14.79	12.34	0.178	5.18	8.48	3.34	1.151	0.387	0.013	-0.49	99.93
JM-22	1		51.46	2.825	14.72	12.50	0.180	5.12	8.56	3.37	1.121	0.403	<0.002	-0.32	99.94
JM-52	1		51.43	2.355	15.45	11.32	0.165	4.92	9.15	3.32	1.133	0.288	0.010	0.81	100.35
JM-113	2		51.93	2.378	15.40	11.87	0.175	4.81	8.96	3.33	1.167	0.289	0.013	0.11	100.42
JM-142	2		51.10	2.594	14.77	12.53	0.184	5.56	9.15	3.21	1.021	0.349	<0.003	-0.07	100.40
Group 4(a)															
JM-2	1		72.72	0.246	13.16	3.72	0.105	0.03	0.69	6.23	3.488	0.012	<0.003	0.17	100.58
JM-4	1		73.86	0.235	12.29	3.77	0.081	0.00	0.40	5.81	3.637	0.006	<0.003	0.11	100.20
JM-36	1		73.23	0.315	12.38	4.29	0.138	-0.01	0.62	5.89	3.295	0.012	<0.003	0.19	100.35
JM-37	1		72.74	0.305	12.19	4.21	0.132	0.00	0.70	6.13	3.320	0.012	<0.003	0.26	100.01

Sample	Session		SiO_2	TiO_2	Al_2O_3	Fe_2O_3	MnO	MgO	CaO	Na_2O	K_2O	P_2O_5	SO_3	LOI	Total
JM-38	1		73.03	0.325	12.53	4.42	0.145	-0.01	0.53	5.92	3.355	0.014	<0.003	0.09	100.35
JM-79	1		73.46	0.241	12.34	3.85	0.102	0.02	0.29	5.83	3.587	0.008	<0.003	0.16	99.89
JM-80	1		73.36	0.233	12.11	3.75	0.100	0.00	0.44	6.13	3.607	0.008	<0.003	0.30	100.04
JM-81	1		73.74	0.234	12.30	3.75	0.090	0.00	0.30	5.90	3.637	0.009	<0.003	0.21	100.17
JM-84	1		73.26	0.250	12.34	3.84	0.100	0.07	0.45	6.07	3.540	0.014	<0.003	0.16	100.09
JM-85	1		72.82	0.231	12.11	3.74	0.099	0.03	0.44	6.11	3.636	0.007	<0.003	0.26	99.48
JM-124	2		72.18	0.234	12.78	3.32	0.077	0.04	0.59	6.12	3.384	0.010	0.081	0.17	98.91
JM-134	2		71.78	0.262	12.93	4.20	0.092	0.10	0.72	5.45	3.235	0.017	0.120	0.85	99.75
JM-172	2		69.11	0.420	13.08	6.16	0.221	0.07	1.55	6.22	2.822	0.036	0.020	-0.08	99.63
JM-145	3		72.27	0.27	13.27	4.01	0.14	0.09	1.03	5.45	3.26	0.02	0.024	1.25	101.11
JM-147	3		71.40	0.26	12.93	3.84	0.14	0.06	1.08	5.34	3.33	0.02	<0.002	2.42	100.81
JM-208	3		74.21	0.27	13.57	3.01	0.13	0.05	1.02	5.70	3.41	0.03	<0.002	0.19	101.58
JM-218	3		72.64	0.30	13.22	4.14	0.15	0.05	1.02	5.64	3.88	0.02	<0.002	0.22	101.29
Group 4(b)															
JM-103	2		65.64	0.478	12.69	6.21	0.221	0.18	2.53	5.06	1.922	0.060	0.101	3.99	98.98
JM-111	2	Hyaloclastite	68.95	0.981	11.72	6.86	0.007	0.08	0.11	5.04	2.496	0.025	0.038	4.31	100.57
JM-114	2		72.05	0.314	13.14	4.66	0.063	0.13	0.33	5.07	3.487	0.019	0.023	0.74	100.01
JM-130	2		69.18	0.404	13.17	4.66	0.162	0.16	1.35	4.89	3.324	0.051	0.019	2.84	100.20
JM-186	2		75.17	0.247	11.88	2.63	0.035	0.10	0.08	4.46	3.854	0.021	0.038	1.31	99.82
JM-187	2		68.53	0.456	13.41	5.95	0.199	0.23	1.76	5.87	2.821	0.055	0.024	0.42	99.72
JM-211	3		76.59	0.32	12.65	1.89	0.04	0.00	0.14	5.78	3.47	0.02	0.244	0.39	101.55
Sultarfell rhyolite															
JM-5	1	Pumiceous	75.55	0.126	13.10	1.48	0.049	0.04	0.81	4.42	4.018	0.013	<0.003	0.31	99.92
JM-76	1	Pumiceous	75.22	0.125	12.98	1.59	0.052	0.05	0.77	4.29	4.139	0.013	<0.003	0.22	99.45

Sample	Session	SiO_2	TiO_2	Al_2O_3	Fe_2O_3	MnO	MgO	CaO	Na_2O	K_2O	P_2O_5	SO_3	LOI	Total
Sediments														
JM-1	1	47.83	3.679	13.43	15.37	0.222	4.07	6.94	1.89	0.632	0.545	0.157	5.25	100.01
JM-49	1	53.66	2.156	13.71	11.16	0.175	3.93	5.50	2.53	1.358	0.441	0.490	5.02	100.12
JM-56	1	58.92	1.952	13.11	10.58	0.198	2.10	4.41	3.72	1.790	0.434	0.311	2.62	100.15
JM-106	2	63.55	1.128	12.79	7.57	0.216	1.11	3.54	3.76	2.087	0.164	0.638	3.88	99.80
JM-146	2	54.27	2.321	13.29	11.10	0.188	2.94	6.28	2.74	1.263	0.397	0.662	4.68	99.46
JM-209	3	45.61	3.11	13.97	13.73	0.19	5.42	8.73	2.16	0.56	0.42	0.139	4.56	98.60
JM-231	3	44.07	2.69	13.47	13.29	0.18	6.57	10.98	1.85	0.49	0.34	0.087	6.41	100.44
JM-241	3	48.58	2.96	14.16	13.17	0.26	4.54	7.45	3.12	1.15	0.43	0.022	2.28	98.13
JM-254	3	45.62	3.64	15.42	14.79	0.20	4.85	9.44	2.82	0.64	0.47	0.017	1.86	99.76
JM-255	3	59.59	1.79	13.22	9.80	0.14	2.09	4.08	2.78	1.46	0.33	1.012	4.40	100.69

A2.2 Trace elements (ppm)

Sample	Ba	Ce	Co	Cu	Ga	La	Mo	Nb	Nd	Pb	Rb	Sc	Sr	Th	U	V	Y	Zn	Zr
Mafic basement																			
JM-54	140.5	53.1	38.6	170.5	25.9	21.1	2.6	26.9	30.5	2.4	11.1	27.5	446.8	2.7	1.9	306.0	32.7	90.6	203.2
JM-55	100.7	49.8	38.5	175.3	23.8	20.5	2.0	23.7	28.8	1.7	4.8	32.3	435.3	2.2	0.7	367.4	27.6	98.6	169.6
JM-117	291.2	101.5	32.5	113.5	24.3	41.8	3.5	44.8	52.8	4.3	31.4	23.5	330.6	6.2	2.3	184.8	54.6	124.3	402.8
JM-215	105.4	57.8	49.6	146.2	22.8	21.2	2.9	28.1	32.5	1.8	8.6	37.0	360.1	2.3	1.7	418.3	34.7	98.5	207.0
Group 1																			
JM-18	134.1	52.3	51.2	124.8	24.2	20.1	2.7	27.3	32.5	1.2	8.2	36.6	441.2	1.6	0.7	424.1	35.5	118.8	187.2
JM-31	101.9	51.6	53.5	144.1	22.8	16.6	2.5	25.5	32.1	1.4	8.3	34.5	401.1	1.2	1.4	334.5	33.1	107.5	200.4
JM-32	129.0	57.2	50.2	177.6	24.3	19.8	2.8	32.0	36.3	1.4	9.4	35.1	399.9	2.0	0.8	370.2	37.2	112.9	212.0
JM-33	137.1	60.4	50.7	106.8	22.9	21.7	2.6	33.5	36.3	2.4	9.7	35.7	405.2	1.2	0.8	386.5	38.1	126.7	220.7
JM-47	142.3	55.6	42.0	140.5	20.6	22.1	3.0	29.3	31.6	2.3	16.3	29.2	313.1	2.1	1.1	287.5	33.8	104.4	227.8
JM-50	159.1	59.6	46.8	148.9	23.2	25.3	2.7	28.9	31.7	2.4	15.3	31.7	324.0	2.8	0.8	313.8	39.1	117.2	245.4
JM-51	153.6	56.8	46.3	155.8	22.1	24.8	2.8	27.6	31.3	1.8	14.8	30.6	310.0	1.8	0.5	297.7	38.1	114.0	238.5
JM-101	199.9	75.8	45.5	111.5	23.1	31.9	3.8	40.2	40.3	2.5	17.0	29.7	406.0	3.4	0.8	318.2	42.9	125.1	284.2
JM-108	281.1	83.0	43.6	16.3	23.6	32.9	4.6	44.7	49.5	2.5	16.4	31.2	427.8	3.0	1.6	338.7	50.6	142.9	301.0
JM-122	174.2	63.0	50.5	75.3	27.3	25.4	3.0	32.1	38.1	2.6	11.1	29.4	541.2	3.2	1.4	344.6	36.2	108.8	223.3
JM-126	110.5	45.7	57.7	125.5	22.4	20.1	2.4	25.4	25.2	2.1	8.6	34.0	371.9	1.7	1.1	320.2	31.7	103.3	175.3
JM-128	110.7	49.8	49.0	122.1	21.8	18.2	2.2	25.9	27.3	1.4	8.6	29.8	377.4	1.5	<0.5	288.4	33.4	98.2	191.9
JM-135	176.9	69.9	44.0	120.1	26.2	26.4	3.1	34.5	36.2	2.2	13.6	29.9	407.4	2.6	1.2	363.7	40.3	122.2	267.5
JM-137	121.2	47.7	49.5	116.4	21.8	19.2	2.7	25.9	26.8	1.5	10.9	32.5	347.9	1.7	0.7	325.3	33.0	106.6	205.0
JM-140	175.7	66.6	52.1	75.3	25.8	21.4	2.5	34.9	33.0	1.6	10.2	33.2	536.9	1.9	0.7	414.6	38.1	132.8	226.3
JM-152	128.1	51.6	43.2	90.5	19.8	18.4	1.8	23.5	30.7	2.1	8.1	35.3	457.1	1.2	0.8	277.7	29.5	108.4	158.5
JM-155	162.2	57.3	48.6	115.2	23.3	22.1	2.5	27.8	33.7	3.0	11.4	34.5	420.7	2.2	1.5	338.3	36.0	100.3	209.2
JM-156	126.0	60.4	50.7	130.4	24.8	19.5	2.5	31.4	30.8	2.6	8.9	36.8	408.0	1.7	1.2	385.2	37.1	124.4	204.1
JM-157	162.8	71.4	48.5	88.2	24.1	26.6	2.7	41.1	40.7	2.2	11.0	34.3	434.0	1.8	0.8	350.2	42.9	121.2	250.4
JM-159	166.5	60.0	42.6	130.2	25.5	23.7	2.7	27.3	34.0	2.8	10.0	32.1	438.9	2.4	0.9	352.1	36.0	95.6	195.4
JM-160	88.6	44.7	54.3	140.4	21.4	14.6	2.6	23.0	25.6	1.3	7.2	36.5	378.0	1.3	1.1	364.7	31.0	111.2	178.4

Sample	Ba	Ce	Co	Cu	Ga	La	Mo	Nb	Nd	Pb	Rb	Sc	Sr	Th	U	V	Y	Zn	Zr
JM-162	171.3	72.9	47.8	75.9	24.2	26.7	2.5	33.0	35.2	2.7	11.0	28.5	551.7	2.2	0.8	372.2	37.9	113.1	226.3
JM-164	108.2	47.2	54.0	121.7	20.5	16.0	2.8	22.2	23.7	1.9	9.5	36.6	302.0	1.7	0.7	316.5	32.0	107.0	182.6
JM-165	147.8	62.8	52.0	77.3	24.6	19.3	2.3	29.2	33.7	2.7	10.7	29.4	524.3	2.2	1.2	365.0	33.1	112.8	209.7
JM-166	109.0	47.1	49.3	114.3	23.8	17.8	2.5	24.5	25.5	2.4	7.8	33.7	340.5	1.5	1.3	332.0	34.2	105.2	195.5
JM-167	185.8	69.4	46.8	70.5	25.3	25.6	2.9	38.0	38.5	2.0	14.2	32.4	426.0	2.6	1.7	343.1	42.4	125.7	298.4
JM-170	97.6	47.0	49.3	113.2	20.1	16.2	2.3	21.5	28.7	1.3	6.7	35.4	327.6	0.8	0.9	334.0	30.5	100.0	172.1
JM-171	175.3	75.0	44.5	78.0	25.2	26.5	2.8	38.4	42.8	2.4	13.9	30.7	429.3	2.3	1.3	359.3	43.5	124.0	298.7
JM-174	237.8	57.2	52.3	90.8	21.5	20.6	2.0	27.0	31.6	1.0	24.8	31.9	376.9	1.9	1.0	371.1	32.5	105.2	202.8
JM-175	66.9	48.8	48.6	113.1	22.4	17.0	2.4	25.2	26.6	1.6	2.2	33.8	363.5	1.1	0.9	405.9	32.0	107.4	182.8
JM-176	121.4	46.7	58.1	102.0	20.5	20.8	2.4	24.4	24.2	2.1	8.4	33.9	328.4	1.3	0.6	280.4	30.7	101.7	197.6
JM-181	124.7	58.5	46.4	87.7	23.8	20.7	2.5	27.7	29.4	2.9	10.2	32.2	338.2	1.6	1.3	356.7	39.5	116.3	228.1
JM-182	132.5	53.5	51.5	134.9	23.2	20.2	2.7	26.1	27.4	2.0	8.7	34.2	406.4	1.6	1.1	408.7	31.5	112.3	181.7
JM-207	181.6	75.8	45.1	155.6	26.1	26.6	2.8	35.7	44.1	1.2	9.6	31.4	483.1	2.2	1.2	330.3	47.9	123.2	241.7
JM-223	235.0	77.3	45.2	75.3	23.9	31.0	3.2	41.0	45.7	2.6	12.3	30.6	338.5	3.8	1.4	308.7	51.8	124.2	345.0
Gabbro nodules																			
JM-26	23.0	13.5	60.3	86.6	16.5	4.0	1.4	4.5	8.2	<0.7	1.6	18.4	419.4	<0.6	<0.5	88.5	6.7	51.0	34.2
JM-27	26.5	6.5	44.1	98.6	16.1	3.1	1.5	2.1	7.2	1.2	2.0	48.8	333.1	<0.6	<0.5	145.7	10.4	37.4	24.1
Group 2																			
JM-34	267.6	129.3	25.9	56.0	28.8	49.1	3.6	57.0	78.4	1.9	19.2	22.9	545.1	2.9	0.6	100.9	72.9	170.0	399.7
JM-35	272.6	128.4	24.6	56.5	28.5	46.5	3.5	56.7	75.7	2.9	24.7	23.4	484.8	4.3	1.5	124.4	77.6	164.6	415.5
JM-39	377.7	130.0	22.0	56.1	30.7	49.9	3.8	58.0	76.0	3.0	14.0	21.4	518.4	3.9	1.6	94.6	68.6	169.7	431.0
JM-141	358.0	129.4	12.3	5.2	32.1	53.7	3.9	63.1	74.6	3.2	23.6	19.4	492.5	4.7	1.8	11.6	78.2	189.9	473.1
JM-151	250.8	114.8	24.9	14.7	27.1	45.5	3.5	49.2	70.1	2.9	18.7	28.4	472.4	3.5	2.2	112.9	72.4	173.5	343.3
JM-168	260.2	114.7	30.0	13.7	27.8	45.1	4.0	52.9	70.5	2.5	19.8	23.7	479.7	4.7	2.3	175.2	72.4	159.2	369.3
JM-201	350.5	129.1	14.9	5.5	32.1	52.2	3.9	59.9	74.5	2.4	25.1	17.3	499.8	4.7	1.9	42.7	73.0	152.2	439.7
JM-212	441.7	140.1	10.0	7.7	32.5	60.5	5.7	72.5	77.0	4.1	33.6	14.1	406.3	5.4	2.4	2.9	81.9	192.4	1048.6

Sample	Ba	Ce	Co	Cu	Ga	La	Mo	Nb	Nd	Pb	Rb	Sc	Sr	Th	U	V	Y	Zn	Zr
Group 3																			
JM-10	290.5	83.6	36.9	124.8	23.6	34.4	3.5	39.0	43.2	3.4	36.9	24.1	296.7	6.0	2.3	235.0	43.2	105.9	294.2
JM-13	295.1	81.6	37.6	117.1	23.3	34.4	3.3	37.3	41.3	4.0	36.8	24.1	305.7	5.5	0.9	212.9	42.4	96.4	291.1
JM-14	290.8	77.4	39.0	118.0	23.5	33.0	3.6	36.7	38.2	3.4	36.2	23.7	302.3	5.7	2.0	223.0	42.2	97.5	279.3
JM-15	296.9	77.6	37.7	110.5	23.3	34.7	3.4	36.7	40.8	3.6	37.2	22.8	297.1	5.5	0.8	216.8	42.1	97.1	275.7
JM-20	241.0	75.5	41.6	122.1	24.3	29.6	3.2	36.5	38.1	3.2	28.2	27.2	363.4	4.6	1.4	274.7	42.7	113.6	279.7
JM-21	216.8	73.4	42.5	125.2	24.8	28.8	3.3	35.9	38.2	3.3	26.6	29.0	368.8	4.3	1.9	294.0	41.7	121.0	271.9
JM-22	228.9	73.8	42.4	120.7	24.3	30.7	3.1	35.0	40.4	3.6	25.4	26.6	380.0	4.5	1.5	260.8	42.1	108.9	273.3
JM-52	236.1	74.0	38.7	138.7	25.5	33.0	3.4	35.0	37.2	2.3	24.5	23.6	354.9	4.5	2.1	251.2	40.4	101.1	333.4
JM-113	241.7	76.7	37.9	92.2	23.7	30.6	3.4	36.4	41.0	3.1	25.3	26.3	337.6	3.6	1.2	262.9	40.0	105.3	341.3
JM-142	214.5	71.3	45.2	84.6	23.7	27.5	3.1	34.4	36.5	3.7	23.0	28.7	338.0	3.4	1.4	280.4	40.3	108.9	280.3
Group 4(a)																			
JM-2	627.8	237.9	2.8	45.2	38.7	112.2	4.1	140.3	121.5	7.7	72.4	<1.0	71.4	12.3	2.9	3.1	130.6	191.1	1034.2
JM-4	469.1	197.8	3.3	45.5	41.6	141.0	2.2	145.9	152.0	7.5	65.2	1.5	16.1	13.2	1.9	2.0	141.1	212.9	1174.2
JM-36	584.2	250.2	3.1	46.2	38.5	101.1	3.3	151.3	116.7	8.2	61.6	1.1	57.3	13.3	2.7	2.2	133.0	223.4	1303.8
JM-37	593.7	251.7	3.0	45.6	36.5	110.3	7.8	150.3	122.2	8.3	76.9	1.8	53.9	12.9	3.7	<0.8	141.9	239.0	1292.7
JM-38	607.6	241.1	1.8	46.2	39.6	98.3	4.4	149.5	113.8	8.5	75.4	2.1	54.7	12.7	3.0	2.0	116.2	216.5	1299.2
JM-79	523.6	270.8	2.4	45.8	40.8	128.6	2.6	138.7	140.9	9.2	65.3	1.3	15.4	13.4	2.8	2.9	130.6	201.6	1083.5
JM-80	576.0	266.5	2.9	46.2	41.0	115.6	8.1	156.0	128.1	9.9	83.0	<1.0	17.9	14.0	4.2	1.8	145.9	249.3	1243.7
JM-81	501.4	292.2	1.8	45.4	42.1	133.5	2.2	150.9	147.8	9.0	79.5	1.0	13.0	13.8	3.7	2.5	133.7	185.6	1193.4
JM-84	603.2	234.9	1.3	46.8	40.4	128.2	4.9	154.8	131.4	8.5	77.5	1.6	20.5	13.3	5.0	2.5	158.0	254.2	1231.4
JM-85	570.1	261.6	2.0	45.7	39.5	113.7	7.8	154.9	128.2	9.5	83.3	1.1	18.1	14.1	4.8	1.4	145.1	247.7	1234.4
JM-124	610.3	246.2	3.1	0.5	38.3	112.0	2.1	133.1	119.3	8.4	68.2	<1.0	55.1	12.7	2.0	1.5	133.6	160.7	921.9
JM-134	703.1	217.0	3.9	2.9	31.5	96.5	3.3	134.7	101.8	6.6	77.4	2.5	98.2	12.4	3.0	2.7	114.9	152.9	911.7
JM-172	635.8	185.1	3.9	<0.5	36.5	79.1	2.3	122.4	93.8	6.3	59.8	2.5	143.4	9.6	2.4	4.2	110.5	176.0	1052.8
JM-145	684.2	220.4	3.8	2.9	31.3	101.7	4.8	133.8	107.2	7.7	68.5	2.6	103.1	12.3	3.7	1.7	117.0	170.0	965.6
JM-147	667.4	221.8	3.9	2.8	30.0	99.4	6.2	133.3	106.5	7.2	74.5	4.0	91.2	12.2	3.8	1.4	115.9	168.5	906.3
JM-208	714.3	229.7	1.7	2.5	31.8	99.2	3.9	126.9	109.1	8.8	77.0	3.7	100.4	13.1	3.6	2.1	110.2	132.7	844.9
JM-218	819.0	217.2	<1.2	1.5	31.2	99.2	7.8	128.1	103.7	8.4	91.1	2.5	81.5	12.9	3.7	<0.9	103.0	170.5	1032.2

Sample	Ba	Ce	Co	Cu	Ga	La	Mo	Nb	Nd	Pb	Rb	Sc	Sr	Th	U	V	Y	Zn	Zr
Group 4(b)																			
JM-103	611.2	193.6	3.5	2.2	31.7	87.0	5.1	114.5	95.5	5.9	79.9	3.5	193.0	9.6	3.6	5.3	105.6	175.4	925.7
JM-111	626.9	92.8	8.6	11.5	37.4	38.0	4.1	78.3	46.3	5.2	60.0	7.5	125.9	6.6	1.6	46.1	59.1	20.2	599.6
JM-114	668.4	216.9	3.1	2.6	34.8	95.0	2.5	140.2	102.6	6.8	78.6	1.9	108.3	11.8	2.8	2.7	117.0	154.6	1087.8
JM-130	631.7	214.9	4.9	3.3	30.0	92.7	5.5	119.8	109.6	6.8	72.1	4.0	138.9	10.8	3.7	7.4	111.4	181.3	958.3
JM-186	364.9	200.4	<1.1	8.2	35.2	83.2	6.7	148.9	93.3	8.5	91.7	2.5	11.8	14.2	4.3	9.3	112.1	192.2	1176.9
JM-187	616.1	201.2	3.7	2.4	34.1	88.3	6.0	123.8	103.1	6.8	59.4	3.9	162.1	10.1	2.6	3.8	110.9	185.9	1054.7
JM-211	573.5	117.1	<1.2	<0.5	36.7	42.9	1.7	148.6	60.4	5.9	74.0	<1.2	46.3	12.7	3.0	3.6	130.5	69.5	1296.4
Sultarfell rhyolite																			
JM-5	618.9	103.8	<1.1	45.7	19.1	50.1	3.2	52.0	49.9	7.9	97.6	3.7	60.3	13.0	3.3	3.0	54.2	54.9	226.0
JM-76	613.4	100.0	<1.1	45.8	18.7	48.9	3.6	53.6	45.5	7.9	103.6	3.7	55.1	13.2	3.6	2.5	55.4	53.1	216.3
Sediments																			
JM-1	178.7	78.7	46.1	140.0	23.2	27.8	2.4	37.4	43.2	2.5	19.0	35.5	348.9	2.6	1.3	324.5	42.3	134.5	270.9
JM-49	318.9	103.6	32.5	101.5	24.4	42.4	2.6	57.2	55.1	2.9	29.3	24.6	314.3	4.1	1.7	179.7	57.5	139.2	447.8
JM-56	394.5	144.3	21.5	71.7	29.4	61.1	3.1	77.9	75.3	4.0	40.0	17.6	296.0	6.1	2.1	132.5	77.6	169.6	590.5
JM-106	526.2	140.6	11.5	21.2	26.6	63.6	3.6	86.7	72.0	4.3	44.1	11.8	217.7	6.9	2.2	88.6	80.2	143.4	688.2
JM-146	326.7	102.6	30.5	53.5	23.6	43.3	2.7	56.5	54.1	3.3	27.9	22.6	311.6	4.4	2.3	225.7	55.8	132.6	439.8
JM-209	141.5	62.1	42.8	83.0	27.4	22.7	2.4	28.3	34.7	1.9	11.4	30.7	397.6	2.0	1.4	288.8	34.8	112.4	216.7
JM-231	125.5	55.6	52.0	104.0	18.7	22.7	1.5	26.7	31.5	2.7	10.5	34.5	403.0	1.2	0.9	334.3	31.4	111.5	194.2
JM-241	312.8	102.3	36.0	48.7	26.0	40.1	3.0	52.4	54.3	3.3	24.6	22.9	422.9	4.0	1.3	200.1	53.1	137.4	385.9
JM-254	169.5	67.9	44.6	63.0	23.2	25.2	2.8	34.6	37.6	1.8	12.7	26.5	507.5	2.2	1.5	294.8	38.8	117.5	251.6
JM-255	371.8	111.6	25.3	47.0	24.0	49.6	3.0	64.6	57.8	3.7	35.4	20.4	238.3	5.9	2.1	179.4	64.7	135.8	530.8

A2.3 BCR-1 reference material data

Trace element data (ppm) from multiple analyses of BCR-1. The sessions during which Tindfjallajökull samples were analysed are in bold.

Date	Run No(s)	Ba	Ce	Co	Cu	Ga	La	Mo	Nb	Nd	Pb	Rb	Sc	Sr	Th	U	V	Y	Zn	Zr
Mar-15	**900-902 (Session 1)**	**733.0**	**61.3**	**38.1**	**84.0**	**22.6**	**27.6**	**2.1**	**12.5**	**29.2**	**14.6**	**49.1**	**30.5**	**331.6**	**6.3**	**1.9**	**383.9**	**39.1**	**124.0**	**198.1**
Aug-15	957-959	713.4	55.5	34.5	40.1	22.7	24.7	2.1	12.5	29.6	15.4	49.3	31.0	332.2	6.1	2.5	389.3	38.9	122.3	198.5
Oct-15	**966-968 (Session 2)**	**738.5**	**59.1**	**35.8**	**39.2**	**22.6**	**26.8**	**2.2**	**12.5**	**30.5**	**15.0**	**49.2**	**30.3**	**332.0**	**6.0**	**1.9**	**388.6**	**38.8**	**124.6**	**195.4**
Oct-15	**969-971 (Session 2)**	**726.3**	**54.5**	**36.8**	**39.7**	**22.1**	**27.6**	**2.1**	**12.2**	**28.7**	**14.3**	**49.3**	**30.3**	**333.3**	**5.4**	**1.8**	**390.3**	**39.1**	**121.9**	**199.1**
Nov-15	975-977	731.9	56.4	36.2	39.3	22.7	26.1	2.2	12.2	29.4	14.1	48.9	31.0	332.1	6.2	1.8	387.2	38.8	124.1	198.3
Nov-15	972-974	722.8	57.7	36.1	38.6	22.5	26.3	1.9	11.9	28.8	14.1	48.5	29.2	332.4	6.2	2.4	386.1	38.5	121.8	198.1
Nov-15	989-991	722.0	54.6	37.2	39.8	22.4	26.4	2.0	11.8	27.7	14.7	48.3	30.3	330.9	5.4	2.0	394.3	38.7	124.1	197.0
Nov-15	981-983	738.4	57.0	37.2	39.8	23.5	26.9	2.1	12.3	26.7	14.5	49.1	29.4	331.6	5.4	1.9	386.6	39.2	122.7	198.1
Nov-16	1066-1068	734.0	58.7	38.5	41.1	22.5	26.4	2.3	12.5	31.4	15.3	48.9	29.3	331.2	6.1	2.2	386.0	38.9	123.2	198.5
Nov-16	**1069-1071 (Session 3)**	**733.5**	**54.2**	**37.3**	**41.5**	**22.6**	**24.1**	**2.1**	**12.6**	**28.9**	**14.0**	**49.4**	**30.5**	**331.6**	**6.3**	**1.8**	**384.3**	**38.7**	**123.1**	**198.7**
Dec-16		730.2	56.9	37.2	41.3	22.7	26.1	2.1	12.3	31.7	14.7	48.7	30.1	331.7	6.1	1.8	383.8	39.3	121.0	198.3
Dec-16		707.0	53.7	34.6	41.5	23.0	22.9	1.9	12.2	29.8	14.2	49.4	27.6	332.4	6.1	1.9	375.1	38.9	123.3	198.0
Dec-16		730.6	57.3	36.1	40.9	22.7	24.6	2.3	12.6	29.3	14.6	49.2	29.0	332.0	5.8	2.1	396.0	39.1	123.4	198.4
Dec-16	3A	728.8	62.4	36.5	40.9	21.4	24.6	2.1	12.3	31.5	13.3	49.2	28.3	331.3	6.0	1.8	396.6	39.1	122.6	198.5
Dec-16	3B	728.8	62.4	36.0	41.6	23.3	24.6	2.2	12.3	31.5	14.5	49.1	28.3	331.5	5.0	1.8	396.6	38.5	123.7	197.9
Dec-16	3C	728.0	54.8	37.5	40.8	23.0	24.5	2.1	12.4	26.4	14.5	48.8	26.8	330.9	6.0	2.3	396.9	38.7	122.3	198.5
Dec-16	3D	723.7	57.2	36.1	40.4	22.2	23.7	2.0	12.1	32.3	14.1	49.0	31.5	331.8	5.9	1.9	397.2	38.5	124.5	198.0
Dec-16	3E	722.6	55.7	36.2	40.7	22.9	23.9	2.1	11.9	31.0	15.5	48.6	28.8	331.6	6.0	2.3	397.5	39.2	121.8	198.0
Jan-17	1079-1081	727.9	57.9	36.4	40.9	22.3	24.7	2.0	12.2	28.6	15.0	48.9	30.4	332.0	6.5	2.1	398.9	38.9	124.3	198.5
Jan-17	1088-1090	741.8	52.4	36.5	40.8	21.4	24.0	1.9	12.1	27.9	14.4	49.1	29.2	332.4	5.8	2.2	395.4	39.4	123.8	198.0
	Avg.	***728.2***	***57.0***	***36.5***	***42.6***	***22.6***	***25.3***	***2.1***	***12.3***	***29.5***	***14.5***	***49.0***	***29.6***	***331.8***	***5.9***	***2.0***	***390.5***	***38.9***	***123.1***	***198.1***
	St.Dev	***8.3***	***2.8***	***1.0***	***9.8***	***0.5***	***1.4***	***0.1***	***0.2***	***1.7***	***0.5***	***0.3***	***1.2***	***0.6***	***0.4***	***0.2***	***6.4***	***0.3***	***1.0***	***0.8***
	RSD (%)	***1.1***	***4.9***	***2.7***	***22.9***	***2.3***	***5.4***	***5.6***	***1.8***	***5.7***	***3.6***	***0.6***	***4.1***	***0.2***	***6.1***	***11.2***	***1.6***	***0.7***	***0.8***	***0.4***
	Recommended values	**683.3**	**53.9**	**37.6**	**19.6**	**22.2**	**25.5**	**1.5**	**12.7**	**28.7**	**13.4**	**46.6**	**32.4**	**334.9**	**5.8**	**1.7**	**404.4**	**36.9**	**128.5**	**190.3**

A2.4 Internal reference materials

Major element data (wt%) from Tindfjallajökull samples run during each analytical session.

Sample	Session	SiO_2	TiO_2	Al_2O_3	Fe_2O_3	MnO	MgO	CaO	Na_2O	K_2O	P_2O_5	SO_3	LOI	Total
JM-31	1	46.60	3.018	14.95	14.02	0.184	7.07	11.02	2.59	0.42	0.34	<0.002	-0.04	100.17
JM-31	2	46.10	3.015	14.90	14.60	0.197	7.13	11.11	2.58	0.41	0.33	<0.003	-0.04	100.34
JM-31	3	46.45	3.10	15.26	14.40	0.19	6.85	11.27	2.57	0.43	0.35	<0.002	-0.04	100.84
	Avg.	***46.39***	***3.05***	***15.04***	***14.34***	***0.19***	***7.02***	***11.13***	***2.58***	***0.42***	***0.34***			
	St.Dev	***0.25***	***0.05***	***0.20***	***0.29***	***0.01***	***0.15***	***0.13***	***0.01***	***0.01***	***0.01***			
	RSD (%)	***0.5***	***1.6***	***1.3***	***2.0***	***3.5***	***2.1***	***1.1***	***0.4***	***2.1***	***3.2***			
JM-39	1	52.44	2.564	13.68	14.58	0.320	2.80	6.57	4.88	1.01	1.16	0.010	-0.29	99.73
JM-39	2	52.13	2.543	13.64	15.20	0.338	2.85	6.61	4.90	0.99	1.15	<0.003	-0.29	100.07
JM-39	3	52.46	2.64	13.94	15.02	0.33	2.65	6.72	4.85	1.03	1.21	<0.002	-0.29	100.55
	Avg.	***52.34***	***2.58***	***13.76***	***14.93***	***0.33***	***2.77***	***6.63***	***4.88***	***1.01***	***1.17***			
	St.Dev	***0.18***	***0.05***	***0.16***	***0.32***	***0.01***	***0.11***	***0.08***	***0.02***	***0.02***	***0.03***			
	RSD (%)	***0.4***	***1.9***	***1.2***	***2.1***	***2.8***	***3.8***	***1.2***	***0.5***	***1.9***	***2.6***			
JM-13	1	55.17	2.190	14.74	10.37	0.155	4.69	7.80	3.42	1.51	0.30	<0.003	-0.15	100.18
JM-13	2	54.74	2.187	14.66	10.78	0.164	4.72	7.87	3.37	1.48	0.29	<0.003	-0.15	100.11
JM-13	3	55.38	2.25	15.02	10.61	0.16	4.49	7.98	3.39	1.54	0.31	<0.002	-0.15	100.96
	Avg.	***55.10***	***2.21***	***14.80***	***10.58***	***0.16***	***4.63***	***7.88***	***3.39***	***1.51***	***0.30***			
	St.Dev	***0.32***	***0.04***	***0.19***	***0.21***	***0.00***	***0.12***	***0.09***	***0.02***	***0.03***	***0.01***			
	RSD (%)	***0.6***	***1.6***	***1.3***	***2.0***	***2.9***	***2.7***	***1.1***	***0.7***	***1.9***	***3.6***			

Sample	Session	SiO_2	TiO_2	Al_2O_3	Fe_2O_3	MnO	MgO	CaO	Na_2O	K_2O	P_2O_5	SO_3	LOI	Total
JM-2	1	72.72	0.246	13.16	3.72	0.105	0.03	0.69	6.23	3.49	0.01	<0.003	0.17	100.58
JM-2	2	69.84	0.234	12.61	3.73	0.106	0.05	0.67	5.97	3.30	0.01	<0.003	0.17	96.69
JM-2	3	71.37	0.24	12.88	3.63	0.11	0.02	0.68	6.00	3.52	0.02	<0.002	0.17	98.64
	Avg.	***71.31***	***0.24***	***12.88***	***3.70***	***0.11***	***0.04***	***0.68***	***6.07***	***3.44***	***0.01***			
	St.Dev	***1.44***	***0.01***	***0.28***	***0.05***	***0.00***	***0.02***	***0.01***	***0.14***	***0.12***	***0.00***			
	RSD (%)	***2.0***	***2.5***	***2.2***	***1.4***	***0.8***	***43.5***	***1.8***	***2.4***	***3.4***	***19.3***			
JM-36	1	73.23	0.315	12.38	4.29	0.138	-0.01	0.62	5.89	3.29	0.01	<0.003	0.19	100.35
JM-36	2	72.39	0.315	12.23	4.39	0.142	0.04	0.63	5.83	3.26	0.01	<0.003	0.19	99.42
JM-36	3	74.07	0.32	12.57	4.29	0.14	0.01	0.63	5.86	3.43	0.02	<0.002	0.19	101.54
	Avg.	***73.23***	***0.32***	***12.39***	***4.33***	***0.14***	***0.01***	***0.62***	***5.86***	***3.33***	***0.01***			
	St.Dev	***0.84***	***0.00***	***0.17***	***0.06***	***0.00***	***0.02***	***0.01***	***0.03***	***0.09***	***0.00***			
	RSD (%)	***1.1***	***0.6***	***1.4***	***1.4***	***1.3***	***165.4***	***1.3***	***0.6***	***2.7***	***15.9***			
JM-76	1	75.22	0.125	12.98	1.59	0.052	0.05	0.77	4.29	4.14	0.01	<0.003	0.22	99.45
JM-76	2	74.28	0.127	12.86	1.62	0.054	0.09	0.77	4.22	4.06	0.01	<0.003	0.22	98.30
JM-76	3	76.25	0.13	13.22	1.51	0.05	0.06	0.77	4.24	4.29	0.01	<0.002	0.22	100.75
	Avg.	***75.25***	***0.13***	***13.02***	***1.57***	***0.05***	***0.07***	***0.77***	***4.25***	***4.16***	***0.01***			
	St.Dev	***0.98***	***0.00***	***0.18***	***0.06***	***0.00***	***0.02***	***0.00***	***0.04***	***0.12***	***0.00***			
	RSD (%)	***1.3***	***0.9***	***1.4***	***3.6***	***2.2***	***32.0***	***0.4***	***0.9***	***2.8***	***16.3***			

Trace element data (ppm) from Tindfjallajökull samples run during each analytical session.

Sample	Session	Ba	Ce	Co	Cu	Ga	La	Mo	Nb	Nd	Pb	Rb	Sc	Sr	Th	U	V	Y	Zn	Zr
JM-31	1	101.9	51.6	53.5	144.1	22.8	16.6	2.5	25.5	32.1	1.4	8.3	34.5	401.1	1.2	1.4	334.5	33.1	107.5	200.4
JM-31	2	104.9	47.6	51.6	100.8	22.3	16.8	2.3	25.1	27.0	1.5	8.5	32.2	402.0	1.9	1.0	340.0	32.9	107.3	199.7
JM-31	3	108.6	50.3	51.9	100.3	23.4	18.0	2.7	25.4	27.6	2.2	8.3	34.4	399.4	1.4	1.0	334.1	32.7	106.5	199.0
	Avg.	***105.2***	***49.8***	***52.3***	***115.1***	***22.8***	***17.1***	***2.5***	***25.3***	***28.9***	***1.7***	***8.4***	***33.7***	***400.8***	***1.5***	***1.2***	***336.2***	***32.9***	***107.1***	***199.7***
	St.Dev	***3.4***	***2.0***	***1.1***	***25.1***	***0.6***	***0.8***	***0.2***	***0.2***	***2.8***	***0.4***	***0.1***	***1.3***	***1.3***	***0.4***	***0.2***	***3.3***	***0.2***	***0.6***	***0.7***
	RSD (%)	***3.2***	***4.1***	***2.0***	***21.8***	***2.5***	***4.4***	***7.9***	***0.8***	***9.6***	***23.5***	***1.2***	***3.9***	***0.3***	***23.9***	***20.1***	***1.0***	***0.6***	***0.5***	***0.3***
JM-39	1	377.7	130.0	22.0	56.1	30.7	49.9	3.8	58.0	76.0	3.0	14.0	21.4	518.4	3.9	1.6	94.6	68.6	169.7	431.0
JM-39	2	394.9	124.6	19.9	11.6	30.5	49.5	3.7	57.9	72.7	2.2	13.9	19.7	520.5	3.4	0.9	102.2	68.6	170.7	433.2
JM-39	3	394.2	129.1	22.5	11.8	31.3	49.2	3.7	57.2	75.3	2.0	13.9	22.7	515.2	2.9	1.0	95.1	68.5	169.0	428.3
	Avg.	***388.9***	***127.9***	***21.5***	***26.5***	***30.8***	***49.5***	***3.8***	***57.7***	***74.7***	***2.4***	***13.9***	***21.3***	***518.0***	***3.4***	***1.2***	***97.3***	***68.6***	***169.8***	***430.8***
	St.Dev	***9.7***	***2.9***	***1.3***	***25.7***	***0.4***	***0.3***	***0.1***	***0.4***	***1.7***	***0.5***	***0.1***	***1.5***	***2.7***	***0.5***	***0.4***	***4.3***	***0.0***	***0.9***	***2.4***
	RSD (%)	***2.5***	***2.2***	***6.3***	***96.8***	***1.4***	***0.7***	***1.8***	***0.8***	***2.3***	***22.1***	***0.6***	***7.0***	***0.5***	***14.8***	***32.8***	***4.4***	***0.0***	***0.5***	***0.6***
JM-13	1	295.1	81.6	37.6	117.1	23.3	34.4	3.3	37.3	41.3	4.0	36.8	24.1	305.7	5.5	0.9	212.9	42.4	96.4	291.1
JM-13	2	302.4	77.5	36.0	74.0	25.7	32.6	3.3	37.3	40.5	3.8	36.8	22.9	307.7	5.7	1.9	214.6	43.2	97.3	292.6
JM-13	3	303.7	80.5	36.7	73.1	24.7	36.6	3.4	37.5	42.2	4.2	36.2	21.6	305.3	6.1	2.0	211.5	42.9	97.4	291.7
	Avg.	***300.4***	***79.9***	***36.8***	***88.0***	***24.6***	***34.5***	***3.3***	***37.4***	***41.3***	***4.0***	***36.6***	***22.9***	***306.2***	***5.7***	***1.6***	***213.0***	***42.9***	***97.0***	***291.8***
	St.Dev	***4.6***	***2.1***	***0.8***	***25.1***	***1.2***	***2.0***	***0.1***	***0.1***	***0.8***	***0.2***	***0.3***	***1.3***	***1.3***	***0.3***	***0.6***	***1.5***	***0.4***	***0.6***	***0.7***
	RSD (%)	***1.5***	***2.6***	***2.2***	***28.6***	***4.8***	***5.8***	***3.1***	***0.3***	***2.0***	***5.0***	***0.9***	***5.5***	***0.4***	***5.3***	***38.8***	***0.7***	***1.0***	***0.6***	***0.3***

Sample	Session	Ba	Ce	Co	Cu	Ga	La	Mo	Nb	Nd	Pb	Rb	Sc	Sr	Th	U	V	Y	Zn	Zr
JM-2	1	627.8	237.9	2.8	45.2	38.7	112.2	4.1	140.3	121.5	7.7	72.4	<1.0	71.4	12.3	2.9	3.1	130.6	191.1	1034.2
JM-2	2	592.7	226.4	2.9	0.6	38.8	109.1	4.1	141.6	116.9	8.4	72.9	1.7	71.1	11.9	3.0	3.1	132.4	192.7	1041.5
JM-2	3	629.4	234.1	1.9	1.1	39.7	115.0	4.2	141.1	123.2	8.0	72.3	<1.2	71.1	12.4	3.2	3.2	131.9	191.7	1039.3
	Avg.	***616.6***	***232.8***	***2.5***	***15.6***	***39.1***	***112.1***	***4.2***	***141.0***	***120.5***	***8.1***	***72.5***		***71.2***	***12.2***	***3.0***	***3.1***	***131.6***	***191.8***	***1038.3***
	St.Dev	***20.7***	***5.9***	***0.6***	***25.6***	***0.6***	***3.0***	***0.0***	***0.6***	***3.3***	***0.3***	***0.3***		***0.2***	***0.3***	***0.1***	***0.0***	***0.9***	***0.8***	***3.8***
	RSD (%)	***3.4***	***2.5***	***21.7***	***164.2***	***1.4***	***2.6***	***1.1***	***0.4***	***2.7***	***4.2***	***0.5***		***0.3***	***2.1***	***4.7***	***1.2***	***0.7***	***0.4***	***0.4***
JM-36	1	584.2	250.2	3.1	46.2	38.5	101.1	3.3	151.3	116.7	8.2	61.6	1.1	57.3	13.3	2.7	2.2	133.0	223.4	1303.8
JM-36	2	588.0	249.6	2.5	1.3	37.2	102.1	3.1	152.5	116.3	8.4	61.8	<1.0	56.4	13.2	2.8	2.5	134.5	226.0	1310.2
JM-36	3	587.5	252.9	3.7	1.3	38.1	103.8	3.2	151.8	117.0	7.7	60.7	1.2	56.5	13.3	3.2	2.2	133.7	223.4	1307.4
	Avg.	***586.6***	***250.9***	***3.1***	***16.2***	***37.9***	***102.3***	***3.2***	***151.9***	***116.7***	***8.1***	***61.4***	***1.1***	***56.8***	***13.3***	***2.9***	***2.3***	***133.7***	***224.3***	***1307.1***
	St.Dev	***2.1***	***1.7***	***0.6***	***25.9***	***0.7***	***1.3***	***0.1***	***0.6***	***0.4***	***0.4***	***0.6***	***0.1***	***0.5***	***0.1***	***0.2***	***0.2***	***0.7***	***1.5***	***3.2***
	RSD (%)	***0.4***	***0.7***	***19.4***	***159.6***	***1.7***	***1.3***	***4.3***	***0.4***	***0.3***	***4.5***	***1.0***	***9.6***	***0.9***	***0.4***	***8.0***	***7.5***	***0.5***	***0.7***	***0.2***
JM-76	1	613.4	100.0	<1.1	45.8	18.7	48.9	3.6	53.6	45.5	7.9	103.6	3.7	55.1	13.2	3.6	2.5	55.4	53.1	216.3
JM-76	2	604.7	101.1	<1.1	0.9	19.6	48.0	3.6	54.2	47.1	8.1	103.6	4.7	54.2	13.6	3.3	2.1	56.1	53.0	217.0
JM-76	3	616.2	101.7	<1.1	1.4	19.4	48.5	3.7	54.1	47.9	7.7	103.7	3.7	54.4	13.4	3.6	2.5	55.9	52.6	217.0
	Avg.	***611.4***	***100.9***		***16.1***	***19.2***	***48.5***	***3.6***	***54.0***	***46.8***	***7.9***	***103.6***	***4.0***	***54.6***	***13.4***	***3.5***	***2.4***	***55.8***	***52.9***	***216.8***
	St.Dev	***6.0***	***0.9***		***25.8***	***0.5***	***0.5***	***0.0***	***0.4***	***1.3***	***0.2***	***0.1***	***0.6***	***0.5***	***0.2***	***0.2***	***0.3***	***0.3***	***0.3***	***0.4***
	RSD (%)	***1.0***	***0.9***		***160.6***	***2.6***	***0.9***	***0.9***	***0.7***	***2.7***	***2.7***	***0.1***	***14.9***	***0.8***	***1.3***	***4.6***	***10.7***	***0.6***	***0.5***	***0.2***

APPENDIX 3: TINDFJALLAJÖKULL $^{40}Ar/^{39}Ar$ DATA

Recommended ages in bold. Uncertainty in ages and initial $^{40}Ar/^{36}Ar$ is 2σ.

A3.1 Samples analysed in 2015 (irradiated 12/02/15)

Sample: JM-12 | Basaltic andesite | Lab sample code: J1 | J: 0.000243292 ± 0.5% | Date of analysis: 12/06/2015

Step	^{40}Ar counts	± σ_{40} counts	^{39}Ar counts	± σ_{39} counts	^{38}Ar counts	± σ_{38} counts	^{37}Ar counts	± σ_{37} counts	^{36}Ar counts	± σ_{36} counts	$^{40}Ar^*/^{39}Ar$	± σ	Age ka	± σ ka
1	5.326E+03	1.342E+02	8.479E+02	7.851E+00	1.552E+01	9.875E-01	1.333E+03	1.083E+01	1.470E+01	8.411E-01	1.158E+00	3.333E-01	508.033	146.269
2	1.015E+04	1.481E+02	2.125E+03	1.027E+01	4.365E+01	2.032E+00	3.171E+03	1.084E+01	2.896E+01	9.108E-01	7.491E-01	1.446E-01	328.759	63.477
3	1.172E+04	1.567E+02	2.768E+03	1.248E+01	5.305E+01	2.032E+00	3.661E+03	1.085E+01	3.280E+01	9.108E-01	7.340E-01	1.126E-01	322.131	49.396
4	1.241E+04	1.567E+02	2.656E+03	1.344E+01	4.982E+01	2.411E+00	3.847E+03	1.085E+01	3.360E+01	1.291E+00	9.358E-01	1.554E-01	410.678	68.198
5	2.411E+04	2.253E+02	5.798E+03	1.933E+01	1.085E+02	2.795E+00	8.781E+03	1.086E+01	7.612E+01	1.645E+00	2.792E-01	9.243E-02	122.556	40.568
6	2.688E+04	2.424E+02	5.275E+03	1.539E+01	1.018E+02	2.892E+00	9.833E+03	1.086E+01	8.418E+01	1.737E+00	3.796E-01	1.076E-01	166.610	47.233
7	3.438E+04	2.870E+02	7.854E+03	1.834E+01	1.509E+02	2.989E+00	1.544E+04	1.087E+01	1.059E+02	1.923E+00	3.944E-01	8.106E-02	173.102	35.574
8	1.173E+04	1.567E+02	3.182E+03	1.248E+01	5.967E+01	2.220E+00	6.391E+03	1.087E+01	3.310E+01	8.846E-01	6.135E-01	9.581E-02	269.238	42.047
9	2.144E+04	2.169E+02	5.638E+03	1.637E+01	1.072E+02	2.795E+00	1.284E+04	1.088E+01	6.341E+01	1.646E+00	4.795E-01	9.444E-02	210.435	41.446
10	3.597E+04	3.053E+02	9.664E+03	2.130E+01	1.757E+02	3.870E+00	2.486E+04	1.088E+01	1.098E+02	1.923E+00	3.633E-01	6.676E-02	159.466	29.300
11	3.362E+04	2.779E+02	7.626E+03	1.933E+01	1.436E+02	3.379E+00	1.994E+04	1.089E+01	1.002E+02	1.830E+00	5.250E-01	7.974E-02	230.430	34.993
12	2.252E+04	2.169E+02	7.089E+03	2.032E+01	1.270E+02	3.282E+00	2.006E+04	1.089E+01	7.059E+01	1.737E+00	2.344E-01	7.862E-02	102.878	34.504
Total:	*250270.534*		*60522.6164*		*1136.4672*		*130158.793*		*753.3991*					

Plateau Age: 188 ± 28 ka Steps 5-11 MSWD: 1.6 Probability: 0.15 74.4% of the ^{39}Ar
Isochron Age: Not determined

Sample: JM-20 Basaltic andesite Lab sample code: J3 J: 0.000243728 ± 0.5% Date of analysis: 15/06/2015

Step	^{40}Ar counts	± σ_{40} counts	^{39}Ar counts	± σ_{39} counts	^{38}Ar counts	± σ_{38} counts	^{37}Ar counts	± σ_{37} counts	^{36}Ar counts	± σ_{36} counts	^{40}Ar*/^{39}Ar	± σ	Age ka	± σ ka
1	1.637E+04	1.499E+02	2.214E+03	1.164E+01	4.676E+01	1.839E+00	4.254E+03	1.539E+01	5.091E+01	1.457E+00	5.992E-01	2.059E-01	263.469	90.516
2	5.083E+03	1.031E+02	1.659E+03	1.023E+01	2.982E+01	1.839E+00	2.676E+03	1.540E+01	1.436E+01	7.910E-01	5.069E-01	1.540E-01	222.860	67.708
3	3.732E+04	2.849E+02	8.037E+03	2.137E+01	1.526E+02	3.083E+00	1.590E+04	1.541E+01	1.146E+02	1.730E+00	4.292E-01	7.282E-02	188.705	32.016
4	2.222E+04	1.924E+02	6.356E+03	1.940E+01	1.143E+02	2.888E+00	1.373E+04	1.542E+01	6.709E+01	1.730E+00	3.762E-01	8.594E-02	165.420	37.785
5	3.268E+04	2.565E+02	6.996E+03	1.940E+01	1.313E+02	3.278E+00	1.944E+04	1.543E+01	9.477E+01	1.916E+00	6.685E-01	8.889E-02	293.911	39.078
6	3.761E+04	2.849E+02	7.723E+03	1.842E+01	1.423E+02	3.180E+00	2.722E+04	1.543E+01	1.074E+02	1.823E+00	7.617E-01	7.893E-02	334.888	34.699
7	2.498E+04	2.103E+02	6.396E+03	1.744E+01	1.072E+02	3.768E+00	2.369E+04	1.544E+01	7.165E+01	2.489E+00	5.954E-01	1.196E-01	261.776	52.578
8	3.116E+04	2.472E+02	8.883E+03	2.137E+01	1.564E+02	3.474E+00	3.514E+04	1.545E+01	9.295E+01	1.823E+00	4.156E-01	6.673E-02	182.733	29.341
9	1.064E+04	1.264E+02	3.605E+03	1.452E+01	6.222E+01	2.120E+00	1.510E+04	1.546E+01	2.958E+01	8.638E-01	5.264E-01	7.903E-02	231.458	34.744
10	8.501E+03	1.150E+02	2.524E+03	1.070E+01	4.847E+01	2.026E+00	1.095E+04	1.546E+01	2.335E+01	8.200E-01	6.338E-01	1.063E-01	278.666	46.724
Total:	*226555.256*		*54394.3272*		*991.3961*		*168095.913*		*666.6318*					

Plateau Age: Not determined
Isochron Age: 130 ± 110 ka MSWD: 2.2 Initial ^{40}Ar/^{36}Ar: 316 ± 39

Sample: JM-34 Trachybasalt Lab sample code: J5 J: 0.000244164 ± 0.5% Date of analysis: 15/06/2015

Step	^{40}Ar counts	± σ_{40} counts	^{39}Ar counts	± σ_{39} counts	^{38}Ar counts	± σ_{38} counts	^{37}Ar counts	± σ_{37} counts	^{36}Ar counts	± σ_{36} counts	^{40}Ar*/^{39}Ar	± σ	Age ka	± σ ka
1	2.275E+04	1.924E+02	1.601E+03	9.301E+00	4.074E+01	1.656E+00	2.995E+03	1.547E+01	7.052E+01	1.638E+00	1.194E+00	3.253E-01	525.669	143.253
2	4.384E+04	3.328E+02	3.535E+03	1.259E+01	8.123E+01	2.502E+00	6.091E+03	1.548E+01	1.320E+02	1.916E+00	1.364E+00	1.859E-01	600.746	81.852
3	6.014E+04	4.399E+02	4.436E+03	1.452E+01	1.118E+02	2.598E+00	8.297E+03	1.549E+01	1.852E+02	2.296E+00	1.219E+00	1.823E-01	537.047	80.299
4	3.305E+04	2.660E+02	2.420E+03	1.164E+01	6.032E+01	2.026E+00	4.248E+03	1.549E+01	9.731E+01	1.638E+00	1.773E+00	2.284E-01	780.963	100.546
5	6.591E+04	5.121E+02	3.771E+03	1.354E+01	1.119E+02	3.066E+00	1.179E+04	1.280E+01	2.020E+02	2.540E+00	1.649E+00	2.410E-01	726.302	106.131
6	1.382E+05	1.007E+03	6.030E+03	1.450E+01	1.982E+02	3.883E+00	2.687E+04	1.280E+01	4.191E+02	3.505E+00	2.373E+00	2.397E-01	1045.107	105.503
7	1.116E+05	8.205E+02	5.378E+03	1.743E+01	1.692E+02	3.606E+00	2.740E+04	1.281E+01	3.451E+02	3.323E+00	1.793E+00	2.380E-01	789.478	104.789
8	9.712E+04	7.327E+02	4.923E+03	1.743E+01	1.529E+02	3.333E+00	2.645E+04	1.281E+01	2.951E+02	3.144E+00	2.015E+00	2.405E-01	887.419	105.866
9	7.207E+04	5.499E+02	3.864E+03	1.450E+01	1.148E+02	4.731E+00	2.294E+04	1.282E+01	2.166E+02	4.531E+00	2.091E+00	3.747E-01	920.665	164.968
10	6.006E+04	4.747E+02	3.227E+03	1.354E+01	8.363E+01	6.080E+00	1.913E+04	1.283E+01	1.762E+02	5.876E+00	2.479E+00	5.580E-01	1091.757	245.635
11	3.763E+04	3.398E+02	2.127E+03	1.067E+01	6.040E+01	2.635E+00	1.349E+04	1.283E+01	1.129E+02	2.221E+00	2.004E+00	3.476E-01	882.403	153.025
12	2.619E+04	2.668E+02	1.486E+03	9.184E+00	4.540E+01	2.234E+00	1.000E+04	1.284E+01	7.960E+01	2.000E+00	1.796E+00	4.366E-01	790.969	192.248
Total:	*768536.636*		*42796.2910*		*1230.5538*		*179693.205*		*2331.6608*					

Plateau Age: 857 ± 83 ka Steps 4-12 MSWD: 0.87 Probability: 0.54 77.6% of the ^{39}Ar

Isochron Age: 96 ± 30 ka MSWD: 0.84 Initial ^{40}Ar/^{36}Ar: 325 ± 14

Sample: JM-36 Rhyolite Lab sample code: J7 J: 0.000246921 ± 0.5% Date of analysis: 16/06/2015

Step	^{40}Ar counts	± σ_{40} counts	^{39}Ar counts	± σ_{39} counts	^{38}Ar counts	± σ_{38} counts	^{37}Ar counts	± σ_{37} counts	^{36}Ar counts	± σ_{36} counts	^{40}Ar*/^{39}Ar	± σ	Age ka	± σ ka
1	1.504E+04	2.127E+02	7.006E+03	1.811E+01	8.408E+01	2.582E+00	3.837E+02	7.091E+00	3.364E+01	1.449E+00	7.283E-01	6.826E-02	325.158	30.471
2	2.130E+04	2.445E+02	1.348E+04	2.711E+01	1.649E+02	3.561E+00	7.577E+02	7.093E+00	3.484E+01	1.276E+00	8.163E-01	3.338E-02	364.441	14.902
3	1.999E+04	2.377E+02	1.458E+04	2.611E+01	1.730E+02	3.070E+00	8.902E+02	7.097E+00	2.640E+01	1.353E+00	8.356E-01	3.193E-02	373.050	14.252
4	2.983E+04	2.817E+02	2.340E+04	3.211E+01	2.800E+02	4.747E+00	1.273E+03	7.099E+00	3.860E+01	2.766E+00	7.872E-01	3.696E-02	351.466	16.498
5	1.330E+04	2.072E+02	1.118E+04	2.311E+01	1.359E+02	3.168E+00	6.592E+02	7.104E+00	1.567E+01	1.058E+00	7.763E-01	3.360E-02	346.597	15.000
6	2.172E+04	2.445E+02	1.087E+04	2.311E+01	1.389E+02	3.758E+00	8.160E+02	7.106E+00	1.972E+01	2.672E+00	1.462E+00	7.607E-02	652.459	33.955
7	1.267E+04	2.146E+02	4.506E+03	1.331E+01	5.699E+01	2.098E+00	3.040E+02	8.843E+00	1.415E+01	1.030E+00	1.883E+00	8.284E-02	840.502	36.970
8	1.088E+04	2.033E+02	2.943E+03	2.023E+01	3.817E+01	1.049E+00	1.817E+02	8.846E+00	8.086E+00	1.013E+00	2.884E+00	1.246E-01	1287.362	55.590
9	4.785E+03	1.952E+02	1.830E+03	1.039E+01	2.116E+01	8.900E-01	1.430E+02	8.853E+00	6.096E+00	1.009E+00	1.630E+00	1.950E-01	727.848	87.029
10	2.004E+04	2.484E+02	8.715E+03	2.321E+01	1.052E+02	2.677E+00	7.955E+02	8.855E+00	2.472E+01	1.438E+00	1.462E+00	5.662E-02	652.495	25.273
11	8.474E+03	2.056E+02	5.127E+03	1.528E+01	6.419E+01	2.194E+00	4.531E+02	8.861E+00	1.231E+01	1.022E+00	9.430E-01	7.129E-02	421.012	31.823
12	5.045E+03	1.960E+02	3.163E+03	1.233E+01	3.417E+01	1.049E+00	2.964E+02	8.864E+00	6.956E+00	1.001E+00	9.450E-01	1.123E-01	421.925	50.123
Total:	*183070.591*		*106801.581*		*1296.7981*		*6953.2206*		*241.2031*					

Plateau Age: **358 ± 15 ka** Steps 1-5 MSWD: 0.80 Probability: 0.53 65.2% of the ^{39}Ar

Isochron Age: 364 ± 39 ka Steps 1-5 (not determinable with all steps) MSWD: 1.16 Initial ^{40}Ar/^{36}Ar: 289 ± 38

Sample: JM-37 Rhyolite Lab sample code: J9 J: 0.000247928 ± 0.5% Date of analysis: 17/06/2015

Step	^{40}Ar counts	± σ_{40} counts	^{39}Ar counts	± σ_{39} counts	^{38}Ar counts	± σ_{38} counts	^{37}Ar counts	± σ_{37} counts	^{36}Ar counts	± σ_{36} counts	^{40}Ar*/^{39}Ar	± σ	Age ka	± σ ka
1	4.975E+03	1.955E+02	7.629E+02	6.694E+00	1.705E+01	8.759E-01	7.956E+01	8.872E+00	1.441E+01	1.026E+00	9.381E-01	4.728E-01	420.528911	211.936327
2	4.782E+03	1.957E+02	1.038E+03	7.620E+00	2.686E+01	1.536E+00	1.399E+02	8.882E+00	1.350E+01	1.026E+00	7.643E-01	3.475E-01	342.627140	155.761155
3	1.008E+04	2.072E+02	2.321E+03	1.136E+01	5.409E+01	2.290E+00	2.002E+02	8.886E+00	2.678E+01	1.072E+00	9.333E-01	1.632E-01	418.378037	73.1389563
4	9.977E+03	2.084E+02	2.642E+03	1.019E+01	5.759E+01	1.908E+00	3.659E+02	8.891E+00	2.564E+01	1.067E+00	9.090E-01	1.431E-01	407.507616	64.1625491
5	9.978E+03	2.068E+02	2.542E+03	1.233E+01	5.779E+01	1.908E+00	2.371E+02	8.894E+00	2.577E+01	1.211E+00	9.296E-01	1.627E-01	416.719923	72.9204605
6	1.256E+04	1.048E+02	3.793E+03	1.426E+01	8.732E+01	3.035E+00	3.043E+02	1.002E+01	3.087E+01	1.072E+00	9.056E-01	8.804E-02	405.979908	39.4625467
7	1.374E+04	1.144E+02	6.138E+03	1.723E+01	1.286E+02	2.942E+00	4.471E+02	1.002E+01	3.113E+01	1.025E+00	7.396E-01	5.278E-02	331.567084	23.6603440
8	2.366E+04	1.829E+02	5.297E+03	1.822E+01	1.205E+02	3.220E+00	4.090E+02	1.003E+01	6.904E+01	1.551E+00	6.158E-01	9.317E-02	276.058348	41.763187
9	1.615E+04	2.027E+02	5.888E+03	3.417E+01	1.296E+02	3.502E+00	4.475E+02	1.003E+01	3.883E+01	1.048E+00	7.933E-01	6.303E-02	355.638415	28.2544253
10	1.824E+04	1.436E+02	7.331E+03	2.021E+01	1.526E+02	3.597E+00	5.595E+02	1.003E+01	4.320E+01	2.171E+00	7.463E-01	8.971E-02	334.547440	40.210939
11	1.151E+05	8.420E+02	5.267E+03	1.624E+01	1.756E+02	4.169E+00	3.987E+02	1.004E+01	3.609E+02	3.021E+00	1.606E+00	2.330E-01	719.985291	104.438630
12	2.463E+03	3.376E+01	2.230E+03	9.957E+00	4.038E+01	1.430E+00	1.609E+02	1.004E+01	4.106E+00	9.393E-01	5.604E-01	1.254E-01	251.237665	56.2121163
13	1.137E+04	9.999E+01	2.511E+03	1.230E+01	5.819E+01	2.403E+00	2.006E+02	1.005E+01	2.840E+01	1.003E+00	1.185E+00	1.247E-01	531.148388	55.8927349
14	8.445E+03	7.931E+01	2.030E+03	8.896E+00	4.278E+01	2.145E+00	1.418E+02	1.005E+01	2.011E+01	1.206E+00	1.233E+00	1.799E-01	552.592359	80.6348915
15	5.125E+03	5.875E+01	1.308E+03	9.957E+00	1.496E+01	3.786E+00	1.057E+02	1.006E+01	5.620E+00	3.698E+00	2.648E+00	8.367E-01	1186.93132	374.878437
Total:	*266650.175*		*51098.9338*		*1163.8355*		*4197.7899*		*738.3423*					

Plateau Age: **350 ± 27 ka** Steps 1-10 MSWD: 0.95 Probability: 0.48 73.9% of the ^{39}Ar

Isochron Age: 310 ± 61 ka MSWD: 2.1 Initial ^{40}Ar/^{36}Ar: 311 ± 11

A3.2 Samples analysed in 2016 (irradiated 09/06/16)

Sample: JM-12 Basaltic andesite Lab sample code: AH1 J: 0.000311897 ± 0.5% Date of analysis: 18/07/2016

Step	^{40}Ar counts	± σ_{40} counts	^{39}Ar counts	± σ_{39} counts	^{38}Ar counts	± σ_{38} counts	^{37}Ar counts	± σ_{37} counts	^{36}Ar counts	± σ_{36} counts	^{40}Ar*/^{39}Ar	± σ	Age ka	± σ ka
1	6.556E+03	9.503E+01	6.312E+02	1.503E+01	1.333E+01	7.227E-01	5.772E+02	2.538E+00	2.937E+01	6.190E-01	-3.364E+00	-3.363E-01	-1893.726	189.418
2	1.898E+03	2.206E+01	4.053E+02	4.523E+00	8.427E+00	3.887E-01	3.789E+02	7.742E-01	5.740E+00	4.880E-01	4.981E-01	3.600E-01	280.251	202.512
3	9.179E+03	2.734E+01	1.448E+03	8.916E+00	3.388E+01	1.609E+00	1.355E+03	7.535E-01	2.463E+01	1.065E+00	1.313E+00	2.182E-01	738.847	122.714
4	1.024E+02	1.240E+01	5.119E+01	1.772E+00	8.883E-01	7.010E-01	7.554E+01	3.806E+00	1.110E+00	6.930E-01	-4.407E+00	-4.010E+00	-2481.424	2259.705
5	1.367E+03	6.585E+01	3.629E+02	4.018E+00	6.906E+00	5.688E-01	6.061E+02	4.078E+00	4.585E+00	4.749E-01	3.471E-02	4.271E-01	19.528	240.345
6	7.752E+03	6.777E+01	1.514E+03	8.921E+00	2.898E+01	1.313E+00	2.824E+03	4.080E+00	2.296E+01	1.106E+00	6.384E-01	2.205E-01	359.204	124.038
7	1.087E+04	6.455E+01	2.376E+03	1.202E+01	5.540E+01	1.637E+00	4.738E+03	3.513E+00	3.784E+01	1.230E+00	-1.296E-01	-1.553E-01	-72.901	87.401
8	1.664E+04	6.493E+01	3.647E+03	1.303E+01	8.648E+01	2.426E+00	7.959E+03	3.514E+00	5.377E+01	7.779E-01	2.067E-01	6.550E-02	116.304	36.855
9	1.209E+04	3.634E+02	3.231E+03	1.203E+01	6.950E+01	2.044E+00	7.566E+03	3.652E+00	3.781E+01	1.279E+00	2.848E-01	1.623E-01	160.257	91.298
10	6.769E+03	3.630E+02	2.052E+03	1.103E+01	4.713E+01	1.654E+00	5.217E+03	3.653E+00	2.096E+01	1.229E+00	2.800E-01	2.502E-01	157.556	140.783
11	6.635E+01	1.209E+02	5.914E+01	1.806E+00	1.157E+00	6.440E-01	1.308E+02	6.094E-01	-3.954E-02	5.058E-01	1.319E+00	3.251E+00	742.238	1828.551
12	4.318E+01	1.171E+02	4.719E+01	1.805E+00	2.708E+00	1.144E+00	1.174E+02	4.064E+00	9.472E-01	8.950E-01	-5.016E+00	-6.131E+00	-2824.419	3455.515
Total:	*73345.2265*		*15826.2990*		*354.7788*		*31544.8974*		*239.6883*					

Plateau Age: 133 ± 60 ka Steps 4-12 MSWD: 1.4 Probability: 0.19 84.3% of the ^{39}Ar

Isochron Age: Not determined

Sample: JM-14 | Basaltic andesite | Lab sample code: AH3 | J: 0.000311335 ± 0.5% | Date of analysis: 24/08/2016

Step	^{40}Ar counts	± σ_{40} counts	^{39}Ar counts	± σ_{39} counts	^{38}Ar counts	± σ_{38} counts	^{37}Ar counts	± σ_{37} counts	^{36}Ar counts	± σ_{36} counts	$^{40}Ar^*/^{39}Ar$	± σ	Age ka	± σ ka
1	4.095E+03	1.476E+01	2.208E+02	3.639E+00	2.581E+00	1.053E+00	5.860E+02	4.307E+00	1.219E+01	1.847E+00	2.233E+00	2.474E+00	1253.949	1388.338
2	2.142E+03	1.540E+02	1.311E+02	2.888E+00	1.487E+00	1.004E+00	3.393E+02	3.590E+00	6.257E+00	1.433E+00	2.232E+00	3.437E+00	1253.115	1929.245
3	2.372E+03	1.539E+02	1.629E+02	3.161E+00	2.034E+00	1.025E+00	5.008E+02	3.591E+00	7.660E+00	1.453E+00	6.657E-01	2.800E+00	373.873	1572.166
4	2.419E+04	5.506E+01	1.437E+03	1.803E+01	3.604E+01	1.702E+00	3.834E+03	1.188E+00	8.072E+01	2.502E+00	2.323E-01	5.158E-01	130.485	289.706
5	2.967E+04	5.982E+01	1.904E+03	1.703E+01	5.535E+01	3.903E+00	5.647E+03	1.188E+00	1.084E+02	3.501E+00	-1.237E+00	-5.446E-01	-694.903	305.980
6	3.204E+04	1.045E+02	1.912E+03	2.004E+01	4.678E+01	1.924E+00	5.306E+03	5.447E+00	1.122E+02	2.695E+00	-5.793E-01	-4.202E-01	-325.419	236.061
7	4.154E+04	1.123E+02	2.351E+03	2.205E+01	5.388E+01	3.814E+00	7.117E+03	5.449E+00	1.410E+02	4.260E+00	-5.430E-02	-5.376E-01	-30.499	301.983
8	5.817E+04	1.296E+02	3.300E+03	2.606E+01	8.471E+01	3.215E+00	1.043E+04	7.124E+00	2.035E+02	4.363E+00	-5.964E-01	-3.927E-01	-335.021	220.611
9	5.287E+04	1.349E+02	2.790E+03	2.505E+01	7.779E+01	4.013E+00	9.200E+03	7.128E+00	1.878E+02	4.461E+00	-9.418E-01	-4.751E-01	-529.055	266.939
10	5.076E+04	1.211E+02	2.766E+03	2.205E+01	8.542E+01	5.615E+00	1.113E+04	6.699E+00	1.882E+02	4.651E+00	-1.755E+00	-4.990E-01	-985.982	280.449
11	3.329E+04	1.159E+02	1.716E+03	1.804E+01	4.953E+01	2.031E+00	7.071E+03	6.701E+00	1.219E+02	3.567E+00	-1.590E+00	-6.183E-01	-893.374	347.474
12	4.198E+04	3.297E+02	2.008E+03	2.004E+01	6.306E+01	5.618E+00	9.613E+03	6.894E+00	1.439E+02	3.429E+00	-2.693E-01	-5.307E-01	-151.263	298.089
13	5.140E+04	3.086E+02	2.417E+03	2.205E+01	7.521E+01	6.216E+00	1.398E+04	7.676E+00	1.747E+02	3.999E+00	-8.928E-02	-5.053E-01	-50.147	283.805
14	1.501E+05	1.862E+02	5.791E+03	3.007E+01	1.885E+02	3.620E+00	3.593E+04	1.217E+01	5.513E+02	6.401E+00	-2.207E+00	-3.284E-01	-1239.794	184.578
15	8.590E+04	9.009E+01	3.165E+03	1.406E+01	1.099E+02	2.427E+00	2.124E+04	1.217E+01	3.047E+02	2.901E+00	-1.303E+00	-2.724E-01	-731.887	153.055
16	1.064E+05	8.168E+01	3.850E+03	1.506E+01	1.350E+02	2.724E+00	2.387E+04	1.218E+01	3.774E+02	3.101E+00	-1.345E+00	-2.390E-01	-755.582	134.318
17	8.779E+04	8.168E+01	3.030E+03	1.206E+01	1.062E+02	2.923E+00	1.819E+04	1.218E+01	3.167E+02	3.201E+00	-1.909E+00	-3.134E-01	-1072.422	176.133
18	7.656E+04	7.923E+01	2.638E+03	1.206E+01	8.488E+01	6.115E+00	1.469E+04	1.219E+01	2.656E+02	6.100E+00	-7.313E-01	-6.841E-01	-410.812	384.334
Total:	*931269.134*		*41587.3655*		*1258.3878*		*198677.406*		*3304.0843*					

Plateau Age: Not determined

Isochron Age: 460 ± 450 ka MSWD: 1.8 Initial $^{40}Ar/^{36}Ar$: 272 ± 15

Sample: JM-20 Basaltic andesite Lab sample code: AH5 J: 0.000310774 ± 0.5% Date of analysis: 02/09/2016

Step	^{40}Ar counts	± σ_{40} counts	^{39}Ar counts	± σ_{39} counts	^{38}Ar counts	± σ_{38} counts	^{37}Ar counts	± σ_{37} counts	^{36}Ar counts	± σ_{36} counts	$^{40}Ar^*/^{39}Ar$	± σ	Age ka	± σ ka
1	5.486E+03	2.384E+01	6.450E+02	4.609E+00	1.445E+01	7.064E-01	2.648E+03	9.553E-01	1.556E+01	5.945E-01	1.377E+00	2.751E-01	771.892	154.147
2	1.120E+02	2.843E+01	3.504E+01	1.552E+00	1.107E+00	7.545E-01	9.542E+01	6.145E+00	1.281E+00	5.571E-01	-7.603E+00	-4.779E+00	-4267.978	2685.669
3	-4.889E+01	2.831E+01	6.050E+00	6.576E-01	5.150E-01	7.674E-01	3.406E+01	6.147E+00	-5.845E-02	5.733E-01	-5.227E+00	-2.840E+01	-2932.905	15948.032
4	4.644E+00	2.246E+01	5.311E+00	4.411E-01	1.126E+00	4.107E-01	3.163E+01	2.047E-01	1.583E+00	3.829E-01	-8.721E+01	-2.290E+01	-49572.773	13194.616
5	1.145E+01	2.248E+01	3.797E+00	5.913E-01	-9.758E-01	5.679E-01	1.437E+01	2.048E-01	-9.849E-01	5.520E-01	7.967E+01	4.511E+01	44125.387	24680.317
6	2.352E+03	1.006E+01	3.580E+02	4.509E+00	7.705E+00	5.902E-01	1.743E+03	1.175E+00	7.775E+00	5.214E-01	1.528E-01	4.313E-01	85.641	241.800
7	6.224E+04	6.800E+01	8.060E+03	1.904E+01	2.112E+02	3.722E+00	4.067E+04	3.461E+00	2.238E+02	2.401E+00	-4.821E-01	-8.843E-02	-270.320	49.588
8	5.472E+04	5.030E+01	9.442E+03	2.104E+01	2.207E+02	3.835E+00	4.853E+04	5.128E+00	1.910E+02	2.464E+00	-1.812E-01	-7.731E-02	-101.588	43.349
9	6.426E+04	5.151E+01	1.139E+04	2.204E+01	2.623E+02	3.904E+00	6.044E+04	2.508E+00	2.288E+02	2.501E+00	-2.954E-01	-6.503E-02	-165.652	36.463
10	5.952E+04	6.550E+01	1.256E+04	2.406E+01	2.843E+02	4.815E+00	6.890E+04	8.745E+00	2.071E+02	2.722E+00	-1.346E-01	-6.423E-02	-75.470	36.013
11	5.086E+04	4.341E+01	1.160E+04	2.308E+01	2.560E+02	3.707E+00	6.364E+04	5.030E+00	1.795E+02	2.202E+00	-1.878E-01	-5.621E-02	-105.288	31.519
12	5.538E+04	4.986E+01	1.300E+04	2.607E+01	2.830E+02	3.824E+00	7.253E+04	6.865E+00	1.986E+02	2.337E+00	-2.534E-01	-5.323E-02	-142.062	29.849
13	1.654E+04	3.372E+01	4.767E+03	1.607E+01	1.039E+02	2.534E+00	2.731E+04	8.027E+00	5.606E+01	1.466E+00	-5.372E-03	-9.118E-02	-3.012	51.119
Total:	*371439.9296*		*71883.2907*		*1645.2095*		*386592.140*		*1310.0127*					

Plateau Age: Not determined

Isochron Age: Not determined

Sample: JM-165 Basalt Lab sample code: AH7 J: 0.000310212 ± 0.5% Date of analysis: 01/09/2016

Step	^{40}Ar counts	$\pm \sigma_{40}$ counts	^{39}Ar counts	$\pm \sigma_{39}$ counts	^{38}Ar counts	$\pm \sigma_{38}$ counts	^{37}Ar counts	$\pm \sigma_{37}$ counts	^{36}Ar counts	$\pm \sigma_{36}$ counts	$^{40}Ar^*/^{39}Ar$	$\pm \sigma$	Age ka	$\pm \sigma$ ka
1	7.344E+03	1.728E+01	1.034E+03	6.925E+00	1.609E+01	7.465E-01	5.707E+03	3.398E+00	2.328E+01	6.963E-01	4.479E-01	1.996E-01	250.639	111.709
2	3.406E+03	1.544E+01	5.087E+02	4.227E+00	8.169E+00	7.214E-01	2.667E+03	3.399E+00	1.090E+01	6.963E-01	3.654E-01	4.056E-01	204.484	226.985
3	2.833E+02	5.272E+01	6.257E+01	1.914E+00	2.219E-01	5.227E-01	3.384E+02	5.504E+00	3.352E-01	5.128E-01	2.945E+00	2.566E+00	1647.394	1434.571
4	2.019E+02	5.268E+01	3.529E+01	1.515E+00	4.712E-01	4.159E-01	1.793E+02	5.506E+00	6.443E-01	4.090E-01	3.272E-01	3.736E+00	183.079	2090.823
5	6.804E+01	1.818E+01	8.703E+00	7.946E-01	3.983E-01	7.838E-01	6.168E+01	9.999E+00	1.454E+00	1.797E+00	-4.156E+01	-6.118E+01	-23410.395	34683.565
6	2.225E+04	3.228E+01	8.888E+02	6.035E+00	2.836E+01	1.624E+00	5.970E+03	1.000E+01	7.734E+01	2.295E+00	-6.776E-01	-7.640E-01	-379.230	427.672
7	-2.339E+02	7.440E+00	6.767E+00	6.683E-01	6.631E-01	6.450E-01	5.475E+01	3.511E+00	7.411E-01	6.031E-01	-6.692E+01	-2.717E+01	-37844.529	15530.094
8	2.904E+04	3.840E+01	2.957E+03	1.107E+01	6.885E+01	2.173E+00	2.246E+04	4.476E-01	9.999E+01	1.906E+00	-1.722E-01	-1.909E-01	-96.350	106.852
9	1.371E+04	2.456E+01	1.360E+03	8.777E+00	3.654E+01	1.694E+00	1.327E+04	4.478E-01	4.808E+01	1.534E+00	-3.686E-01	-3.338E-01	-206.275	186.804
10	1.799E+04	4.310E+01	1.579E+03	9.251E+00	4.153E+01	1.905E+00	1.601E+04	1.318E+01	6.584E+01	2.206E+00	-9.295E-01	-4.138E-01	-520.265	231.647
11	9.855E+04	8.309E+01	9.933E+03	2.010E+01	2.263E+02	3.703E+00	8.259E+04	1.319E+01	3.463E+02	3.187E+00	-3.801E-01	-9.518E-02	-212.734	53.272
12	1.680E+05	1.805E+02	1.221E+04	4.609E+01	3.065E+02	7.827E+00	1.010E+05	4.143E+00	5.909E+02	7.122E+00	-5.455E-01	-1.731E-01	-305.327	96.875
13	2.309E+04	3.254E+01	2.240E+03	9.059E+00	5.325E+01	2.038E+00	2.233E+04	4.145E+00	7.897E+01	1.742E+00	-1.098E-01	-2.303E-01	-61.460	128.887
Total:	*383660.6550*		*32819.3040*		*787.3372*		*272665.361*		*1344.8052*					

Plateau Age: Not determined

Isochron Age: 380 ± 840 ka MSWD: 1.8 Initial $^{40}Ar/^{36}Ar$: 269 ± 22

Sample: JM-164 Basalt Lab sample code: AH9 J: 0.000300225 ± 0.5% Date of analysis: 31/08/2016

Step	^{40}Ar	± σ_{40}	^{39}Ar	± σ_{39}	^{38}Ar	± σ_{38}	^{37}Ar	± σ_{37}	^{36}Ar	± σ_{36}	^{40}Ar*/^{39}Ar	± σ	Age	± σ
	counts	counts	counts	counts	counts	counts	counts	counts	counts	counts			ka	ka
1	5.226E+04	4.948E+01	3.245E+03	1.404E+01	9.068E+01	2.277E+00	4.111E+04	4.352E+00	1.840E+02	2.273E+00	-6.514E-01	-2.076E-01	-353.753	112.763
2	2.024E+03	2.167E+01	2.891E+02	3.854E+00	7.636E+00	1.131E+00	3.027E+03	4.353E+00	6.271E+00	8.132E-01	5.896E-01	8.346E-01	320.159	453.148
3	3.127E+02	1.768E+01	8.660E+01	2.260E+00	1.424E-01	6.666E-01	9.376E+02	3.845E+00	-1.680E+00	6.294E-01	9.345E+00	2.171E+00	5067.748	1175.688
4	8.392E+02	1.136E+01	1.147E+02	2.352E+00	9.327E-01	7.007E-01	1.374E+03	3.641E+00	1.848E+00	6.721E-01	2.555E+00	1.735E+00	1386.841	941.634
5	7.225E+02	9.421E+00	7.664E+01	2.349E+00	-5.644E-01	9.799E-01	1.009E+03	5.028E+00	4.994E-01	9.596E-01	7.502E+00	3.709E+00	4069.174	2009.769
6	3.947E+02	8.698E+00	4.126E+01	1.887E+00	-5.894E-01	9.226E-01	6.103E+02	5.030E+00	-6.469E-01	9.130E-01	1.420E+01	6.574E+00	7694.180	3555.022
7	1.986E+02	7.454E+00	1.893E+01	7.896E-01	-5.025E-02	6.444E-01	3.827E+02	3.647E+00	-3.074E+00	7.661E-01	5.850E+01	1.221E+01	31489.559	6518.172
8	1.420E+02	7.529E+00	2.417E+01	1.476E+00	-6.165E-01	6.157E-01	3.586E+02	3.648E+00	-7.189E-01	6.224E-01	1.467E+01	7.670E+00	7946.641	4146.852
9	1.378E+04	2.656E+01	1.706E+03	8.626E+00	4.222E+01	1.845E+00	2.788E+04	3.389E+00	4.336E+01	1.352E+00	5.700E-01	2.347E-01	309.485	127.424
10	1.083E+04	2.248E+01	1.521E+03	9.426E+00	3.722E+01	2.050E+00	2.493E+04	3.599E+00	3.166E+01	1.024E+00	9.710E-01	1.996E-01	527.245	108.352
11	9.226E+03	2.420E+01	1.447E+03	7.731E+00	3.234E+01	1.675E+00	2.711E+04	3.653E+00	2.703E+01	1.029E+00	8.553E-01	2.110E-01	464.390	114.526
12	6.793E+03	2.136E+01	1.043E+03	6.632E+00	2.006E+01	8.470E-01	2.014E+04	3.654E+00	2.102E+01	7.845E-01	5.586E-01	2.232E-01	303.330	121.185
13	1.464E+04	2.595E+01	2.054E+03	8.734E+00	4.577E+01	2.258E+00	3.191E+04	3.921E+00	4.660E+01	1.869E+00	4.236E-01	2.692E-01	230.007	146.145
Total:	*112172.7615*		*11667.1502*		*275.1901*		*180783.746*		*356.1825*					

Plateau Age: 390 ± 110 ka Steps 9-13 MSWD: 1.03 Probability: 0.39 66.6% of the ^{39}Ar

Isochron Age: 830 ± 200 ka MSWD: 1.3 Initial ^{40}Ar/^{36}Ar: 257 ± 11

Sample: JM-160 Basalt Lab sample code: AH11 J: 0.000281376 ± 0.5% Date of analysis: 09/09/2016

Step	^{40}Ar counts	$\pm \sigma_{40}$ counts	^{39}Ar counts	$\pm \sigma_{39}$ counts	^{38}Ar counts	$\pm \sigma_{38}$ counts	^{37}Ar counts	$\pm \sigma_{37}$ counts	^{36}Ar counts	$\pm \sigma_{36}$ counts	$^{40}Ar^*/^{39}Ar$	$\pm \sigma$	Age ka	$\pm \sigma$ ka
1	6.915E+02	1.078E+01	1.283E+01	1.180E+00	-6.005E-01	6.444E-01	8.504E+01	4.032E+00	2.267E+00	6.297E-01	1.672E+00	1.453E+01	848.716	7371.628
2	2.003E+02	1.034E+01	1.011E-01	7.013E-01	-5.605E-01	6.818E-01	1.406E+01	4.034E+00	5.163E-01	6.903E-01	4.719E+02	3.848E+03	224933.911	1724335.31
3	6.527E+03	1.783E+01	4.899E+02	4.631E+00	1.104E+01	7.226E-01	4.385E+03	4.343E+00	1.995E+01	7.061E-01	1.290E+00	4.277E-01	654.725	217.010
4	2.001E+04	3.105E+01	7.021E+02	5.629E+00	2.158E+01	1.182E+00	6.958E+03	4.344E+00	6.629E+01	1.754E+00	6.069E-01	7.394E-01	308.052	375.289
5	9.523E+03	1.942E+01	9.691E+02	6.429E+00	2.399E+01	1.290E+00	1.043E+04	8.572E+00	3.178E+01	1.275E+00	1.372E-01	3.892E-01	69.667	197.565
6	-2.018E+02	6.350E+01	4.979E+01	1.812E+00	-6.806E-01	7.648E-01	6.113E+02	1.060E+01	-2.022E+00	7.669E-01	7.947E+00	4.736E+00	4029.370	2398.567
7	8.244E+01	3.305E+02	5.788E+01	1.818E+00	1.932E+00	5.892E-01	7.023E+02	1.695E+01	4.039E-01	8.940E-01	-6.376E-01	-7.310E+00	-323.687	3711.574
8	-8.087E+01	3.305E+02	3.884E+01	1.619E+00	1.531E+00	8.278E-01	5.233E+02	1.695E+01	2.713E-01	1.054E+00	-4.146E+00	-1.169E+01	-2106.013	5943.436
9	6.318E+03	1.696E+01	7.856E+02	6.313E+00	2.043E+01	1.104E+00	1.098E+04	5.460E+00	1.842E+01	8.017E-01	1.113E+00	3.025E-01	564.907	153.487
10	4.963E+01	1.078E+01	9.263E+00	5.359E-01	5.254E-01	4.583E-01	1.385E+02	5.463E+00	4.330E-02	6.684E-01	3.977E+00	2.136E+01	2017.667	10829.160
11	7.489E+01	5.981E+00	1.242E+01	8.116E-01	4.053E-01	4.482E-01	2.286E+02	3.194E+00	5.694E-01	4.011E-01	-7.518E+00	-9.568E+00	-3820.407	4867.262
12	3.579E+01	6.211E+00	1.066E+01	1.325E+00	2.147E+00	8.797E-01	1.440E+02	3.195E+00	1.382E+00	8.505E-01	-3.494E+01	-2.398E+01	-17824.484	12291.694
13	5.241E+01	1.563E+01	6.002E+00	7.975E-01	5.705E-01	6.161E-01	9.903E+01	1.260E+00	1.764E+00	1.027E+00	-7.810E+01	-5.168E+01	-40088.097	26822.060
14	5.448E+01	1.560E+01	7.253E+00	7.975E-01	6.906E-01	6.026E-01	1.171E+02	1.261E+00	2.169E+00	1.023E+00	-8.086E+01	-4.268E+01	-41519.066	22168.922
Total:	*43339.4129*		*3151.6928*		*83.0003*		*35414.4080*		*143.7952*					

Plateau Age: 440 ± 200 ka Steps 1-13 MSWD: 1.09 Probability: 0.37 99.77% of the ^{39}Ar

Isochron Age: Not determined

Sample: JM-151 Basalt Lab sample code: AH13 J: 0.000262527 ± 0.5% Date of analysis: 12/09/2016

Step	^{40}Ar counts	± σ_{40} counts	^{39}Ar counts	± σ_{39} counts	^{38}Ar counts	± σ_{38} counts	^{37}Ar counts	± σ_{37} counts	^{36}Ar counts	± σ_{36} counts	^{40}Ar*/^{39}Ar	± σ	Age ka	± σ ka
1	1.728E+04	2.898E+01	9.856E+02	6.213E+00	2.933E+01	1.819E+00	2.332E+03	6.484E-01	5.683E+01	1.600E+00	4.912E-01	4.807E-01	232.630	227.631
2	2.393E+04	3.243E+01	1.708E+03	8.928E+00	5.360E+01	1.720E+00	4.551E+03	1.668E+00	7.864E+01	1.513E+00	4.069E-01	2.623E-01	192.698	124.240
3	2.191E+04	3.618E+01	1.776E+03	9.438E+00	4.687E+01	1.853E+00	5.708E+03	3.162E+00	7.141E+01	1.585E+00	4.556E-01	2.645E-01	215.759	125.237
4	2.919E+04	3.736E+01	2.470E+03	9.521E+00	7.088E+01	2.109E+00	9.359E+03	8.245E-01	9.824E+01	1.876E+00	6.522E-02	2.249E-01	30.888	106.494
5	4.811E+04	4.996E+01	3.515E+03	1.403E+01	1.076E+02	2.707E+00	1.688E+04	5.185E-01	1.548E+02	2.105E+00	6.741E-01	1.776E-01	319.237	84.096
6	6.763E+04	5.731E+01	4.202E+03	1.603E+01	1.399E+02	2.702E+00	2.318E+04	4.964E+00	2.228E+02	2.505E+00	4.229E-01	1.767E-01	200.259	83.669
7	7.651E+04	8.703E+01	4.301E+03	1.203E+01	1.561E+02	2.903E+00	2.891E+04	3.181E+00	2.619E+02	2.437E+00	-2.028E-01	-1.686E-01	-96.046	79.875
8	1.038E+05	7.639E+01	6.635E+03	1.603E+01	2.201E+02	3.912E+00	4.782E+04	7.597E+00	3.501E+02	3.218E+00	5.067E-02	1.438E-01	23.997	68.089
9	1.025E+05	8.537E+01	6.579E+03	1.904E+01	2.013E+02	8.524E+00	5.133E+04	8.907E+00	3.377E+02	8.416E+00	4.112E-01	3.783E-01	194.761	179.133
10	8.178E+04	6.818E+01	5.545E+03	1.606E+01	1.738E+02	7.139E+00	4.444E+04	1.241E+01	2.645E+02	6.875E+00	6.523E-01	3.666E-01	308.926	173.591
11	5.304E+04	9.170E+01	3.852E+03	2.806E+01	1.268E+02	6.206E+00	3.200E+04	3.501E+00	1.835E+02	4.902E+00	-3.103E-01	-3.768E-01	-146.977	178.486
12	2.768E+03	4.124E+01	2.692E+02	3.512E+00	8.816E+00	8.165E-01	2.187E+03	1.250E+00	7.936E+00	5.815E-01	1.570E+00	6.567E-01	743.307	310.907
Total:	*628427.6268*		*41839.1890*		*1335.1411*		*268710.832*		*2088.3861*					

Plateau Age: 4 ± 92 ka Steps 7-11 MSWD: 1.6 Probability: 0.16 64.3% of the ^{39}Ar

Isochron Age: Not determined

Sample: JM-124 Rhyolite Lab sample code: AH15 J: 0.000245488 ± 0.5% Date of analysis: 04/07/2016

Step	^{40}Ar counts	± σ_{40} counts	^{39}Ar counts	± σ_{39} counts	^{38}Ar counts	± σ_{38} counts	^{37}Ar counts	± σ_{37} counts	^{36}Ar counts	± σ_{36} counts	$^{40}Ar^*/^{39}Ar$	± σ	Age ka	± σ ka
1	1.455E+03	1.099E+02	6.571E+02	8.768E+00	1.018E+01	8.635E-01	4.428E+01	4.963E+00	5.845E+00	1.893E+00	-4.146E-01	-8.676E-01	154.089802	325.577194
2	7.074E+03	1.141E+02	5.455E+03	4.207E+01	8.204E+01	2.427E+00	2.912E+02	4.966E+00	1.418E+01	1.464E+00	5.286E-01	8.211E-02	198.347722	30.8090288
3	1.296E+04	4.001E+01	1.211E+04	3.529E+01	1.766E+02	2.943E+00	7.153E+02	2.842E+00	2.160E+01	7.407E-01	5.427E-01	1.844E-02	203.619311	6.91847957
4	4.459E+04	5.308E+01	4.986E+04	1.202E+02	7.061E+02	7.123E+00	2.787E+03	2.844E+00	5.785E+01	9.021E-01	5.514E-01	5.611E-03	206.882614	2.10517563
5	4.612E+04	8.640E+01	5.858E+04	3.105E+02	8.322E+02	1.802E+01	3.088E+03	2.846E+00	5.117E+01	8.473E-01	5.291E-01	5.321E-03	198.548096	1.99633122
6	5.105E+04	5.480E+01	6.739E+04	1.703E+02	9.393E+02	8.122E+00	3.040E+03	2.848E+00	4.568E+01	8.407E-01	5.572E-01	4.029E-03	209.080965	1.51168194
7	5.342E+04	6.436E+01	7.090E+04	2.304E+02	1.009E+03	8.521E+00	3.059E+03	2.850E+00	4.588E+01	8.473E-01	5.623E-01	4.079E-03	211.004932	1.53026808
8	3.302E+04	4.899E+01	4.376E+04	1.102E+02	6.160E+02	6.225E+00	1.747E+03	2.852E+00	2.903E+01	7.906E-01	5.586E-01	5.634E-03	209.606215	2.11394486
9	2.521E+04	4.432E+01	3.154E+04	7.822E+01	4.649E+02	5.726E+00	1.319E+03	2.854E+00	2.684E+01	7.675E-01	5.479E-01	7.452E-03	205.578814	2.79611318
10	1.361E+04	4.140E+01	1.732E+04	9.422E+01	2.607E+02	1.002E+01	7.603E+02	2.855E+00	1.309E+01	1.014E+00	5.627E-01	1.773E-02	211.120726	6.65339772
11	8.312E+03	3.742E+01	1.041E+04	2.933E+01	1.516E+02	3.240E+00	5.591E+02	2.857E+00	8.742E+00	9.605E-01	5.504E-01	2.755E-02	206.506842	10.3361655
Total:	*296820.3233*		*367973.111*		*5248.7452*		*17410.2222*		*319.9101*					

Plateau Age: **209.5 ± 2.8 ka** Steps 6-11 MSWD: 0.63 Probability: 0.68 65.6% of the ^{39}Ar

Isochron Age: 253 ± 13 ka MSWD: 2.8 Initial $^{40}Ar/^{36}Ar$: 274 ± 34

Sample: JM-186 Rhyolite Lab sample code: AH18 J: 0.000217005 ± 0.5% Date of analysis: 4/10/2016

Step	^{40}Ar counts	± σ_{40} counts	^{39}Ar counts	± σ_{39} counts	^{38}Ar counts	± σ_{38} counts	^{37}Ar counts	± σ_{37} counts	^{36}Ar counts	± σ_{36} counts	^{40}Ar*/^{39}Ar	± σ	Age ka	± σ ka
1	3.901E+03	3.410E+02	3.002E+03	1.103E+01	3.455E+01	9.835E-01	1.401E+01	4.001E+00	9.036E+00	1.227E+00	4.100E-01	1.658E-01	159.341	64.415
2	9.750E+03	2.128E+02	1.022E+04	4.910E+01	1.243E+02	2.808E+00	3.504E+01	4.004E+00	2.154E+01	1.076E+00	3.314E-01	3.749E-02	128.792	14.567
3	7.626E+03	2.664E+02	9.696E+03	2.210E+01	1.250E+02	3.027E+00	4.257E+01	5.008E-01	1.545E+01	1.149E+00	3.155E-01	4.452E-02	122.616	17.301
4	4.544E+03	2.149E+02	6.941E+03	1.806E+01	8.794E+01	2.510E+00	4.310E+01	1.002E+01	8.274E+00	7.530E-01	3.024E-01	4.457E-02	117.506	17.320
5	1.342E+03	6.668E+01	1.799E+03	9.525E+00	2.101E+01	8.312E-01	1.304E+01	1.103E+01	1.802E+00	7.491E-01	4.500E-01	1.285E-01	174.851	49.932
6	4.471E+02	1.318E+01	4.878E+02	5.228E+00	7.115E+00	6.199E-01	1.054E+01	1.355E+01	3.027E+00	7.666E-01	-9.172E-01	-4.653E-01	-356.480	180.856
7	2.414E+02	5.325E+00	1.736E+02	2.806E+00	3.119E+00	4.117E-01	2.460E+01	3.515E+00	3.235E-01	6.297E-01	8.402E-01	1.073E+00	326.495	416.708
8	2.352E+02	7.041E+00	8.470E+01	2.118E+00	1.947E+00	4.415E-01	1.558E+01	1.256E+01	7.709E-01	4.224E-01	8.721E-02	1.476E+00	33.890	573.619
9	3.736E+02	5.807E+00	6.763E+01	1.925E+00	1.892E+00	4.598E-01	-4.525E+00	7.542E+00	1.581E+00	3.625E-01	-1.385E+00	-1.587E+00	-538.373	616.745
10	4.478E+02	8.793E+00	5.504E+01	9.827E-01	1.523E+00	5.496E-01	-2.012E+01	2.012E+00	1.535E+00	5.315E-01	-1.072E-01	-2.858E+00	-41.659	1110.716
Total:	*28907.9285*		*32523.7558*		*408.4435*		*173.8163*		*63.3389*					

Plateau Age: **126 ± 18 ka** Steps 1-10 MSWD: 1.12 Probability: 0.34 100% of the ^{39}Ar

Isochron Age: 125 ± 97 ka MSWD: 1.3 Initial ^{40}Ar/^{36}Ar: 298 ± 76

Sample: JM-168 Basalt Lab sample code: AH21 J: 0.000203097 ± 0.5% Date of analysis: 13/07/2016

Step	^{40}Ar counts	$\pm \sigma_{40}$ counts	^{39}Ar counts	$\pm \sigma_{39}$ counts	^{38}Ar counts	$\pm \sigma_{38}$ counts	^{37}Ar counts	$\pm \sigma_{37}$ counts	^{36}Ar counts	$\pm \sigma_{36}$ counts	$^{40}Ar^*/^{39}Ar$	$\pm \sigma$	Age ka	$\pm \sigma$ ka
1	1.382E+05	1.542E+03	1.081E+02	2.459E+00	6.049E+01	1.316E+00	3.395E+02	2.277E+00	4.149E+02	5.799E+00	1.439E+02	2.157E+01	51963.683	7680.466
2	4.787E+05	1.735E+03	3.809E+02	3.607E+01	1.930E+02	3.504E+01	1.329E+03	2.279E+00	1.457E+03	3.628E+01	1.268E+02	3.094E+01	45871.760	11050.837
3	1.997E+04	1.540E+03	2.006E+01	1.186E+00	9.844E+00	9.899E-01	4.615E+01	2.282E+00	5.980E+01	4.512E+00	1.143E+02	1.018E+02	41412.325	36441.417
4	4.501E+04	1.540E+03	6.976E+01	1.355E+00	2.125E+01	1.038E+00	1.670E+02	2.283E+00	1.300E+02	4.576E+00	9.463E+01	2.944E+01	34342.334	10583.295
5	9.239E+04	1.541E+03	1.432E+02	2.732E+00	4.858E+01	1.929E+00	3.346E+02	2.284E+00	2.859E+02	5.218E+00	5.515E+01	1.526E+01	20095.402	5530.784
6	2.584E+05	1.574E+03	2.832E+02	8.186E+00	1.259E+02	2.946E+00	6.172E+02	2.285E+00	8.159E+02	1.280E+01	6.103E+01	1.458E+01	22223.307	5276.170
7	2.684E+05	1.581E+03	4.214E+02	2.506E+01	1.269E+02	3.137E+00	6.313E+02	2.287E+00	8.508E+02	1.280E+01	4.024E+01	1.002E+01	14684.149	3642.029
8	3.205E+05	1.560E+03	3.883E+02	2.306E+01	1.219E+02	2.204E+01	6.549E+02	2.287E+00	1.007E+03	2.343E+01	5.910E+01	1.861E+01	21524.660	6737.817
9	3.155E+05	1.555E+03	4.072E+02	4.249E+00	1.610E+02	3.813E+00	8.251E+02	2.289E+00	1.027E+03	6.778E+00	2.957E+01	6.235E+00	10803.455	2270.716
10	3.986E+05	1.568E+03	6.663E+02	2.406E+01	1.710E+02	2.404E+01	1.401E+03	2.289E+00	1.297E+03	2.441E+01	2.318E+01	1.111E+01	8472.363	4052.311
11	2.724E+05	1.551E+03	4.982E+02	5.616E+00	1.470E+02	3.042E+00	1.123E+03	2.291E+00	8.867E+02	6.930E+00	2.080E+01	5.162E+00	7605.843	1883.437
12	1.862E+05	1.544E+03	4.629E+02	1.307E+01	7.680E+01	1.204E+01	1.514E+03	2.292E+00	5.836E+02	1.375E+01	2.978E+01	9.425E+00	10878.939	3432.712
13	9.349E+04	1.541E+03	3.148E+02	4.735E+00	4.878E+01	1.199E+00	1.290E+03	2.293E+00	3.017E+02	5.167E+00	1.379E+01	6.894E+00	5047.445	2519.051
14	3.980E+04	1.540E+03	1.679E+02	3.197E+00	2.105E+01	1.096E+00	7.566E+02	2.294E+00	1.278E+02	4.893E+00	1.208E+01	1.258E+01	4420.163	4598.790
Total:	*2927465.9898*		*4332.0998*		*1333.5332*		*11029.2453*		*9244.1152*					

Plateau Age: Not determined

Isochron Age: Not determined

APPENDIX 4: EPMA DATA

All oxides in weight %. Total iron expressed as FeO.

A4.1 Torfajökull rhyolite lavas

	SiO_2	TiO_2	Al_2O_3	MgO	CaO	MnO	FeO	Na_2O	K_2O	Total
RFR - Kirkjufell	75.38	0.24	12.21	0.01	0.35	0.07	2.54	5.46	4.20	100.49
TJ99-2	75.00	0.13	12.22	0.01	0.34	0.10	2.45	5.34	4.19	99.77
n=18	75.41	0.23	12.27	0.01	0.32	0.08	2.55	5.33	4.21	100.38
Analytical period 2	75.06	0.18	12.00	0.00	0.33	0.08	2.62	5.43	4.19	99.90
	74.86	0.22	12.16	0.01	0.36	0.09	2.56	5.15	4.17	99.61
	75.06	0.19	12.17	0.00	0.35	0.09	2.58	5.32	4.16	99.93
	75.30	0.19	12.08	0.00	0.31	0.08	2.53	5.31	4.16	99.98
	74.69	0.19	11.92	0.00	0.33	0.09	2.42	5.03	4.18	98.85
	74.88	0.21	12.32	0.01	0.34	0.09	2.67	5.42	4.16	100.11
	74.88	0.18	12.20	0.01	0.35	0.09	2.60	5.54	4.19	100.02
	74.96	0.22	12.33	0.00	0.36	0.09	2.65	5.55	4.18	100.35
	74.74	0.21	12.23	0.01	0.35	0.10	2.67	5.54	4.16	100.00
	74.72	0.22	12.36	0.02	0.37	0.09	2.59	5.58	4.19	100.17
	75.07	0.20	12.09	0.01	0.34	0.09	2.64	5.42	4.13	100.00
	75.09	0.20	12.21	0.02	0.35	0.08	2.56	5.44	4.12	100.08
	75.01	0.18	12.17	0.00	0.35	0.09	2.59	5.43	4.19	100.00
	74.92	0.23	12.04	0.02	0.35	0.09	2.65	5.29	4.13	99.71
	75.06	0.21	11.95	0.03	0.35	0.08	2.57	5.41	4.16	99.80
Mean	75.01	0.20	12.16	0.01	0.34	0.09	2.58	5.39	4.17	99.95
St. dev.	0.21	0.03	0.13	0.01	0.01	0.01	0.07	0.14	0.02	0.36
Mean of normalised data	75.04	0.20	12.17	0.01	0.34	0.09	2.58	5.39	4.17	100.00
St. dev. of normalised data	0.23	0.02	0.10	0.01	0.01	0.01	0.06	0.13	0.03	0.00
RFR - Kirkjufell	74.90	0.16	12.42	0.02	0.36	0.09	2.56	5.46	4.14	100.12
TJ99-4	74.74	0.24	12.51	0.00	0.36	0.09	2.58	5.66	4.14	100.31
n=19	74.70	0.20	12.72	0.02	0.38	0.10	2.62	5.38	4.13	100.24
Analytical period 2	74.66	0.22	12.70	0.02	0.37	0.09	2.59	5.61	4.15	100.42
	74.58	0.22	12.63	0.00	0.37	0.08	2.60	5.33	4.13	99.95
	74.61	0.22	12.56	0.01	0.36	0.10	2.53	5.49	4.16	100.04
	74.76	0.20	12.35	0.02	0.34	0.09	2.58	5.70	4.14	100.19
	75.00	0.24	12.51	0.01	0.34	0.10	2.55	5.38	4.10	100.27
	74.90	0.19	12.36	0.01	0.38	0.09	2.70	5.45	4.15	100.23
	74.78	0.22	12.33	0.02	0.37	0.09	2.60	5.72	4.12	100.26
	75.10	0.20	12.51	0.01	0.36	0.10	2.63	5.74	4.15	100.81
	75.07	0.16	12.31	0.00	0.37	0.12	2.75	5.51	4.16	100.44
	74.76	0.16	12.52	0.01	0.37	0.11	2.61	5.45	4.15	100.13
	74.88	0.21	12.46	0.01	0.36	0.10	2.58	5.47	4.12	100.19

	SiO_2	TiO_2	Al_2O_3	MgO	CaO	MnO	FeO	Na_2O	K_2O	Total
	74.72	0.22	12.39	0.01	0.35	0.09	2.58	5.46	4.15	99.98
	74.45	0.20	12.48	0.00	0.35	0.09	2.65	5.48	4.19	99.89
	74.68	0.24	12.60	0.01	0.35	0.10	2.52	5.58	4.15	100.26
	75.01	0.23	12.18	0.01	0.38	0.09	2.66	5.44	4.14	100.14
	74.90	0.22	12.25	0.01	0.37	0.10	2.62	5.46	4.14	100.05
Mean	74.80	0.21	12.46	0.01	0.36	0.09	2.60	5.51	4.14	100.21
St. dev.	0.17	0.03	0.15	0.01	0.01	0.01	0.06	0.12	0.02	0.21
Mean of normalised data	74.65	0.21	12.44	0.01	0.36	0.09	2.60	5.50	4.13	100.00
St. dev. of normalised data	0.15	0.03	0.15	0.01	0.01	0.01	0.05	0.11	0.02	0.00
RFR - Illihnúkur	73.94	0.30	13.12	0.02	0.43	0.12	2.65	5.47	4.39	100.45
TJ97-16	74.34	0.30	13.07	0.06	0.48	0.10	2.66	5.14	4.53	100.68
n=21	74.69	0.32	12.98	0.02	0.39	0.10	2.49	5.31	4.46	100.75
Analytical period 2	74.50	0.24	12.81	0.04	0.38	0.12	2.72	5.27	4.36	100.47
	74.18	0.28	13.26	0.03	0.40	0.10	2.63	5.29	4.40	100.59
	74.20	0.28	13.01	0.04	0.41	0.13	2.82	5.65	4.37	100.91
	74.69	0.36	12.80	0.00	0.35	0.11	2.01	5.20	4.44	99.96
	74.61	0.28	13.32	0.04	0.37	0.10	2.62	5.38	4.39	101.12
	74.27	0.24	13.14	0.05	0.41	0.11	2.77	5.53	4.38	100.93
	74.17	0.31	13.16	0.05	0.43	0.10	2.69	5.39	4.43	100.76
	74.37	0.27	12.89	0.04	0.45	0.10	2.60	5.55	4.43	100.71
	74.02	0.26	13.10	0.04	0.43	0.10	2.60	5.34	4.38	100.27
	73.79	0.23	13.05	0.03	0.40	0.09	2.63	5.59	4.39	100.25
	74.22	0.28	13.05	0.06	0.41	0.12	2.76	5.69	4.36	100.98
	74.22	0.23	12.97	0.04	0.40	0.13	2.86	5.55	4.34	100.76
	73.69	0.22	13.08	0.05	0.43	0.12	2.76	5.58	4.38	100.31
	74.21	0.29	12.85	0.05	0.46	0.13	2.82	6.31	3.77	100.92
	74.35	0.27	13.13	0.04	0.43	0.12	2.69	5.73	4.35	101.12
	74.31	0.26	13.16	0.04	0.44	0.11	2.82	5.44	4.38	100.96
	73.81	0.29	13.07	0.06	0.77	0.13	2.79	5.50	4.30	100.71
	73.90	0.27	13.13	0.05	0.43	0.12	2.87	5.45	4.32	100.55
Mean	74.21	0.27	13.05	0.04	0.43	0.11	2.68	5.49	4.36	100.67
St. dev.	0.28	0.03	0.14	0.01	0.08	0.01	0.18	0.24	0.14	0.31
Mean of normalised data	73.72	0.27	12.97	0.04	0.43	0.11	2.66	5.46	4.33	100.00
St. dev. of normalised data	0.31	0.03	0.13	0.01	0.08	0.01	0.18	0.24	0.15	0.00
RFR - Illihnúkur	74.74	0.24	13.24	0.03	0.49	0.13	2.60	5.40	4.38	101.28
TJ97-18	74.88	0.28	13.29	0.05	0.52	0.11	2.64	5.46	4.26	101.50
n=14	74.59	0.25	13.32	0.04	0.51	0.13	2.56	5.52	4.39	101.33
Analytical period 3	74.69	0.25	13.25	0.04	0.53	0.11	2.66	5.51	4.37	101.44
	74.46	0.26	13.09	0.03	0.48	0.11	2.55	5.45	4.28	100.71
	74.73	0.24	13.22	0.04	0.52	0.13	2.68	5.36	4.38	101.34
	74.55	0.26	13.04	0.04	0.50	0.13	2.67	5.54	3.91	100.64
	74.87	0.25	13.05	0.03	0.46	0.11	2.60	5.35	4.31	101.03

	SiO_2	TiO_2	Al_2O_3	MgO	CaO	MnO	FeO	Na_2O	K_2O	Total
	74.62	0.25	12.98	0.04	0.50	0.11	2.62	5.56	4.33	101.02
	74.21	0.24	13.05	0.03	0.51	0.10	2.64	5.33	4.31	100.46
	74.75	0.24	13.15	0.04	0.51	0.14	2.63	5.33	4.37	101.18
	74.64	0.26	13.22	0.03	0.51	0.13	2.63	5.41	4.31	101.14
	74.75	0.26	13.11	0.04	0.45	0.11	2.67	5.20	4.34	100.96
	74.76	0.27	13.08	0.03	0.49	0.12	2.60	5.31	4.37	101.03
Mean	74.66	0.25	13.15	0.04	0.50	0.12	2.63	5.41	4.31	101.08
St. dev.	0.17	0.01	0.11	0.01	0.02	0.01	0.04	0.10	0.12	0.31
Mean of normalised data	73.87	0.25	13.01	0.04	0.49	0.12	2.60	5.35	4.26	100.00
St. dev. of normalised data	0.15	0.01	0.08	0.01	0.02	0.01	0.04	0.10	0.11	0.00
RFR - Laufafell	76.44	0.20	12.16	0.00	0.37	0.07	2.33	5.27	4.19	101.04
JM-40	76.60	0.24	12.32	0.00	0.39	0.09	2.34	5.00	4.26	101.24
n=19	76.47	0.24	12.28	0.03	0.39	0.09	2.41	5.01	4.27	101.20
Analytical period 2	76.59	0.15	12.33	0.02	0.35	0.10	2.33	5.03	4.24	101.14
	76.62	0.20	12.30	0.01	0.41	0.08	2.34	5.14	4.29	101.40
	76.39	0.21	12.10	0.03	0.37	0.07	2.32	4.84	4.23	100.61
	76.66	0.15	12.37	0.00	0.38	0.09	2.26	4.77	4.33	101.05
	75.09	0.18	11.82	0.02	0.34	0.08	2.33	4.75	4.22	98.84
	76.56	0.21	12.17	0.01	0.39	0.10	2.41	4.57	4.32	100.74
	76.66	0.19	12.20	0.02	0.38	0.07	2.32	5.12	4.35	101.32
	76.43	0.24	12.00	0.01	0.36	0.06	2.29	4.91	4.32	100.62
	76.43	0.23	12.21	0.01	0.37	0.11	2.39	4.54	4.49	100.81
	76.29	0.23	12.31	0.04	0.38	0.08	2.31	4.84	4.55	101.03
	76.38	0.23	12.35	0.01	0.39	0.08	2.38	4.87	4.44	101.13
	76.48	0.25	12.14	0.01	0.34	0.10	2.22	4.73	4.39	100.64
	76.05	0.18	12.41	0.00	0.40	0.10	2.38	4.85	4.34	100.72
	76.22	0.23	12.39	0.01	0.40	0.09	2.31	4.84	4.30	100.79
	76.03	0.19	12.07	0.02	0.37	0.10	2.39	4.72	4.33	100.25
	75.81	0.21	11.99	0.02	0.37	0.11	2.46	4.79	4.37	100.13
Mean	76.33	0.21	12.21	0.01	0.38	0.09	2.34	4.87	4.33	100.77
St. dev.	0.38	0.03	0.16	0.01	0.02	0.01	0.06	0.19	0.09	0.58
Mean of normalised data	75.74	0.21	12.11	0.01	0.37	0.09	2.33	4.84	4.29	100.00
St. dev. of normalised data	0.17	0.03	0.11	0.01	0.02	0.01	0.06	0.17	0.09	0.00
RFR - Rauðfossafjöll	76.53	0.21	12.38	0.00	0.36	0.07	2.48	4.98	4.23	101.24
TJ97-29	76.25	0.23	12.40	0.00	0.41	0.11	2.46	5.17	4.20	101.22
n=10	76.15	0.19	12.10	0.00	0.39	0.11	2.46	4.70	4.24	100.36
Analytical period 2	75.88	0.21	12.28	0.01	0.41	0.12	2.54	4.97	4.16	100.59
	75.92	0.21	12.36	0.00	0.40	0.06	2.43	5.31	4.27	101.02
	75.17	0.23	12.18	0.00	0.40	0.08	2.45	5.26	4.25	100.01
	75.71	0.18	12.33	0.00	0.39	0.07	2.52	5.15	4.23	100.61
	75.55	0.19	12.23	0.00	0.41	0.07	2.56	4.95	4.25	100.24
	75.02	0.15	12.11	0.01	0.39	0.10	2.47	4.72	4.31	99.28

	SiO_2	TiO_2	Al_2O_3	MgO	CaO	MnO	FeO	Na_2O	K_2O	Total
	75.51	0.22	12.12	0.01	0.37	0.09	2.45	5.18	4.33	100.28
Mean	75.77	0.20	12.25	0.00	0.39	0.09	2.48	5.04	4.25	100.49
St. dev.	0.47	0.02	0.12	0.00	0.02	0.02	0.04	0.21	0.05	0.60
Mean of normalised data	75.40	0.20	12.19	0.00	0.39	0.09	2.47	5.01	4.23	100.00
St. dev. of normalised data	0.22	0.02	0.07	0.00	0.02	0.02	0.05	0.20	0.07	0.00
RFR - Rauðfossafjöll	76.23	0.24	12.55	0.01	0.41	0.08	2.40	5.32	4.26	101.51
TJ98-18	76.10	0.21	12.59	0.02	0.41	0.11	2.40	5.24	4.25	101.35
n=13	76.44	0.26	12.63	0.02	0.40	0.09	2.39	5.39	4.25	101.88
Analytical period 3	76.18	0.23	12.63	0.02	0.41	0.09	2.34	4.86	4.23	101.04
	76.55	0.20	12.55	0.02	0.40	0.08	2.41	5.42	4.25	101.89
	76.65	0.20	12.56	0.03	0.40	0.09	2.36	5.37	4.25	101.91
	76.41	0.20	12.57	0.02	0.40	0.08	2.41	4.91	4.23	101.24
	76.22	0.22	12.62	0.02	0.41	0.09	2.40	5.01	4.25	101.24
	76.40	0.24	12.57	0.00	0.38	0.10	2.37	5.34	4.28	101.70
	76.30	0.22	12.62	0.01	0.72	0.11	2.35	5.08	4.22	101.65
	76.49	0.20	12.60	0.02	0.38	0.08	2.35	5.19	4.26	101.57
	76.59	0.22	12.48	0.00	0.38	0.10	2.30	5.25	4.25	101.58
	76.83	0.21	12.56	0.02	0.36	0.08	2.21	5.02	4.25	101.55
Mean	76.41	0.22	12.58	0.02	0.42	0.09	2.36	5.18	4.25	101.55
St. dev.	0.21	0.02	0.04	0.01	0.09	0.01	0.06	0.19	0.02	0.27
Mean of normalised data	75.25	0.22	12.39	0.02	0.41	0.09	2.32	5.11	4.18	100.00
St. dev. of normalised data	0.19	0.02	0.06	0.01	0.09	0.01	0.06	0.18	0.02	0.00
RFR - Rauðfossafjöll	75.31	0.36	13.16	0.08	0.46	0.13	2.11	5.02	4.18	100.86
TJ98-43	75.38	0.40	12.95	0.14	0.43	0.11	2.32	5.17	4.19	101.14
n=10	75.34	0.32	12.91	0.13	0.48	0.10	2.17	5.03	4.25	100.76
Analytical period 2	75.05	0.35	12.85	0.10	0.48	0.14	2.23	4.83	4.19	100.24
	75.64	0.30	13.11	0.11	0.46	0.11	2.44	5.02	4.26	101.46
	75.55	0.31	12.90	0.10	0.39	0.09	2.19	4.95	4.26	100.74
	75.20	0.37	13.01	0.09	0.45	0.10	2.15	4.92	4.22	100.51
	75.07	0.41	12.98	0.11	0.46	0.10	2.26	4.97	4.24	100.64
	74.72	0.34	13.04	0.11	0.48	0.12	2.24	5.18	4.24	100.51
	74.88	0.31	12.86	0.12	0.49	0.15	2.33	5.10	4.17	100.44
Mean	75.21	0.35	12.98	0.11	0.46	0.12	2.24	5.02	4.22	100.73
St. dev.	0.29	0.04	0.10	0.02	0.03	0.02	0.10	0.11	0.03	0.36
Mean of normalised data	74.67	0.34	12.88	0.11	0.45	0.11	2.23	4.98	4.19	100.00
St. dev. of normalised data	0.19	0.04	0.09	0.02	0.03	0.02	0.09	0.10	0.03	0.00
Unnamed ridge A	74.45	0.21	12.98	0.04	0.38	0.06	2.69	5.20	4.54	100.55
TJ98-05	74.19	0.19	13.21	0.03	0.37	0.10	2.66	5.31	4.56	100.62
n=10	73.84	0.21	13.05	0.05	0.38	0.03	2.45	5.30	4.63	99.96
Analytical period 2	74.47	0.13	13.27	0.05	0.40	0.05	2.62	5.04	4.52	100.57

	SiO_2	TiO_2	Al_2O_3	MgO	CaO	MnO	FeO	Na_2O	K_2O	Total
	74.27	0.24	13.23	0.04	0.34	0.05	2.37	5.36	4.64	100.55
	74.63	0.17	13.39	0.05	0.40	0.06	2.33	5.30	4.55	100.90
	74.50	0.23	13.06	0.05	0.28	0.06	2.64	5.10	4.67	100.61
	74.77	0.27	12.71	0.07	0.49	0.07	2.86	5.21	4.37	100.82
	74.18	0.21	12.80	0.07	0.78	0.08	2.96	5.29	4.34	100.77
	74.54	0.20	13.23	0.04	0.38	0.06	2.68	5.31	4.66	101.10
Mean	74.38	0.21	13.09	0.05	0.42	0.06	2.63	5.24	4.55	100.65
St. dev.	0.27	0.04	0.22	0.01	0.14	0.02	0.20	0.10	0.11	0.30
Mean of normalised data	73.91	0.20	13.01	0.05	0.42	0.06	2.61	5.21	4.52	100.00
St. dev. of normalised data	0.18	0.04	0.21	0.01	0.14	0.02	0.20	0.10	0.12	0.00
Unnamed ridge B	74.35	0.24	12.74	0.01	0.32	0.09	3.11	5.38	4.31	100.55
TJ97-09	74.36	0.22	12.70	0.01	0.27	0.11	3.44	5.88	4.30	101.32
n=11	74.22	0.29	12.68	0.01	0.25	0.10	3.39	5.54	4.30	100.79
Analytical period 3	74.12	0.26	12.74	0.03	0.29	0.10	3.52	5.77	4.28	101.10
	74.35	0.23	12.75	0.01	0.35	0.08	3.21	5.60	4.32	100.90
	74.15	0.26	12.71	0.02	0.39	0.09	3.35	5.46	4.30	100.73
	74.20	0.23	12.85	0.01	0.24	0.11	3.41	5.75	4.28	101.08
	74.05	0.23	12.64	0.00	0.29	0.10	3.54	5.50	4.26	100.65
	74.08	0.24	12.71	0.01	0.26	0.10	3.38	5.67	4.31	100.77
	74.31	0.26	12.76	0.01	0.24	0.08	3.36	5.35	4.32	100.70
	74.31	0.25	12.86	0.02	0.28	0.09	3.40	5.69	4.28	101.21
Mean	74.23	0.25	12.74	0.01	0.29	0.10	3.37	5.60	4.30	100.89
St. dev.	0.12	0.02	0.07	0.01	0.05	0.01	0.12	0.17	0.02	0.25
Mean of normalised data	73.57	0.24	12.63	0.01	0.29	0.09	3.34	5.55	4.26	100.00
St. dev. of normalised data	0.19	0.02	0.06	0.01	0.05	0.01	0.12	0.16	0.02	0.00
Unnamed ridge B	73.87	0.24	12.70	0.02	0.55	0.11	3.62	6.00	4.23	101.36
TJ97-12	73.67	0.23	12.76	0.02	0.55	0.11	3.56	5.66	4.25	100.84
n=15	73.81	0.26	12.86	0.04	0.54	0.11	3.56	6.05	4.27	101.52
Analytical period 3	73.68	0.25	12.70	0.01	0.55	0.11	3.56	5.77	4.27	100.92
	73.77	0.23	12.68	0.01	0.55	0.11	3.59	5.61	4.26	100.85
	73.89	0.24	12.74	0.02	0.56	0.11	3.56	5.95	4.25	101.32
	73.76	0.25	12.72	0.03	0.53	0.11	3.58	5.85	4.24	101.08
	73.76	0.26	12.76	0.03	0.55	0.11	3.61	5.71	4.24	101.02
	73.73	0.24	12.68	0.02	0.54	0.11	3.52	5.73	4.23	100.81
	73.94	0.24	12.72	0.00	0.57	0.09	3.60	5.76	4.23	101.17
	73.95	0.22	12.79	0.02	0.57	0.10	3.53	5.64	4.27	101.10
	73.89	0.27	12.64	0.02	0.55	0.12	3.63	5.43	4.26	100.82
	73.71	0.25	12.73	0.02	0.55	0.11	3.56	5.93	4.28	101.14
	73.83	0.25	12.61	0.01	0.55	0.12	3.53	5.72	4.27	100.89
	73.85	0.25	12.71	0.02	0.58	0.12	3.52	5.83	4.27	101.17
Mean	73.81	0.25	12.72	0.02	0.55	0.11	3.57	5.78	4.25	101.07
St. dev.	0.09	0.01	0.06	0.01	0.01	0.01	0.04	0.16	0.02	0.22

	SiO_2	TiO_2	Al_2O_3	MgO	CaO	MnO	FeO	Na_2O	K_2O	Total
Mean of normalised data	73.03	0.24	12.59	0.02	0.55	0.11	3.53	5.71	4.21	100.00
St. dev. of normalised data	0.15	0.01	0.05	0.01	0.01	0.01	0.04	0.15	0.02	0.00
Bláhnúkur	71.26	0.24	14.53	0.14	0.67	0.10	2.41	5.95	4.54	99.86
TJ98-40	71.42	0.23	14.69	0.16	0.68	0.07	2.42	5.55	4.54	99.77
n=15	71.98	0.19	14.72	0.12	0.51	0.06	2.01	5.99	4.55	100.14
Analytical period 3	71.45	0.25	14.69	0.14	0.64	0.08	2.46	5.72	4.59	100.06
	71.33	0.23	14.63	0.13	0.65	0.07	2.40	5.69	4.62	99.77
	71.66	0.24	14.57	0.13	0.59	0.08	2.35	5.79	4.60	100.01
	71.59	0.24	14.56	0.17	0.78	0.07	2.52	5.70	4.50	100.14
	71.60	0.22	14.45	0.16	0.73	0.07	2.49	5.80	4.50	100.07
	71.58	0.22	14.41	0.13	0.69	0.08	2.47	5.62	4.53	99.74
	71.63	0.23	14.56	0.12	0.57	0.08	2.28	5.75	4.25	99.49
	71.53	0.21	14.55	0.14	0.73	0.08	2.42	5.66	4.51	99.86
	71.69	0.20	14.51	0.12	0.67	0.06	2.41	5.73	4.56	99.95
	71.68	0.22	14.53	0.14	0.67	0.07	2.46	5.81	4.52	100.10
	71.70	0.20	14.62	0.12	0.62	0.06	2.32	5.88	4.54	100.08
	71.83	0.20	14.56	0.14	0.68	0.07	2.42	6.11	4.48	100.50
Mean	71.68	0.21	14.56	0.13	0.66	0.07	2.39	5.82	4.48	100.00
St. dev.	0.10	0.01	0.04	0.01	0.06	0.01	0.07	0.16	0.11	0.33
Mean of normalised data	71.62	0.22	14.58	0.14	0.66	0.07	2.39	5.78	4.52	100.00
St. dev. of normalised data	0.17	0.02	0.09	0.02	0.07	0.01	0.12	0.14	0.08	0.00
Hábarmur	76.48	0.25	10.83	0.01	0.04	0.05	3.02	4.74	4.55	99.96
TJ97-14	75.15	0.22	10.76	0.00	0.08	0.09	3.72	4.80	4.62	99.45
n=15	74.85	0.30	10.48	0.00	0.28	0.12	4.15	4.60	4.74	99.53
Analytical period 3	74.26	0.27	10.53	0.00	0.14	0.08	4.35	4.74	4.76	99.15
	75.31	0.28	10.60	0.00	0.02	0.08	4.20	4.93	4.64	100.07
	75.27	0.26	10.45	0.01	0.33	0.13	4.69	5.51	3.86	100.52
	76.19	0.26	10.37	0.00	0.10	0.08	3.85	5.42	3.64	99.93
	73.22	0.37	10.51	0.01	0.23	0.15	4.97	5.66	3.72	98.85
	74.91	0.32	10.21	0.00	0.16	0.15	4.58	5.71	3.54	99.58
	74.65	0.28	10.40	0.01	0.38	0.11	4.16	5.87	3.22	99.11
	74.92	0.27	10.63	0.01	0.28	0.10	4.48	5.45	3.80	99.96
	75.15	0.27	10.76	0.00	0.02	0.08	4.31	5.67	3.69	99.95
	74.45	0.33	10.25	0.01	0.82	0.16	5.09	5.62	3.79	100.52
	74.60	0.26	10.53	0.00	0.24	0.07	4.08	5.66	3.77	99.22
	75.44	0.27	10.20	0.01	0.49	0.09	4.40	5.04	3.99	99.97
Mean	74.99	0.28	10.50	0.00	0.24	0.10	4.27	5.29	4.02	99.72
St. dev.	0.77	0.04	0.20	0.01	0.21	0.03	0.51	0.43	0.50	0.50
Mean of normalised data	75.20	0.28	10.53	0.00	0.24	0.10	4.28	5.31	4.03	100.00
St. dev. of normalised data	0.65	0.04	0.21	0.01	0.21	0.03	0.51	0.44	0.50	0.00

	SiO_2	TiO_2	Al_2O_3	MgO	CaO	MnO	FeO	Na_2O	K_2O	Total
North Hábarmur	75.84	0.23	10.60	0.00	0.16	0.11	4.13	5.17	4.49	100.75
TJ98-34	75.91	0.26	10.78	0.00	0.12	0.16	3.92	5.27	4.50	100.97
n=10	75.42	0.28	10.89	0.00	0.28	0.12	4.03	5.48	4.54	101.04
Analytical period 2	75.75	0.24	10.91	0.00	0.18	0.14	4.20	5.49	4.47	101.37
	75.58	0.30	10.94	0.00	0.14	0.11	4.03	5.44	4.42	100.95
	75.40	0.32	10.90	0.00	0.11	0.07	3.96	5.35	4.49	100.63
	74.03	0.31	10.60	0.00	0.41	0.16	4.23	5.32	4.32	99.40
	75.55	0.31	10.90	0.00	0.13	0.08	3.93	5.62	4.46	100.99
	75.15	0.26	10.81	0.00	0.17	0.12	3.94	5.41	4.49	100.36
	75.07	0.22	10.83	0.00	0.15	0.11	4.01	5.65	4.42	100.53
Mean	75.37	0.27	10.82	0.00	0.19	0.12	4.04	5.42	4.46	100.70
St. dev.	0.54	0.04	0.12	0.00	0.09	0.03	0.11	0.15	0.06	0.54
Mean of normalised data	74.85	0.27	10.74	0.00	0.18	0.12	4.01	5.38	4.43	100.00
St. dev. of normalised data	0.24	0.04	0.10	0.00	0.09	0.03	0.12	0.14	0.05	0.00
Gvendarhyrna	75.81	0.23	9.78	0.00	0.23	0.12	4.40	4.91	4.41	99.90
TJ97-22	75.59	0.33	9.78	0.00	0.22	0.10	4.32	5.23	4.46	100.04
n=12	75.97	0.23	9.85	0.01	0.23	0.14	4.27	5.08	4.43	100.20
Analytical period 2	75.86	0.30	9.93	0.01	0.20	0.12	4.41	4.82	4.43	100.09
	76.24	0.27	9.88	0.00	0.20	0.10	4.36	4.85	4.45	100.35
	75.78	0.24	9.91	0.02	0.23	0.13	4.31	5.08	4.43	100.14
	75.82	0.26	9.74	0.00	0.26	0.10	4.20	4.78	4.46	99.62
	76.20	0.22	9.87	0.00	0.21	0.10	4.20	5.13	4.50	100.42
	76.12	0.31	9.89	0.01	0.22	0.06	4.21	4.93	4.45	100.22
	76.02	0.28	9.72	0.01	0.21	0.12	4.36	4.93	4.51	100.15
	75.66	0.26	9.72	0.00	0.23	0.12	4.40	5.05	4.51	99.94
	75.84	0.25	9.78	0.01	0.20	0.09	4.41	4.71	4.62	99.92
Mean	75.91	0.27	9.82	0.01	0.22	0.11	4.32	4.96	4.47	100.08
St. dev.	0.20	0.03	0.08	0.01	0.02	0.02	0.08	0.16	0.06	0.22
Mean of normalised data	75.85	0.26	9.81	0.01	0.22	0.11	4.32	4.95	4.47	100.00
St. dev. of normalised data	0.15	0.03	0.06	0.01	0.02	0.02	0.08	0.15	0.06	0.00

A4.2 Thórsmörk Ignimbrite fiamme

	SiO_2	TiO_2	Al_2O_3	MgO	CaO	MnO	FeO	Na_2O	K_2O	Total
JM-252	74.40	0.14	11.78	0.00	0.50	0.03	2.22	4.12	5.31	98.50
n=10	75.46	0.12	11.95	0.00	0.10	0.04	2.07	4.36	5.42	99.53
Analytical period 2	75.17	0.19	11.98	0.00	0.33	0.06	2.13	4.14	5.21	99.21
	75.10	0.15	11.89	0.00	0.29	0.07	2.44	4.07	5.30	99.31
	76.02	0.15	12.20	0.00	0.05	0.04	1.59	4.29	5.35	99.71
	74.89	0.22	12.09	0.01	0.05	0.03	2.54	4.21	5.38	99.42
	74.53	0.17	12.01	0.00	0.68	0.10	3.24	4.69	5.24	100.66
	73.69	0.19	11.82	0.01	0.55	0.04	3.40	4.87	4.81	99.39
	75.82	0.18	12.12	0.00	0.21	0.04	2.50	5.88	2.98	99.74
	76.41	0.14	12.26	0.00	0.21	0.05	2.44	5.88	2.91	100.37
Mean	75.15	0.17	12.01	0.00	0.30	0.05	2.46	4.65	4.79	99.58
St. dev.	0.82	0.03	0.16	0.00	0.22	0.02	0.54	0.70	0.99	0.60
Mean of normalised data	75.46	0.17	12.06	0.00	0.30	0.05	2.47	4.67	4.81	100.00
St. dev. of normalised data	0.77	0.03	0.12	0.00	0.22	0.02	0.53	0.68	1.00	0.00
JM-253	74.69	0.16	12.06	0.00	0.53	0.08	2.61	4.19	5.62	99.94
n=8	74.34	0.14	11.72	0.00	0.27	0.07	2.70	4.08	5.59	98.91
Analytical period 2	74.59	0.20	11.95	0.00	0.53	0.07	2.32	4.19	5.74	99.62
	74.32	0.21	11.93	0.00	0.43	0.06	2.64	4.03	5.57	99.21
	74.36	0.16	11.93	0.00	0.63	0.07	2.79	4.20	5.54	99.69
	73.82	0.15	11.83	0.00	0.62	0.11	3.00	4.32	5.54	99.38
	74.05	0.16	12.01	0.01	0.34	0.06	2.44	4.16	5.61	98.83
	75.14	0.20	12.13	0.01	0.23	0.07	2.25	4.38	5.52	99.94
Mean	74.41	0.17	11.95	0.00	0.45	0.07	2.59	4.19	5.59	99.44
St. dev.	0.40	0.03	0.13	0.00	0.15	0.02	0.25	0.11	0.07	0.43
Mean of normalised data	74.83	0.17	12.01	0.00	0.45	0.07	2.61	4.22	5.62	100.00
St. dev. of normalised data	0.30	0.03	0.11	0.00	0.15	0.02	0.25	0.11	0.08	0.00

A4.3 Tindfjallajökull rhyolite lavas

	SiO_2	TiO_2	Al_2O_3	MgO	CaO	MnO	FeO	Na_2O	K_2O	Total
JM-130	74.13	0.39	10.60	0.04	0.56	0.10	3.86	2.41	5.12	97.23
n=15	73.6	0.34	11	0.03	0.69	0.1	3.81	3.57	4.05	97.26
Analytical period 3	74.12	0.36	10.31	0.05	0.57	0.11	3.99	2.63	4.91	97.09
	74.80	0.32	11.23	0.04	0.81	0.12	3.74	4.20	3.74	99.18
	74.58	0.35	10.81	0.03	0.51	0.12	3.65	2.27	4.00	96.38
	75.24	0.34	10.93	0.04	0.54	0.11	3.67	2.95	4.15	98.02
	74.33	0.34	10.82	0.05	0.66	0.12	4.20	2.94	4.34	97.86
	74.71	0.35	10.72	0.03	0.55	0.12	3.77	1.97	4.07	96.33
	74.96	0.34	10.74	0.05	0.58	0.12	4.03	2.31	4.13	97.28
	75.78	0.33	11.14	0.03	0.47	0.1	3.52	3.2	4.39	99.01
	75.02	0.3	10.87	0.04	0.51	0.1	3.6	1.66	3.61	95.73
	74.71	0.33	10.86	0.04	0.62	0.12	3.98	2.07	3.79	96.54
	73.97	0.33	10.61	0.06	0.58	0.12	3.89	1.68	3.75	95.01
	74.99	0.31	10.89	0.03	0.54	0.11	3.69	1.82	3.48	95.92
	74.65	0.33	10.64	0.04	0.55	0.12	3.75	2.21	4.75	97.12
Mean	74.64	0.34	10.81	0.04	0.58	0.11	3.81	2.53	4.15	97.06
St. dev.	0.55	0.02	0.23	0.01	0.08	0.01	0.18	0.73	0.48	1.15
Mean of normalised data	76.90	0.35	11.14	0.04	0.60	0.12	3.93	2.60	4.28	100.00
St. dev. of normalised data	0.89	0.02	0.20	0.01	0.08	0.01	0.20	0.72	0.48	0.00
JM-147	73.51	0.19	11.43	0.00	0.52	0.12	3.30	4.78	3.87	97.73
n=11	74.36	0.20	10.79	0.01	0.44	0.13	3.15	4.46	4.27	97.84
Analytical period 3	73.53	0.17	12.31	0.01	0.65	0.11	3.02	5.38	3.72	98.92
	74.31	0.26	11.45	0.02	0.56	0.11	3.41	4.87	3.55	98.56
	73.13	0.27	11.81	0.03	0.61	0.12	3.47	4.03	4.31	97.78
	72.64	0.25	11.99	0.03	0.63	0.13	3.64	4.40	4.34	98.08
	73.55	0.25	11.55	0.02	0.68	0.12	3.37	4.68	3.54	97.78
	73.28	0.24	11.94	0.01	0.53	0.12	3.25	4.22	4.45	98.04
	74.10	0.24	10.94	0.01	0.55	0.11	3.47	4.13	4.18	97.74
	74.72	0.23	10.68	0.01	0.47	0.12	3.48	4.67	4.18	98.56
	72.97	0.20	11.53	0.01	0.58	0.11	3.22	5.62	3.82	98.07
Mean	73.65	0.23	11.49	0.01	0.57	0.12	3.34	4.66	4.02	98.10
St. dev.	0.65	0.03	0.52	0.01	0.07	0.01	0.18	0.50	0.33	0.40
Mean of normalised data	75.07	0.23	11.72	0.01	0.58	0.12	3.41	4.75	4.10	100.00
St. dev. of normalised data	0.66	0.03	0.52	0.01	0.08	0.01	0.18	0.50	0.34	0.00
JM-80	74.87	0.25	12.30	0.01	0.47	0.09	3.46	5.71	3.72	100.86
n=12	74.81	0.24	12.34	0.00	0.43	0.09	3.37	5.81	3.70	100.83
Analytical period 3	74.71	0.21	12.28	0.01	0.41	0.10	3.34	5.82	3.70	100.57
	74.64	0.23	12.44	0.01	0.45	0.10	3.50	5.91	3.72	101.00
	74.62	0.22	12.40	0.00	0.43	0.08	3.54	5.90	3.69	100.89
	74.85	0.20	12.31	0.00	0.42	0.10	3.55	5.68	3.72	100.82

	SiO_2	TiO_2	Al_2O_3	MgO	CaO	MnO	FeO	Na_2O	K_2O	Total
	74.34	0.23	12.34	0.02	0.43	0.11	3.42	5.92	3.67	100.47
	74.44	0.25	12.29	0.01	0.42	0.11	3.40	5.99	3.68	100.59
	74.49	0.22	12.31	0.01	0.44	0.09	3.45	6.03	3.70	100.75
	74.69	0.22	12.23	0.01	0.45	0.11	3.36	6.03	3.72	100.81
	74.87	0.20	12.37	0.00	0.43	0.09	3.46	5.93	3.66	101.03
	74.51	0.23	12.35	0.02	0.43	0.08	3.32	5.94	3.71	100.59
Mean	74.65	0.22	12.33	0.01	0.43	0.10	3.43	5.89	3.70	100.77
St. dev.	0.18	0.02	0.06	0.01	0.02	0.01	0.08	0.12	0.02	0.18
Mean of normalised data	74.08	0.22	12.24	0.01	0.43	0.09	3.41	5.84	3.67	100.00
St. dev. of normalised data	0.13	0.02	0.05	0.01	0.01	0.01	0.07	0.12	0.02	0.00
JM-37	74.45	0.30	12.27	0.00	0.63	0.12	3.76	5.03	3.59	100.18
n=13	74.62	0.29	12.35	0.00	0.62	0.12	3.61	5.75	3.59	100.98
Analytical period 3	74.43	0.30	12.23	0.00	0.63	0.13	3.50	5.68	3.61	100.51
	74.43	0.35	12.36	0.00	0.56	0.12	3.66	5.63	3.54	100.68
	74.59	0.31	12.18	0.00	0.63	0.11	3.75	5.55	3.57	100.71
	74.47	0.33	12.16	0.00	0.62	0.12	3.68	5.79	3.61	100.78
	74.56	0.26	12.34	0.00	0.61	0.13	3.81	5.49	3.62	100.82
	74.43	0.33	12.24	0.00	0.61	0.11	3.71	5.88	3.57	100.87
	74.49	0.27	12.26	0.00	0.63	0.11	3.75	5.80	3.62	100.94
	74.46	0.29	12.26	0.00	0.62	0.12	3.66	5.70	3.64	100.75
	74.48	0.26	12.32	0.00	0.60	0.12	3.75	5.88	3.54	100.94
	74.51	0.27	12.25	0.00	0.66	0.12	3.67	5.84	3.62	100.96
	74.31	0.28	12.33	0.00	0.62	0.11	3.63	5.64	3.59	100.51
Mean	74.48	0.30	12.27	0.00	0.62	0.12	3.69	5.66	3.59	100.74
St. dev.	0.08	0.03	0.06	0.00	0.02	0.01	0.08	0.23	0.03	0.23
Mean of normalised data	73.93	0.29	12.18	0.00	0.61	0.12	3.66	5.62	3.57	100.00
St. dev. of normalised data	0.15	0.03	0.07	0.00	0.02	0.01	0.08	0.22	0.03	0.00

A4.4 Thorsmork Ignimbrite ash

All analytical period 1. Bold shards have corresponding trace element data.

	SiO_2	TiO_2	Al_2O_3	MgO	CaO	MnO	FeO	Na_2O	K_2O	Total
JM-184 1	72.27	0.17	12.01	0.00	0.38	0.06	2.68	5.12	4.14	96.82
JM-184 2	72.86	0.15	11.98	0.00	0.38	0.05	2.44	5.35	4.04	97.25
JM-184 3	72.46	0.18	12.02	0.00	0.38	0.05	2.45	5.10	3.97	96.62
JM-184 4	74.06	0.12	11.94	0.00	0.46	0.07	2.54	4.86	4.30	98.36
JM-184 5	72.52	0.20	11.96	0.00	0.37	0.07	2.41	5.42	3.99	96.92
JM-184 6	72.62	0.21	11.79	0.01	0.38	0.08	2.38	5.20	4.04	96.74
JM-184 7	71.63	0.18	11.91	0.00	0.37	0.08	2.49	5.00	4.01	95.67
JM-184 8	72.42	0.20	11.89	0.00	0.38	0.07	2.55	5.19	4.04	96.74
JM-184 9	72.15	0.18	11.77	0.00	0.40	0.05	2.57	5.37	3.97	96.47
JM-184 10	71.05	0.13	11.89	0.00	0.38	0.08	2.46	4.79	3.89	94.70
JM-184 11	72.57	0.19	11.89	0.00	0.37	0.08	2.42	5.26	4.01	96.80
JM-184 12	72.89	0.23	11.92	0.00	0.39	0.07	2.66	5.36	4.07	97.60
JM-184 13	71.59	0.17	11.96	0.00	0.38	0.06	2.63	5.47	3.86	96.13
JM-184 14	71.83	0.17	11.95	0.00	0.37	0.05	2.55	5.46	4.07	96.45
JM-184 15	72.69	0.14	11.96	0.00	0.38	0.06	2.46	5.30	4.10	97.09
JM-184 16	72.77	0.16	11.96	0.00	0.39	0.06	2.40	5.29	4.04	97.07
JM-184 17	73.56	0.14	11.85	0.00	0.37	0.07	2.54	5.15	3.97	97.65
JM-184 18	74.26	0.19	12.14	0.00	0.38	0.07	2.50	5.50	4.07	99.12
JM-184 19	73.99	0.13	12.31	0.00	0.39	0.08	2.57	5.36	4.13	98.97
JM-184 20	74.52	0.16	12.47	0.00	0.39	0.07	2.53	5.60	4.09	99.86
JM-205 1	74.00	0.17	12.27	0.00	0.40	0.06	2.48	5.61	4.05	99.04
JM-205 2	73.61	0.14	12.08	0.00	0.39	0.05	2.56	5.34	4.04	98.21
JM-205 3	72.75	0.20	11.97	0.00	0.38	0.07	2.47	5.52	3.96	97.33
JM-205 4	73.65	0.17	12.19	0.00	0.37	0.07	2.58	5.66	4.00	98.70
JM-205 5	75.68	0.20	12.33	0.00	0.38	0.07	2.61	5.28	4.13	100.71
JM-205 6	74.38	0.18	12.06	0.00	0.39	0.08	2.64	5.53	4.05	99.32
JM-205 7	75.16	0.14	12.07	0.00	0.38	0.07	2.51	5.46	4.03	99.83
JM-205 8	73.94	0.15	11.93	0.00	0.37	0.07	2.49	5.52	4.03	98.50
JM-205 9	75.54	0.18	12.15	0.00	0.40	0.07	2.57	5.39	4.07	100.38
JM-205 10	75.30	0.17	12.31	0.00	0.37	0.07	2.67	5.42	4.11	100.43
JM-205 11	73.67	0.17	11.78	0.00	0.38	0.06	2.50	5.59	4.00	98.16
JM-205 12	75.66	0.21	12.35	0.00	0.39	0.07	2.75	5.45	4.15	101.05
JM-205 13	74.22	0.19	12.15	0.00	0.40	0.06	2.55	5.44	4.11	99.15
JM-205 14	74.25	0.13	12.06	0.00	0.39	0.07	2.64	5.51	4.05	99.13
JM-205 15	73.39	0.17	12.14	0.00	0.38	0.07	2.51	4.97	4.15	97.79
JM-219 1	73.46	0.16	12.24	0.00	0.38	0.07	2.50	5.51	4.11	98.44
JM-219 2	74.47	0.20	12.27	0.00	0.39	0.07	2.55	5.01	4.15	99.12
JM-219 3	74.71	0.15	12.31	0.00	0.39	0.07	2.60	5.66	4.09	100.00
JM-219 4	74.75	0.16	12.22	0.00	0.38	0.06	2.53	5.34	4.09	99.57

	SiO_2	TiO_2	Al_2O_3	MgO	CaO	MnO	FeO	Na_2O	K_2O	Total
JM-219 5	73.15	0.17	12.08	0.00	0.37	0.05	2.57	5.41	4.04	97.84
JM-219 6	73.03	0.19	11.91	0.00	0.38	0.07	2.51	5.36	4.10	97.55
JM-219 7	69.44	0.14	11.35	0.00	0.35	0.06	2.35	5.06	3.75	92.51
JM-219 8	75.05	0.20	12.23	0.00	0.38	0.05	2.59	5.56	4.10	100.17
JM-219 9	73.76	0.14	12.25	0.00	0.38	0.07	2.58	5.58	3.99	98.76
JM-219 10	74.30	0.19	12.10	0.00	0.40	0.06	2.62	5.48	4.15	99.29
JM-219 11	73.18	0.17	11.88	0.00	0.38	0.08	2.54	5.15	4.12	97.50
JM-228 1	73.38	0.17	12.09	0.01	0.19	0.07	2.44	5.30	4.16	97.82
JM-228 2	74.15	0.13	12.04	0.00	0.22	0.05	2.57	5.17	4.22	98.55
JM-228 3	73.93	0.16	11.92	0.00	0.36	0.06	2.49	5.31	4.09	98.33
JM-228 4	73.48	0.17	12.14	0.00	0.28	0.08	2.63	5.43	4.10	98.31
JM-228 5	73.60	0.17	12.18	0.00	0.26	0.07	2.62	5.39	4.17	98.47
JM-228 6	73.12	0.16	11.77	0.00	0.12	0.03	2.41	5.25	4.21	97.09
JM-228 7	73.47	0.24	12.14	0.00	0.18	0.06	2.43	5.24	4.12	97.87
JM-228 8	73.95	0.17	12.00	0.00	0.09	0.07	2.59	5.19	4.20	98.29
JM-228 9	74.16	0.12	12.07	0.00	0.15	0.06	2.41	5.07	4.20	98.26
JM-228 10	72.01	0.20	11.74	0.00	0.13	0.05	2.35	4.94	4.08	95.54
JM-228 15	75.88	0.19	12.53	0.00	0.39	0.07	2.59	5.29	4.14	101.09
JM-228 16	73.90	0.17	12.36	0.00	0.21	0.06	2.58	5.27	4.10	98.65
JM-228 17	73.75	0.15	12.24	0.00	0.21	0.05	2.52	5.22	4.07	98.22
JM-228 19	73.90	0.13	12.33	0.00	0.29	0.07	2.61	5.37	4.03	98.75
JM-228 20	73.48	0.17	12.27	0.00	0.24	0.08	2.54	5.36	4.12	98.28

A4.5 NAAZ II (II-RHY-1) ash

All analytical period 1. Bold shards have corresponding trace element data.

	SiO_2	TiO_2	Al_2O_3	MgO	CaO	MnO	FeO	Na_2O	K_2O	Total
MD01-01-25	73.28	0.13	12.14	0.00	0.38	0.06	2.43	5.41	3.89	97.72
MD01-02-25	71.74	0.18	11.79	0.00	0.38	0.07	2.39	4.97	3.82	95.35
MD01-03-25	72.24	0.17	11.60	0.00	0.38	0.07	2.46	5.12	3.91	95.95
MD01-04-25	71.65	0.21	11.95	0.00	0.37	0.05	2.49	5.26	4.00	95.98
MD01-05-25	71.50	0.19	11.63	0.00	0.37	0.08	2.57	4.93	3.90	95.18
MD01-06-25	72.48	0.18	12.08	0.00	0.38	0.07	2.61	5.50	3.99	97.32
MD01-07-25	72.44	0.18	12.10	0.00	0.38	0.07	2.51	5.58	3.95	97.24
MD01-08-25	74.92	0.19	12.29	0.00	0.39	0.07	2.56	5.20	4.19	99.81
MD01-09-25	72.45	0.18	11.85	0.00	0.38	0.05	2.50	5.31	3.83	96.55
MD01-10-25	74.40	0.17	12.07	0.00	0.39	0.06	2.43	5.55	4.12	99.20
MD01-11-25	71.02	0.17	11.91	0.00	0.37	0.07	2.49	4.98	3.82	94.85
MD01-02-40	71.74	0.21	12.06	0.00	0.37	0.06	2.37	5.18	3.88	95.89
MD01-06-40	71.80	0.16	11.93	0.00	0.36	0.07	2.54	5.23	3.90	95.99
MD01-08-40	71.51	0.16	12.17	0.00	0.39	0.07	2.48	4.90	3.94	95.61
MD01-10-40	71.11	0.17	12.00	0.00	0.38	0.07	2.42	5.14	3.84	95.15
MD01-12-40	72.59	0.11	12.03	0.01	0.38	0.07	2.40	5.15	3.92	96.69
MD01-13-40	72.47	0.15	12.06	0.00	0.40	0.05	2.65	5.41	3.91	97.10
MD01-15-40	72.23	0.16	11.84	0.00	0.37	0.07	2.46	5.26	3.97	96.37
MD01-16-40	71.94	0.20	12.24	0.00	0.37	0.07	2.42	5.26	3.89	96.40
MD01-18-40	69.02	0.17	11.34	0.00	0.37	0.06	2.33	5.02	3.88	92.20
MD01-20-40	72.68	0.18	11.93	0.00	0.38	0.08	2.44	5.58	3.95	97.23
MD04-01-25	72.30	0.17	11.92	0.00	0.37	0.07	2.46	5.33	4.02	96.64
MD04-02-25	73.83	0.15	12.03	0.00	0.38	0.06	2.46	5.34	4.02	98.28
MD04-03-25	71.45	0.14	12.10	0.00	0.38	0.06	2.47	5.49	3.98	96.09
MD04-04-25	72.58	0.20	12.01	0.00	0.38	0.06	2.48	5.56	3.93	97.23
MD04-05-25	74.62	0.17	12.38	0.00	0.38	0.06	2.53	5.54	4.14	99.83
MD04-06-25	72.96	0.18	12.23	0.00	0.37	0.05	2.48	5.67	3.96	97.91
MD04-07-25	72.58	0.21	12.15	0.00	0.39	0.06	2.35	5.28	3.88	96.92
MD04-08-25	72.47	0.14	11.98	0.00	0.38	0.07	2.39	5.18	3.92	96.52
MD04-09-25	72.41	0.13	11.98	0.00	0.38	0.07	2.55	5.23	3.87	96.62
MD04-10-25	71.84	0.17	12.03	0.00	0.38	0.06	2.53	5.27	3.81	96.11
MD04-11-25	72.11	0.20	12.11	0.00	0.38	0.07	2.43	5.66	3.97	96.91
MD04-04-40	72.09	0.18	11.77	0.01	0.38	0.06	2.46	5.35	3.79	96.09
MD04-05-40	72.06	0.19	11.69	0.00	0.40	0.07	2.38	4.94	3.99	95.72
MD04-09-40	72.09	0.15	11.96	0.00	0.37	0.06	2.47	5.29	3.99	96.39
MD04-11-40	72.09	0.17	12.02	0.00	0.38	0.06	2.46	5.37	3.96	96.53
MD04-14-40	72.13	0.15	12.03	0.00	0.38	0.08	2.32	5.23	3.96	96.28
MD04-15-40	72.02	0.19	11.86	0.00	0.38	0.05	2.47	5.07	3.99	96.05
MD04-03-50	71.20	0.21	11.35	0.01	0.37	0.06	2.47	4.86	3.91	94.47

	SiO_2	TiO_2	Al_2O_3	MgO	CaO	MnO	FeO	Na_2O	K_2O	Total
MD99-01-25	73.78	0.18	11.89	0.00	0.37	0.06	2.46	5.39	3.99	98.12
MD99-02-25	72.63	0.11	11.77	0.00	0.38	0.07	2.30	5.49	3.96	96.71
MD99-03-25	72.81	0.15	11.72	0.00	0.38	0.07	2.41	5.37	3.99	96.89
MD99-04-25	72.76	0.18	11.95	0.00	0.38	0.07	2.40	5.46	3.92	97.12
MD99-05-25	73.43	0.17	11.79	0.00	0.38	0.06	2.33	5.05	4.25	97.46
MD99-06-25	72.42	0.15	12.18	0.01	0.38	0.06	2.59	4.00	3.95	95.76
MD99-07-25	72.07	0.15	11.85	0.00	0.38	0.06	2.51	5.26	4.00	96.27
MD99-08-25	71.55	0.15	11.74	0.00	0.36	0.06	2.45	5.03	3.91	95.26
MD99-09-25	72.61	0.17	11.96	0.00	0.39	0.06	2.39	5.10	4.06	96.76
MD99-10-25	71.96	0.20	11.83	0.00	0.38	0.07	2.53	5.82	3.86	96.66
MD99-11-25	73.09	0.21	11.96	0.00	0.38	0.07	2.43	5.20	4.18	97.51
MD99-12-25	71.50	0.19	12.19	0.00	0.38	0.06	2.41	4.94	3.99	95.66
MD99-13-25	72.28	0.15	11.78	0.00	0.38	0.07	2.50	5.03	4.03	96.23
MD99-14-25	72.17	0.15	11.88	0.00	0.37	0.07	2.55	5.12	3.92	96.26
MD99-01-40	73.15	0.16	12.30	0.00	0.39	0.06	2.60	5.63	4.03	98.33
MD99-02-40	72.40	0.22	12.04	0.00	0.37	0.05	2.44	4.98	3.91	96.43
MD99-09-50	73.40	0.18	12.15	0.00	0.38	0.06	2.56	5.35	4.07	98.16
MD99-11-50	73.09	0.19	11.91	0.00	0.37	0.07	2.44	5.25	3.89	97.22
GIK23-01-25	71.84	0.17	11.92	0.01	0.39	0.06	2.33	5.26	3.96	95.94
GIK23-02-25	71.20	0.19	11.71	0.00	0.37	0.06	2.28	5.11	3.98	94.91
GIK23-05-25	72.00	0.18	11.90	0.00	0.38	0.07	2.55	5.31	3.97	96.41
GIK23-06-25	71.63	0.23	11.90	0.00	0.37	0.06	2.38	4.84	4.03	95.44
GIK23-07-25	71.72	0.19	11.67	0.00	0.37	0.07	2.49	4.73	3.99	95.23
GIK23-09-25	72.01	0.18	11.87	0.00	0.38	0.08	2.46	5.10	3.97	96.06
GIK23-10-25	71.56	0.18	11.92	0.00	0.38	0.06	2.49	5.23	4.10	95.93
GIK23-11-25	72.31	0.19	11.92	0.00	0.41	0.07	2.40	5.41	3.93	96.66
GIK23-01-40	72.20	0.18	11.79	0.00	0.37	0.07	2.46	5.33	4.03	96.44
GIK23-10-40	72.34	0.19	11.96	0.00	0.38	0.06	2.38	5.27	4.06	96.65
GIK23-14-40	70.99	0.15	11.83	0.01	0.37	0.07	2.49	5.21	3.96	95.07
GIK23-17-40	71.51	0.10	11.84	0.00	0.37	0.06	2.37	5.37	4.00	95.64
GIK23-18-40	73.17	0.13	12.13	0.00	0.38	0.05	2.51	5.40	4.02	97.80
GIK23-19-40	70.89	0.16	11.67	0.01	0.36	0.05	2.31	5.52	3.93	94.90
GIK23-20-40	73.49	0.14	12.31	0.00	0.39	0.08	2.48	5.09	4.16	98.14
GIK23-05-85	73.14	0.18	11.75	0.00	0.38	0.06	2.48	5.61	4.05	97.65
GIK23-13-85	72.97	0.15	11.91	0.00	0.38	0.06	2.52	5.44	4.05	97.49

A4.6 Secondary standard VG-568 rhyolite glass

	SiO_2	TiO_2	Al_2O_3	MgO	CaO	MnO	FeO	Na_2O	K_2O	Total
Analytical period 1	77.46	0.11	12.28	0.04	0.45	0.02	1.15	3.93	4.93	100.39
06/04/2017 - 07/04/2017	77.39	0.06	12.15	0.04	0.43	0.02	1.09	4.09	4.94	100.21
	77.32	0.09	12.04	0.03	0.44	0.03	1.17	4.09	4.91	100.15
	77.68	0.08	12.21	0.02	0.43	0.01	1.14	4.05	4.93	100.55
	77.63	0.04	12.48	0.03	0.42	0.04	1.04	4.03	4.90	100.62
	77.39	0.11	12.38	0.03	0.45	0.03	1.07	4.06	4.92	100.44
	77.32	0.07	12.24	0.03	0.42	0.01	0.94	4.06	4.93	100.04
	77.20	0.12	12.39	0.04	0.43	0.03	1.03	4.09	4.90	100.23
	77.18	0.06	12.18	0.02	0.45	0.03	1.19	4.13	4.91	100.17
	77.04	0.08	12.05	0.01	0.42	0.03	1.09	3.92	4.89	99.53
	77.11	0.05	12.26	0.03	0.44	0.02	1.13	4.00	4.88	99.93
	77.43	0.06	12.25	0.02	0.44	0.02	1.13	3.99	4.93	100.28
	77.55	0.06	12.48	0.04	0.44	0.02	1.05	4.07	4.87	100.61
	77.50	0.07	12.33	0.04	0.44	0.02	1.10	2.63	4.87	98.99
	77.74	0.05	12.49	0.02	0.44	0.01	1.14	4.03	4.90	100.83
	77.73	0.12	12.25	0.02	0.42	0.03	1.05	3.98	4.93	100.52
	77.74	0.07	12.21	0.03	0.44	0.02	1.16	4.15	4.83	100.67
	77.56	0.08	12.20	0.03	0.44	0.03	1.04	3.99	4.88	100.27
	77.49	0.09	12.16	0.03	0.44	0.02	1.14	3.83	4.91	100.13
	77.20	0.09	12.19	0.03	0.43	0.03	1.18	4.12	4.90	100.20
	77.30	0.11	12.24	0.03	0.43	0.01	1.28	4.10	4.95	100.44
	77.77	0.10	12.37	0.03	0.44	0.02	1.12	4.05	4.90	100.79
	77.74	0.10	12.33	0.02	0.44	0.03	1.03	4.15	4.92	100.75
	77.29	0.08	12.20	0.04	0.44	0.01	1.04	3.98	4.90	99.98
	77.36	0.13	12.15	0.02	0.44	0.02	1.04	4.06	4.93	100.15
Mean	77.44	0.08	12.26	0.03	0.44	0.02	1.10	3.98	4.91	100.27
St. dev.	0.22	0.02	0.12	0.01	0.01	0.01	0.07	0.29	0.03	0.40
Analytical period 2	77.44	0.05	12.35	0.02	0.46	0.00	1.17	3.89	4.94	100.33
28/04/2017	77.05	0.06	12.25	0.02	0.47	0.02	1.15	3.73	4.95	99.70
	76.33	0.12	12.17	0.02	0.46	0.01	1.11	3.97	5.00	99.24
	77.19	0.08	12.26	0.04	0.42	0.04	1.10	3.92	4.90	99.95
	76.79	0.09	12.01	0.03	0.40	0.01	0.97	3.60	5.02	98.92
	76.25	0.10	11.96	0.02	0.45	0.03	1.06	3.57	5.02	98.47
	77.06	0.10	12.15	0.03	0.43	0.02	1.17	3.69	4.96	99.63
	77.15	0.07	12.17	0.02	0.44	0.02	1.14	3.51	4.84	99.37
	77.28	0.06	12.14	0.02	0.43	0.02	1.06	3.67	4.92	99.61
	77.31	0.08	12.04	0.03	0.43	0.02	1.13	3.79	4.90	99.74
	77.33	0.09	12.26	0.05	0.45	0.02	1.13	3.77	4.90	100.02
	77.31	0.08	12.27	0.03	0.45	0.02	1.27	3.80	4.94	100.17
	77.46	0.07	12.14	0.04	0.44	0.01	1.13	3.83	4.94	100.06
	77.31	0.09	12.35	0.03	0.44	0.03	1.14	3.56	4.95	99.93
Mean	77.09	0.08	12.18	0.03	0.44	0.02	1.12	3.74	4.94	99.65
St. dev.	0.38	0.02	0.12	0.01	0.02	0.01	0.07	0.14	0.05	0.51

	SiO_2	TiO_2	Al_2O_3	MgO	CaO	MnO	FeO	Na_2O	K_2O	Total
Analytical period 3	77.83	0.07	12.38	0.02	0.44	0.01	1.15	3.98	4.94	100.83
25/10/2017 - 26/10/2017	77.51	0.09	12.52	0.04	0.43	0.03	1.14	3.92	4.87	100.54
	77.74	0.06	12.46	0.02	0.45	0.02	1.11	3.94	4.93	100.75
	77.21	0.07	12.32	0.04	0.45	0.03	1.08	3.89	4.93	100.03
	77.10	0.08	12.18	0.03	0.45	0.02	1.11	3.89	4.90	99.78
	77.12	0.11	12.31	0.03	0.42	0.01	1.04	4.19	4.93	100.18
	77.04	0.08	12.31	0.03	0.46	0.01	1.13	4.02	4.89	99.97
	76.83	0.08	12.22	0.03	0.46	0.02	1.09	3.99	4.91	99.65
	77.79	0.07	12.25	0.03	0.45	0.03	1.13	3.67	4.77	100.20
	77.70	0.08	12.16	0.04	0.42	0.03	1.04	3.84	4.91	100.25
	77.88	0.07	12.14	0.04	0.46	0.02	1.17	3.68	4.94	100.39
	77.90	0.08	12.15	0.03	0.45	0.02	1.11	3.70	4.92	100.36
	78.06	0.08	12.21	0.03	0.44	0.02	1.14	3.80	4.88	100.68
	78.03	0.08	12.16	0.02	0.44	0.02	1.03	3.85	4.94	100.58
	77.44	0.08	11.91	0.02	0.45	0.02	1.16	3.69	4.94	99.72
	77.61	0.10	12.06	0.03	0.46	0.03	1.12	3.56	4.95	99.94
	77.74	0.09	12.16	0.02	0.44	0.02	1.19	4.00	4.93	100.60
	77.34	0.06	12.17	0.04	0.45	0.03	1.09	5.01	4.94	101.13
	77.51	0.10	12.19	0.02	0.47	0.02	1.19	3.90	4.91	100.30
	77.22	0.07	12.21	0.02	0.45	0.01	1.15	3.84	4.94	99.93
	77.16	0.07	12.13	0.04	0.46	0.02	1.17	3.90	4.96	99.92
	77.33	0.09	12.16	0.03	0.45	0.01	1.11	3.90	4.95	100.05
	77.16	0.09	12.27	0.02	0.44	0.03	1.12	3.92	4.94	99.98
	76.83	0.11	12.37	0.03	0.44	0.01	1.12	3.99	4.94	99.87
	77.07	0.09	12.29	0.02	0.42	0.01	1.05	3.90	4.95	99.80
	76.52	0.06	12.31	0.01	0.44	0.00	1.09	3.88	4.92	99.24
Mean	77.41	0.08	12.23	0.03	0.45	0.02	1.12	3.92	4.92	100.18
St. dev.	0.40	0.01	0.13	0.01	0.01	0.01	0.04	0.26	0.04	0.43

Smithsonian values	**SiO_2**	**TiO_2**	**Al_2O_3**	**MgO**	**CaO**	**MnO**	**FeO**	**Na_2O**	**K_2O**	**Total**
	76.71	**0.12**	**12.06**	**<0.1**	**0.50**	**0.03**	**1.23**	**3.75**	**4.89**	**99.29**

APPENDIX 5: LA-ICP-MS DATA

All in ppm.

A5.1 Torfajökull rhyolite lavas

RFR - Kirkjufell - TJ99-2 Analytical session 1

	1	2	3	4	5	6	7	8	9	10	11	12	13	14	15	16	Mean	St. dev.
Li	44.54	39.50	47.07	44.66	44.42	43.82	44.18	45.50	44.66	44.78	47.31	44.30	46.10	44.78	45.74	45.74	44.82	1.74
Sc	1.97	1.83	2.07	1.46	1.82	2.12	1.83	1.77	1.93	1.67	1.77	1.97	1.33	1.62	1.92	1.59	1.79	0.22
Zn	272.89	293.41	263.66	283.15	276.99	255.45	274.94	261.60	278.02	259.55	272.89	283.15	259.24	262.63	268.79	271.86	271.14	10.44
Rb	106.36	108.16	110.65	108.06	105.56	106.76	106.26	106.76	107.66	106.26	108.06	105.16	104.96	106.66	108.75	105.76	106.99	1.49
Sr	9.83	9.84	9.86	9.80	10.15	9.88	10.23	10.53	11.11	11.24	11.10	10.65	11.37	11.00	10.73	10.73	10.50	0.56
Y	115.79	120.53	121.27	124.53	119.90	117.79	121.16	123.06	121.27	122.11	122.11	121.37	122.11	120.32	123.06	123.37	121.23	2.15
Zr	919.05	942.30	943.41	953.37	944.52	929.01	943.41	971.09	981.06	998.77	1016.49	1002.10	1009.85	1015.38	1046.39	1014.28	976.90	38.48
Nb	186.48	184.54	184.89	193.42	181.93	181.36	182.95	186.82	202.98	206.39	209.92	209.92	211.05	210.26	206.39	201.72	196.31	11.92
Cs	1.11	1.00	1.14	1.06	1.04	1.06	1.17	1.08	1.10	1.19	1.24	1.19	1.18	1.18	1.25	1.25	1.14	0.08
Ba	391.03	382.22	394.33	393.23	391.03	380.01	391.03	406.45	385.52	392.13	393.23	387.72	394.33	386.62	386.62	391.03	390.41	6.02
La	113.63	122.50	116.69	134.12	115.53	114.47	114.58	117.22	120.28	119.44	121.34	119.54	119.12	122.50	121.87	120.71	119.60	4.87
Ce	245.87	262.75	250.93	285.97	250.72	245.87	248.61	253.15	250.51	249.04	251.04	249.14	248.72	249.04	253.36	252.41	252.95	9.62
Pr	26.72	27.05	27.13	29.84	27.53	26.72	28.33	28.59	30.69	31.66	32.41	31.87	33.70	32.95	32.41	31.50	29.94	2.48
Nd	112.78	115.01	114.16	129.68	112.99	109.17	111.19	112.46	108.74	111.29	114.16	109.38	113.31	114.91	116.29	112.04	113.60	4.81
Sm	23.77	22.60	22.01	24.07	22.50	23.38	22.80	24.36	21.43	23.09	22.89	22.21	21.13	22.70	22.80	22.11	22.74	0.88
Eu	3.70	3.59	3.12	3.53	3.73	3.32	3.10	3.37	3.40	3.17	3.15	3.50	3.23	3.23	3.12	3.21	3.34	0.21
Gd	22.15	23.25	23.36	23.80	22.26	22.48	22.48	23.58	23.80	23.69	22.48	22.15	22.26	22.59	24.13	23.03	22.97	0.69
Tb	3.41	3.28	3.53	3.45	3.48	3.23	3.42	3.68	3.44	3.80	3.65	3.70	3.74	3.79	3.66	3.47	3.55	0.17

Dy	20.14	20.72	21.30	20.43	20.05	20.53	20.72	21.49	20.34	21.01	19.85	21.49	20.20	20.24	20.34	20.91	20.61	0.51
Ho	4.33	4.20	4.60	4.53	4.41	4.43	4.65	4.67	4.58	4.69	4.65	4.65	4.64	4.44	4.58	4.65	4.54	0.14
Er	13.40	13.50	13.21	13.03	13.39	13.32	13.63	13.24	13.91	14.11	14.72	14.74	13.82	14.08	14.38	14.84	13.83	0.59
Tm	1.86	1.59	1.99	1.76	1.87	1.81	1.73	1.81	1.91	1.84	1.78	1.83	2.07	1.88	1.90	1.92	1.85	0.11
Yb	12.77	12.58	13.54	13.56	13.80	13.97	13.13	13.14	13.31	13.68	13.18	13.19	13.63	13.30	13.92	13.80	13.41	0.40
Lu	1.63	1.58	1.63	1.73	1.67	1.72	1.77	1.71	1.77	1.64	1.93	1.83	1.83	1.79	1.94	1.81	1.75	0.11
Hf	25.90	26.23	26.34	25.57	27.66	25.90	25.68	26.93	26.12	26.01	25.90	25.34	26.89	26.58	26.78	26.62	26.28	0.60
Ta	11.09	10.95	11.86	11.79	11.58	10.90	11.70	11.52	11.47	11.50	11.30	11.31	11.46	11.28	11.77	11.19	11.42	0.29
Pb	9.79	9.72	10.14	9.87	10.17	10.25	10.42	10.36	10.62	10.32	10.37	10.31	10.33	10.37	10.38	10.17	10.22	0.24
Th	15.52	15.93	16.26	15.80	16.25	16.04	16.50	17.17	17.54	18.67	18.53	18.56	18.78	18.66	18.45	18.34	17.31	1.24
U	4.96	4.57	4.83	4.75	4.79	4.89	5.03	5.07	5.20	5.77	5.72	5.74	5.61	5.54	5.58	5.55	5.22	0.41

RFR - Kirkjufell - TJ99-4 Analytical session 5

	1	2	3	4	5	6	7	8	9	10	11	12	13	14	15	16	Mean	St. dev.
Li	35.67	35.48	33.33	33.61	35.01	35.67	35.57	35.76	35.48	37.81	35.95	37.16	37.35	37.63	37.25	37.35	36.00	1.35
Sc	1.93	1.93	1.86	1.84	1.84	1.81	1.90	1.83	1.86	2.00	1.84	1.83	1.85	1.80	1.82	1.80	1.86	0.05
Zn	348.21	352.24	339.12	344.17	355.27	357.29	351.23	349.22	351.23	370.41	362.34	348.21	359.31	364.36	364.36	357.29	354.64	8.26
Rb	101.11	103.33	99.37	99.28	102.56	101.88	106.13	108.73	102.27	108.92	109.02	113.07	106.80	109.12	106.61	109.60	105.49	4.14
Sr	11.09	11.10	10.52	12.04	10.99	11.23	11.27	11.20	11.23	11.37	11.42	11.64	11.72	11.47	11.52	11.57	11.34	0.35
Y	98.86	100.47	95.37	96.12	99.15	101.42	102.27	98.86	98.68	104.91	103.12	104.35	106.43	106.71	104.91	106.24	101.74	3.67
Zr	746.06	763.92	719.27	728.20	763.92	772.84	773.84	768.88	750.03	791.69	783.76	787.73	794.67	796.65	787.73	786.73	769.74	23.49
Nb	170.94	175.48	166.85	167.30	175.48	175.04	175.70	178.91	170.28	179.57	173.71	174.48	176.92	177.25	175.37	173.82	174.19	3.68
Cs	1.19	1.20	1.15	1.17	1.20	1.20	1.24	1.23	1.23	1.29	1.25	1.28	1.29	1.27	1.28	1.29	1.24	0.05
Ba	387.10	391.48	372.89	405.69	396.94	396.94	402.41	403.50	401.32	418.81	412.25	414.44	419.91	422.09	417.72	417.72	405.08	13.80
La	112.09	114.79	110.42	111.78	116.98	117.08	119.68	119.99	118.12	125.09	123.63	125.40	124.25	127.48	123.32	124.46	119.66	5.43
Ce	264.28	266.19	258.12	260.14	271.94	270.63	273.25	272.04	276.68	294.22	287.57	293.82	288.37	296.04	290.39	291.40	278.44	13.07
Pr	26.07	26.01	24.46	24.71	25.27	25.39	26.38	26.38	31.19	33.97	33.41	33.97	34.07	34.50	33.65	33.11	29.53	4.17
Nd	109.53	111.73	106.29	108.28	113.29	113.08	113.61	113.08	114.02	120.92	118.62	120.82	120.61	125.21	121.34	119.77	115.64	5.47
Sm	23.55	23.53	22.49	22.69	24.02	23.31	24.02	23.92	23.37	24.71	24.42	25.01	24.12	24.89	24.83	24.83	23.98	0.78
Eu	3.13	3.29	3.00	3.09	3.08	3.30	3.21	3.14	3.20	3.31	3.31	3.34	3.28	3.35	3.42	3.32	3.24	0.12
Gd	20.28	20.93	19.87	20.28	20.84	20.57	21.46	20.95	20.84	21.79	22.16	22.32	22.76	23.07	22.13	22.29	21.41	0.97
Tb	3.51	3.52	3.39	3.32	3.54	3.57	3.62	3.52	3.49	3.61	3.65	3.68	3.68	3.86	3.77	3.77	3.59	0.14
Dy	22.00	22.38	21.62	21.44	22.81	22.44	22.74	22.28	22.46	23.77	23.30	23.73	23.30	23.81	23.49	23.58	22.82	0.77
Ho	4.47	4.42	4.38	4.37	4.49	4.51	4.60	4.55	4.50	4.83	4.65	4.73	4.76	4.92	4.73	4.80	4.61	0.17
Er	12.67	12.95	12.28	12.26	12.64	13.06	13.18	12.97	12.91	13.67	13.41	13.70	13.62	14.06	13.48	13.82	13.17	0.54
Tm	1.73	1.70	1.54	1.55	1.63	1.63	1.65	1.67	1.94	2.06	2.09	2.07	2.14	2.20	2.21	2.16	1.87	0.25
Yb	12.40	12.80	11.85	12.13	12.93	12.91	12.80	12.92	12.87	13.40	13.53	13.41	13.10	13.50	13.70	13.67	13.00	0.54
Lu	1.74	1.65	1.67	1.65	1.72	1.78	1.76	1.78	1.77	1.92	1.90	1.93	1.91	1.97	1.95	1.93	1.81	0.11
Hf	27.01	27.47	25.93	26.68	27.51	27.33	27.70	27.79	27.61	29.28	28.35	29.28	29.46	29.46	29.56	29.28	28.11	1.15
Ta	12.56	12.82	12.02	12.40	13.00	13.03	13.05	13.26	13.20	13.99	14.11	14.00	14.01	14.27	13.98	13.95	13.35	0.70
Pb	12.95	13.21	12.01	11.98	12.05	12.65	12.69	12.98	14.10	15.68	15.50	15.65	16.33	16.59	16.83	16.46	14.23	1.85
Th	18.48	18.86	17.91	18.08	18.84	18.91	19.31	19.14	18.97	20.25	19.94	20.34	20.25	20.68	20.33	20.27	19.41	0.89
U	6.63	6.59	6.31	6.40	6.43	6.50	6.59	6.63	6.58	6.83	6.56	6.90	6.83	7.08	6.88	6.97	6.67	0.22

RFR - Illihnúkur - TJ97-16 Analytical session 5

	1	2	3	4	5	6	7	8	9	10	11	12	13	Mean	St. dev.
Li	24.94	31.16	26.99	33.29	32.55	27.82	33.01	34.22	32.46	28.10	31.81	31.81	30.88	30.70	2.82
Sc	2.49	2.32	2.24	2.25	2.22	2.18	2.25	2.35	2.36	2.33	2.35	2.34	2.25	2.30	0.08
Zn	265.66	288.72	292.73	279.69	281.70	275.68	255.63	272.68	259.64	247.61	240.60	233.58	268.67	266.35	18.24
Rb	88.93	102.34	82.89	98.80	94.87	90.94	98.70	97.36	96.50	88.16	95.44	92.57	90.65	93.70	5.32
Sr	33.81	28.92	40.80	31.76	33.27	30.58	32.41	31.65	29.63	39.94	32.84	32.94	36.43	33.46	3.61
Y	100.92	95.29	91.91	90.41	94.35	94.82	96.88	96.13	99.51	101.20	98.10	98.20	95.19	96.38	3.23
Zr	789.31	741.02	714.42	699.64	726.24	723.29	737.08	729.20	768.61	791.28	777.48	757.78	722.30	744.43	29.63
Nb	190.44	183.19	179.13	173.86	177.48	175.61	177.59	181.10	190.77	191.65	191.98	191.10	176.16	183.08	7.07
Cs	1.09	1.10	1.09	1.10	1.07	1.09	1.04	1.06	1.05	0.99	0.99	0.93	1.05	1.05	0.05
Ba	461.61	463.78	472.47	462.69	463.78	449.66	454.00	461.61	443.14	497.45	427.94	414.90	477.90	457.76	21.10
La	110.92	110.20	108.65	108.23	110.71	107.20	105.86	108.23	109.16	108.54	106.48	100.80	107.82	107.91	2.62
Ce	244.16	249.07	243.46	241.66	254.48	246.37	235.35	239.36	236.55	230.34	224.33	217.32	242.76	238.86	10.17
Pr	26.75	27.55	27.69	27.37	29.38	28.64	25.89	25.95	25.48	24.40	23.23	22.60	25.71	26.20	1.99
Nd	106.61	105.99	104.22	105.47	108.79	105.05	101.94	105.78	103.08	102.87	97.58	94.78	107.13	103.79	3.90
Sm	21.83	22.34	22.22	22.24	22.65	22.06	21.43	22.19	22.14	21.23	20.42	19.91	21.93	21.74	0.80
Eu	3.03	3.31	3.42	3.19	3.30	3.19	3.16	3.23	3.12	3.26	3.13	2.91	3.35	3.20	0.14
Gd	19.85	19.25	19.36	18.54	19.80	18.84	18.73	19.00	18.92	18.26	17.79	17.31	19.33	18.84	0.74
Tb	3.32	3.27	3.24	3.30	3.28	3.21	3.14	3.22	3.21	3.11	3.05	2.91	3.28	3.20	0.12
Dy	20.32	20.62	20.00	20.04	20.38	20.09	19.27	20.52	19.72	19.35	19.26	17.87	20.25	19.82	0.75
Ho	4.09	4.17	4.11	4.04	4.26	3.98	4.01	4.03	3.95	3.84	3.72	3.56	3.95	3.98	0.19
Er	11.53	11.39	11.18	11.21	11.61	11.36	11.24	11.57	11.33	11.17	10.51	9.87	11.29	11.17	0.48
Tm	1.64	1.69	1.70	1.73	1.72	1.70	1.59	1.60	1.55	1.47	1.42	1.29	1.53	1.59	0.13
Yb	11.48	11.57	11.16	11.54	12.10	11.03	11.25	11.76	11.46	11.10	10.16	9.92	11.26	11.22	0.60
Lu	1.56	1.60	1.59	1.59	1.58	1.56	1.48	1.52	1.47	1.45	1.38	1.30	1.55	1.51	0.09
Hf	23.28	23.63	23.82	23.63	24.39	23.08	22.16	23.26	22.22	21.69	20.59	20.13	23.63	22.73	1.30
Ta	11.60	12.22	12.16	12.05	12.46	11.95	11.18	11.80	11.32	10.81	10.25	9.90	11.84	11.50	0.78
Pb	10.42	12.92	12.39	13.09	13.16	13.60	9.63	10.11	9.15	8.21	7.58	7.37	9.79	10.57	2.23
Th	16.34	17.30	17.21	17.26	17.84	16.96	16.14	17.16	16.35	15.58	14.69	13.98	17.30	16.47	1.13
U	5.24	5.70	5.85	5.83	5.76	5.64	5.09	5.57	5.07	4.54	4.33	4.08	5.59	5.25	0.60

RFR - Illihnúkur - TJ97-18 Analytical session 1

	1	2	3	4	5	6	7	8	9	10	11	12	13	14	15	Mean	St. dev.
Li	50.51	46.37	47.20	45.54	44.36	46.02	44.60	45.31	43.53	43.89	47.32	43.77	43.41	44.60	42.23	45.24	2.05
Sc	2.81	2.07	2.24	2.25	2.22	2.11	2.18	2.19	2.08	2.12	2.15	1.87	2.28	2.22	2.73	2.24	0.24
Zn	210.29	215.11	218.01	201.61	213.18	202.57	208.36	203.54	206.43	201.61	206.43	198.71	200.64	189.07	196.78	204.82	7.52
Rb	118.05	112.07	117.50	116.74	119.89	117.29	122.72	115.00	115.66	114.89	122.18	118.92	119.24	114.46	116.63	117.42	2.89
Sr	35.24	36.59	34.90	35.24	29.04	27.69	28.48	33.77	29.72	35.57	32.11	35.80	31.09	35.57	35.12	33.06	3.07
Y	107.39	102.97	105.49	100.86	105.92	106.55	108.13	103.18	105.07	104.65	105.70	105.18	106.76	105.81	108.23	105.46	1.99
Zr	835.92	830.39	840.33	812.73	863.52	848.06	845.85	811.62	827.08	831.50	824.87	830.39	843.65	840.33	834.81	834.74	13.35
Nb	200.67	194.07	198.24	193.26	203.44	199.97	200.55	191.64	194.65	197.19	196.15	196.38	196.15	191.41	194.53	196.55	3.49
Cs	1.18	1.20	1.12	1.14	1.15	1.17	1.08	1.10	1.00	1.12	1.16	1.21	1.16	1.13	1.15	1.14	0.05
Ba	509.57	503.70	511.92	517.79	474.34	469.65	479.04	514.26	480.21	502.52	504.87	515.44	490.78	502.52	508.39	499.00	16.02
La	121.73	121.95	122.61	119.33	129.28	122.61	125.56	119.00	121.52	122.94	121.84	121.95	122.61	120.09	122.39	122.36	2.48
Ce	260.71	257.95	258.06	254.08	276.18	261.04	266.13	257.07	258.61	259.61	261.82	258.50	258.28	256.29	258.50	260.19	5.20
Pr	29.20	29.20	28.45	28.55	31.02	28.77	29.85	28.14	29.20	28.77	28.81	28.77	29.38	29.22	29.09	29.09	0.68
Nd	114.72	114.61	114.06	111.86	119.67	110.64	116.04	112.96	108.66	115.71	112.19	109.98	111.75	109.76	112.19	112.99	2.88
Sm	22.51	20.74	19.90	21.57	21.42	22.20	21.88	20.63	19.80	20.95	21.26	21.26	20.32	20.74	21.47	21.11	0.78
Eu	3.96	3.60	3.81	3.75	3.51	3.52	3.43	3.77	3.61	3.58	3.52	3.54	3.63	3.18	3.23	3.58	0.20
Gd	21.60	20.95	21.27	17.70	19.97	20.84	21.82	21.17	20.35	19.97	18.87	19.20	20.26	21.38	20.73	20.40	1.13
Tb	3.32	3.46	3.28	3.27	3.58	3.62	3.45	3.43	3.58	3.48	3.45	3.30	3.17	3.51	3.47	3.42	0.13
Dy	21.14	20.92	21.59	21.59	21.93	22.27	22.04	21.36	20.85	21.25	21.70	21.59	20.80	20.86	20.84	21.38	0.48
Ho	4.30	4.11	4.13	4.34	4.32	4.35	4.18	4.21	4.05	4.05	4.16	4.40	4.20	4.16	4.37	4.22	0.12
Er	12.89	12.77	12.26	11.95	12.94	13.05	12.24	12.90	11.94	11.71	11.74	12.40	12.50	12.47	12.01	12.38	0.45
Tm	1.84	1.72	1.83	1.50	1.67	1.82	1.86	1.74	1.88	1.82	1.84	1.77	1.89	1.82	1.67	1.78	0.10
Yb	13.54	11.94	10.81	12.68	13.96	12.48	12.34	11.08	11.94	12.55	12.80	12.37	11.86	11.89	13.05	12.35	0.83
Lu	1.46	1.55	1.53	1.30	1.48	1.49	1.61	1.48	1.49	1.53	1.43	1.46	1.43	1.53	1.48	1.48	0.07
Hf	22.42	23.53	23.42	22.19	23.75	23.87	23.87	22.53	22.86	21.86	23.64	23.20	22.86	22.53	21.97	22.97	0.70
Ta	11.44	11.50	11.94	11.36	12.07	12.01	11.92	11.35	11.64	11.65	11.87	11.45	11.81	11.68	11.64	11.69	0.24
Pb	10.64	10.78	10.77	10.56	11.01	10.56	10.95	10.44	10.78	10.19	10.99	10.37	10.76	10.86	10.37	10.67	0.25
Th	18.19	18.08	17.87	17.92	18.67	18.49	18.99	17.90	18.25	17.38	17.65	17.36	17.83	17.89	17.81	18.02	0.45
U	5.67	5.71	5.41	5.58	5.79	5.85	6.14	5.61	5.56	5.36	5.42	5.51	5.74	5.92	5.76	5.67	0.21

RFR - Laufafell – JM-40 Analytical session 3

	1	2	3	4	5	6	7	8	9	10	11	12	13	14	15	Mean	St. dev.
Li	33.60	37.98	37.69	37.20	37.98	35.64	37.11	37.20	38.18	35.26	36.03	39.74	36.33	34.77	39.15	36.92	1.66
Sc	1.52	1.50	1.50	1.52	1.61	1.38	1.54	1.70	1.59	1.55	1.62	1.73	1.64	1.74	1.81	1.60	0.11
Zn	270.49	276.15	278.41	267.09	279.54	244.46	270.49	261.43	286.33	245.59	250.12	264.83	268.22	262.56	297.65	268.22	14.63
Rb	108.92	126.24	113.42	108.62	124.28	106.66	120.17	115.47	123.69	108.43	106.66	112.63	113.81	108.03	121.34	114.56	6.92
Sr	11.98	12.29	11.72	11.78	12.41	11.34	12.31	11.95	12.27	11.71	11.28	12.60	12.29	11.68	12.47	12.00	0.41
Y	94.95	102.01	99.11	97.56	103.37	95.72	102.21	104.04	108.69	102.59	105.88	113.14	111.98	106.46	119.92	104.51	6.83
Zr	673.71	702.16	684.88	680.82	715.37	662.53	719.43	736.71	774.31	716.39	714.35	786.50	778.37	743.82	830.19	727.97	47.37
Nb	178.35	199.33	187.79	187.79	195.13	176.25	198.28	199.33	212.97	187.79	188.84	202.48	204.58	199.33	214.02	195.48	11.08
Cs	1.15	1.31	1.22	1.24	1.26	1.15	1.21	1.25	1.25	1.16	1.16	1.18	1.20	1.17	1.31	1.21	0.06
Ba	284.71	285.80	283.61	272.66	290.18	265.00	281.42	294.56	284.71	280.33	280.33	301.13	286.90	289.09	316.46	286.46	11.86
La	99.28	104.67	99.49	97.72	103.53	94.20	100.42	107.36	104.15	99.80	101.66	106.01	105.91	101.97	113.99	102.68	4.72
Ce	219.93	227.15	217.86	216.83	226.12	206.50	216.83	233.35	227.15	211.67	212.70	227.15	224.06	212.70	247.80	221.85	10.32
Pr	24.34	25.77	24.85	24.65	25.97	24.04	26.58	26.99	26.38	24.95	25.46	26.28	25.77	24.75	27.40	25.61	1.00
Nd	90.93	93.30	87.83	87.83	91.03	84.21	92.89	95.06	93.61	88.86	90.41	94.85	94.96	93.41	103.12	92.15	4.36
Sm	18.72	19.97	19.03	19.03	18.82	17.47	18.82	19.66	20.49	18.51	19.24	20.38	20.70	19.66	21.84	19.49	1.07
Eu	2.01	2.27	2.20	2.21	2.23	2.09	2.35	2.39	2.35	2.21	2.31	2.40	2.34	2.26	2.37	2.27	0.11
Gd	17.19	18.50	18.10	18.20	17.69	16.78	17.89	18.70	18.70	18.20	18.40	19.37	18.90	18.20	20.72	18.37	0.92
Tb	2.70	2.95	2.85	2.81	2.81	2.81	2.87	3.00	3.11	2.84	2.97	3.11	3.16	3.03	3.47	2.96	0.19
Dy	17.33	18.12	17.72	16.83	17.42	16.14	17.42	18.02	18.91	17.72	17.92	19.56	19.80	17.82	20.89	18.11	1.22
Ho	3.60	3.83	3.95	3.95	4.01	3.52	3.79	4.08	4.07	3.82	4.07	4.26	4.12	3.98	4.70	3.98	0.28
Er	10.95	11.51	10.95	11.00	11.12	10.49	11.23	12.02	12.05	11.16	11.46	11.51	11.57	11.62	13.16	11.46	0.63
Tm	1.60	1.61	1.59	1.56	1.55	1.44	1.58	1.61	1.63	1.54	1.62	1.63	1.70	1.61	1.83	1.61	0.08
Yb	10.89	11.01	10.61	10.44	11.00	9.89	10.74	11.14	11.26	10.72	10.61	12.04	11.51	10.51	12.64	11.00	0.67
Lu	1.34	1.47	1.36	1.35	1.38	1.23	1.46	1.45	1.42	1.37	1.42	1.59	1.44	1.45	1.62	1.42	0.10
Hf	19.65	19.75	19.75	19.04	19.55	18.02	19.75	20.26	21.38	19.44	19.95	21.79	20.56	20.06	23.21	20.14	1.23
Ta	10.80	11.02	11.02	10.69	11.21	10.31	11.58	11.42	11.72	11.02	10.75	11.67	11.52	10.86	12.76	11.22	0.59
Pb	10.63	12.02	11.78	11.36	11.59	10.27	11.19	11.79	11.95	10.14	11.29	11.24	10.62	10.86	12.15	11.26	0.64
Th	15.24	16.38	15.50	15.14	15.38	14.10	15.45	16.17	16.27	15.03	15.55	16.93	16.57	16.03	18.25	15.87	0.97
U	5.18	5.79	5.38	5.15	5.31	4.77	5.28	5.38	5.32	4.95	5.08	5.30	5.34	4.84	5.69	5.25	0.28

RFR - Rauðfossafjöll - TJ97-29 Analytical session 5

	1	2	3	4	5	6	7	8	9	10	11	12	13	14	15	16	Mean	St. dev.
Li	34.13	35.90	34.97	32.36	36.08	34.87	34.60	34.78	36.36	35.99	35.06	34.32	32.64	34.97	33.57	33.48	34.63	1.18
Sc	1.78	1.78	1.75	1.72	1.87	1.90	1.88	1.87	1.99	1.89	1.78	1.86	1.83	1.87	1.78	1.84	1.83	0.07
Zn	264.40	258.37	259.37	240.27	275.46	262.39	249.32	258.37	279.48	268.42	268.42	262.39	258.37	267.41	251.33	260.38	261.51	9.65
Rb	105.32	104.17	107.53	98.21	107.53	104.55	104.55	103.69	114.16	110.80	101.67	107.15	101.67	109.26	101.77	100.52	105.16	4.12
Sr	11.21	11.22	11.15	10.61	11.75	11.55	11.12	11.07	12.47	11.93	11.27	11.76	11.19	12.22	11.41	11.36	11.46	0.47
Y	100.26	100.83	104.31	96.22	106.95	104.78	105.16	103.75	112.97	109.11	104.78	107.32	103.46	108.36	101.11	102.81	104.51	3.99
Zr	737.18	740.15	766.83	716.43	780.66	755.96	758.92	761.89	829.09	795.49	774.74	802.40	779.68	807.35	763.87	769.79	771.28	28.35
Nb	185.03	187.56	182.83	178.42	193.84	190.65	181.72	182.83	200.78	199.35	189.43	194.94	188.88	196.70	187.78	182.83	188.97	6.66
Cs	1.10	1.11	1.04	1.08	1.14	1.12	1.11	1.06	1.15	1.15	1.09	1.12	1.06	1.11	1.03	1.01	1.09	0.04
Ba	302.80	302.80	310.42	295.17	311.51	313.69	302.80	301.71	330.03	321.31	313.69	313.69	300.62	318.04	304.97	297.35	308.79	9.42
La	98.80	97.87	98.29	93.73	103.67	103.88	102.12	100.36	110.40	107.92	105.12	105.22	102.53	109.47	102.64	100.98	102.69	4.43
Ce	228.99	233.00	226.98	214.92	237.02	227.98	217.94	226.98	237.02	222.96	225.97	225.97	213.92	226.98	214.92	213.92	224.72	7.71
Pr	25.75	25.75	25.75	23.83	26.17	25.30	24.26	24.79	26.60	25.64	25.85	25.43	24.47	25.64	24.68	23.94	25.24	0.82
Nd	90.36	91.71	92.86	87.03	95.98	94.73	91.30	91.30	102.75	97.96	95.98	96.09	92.55	97.96	93.90	91.61	94.00	3.75
Sm	18.25	19.06	19.67	17.94	19.97	20.35	19.97	19.36	21.90	20.98	20.88	20.98	20.58	21.19	20.59	20.68	20.15	1.08
Eu	2.11	2.31	2.28	2.26	2.31	2.37	2.48	2.31	2.55	2.63	2.47	2.56	2.25	2.41	2.32	2.20	2.36	0.14
Gd	18.03	17.65	17.46	16.22	17.65	18.60	18.79	18.31	19.45	18.97	18.82	17.93	18.12	18.97	18.03	17.46	18.15	0.79
Tb	3.00	2.94	3.08	2.95	3.09	3.17	3.06	3.13	3.38	3.14	3.11	3.17	3.06	3.13	3.07	3.05	3.10	0.10
Dy	18.57	18.10	18.20	17.64	19.59	19.24	18.75	18.66	20.52	20.15	19.13	19.59	19.40	19.78	19.13	19.13	19.10	0.76
Ho	3.77	3.68	3.63	3.54	4.02	3.79	3.73	3.80	4.26	4.06	3.87	3.98	3.65	3.96	3.78	3.71	3.83	0.19
Er	10.86	10.52	10.51	9.68	10.84	11.08	10.76	10.61	11.77	10.80	10.69	11.10	10.34	11.19	10.22	10.48	10.72	0.47
Tm	1.54	1.55	1.67	1.58	1.59	1.67	1.56	1.58	1.74	1.53	1.62	1.68	1.56	1.61	1.50	1.45	1.59	0.07
Yb	9.95	9.61	10.21	9.79	10.56	10.59	10.21	9.93	11.66	10.45	10.60	10.55	10.24	10.57	10.24	10.39	10.35	0.47
Lu	1.38	1.34	1.38	1.32	1.41	1.47	1.30	1.41	1.59	1.47	1.45	1.42	1.35	1.34	1.36	1.32	1.39	0.07
Hf	20.09	20.27	20.09	19.26	21.11	21.29	20.46	21.20	22.59	21.57	21.11	22.03	20.37	21.76	20.65	20.09	20.87	0.87
Ta	10.25	10.24	10.19	9.76	10.59	10.86	10.44	10.35	11.25	10.94	10.56	10.58	10.46	10.93	10.48	10.47	10.52	0.36
Pb	10.48	10.43	10.04	9.53	9.95	9.76	9.41	9.38	11.01	10.36	9.89	10.43	9.91	10.19	9.76	9.45	10.00	0.46
Th	14.92	14.85	14.51	14.16	15.59	15.31	15.11	14.80	16.40	15.78	15.03	15.33	14.87	15.48	14.54	14.54	15.08	0.56
U	4.79	4.86	4.75	4.52	4.93	4.88	4.68	4.76	5.25	5.07	4.71	4.83	4.66	4.90	4.54	4.67	4.80	0.19

RFR - Rauðfossafjöll - TJ98-18 Analytical session 5

	1	2	3	4	5	6	7	8	9	10	11	12	13	14	15	16	Mean	St. dev.
Li	33.48	34.19	35.09	33.96	34.44	34.24	34.15	34.81	35.38	35.38	35.00	35.19	34.71	35.94	36.89	36.32	34.95	0.90
Sc	1.99	1.98	2.03	1.99	1.97	1.97	1.96	1.90	2.12	2.01	2.01	2.00	1.95	2.03	2.04	2.06	2.00	0.05
Zn	275.79	274.81	283.07	283.39	277.74	278.83	278.18	291.10	331.93	331.17	331.38	327.91	321.50	327.91	328.99	325.52	304.33	25.13
Rb	110.42	112.42	115.42	115.82	111.12	112.52	112.92	112.82	116.82	116.32	116.22	114.72	111.82	113.32	118.32	112.02	113.94	2.31
Sr	12.69	12.78	13.08	12.45	12.47	12.95	12.74	12.59	13.10	12.64	12.72	12.45	12.72	12.93	13.28	12.92	12.78	0.24
Y	93.37	96.92	98.45	98.35	97.97	99.69	99.89	102.47	106.78	103.43	103.43	103.33	101.23	103.05	103.91	102.28	100.91	3.34
Zr	559.69	560.69	575.57	573.59	580.53	600.38	608.32	635.11	710.53	698.62	699.62	686.72	674.81	671.83	674.81	670.84	636.35	55.23
Nb	172.18	170.54	177.49	172.89	171.05	175.65	172.28	176.57	185.15	180.86	180.55	181.17	177.39	179.74	184.44	182.70	177.54	4.79
Cs	1.30	1.32	1.35	1.33	1.30	1.32	1.32	1.33	1.37	1.34	1.32	1.33	1.31	1.34	1.38	1.36	1.33	0.02
Ba	317.33	317.66	328.35	323.99	318.97	335.99	327.26	327.37	337.08	340.35	333.59	334.90	320.72	328.35	333.81	329.44	328.45	7.22
La	103.56	106.63	110.52	109.81	110.63	111.45	113.60	114.21	110.11	108.27	107.04	104.28	102.64	104.58	105.81	103.35	107.91	3.71
Ce	233.23	239.14	243.11	240.67	241.79	241.79	246.78	252.38	270.21	267.97	264.30	262.06	254.52	259.31	259.92	249.43	251.66	11.34
Pr	26.37	26.75	27.32	27.24	27.15	27.72	27.62	27.94	28.40	28.20	28.07	27.90	27.34	27.32	27.60	27.43	27.52	0.53
Nd	96.12	95.72	98.16	99.07	100.29	102.84	102.63	105.38	106.80	104.97	104.57	104.06	101.21	101.51	103.75	102.23	101.83	3.26
Sm	22.03	21.54	22.27	22.58	22.26	22.12	21.79	22.42	23.15	23.08	22.82	22.94	22.66	23.19	23.80	23.69	22.65	0.64
Eu	2.47	2.48	2.55	2.55	2.45	2.56	2.61	2.63	2.71	2.62	2.60	2.62	2.68	2.59	2.76	2.65	2.60	0.09
Gd	19.17	20.22	20.08	20.08	20.21	21.07	21.07	21.03	21.71	21.02	22.04	21.69	21.10	21.41	21.64	21.60	20.95	0.78
Tb	3.09	3.13	3.16	3.25	3.27	3.35	3.36	3.45	3.73	3.72	3.71	3.63	3.50	3.53	3.60	3.41	3.43	0.21
Dy	19.72	19.90	21.25	20.31	21.19	21.20	21.63	22.24	23.96	23.76	23.12	22.74	22.70	22.35	23.27	22.75	22.01	1.32
Ho	3.97	4.01	4.21	4.09	4.12	4.25	4.28	4.47	4.88	4.74	4.77	4.59	4.63	4.59	4.62	4.44	4.42	0.29
Er	12.23	12.27	13.09	12.54	12.73	13.00	12.93	13.27	14.10	13.88	14.06	13.48	13.59	13.67	13.47	13.99	13.27	0.61
Tm	1.66	1.66	1.82	1.72	1.75	1.77	1.81	1.82	1.99	2.03	2.00	2.01	1.97	1.95	1.98	1.98	1.87	0.13
Yb	11.79	11.99	12.76	12.43	12.93	13.06	13.14	13.18	13.58	13.93	14.02	13.45	13.03	13.28	14.34	13.54	13.15	0.69
Lu	1.55	1.60	1.65	1.62	1.67	1.74	1.72	1.74	1.84	1.85	1.83	1.78	1.72	1.74	1.73	1.78	1.72	0.09
Hf	21.22	21.38	21.84	21.93	22.78	23.55	23.62	24.98	26.99	27.17	26.95	26.67	25.90	25.67	25.76	25.15	24.47	2.13
Ta	12.64	12.81	13.32	13.23	13.26	13.65	13.65	13.85	14.62	14.51	14.67	14.39	14.07	14.30	14.43	14.17	13.85	0.65
Pb	13.81	13.58	14.17	14.28	13.98	14.45	14.12	14.60	15.19	14.85	14.93	15.51	15.04	15.17	15.47	14.91	14.63	0.59
Th	18.84	19.31	20.21	20.04	20.10	20.48	20.61	20.84	22.01	21.75	21.85	21.78	21.48	21.64	21.96	21.65	20.91	1.00
U	4.85	4.71	4.79	4.76	4.89	5.11	5.47	5.98	7.39	7.31	7.19	7.03	6.66	6.65	6.57	6.57	5.99	1.03

RFR - Rauðfossafjöll - TJ98-43 Analytical session 1

	1	2	3	4	5	6	7	8	9	10	11	12	13	14	15	16	Mean	St. dev.
Li	42.04	43.09	41.57	42.74	41.11	43.79	42.27	41.22	38.55	42.74	44.13	40.29	41.81	40.18	39.59	42.04	41.70	1.51
Sc	3.91	3.05	3.00	3.22	3.89	3.23	3.32	3.18	3.09	2.85	3.04	2.69	3.21	3.02	3.13	3.46	3.21	0.33
Zn	197.52	178.52	177.57	179.47	173.78	164.28	169.98	164.28	172.83	169.03	180.42	171.88	162.38	162.38	169.03	156.68	171.88	9.71
Rb	120.06	118.45	116.10	115.24	115.67	119.52	119.10	122.41	114.71	114.82	120.17	116.21	116.74	118.03	117.06	117.81	117.63	2.21
Sr	39.65	39.01	40.01	41.11	33.80	39.23	39.01	29.26	38.23	37.90	38.68	40.12	39.12	37.57	39.67	32.24	37.79	3.22
Y	101.36	96.91	98.56	96.80	94.11	99.70	97.84	95.66	94.73	93.49	95.56	96.08	93.59	93.49	95.97	91.62	95.97	2.54
Zr	763.10	744.62	726.14	726.14	702.23	740.27	733.75	726.14	714.19	704.40	750.06	741.36	727.23	728.32	746.80	712.01	730.42	16.92
Nb	207.22	200.27	198.22	193.21	189.45	203.46	195.49	196.06	192.18	193.89	201.98	195.72	195.60	193.32	194.69	191.73	196.41	4.73
Cs	1.24	1.23	1.01	1.08	1.22	1.12	1.12	1.01	1.04	1.12	1.21	1.11	1.10	1.09	1.12	0.97	1.11	0.08
Ba	484.29	479.67	463.48	472.73	451.93	479.67	467.07	438.06	465.80	464.64	470.42	484.29	471.58	465.80	480.82	457.71	468.62	12.40
La	124.90	120.70	117.36	118.98	115.96	121.56	119.95	118.87	118.33	118.33	121.02	119.73	118.87	118.33	120.16	115.53	119.29	2.24
Ce	259.91	255.56	247.08	250.12	243.60	254.37	252.63	248.17	244.69	249.04	254.37	252.73	250.12	250.56	254.47	240.77	250.51	4.93
Pr	28.21	27.47	27.17	27.16	26.52	28.64	27.58	27.80	27.60	27.69	28.11	26.95	26.74	27.42	28.21	26.37	27.48	0.64
Nd	109.79	107.08	106.21	108.81	103.61	109.14	108.60	105.99	102.74	108.38	107.29	104.15	106.75	102.96	110.76	104.48	106.67	2.51
Sm	20.93	21.34	21.03	21.54	20.41	22.36	20.21	20.41	20.31	20.41	20.41	19.49	21.03	17.23	19.18	18.88	20.32	1.20
Eu	3.57	3.45	3.10	2.98	3.19	3.09	3.27	3.10	3.27	3.29	3.42	3.18	2.86	3.25	3.14	3.24	3.21	0.18
Gd	19.02	18.80	18.80	18.47	20.08	19.22	17.72	18.04	17.61	17.29	17.51	18.15	17.29	15.36	18.15	16.75	18.02	1.11
Tb	3.04	2.91	3.02	3.06	2.98	3.04	3.19	2.88	2.91	2.99	3.16	3.04	3.01	2.90	3.04	2.81	3.00	0.10
Dy	19.04	19.72	19.38	19.93	18.82	19.13	18.82	21.03	19.48	19.26	18.60	19.48	18.90	19.37	20.15	18.71	19.36	0.63
Ho	4.03	3.84	3.92	3.74	3.95	4.13	3.88	3.88	3.73	3.93	3.64	3.70	4.14	3.49	3.74	3.93	3.85	0.17
Er	11.36	10.41	10.75	11.50	11.79	11.85	11.42	11.06	10.92	10.79	11.58	11.44	11.40	10.95	11.97	11.13	11.27	0.44
Tm	1.65	1.68	1.54	1.70	1.57	1.80	1.68	1.60	1.60	1.61	1.76	1.60	1.64	1.60	1.91	1.53	1.65	0.10
Yb	11.15	12.12	11.22	11.28	11.23	12.36	11.64	10.55	11.68	11.52	12.03	11.46	11.63	11.03	11.39	11.03	11.46	0.46
Lu	1.39	1.53	1.46	1.50	1.34	1.50	1.38	1.46	1.25	1.27	1.32	1.37	1.40	1.37	1.32	1.54	1.40	0.09
Hf	19.97	21.63	20.62	21.30	21.19	22.00	21.08	21.08	20.53	19.98	21.52	20.31	20.53	20.31	23.27	20.31	20.98	0.86
Ta	11.90	12.00	11.92	11.69	11.49	12.03	12.18	11.51	11.39	11.59	12.07	11.52	11.72	11.21	11.95	11.32	11.72	0.30
Pb	11.20	11.11	11.05	10.65	10.94	11.17	11.24	11.01	10.68	10.70	11.03	10.73	10.73	10.60	10.69	10.90	10.90	0.22
Th	18.91	19.19	18.56	18.78	18.96	19.43	19.34	18.70	18.83	18.52	19.13	18.95	19.08	18.96	19.28	18.90	18.97	0.26
U	6.20	5.77	5.94	5.86	5.86	5.90	5.96	5.89	5.91	6.11	6.13	6.05	5.73	6.08	6.26	6.01	5.98	0.15

RFR – Unnamed Ridge A - TJ98-05 Analytical session 1

	1	2	3	4	5	6	7	8	9	10	11	12	13	14	15	16	Mean	St. dev.
Li	41.22	39.01	41.92	38.08	41.69	37.49	42.73	39.71	40.75	35.98	39.12	36.10	41.10	36.56	44.13	33.07	39.29	2.94
Sc	1.60	2.06	1.79	1.47	1.37	1.46	1.65	1.39	1.38	1.07	1.44	1.36	1.49	1.27	1.50	1.03	1.46	0.25
Zn	189.91	198.45	190.85	207.95	183.26	190.95	186.11	180.41	185.82	193.70	187.06	199.40	184.11	201.30	173.76	200.35	190.84	8.94
Rb	117.70	122.62	119.19	118.77	116.52	114.91	117.80	115.13	114.81	106.89	112.13	111.49	110.21	107.75	112.99	106.57	114.09	4.70
Sr	21.61	19.06	19.56	19.78	21.05	20.28	20.49	21.72	21.00	19.66	21.50	20.17	19.99	20.83	20.05	24.93	20.73	1.37
Y	98.56	101.77	99.39	101.98	98.14	99.28	99.28	99.49	100.32	96.59	100.32	97.73	97.83	97.31	97.94	95.76	98.86	1.72
Zr	782.61	813.05	789.13	804.35	783.70	800.00	790.22	780.44	779.35	757.61	785.87	778.26	776.09	776.09	770.66	771.74	783.70	13.66
Nb	161.76	169.16	165.17	168.25	162.55	162.33	165.97	163.35	164.26	155.04	164.03	162.44	163.35	158.45	163.24	158.22	162.97	3.57
Cs	1.22	1.29	1.32	1.24	1.27	1.28	1.16	1.19	1.27	1.28	1.26	1.22	1.29	1.23	1.35	1.07	1.25	0.07
Ba	527.02	514.30	527.02	527.02	538.57	528.17	516.62	528.17	535.11	491.19	535.11	509.68	515.46	507.37	518.93	552.44	523.26	14.44
La	115.85	117.46	114.12	116.49	116.71	113.91	118.97	115.95	115.63	108.52	115.63	110.46	114.88	111.65	116.17	108.63	114.44	3.08
Ce	238.14	243.69	238.36	240.97	239.56	233.47	238.80	234.34	232.71	214.22	238.14	221.83	229.45	226.18	230.75	217.05	232.35	8.67
Pr	26.20	26.31	26.94	27.46	27.37	25.99	26.42	25.57	26.41	24.30	26.52	24.83	25.68	24.30	25.81	23.56	25.86	1.12
Nd	98.62	100.57	99.70	103.82	99.70	97.86	98.62	96.67	100.13	89.41	99.92	93.63	98.62	92.77	98.18	91.36	97.47	3.81
Sm	18.67	19.49	21.03	19.69	19.59	18.57	19.49	19.80	20.82	18.05	19.69	18.57	18.05	19.28	19.08	17.13	19.19	1.01
Eu	2.42	2.88	2.86	2.61	3.04	2.48	2.60	2.99	2.74	2.52	3.05	2.39	2.65	2.67	2.78	2.53	2.70	0.22
Gd	18.04	18.79	17.40	19.01	20.30	18.58	17.83	19.12	18.79	17.50	19.12	16.86	18.58	17.72	18.04	15.25	18.18	1.15
Tb	2.87	3.10	3.20	3.00	3.15	2.89	3.17	2.94	2.93	2.60	2.89	2.97	3.12	2.55	3.02	2.69	2.94	0.20
Dy	19.70	17.49	19.59	17.71	19.81	18.71	19.81	18.82	17.82	17.79	19.70	18.38	18.38	19.26	18.96	17.49	18.71	0.87
Ho	3.75	3.71	3.43	3.66	3.83	3.69	3.72	3.71	3.75	3.47	3.72	3.51	3.85	3.60	3.55	3.36	3.64	0.14
Er	11.31	10.97	10.98	11.17	11.82	10.92	11.13	10.58	10.57	9.71	10.76	9.85	11.64	10.21	11.36	10.58	10.85	0.59
Tm	1.58	1.73	1.61	1.71	1.68	1.59	1.64	1.78	1.58	1.47	1.55	1.56	1.62	1.52	1.79	1.55	1.62	0.09
Yb	10.78	11.47	11.22	11.58	11.69	11.15	10.90	10.42	11.09	9.38	10.90	9.07	11.78	10.18	10.53	9.33	10.72	0.85
Lu	1.38	1.30	1.49	1.34	1.59	1.29	1.38	1.13	1.58	1.09	1.27	1.10	1.36	1.27	1.37	1.12	1.32	0.15
Hf	22.72	21.54	21.30	21.95	23.49	20.97	22.50	20.42	22.17	19.21	22.22	19.21	21.95	18.22	21.85	20.09	21.24	1.45
Ta	9.72	9.57	9.99	9.51	9.80	9.42	9.96	9.36	9.83	8.17	9.13	8.50	9.39	8.93	9.75	8.92	9.37	0.52
Pb	10.57	10.81	11.04	10.84	11.17	10.42	11.09	10.26	10.95	9.37	10.43	9.39	10.67	9.81	10.89	9.49	10.45	0.62
Th	16.68	16.81	17.19	16.36	16.69	16.05	16.79	16.54	16.44	13.87	15.94	14.65	16.46	14.86	16.37	14.70	16.02	0.96
U	5.16	5.06	4.85	4.78	5.12	4.81	5.17	4.99	5.28	4.49	5.05	4.65	5.10	4.62	5.06	4.48	4.92	0.25

Unnamed Ridge B - TJ97-12 Analytical session 5

	1	2	3	4	5	6	7	8	9	10	11	12	13	14	15	16	Mean	St. dev.
Li	34.70	34.23	33.85	33.85	34.89	34.32	34.13	34.70	34.42	34.70	33.28	34.32	34.23	32.71	32.62	33.09	34.00	0.72
Sc	1.97	1.87	1.86	2.01	1.87	1.92	1.91	1.92	1.99	1.90	1.94	2.01	1.97	1.86	1.91	1.94	1.93	0.05
Zn	374.40	358.08	359.16	365.70	356.99	353.72	364.61	356.99	378.76	404.88	397.26	405.97	408.14	364.61	361.34	382.02	374.54	19.38
Rb	104.17	101.97	101.87	102.57	100.37	100.67	105.07	99.57	107.38	108.38	102.97	102.97	107.98	100.97	99.97	105.38	103.27	2.87
Sr	27.73	26.98	26.55	25.91	26.87	26.34	26.87	25.91	26.98	26.76	26.98	26.98	28.16	26.01	25.16	26.12	26.64	0.73
Y	113.95	116.35	113.66	111.74	114.33	116.73	119.52	111.84	119.04	118.56	120.67	119.42	121.53	113.85	111.64	113.66	116.03	3.37
Zr	1299.12	1296.14	1290.17	1283.20	1279.2	1304.1	1377.7	1299.1	1372.7	1328.0	1328.0	1332.0	1400.6	1274.3	1273.3	1296.1	1314.60	39.03
Nb	203.83	193.99	196.66	199.73	197.68	200.75	205.87	201.78	214.07	202.80	202.19	211.00	215.09	205.16	202.80	209.97	203.96	6.04
Cs	1.06	0.99	1.03	0.98	1.01	1.03	1.02	1.03	1.07	1.07	1.05	1.05	1.10	0.99	1.00	1.03	1.03	0.03
Ba	430.83	403.49	404.58	399.12	405.68	411.14	417.71	410.05	425.36	414.43	420.99	423.17	435.20	389.28	386.00	399.12	411.01	14.13
La	127.22	120.85	118.18	120.44	117.46	121.57	125.68	117.36	122.49	124.14	125.47	128.24	136.97	122.80	121.98	124.96	123.49	4.87
Ce	270.65	281.89	264.53	269.63	267.59	271.68	271.68	261.46	278.82	299.25	294.14	301.29	316.61	284.95	288.02	293.12	282.21	15.54
Pr	29.50	30.02	28.86	28.65	28.65	28.55	29.50	28.65	30.02	30.65	29.39	30.23	31.18	27.81	27.71	28.44	29.24	0.99
Nd	120.72	113.58	110.63	107.57	106.14	110.12	111.85	111.75	121.33	122.66	122.25	125.00	132.75	115.62	115.21	118.89	116.63	7.17
Sm	26.69	24.26	23.24	23.75	22.63	24.36	24.46	23.95	24.97	24.77	25.07	24.46	26.49	22.63	22.84	23.04	24.23	1.23
Eu	3.97	3.85	3.71	3.89	3.71	3.85	3.89	3.78	3.91	4.00	3.87	3.83	4.20	3.67	3.65	3.62	3.84	0.15
Gd	22.20	22.30	21.90	21.51	22.69	22.20	23.09	21.90	23.58	22.99	22.89	23.88	24.57	22.00	21.11	20.82	22.48	1.00
Tb	3.81	3.60	3.71	3.54	3.53	3.62	3.74	3.64	3.85	3.72	3.73	3.80	4.05	3.37	3.51	3.43	3.66	0.17
Dy	24.18	21.81	21.91	22.40	20.92	22.31	23.19	22.60	23.00	23.00	23.29	23.10	24.58	21.22	22.11	21.71	22.58	0.99
Ho	4.83	4.67	4.59	4.47	4.35	4.44	4.61	4.28	4.59	4.81	4.90	4.95	5.29	4.94	4.77	4.91	4.71	0.26
Er	12.64	13.04	12.55	12.43	12.54	12.45	13.10	12.16	13.12	13.25	12.98	12.56	13.40	11.99	11.66	11.95	12.62	0.51
Tm	1.82	1.87	1.81	1.75	1.77	1.80	1.79	1.77	1.81	1.79	1.87	1.78	1.77	1.57	1.66	1.64	1.77	0.08
Yb	12.86	12.46	12.47	11.67	12.04	12.39	12.05	11.91	11.79	12.14	12.48	12.13	12.72	10.81	11.24	11.31	12.03	0.56
Lu	1.74	1.73	1.63	1.61	1.61	1.69	1.67	1.53	1.60	1.80	1.78	1.73	1.91	1.68	1.65	1.70	1.69	0.09
Hf	34.24	33.34	32.94	33.04	33.24	33.64	34.54	32.94	31.84	32.74	33.14	32.84	33.94	30.83	29.73	30.83	32.74	1.31
Ta	12.39	11.08	11.21	11.26	11.15	11.41	11.63	11.36	11.43	11.39	11.48	11.49	11.74	10.55	10.54	10.68	11.30	0.46
Pb	11.04	10.94	11.12	10.48	11.05	11.10	10.92	10.76	11.27	11.58	11.61	11.30	10.89	10.62	10.57	11.16	11.03	0.33
Th	16.68	15.34	15.66	15.40	15.28	15.53	16.04	15.63	16.32	16.65	16.69	16.56	17.08	15.03	14.91	15.72	15.91	0.67
U	5.58	5.14	5.23	5.15	5.27	5.12	5.33	5.19	5.31	5.57	5.57	5.69	5.70	5.28	5.35	5.40	5.37	0.20

Hábarmur - TJ97-14 Analytical session 5

	1	2	3	4	5	6	7	8	9	10	11	12	13	14	15	16	Mean	St. dev.
Li	31.03	33.66	29.77	28.70	33.76	30.45	20.53	22.76	31.81	20.53	27.05	31.81	32.88	20.24	24.13	25.59	27.79	4.88
Sc	1.83	1.86	1.87	1.86	1.73	1.86	1.83	1.86	1.94	1.92	2.00	2.01	1.77	1.64	1.89	1.72	1.85	0.10
Zn	542.74	549.44	538.28	544.98	560.61	531.57	412.08	415.43	510.36	484.67	452.29	437.77	403.15	377.46	390.86	409.85	472.60	66.44
Rb	108.43	87.88	102.57	118.40	120.76	122.72	94.04	121.28	139.26	101.65	113.57	113.57	135.36	80.68	119.74	97.23	111.07	16.27
Sr	3.39	3.39	3.62	3.43	3.28	3.30	3.86	3.73	3.41	4.93	4.24	3.72	2.90	3.88	3.02	3.78	3.62	0.49
Y	68.16	64.62	86.88	81.56	54.57	73.97	98.60	87.66	60.97	118.20	100.76	86.88	65.80	85.99	59.00	69.05	78.92	17.50
Zr	1424.9	1488.13	1499.36	1471.80	1278.9	1442.20	1578.97	1643.27	1506.50	1721.86	1689.20	1707.57	1468.74	1470.78	1424.85	1369.73	1511.67	125.43
Nb	199.37	203.46	201.78	203.15	174.98	196.21	218.60	223.85	202.94	235.41	235.41	238.57	216.50	222.80	207.04	206.93	211.69	16.91
Cs	0.94	1.01	1.03	0.82	0.84	0.91	0.70	0.79	0.79	0.99	0.84	0.74	0.68	0.72	0.81	0.73	0.83	0.11
Ba	103.67	102.77	109.62	100.87	99.86	103.90	91.55	95.26	101.76	114.78	94.81	87.96	80.56	89.42	89.87	87.96	97.16	9.04
La	70.27	69.01	83.76	71.85	59.84	71.22	80.28	71.11	52.47	102.72	80.17	63.21	48.88	70.38	55.63	67.53	69.90	13.14
Ce	175.74	166.63	203.30	177.42	137.91	168.72	165.16	147.66	114.65	235.79	188.11	152.06	112.87	156.15	122.19	150.70	160.94	32.26
Pr	19.27	18.39	23.08	20.74	15.35	18.75	18.88	16.97	13.36	26.65	21.62	17.69	12.73	17.94	14.05	17.80	18.33	3.61
Nd	71.24	67.37	85.05	75.85	57.44	69.57	72.81	65.07	51.58	106.92	82.75	68.32	48.75	70.51	54.61	68.73	69.79	14.18
Sm	15.61	15.03	19.65	17.40	11.83	16.25	16.53	14.67	10.24	22.01	17.99	14.55	10.20	15.00	11.05	14.36	15.15	3.28
Eu	2.28	2.12	2.83	2.61	1.79	2.17	2.30	1.91	1.48	3.00	2.53	2.05	1.42	2.06	1.52	1.85	2.12	0.47
Gd	15.26	14.38	19.21	17.63	11.85	15.52	17.62	14.39	10.42	21.35	17.61	14.38	9.61	13.97	9.72	13.21	14.76	3.38
Tb	2.68	2.58	3.23	2.98	2.01	2.69	2.87	2.47	1.91	3.71	2.97	2.51	1.87	2.42	1.68	2.16	2.55	0.54
Dy	18.51	18.26	22.32	20.14	13.74	17.73	18.33	17.11	12.23	23.39	19.14	17.11	12.36	15.46	11.03	13.23	16.88	3.62
Ho	3.92	3.91	4.97	4.46	3.03	4.01	4.10	3.71	2.60	4.67	3.83	3.28	2.57	2.98	2.23	2.49	3.55	0.83
Er	12.49	12.63	14.46	13.81	8.79	12.07	11.80	10.56	8.51	14.58	12.60	11.61	8.68	10.29	7.63	7.90	11.15	2.31
Tm	1.89	1.89	2.15	2.12	1.38	1.80	1.63	1.70	1.40	2.25	2.00	1.73	1.36	1.55	1.05	1.17	1.69	0.36
Yb	13.51	13.80	15.33	15.26	10.20	13.35	12.02	12.02	10.43	15.07	14.21	13.25	10.38	10.96	8.75	8.81	12.34	2.21
Lu	2.09	2.15	2.33	2.41	1.75	2.13	1.82	1.81	1.64	2.05	2.06	1.88	1.54	1.64	1.28	1.18	1.86	0.35
Hf	47.25	49.00	51.36	49.41	43.66	47.46	37.19	38.62	39.34	43.55	40.06	38.62	31.23	31.54	30.51	31.33	40.63	7.08
Ta	16.04	16.38	16.86	16.50	16.06	16.40	12.54	14.01	15.55	15.50	13.89	13.85	13.00	12.28	12.04	11.73	14.54	1.82
Pb	17.98	20.32	18.43	17.73	11.15	15.28	11.72	11.76	9.33	13.95	12.06	12.25	12.84	10.40	8.28	6.97	13.15	3.85
Th	21.68	22.73	23.84	22.49	21.49	22.14	17.29	17.69	20.81	22.10	20.03	18.60	16.02	14.92	15.70	16.20	19.61	2.94
U	7.62	7.77	8.16	7.86	6.04	7.22	5.03	4.96	4.02	5.48	4.78	4.35	3.88	3.91	3.43	3.51	5.50	1.70

North Hábarmur - TJ98-34 Analytical session 5

	1	2	3	4	5	6	7	8	9	10	11	12	13	14	15	16	Mean	St. dev.
Li	38.54	38.17	37.15	37.80	38.63	39.10	39.19	40.86	41.42	41.14	39.01	38.91	41.33	40.21	41.61	38.36	39.46	1.43
Sc	1.77	1.74	1.63	1.69	1.72	1.72	1.68	1.71	1.76	1.69	1.72	1.67	1.75	1.74	1.71	1.61	1.71	0.04
Zn	562.21	538.11	544.14	545.14	559.20	563.21	561.20	576.26	593.33	573.25	573.25	547.15	574.26	575.26	595.34	541.13	563.90	17.62
Rb	119.67	121.11	115.54	122.74	123.80	123.51	120.53	127.35	128.88	127.25	124.47	120.63	132.63	125.91	131.86	121.30	124.20	4.59
Sr	10.61	11.61	10.49	10.58	10.57	10.58	10.75	10.89	10.88	10.90	10.61	11.37	10.62	10.85	11.01	10.97	10.83	0.31
Y	142.90	136.23	133.13	138.39	142.43	140.46	139.71	145.07	141.40	145.54	137.55	138.58	143.66	140.65	148.73	136.04	140.65	4.03
Zr	1506.90	1457.56	1412.17	1501.97	1501.0	1492.10	1491.11	1555.3	1525.65	1574.99	1496.05	1476.31	1548.35	1514.80	1599.66	1447.69	1506.35	47.75
Nb	239.00	231.63	219.64	236.25	240.76	234.82	232.84	241.86	242.63	246.04	233.50	233.28	243.07	242.41	247.69	232.62	237.38	6.98
Cs	1.35	1.29	1.27	1.30	1.33	1.33	1.32	1.40	1.42	1.38	1.33	1.34	1.42	1.42	1.40	1.27	1.35	0.05
Ba	369.82	420.94	370.91	377.44	370.91	373.08	374.17	391.58	390.49	376.35	380.70	400.28	377.44	387.23	391.58	382.00	383.43	13.44
La	172.62	164.14	154.11	165.69	172.83	163.83	165.48	169.93	166.72	168.17	161.04	157.62	168.07	164.24	172.41	159.38	165.39	5.43
Ce	392.15	371.59	356.05	380.12	389.15	375.10	377.11	391.15	391.15	405.19	388.14	382.13	402.18	397.17	423.25	395.16	388.55	15.45
Pr	42.60	40.27	38.35	40.69	41.33	39.84	39.95	41.44	42.71	43.56	42.71	42.18	43.99	43.03	45.69	41.44	41.86	1.83
Nd	170.70	161.87	154.59	166.54	172.89	165.61	167.06	172.68	169.25	171.53	167.48	163.43	169.25	166.34	176.84	158.33	167.15	5.65
Sm	35.43	33.71	31.68	34.42	35.13	34.52	34.32	34.82	34.52	35.33	33.71	33.30	34.92	34.62	36.85	33.30	34.41	1.15
Eu	6.21	6.00	5.78	6.14	6.38	6.22	6.21	6.48	6.33	6.30	6.15	6.18	6.29	6.19	6.60	6.01	6.22	0.20
Gd	32.50	30.79	29.75	31.74	31.64	31.83	31.83	32.21	31.46	32.02	30.98	30.89	31.74	31.74	33.35	30.51	31.56	0.85
Tb	5.38	5.06	5.02	5.34	5.41	5.39	5.28	5.46	5.59	5.54	5.38	5.29	5.54	5.40	5.63	5.23	5.37	0.17
Dy	32.82	30.97	30.04	32.26	33.10	32.64	33.28	34.21	34.12	34.21	32.45	33.10	34.58	33.38	35.32	31.62	33.01	1.37
Ho	6.55	6.29	6.12	6.42	6.60	6.55	6.62	6.88	6.68	6.93	6.46	6.49	6.73	6.67	7.00	6.43	6.59	0.23
Er	18.47	17.86	17.32	18.32	18.46	18.45	18.05	19.72	18.49	18.76	18.27	17.97	19.13	18.74	19.60	17.77	18.46	0.64
Tm	2.58	2.39	2.34	2.48	2.57	2.54	2.50	2.67	2.62	2.60	2.53	2.54	2.56	2.53	2.67	2.32	2.53	0.10
Yb	17.95	17.07	16.79	17.82	17.62	17.94	17.89	18.95	18.51	18.70	17.95	17.81	18.92	18.34	18.93	17.76	18.06	0.64
Lu	2.49	2.33	2.39	2.44	2.47	2.42	2.48	2.56	2.58	2.60	2.44	2.45	2.56	2.49	2.62	2.44	2.48	0.08
Hf	48.17	45.67	44.75	47.34	48.35	47.71	48.08	50.20	49.37	49.65	48.54	47.80	49.46	48.54	51.96	45.86	48.21	1.80
Ta	18.01	17.80	16.86	17.98	18.06	18.05	17.87	19.12	17.96	18.26	17.83	17.39	18.47	18.14	19.08	17.51	18.02	0.56
Pb	17.39	16.59	16.14	16.15	16.50	16.84	16.03	17.39	19.19	19.85	18.97	18.55	19.74	18.92	19.91	17.57	17.86	1.43
Th	24.49	23.46	23.07	24.40	24.92	24.64	24.40	25.53	25.16	25.36	24.28	24.02	25.53	24.78	25.94	23.93	24.62	0.78
U	8.32	8.16	8.00	8.36	8.71	8.59	8.76	9.09	9.04	9.21	8.64	8.83	9.02	8.95	9.04	8.31	8.69	0.37

A5.2 Thórsmörk Ignimbrite

Fiamme, analytical session 3:

JM-252	1	2	3	4	5	6	7	8	9	10	11	12	13	14	15	Mean	St. dev.
Li	65.62	66.32	64.64	66.51	66.02	65.82	72.04	67.50	60.99	64.14	61.58	63.65	62.86	48.45	63.65	63.99	5.05
Sc	0.84	0.88	0.85	0.88	0.80	0.79	0.89	0.81	0.77	0.76	0.79	0.81	0.76	0.74	0.74	0.81	0.05
Zn	386.46	384.17	368.11	400.22	387.61	374.99	388.75	386.46	371.55	394.49	378.43	391.05	393.34	388.75	388.75	385.54	8.81
Rb	120.08	119.09	113.73	124.14	113.83	166.58	163.61	151.71	126.52	121.07	123.45	127.52	136.24	121.76	174.52	133.59	20.27
Sr	8.96	9.16	8.61	9.01	8.78	8.12	8.51	7.78	8.24	9.64	8.55	8.93	9.33	7.67	8.83	8.68	0.55
Y	98.95	98.66	94.64	97.38	93.56	91.40	91.20	89.15	88.36	93.07	89.34	91.89	90.91	90.32	91.89	92.72	3.36
Zr	718.69	719.72	695.00	720.75	684.71	675.44	665.15	713.54	645.58	669.26	656.91	664.12	673.38	666.18	673.38	682.79	24.78
Nb	157.65	159.77	151.80	153.82	149.57	146.27	149.36	140.75	143.08	150.53	150.31	147.87	151.38	151.48	152.65	150.42	4.88
Cs	1.48	1.46	1.44	1.46	1.44	1.46	1.44	1.50	1.48	1.53	1.48	1.52	1.49	1.57	1.50	1.48	0.04
Ba	452.70	468.24	438.28	468.24	451.59	430.51	450.48	451.59	442.72	472.67	444.94	470.46	477.11	449.37	487.10	457.07	15.97
La	98.50	99.44	95.24	99.76	94.61	93.35	94.40	94.19	94.30	97.87	94.09	95.14	95.87	95.56	96.92	95.95	2.06
Ce	218.03	223.89	215.10	228.08	219.50	218.66	220.75	219.71	221.80	231.53	223.89	231.63	230.59	231.21	232.89	224.48	5.98
Pr	25.18	25.70	25.25	26.32	25.39	25.49	25.86	25.90	26.01	27.25	26.42	27.25	27.45	27.45	28.18	26.34	0.95
Nd	105.43	107.32	101.66	108.36	105.64	100.82	103.76	102.92	102.92	105.22	104.38	105.54	106.16	103.97	105.22	104.62	2.02
Sm	22.66	22.34	21.71	22.33	21.92	20.55	21.08	20.76	21.18	21.54	21.71	22.34	22.72	22.56	23.60	21.93	0.83
Eu	2.88	2.84	2.64	2.66	2.58	2.58	2.55	2.69	2.58	2.85	2.55	2.71	2.64	2.62	2.69	2.67	0.11
Gd	22.13	21.61	20.93	21.61	21.61	20.79	21.31	21.51	21.51	22.43	21.82	22.08	21.82	21.23	21.92	21.62	0.44
Tb	3.38	3.45	3.31	3.39	3.28	3.17	3.24	3.26	3.35	3.42	3.29	3.39	3.39	3.48	3.43	3.35	0.09
Dy	22.77	21.57	21.13	22.07	21.17	20.67	21.17	20.26	21.17	20.75	20.71	20.76	21.25	21.64	21.47	21.23	0.62
Ho	4.61	4.59	4.52	4.65	4.42	4.38	4.36	4.32	4.26	4.32	4.42	4.39	4.51	4.53	4.53	4.45	0.12
Er	12.53	12.80	12.17	12.68	12.36	12.30	12.32	12.42	12.04	12.87	12.60	12.33	12.70	12.00	12.53	12.44	0.26
Tm	1.74	1.87	1.74	1.77	1.75	1.73	1.76	1.72	1.64	1.81	1.72	1.76	1.76	1.68	1.76	1.75	0.05
Yb	11.78	11.98	11.29	11.83	11.51	11.57	11.08	11.22	10.93	11.46	11.29	11.45	11.23	11.46	11.52	11.44	0.28
Lu	1.45	1.51	1.45	1.50	1.47	1.42	1.45	1.42	1.43	1.51	1.43	1.45	1.43	1.48	1.47	1.46	0.03
Hf	24.76	25.17	23.78	24.96	24.55	23.83	24.35	24.96	23.73	24.61	24.45	24.86	25.07	24.76	25.17	24.60	0.49
Ta	11.14	11.02	10.89	11.20	11.01	10.69	10.78	10.65	10.67	11.20	11.04	11.23	11.19	11.03	10.98	10.98	0.20
Pb	12.08	13.03	12.46	12.89	12.19	12.46	12.56	12.99	12.74	13.65	12.79	13.91	13.80	13.51	13.51	12.97	0.59
Th	16.08	16.16	15.54	16.19	15.56	15.29	15.38	15.11	15.43	16.15	15.81	16.04	16.37	16.03	16.72	15.86	0.46
U	5.16	5.27	5.07	5.51	5.37	5.35	5.28	5.37	5.46	5.65	5.58	5.63	5.72	5.72	5.85	5.47	0.22

JM-253

	1	2	3	4	5	6	7	8	9	10	11	12	13	14	15	Mean	St. dev.
Li	86.47	80.83	87.16	85.18	85.97	76.09	82.02	78.07	80.04	77.67	81.62	91.31	92.69	80.34	78.17	82.91	5.02
Sc	0.77	0.77	0.78	0.79	0.75	0.79	0.77	0.79	0.89	0.73	0.77	0.83	0.87	0.79	0.85	0.80	0.05
Zn	391.59	383.55	383.55	395.03	396.18	284.79	287.09	314.65	288.24	299.72	281.35	316.94	316.94	281.35	284.79	327.05	47.74
Rb	111.11	103.86	107.24	115.38	117.96	115.18	124.12	156.88	115.18	126.10	198.59	224.40	172.77	125.61	130.07	136.30	35.86
Sr	8.46	8.03	8.28	8.24	8.20	7.33	7.10	6.66	7.11	7.24	8.42	8.58	9.49	7.18	8.77	7.94	0.79
Y	91.82	88.09	87.99	89.66	91.72	83.38	83.67	80.82	81.61	80.72	98.99	101.25	106.85	95.65	96.54	90.58	8.02
Zr	660.91	628.95	636.16	644.41	662.97	612.45	643.38	603.17	628.95	618.64	741.33	752.67	775.36	720.71	725.87	670.39	56.78
Nb	156.38	154.78	152.01	158.93	158.93	157.55	166.06	172.45	163.93	162.87	174.15	176.49	184.16	167.13	166.06	164.79	8.97
Cs	1.56	1.50	1.55	1.50	1.52	1.18	1.29	1.49	1.17	1.26	1.34	1.43	1.39	1.42	1.23	1.39	0.13
Ba	461.11	448.88	453.33	451.11	463.33	333.33	336.66	335.55	337.77	334.44	404.44	426.66	437.77	367.77	387.77	398.66	53.24
La	95.06	90.22	89.27	90.22	91.48	68.87	67.82	72.98	68.56	70.35	84.12	89.48	90.33	83.39	80.55	82.18	9.83
Ce	233.00	225.04	224.20	226.30	231.11	164.48	166.58	179.15	165.53	171.82	189.63	207.44	209.95	189.52	183.34	197.81	25.82
Pr	26.66	25.94	25.53	25.73	26.10	18.91	19.33	19.33	19.12	18.50	22.74	24.60	24.60	21.60	21.19	22.66	3.08
Nd	104.42	100.23	100.02	99.60	102.96	72.45	72.45	75.28	73.29	72.34	85.76	91.42	94.25	83.46	80.00	87.19	12.42
Sm	24.69	24.06	23.85	24.80	24.91	18.04	18.26	18.78	18.47	19.10	22.16	23.22	24.48	21.10	19.84	21.72	2.73
Eu	3.09	3.17	3.03	3.19	3.41	2.44	2.51	2.45	2.36	2.35	2.79	3.01	3.15	2.54	2.44	2.80	0.37
Gd	21.50	20.45	19.86	20.79	21.25	14.87	15.90	16.00	15.18	15.39	18.98	19.49	20.62	17.85	17.54	18.38	2.41
Tb	3.55	3.41	3.42	3.52	3.59	2.53	2.77	2.71	2.49	2.66	3.11	3.32	3.46	3.03	3.01	3.11	0.39
Dy	22.60	21.90	21.80	22.10	22.81	16.37	17.18	17.08	16.68	16.88	20.89	21.20	22.00	19.29	18.68	19.83	2.46
Ho	4.40	4.25	4.23	4.29	4.39	3.13	3.21	3.04	2.92	3.00	3.63	3.83	4.07	3.50	3.49	3.69	0.55
Er	12.27	12.14	11.69	12.02	12.11	8.46	8.77	8.55	8.37	8.20	10.01	10.73	11.52	9.82	9.58	10.28	1.58
Tm	1.78	1.71	1.57	1.60	1.66	1.10	1.15	1.12	1.11	1.12	1.37	1.46	1.52	1.32	1.28	1.39	0.24
Yb	11.38	10.28	10.56	10.68	10.75	7.15	7.85	7.07	7.39	7.21	9.09	10.13	10.05	8.87	8.65	9.14	1.51
Lu	1.36	1.41	1.32	1.32	1.42	0.89	0.97	0.99	0.96	0.91	1.07	1.20	1.27	1.07	1.09	1.15	0.19
Hf	25.10	23.55	22.83	23.55	24.01	16.01	16.22	16.22	15.39	15.49	20.14	21.41	21.80	19.01	18.80	19.97	3.47
Ta	11.06	10.63	10.61	10.61	10.77	7.60	8.03	7.62	7.90	8.15	9.20	10.10	9.96	8.95	8.51	9.31	1.28
Pb	13.03	12.32	12.75	12.93	13.11	8.17	8.74	8.22	9.31	8.60	8.91	10.00	9.65	8.73	8.48	10.20	1.99
Th	16.60	16.17	15.65	15.93	16.37	10.74	11.15	10.77	10.73	10.94	13.10	14.01	14.55	12.70	12.10	13.43	2.30
U	5.84	5.66	5.73	5.88	5.79	3.89	4.17	3.99	3.97	3.98	4.12	4.60	4.54	4.16	3.87	4.68	0.83

Ash, analytical session 4:

JM-184	1	2	3	4	5	6	7	8	9	10	11	12	13	14	15	16
Li	46.87	48.75	53.65	29.45	49.11	50.06	50.71	45.38	47.42	52.69	52.88	45.55	53.73	56.71	45.32	48.75
Sc	2.90	1.03	1.09	1.07	1.12	0.94	1.12	1.07	0.87	1.23	1.13	1.03	1.04	1.66	1.46	1.01
Zn	139.26	390.88	294.78	395.81	357.85	385.82	307.31	213.69	371.43	389.28	371.35	368.30	301.06	184.56	175.06	359.67
Rb	139.81	132.08	140.52	135.97	131.80	132.46	139.58	140.03	129.57	140.47	135.74	136.40	134.68	141.30	137.22	133.69
Sr	19.36	12.31	14.36	13.41	12.86	12.66	14.88	15.55	12.30	13.97	13.16	13.38	13.84	16.00	15.89	12.33
Y	148.17	132.06	146.72	130.46	133.71	133.30	151.94	159.89	125.55	135.61	130.81	137.11	140.20	156.20	154.19	127.07
Zr	1064.14	934.01	1041.83	918.65	945.74	940.16	1041.03	1091.95	886.32	969.16	938.35	973.13	969.53	1078.04	1048.98	911.34
Nb	203.35	187.14	190.12	191.04	184.84	190.83	195.10	196.94	188.18	197.94	192.59	196.37	196.53	200.95	195.06	189.71
Cs	3.39	2.13	2.32	2.26	2.19	2.10	2.17	2.14	1.98	2.32	2.14	2.19	2.14	2.70	2.77	2.25
Ba	708.98	623.12	675.85	630.96	605.84	605.89	665.08	687.97	571.84	600.18	574.21	597.34	597.78	629.37	615.54	546.78
La	148.71	131.35	143.45	131.77	129.08	130.00	142.24	147.25	118.54	126.43	124.48	129.65	127.52	143.02	141.86	119.73
Ce	280.07	274.77	287.59	277.69	276.83	279.28	290.96	295.08	269.84	296.85	286.24	288.34	290.28	295.45	293.51	288.49
Pr	34.99	32.90	34.45	31.52	32.09	32.04	35.47	36.05	29.77	32.42	31.82	34.92	34.73	38.01	39.50	35.62
Nd	143.00	124.57	135.30	128.72	128.93	127.36	145.58	148.02	114.47	122.05	118.66	126.23	127.52	144.19	148.44	131.70
Sm	34.77	32.58	37.23	33.66	32.23	31.61	34.95	37.07	30.10	33.57	31.59	34.49	34.10	36.38	32.74	30.48
Eu	4.95	3.62	4.07	3.86	4.09	3.84	4.28	4.44	3.79	4.10	4.07	3.97	3.95	4.65	4.59	3.60
Gd	31.57	30.45	31.30	29.25	30.77	28.75	33.05	32.91	27.85	30.38	28.95	29.58	29.59	32.02	33.00	27.89
Tb	6.32	5.35	5.93	5.41	5.14	4.97	5.54	5.90	4.46	5.10	4.77	5.30	4.92	5.71	5.59	4.83
Dy	33.21	28.28	31.71	29.91	29.42	29.37	32.87	34.91	29.03	31.92	30.29	31.08	31.34	33.54	33.95	30.83
Ho	7.48	6.15	6.69	6.23	6.30	6.23	6.62	7.09	4.93	6.05	5.80	6.25	5.94	6.70	7.42	6.29
Er	19.30	17.83	19.57	17.35	17.78	17.78	19.23	19.43	15.92	17.68	16.24	17.13	17.78	20.55	18.54	15.78
Tm	3.69	2.25	2.55	2.38	2.38	2.27	2.55	2.88	2.19	2.40	2.41	2.43	2.51	3.30	3.21	2.55
Yb	17.43	16.14	17.81	16.72	16.18	15.78	17.19	19.36	14.56	16.79	15.52	16.40	16.37	18.40	17.61	15.16
Lu	2.88	1.88	2.05	1.95	2.10	2.15	2.18	2.21	1.71	2.07	2.01	2.01	1.86	2.58	2.55	1.87
Hf	40.57	36.93	40.77	36.28	37.30	35.57	40.69	42.28	33.51	35.97	34.23	35.37	35.07	37.84	37.47	32.70
Ta	15.54	14.27	15.05	14.38	14.33	14.21	14.75	14.63	13.54	14.63	13.96	14.47	14.17	14.68	14.73	13.95
Pb	15.99	17.62	17.57	18.68	17.37	17.23	16.76	15.13	15.14	16.32	15.70	16.22	16.23	18.39	16.07	18.65
Th	23.91	22.77	24.90	22.92	22.92	22.87	24.96	26.31	21.72	24.11	22.87	23.91	23.35	26.22	24.77	22.57
U	7.37	7.68	7.66	7.82	7.72	7.81	7.58	7.65	7.39	8.01	7.84	7.78	7.54	7.96	7.38	7.95

	JM-205 5	JM-205 6	JM-205 7	JM-219 2	JM-228 9	JM-228 15	JM-228 16	JM-228 19	JM-228 20
Li	37.82	36.60	37.69	43.89	17.33	19.61	20.37	19.70	17.66
Sc	1.16	1.03	1.05	1.16	1.45	1.02	1.17	0.84	1.19
Zn	263.55	220.27	396.03	421.72	158.69	221.91	272.43	251.91	148.03
Rb	129.28	128.82	126.30	146.01	109.11	104.51	101.24	104.01	106.50
Sr	41.40	14.90	11.78	13.12	10.19	10.09	10.23	10.22	11.28
Y	157.13	168.20	132.15	153.81	121.75	127.29	124.57	113.29	132.47
Zr	1139.09	1215.22	978.42	1060.42	866.98	836.64	884.41	807.53	947.27
Nb	178.89	184.55	174.53	213.64	176.93	171.82	179.35	152.95	163.56
Cs	1.90	1.86	1.93	2.10	1.39	1.42	1.45	1.29	1.35
Ba	698.90	659.16	556.17	601.65	498.42	450.85	459.78	449.36	429.27
La	142.24	152.22	122.90	137.76	104.20	108.13	103.64	99.13	108.35
Ce	284.86	299.97	274.72	305.86	204.33	205.91	202.00	205.79	196.74
Pr	36.67	39.21	32.76	38.18	25.82	25.33	24.35	25.18	26.70
Nd	157.06	168.85	135.64	151.72	111.87	103.63	107.08	98.10	102.25
Sm	33.74	37.31	29.37	35.02	25.11	22.37	25.92	21.98	26.37
Eu	4.85	4.78	3.88	4.06	1.82	2.61	2.50	2.50	2.44
Gd	32.99	34.04	28.93	31.02	23.37	23.46	25.82	20.80	25.32
Tb	5.10	5.35	4.30	5.60	3.94	3.59	3.95	3.28	3.55
Dy	33.70	35.84	28.69	35.80	26.25	23.90	23.89	22.20	24.58
Ho	7.22	7.46	6.03	7.42	4.79	4.59	4.81	4.55	5.02
Er	18.62	19.23	15.86	19.66	13.96	13.60	13.94	11.72	12.94
Tm	2.49	2.68	2.26	2.56	1.46	1.75	1.52	1.59	1.58
Yb	18.46	20.44	15.70	18.20	12.00	11.51	10.11	9.38	12.08
Lu	2.03	2.33	1.85	2.35	1.38	1.41	1.60	1.31	1.34
Hf	38.40	41.58	33.83	43.47	24.73	24.20	24.56	21.39	24.17
Ta	15.52	15.47	14.65	16.69	10.28	10.86	11.01	10.37	9.76
Pb	13.35	14.29	15.39	18.04	7.98	8.17	10.09	8.38	7.41
Th	24.68	26.27	21.59	24.11	16.29	16.15	16.07	14.97	15.77
U	8.17	8.47	9.02	8.22	4.16	3.79	3.94	3.59	3.42

A5.3 NAAZ II (II-RHY-1)

Analytical session 2:

	MD01-08-40	MD01-10-40	MD01-13-40	MD01-15-40	MD01-16-40	MD01-18-40	MD01-20-40	MD04-04-40	MD04-05-40	MD04-15-40	MD04-03-50
Li	34.13	34.50	38.88	37.09	32.49	34.41	37.48	32.45	29.93	34.27	29.70
Sc	0.97	0.80	1.22	1.08	0.97	1.11	1.19	1.26	1.37		0.89
Zn	199.91	161.19	177.99	228.03	204.21	193.65	195.41	238.32	218.73	108.05	266.02
Rb	100.87	96.28	95.90	92.66	88.87	93.24	91.73	80.93	94.62	106.94	91.67
Sr	11.96	9.65	10.21	8.98	7.97	10.30	9.31	8.41	9.34	11.04	8.18
Y	110.50	97.17	112.28	100.35	88.22	109.38	105.18	100.52	107.92	105.19	96.25
Zr	745.43	665.55	800.62	731.31	662.80	797.62	759.86	748.91	820.40	746.47	738.75
Nb	148.75	142.08	148.76	144.22	132.60	151.23	146.84	156.00	162.20	160.85	166.95
Cs	1.45	1.50	1.39	1.37	1.38	1.53	1.40	1.22	1.23	1.38	1.24
Ba	510.34	440.60	555.28	511.15	472.33	559.52	515.01	382.42	400.35	471.17	338.64
La	104.91	96.33	121.22	110.10	100.28	121.99	116.26	81.06	90.83	103.83	83.24
Ce	228.78	208.67	247.99	224.91	207.11	259.61	242.89	172.55	193.62	205.98	177.07
Pr	27.90	24.90	31.49	28.03	26.75	32.30	29.26	21.33	22.99	24.12	20.33
Nd	109.76	107.69	135.79	115.91	103.96	133.60	117.43	80.49	92.04	110.98	80.17
Sm	26.81	24.03	30.56	27.68	24.68	29.06	27.44	18.18	22.31	26.60	18.82
Eu	3.47	2.95	3.84	3.18	2.88	3.71	3.14	2.36	2.46	2.85	2.62
Gd	23.34	20.72	26.87	24.99	19.72	30.47	26.83	21.16	19.13	22.66	14.90
Tb	3.77	3.76	4.96	3.92	3.86	4.92	4.50	3.02	3.26	3.60	2.47
Dy	26.30	20.95	27.68	24.89	22.24	30.66	26.93	18.73	20.10	23.20	17.21
Ho	4.89	4.54	5.66	5.20	4.32	6.23	5.49	3.58	3.90	4.14	3.43
Er	12.25	12.92	15.32	13.40	12.63	15.24	14.66	10.31	10.95	13.24	9.84
Tm	2.10	1.90	2.24	1.76	1.76	2.00	2.11	1.22	1.52	1.57	1.17
Yb	12.61	11.15	15.02	12.26	9.88	13.47	13.18	7.02	7.89	11.25	8.78
Lu	1.67	1.65	1.65	1.74	1.46	1.84	1.74	1.10	1.08	1.44	1.19
Hf	23.82	21.94	29.80	28.06	23.62	31.52	28.54	17.57	19.09	21.41	16.43
Ta	11.51	10.78	12.45	12.42	10.57	13.35	12.39	8.10	8.70	10.27	8.36
Pb	13.19	12.87	13.86	12.46	11.58	13.29	12.97	7.92	8.44	10.57	7.45
Th	19.68	17.89	19.80	17.41	14.80	20.41	18.49	11.18	11.95	16.17	12.14
U	5.66	5.07	6.13	5.99	5.15	6.73	5.88	3.89	3.85	4.60	3.47

	MD99-02-40	MD99-09-50	MD99-11-50	GIK23-10-40	GIK23-14-40	GIK23-17-40	GIK23-19-40	GIK23-05-85	GIK23-13-85
Li	38.83	37.28	38.73	31.06	28.83	25.72	28.46	34.75	33.34
Sc	0.98	1.22	0.83	1.24	0.96	1.05	1.72	0.95	0.82
Zn	236.20	235.01	357.91	252.24	179.38	160.36	135.08	163.34	270.80
Rb	99.91	100.67	100.90	99.57	98.69	95.26	102.90	103.69	100.08
Sr	10.45	10.12	10.80	10.57	10.19	9.63	10.29	9.59	8.97
Y	113.85	100.78	111.75	112.80	106.88	98.04	96.50	111.47	102.75
Zr	759.10	735.70	809.37	794.95	822.49	772.49	752.21	813.35	757.33
Nb	157.09	155.63	166.71	169.65	180.69	170.28	185.71	161.39	158.80
Cs	1.48	1.57	1.58	1.30	1.20	1.02	1.22	1.41	1.36
Ba	490.30	510.55	529.24	396.41	390.75	368.93	354.63	424.00	388.77
La	111.57	109.80	118.86	94.60	88.04	85.14	82.33	99.01	90.28
Ce	241.93	234.09	263.65	182.60	169.40	158.01	154.59	202.95	195.43
Pr	31.20	29.45	33.13	21.30	20.03	18.98	17.73	24.21	22.44
Nd	125.76	109.90	126.45	82.13	75.92	79.82	72.02	94.17	89.52
Sm	28.02	24.08	29.38	20.67	17.61	18.84	17.52	22.06	22.09
Eu	3.98	3.83	4.68	2.19	1.85	2.48	1.96	2.80	2.89
Gd	28.53	22.91	24.59	17.47	15.27	16.05	19.03	21.61	19.56
Tb	4.38	3.80	4.53	3.15	3.11	2.48	2.97	3.41	3.04
Dy	27.52	24.17	29.34	16.42	18.53	15.75	14.41	20.97	20.62
Ho	5.36	5.52	6.08	3.49	3.62	3.23	2.50	4.38	3.86
Er	14.55	13.29	16.46	10.30	9.42	8.94	7.53	11.86	10.37
Tm	1.94	2.35	2.41	1.28	1.29	1.32	0.95	1.44	1.43
Yb	14.25	13.52	14.76	9.48	8.37	8.19	8.76	9.98	9.16
Lu	1.99	1.82	2.04	1.05	0.94	0.85	0.96	1.49	1.30
Hf	30.26	26.79	33.15	17.18	16.72	14.38	15.62	21.70	20.03
Ta	12.81	12.59	14.33	7.74	7.36	6.50	6.55	9.84	9.44
Pb	12.82	13.46	14.05	6.59	7.17	6.63	5.11	9.05	9.30
Th	21.95	18.77	22.35	13.33	12.52	11.17	10.22	14.02	13.23
U	6.41	5.59	6.52	3.70	3.53	3.12	2.93	3.83	4.13

Analytical session 3:

	MD01-01-25	MD01-02-25	MD01-03-25	MD01-05-25	MD01-06-25	MD01-07-25	MD01-08-25	MD01-10-25	MD01-11-25
Li	36.13	34.64	35.87	33.97	33.84	33.66	32.99	32.50	35.55
Sc	0.86	1.30		0.93		1.19	1.29		0.67
Zn	374.22	278.36	365.14	344.55	259.40	257.18	356.93	181.94	351.97
Rb	100.97	100.41	105.14	98.90	100.14	102.50	100.47	106.77	99.88
Sr	11.10	11.02	11.30	10.67	9.73	9.82	9.80	9.81	9.38
Y	108.47	106.88	113.08	108.74	110.90	108.66	113.02	110.74	112.11
Zr	786.72	806.27	817.06	784.39	768.34	786.99	805.36	779.69	767.41
Nb	156.76	163.29	167.03	167.66	159.40	164.69	173.15	162.70	165.47
Cs	1.45	1.39	1.38	1.32	1.66	1.15	1.35	1.39	1.38
Ba	497.31	521.16	509.02	508.02	485.58	501.01	511.30	520.58	513.64
La	108.84	110.12	110.96	106.05	109.28	111.58	118.77	115.52	112.84
Ce	234.82	234.59	242.16	231.04	227.79	235.06	241.82	239.83	237.94
Pr	29.74	28.52	28.80	27.54	28.85	27.63	29.56	27.75	27.98
Nd	120.00	129.01	129.37	126.99	121.54	120.02	123.02	123.66	115.21
Sm	27.33	25.44	26.10	28.76	28.93	26.78	27.88	24.79	26.40
Eu	3.43	3.27	3.31	3.05	3.06	2.12	3.33	3.33	3.12
Gd	26.08	25.94	30.70	24.42	26.18	26.20	31.13	27.06	26.34
Tb	4.46	3.81	4.46	4.44	4.80	4.43	3.89	3.44	4.38
Dy	27.17	27.72	25.12	28.75	24.77	27.90	29.28	23.48	28.85
Ho	5.78	5.86	5.07	5.30	5.10	5.43	5.60	4.73	5.29
Er	14.33	14.07	16.05	14.95	15.10	14.04	16.25	15.17	14.02
Tm	2.04	1.89	2.33	2.02	1.69	1.86	2.22	1.88	2.12
Yb	12.77	11.86	15.03	13.11	14.96	12.43	14.84	15.98	12.47
Lu	2.38	2.37	2.46	2.30	1.81	2.25	2.45	1.82	2.50
Hf	27.44	26.21	29.36	27.93	25.33	27.81	26.29	27.94	27.55
Ta	11.28	11.40	11.75	11.53	11.20	11.17	12.17	11.30	11.77
Pb	13.17	12.40	12.81	12.42	13.22	12.76	12.08	15.43	13.57
Th	18.44	18.17	19.75	18.68	18.06	18.24	19.15	17.67	18.47
U	5.47	5.27	5.74	5.53	5.55	5.30	5.67	5.37	5.65

	MD04-01-25	MD04-02-25	MD04-04-25	MD04-06-25	MD04-08-25	MD04-09-25	MD04-10-25
Li	34.49	31.29	34.28	33.23	32.47	35.72	36.95
Sc	1.73	1.18	0.91		0.73		1.60
Zn	302.72	283.27	333.64	279.52	314.10	268.60	288.44
Rb	98.03	97.42	99.61	96.55	97.21	113.37	110.51
Sr	9.83	10.58	10.25	10.44	9.99	11.11	12.33
Y	117.79	98.15	110.65	109.88	110.17	128.03	126.82
Zr	785.84	716.85	790.68	778.03	786.81	937.15	915.38
Nb	158.63	144.48	152.38	150.51	155.75	185.12	183.49
Cs	1.46	1.36	1.49	1.37	1.15	1.37	1.28
Ba	485.22	484.56	499.81	490.12	475.73	502.97	515.77
La	111.46	106.84	118.91	112.20	113.23	116.74	113.13
Ce	245.03	226.24	246.41	238.11	238.43	236.80	234.82
Pr	27.46	25.33	28.87	28.79	29.09	27.35	27.73
Nd	109.47	104.21	111.12	111.50	112.29	103.90	101.87
Sm	23.03	21.40	21.75	27.05	26.06	23.96	26.63
Eu	2.30	2.72	3.33	3.04	3.23	3.08	2.65
Gd	28.94	21.37	25.57	28.44	23.95	29.85	23.93
Tb	4.07	3.35	4.05	3.83	3.89	4.19	3.94
Dy	28.32	23.46	26.23	23.90	27.63	22.54	21.69
Ho	4.86	4.76	4.88	5.52	5.28	5.35	4.81
Er	13.28	12.58	14.64	13.58	14.02	12.32	12.99
Tm	2.28	1.88	1.96	1.86	2.57	1.90	1.82
Yb	16.00	9.78	14.97	13.80	13.46	16.27	14.60
Lu	2.11	2.15	2.37	1.92	1.72	1.93	1.45
Hf	26.22	23.58	27.58	25.64	25.78	25.75	24.23
Ta	11.34	10.46	10.74	10.96	11.03	11.19	10.54
Pb	13.08	12.27	12.52	11.72	11.11	7.92	10.13
Th	16.56	15.46	18.39	17.08	16.95	15.53	15.57
U	5.42	5.17	5.70	5.56	5.28	5.01	4.51

	MD99-01-25	MD99-02-25	MD99-03-25	MD99-04-25	MD99-05-25	MD99-07-25	MD99-08-25	MD99-10-25	MD99-11-25	MD99-12-25	MD99-13-25
Li	33.76	39.49	39.92	35.23	35.93	32.56	37.28	36.32	36.82	29.65	37.31
Sc		1.25	0.89	1.22	1.24		1.05	1.40	0.93		0.79
Zn	224.82	352.52	351.86	336.45	295.34	213.21	338.07	360.02	333.90	135.65	327.31
Rb	96.35	100.56	99.86	98.27	101.34	104.05	99.24	100.51	99.84	101.46	99.49
Sr	9.91	9.71	10.04	10.37	10.73	11.61	10.19	10.05	11.25	10.40	11.44
Y	111.96	117.82	117.72	114.75	118.31	113.17	115.09	108.96	112.78	97.28	112.04
Zr	754.93	809.43	819.98	808.42	835.57	788.86	819.30	814.68	823.16	740.15	817.11
Nb	160.08	163.00	155.16	157.26	155.54	145.60	146.79	147.61	150.31	133.05	147.09
Cs	1.35	1.42	1.28	1.36	1.60	1.34	1.44	1.48	1.42	1.46	1.28
Ba	480.38	523.91	527.96	535.49	532.37	506.06	517.82	550.64	542.09	457.09	517.66
La	102.75	113.01	113.15	109.04	115.50	112.94	111.77	115.52	114.51	99.97	114.16
Ce	225.47	252.33	251.63	253.09	264.42	250.59	258.97	263.39	258.24	223.14	261.67
Pr	27.83	29.37	29.66	30.26	30.38	28.71	29.47	30.41	30.93	27.63	30.20
Nd	121.58	126.49	131.72	125.03	133.14	121.58	130.19	129.70	132.73	114.12	127.71
Sm	22.34	29.46	29.98	23.72	26.83	26.94	27.34	26.48	26.59	23.97	26.71
Eu	3.32	2.96	3.46	3.27	3.01	2.92	3.34	3.01	3.50	2.92	3.52
Gd	24.32	25.06	24.37	24.44	25.25	22.72	24.79	27.00	26.13	23.78	25.83
Tb	3.69	4.40	4.56	4.17	3.97	3.54	4.23	3.98	4.32	4.00	4.31
Dy	25.28	28.42	26.08	27.70	27.72	23.83	26.89	25.30	28.06	22.52	24.93
Ho	4.55	5.78	5.52	5.48	5.66	5.44	5.59	6.19	5.46	4.46	5.46
Er	12.13	12.91	13.97	13.69	15.32	12.60	14.70	14.12	13.40	10.98	14.91
Tm	1.60	2.10	2.16	2.22	2.10	2.29	1.79	1.71	1.92	1.59	2.12
Yb	11.65	15.32	13.81	15.92	13.20	11.61	13.64	14.65	13.86	11.14	14.31
Lu	1.40	1.87	2.21	1.61	2.17	1.68	2.26	2.14	2.17	1.32	1.71
Hf	23.85	29.49	28.38	28.66	27.63	27.61	28.98	28.80	27.73	21.50	28.10
Ta	11.73	12.02	12.32	12.18	11.92	11.78	12.32	12.67	11.96	10.38	12.04
Pb	11.11	11.75	11.61	12.77	12.49	12.64	11.68	12.95	12.01	10.66	11.81
Th	15.60	18.45	18.90	18.47	18.38	16.87	19.47	19.52	18.36	15.02	18.74
U	5.07	5.53	5.81	5.69	5.79	5.32	5.95	6.36	6.12	4.54	6.07

	GIK23-01-25	GIK23-02-25	GIK23-05-25	GIK23-07-25	GIK23-09-25	GIK23-10-25	GIK23-11-25
Li	35.56	31.04	39.30	32.91	34.90	33.60	42.99
Sc	1.01		0.85		1.29		1.55
Zn	217.63	170.28	269.19	164.75	131.40	102.06	296.56
Rb	116.38	112.23	110.48	107.52	107.53	115.13	112.28
Sr	10.84	9.78	11.37	12.09	10.82	12.59	10.45
Y	132.84	118.14	126.31	112.02	116.37	131.55	127.04
Zr	917.00	837.09	923.44	863.72	851.39	923.19	910.17
Nb	193.46	183.65	208.26	192.98	190.13	206.33	207.84
Cs	1.48	1.45	1.44	1.25	1.20	1.47	1.44
Ba	550.96	494.06	526.80	473.22	457.72	540.86	492.68
La	112.97	102.30	108.32	99.83	98.61	110.28	110.50
Ce	231.76	206.16	229.47	197.29	199.06	217.87	230.61
Pr	28.81	26.46	30.26	23.03	25.00	29.49	28.93
Nd	113.43	106.72	112.41	96.91	99.70	116.14	118.41
Sm	24.13	22.04	26.32	17.06	24.56	20.77	26.37
Eu	2.05	3.00	3.06	1.63	2.18	2.17	2.73
Gd	25.52	25.80	24.75	25.84	22.00	26.95	25.72
Tb	3.97	3.56	3.63	2.80	2.69	4.63	3.75
Dy	25.85	21.59	23.19	23.23	22.30	21.48	26.14
Ho	5.16	4.08	4.28	4.14	4.29	5.03	4.10
Er	13.38	11.06	13.19	10.41	9.84	13.13	12.19
Tm	2.22	1.84	1.83	1.22	1.67	1.40	1.84
Yb	14.49	11.64	11.05	14.74	14.20	12.73	11.56
Lu	1.73	1.19	1.79	1.29	1.24	1.79	2.02
Hf	25.34	19.39	24.86	22.79	21.88	20.84	24.21
Ta	9.88	8.58	11.03	9.46	8.14	10.84	11.18
Pb	11.84	10.02	11.54	10.35	9.05	12.81	11.27
Th	16.08	13.91	16.17	13.25	12.89	15.22	15.88
U	4.54	3.80	4.57	3.75	3.70	4.08	4.56

A5.4 BCR-2G secondary standard raw data

Prior to correction to preferred values.

Preferred values	
Li	**8.85**
Sc	**34.36**
Zn	**168.25**
Rb	**48.69**
Sr	**338.78**
Y	**32.34**
Zr	**180.60**
Nb	**12.70**
Cs	**1.20**
Ba	**705.50**
La	**24.50**
Ce	**51.13**
Pr	**6.46**
Nd	**27.53**
Sm	**6.41**
Eu	**1.98**
Gd	**6.29**
Tb	**0.97**
Dy	**6.08**
Ho	**1.24**
Er	**3.46**
Tm	**0.48**
Yb	**3.42**
Lu	**0.49**
Hf	**4.76**
Ta	**0.73**
Pb	**10.90**
Th	**5.82**
U	**1.66**

Analytical session 1 - 19/02/16								
	1	2	3	4	5	Mean	St. dev.
Li	7.09	7.66	8.00	7.44	7.22	7.48	0.36
Sc	28.70	32.50	31.20	29.70	29.70	30.36	1.49
Zn	166.00	162.00	165.00	190.00	173.00	171.20	11.26
Rb	48.90	48.70	46.00	44.30	45.30	46.64	2.06
Sr	298.00	326.00	316.00	286.00	309.00	307.00	15.56
Y	29.10	32.30	31.40	30.40	31.20	30.88	1.20
Zr	151.60	174.60	166.00	163.40	165.70	164.26	8.26
Nb	10.35	11.98	11.54	10.39	11.30	11.11	0.72
Cs	1.14	1.24	1.20	1.11	1.20	1.18	0.05
Ba	613.00	668.00	610.00	590.00	619.00	620.00	28.96
La	22.40	24.00	23.50	22.21	22.10	22.84	0.85
Ce	47.90	49.00	48.20	46.10	45.80	47.40	1.39
Pr	5.63	6.41	6.18	5.75	6.29	6.05	0.34
Nd	25.30	26.50	27.30	23.30	25.10	25.50	1.52
Sm	7.18	5.93	6.72	5.91	6.00	6.35	0.57
Eu	1.70	1.81	1.67	1.62	1.69	1.70	0.07
Gd	5.85	5.57	5.26	6.31	5.89	5.78	0.39
Tb	0.87	1.02	0.90	0.80	0.96	0.91	0.09
Dy	5.90	6.72	5.86	5.05	5.46	5.80	0.62
Ho	1.18	1.17	1.19	1.11	1.05	1.14	0.06
Er	2.85	3.26	3.21	3.01	2.99	3.06	0.17
Tm	0.43	0.44	0.42	0.38	0.40	0.41	0.02
Yb	2.72	2.88	3.08	2.32	3.01	2.80	0.30
Lu	0.36	0.52	0.48	0.39	0.48	0.44	0.06
Hf	3.72	4.91	4.45	3.96	4.50	4.31	0.47
Ta	0.64	0.67	0.63	0.57	0.64	0.63	0.04
Pb	10.61	11.34	10.18	9.00	10.28	10.28	0.85
Th	4.75	5.79	5.10	4.78	4.83	5.05	0.44
U	1.39	1.72	1.41	1.33	1.40	1.45	0.15

Analytical session 2 - 15/03/16

	1	2	3	4	5	6	7	8	9	10	Mean	St. dev.
Li	8.96	8.66	8.18	8.34	9.34	9.44	9.35	9.23	8.52	8.71	8.87	0.45
Sc	32.60	31.30	30.90	31.50	32.00	31.20	37.40	37.30	30.30	30.50	32.50	2.64
Zn	144.40	149.00	138.00	143.00	148.90	158.70	155.90	150.00	127.90	133.20	144.90	9.70
Rb	49.80	50.20	43.00	45.20	49.10	52.90	51.60	51.60	46.80	48.10	48.83	3.10
Sr	312.00	308.00	286.00	296.00	320.00	331.00	356.00	360.00	297.00	301.00	316.70	25.25
Y	30.70	30.80	28.40	29.40	28.60	30.10	36.40	36.70	29.80	30.10	31.10	2.98
Zr	162.00	157.60	153.70	160.90	157.70	162.90	193.10	188.00	154.20	158.40	164.85	13.92
Nb	11.11	11.42	11.04	11.09	12.09	11.58	12.89	12.71	10.66	10.91	11.55	0.77
Cs	1.17	1.24	1.16	1.12	1.17	1.31	1.25	1.27	1.06	1.12	1.19	0.08
Ba	599.00	630.00	573.00	598.00	606.00	629.00	687.00	683.00	566.00	594.00	616.50	41.42
La	21.50	21.50	20.96	21.20	22.60	21.50	26.70	25.30	21.80	21.07	22.41	1.97
Ce	45.10	45.50	45.80	47.10	46.60	48.00	54.30	52.50	44.40	44.60	47.39	3.38
Pr	5.75	5.85	5.74	5.57	5.90	6.21	7.03	6.91	5.51	5.71	6.02	0.54
Nd	23.00	23.40	22.90	24.40	26.00	27.00	29.50	29.30	23.90	25.10	25.45	2.46
Sm	5.60	4.95	6.00	5.71	5.61	5.45	6.67	6.67	5.54	5.64	5.78	0.53
Eu	1.68	1.88	1.79	1.57	1.84	1.73	2.00	2.00	1.31	1.56	1.74	0.21
Gd	5.90	5.00	5.22	5.80	4.70	5.36	7.00	6.66	5.70	5.83	5.72	0.71
Tb	0.70	0.89	0.86	0.90	0.83	0.83	1.03	1.15	0.89	0.84	0.89	0.12
Dy	5.31	5.57	5.10	5.53	5.06	4.92	6.71	6.18	5.12	4.98	5.45	0.58
Ho	1.07	1.00	1.02	1.01	1.15	1.11	1.39	1.34	0.95	0.96	1.10	0.15
Er	2.55	2.91	3.16	2.83	3.24	3.04	3.83	3.70	2.79	2.94	3.10	0.40
Tm	0.49	0.32	0.33	0.31	0.45	0.39	0.57	0.51	0.38	0.31	0.41	0.09
Yb	2.85	2.87	2.54	2.76	3.00	3.00	3.68	3.62	2.65	2.71	2.97	0.39
Lu	0.39	0.36	0.46	0.38	0.32	0.46	0.51	0.50	0.36	0.39	0.41	0.06
Hf	3.92	3.46	4.19	4.19	4.12	4.18	5.31	4.97	3.92	3.93	4.22	0.54
Ta	0.62	0.58	0.57	0.57	0.61	0.69	0.73	0.74	0.55	0.58	0.62	0.07
Pb	8.70	8.31	9.10	9.40	9.04	9.36	10.58	10.63	8.45	8.70	9.23	0.81
Th	4.78	4.99	4.58	4.62	4.92	5.26	6.24	6.01	4.53	4.57	5.05	0.61
U	1.37	1.45	1.42	1.43	1.41	1.57	1.69	1.64	1.41	1.51	1.49	0.11

Analytical session 3 - 16/03/16

	1	2	3	4	5	6	7	8	9	10	11	12	13	14	15	16	Mean	St. dev.
Li	8.52	8.30	9.80	7.60	8.20	8.40	11.20	9.40	9.03	9.11	9.21	9.23	8.20	9.41	8.98	8.90	8.97	0.83
Sc	31.20	29.90	31.40	28.50	32.20	31.60	31.90	29.60	35.70	37.10	35.20	34.70	31.80	33.40	34.50	32.80	32.59	2.37
Zn	144.00	138.00	150.00	151.00	125.00	138.00	151.00	144.00	155.80	155.30	135.00	148.60	142.00	147.00	145.70	149.00	144.96	8.01
Rb	49.90	47.10	49.10	47.00	46.60	45.40	52.00	49.80	52.70	50.90	49.00	50.80	45.80	46.70	48.30	50.20	48.83	2.23
Sr	319.00	319.00	298.00	294.00	282.00	298.00	321.00	293.00	343.00	354.00	334.00	337.00	309.00	320.00	341.00	337.00	318.69	21.31
Y	29.10	28.20	27.80	29.90	28.90	28.60	28.60	26.90	35.20	36.20	34.00	33.90	29.60	30.80	33.20	32.00	30.81	2.89
Zr	163.00	150.00	143.00	156.00	154.00	156.00	157.60	157.00	189.00	195.00	179.00	178.60	156.00	167.00	178.20	166.00	165.34	14.67
Nb	11.00	10.80	12.30	11.30	10.40	11.00	11.23	11.00	12.41	12.77	12.00	12.07	11.08	11.58	12.17	11.90	11.56	0.68
Cs	1.44	1.13	1.09	1.25	1.32	1.28	1.32	1.17	1.27	1.23	1.12	1.27	1.08	1.16	1.20	1.21	1.22	0.10
Ba	618.00	564.00	601.00	595.00	532.00	539.00	603.00	582.00	654.00	658.00	641.00	637.00	604.00	634.00	643.00	636.00	608.81	38.93
La	23.90	22.50	22.00	22.20	18.50	20.40	22.30	21.80	24.20	25.10	24.00	24.30	20.70	22.50	23.80	22.80	22.56	1.70
Ce	49.90	49.60	44.60	43.90	45.10	43.30	46.10	45.40	50.10	51.30	48.90	50.40	44.30	47.80	48.90	50.80	47.53	2.78
Pr	6.44	6.48	5.88	6.13	4.81	6.06	5.97	5.36	6.75	6.76	6.18	6.23	5.57	6.31	6.36	6.12	6.09	0.50
Nd	26.10	22.10	26.10	27.30	22.40	21.40	24.80	25.50	28.00	28.60	25.80	26.90	23.00	26.00	26.50	26.40	25.43	2.14
Sm	5.00	6.00	6.70	6.60	5.00	4.60	5.80	6.40	6.28	6.55	6.42	6.29	5.34	5.67	6.49	5.84	5.94	0.65
Eu	1.78	1.81	1.87	1.75	2.33	1.72	2.12	1.91	2.07	2.01	1.80	1.94	1.50	1.67	1.97	1.87	1.88	0.20
Gd	5.90	3.30	3.40	5.90	4.50	5.80	5.20	6.50	6.67	6.56	5.70	6.67	5.40	5.82	6.45	6.07	5.62	1.06
Tb	0.69	0.84	0.79	1.00	0.71	0.86	1.02	0.85	1.07	1.07	0.97	1.03	0.89	0.87	1.03	0.95	0.91	0.12
Dy	5.58	5.40	6.10	4.70	4.70	3.60	6.20	5.50	6.37	6.50	6.08	6.07	5.46	5.70	6.35	6.16	5.65	0.77
Ho	0.95	0.97	1.02	1.14	0.89	1.02	1.07	1.10	1.31	1.36	1.22	1.20	1.01	1.22	1.18	1.14	1.11	0.13
Er	2.76	3.32	3.07	3.41	2.80	2.31	3.41	2.65	3.83	3.67	3.24	3.37	2.87	3.21	3.36	3.37	3.17	0.40
Tm	0.47	0.26	0.45	0.35	0.28	0.44	0.50	0.40	0.49	0.50	0.48	0.49	0.38	0.43	0.46	0.47	0.43	0.08
Yb	2.80	2.79	2.83	2.43	1.91	3.80	2.49	2.00	3.37	3.45	3.27	3.23	2.78	2.70	3.27	3.16	2.89	0.52
Lu	0.34	0.40	0.29	0.32	0.47	0.23	0.32	0.33	0.54	0.51	0.51	0.51	0.39	0.44	0.47	0.44	0.41	0.09
Hf	4.20	4.50	4.33	3.87	3.62	4.20	4.80	3.97	4.92	5.08	4.72	4.70	3.74	4.46	4.85	4.56	4.41	0.44
Ta	0.82	0.58	0.64	0.64	0.50	0.72	0.73	0.43	0.75	0.73	0.68	0.69	0.63	0.67	0.68	0.67	0.66	0.10
Pb	10.30	10.00	10.40	9.50	8.70	7.50	9.10	9.70	10.93	10.16	9.48	10.58	8.66	9.36	9.89	9.99	9.64	0.86
Th	5.20	4.90	4.98	5.03	4.74	4.86	5.07	5.09	6.02	6.07	5.57	5.65	4.86	5.33	5.62	5.40	5.27	0.41
U	1.56	1.58	1.52	1.43	1.51	1.53	1.64	1.52	1.62	1.77	1.57	1.63	1.49	1.63	1.58	1.65	1.58	0.08

Analytical session 4 - 17/03/16

	1	2	3	4	5	6	7	8	9	10	11	12	13	14	15	Mean	St. dev.
Li	9.40	9.71	10.30	8.80	8.20	7.65	8.20	10.50	9.30	9.30	9.30	9.78	9.50	8.70	10.80	9.30	0.88
Sc	31.60	30.40	27.30	28.50	27.80	27.80	25.80	32.80	33.20	29.10	33.30	31.20	27.50	26.30	30.60	29.55	2.51
Zn	146.00	140.00	157.00	155.00	161.00	166.00	140.00	155.00	159.00	140.00	132.00	173.00	137.00	138.00	158.00	150.47	12.25
Rb	49.50	50.30	48.70	47.00	48.90	50.90	49.00	48.90	49.50	43.40	49.70	52.20	47.70	48.00	51.20	48.99	2.06
Sr	304.00	313.00	311.00	296.00	308.00	323.00	277.00	346.00	329.00	314.00	312.00	337.00	288.00	289.00	321.00	311.20	18.77
Y	29.20	29.60	27.20	26.00	27.00	27.80	27.00	31.30	31.70	30.00	29.20	31.30	26.80	24.60	28.90	28.51	2.10
Zr	153.00	155.10	152.00	139.00	133.00	142.00	135.00	151.00	166.00	139.00	154.00	157.00	143.00	129.00	139.00	145.81	10.45
Nb	11.00	10.72	11.40	11.00	10.70	11.10	10.80	11.70	11.20	10.70	11.10	12.40	11.60	10.90	12.20	11.23	0.53
Cs	1.24	1.25	1.21	1.13	1.19	1.24	1.09	1.32	1.11	1.13	1.17	1.38	1.11	1.13	1.27	1.20	0.09
Ba	671.00	664.00	657.00	612.00	611.00	638.00	594.00	720.00	736.00	605.00	640.00	713.00	591.00	602.00	676.00	648.67	47.63
La	22.20	21.30	22.60	24.70	21.00	20.70	20.60	23.40	23.40	21.70	20.80	26.10	22.00	19.70	22.30	22.17	1.69
Ce	52.40	53.20	51.70	56.10	47.00	48.70	47.40	52.80	52.60	51.20	50.80	56.40	47.90	46.30	56.70	51.41	3.42
Pr	6.05	5.95	5.94	6.32	5.90	5.98	5.57	6.28	6.28	6.88	6.57	6.71	5.79	5.62	6.30	6.14	0.38
Nd	25.00	26.30	23.90	21.30	22.00	24.50	21.80	26.50	26.30	26.80	27.30	27.80	23.00	23.80	26.00	24.82	2.11
Sm	5.74	5.91	5.21	5.38	4.98	5.71	6.00	5.80	5.85	6.30	5.37	6.09	5.67	4.79	6.02	5.65	0.43
Eu	1.80	2.02	1.48	2.01	1.63	1.59	1.89	1.60	2.50	2.06	1.86	2.01	1.57	1.76	1.92	1.85	0.26
Gd	5.74	6.05	4.79	5.30	5.11	4.55	4.71	5.30	5.90	6.80	5.80	6.04	4.87	4.98	5.55	5.43	0.62
Tb	0.84	0.85	0.74	0.81	0.78	0.77	0.69	0.88	0.92	0.82	0.89	1.09	0.85	0.78	0.83	0.84	0.09
Dy	5.34	5.95	5.04	4.60	4.73	5.34	4.15	5.80	5.46	6.30	6.50	6.19	5.13	4.36	4.96	5.32	0.72
Ho	1.08	1.13	0.95	0.92	0.97	1.01	0.99	1.08	1.26	1.18	1.26	1.20	0.96	0.89	1.11	1.07	0.12
Er	3.03	3.29	2.90	2.75	2.74	2.86	2.73	3.00	3.40	2.95	2.80	3.57	3.26	2.49	2.76	2.97	0.29
Tm	0.49	0.45	0.37	0.29	0.42	0.47	0.41	0.42	0.61	0.42	0.45	0.44	0.41	0.37	0.51	0.43	0.07
Yb	2.76	3.26	2.45	2.46	2.49	2.76	2.29	3.41	3.56	2.57	3.02	2.97	2.99	2.76	2.80	2.84	0.37
Lu	0.39	0.44	0.39	0.37	0.43	0.38	0.38	0.46	0.61	0.46	0.56	0.52	0.47	0.34	0.43	0.44	0.08
Hf	4.22	4.22	3.31	3.13	3.76	4.02	3.92	3.70	4.30	4.30	4.12	4.28	4.01	3.43	4.22	3.93	0.38
Ta	0.67	0.63	0.60	0.69	0.58	0.61	0.50	0.66	0.70	0.74	0.62	0.74	0.59	0.56	0.58	0.63	0.07
Pb	10.38	10.48	11.00	11.00	10.60	11.30	9.20	9.60	9.30	9.10	10.00	10.97	10.00	10.30	11.20	10.30	0.74
Th	5.40	5.57	4.66	4.76	4.68	4.57	4.48	5.45	5.55	5.06	4.67	5.50	4.73	4.37	4.94	4.96	0.43
U	1.60	1.70	1.66	1.75	1.56	1.68	1.44	1.52	1.88	1.76	1.53	1.72	1.55	2.05	2.08	1.70	0.19

Analytical session 5 - 25/04/16

	1	2	3	4	5	6	7	8	9	10	11	12	13	14	15	16	17
Li	9.18	8.99	9.18	9.26	8.91	9.06	9.06	9.42	9.22	9.67	9.22	9.57	8.99	9.68	9.70	9.10	9.39
Sc	38.30	36.60	35.00	33.90	34.80	34.10	31.00	35.30	36.70	37.00	32.50	35.80	35.60	37.50	34.90	32.80	35.60
Zn	154.80	151.00	146.00	156.90	158.00	163.00	145.40	151.00	153.90	155.00	141.00	150.40	143.20	156.00	162.60	165.00	173.90
Rb	51.60	49.50	44.80	47.10	49.40	47.70	45.80	46.60	50.90	49.10	47.50	49.90	47.80	48.90	47.70	47.10	51.90
Sr	320.00	317.00	299.00	315.00	295.00	310.00	295.00	321.00	323.00	326.00	310.00	338.00	320.00	325.00	311.00	297.00	314.00
Y	35.90	36.50	32.30	32.40	32.80	33.60	30.40	33.40	36.60	35.30	29.30	35.00	33.00	35.00	32.20	31.00	34.60
Zr	188.00	191.10	172.00	172.00	180.00	181.00	167.00	176.00	199.00	187.00	159.20	190.00	181.00	188.30	179.60	170.00	178.40
Nb	12.87	12.50	12.30	12.23	11.67	12.05	11.18	11.44	12.44	12.42	12.07	12.74	12.72	12.93	13.00	12.26	11.97
Cs	1.25	1.24	1.12	1.19	1.17	1.20	1.18	1.20	1.19	1.19	1.18	1.19	1.16	1.20	1.17	1.18	1.34
Ba	641.00	648.00	597.00	613.00	644.00	669.00	612.00	634.00	663.00	658.00	636.00	668.00	644.00	676.00	631.00	605.00	671.00
La	25.00	24.61	21.80	21.50	23.70	23.90	21.10	23.50	24.60	24.50	21.40	24.36	23.20	24.90	26.50	24.10	24.20
Ce	49.10	50.70	46.80	46.00	50.60	52.00	48.20	47.70	49.60	50.50	48.80	51.20	48.20	49.20	54.40	51.40	51.30
Pr	6.29	6.33	5.69	5.97	6.14	6.19	5.92	6.07	6.08	6.05	5.89	6.46	5.97	6.44	5.94	5.90	5.72
Nd	27.70	28.60	24.60	25.40	27.40	26.50	25.00	26.80	27.80	26.40	25.60	28.60	25.60	27.30	28.60	26.60	26.00
Sm	6.40	6.31	6.04	5.97	6.36	6.64	5.74	6.06	6.61	6.77	5.62	6.63	6.29	6.60	6.06	6.17	6.09
Eu	1.80	1.92	1.63	1.80	1.77	1.73	1.56	1.75	1.79	1.75	1.81	1.94	1.80	1.97	1.79	1.70	1.79
Gd	6.90	6.69	6.01	6.71	6.24	6.07	5.97	6.86	6.64	6.24	5.54	6.46	6.17	6.54	6.35	5.82	6.44
Tb	0.98	1.08	0.91	0.88	1.01	1.00	0.88	0.94	1.07	1.05	0.87	1.08	0.94	0.98	0.94	0.96	0.95
Dy	6.44	6.51	5.99	5.89	5.80	6.23	5.48	6.14	6.58	6.73	5.28	6.49	5.91	6.47	5.97	5.87	6.42
Ho	1.20	1.25	1.10	1.16	1.27	1.27	1.14	1.29	1.45	1.46	1.10	1.28	1.18	1.30	1.43	1.25	1.38
Er	3.82	3.66	3.44	3.57	3.61	3.62	3.23	3.76	3.89	3.67	2.93	3.68	3.23	3.38	3.26	3.29	3.62
Tm	0.50	0.50	0.48	0.45	0.47	0.49	0.48	0.48	0.60	0.49	0.48	0.54	0.44	0.49	0.47	0.42	0.47
Yb	3.52	3.30	3.36	3.28	3.42	3.62	3.09	3.25	3.48	3.41	3.05	3.50	3.25	3.31	3.30	2.86	3.45
Lu	0.50	0.51	0.40	0.45	0.53	0.50	0.45	0.55	0.54	0.56	0.42	0.51	0.43	0.51	0.51	0.47	0.52
Hf	4.98	5.16	4.33	4.30	4.71	5.00	4.56	4.80	5.25	5.02	3.97	4.90	4.57	4.97	4.55	4.32	4.96
Ta	0.77	0.76	0.70	0.70	0.74	0.71	0.60	0.75	0.78	0.79	0.72	0.79	0.68	0.78	0.68	0.71	0.74
Pb	11.20	10.34	9.73	10.92	10.54	10.56	10.44	10.08	10.47	10.27	10.03	10.14	10.20	10.77	10.23	10.61	10.75
Th	5.90	5.98	5.61	5.66	5.67	5.69	5.19	5.78	6.28	6.15	5.26	6.19	5.49	6.03	5.70	5.38	6.02
U	1.44	1.56	1.37	1.37	1.77	1.73	1.66	1.58	1.74	1.79	1.61	1.63	1.54	1.63	1.71	1.62	1.74

Analytical session 5 (cont.) - 25/04/16

	18	19	20	21	22	23	24	25	26	27	28	29	30	31	32	Mean	St. dev.
Li	9.73	9.77	9.78	9.22	9.39	9.46	9.36	9.44	9.24	9.04	10.24	9.67	9.46	8.96	9.39	9.37	0.30
Sc	33.70	32.80	32.80	32.40	35.20	35.10	37.00	35.80	35.50	33.20	33.40	33.50	34.90	33.10	33.70	34.67	1.71
Zn	184.20	160.00	174.00	158.00	161.00	154.00	154.10	164.00	172.90	168.00	170.00	168.00	178.80	160.00	162.70	159.90	10.30
Rb	52.20	53.00	51.90	50.60	48.80	49.70	48.20	48.20	51.20	50.40	51.20	48.50	54.10	46.90	49.60	49.31	2.17
Sr	314.00	289.00	306.00	294.00	312.00	309.00	321.00	321.00	329.00	313.00	317.00	312.00	327.00	303.00	313.00	313.00	11.42
Y	33.90	32.70	33.30	32.80	34.90	34.40	36.90	35.40	35.70	32.70	33.90	34.20	34.40	33.20	33.80	33.80	1.76
Zr	179.00	173.00	175.00	175.00	188.00	181.00	191.50	187.80	192.00	177.00	187.00	182.00	186.00	176.00	180.00	180.93	8.43
Nb	11.56	10.64	11.18	10.80	11.33	11.60	11.65	11.60	11.89	11.29	11.60	11.50	12.02	11.29	11.65	11.89	0.62
Cs	1.34	1.27	1.31	1.29	1.22	1.24	1.22	1.24	1.28	1.24	1.28	1.28	1.34	1.22	1.29	1.23	0.06
Ba	676.00	625.00	640.00	601.00	654.00	615.00	656.00	635.00	670.00	620.00	659.00	647.00	682.00	615.00	643.00	642.13	23.87
La	24.40	22.60	23.20	21.50	23.90	22.30	24.00	23.70	24.60	23.10	24.00	23.90	25.00	22.90	23.20	23.60	1.24
Ce	53.10	49.10	52.10	47.50	48.70	53.70	53.50	50.40	51.50	48.10	49.60	50.90	51.50	48.80	50.40	50.14	2.04
Pr	5.78	6.02	6.14	5.46	5.90	5.95	6.33	6.02	6.18	6.05	6.13	6.65	6.62	5.66	6.04	6.06	0.27
Nd	27.50	25.50	25.80	24.40	26.50	24.00	26.90	26.10	27.60	25.60	26.60	27.00	28.50	26.00	26.90	26.54	1.23
Sm	6.36	5.58	5.94	5.75	6.19	6.07	6.36	6.44	6.55	6.48	6.88	6.50	6.66	6.36	6.48	6.28	0.33
Eu	1.81	1.63	1.72	1.62	1.94	1.80	1.81	1.82	1.90	1.81	1.94	1.83	1.79	1.80	1.90	1.79	0.10
Gd	6.76	5.81	6.58	6.10	6.59	6.37	7.36	6.61	6.99	6.57	6.88	6.64	6.73	6.45	6.68	6.46	0.39
Tb	0.98	0.97	1.00	0.96	1.05	0.93	1.04	1.05	1.18	0.98	1.00	1.02	1.04	1.03	1.08	0.99	0.07
Dy	6.65	6.35	6.36	5.96	6.66	6.01	6.62	7.01	6.79	6.28	6.58	6.57	6.85	6.66	6.48	6.31	0.40
Ho	1.41	1.30	1.35	1.28	1.36	1.24	1.38	1.36	1.47	1.33	1.38	1.32	1.36	1.32	1.39	1.30	0.10
Er	3.92	3.62	3.49	3.59	3.87	3.50	4.06	3.70	3.85	3.68	3.93	4.04	4.05	3.71	4.00	3.65	0.27
Tm	0.50	0.48	0.48	0.47	0.57	0.42	0.55	0.54	0.56	0.54	0.56	0.62	0.54	0.51	0.48	0.50	0.05
Yb	3.36	3.53	3.51	2.96	3.66	3.29	3.63	3.70	3.85	3.43	3.59	3.45	3.80	3.60	3.71	3.42	0.23
Lu	0.54	0.50	0.52	0.46	0.58	0.51	0.53	0.51	0.57	0.52	0.54	0.54	0.56	0.49	0.56	0.51	0.04
Hf	5.15	4.72	4.77	4.76	5.17	4.88	5.28	5.51	5.40	5.13	5.28	5.12	5.44	4.98	5.21	4.91	0.36
Ta	0.80	0.72	0.73	0.71	0.71	0.69	0.75	0.78	0.77	0.72	0.75	0.79	0.80	0.75	0.80	0.74	0.05
Pb	11.78	12.80	12.30	10.51	10.21	9.74	10.47	10.00	10.36	10.71	11.78	13.51	13.86	9.96	10.74	10.81	1.02
Th	6.18	5.58	5.93	5.47	6.08	5.56	6.35	6.18	6.32	6.02	6.29	6.37	6.57	6.22	6.36	5.92	0.36
U	1.77	1.76	1.75	1.70	1.72	1.67	1.66	1.72	1.82	1.80	1.85	1.83	1.93	1.70	1.70	1.68	0.13

APPENDIX 6: TORFAJÖKULL $^{40}Ar/^{39}Ar$ DATA

Recommended ages in bold. Uncertainty in ages and initial $^{40}Ar/^{36}Ar$ is 2σ.

Steps in grey have negative 36Ar and were excluded from inverse isochrons.

A6.1 Samples analysed in 2017 (irradiated 02/02/17)

Thórsmörk Ignimbrite

Sample: JM-252 | Fiamme (rhyolite glass) | Lab sample code: AS3 | J: 0.00033865 ± 0.5% | Blank correction: Average of day | Date of analysis: 22/09/2017

Step	^{40}Ar V	± σ_{40} V	^{39}Ar V	± σ_{39} V	^{38}Ar V	± σ_{38} V	^{37}Ar V	± σ_{37} V	^{36}Ar V	± σ_{36} V	$^{40}Ar^*/^{39}Ar$	± σ	Age (ka)	± σ (ka)
1	1.7599E-03	6.3763E-04	1.0454E-03	8.5983E-05	-7.1546E-06	2.7822E-05	-3.9301E-04	3.1441E-03	-4.8959E-06	2.3360E-05	3.0817E+00	6.7040E+00	1886.176	4101.109
2	3.6826E-02	7.4527E-04	5.8495E-02	5.8135E-04	1.2091E-03	6.4164E-05	5.5037E-03	3.1450E-03	1.2354E-04	2.3360E-05	-1.0086E-03	-1.1991E-01	-0.618	73.431
3	6.3405E-02	6.8563E-04	2.3351E-01	9.6349E-04	4.5513E-03	1.6462E-04	1.4357E-02	3.1466E-03	1.3120E-04	2.3360E-05	1.0379E-01	3.0015E-02	63.557	18.380
4	6.5279E-02	8.2599E-04	3.6072E-01	1.4391E-03	6.9635E-03	1.6462E-04	9.4459E-03	3.1486E-03	1.1250E-04	2.3360E-05	8.7857E-02	1.9473E-02	53.801	11.924
5	6.6187E-02	7.3800E-04	4.5780E-01	2.1012E-03	8.8645E-03	1.8494E-04	1.7328E-02	3.1506E-03	1.1041E-04	2.3360E-05	7.2572E-02	1.5323E-02	44.441	9.383
6	1.2011E-01	2.0875E-03	9.6505E-01	6.9334E-03	1.8687E-02	1.5447E-04	3.2114E-02	3.1523E-03	1.4649E-04	2.3360E-05	7.9138E-02	7.5652E-03	48.462	4.633
7	6.3323E-02	6.7904E-04	5.2076E-01	2.3391E-03	9.8253E-03	2.0529E-04	1.7347E-02	3.1541E-03	4.0403E-05	2.3360E-05	9.8434E-02	1.3463E-02	60.278	8.244
8	6.4777E-02	7.4580E-04	5.3275E-01	2.0495E-03	9.6004E-03	6.4164E-05	1.5385E-02	3.1558E-03	7.0923E-05	2.3360E-05	8.1845E-02	1.3170E-02	50.120	8.065
9	1.0280E-01	1.0651E-03	8.1921E-01	3.8084E-03	1.5672E-02	2.9700E-04	2.8220E-02	3.1575E-03	8.7522E-05	2.3360E-05	9.3595E-02	8.6233E-03	57.315	5.281
10	8.2901E-02	7.0809E-04	6.3624E-01	2.1219E-03	1.2289E-02	1.8494E-04	3.2185E-02	3.1593E-03	1.1647E-04	2.3360E-05	7.5644E-02	1.1021E-02	46.323	6.749
11	6.6277E-02	6.1320E-04	5.2213E-01	2.1840E-03	1.0142E-02	1.9511E-04	2.5288E-02	3.1610E-03	5.8299E-05	2.3360E-05	9.3600E-02	1.3415E-02	57.318	8.215
12	1.0663E-01	1.0739E-03	7.1058E-01	2.0391E-03	1.3270E-02	1.3420E-04	3.6173E-02	3.1627E-03	1.5541E-04	2.3360E-05	8.4761E-02	9.9338E-03	51.906	6.083
13	1.1354E-01	1.0464E-03	8.3656E-01	1.6357E-03	1.4936E-02	2.0529E-04	3.4206E-02	3.1636E-03	1.6594E-04	2.3360E-05	7.6498E-02	8.4317E-03	46.845	5.163
Total:	*0.9538*		*6.6548*		*0.1260*		*0.2672*		*0.0013*					

Plateau Age: **51.3 ± 4.2 ka** Steps 2-13 MSWD: 0.57 Probability: 0.86 100.0% of the ^{39}Ar

Isochron Age: 52 ± 11 ka MSWD: 0.63 Initial $^{40}Ar/^{36}Ar$: 291 ± 77

North Atlantic Ash Zone II (II-RHY-1)

Sample: MD99-2251, 2014-2015 cm | Rhyolite glass shards | Lab sample code: AS1 | J: 0.00033794 ± 0.5% | Blank correction: Average of day | Date of analysis: 05/10/2017

Step	^{40}Ar	± σ_{40}	^{39}Ar	± σ_{39}	^{38}Ar	± σ_{38}	^{37}Ar	± σ_{37}	^{36}Ar	± σ_{36}	^{40}Ar*/^{39}Ar	± σ	Age	± σ
	V	V	V	V	V	V	V	V	V	V			(ka)	(ka)
1	1.4280E+00	6.5375E-03	7.0384E-02	4.0527E-04	2.5435E-03	1.6709E-04	8.9959E-02	7.5368E-03	2.0190E-03	9.4600E-05	1.1724E+01	4.1747E-01	7203.357	255.989
2	1.6307E+00	4.7177E-03	1.0827E-01	9.3214E-04	3.6883E-03	2.0728E-04	2.3552E-02	7.5411E-03	2.7666E-03	5.7900E-05	7.4322E+00	1.7745E-01	4569.765	108.967
3	1.9146E+00	1.0302E-02	1.8787E-01	9.4248E-04	5.8244E-03	7.9300E-05	2.3566E-02	7.5453E-03	2.9666E-03	5.7900E-05	5.4767E+00	1.1059E-01	3368.561	67.956
4	1.8087E+00	6.2390E-03	2.4443E-01	1.7701E-03	7.1327E-03	7.9300E-05	2.3580E-02	7.5499E-03	2.5366E-03	6.6700E-05	4.3014E+00	9.0915E-02	2646.156	55.889
5	3.3838E+00	1.4653E-02	3.9229E-01	2.0598E-03	1.0383E-02	2.0728E-04	3.5115E-02	7.5540E-03	4.2836E-03	8.5200E-05	5.3657E+00	7.9938E-02	3300.335	49.123
6	1.8336E+00	6.4976E-03	2.6489E-01	6.3236E-04	6.5910E-03	1.2736E-04	9.5156E-03	7.5583E-03	1.9103E-03	5.7900E-05	4.7690E+00	7.0647E-02	2933.617	43.423
7	3.7962E+00	8.6766E-03	3.9437E-01	9.9419E-04	9.8208E-03	1.4715E-04	1.4647E-02	7.5624E-03	2.3990E-03	6.6700E-05	7.8098E+00	5.8513E-02	4801.644	35.928
8	5.4946E+00	1.0405E-02	4.5412E-01	1.5427E-03	1.0851E-02	2.0566E-04	1.6969E-02	4.3943E-03	2.2888E-03	4.1500E-05	1.0595E+01	5.0648E-02	6510.746	31.069
9	3.2364E+00	1.5269E-02	2.5611E-01	7.5681E-04	6.2722E-03	1.2472E-04	1.0448E-02	4.3968E-03	1.8906E-03	6.1000E-05	1.0433E+01	9.7799E-02	6411.377	59.996
10	2.2383E+00	5.0736E-03	1.9595E-01	6.8450E-04	4.5858E-03	1.4487E-04	7.8406E-03	4.3992E-03	1.0913E-03	3.2000E-05	9.7602E+00	6.4879E-02	5998.783	39.810
11	3.9872E+00	1.9936E-02	1.5682E-01	1.0049E-03	3.9929E-03	1.1468E-04	-7.0900E-18	4.4017E-03	1.1433E-03	6.1000E-05	2.3249E+01	2.2770E-01	14256.465	139.083
12	4.1444E+00	1.1803E-02	1.2547E-01	4.6784E-04	2.8278E-03	1.4487E-04	2.6166E-03	4.4044E-03	1.3626E-03	6.1000E-05	2.9788E+01	2.0560E-01	18246.551	125.302
Total:	*34.8965*		*2.8510*		*0.0745*		*0.2578*		*0.0267*					

Plateau Age: Not determined
Isochron Age: Not determined

Torfajökull Ring Fracture Rhyolites

Kirkjufell

TJ99-4 Rhyolite glass Lab sample code: AS18 J: 0.00034189 ± 0.5% Blank correction: Average of day Date of analysis: 17/10/2017

Step	^{40}Ar	± σ_{40}	^{39}Ar	± σ_{39}	^{38}Ar	± σ_{38}	^{37}Ar	± σ_{37}	^{36}Ar	± σ_{36}	^{40}Ar*/^{39}Ar	± σ	Age	± σ
	V	V	V	V	V	V	V	V	V	V			(ka)	(ka)
1	5.8765E-01	7.5105E-03	9.2329E-02	1.2746E-03	1.9176E-03	1.1382E-04	1.3023E-02	4.7941E-03	1.8396E-03	6.3183E-05	4.1607E-01	2.1999E-01	257.214	135.986
2	3.5990E-01	4.6153E-03	1.5610E-01	1.2746E-03	2.7250E-03	1.2392E-04	1.7870E-02	4.7967E-03	1.0983E-03	5.3779E-05	2.0486E-01	1.0703E-01	126.651	66.169
3	5.5833E-01	4.4510E-03	2.4194E-01	2.1330E-03	4.3808E-03	2.1537E-04	1.1423E-02	4.7992E-03	1.8000E-03	6.3183E-05	8.6395E-02	8.0115E-02	53.413	49.529
4	4.3058E-01	3.8165E-03	2.8068E-01	2.1020E-03	4.6466E-03	1.3405E-04	3.2429E-02	4.8024E-03	1.3245E-03	5.3779E-05	1.2519E-01	5.8807E-02	77.397	36.355
5	2.6341E-01	1.3516E-03	3.5846E-01	1.0162E-03	6.3534E-03	1.2392E-04	1.7901E-02	4.8049E-03	7.8833E-04	3.5947E-05	7.8243E-02	3.0177E-02	48.373	18.657
6	2.8530E-01	1.9359E-03	4.6722E-01	1.8951E-03	7.6924E-03	1.8483E-04	3.2465E-02	4.8079E-03	7.3447E-04	2.8145E-05	1.4130E-01	1.8465E-02	87.354	11.415
7	3.1473E-01	1.6483E-03	4.7392E-01	2.0192E-03	7.8763E-03	2.1537E-04	1.9539E-02	4.8104E-03	7.8790E-04	5.3779E-05	1.6774E-01	3.4065E-02	103.704	21.059
8	1.2610E-01	1.4107E-03	4.7486E-01	3.0332E-03	7.5084E-03	1.9500E-04	4.0593E-02	4.8129E-03	3.1232E-04	2.8145E-05	6.9176E-02	1.7949E-02	42.767	11.097
9	1.3059E-01	1.0185E-03	4.8930E-01	2.0192E-03	7.8048E-03	1.7466E-04	1.7940E-02	4.8154E-03	2.3832E-04	3.5947E-05	1.2147E-01	2.2038E-02	75.095	13.624
10	1.0479E-01	1.0702E-03	4.5501E-01	1.3779E-03	7.3653E-03	2.0518E-04	2.6052E-02	4.8180E-03	2.2617E-04	2.8145E-05	8.1887E-02	1.8619E-02	50.626	11.511
11	1.2291E-01	1.1623E-03	5.1343E-01	1.8847E-03	8.5407E-03	1.2392E-04	2.9308E-02	4.8205E-03	2.3531E-04	3.5947E-05	1.0255E-01	2.1029E-02	63.400	13.000
12	8.5108E-02	1.0309E-03	4.0771E-01	7.4777E-04	6.5783E-03	1.3405E-04	2.7701E-02	4.8230E-03	1.4574E-04	3.5947E-05	1.0203E-01	2.6445E-02	63.077	16.349
13	1.1610E-01	9.4394E-04	4.2092E-01	1.2539E-03	6.8236E-03	1.7466E-04	2.1224E-02	4.8256E-03	2.8745E-04	2.8145E-05	7.1938E-02	2.0091E-02	44.475	12.421
14	5.7301E-02	1.0437E-03	1.1789E-01	2.0089E-03	1.8665E-03	1.0373E-04	1.7982E-02	4.8268E-03	1.7831E-04	2.8146E-05	3.4476E-02	7.1829E-02	21.314	44.407
Total:	*3.5428*		*4.9498*		*0.0821*		*0.3254*		*0.0100*					

Plateau Age: 61.7 ± 8.9 ka Steps 3-13 MSWD: 1.7 Probability: 0.086 92.6% of the ^{39}Ar

Isochron Age: **53 ± 13 ka** MSWD: 1.3 Initial ^{40}Ar/^{36}Ar: 312 ± 12

Rauðfossafjöll (N)

TJ98-43 Rhyolite glass Lab sample code: AS15 J: 0.00033797 ± 0.5% Blank correction: Average of day Date of analysis: 21/09/2017

Step	^{40}Ar	± σ_{40}	^{39}Ar	± σ_{39}	^{38}Ar	± σ_{38}	^{37}Ar	± σ_{37}	^{36}Ar	± σ_{36}	^{40}Ar*/^{39}Ar	± σ	Age	± σ
	V	V	V	V	V	V	V	V	V	V			(ka)	(ka)
1	3.5835E-03	1.1917E-03	8.3575E-04	7.2094E-05	8.1767E-06	2.7979E-05	-5.7816E-03	2.7705E-03	-4.6787E-07	2.2874E-05	4.4549E+00	8.3037E+00	2720.592	5067.230
2	7.3014E-02	1.4499E-03	5.2007E-02	4.9806E-04	9.4849E-04	6.4232E-05	9.6439E-03	2.7728E-03	2.8544E-04	3.1988E-05	-2.3474E-01	-1.8575E-01	-143.471	113.531
3	1.1424E-01	1.8434E-03	1.2142E-01	1.1079E-03	1.9093E-03	1.0398E-04	1.3509E-02	2.7743E-03	4.0442E-04	3.1988E-05	-5.3541E-02	-8.0108E-02	-32.722	48.959
4	1.0465E-01	1.4363E-03	1.3168E-01	6.7362E-04	2.1443E-03	1.0398E-04	6.7579E-03	2.7758E-03	3.6621E-04	3.1988E-05	-3.5554E-02	-7.3342E-02	-21.729	44.824
5	1.5446E-01	1.4364E-03	1.7521E-01	1.0768E-03	2.5634E-03	1.2413E-04	1.6421E-02	2.7773E-03	5.0365E-04	3.1988E-05	2.3325E-02	5.5121E-02	14.255	33.687
6	1.3553E-01	1.6486E-03	2.8152E-01	1.9044E-03	4.1476E-03	5.4558E-05	1.8364E-02	2.7789E-03	3.7313E-04	2.2874E-05	8.5702E-02	2.4962E-02	52.377	15.255
7	1.5001E-01	2.1844E-03	3.3131E-01	1.5320E-03	5.1595E-03	1.4436E-04	2.6110E-02	2.7804E-03	4.7108E-04	4.1512E-05	2.8254E-02	3.7985E-02	17.268	23.214
8	1.1949E-01	1.7523E-03	3.1929E-01	9.8375E-04	4.6995E-03	1.6465E-04	3.5803E-02	2.7822E-03	3.3851E-04	3.1988E-05	5.7714E-02	3.0410E-02	35.272	18.585
9	1.2291E-01	1.8604E-03	4.3949E-01	2.7839E-03	6.9072E-03	1.7480E-04	3.9695E-02	2.7837E-03	2.6748E-04	2.2874E-05	9.7956E-02	1.6117E-02	59.865	9.850
10	1.3338E-01	1.7688E-03	4.7947E-01	1.4078E-03	7.1628E-03	2.2567E-04	3.6810E-02	2.7851E-03	3.5825E-04	2.2874E-05	5.5102E-02	1.4714E-02	33.675	8.992
11	1.3224E-01	1.6179E-03	5.2842E-01	2.9287E-03	7.9089E-03	2.8682E-04	3.6830E-02	2.7867E-03	2.6824E-04	3.1988E-05	9.8701E-02	1.8339E-02	60.320	11.208
12	1.1886E-01	1.5279E-03	4.0933E-01	2.3907E-03	6.2429E-03	1.8496E-04	2.7154E-02	2.7883E-03	2.7080E-04	3.1988E-05	9.2867E-02	2.3634E-02	56.756	14.444
13	1.0465E-01	1.6565E-03	4.2130E-01	2.4735E-03	6.7437E-03	1.3424E-04	3.3961E-02	2.7898E-03	2.0900E-04	3.1988E-05	1.0028E-01	2.3015E-02	61.284	14.065
14	9.9174E-02	1.2940E-03	3.2298E-01	6.3230E-04	4.8222E-03	1.5450E-04	4.1745E-02	2.7913E-03	2.6694E-04	4.1512E-05	6.0305E-02	3.8581E-02	36.855	23.579
Total:	*1.5662*		*4.0143*		*0.0614*		*0.3370*		*0.0044*					

Plateau Age: 48.5 ± 8.8 ka Steps 5-14 MSWD: 1.11 Probability: 0.35 92.4% of the ^{39}Ar

Isochron Age: **67 ± 15 ka** MSWD: 0.88 Initial ^{40}Ar/^{36}Ar: 258 ± 24

Rauðfossafjöll (SW)

JM-247 | Rhyolite non-glassy groundmass | Lab sample code: AS25 | J: 0.00034221 ± 0.5% | Blank correction: Moving average through day | Date of analysis: 13/10/2017

Step	^{40}Ar	± σ_{40}	^{39}Ar	± σ_{39}	^{38}Ar	± σ_{38}	^{37}Ar	± σ_{37}	^{36}Ar	± σ_{36}	^{40}Ar*/^{39}Ar	± σ	Age	± σ
	V	V	V	V	V	V	V	V	V	V			(ka)	(ka)
1	1.0671E+00	4.7724E-03	2.7229E-02	4.5541E-04	1.3696E-03	1.0255E-04	7.4436E-03	1.2155E-03	3.4880E-03	9.2557E-05	9.4444E-01	1.0300E+00	584.342	637.190
2	2.6368E+00	6.7114E-03	1.7965E-01	1.3351E-03	5.1104E-03	1.2293E-04	2.2343E-02	1.2162E-03	8.5441E-03	1.0231E-04	4.7787E-01	1.7412E-01	295.691	107.729
3	1.4217E+00	7.2054E-03	2.6712E-01	1.9777E-03	5.0427E-03	2.0499E-04	1.7884E-02	5.4248E-03	4.6228E-03	1.3085E-04	1.5546E-01	1.4872E-01	96.199	92.025
4	8.5550E-01	4.6426E-03	4.0276E-01	1.5428E-03	6.3328E-03	1.5434E-04	2.8033E-02	6.1408E-03	2.6086E-03	5.0662E-05	1.9040E-01	3.9291E-02	117.819	24.312
5	4.9340E-01	2.2283E-03	4.1637E-01	1.1187E-03	6.0058E-03	1.1383E-04	2.0589E-02	6.1441E-03	1.5405E-03	4.0825E-05	8.0353E-02	2.9759E-02	49.724	18.415
6	2.3693E-01	1.3242E-03	3.5392E-01	1.6255E-03	4.6771E-03	1.1383E-04	5.6723E-03	6.1474E-03	6.5450E-04	3.1091E-05	1.1733E-01	2.6499E-02	72.603	16.397
7	1.4764E-01	9.1508E-04	2.6847E-01	1.1807E-03	3.2257E-03	1.2394E-04	1.1948E-03	6.1508E-03	3.6568E-04	3.1091E-05	1.4326E-01	3.4749E-02	88.651	21.502
8	1.0957E-01	8.4141E-04	2.1034E-01	9.1185E-04	2.9053E-03	8.3152E-05	3.7359E-03	5.0122E-03	2.9151E-04	3.2719E-05	1.0714E-01	4.6615E-02	66.301	28.845
9	8.7838E-02	8.8456E-04	2.0266E-01	1.0875E-03	2.6268E-03	1.0343E-04	1.9736E-02	3.0495E-03	2.0277E-04	2.1369E-05	1.3470E-01	3.1791E-02	83.356	19.672
10	1.3888E-01	1.2262E-03	3.5702E-01	1.5737E-03	4.7425E-03	1.3381E-04	2.9919E-04	3.0511E-03	3.4792E-04	3.0930E-05	9.8050E-02	2.6096E-02	60.674	16.148
11	1.5731E-01	1.1421E-03	4.3173E-01	1.5220E-03	5.4068E-03	1.0343E-04	2.1255E-02	3.0529E-03	4.0237E-04	3.0930E-05	8.6122E-02	2.1555E-02	53.293	13.338
12	1.3898E-01	7.8274E-04	4.1543E-01	1.2212E-03	4.9735E-03	1.7502E-04	7.1886E-03	1.7465E-03	3.3410E-04	3.0401E-05	9.4443E-02	2.1932E-02	58.442	13.571
13	1.5705E-01	1.1588E-03	4.8153E-01	1.5605E-03	5.6480E-03	1.3453E-04	1.6183E-02	1.7474E-03	3.6171E-04	3.0401E-05	1.0187E-01	1.9005E-02	63.039	11.760
14	1.3702E-01	1.6049E-03	4.1446E-01	1.9539E-03	5.1343E-03	9.4355E-05	1.6991E-02	1.8698E-03	3.3216E-04	2.0554E-05	9.1311E-02	1.5310E-02	56.504	9.474
15	6.0424E-02	7.0913E-04	1.8608E-01	1.0503E-03	2.0987E-03	5.5251E-05	1.5500E-02	1.8708E-03	1.9256E-04	3.0372E-05	1.5767E-02	4.8880E-02	9.757	30.247
Total:	*7.8461*		*4.6148*		*0.0653*		*0.2040*		*0.0243*					

Plateau Age: 63.9 ± 9.2 ka Steps 3-14 MSWD: 0.88 Probability: 0.56 91.5% of the ^{39}Ar

Isochron Age: **56 ± 11 ka** MSWD: 0.73 Initial ^{40}Ar/^{36}Ar: 307 ± 5.7

Laufafell

JM-250 | Rhyolite non-glassy groundmass | Lab sample code: AS29 | J: 0.00033932 ± 0.5% | Blank correction: Average of day | Date of analysis: 12/10/2017

Step	^{40}Ar	± σ_{40}	^{39}Ar	± σ_{39}	^{38}Ar	± σ_{38}	^{37}Ar	± σ_{37}	^{36}Ar	± σ_{36}	^{40}Ar*/^{39}Ar	± σ	Age	± σ
	V	V	V	V	V	V	V	V	V	V			(ka)	(ka)
1	9.1650E-01	3.1576E-03	1.3651E-02	1.5952E-04	7.1972E-04	5.4478E-05	9.7449E-04	4.1914E-03	2.9297E-03	5.5689E-05	3.0619E+00	1.2403E+00	1877.830	760.258
2	2.9211E+00	9.8459E-03	1.2935E-01	4.7750E-04	4.1846E-03	1.7478E-04	1.5600E-02	4.1936E-03	9.5059E-03	1.6187E-04	6.4185E-01	3.8130E-01	393.803	233.916
3	2.4942E+00	6.7151E-03	2.4861E-01	6.7373E-04	6.0448E-03	1.5447E-04	1.9998E-02	4.1958E-03	8.0847E-03	1.1270E-04	3.2343E-01	1.3802E-01	198.448	84.679
4	1.4976E+00	7.5655E-03	3.4996E-01	1.6770E-03	6.5865E-03	1.5447E-04	2.1473E-02	4.1981E-03	4.8243E-03	9.3280E-05	1.6364E-01	8.2468E-02	100.410	50.600
5	1.3243E+00	4.0595E-03	4.3200E-01	1.6874E-03	7.4961E-03	2.1547E-04	6.6893E-02	4.2003E-03	4.0523E-03	7.4170E-05	2.6500E-01	5.2124E-02	162.596	31.981
6	1.4064E+00	3.4141E-03	4.2464E-01	1.2218E-03	6.9340E-03	1.2409E-04	4.4945E-02	4.2025E-03	4.4881E-03	5.5689E-05	1.5655E-01	3.9974E-02	96.055	24.527
7	4.1750E-01	3.1926E-03	3.1903E-01	1.9668E-03	4.9409E-03	1.7478E-04	2.5907E-02	4.2049E-03	1.3031E-03	4.6917E-05	8.9120E-02	4.5036E-02	54.683	27.633
8	9.4883E-01	2.9944E-03	3.8234E-01	1.2115E-03	6.0652E-03	1.6462E-04	2.0052E-02	4.2071E-03	2.9347E-03	5.5689E-05	1.9000E-01	4.4189E-02	116.583	27.113
9	3.5829E-01	2.6582E-03	3.0671E-01	1.2632E-03	4.3686E-03	7.3993E-05	1.8594E-02	4.2093E-03	1.0651E-03	6.4817E-05	1.3141E-01	6.3689E-02	80.630	39.078
10	2.8412E-01	2.0613E-03	2.9949E-01	1.1184E-03	3.9699E-03	8.3917E-05	1.5667E-02	4.2117E-03	8.4585E-04	4.6917E-05	1.0547E-01	4.7277E-02	64.715	29.009
11	3.4477E-01	2.2769E-03	3.5977E-01	1.4908E-03	5.1249E-03	1.3420E-04	2.7432E-02	4.2139E-03	9.7273E-04	3.8746E-05	1.5107E-01	3.2777E-02	92.694	20.111
12	2.5387E-01	2.4453E-03	2.6789E-01	1.0046E-03	3.6429E-03	1.1400E-04	1.2742E-02	4.2157E-03	7.6662E-04	3.1643E-05	9.3275E-02	3.6429E-02	57.233	22.352
13	2.9239E-01	2.3579E-03	3.2644E-01	1.2431E-03	4.2939E-03	9.4286E-05	1.4502E-02	6.1160E-03	7.8949E-04	3.6398E-05	1.7362E-01	3.4071E-02	106.531	20.905
14	3.4741E-01	1.1891E-03	4.0757E-01	8.8136E-04	5.5306E-03	1.6484E-04	2.0879E-02	6.1193E-03	1.0378E-03	4.4998E-05	9.2176E-02	3.3092E-02	56.559	20.305
15	3.8761E-01	1.8100E-03	4.4741E-01	2.5466E-03	6.1439E-03	1.2438E-04	2.7257E-02	6.1210E-03	1.0561E-03	4.4998E-05	1.6159E-01	3.0313E-02	99.150	18.599
Total:	*14.1949*		*4.7149*		*0.0760*		*0.3529*		*0.0447*					

Plateau Age: 89 ± 14 ka Steps 3-15 MSWD: 1.3 Probability: 0.19 97.0% of the ^{39}Ar

Isochron Age: **66 ± 22 ka** MSWD: 0.92 Initial ^{40}Ar/^{36}Ar: 306.7 ± 4.9

Illihnúkur

TJ97-16 | Rhyolite glass | Lab sample code: AS13 | J: 0.00033288 ± 0.5% | Blank correction: Average of each day | Date of analysis: 02/10/2017

Step	^{40}Ar	± σ_{40}	^{39}Ar	± σ_{39}	^{38}Ar	± σ_{38}	^{37}Ar	± σ_{37}	^{36}Ar	± σ_{36}	^{40}Ar*/^{39}Ar	± σ	Age	± σ
	V	V	V	V	V	V	V	V	V	V			(ka)	(ka)
1	1.8703E-01	1.3609E-03	3.0310E-03	1.0498E-04	1.8398E-04	2.2080E-05	7.2298E-03	1.9677E-03	6.1142E-04	4.0280E-05	1.4799E+00	3.9934E+00	897.206	2420.484
2	5.6226E-01	2.5057E-03	2.7606E-02	2.2836E-04	7.0524E-04	6.1890E-05	-3.6172E-03	1.9689E-03	1.9743E-03	9.0125E-05	-9.8461E-01	-9.7894E-01	-597.195	593.854
3	1.3947E+00	5.8365E-03	8.4487E-02	4.8672E-04	2.3201E-03	4.1726E-05	7.2383E-03	1.9700E-03	4.7714E-03	1.0011E-04	-3.5282E-01	-3.6046E-01	-213.973	218.621
4	2.4327E+00	5.1611E-03	9.8471E-02	9.4260E-04	2.9801E-03	1.7477E-04	1.0474E-02	3.7442E-03	8.2772E-03	1.7034E-04	-3.9098E-01	-5.1913E-01	-237.117	314.854
5	2.7932E+00	6.6555E-03	1.5307E-01	9.0124E-04	3.9920E-03	1.4432E-04	8.0350E-03	3.7464E-03	9.6479E-03	1.1052E-04	-5.6983E-01	-2.1993E-01	-345.592	133.399
6	9.7096E+00	3.1621E-02	2.9062E-01	1.3149E-03	1.0687E-02	1.2408E-04	3.1285E-02	3.7485E-03	3.2962E-02	2.1027E-04	-4.5229E-01	-2.4188E-01	-274.305	146.708
7	2.8216E+00	9.1224E-03	1.3356E-01	8.1854E-04	3.9306E-03	8.3903E-05	1.7837E-02	3.7507E-03	9.7953E-03	1.0057E-04	-7.7018E-01	-2.3502E-01	-467.120	142.559
8	5.5020E+00	2.9461E-02	2.6660E-01	7.6686E-04	7.5897E-03	1.4432E-04	1.9072E-02	3.7528E-03	1.8815E-02	1.2048E-04	-4.3278E-01	-1.7441E-01	-262.470	105.781
9	6.8915E+00	2.3398E-02	4.0135E-01	1.7287E-03	1.0574E-02	2.2564E-04	2.7662E-02	3.7549E-03	2.3273E-02	2.7021E-04	-1.4146E-01	-2.0929E-01	-85.787	126.926
10	3.4273E+00	1.7411E-02	2.6151E-01	7.2553E-04	6.0770E-03	1.2408E-04	1.0513E-02	3.7581E-03	1.1967E-02	1.3044E-04	-5.5684E-01	-1.6314E-01	-337.717	98.949
Total:	*35.7221*		*1.7203*		*0.0490*		*0.1357*		*0.1221*					

Plateau Age: Not determined

Isochron Age: Not determined

APPENDIX 7: JOURNAL OF MAPS PAPER

JOURNAL OF MAPS, 2018
VOL. 14, NO. 2, 22–31
https://doi.org/10.1080/17445647.2018.1425163

Taylor & Francis
Taylor & Francis Group

Science

Geology of Tindfjallajökull volcano, Iceland

Jonathan D. Moles[a], Dave McGarvie[a], John A. Stevenson[b] and Sarah C. Sherlock[a]

[a]Faculty of Science, Technology, Engineering & Mathematics, The Open University, Milton Keynes, UK; [b]British Geological Survey, The Lyell Centre, Edinburgh, UK

ABSTRACT

The geology of Tindfjallajökull volcano, southern Iceland, is presented as a 1:50,000 scale map. Field mapping was carried out with a focus on indicators of past environments. A broad stratocone of interbedded fragmental rocks and lavas was constructed during Tindfjallajökull's early development. This stratocone has been dissected by glacial erosion and overlain by a variety of mafic to silicic volcanic landforms. Eruption of silicic magma, which probably occurred subglacially, constructed a thick pile of breccia and lava lobes in the summit area. Mafic to intermediate flank eruptions continued through to the end of the last glacial period, producing lavas, hyaloclastite-dominated units and tuyas that preserve evidence of volcano-ice interactions. The Thórsmörk Ignimbrite, a regionally important chronostratigraphic marker, is present on the SE flank of the volcano. The geological mapping of Tindfjallajökull gives insights into the evolution of stratovolcanoes in glaciated regions and the influence of ice in their development.

ARTICLE HISTORY
Received 24 April 2017
Revised 3 January 2018
Accepted 4 January 2018

KEYWORDS
Tindfjallajökull; Tindfjöll; volcano; Iceland; volcano-ice interactions

1. Introduction

Tindfjallajökull (alternatively known as Tindfjöll) is an ~300 km^2 stratovolcano in the Eastern Volcanic Zone of southern Iceland (63°47′N 19°35′W). Like nearby Eyjafjallajökull, the name 'Tindfjallajökull' strictly refers to the volcano's ice cap, but is commonly used to refer to the volcano as a whole (in this paper, it is used to refer to the whole volcano). The upper flanks of Tindfjallajökull currently host ~13 km^2 of ice, and the ice-free summit rises to 1464 m above mean sea level (Figure 1).

The geology of Tindfjallajökull is largely unknown. A study of gabbro nodules by Larsen (1979) includes the most detailed geological map previously published. Jakobsson (1979) speculated that Tindfjallajökull is the oldest active volcano in the Eastern Volcanic Zone, and that it probably last erupted in late-glacial or post-glacial time.

Tindfjallajökull is best known as a proposed source of the Thórsmörk Ignimbrite (Jørgensen, 1980). This 1.5–2 km^3 (dense-rock equivalent) peralkaline ignimbrite outcrops to the SE of the volcano (Thórarinsson, 1969) and has been correlated with the rhyolitic component of the widespread North Atlantic Ash Zone II (Lacasse, Sigurdsson, Carey, Paterne, & Guichard, 1996; Sigurdsson, 1982; Tomlinson, Thordarson, Müller, Thirlwall, & Menzies, 2010).

A 1:50,000 geological map (Main map) of Tindfjallajökull is presented here with the aim of documenting the volcano's eruptive products and to provide context for further research. The map was produced as part of a research project on the volcanological development of Tindfjallajökull, focussing particularly on the role of ice in the shaping of the volcano. As is common for Icelandic volcanoes, the influence of past ice is evident in the geomorphology of the volcano, in the presence of glacially worked sediments and in the characteristics of the erupted products.

2. Methods

Geological mapping was undertaken at Tindfjallajökull during the summers of 2014, 2015 and 2016. In the field, lithofacies were mapped onto topographic maps (USA Defence Mapping Agency, 1989) and aerial images (Google Earth Pro, 2010).

Geographical data of topography (contours and spot heights), place names, hydrology, buildings and tracks were sourced from the IS 50 V digital map database (Landmælingar Íslands, 2016). These data were supplemented by field mapping of geomorphological features (mass-wasting scarps and subsidence pits) and superficial deposits (mass-wasting deposits and moraines).

To transform the mapped lithofacies data into the classes displayed on the final map, a division was first made according to the volcanic system. Although most of the mapped area consists of the products of Tindfjallajökull volcano, the products of neighbouring

CONTACT Jonathan D. Moles jonathan.moles@open.ac.uk School of Environment, Earth & Ecosystem Sciences, Faculty of Science, Technology, Engineering & Mathematics, The Open University, Walton Hall, Milton Keynes MK7 6AA, UK

Figure 1. Oblique aerial photograph of Tindfjallajökull from the SE, August 1999. Source: Oddur Sigurðsson. To the right of the glacier-covered shoulder are the orange/brown twin peaks of Ýmir and Ýma, the highest points of the central silicic edifice. The mafic-dominated ridge of Tindfjöll is to the left. The valleys in front contain sediments deposited during the last glacial period.

and older systems are also present. Sediments, which potentially include material from multiple volcanic systems, form a separate category.

Within the categories defined above, divisions were then made based on age. Due to a lack of widespread marker horizons, major stratigraphic discontinuities or radiometric dates, it is only possible to divide Tindfjallajökull into broad stratigraphic groups: Early, Middle and Late Tindfjallajökull (the latter group is subdivided into A and B). The presence of the Thórsmörk Ignimbrite, which has an unpublished $^{40}Ar/^{39}Ar$ age of 54.5 ± 2 ka (see Sigurdsson, McIntosh, Dunbar, Lacasse, & Carey, 1998), aids the identification of sediments and volcanic units deposited during the last glacial period (i.e. the Weichselian glaciation).

Within the broad stratigraphic groups defined above, volcanic rocks were further subdivided according to composition (i.e. mafic, intermediate or silicic) and lithofacies. Without strict stratigraphic control, these subdivisions group together eruptive units that formed through similar processes and that may have formed in similar environments (Loughlin, 2002). Classification in this way is useful for the study of past glacial environments. However, the constituents of each subdivision are not strictly related in time and will represent a range of ages that are likely to overlap with other subdivisions of the same stratigraphic group (Figure 2). Distinct assemblages of related lithofacies are grouped into lithofacies associations (e.g. hyaloclastite-dominated units, which can also include pillow lavas and lobate or sheet-like intrusions). Note that the term hyaloclastite is used here to encompass fragmental rocks generated through both quench fragmentation (hyaloclastite; Rittman, 1958) and explosive phreatomagmatic fragmentation (hyalotuff; Honnorez & Kirst, 1975) of magma.

Vent locations relating to individual eruptive units were identified at numerous locations and are marked on the map. These vents are all extant scoria cones that are associated with the mafic to intermediate lavas and tuyas of Late Tindfjallajökull B. The vents of the older rocks of Early and Middle Tindfjallajökull have been removed by erosion and their locations could not be determined. Additional ornamentations on the map highlight tuya lava caps and areas of lava delta or highly jointed lava.

Where the position of a geological boundary has an uncertainty of more than ±50 m (due to the presence of overlying superficial deposits and/or soils), it is classed as an approximate geological boundary.

3. Geology and past environments of Tindfjallajökull volcano

In this section, the products of Tindfjallajökull volcanic system are described, from oldest stratigraphic group to youngest, with a focus on indicators of past environments. Mapped units that are associated with other volcanic systems are then described, followed by the sediments and superficial deposits. UTM grid references are abbreviated to four digits representing 1 × 1 km^2, e.g. Sindri: *71 76*.

3.1. Early Tindfjallajökull

3.1.1. Mafic undifferentiated (Emu)

Most of the volume of Tindfjallajökull consists of a succession of interbedded mafic hyaloclastite and lava

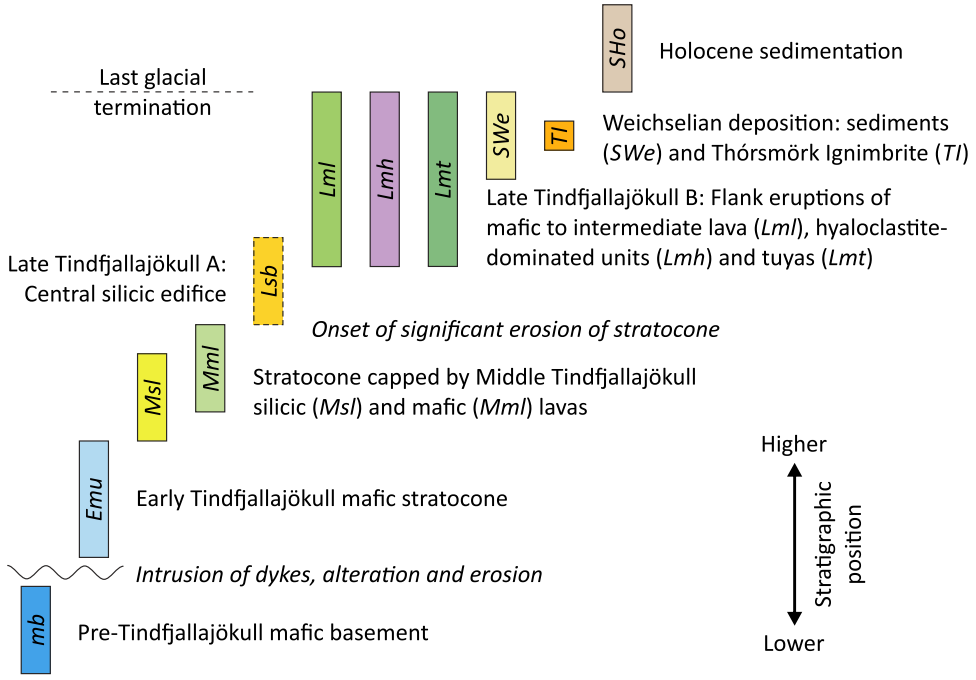

Figure 2. Stratigraphy of the mapped classes on Tindfjallajökull (not drawn to scale). It is not known if there is stratigraphic overlap between Late Tindfjallajökull A and Late Tindfjallajökull B. The eruptive products of Katla volcanic system and the fissure swarm NE of Tindfjallajökull are not included.

sheets, overlying the Pre-Tindfjallajökull basement. The basal contact has not been directly observed. Dykes and alteration in the basement have not been seen to pass into the overlying succession, suggesting that the contact is unconformable. In general, the Early Tindfjallajökull sheets dip gently outward from a central point roughly coincident with the present-day main ice cap. This parallel stratification is occasionally disrupted by minor palaeo-valleys and -gulleys. As a whole, the structure forms a dissected stratocone with an observed vertical extent of 1200 m (present-day maximum elevation: 1299 m above mean sea level, *69 76*).

3.2. Middle Tindfjallajökull

3.2.1. Silicic lava (Msl)

Three main areas of silicic lava are present on Tindfjallajökull, all of which immediately overlie the Early Tindfjallajökull stratocone. Erosion of the lavas has revealed lava lobe thicknesses of 20–60 m. Individual lava lobes have folded glassy margins with some areas of columnar jointing, and microcrystalline interiors which often develop platy structures. Ogives are preserved, or have been exhumed, on the surface of the upper lava lobe at Jökulskarð (~20 m wavelength; *73 76*). The vents of these lavas have not been preserved. A fragmental deposit (0–30 m thick) underlies the lava at Hestur (*72 68*) and is thought to have been emplaced during an initial phase of the same eruption.

These silicic lavas are not diagnostic of a particular eruptive environment, though the presence of ogives suggests that the upper lava lobe at Jökulskarð was emplaced in a subaerial setting.

3.2.2. Mafic lava (Mml)

Much of the west flank of Tindfjallajökull consists of a plateau surfaced with mafic lavas, capping the Early Tindfjallajökull stratocone. Isolated outcrops of capping lava are located on Vestriöxl (*75 75*) and on the NE side of Austurdalur (*66 77*). Individual lavas and vents are not distinct and have not been mapped in these areas. The unconfined nature of the lavas and the lack of evidence of enhanced cooling indicate that the eruptive environment was ice-free.

Since the formation of the Early Tindfjallajökull stratocone and the Middle Tindfjallajökull capping lavas, glacial erosion has cut the major valleys that emanate from the present-day ice cap.

3.3. Late Tindfjallajökull

3.3.1. A: Central silicic edifice

Silicic breccia with coherent lava lobes (Lsb). The summit of Tindfjallajökull (*70 74*) marks the top of a voluminous steep-sided pile of silicic breccia (Figure 3(a)), covering an area of perhaps 10 km^2 (when overlying volcanic rock and ice is removed). The breccia comprises poorly consolidated angular clasts 1–50 mm across. Coherent lobes of columnar-jointed silicic lava (~100 m wide) are present within the pile, and lava clasts are present within the surrounding breccia. The breccia has been subjected to pervasive hydrothermal alteration, and a hot spring in Hitagil (>60°C,

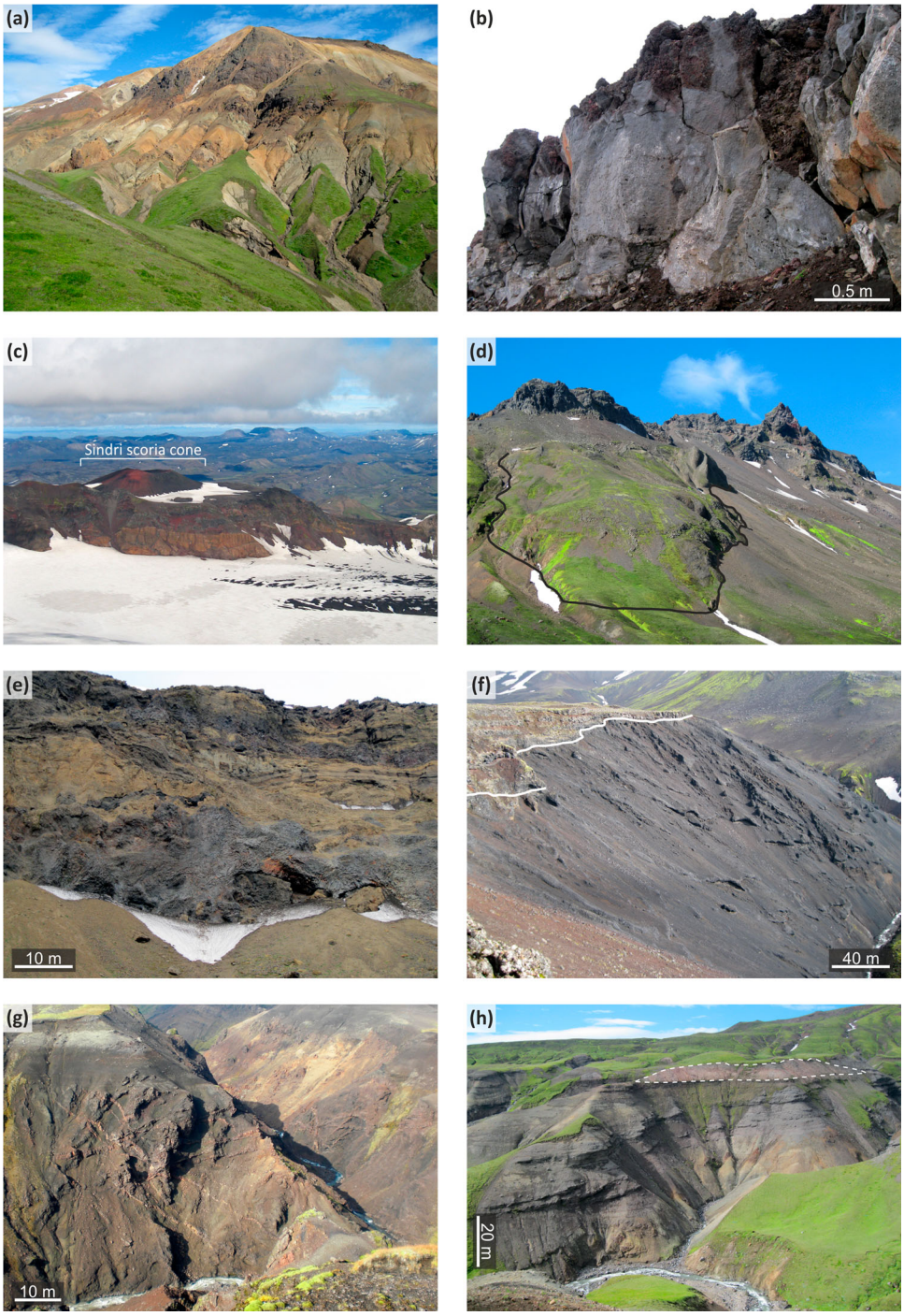

Figure 3. Photographs of selected geological features on Tindfjallajökull. (a) The view north from Botn of the pile of altered silicic breccia and lava lobes (dark) that make up the central silicic edifice of the volcano (Late Tindfjallajökull A). (b) An ~3 m thick mafic a'a lava in Tindfjallajökulsdalur (Late Tindfjallajökull B; *67 72*). This lava flowed into the valley from the Búri scoria cone. (c) Sindri scoria cone (*70 76*) viewed from Ýmir. The 500 m wide scoria cone sits on top of the Early Tindfjallajökull succession. (d) The east side of Tindur (*70 70*) viewed from Botn. A lava of Late Tindfjallajökull B age, outlined in black and ~250 m wide, becomes highly jointed where it has descended into the valley from a vent on the ridge. (e) The interior of a tuff cone has been exposed through mass-wasting at Hitagilsbrún (*72 71*). Mafic sills (grey) intrude bedded hyaloclastite (brown). (f) The lava cap (top left) and lava delta of Bláfell tuya (*66 71*). The white line indicates the passage zone between shallow-dipping a'a lavas and steeply dipping lava lobes and breccia. (g) Pre-Tindfjallajökull mafic basement exposed in a gorge (*73 70*). The lavas and hyaloclastites have been altered and intruded by numerous dykes. (h) The Weichselian depositional succession at Botn (*71 70*) composed of bedded diamictite and the Thórsmörk Ignimbrite (outlined with white dashes).

Ármannsson, 2016; *72 71*) indicates that hydrothermal circulation is still active.

The base of the central silicic edifice was not observed. The lowest outcrop is at ~600 m elevation, over 800 m beneath the highest outcrop. Significant erosion and/or down-faulting of Early and Middle Tindfjallajökull material, which forms ridges up to 1300 m altitude surrounding the central edifice, must have occurred before the breccias were emplaced. It is possible that a caldera formed at Tindfjallajökull

(as marked by Jóhannesson & Sæmundsson, 1989), but no direct evidence for subsidence (e.g. displacement on a fault) has been observed. Syn- or post-eruption subsidence into the top of a magma chamber is necessary for a volcanic structure to be termed a caldera, as defined by Cole, Milner, and Spinks (2005).

Extensive fragmentation of silicic lava and the confinement of a steep-sided pile of erupted material can indicate the presence of ice during an eruption (McGarvie, Stevenson, Burgess, Tuffen, & Tindle, 2007; Stevenson, Gilbert, McGarvie, & Smellie, 2011; Tuffen, Gilbert, & McGarvie, 2001). Angular clasts and jointed lava lobes at all levels of the central silicic edifice suggest that cooling may have been enhanced by a thick body of ice, though further work is needed to reduce ambiguity.

3.3.2. B: Flank volcanism

This category consists of a variety of well-preserved eruptive units that are sourced from dispersed vents and fissures on the flanks of Tindfjallajökull. The preservation of features such as scoria cones and the stratigraphic association of some of the units with the Thórsmörk Ignimbrite suggests that the majority of the units were emplaced during the Weichselian glacial period. There is likely to be chronological overlap between the members of this category (Figure 2), as they are subdivided by lithofacies rather than stratigraphic position.

Mafic to intermediate lava (Lml). Twelve mafic to intermediate lavas that have experienced little erosion have been mapped on Tindfjallajökull's upper flanks. The lavas are typically a'a with autobrecciated bases and tops (where preserved; Figure 3(b)). The remnants of scoria cones are present at the vent of each lava, where not obscured by younger lava or ice. The scoria cone at Sindri (Figure 3(c); *70 76*) is particularly well preserved, suggesting that it has not been subjected to glaciation and probably post-dates the last glacial maximum. Unconfined lavas with no evidence of enhanced cooling are indicative of an ice-free eruptive environment.

Highly jointed lava: In some instances, lavas that have flowed down steep slopes transition from a normal widely spaced jointing pattern to closely spaced pseudopillow fractures and cube-jointing. This occurs on the south side of Sindri (*71 76*), on the southern rim of Austurdalur (*65 74*) and on the east side of Tindur (Figure 3(d); *70 70*). The closely spaced jointing patterns indicate that the lavas were cooled rapidly due to the presence of water (Forbes, Blake, McGarvie, & Tuffen, 2012). Topographic depressions suitable for the ponding of water are not present in these localities, so it is likely that water was instead derived through the melting of ice or snow. The elevation of the transition from subaerial lava to highly jointed lava (marked with white lines on the map) provides constraints on the upper limits of ice or snow within glaciated valleys at the time of each eruption.

Mafic hyaloclastite-dominated units (Lmh). Hyaloclastite-dominated units on Tindfjallajökull exist as hyaloclastite ridges, tuff cones, breccia mounds and hyaloclastite sheets. Each type can include a variable proportion of pillow lava and/or intrusive dykes, sills or lobes (Figure 3(e)), but capping lavas are not present.

Hyaloclastite ridges on Tindfjallajökull have a range of fissure orientations, with approximate groupings at 040–067° (perpendicular to the regional spreading direction), 104–111° and ~155°. Tuff cones and breccia mounds are sourced from point vents with no linear orientation. Hyaloclastite sheets (2–10 m thick) typically constitute the more distal deposits of tuff cones and are common within a succession of Weichselian sediments on the SE side of Tindfjallajökull (around *73 70*).

Both hyaloclastite and pillow lava lithofacies indicate the presence of water during an eruption. This is commonly an indicator for the presence of ice in this topographical setting (Jones, 1969; Mathews, 1947). The prevalence of water interaction throughout all lithofacies in these units suggests that water or ice was present at the vent for the duration of each eruption.

Mafic tuyas (Lmt). Tuyas are defined here as hyaloclastite-dominated units that are capped with shallow-dipping lavas. Eight tuyas have been mapped on Tindfjallajökull, predominantly on the western upper flank. The footprint area of the tuyas ranges from 0.1 km^2 to the 8 km^2 Þórólfsfell tuya (*66 66*). Scoria cones are preserved at the vents of some of the tuyas, and there are subsidence pits on the a'a lava cap of Bláfell tuya (*66 71*). The five largest tuyas have extensive lava deltas preserved on their flanks, composed of steeply dipping highly jointed lava lobes and lava breccia (Figure 3(f)).

Tuyas are common in Iceland and are interpreted to form when subglacial eruptions breach the upper ice surface (Jones, 1966; Mathews, 1947). When this occurs, the eruption transitions from phreatomagmatic conditions, producing pillow lavas and hyaloclastites, to 'dry' conditions during which a lava cap is emplaced. Meltwater is typically ponded around the growing tuya during the eruption. Where lava flows from the shallow-dipping top into the ice-dammed lake, a lava delta is formed, and the change in lithofacies at this water level is called a passage zone. The level of the passage zone from subaerial to subaqueous lava emplacement can be used to estimate the thickness of the surrounding ice body (Russell, Edwards, Porritt, & Ryane, 2014; Skilling, 2009). The subsidence pits on

Bláfell tuya may have been formed through the draining of subsurface magma or meltwater.

3.4. Other volcanic systems

3.4.1. Pre-Tindfjallajökull (volcanic system unknown)

Mafic basement (mb). The oldest rocks on the map are found on the SE side of Tindfjallajökull (Figure 3(g); *73 70*). These mafic hyaloclastites and lavas have been extensively altered, intruded by dykes, and their pore spaces have been infilled through secondary mineralisation. The extent of alteration and intrusion suggests that these rocks pre-date the unaltered rocks of Tindfjallajökull and most likely constitute part of an older volcanic system that has been largely buried by recent volcanic activity.

3.4.2. Torfajökull volcanic system (speculative)

Mafic hyaloclastite-dominated units in fissure swarm between Tindfjallajökull and Torfajökull (mh). The fissure swarm stretching NE from Tindfjallajökull has been the subject of little study, but is tentatively considered to be part of the Torfajökull volcanic system (Sæmundsson & Larsen, 2016). Mafic eruptions in this area have produced SW-NE oriented parallel hyaloclastite ridges. Pillow lavas are found in the cores of the ridges, where exposed through fluvial erosion. The confinement of material along eruptive fissures and the prevalence of magma-water interaction indicate that these ridges were emplaced subglacially. The ridges show relatively little sign of glacial erosion, suggesting that they were emplaced during the Weichselian glaciation.

Silicic breccia with coherent lava lobes in fissure swarm (sb). Sultarfell is a pale-coloured steep-sided hill (~0.03 km^3; *74 79*) situated in the fissure swarm NE of Tindfjallajökull. It is composed of jointed rhyolitic lava lobes (a few metres across) bounded by unconsolidated breccia of cogenetic fragmented rhyolite. Lobes of fractured lava can be seen in close association with lava fragments that have spalled off the lobes during cooling, which may have been enhanced by the presence of water and/or ice. Like the neighbouring mafic hyaloclastite ridges, the level of preservation of Sultarfell suggests it was emplaced during the Weichselian glaciation.

Thórsmörk Ignimbrite (TI). Most of the preserved volume of the Thórsmörk Ignimbrite outcrops to the south of the Markarfljót, beyond the scope of this map (Jørgensen, 1980). The internal structure of the ignimbrite is complex and both welded and unwelded domains are present. Within the area of the map, the ignimbrite is intercalated within a succession of diamictite (Figures 3(h) and 5) and typically forms a layer up to 10 m thick, though it is sometimes entirely absent from the stratigraphy. Within 5 km of Tindfjallajökull's summit, lithic clasts make up <5% of the ignimbrite and are <3 mm in diameter. In comparison, exposures south of the Markarfljót have a thickness of ~30 m with ~10% lithic clasts, which are up to 20 cm in diameter (Jørgensen, 1980).

Jørgensen (1980) proposed that Tindfjallajökull is the source of the Thórsmörk Ignimbrite, based on the broad patterns of welding, crystallisation, and outcrop distribution of the deposit. However, geological mapping on Tindfjallajökull has not found evidence to support this. In particular, the relatively low abundance and small size of lithic clasts entrained within the ignimbrite close to Tindfjallajökull and the continuity of diamictite deposition before and after ignimbrite emplacement suggests that Tindfjallajökull is not the source of this major eruption. Further work is being undertaken to trace the source of the ignimbrite. Torfajökull volcano is a possible alternative source, as Grönvold et al. (1995) noted a geochemical similarity between rhyolites at Torfajökull and North Atlantic Ash Zone II (the distal correlative of the Thórsmörk Ignimbrite).

3.4.3. Katla volcanic system

Mafic lava (Kml). A series of Holocene pahoehoe lavas have infilled the Markarfljót valley SE of Tindfjallajökull (*74 66*, SE extremity of map). The source of the lavas is located to the east of the map margin in the Katla volcanic system (Larsen, 2000). The interiors of the lavas have developed an entablature jointing pattern during cooling, and the lavas have subsequently been scoured by jökulhlaups (Smith & Dugmore, 2006). The unconfined nature of the lavas indicates a subaerial eruptive environment, with the entablature interiors indicating enhanced cooling of the lava following the introduction of river water (Lyle, 2000). This indicates that the valley was occupied by an active river at the time of lava emplacement.

3.5. Sediments

3.5.1. Last glacial period (Weichselian; SWe)

A depositional succession (maximum observed thickness of 160 m) extends from the Vestri-Botná valley (*71 71*) to the low-lying Fauskheiði ridge (*71 65*). The dominant lithofacies is diamictite (Figure 4(a)), with occasional water-lain gravels. Clast sizes in the diamictite range from silt to boulders 60 cm across. The clasts are typically faceted and striated, indicating a glacial influence in their transport. Crucially, the 54.5 ± 2 ka Thórsmörk Ignimbrite is present within the succession, dating it to the last glacial period (Sigurdsson et al., 1998). Other pre-Holocene outcrops of glacially worked material are found on the southern flank of Tindfjallajökull (*68 68*) and in the Eystri-Botná valley (*74 73*).

Figure 4. Photographs of sediments deposited (a) during and (b) after the last glacial period. (a) Diamictite exposed in Hitagil (*73 71*). Inset: striated cobble within the diamictite and (b) Rhythmite with alternating laminae of fine sand and silt (*76 74*).

3.5.2. Holocene and last glacial termination (SHo)

Sediments deposited during and after the retreat of the Weichselian Icelandic Ice Sheet infill valleys to the NE and S of Tindfjallajökull. The youngest sediments are conglomerates that are associated with the presently active fluvial systems, such as the braided river plain of the Markarfljót (in the extreme south of the map). Between the hyaloclastite ridges to the NE of Tindfjallajökull, rhythmites are common (Figure 4(b)). These deposits have 3–10 mm thick laminae of alternating fine sands and silts which are characteristic of lacustrine depositional environments, and suggest that lakes (now drained) once occupied the valleys between the parallel ridges.

3.6. Superficial deposits

With the exception of tephra, the present-day ice cap entrains only a small volume of rock debris. This is reflected in the lack of significant deposits of moraine around the margins of the ice. Only one area of hummocky moraine has been mapped, near to the eastern and lowest altitude termination of the present ice cap (*73 74*).

Features produced through the collapse of ice-eroded and ice-confined eruptive units are present on Tindfjallajökull. Mass-wasting has taken place as coherent slumps (e.g. at Bláfell tuya *65 71*) or more chaotic rockslides and falls (e.g. at Hitagilsbrún *73 72*).

4. Geological development of Tindfjallajökull volcano

4.1. Evolution of Tindfjallajökull

Geological mapping of Tindfjallajökull has given insight into the evolution of the volcano over time. Mafic basement rocks were emplaced during a volcanic episode prior to the construction of Tindfjallajökull. Volcanism in this area has been ongoing for perhaps 1–2 million years, building on top of the crust that formed several million years ago (Óskarsson, Steinthórsson, & Sigvaldason, 1985; Sæmundsson, 1974).

The construction of the Early Tindfjallajökull stratocone, a thick succession with consistent radial dip, was a highly productive phase of Tindfjallajökull's initial development. It is likely that the volcano was glaciated during much of this stage and that some erosion took place, but glacial erosion was surpassed by volcanism as the main driver of landscape evolution. Following the construction of the stratocone, all or most of its surface was capped by the subaerially emplaced Middle Tindfjallajökull lavas of mafic and silicic compositions (Figure 5). Glacial erosion has subsequently resulted in extensive modification of the Early-Middle Tindfjallajökull edifice, particularly through the deepening of the valleys that radiate from the centre of the volcano.

At the onset of the Late Tindfjallajökull stage, the eruption of silicic breccia with coherent lava lobes formed the central silicic edifice. It is unclear if the eruption of this material was accompanied by caldera subsidence. Mafic to intermediate flank volcanism has continued through to the end of the last glacial period during various ice-thickness conditions. These eruptions, on the upper west flank in particular, produced a variety of landforms including hyaloclastite ridges, tuyas and lavas.

On the SE side of Tindfjallajökull, a depositional succession records a detailed history of glacially influenced sedimentation and local mafic volcanism during the last glacial period. The Thórsmörk Ignimbrite provides a valuable chronostratigraphic marker within this succession (Figure 5). During and after the retreat of

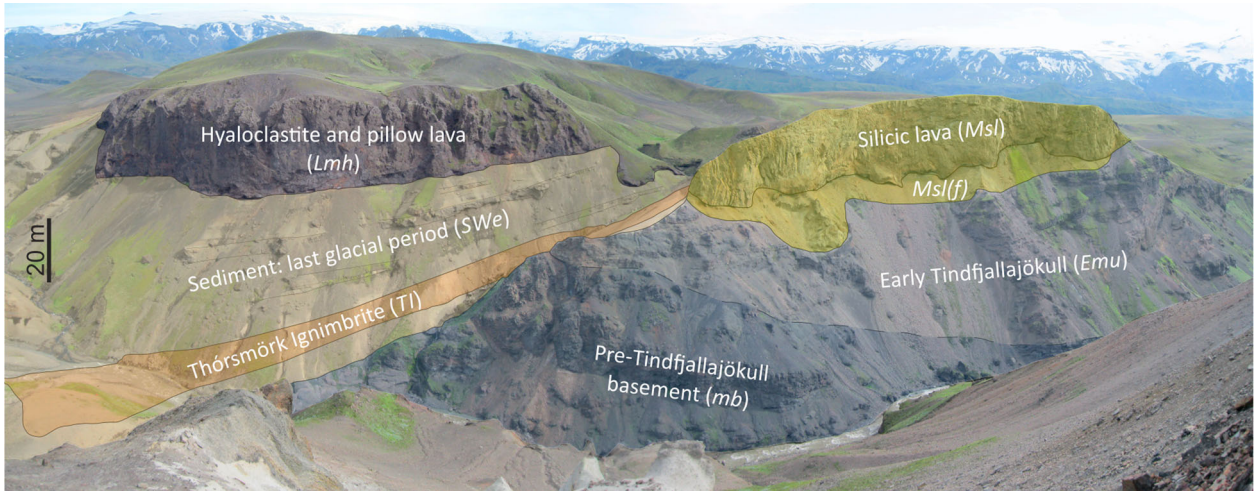

Figure 5. Annotated panorama of the SE side of the Gilsá gorge (*73 68*) viewed from Hestur. Sedimentary and volcanic deposits dating to the last glacial period (left) onlap onto an older succession of volcanic rocks (right).

the Weichselian glaciation, sedimentation has occurred in lacustrine and fluvial settings around the foot of Tindfjallajökull.

4.2. Comparison to neighbouring volcanoes

Several broad characteristics of Tindfjallajökull volcano are comparable to Eyjafjallajökull volcano. The summit of Eyjafjallajökull is only 18 km south of the summit of Tindfjallajökull, and the two volcanoes are of similar size.

The oldest mapped rocks on Eyjafjallajökull are the Laugará Group, exposed on the southern flank of the volcano (Jónsson, 1988). Like the Pre-Tindfjallajökull basement, the Laugará Group is composed of altered basaltic hyaloclastite, pillow breccia and fragmented lava, with numerous intrusive sheets (Loughlin, 1995). The oldest rocks at Eyjafjallajökull were emplaced prior to the Brunhes-Matuyama geomagnetic reversal (~780 ka), and a K/Ar date of 780 ± 30 ka has been obtained from a lava with reversed polarity (Kristjansson, Johannesson, Eiriksson, & Gudmundsson, 1988).

Like Tindfjallajökull, much of Eyjafjallajökull consists of a thick succession of mafic to intermediate hyaloclastites and lavas (Loughlin, 2002). Furthermore, this succession is capped by lavas that surface much of the upper flanks of both volcanoes (Jónsson, 1988; Loughlin, 1995).

Glacial valleys are thought to have formed in the mid-late period of Eyjafjallajökull's development (Loughlin, 1995). Dissection of Tindfjallajökull's edifice is more advanced than at Eyjafjallajökull. The existence of accommodation space for sedimentary successions within a few kilometres of Tindfjallajökull's summit attests to the greater degree of focussed dissection that has occurred. It is not clear if caldera subsidence is an additional factor that may have contributed to the accommodation of sediment at Tindfjallajökull.

Finally, the mapping of Tindfjallajökull has indicated that it has more extensive deposits of silicic rock in comparison to Eyjafjallajökull (Loughlin, 1995). The presence of a suspected caldera and a high ratio of evolved rock to basalt led Jakobsson (1979) to speculate that Tindfjallajökull is the most mature active volcano in the Eastern Volcanic Zone. However, possible caldera structures and significant volumes of silicic material are also features of the larger nearby volcanoes of Katla and Torfajökull (Jóhannesson & Sæmundsson, 1989).

5. Conclusions

A 1:50,000 scale geological map of Tindfjallajökull provides the first comprehensive survey of this ice-capped stratovolcano. The map enables a reconstruction of the evolution of Tindfjallajökull through time and a comparison to other nearby volcanoes. Much of the volcano is similar to neighbouring Eyjafjallajökull, though Tindfjallajökull has a higher proportion of silicic volcanic rocks and a higher degree of erosion.

Field mapping of volcanic lithofacies and lithofacies associations allows the mapped classes to broadly reflect the environment at the time of each eruption. As is typical in Iceland, ice has had a significant influence on the development of Tindfjallajökull, though the extent of ice has varied widely through time. Lavas, tuyas and hyaloclastite-dominated units have interacted with ice of variable thicknesses. A depositional succession on the SE side of Tindfjallajökull records glacially influenced sedimentation and eruptions dating to the last glacial period. Information on past glacial environments on Tindfjallajökull, if combined with chronological data, could fit into larger scale models of late Pleistocene to Holocene palaeoenvironments in Iceland.

Software

Geological boundaries were digitised using Google Earth Pro and the maps and cross-sections were

produced using ESRI ArcGIS. The map page was constructed and edited using CorelDRAW X6.

Acknowledgements

For assistance in the field, we gratefully acknowledge Mike Widdowson, Matthew Saker-Clark, Eleni Wood, Jack McGarvie, Björn Oddsson and Paul & Judi Stevens. We thank the reviewers Juliane Cron, Marco Neri and Alison H. Graettinger for their valuable comments, which helped to improve the map and manuscript.

Disclosure statement

No potential conflict of interest was reported by the authors.

Funding

This work was supported by the Natural Environment Research Council [grant number NE/L002493/1]. JAS was funded by a Royal Society of Edinburgh Personal Research Fellowship held at the University of Edinburgh.

References

Ármannsson, H. (2016). The fluid geochemistry of Icelandic high temperature geothermal areas. *Applied Geochemistry*, *66*, 14–64. doi:10.1016/j.apgeochem.2015.10.008

Cole, J. W., Milner, D. M., & Spinks, K. D. (2005). Calderas and caldera structures: A review. *Earth-Science Reviews*, *69*, 1–26. doi:10.1016/j.earscirev.2004.06.004

Forbes, A. E. S., Blake, S., McGarvie, D. W., & Tuffen, H. (2012). Pseudopillow fracture systems in lavas: Insights into cooling mechanisms and environments from lava flow fractures. *Journal of Volcanology and Geothermal Research*, *245–246*, 68–80. doi:10.1016/j.jvolgeores.2012.07.007

Google Earth Pro. (2010). *Tindfjallajökull 63°47′N 19°35′W*. DigitalGlobe 2012.

Grönvold, K., Óskarsson, N., Johnsen, S. J., Clausen, H. B., Hammer, C. U., Bond, G., & Bard, E. (1995). Ash layers from Iceland in the Greenland GRIP ice core correlated with oceanic and land sediments. *Earth and Planetary Science Letters*, *135*(1–4), 149–155. doi:10.1016/0012-821X(95)00145-3

Honnorez, J., & Kirst, P. (1975). Submarine basaltic volcanism: Morphometric parameters for discriminating hyaloclastites from hyalotuffs. *Bulletin Volcanologique*, *39*, 441–465. doi:10.1007/BF02597266

Jakobsson, S. V. (1979). Petrology of recent basalts of the Eastern Volcanic Zone, Iceland. *Acta Naturalia Islandica*, *26*. doi:10.1016/0198-0254(81)91274-7

Jóhannesson, H., & Sæmundsson, K. (1989). *Geological map of Iceland, 1:500,000, bedrock geology*. Reykjavik: Icelandic Institute of Natural History.

Jones, J. G. (1966). Intraglacial volcanoes of South-west Iceland and their significance in the interpretation of the form of the marine basaltic volcanoes. *Nature*, *212*, 586–588. doi:10.1038/212586a0

Jones, J. G. (1969). Intraglacial volcanoes of the Laugarvatn region, south-west Iceland. *Quarterly Journal of the Geological Society of London*, *124*, 197–211. doi:10.1144/gsjgs.124.1.0197

Jónsson, J. (1988). *Geological Map Eyjafjöll, 1:50,000*. Research Institute Neðri Ás Hveragerði.

Jørgensen, K. A. (1980). The Thorsmörk ignimbrite: An unusual comenditic pyroclastic flow in Southern Iceland. *Journal of Volcanology and Geothermal Research*, *8*, 7–22. doi:10.1016/0377-0273(80)90004-9

Kristjansson, L., Johannesson, H., Eiriksson, J., & Gudmundsson, A. I. (1988). Brunhes- Matuyama paleomagnetism in three lava sections in Iceland. *Canadian Journal of Earth Sciences*, *25*(2), 215–225. doi:10.1139/e88-024

Lacasse, C., Sigurdsson, H., Carey, S., Paterne, M., & Guichard, F. (1996). North Atlantic deep-sea sedimentation of Late Quaternary tephra from the Iceland hotspot. *Marine Geology*, *129*(3–4), 207–235. doi:10.1016/0025-3227(96)83346-9

Landmælingar Íslands. (2016). *IS 50V digital map database*. Retrieved from http://www.lmi.is/en/stafraen-gogn/is-50v-nytt/; Licence: http://www.lmi.is/wp-content/uploads/2013/10/licenceNLSI.pdf

Larsen, J. G. (1979). Glass-bearing gabbro inclusions in hyaloclastites from Tindfjallajökull, Iceland. *Lithos*, *12*(4), 289–302. doi:10.1016/0024-4937(79)90021-5

Larsen, J. G. (2000). Holocene eruptions within the Katla volcanic system, south Iceland: Characteristics and environmental impact. *Jökull*, *49*, 1–28.

Loughlin, S. C. (1995). *The evolution of the Eyjafjöll volcanic system, southern Iceland* (PhD thesis). Durham University.

Loughlin, S. C. (2002). Facies analysis of proximal subglacial and proglacial volcaniclastic successions at the Eyjafjallajökull central volcano, southern Iceland. *Geological Society, London, Special Publications*, *202*, 149–178. doi:10.1144/GSL.SP.2002.202.01.08

Lyle, P. (2000). The eruption environment of multi-tiered columnar basalt lava flows. *Journal of the Geological Society*, *157*, 715–722. doi:10.1144/jgs.157.4.715

Mathews, W. H. (1947). "Tuyas," flat-topped volcanoes in northern British Columbia. *American Journal of Science*. doi:10.2475/ajs.245.9.560

McGarvie, D. W., Stevenson, J. A., Burgess, R., Tuffen, H., & Tindle, A. G. (2007). Volcano – ice interactions at Prestahnukur, Iceland: rhyolite eruption during the last interglacial – glacial transition. *Annals of Glaciology*, *45*, 38–47. doi:10.3189/172756407782282453

Óskarsson, N., Steinthórsson, S., & Sigvaldason, G. E. (1985). Iceland geochemical anomaly: Origin, volcanotectonics, chemical fractionation and isotope evolution of the crust. *Journal of Geophysical Research*, *90*(B12), 10011. doi:10.1029/JB090iB12p10011

Rittman, A. (1958). Il meccanismo di formazione delle lave a pillows e dei cosidelti tufi palagonitici. *Atti Acc. Gioenia*, *4*, 310–317.

Russell, J. K., Edwards, B. R., Porritt, L., & Ryane, C. (2014). Tuyas: A descriptive genetic classification. *Quaternary Science Reviews*, *87*, 70–81. doi:10.1016/j.quascirev.2014.01.001

Sæmundsson, K. (1974). Evolution of the axial rifting zone in Northern Iceland and the Tjörnes fracture. *Geological Society of America Bulletin*, *85*, 495–504. doi:10.1130/0016-7606(1974)85<495

Sæmundsson, K., & Larsen, G. (2016). Torfajökull. In E. Ilyinskaya, G. Larsen, & M. T. Gudmundsson (Eds.), *Catalogue of Icelandic volcanoes*. IMO, UI, CPD-NCIP. Retrieved from http://icelandicvolcanoes.is/

Sigurdsson, H. (1982). Útbreidsla íslenskra gjóskulaga á botni Atlantshafs. In H. Thorarinsdóttir, O. H.

Oskarsson, S. Steinthorsson, & T. Einersson (Eds.), *Eldur er í nordri* (pp. 119–127). Reykjavik: Sögufélag.

Sigurdsson, H., McIntosh, W. C., Dunbar, N., Lacasse, C., & Carey, S. N. (1998). Thorsmork Ignimbrite in Iceland; possible source of North Atlantic ash zone 2? In *AGU 1998 Spring Meeting. Eos (Transactions, American Geophysical Union) 79* (p. 377).

Skilling, I. P. (2009). Subglacial to emergent basaltic volcanism at Hlöðufell, south-west Iceland: A history of ice-confinement. *Journal of Volcanology and Geothermal Research*, *185*(4), 276–289. doi:10.1016/j.jvolgeores.2009.05.023

Smith, K. T., & Dugmore, A. J. (2006). Jökulhlaups circa Landnám: Mid- to late first millennium AD floods in South Iceland and their implications for landscapes of settlement. *Geografiska Annaler*, *88 A*(2), 165–176. doi:10.1111/j.0435-3676.2006.00292.x

Stevenson, J. A., Gilbert, J. S., McGarvie, D. W., & Smellie, J. L. (2011). Explosive rhyolite tuya formation: Classic examples from Kerlingarfjöll, Iceland. *Quaternary Science Reviews*, *30*(1–2), 192–209. doi:10.1016/j.quascirev.2010.10.011

Thórarinsson, S. (1969). Ignimbrít í Þörsmórk. *Náttúrufræðingurinn*, *39*, 139–155.

Tomlinson, E. L., Thordarson, T., Müller, W., Thirlwall, M., & Menzies, M. A. (2010). Microanalysis of tephra by LA-ICP-MS — Strategies, advantages and limitations assessed using the Thorsmörk ignimbrite (Southern Iceland). *Chemical Geology*, *279*(3–4), 73–89. doi:10.1016/j.chemgeo.2010.09.013

Tuffen, H., Gilbert, J., & McGarvie, D. (2001). Products of an effusive subglacial rhyolite eruption: Bláhnúkur, Torfajökull, Iceland. *Bulletin of Volcanology*, *63*(2–3), 179–190. doi:10.1007/s004450100134

USA Defence Mapping Agency. (1989). *Iceland DMA-C761 topographic maps, 1:50,000*. Washington, DC: Defence Mapping Agency. Retrieved from http://www.lmi.is/landupplysingar/kortasafn/

Appendix 8:
Geological map of Tindfjallajökull volcano, Iceland

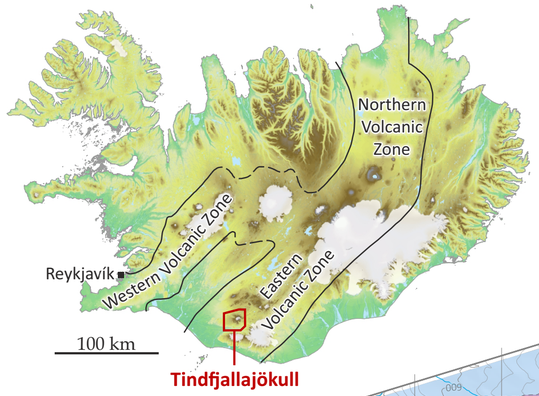

mh and *SHo* dominate for a further 8.5 km NE to Torfajökull volcano

TINDFJALLAJÖKULL

Sediments

- *SHo* — Holocene and last glacial termination. Includes rhythmites and conglomerates
- *SWe* — Last glacial period (Weichselian). Dominant lithofacies: diamict

Late Tindfjallajökull

B: Flank volcanism (≈Weichselian)

- *Lml* — Mafic to intermediate lava (individual lavas mapped)
- Scoria cone
- Highly jointed lava (white line indicates passage zone)
- *Lmh* — Mafic hyaloclastite-dominated units (can also include pillow lava and/or intrusions)
- *Lmt* — Mafic to intermediate tuyas: hyaloclastite-dominated units capped with lava
- Lava cap; with scoria cone
- Lava delta (white line indicates passage zone, dashed if approximate)

A: Central silicic edifice

- *Lsb* — Silicic breccia with coherent lava lobes

Middle Tindfjallajökull

Lavas capping Early stratocone

- *Mml* — Mafic lava (undifferentiated lava plateau)
- *Msl* — Silicic lava. *(f)* = underlying fragmental lithofacies

Early Tindfjallajökull

Shallow-dipping stratocone constructed of hyaloclastite and lava sheets

- *Emu* — Mafic to intermediate, undifferentiated

Other volcanic systems

Katla volcanic system

- *Kml* — Mafic lava (Holocene)

?Torfajökull volcanic system

- *Tl* — Thórsmörk Ignimbrite (Weichselian)
- *mh* — Mafic hyaloclastite-dominated units in fissure swarm between Tindfjallajökull and Torfajökull (?Weichselian)
- *sb* — Silicic breccia with coherent lava lobes in fissure swarm (?Weichselian)

Pre-Tindfjallajökull (volcanic system unknown)

- *mb* — Mafic basement: undifferentiated lavas and hyaloclastites, intruded by dykes and highly altered

Symbols

- Geological boundary
- Approximate geological boundary
- Superficial deposit boundary
- Fissure orientation
- Hot spring
- Mass-wasting scarp
- Subsidence pit
- Track; 20 m contours
- Glacier; rivers
- Superficial: mass-wasting deposit
- Superficial: moraine

Cross section of upper Tindfjallajökull
2× vertical exaggeration

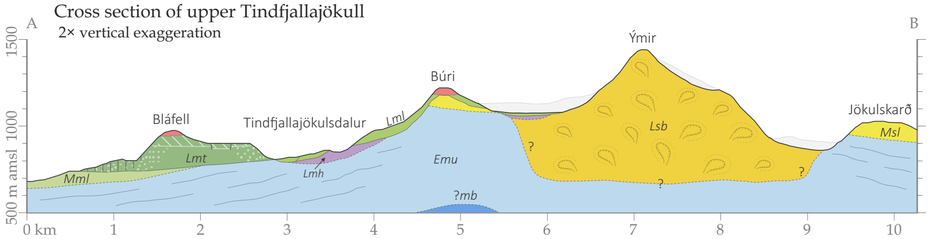

Cross section of SSE Tindfjallajökull
2× vertical exaggeration

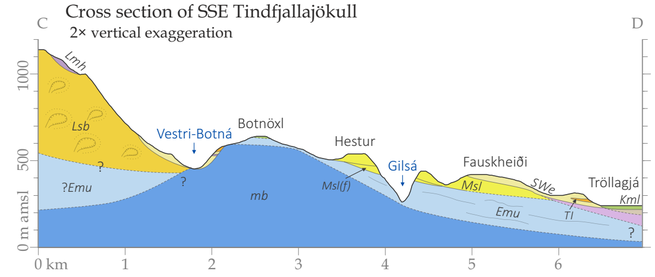

1:50,000

0 kilometres 2

N

UTM Projection, Zone 27N
Hjörsey 1955 Datum

Hydrology, buildings, tracks, place names and topography data sourced from Landmælingar Íslands